



11-05  
30-3  
NASA Contractor Report 4665

P. 433

# Aeroelasticity and Structural Optimization of Composite Helicopter Rotor Blades With Swept Tips

K. A. Yuan and P. P. Friedmann

(NASA-CR-4665) AEROELASTICITY AND  
STRUCTURAL OPTIMIZATION OF  
COMPOSITE HELICOPTER ROTOR BLADES  
WITH SWEPT TIPS (California Univ.)  
433 p

N95-28262

Unclass

H1/05 0050098

Grant NAG1-833  
Prepared for Langley Research Center

May 1995





NASA Contractor Report 4665

# Aeroelasticity and Structural Optimization of Composite Helicopter Rotor Blades With Swept Tips

---

*K. A. Yuan and P. P. Friedmann  
University of California • Los Angeles, California*

National Aeronautics and Space Administration  
Langley Research Center • Hampton, Virginia 23681-0001

Prepared for Langley Research Center  
under Grant NAG1-833

May 1995

Printed copies available from the following:

NASA Center for AeroSpace Information  
800 Elkridge Landing Road  
Linthicum Heights, MD 21090-2934  
(301) 621-0390

National Technical Information Service (NTIS)  
5285 Port Royal Road  
Springfield, VA 22161-2171  
(703) 487-4650

## PREFACE

This report describes in detail innovative analytical research aimed at demonstrating the remarkable potential for structural optimization and aeroelastic tailoring present in swept tip composite helicopter rotor blades. It is shown that by a judicious combination of composite ply orientation in the primary blade structure and the swept tip; remarkable reductions in the vibration levels in forward flight, at the blade hub, can be achieved.

The research described in this report was carried out in the Mechanical, Aerospace and Nuclear Engineering Department at UCLA, and it was funded by NASA Grant NAG 1-833 with Dr. H. Adelman, from NASA Langley, as the grant monitor. The authors hereby express their appreciation to the grant monitor for his useful comments and suggestions.

The principal investigator for this sponsored research activity was Professor Peretz P. Friedmann. This constitutes essentially the first author's Ph.D. dissertation; however, certain changes were made to the dissertation, so as to improve it, before turning it into this report.

Finally, the authors gratefully acknowledge the help and advice received during this research from Professor L.A. Schmit, Jr. and Dr. C. Venkatesan.



## CONTENTS

List of Figures .....	ix
List of Tables .....	xvii
Nomenclature .....	xviii
SUMMARY .....	xxx

<u>Chapter</u>	<u>page</u>
I. Introduction and Literature Review .....	1
Introduction .....	1
Literature Review .....	3
Structural Modeling of Isotropic Rotor Blades .....	3
Structural Modeling of Composite Rotor Blades .....	6
Structural Modeling of Swept-tip Blades .....	13
Structural Optimization for Vibration Reduction .....	16
Objectives of the Research .....	19
II. Model Description and Coordinate Systems .....	21
Basic Assumptions .....	21
Ordering Scheme .....	24
Coordinate Systems .....	25
Nonrotating, Hub-fixed Coordinate System .....	26
Rotating, Hub-fixed Coordinate System .....	26
Preconed, Pitched, Blade-fixed Coordinate System .....	26
Undeformed Element Coordinate System .....	27
Undeformed Curvilinear Coordinate System .....	27
Deformed Curvilinear Coordinate System .....	28
Preconed, Blade-fixed Coordinate System .....	28
Coordinate Transformations .....	29
Rotating to Nonrotating Transformation .....	29
Blade-fixed to Hub-fixed Transformation .....	30
Element to Blade Transformation .....	30
Undeformed Curvilinear to Undeformed Element Transformation .....	31
Deformed to Undeformed Curvilinear Transformation .....	32
Deformed Curvilinear to Undeformed Element Transformation .....	33

	Preconed, Blade-fixed to Preconed, Pitched, Blade-fixed Transformation . . . . .	33
III.	Structural Modeling of the Composite Rotor Blade . . . . .	34
	Kinematics of Deformation . . . . .	35
	Strain Components . . . . .	39
	Strain Components in Curvilinear Coordinates . . . . .	39
	Strain Components in Local Cartesian Coordinates . . . . .	40
	Explicit Strain-Displacement Relations . . . . .	45
	Constitutive Relations . . . . .	51
IV.	Formulation of the Finite Element Equations of Motion . . . . .	55
	Strain Energy Contributions . . . . .	56
	Kinetic Energy Contributions . . . . .	74
	External Work Contributions . . . . .	97
	Summary of the Partial Differential Equations of Motion . . . . .	101
	Finite Element Discretization of the Equations of Motion . . . . .	105
	Element Matrices Associated with the Strain Energy Variation . . . . .	109
	Element Matrices Associated with the Kinetic Energy Variation . . . . .	110
	Element Matrices Associated with the Virtual Work of External Loads . . . . .	110
	Summary of the Beam Finite Element Equations of Motion . . . . .	111
	Local-to-global Coordinate Transformation . . . . .	112
V.	Incorporation of Aerodynamics in the Equations of Motion . . . . .	118
	Aerodynamic Lift and Pitching Moment . . . . .	118
	Blade Velocity Relative to Air . . . . .	121
	Blade Pitch Angle with respect to Free Stream . . . . .	124
	Aerodynamic Forces and Moments in the Undeformed Element Coordinate System . . . . .	125
	Treatment of Reverse Flow . . . . .	126
VI.	Method of Solution . . . . .	128
	Treatment of the Axial Degree of Freedom . . . . .	128
	Free Vibration Analysis . . . . .	132
	Modal Coordinate Transformation and Assembly Procedure . . . . .	133
	Hover Analysis . . . . .	135
	Forward Flight Analysis . . . . .	139
	Trim Analysis . . . . .	140
	Distributed Loads on the blade . . . . .	145
	Inertial Loads . . . . .	145
	Aerodynamic Loads . . . . .	146
	Rotor Hub Loads . . . . .	147

	Coupled Trim and Aeroelastic Response Solution Using Harmonic Balance .....	153
	Vibratory Hub shears and Moments .....	156
	Stability in Forward Flight .....	158
VII.	Structural Optimization for Vibration Reduction .....	161
	Statement of the Optimization Problem .....	161
	Design Variables .....	162
	Constraints .....	163
	Objective Function .....	165
	Formulation of Approximate Problem .....	166
	Detailed Description of the Optimization Process .....	167
VIII.	Model Verification .....	170
	Validation for the Case of Hover .....	171
	Isotropic Blade .....	171
	Single-cell Composite Blade .....	174
	Validation for the Case of Forward Flight .....	177
	Trim Results .....	181
	Blade Response .....	182
	Blade Stability .....	183
	Vibratory Hub Loads .....	185
IX.	Free Vibration and Aeroelastic Behavior in Hover .....	187
	Free Vibration Analysis .....	187
	Influence of Ply Orientation .....	187
	Single-cell Composite Blade .....	188
	Two-cell Composite Blade. ....	189
	Effects of Tip Sweep and Anhedral .....	191
	Aeroelastic Stability in Hover .....	192
	Effects of Swept Tip .....	193
	Single-cell Composite Blade .....	196
	Two-cell Composite Blade .....	197
X.	Aeroelastic Behavior in Forward Flight .....	200
	Blade Response .....	203
	Trim Variables .....	205
	Vibratory Hub Loads .....	206
	Blade Stability .....	207
	Combined Effect of Sweep and Ply Orientation .....	210
XI.	Structural Optimization Results .....	212
XII.	Concluding Remarks .....	223
References	.....	228

Figures .....	238
---------------	-----

Appendix page

A.	Comparison of the Transformation Matrices Between Deformed and Undeformed Coordinate Systems .....	365
B.	Finite Element Matrices for the Composite Beam Model ...	370
	Finite Element Matrices Associated with the Strain Energy Variation .....	370
	Finite Element Matrices Associated with the Kinetic Energy Variation .....	381
	Finite Element Matrices Associated with the Virtual Work of the External Loads .....	394
C.	Local-To-Global Transformation Matrices .....	396
	Transformation for Rotational Degrees of Freedom ....	396
	Transformation for the Vector of Nodal Degrees of Freedom .....	398

## LIST OF FIGURES

<u>Figure</u>	<u>page</u>
1. 1 Rotor blade with tip sweep and anhedral .....	239
2. 1 Nonrotating, hub-fixed coordinate system and rotating, hub-fixed coordinate system .....	240
2. 2 Preconed, pitched, blade-fixed coordinate system .....	241
2. 3 Undeformed element coordinate system .....	242
2. 4 Undeformed curvilinear coordinate system .....	243
3. 1 Deformation sequence and Euler angles .....	244
4. 1 Motion of an element on the deformed elastic axis during the virtual displacement .....	245
4. 2 Finite element nodal degrees of freedom .....	246
5. 1 Components of blade velocity relative to the air .....	247
5. 2 Components of aerodynamic force acting on the blade .....	248
5. 3 Reverse flow region .....	249
6. 1 Schematic of a four-bladed helicopter .....	250
6. 2 Forces on the helicopter in steady, level flight .....	251
7. 1 Finite element model for two-cell composite cross section .....	252
7. 2 Organization of the optimization process .....	253
8. 1 Nonlinear equilibrium position of isotropic blade in hover, as a function of blade collective pitch. ....	254
8. 2 Imaginary part of hover eigenvalues of isotropic blade, as a function of blade collective pitch. ....	255

8. 3	Real part of hover eigenvalues of isotropic blade, as a function of blade collective pitch. . . . .	256
8. 4	Effect of axial mode on the nonlinear equilibrium position of isotropic blade in hover. Analysis with substitution. . . . .	257
8. 5	Effect of axial mode on the imaginary part of hover eigenvalues of isotropic blade. Analysis with substitution. . . . .	258
8. 6	Effect of axial mode on the real part of hover eigenvalues of isotropic blade. Analysis with substitution. . . . .	259
8. 7	Single-cell composite rectangular box beam . . . . .	260
8. 8	Real part of hover eigenvalues for single-cell composite blade as a function of (thrust coefficient/solidity). . . . .	261
8. 9	Trim variables for soft-in-plane isotropic blade in forward flight; pitch setting. . . . .	262
8.10	Trim variables for soft-in-plane isotropic blade in forward flight; inflow and rotor angle of attack. . . . .	263
8.11	Trim variables for stiff-in-plane isotropic blade in forward flight; pitch setting. . . . .	264
8.12	Trim variables for stiff-in-plane isotropic blade in forward flight; inflow and rotor angle of attack. . . . .	265
8.13	Blade tip response for soft-in-plane isotropic blade ( $\mu = 0.30$ ). . .	266
8.14	Blade tip response for stiff-in-plane isotropic blade ( $\mu = 0.30$ ). . .	267
8.15	Blade damping for soft-in-plane isotropic blade in forward flight; first and second lag modes. . . . .	268
8.16	Blade damping for soft-in-plane isotropic blade in forward flight; first flap and torsion modes. . . . .	269
8.17	Blade damping for soft-in-plane isotropic blade in forward flight; second and third flap modes. . . . .	270
8.18	Blade damping for stiff-in-plane isotropic blade in forward flight; first and second lag modes. . . . .	271
8.19	Blade damping for stiff-in-plane isotropic blade in forward flight; first flap mode. . . . .	272

8.20	Blade damping for stiff-in-plane isotropic blade in forward flight; first torsion, second and third flap modes. . . . .	273
8.21	The 4/rev hub loads for soft-in-plane isotropic blade in forward flight; logitudinal shear and rolling moment. . . . .	274
8.22	The 4/rev hub loads for soft-in-plane isotropic blade in forward flight; lateral shear and pitching moment. . . . .	275
8.23	The 4/rev hub loads for soft-in-plane isotropic blade in forward flight; vertical shear and yawing moment. . . . .	276
8.24	The 4/rev hub loads for stiff-in-plane isotropic blade in forward flight; logitudinal shear and rolling moment. . . . .	277
8.25	The 4/rev hub loads for stiff-in-plane isotropic blade in forward flight; lateral shear and pitching moment. . . . .	278
8.26	The 4/rev hub loads for stiff-in-plane isotropic blade in forward flight; vertical shear and yawing moment. . . . .	279
9. 1	Natural frequencies as a function of ply angle in vertical wall for single-cell composite blade. . . . .	280
9. 2	Natural frequencies as a function of ply angle in horizontal wall for single-cell composite blade. . . . .	281
9. 3	Natural frequencies as a function of ply angle in vertical wall for two-cell composite blade. . . . .	282
9. 4	Natural frequencies as a function of ply angle in horizontal wall for two-cell composite blade. . . . .	283
9. 5	Natural frequencies as a function of tip sweep angle for two-cell composite blade with zero ply angle. . . . .	284
9. 6	Natural frequencies as a function of tip anedral angle for two-cell composite blade with zero ply angle. . . . .	285
9. 7	Effect of tip sweep on the imaginary part of hover eigenvalues of isotropic blade, baseline configuration. . . . .	286
9. 8	Effect of tip sweep on the real part of hover eigenvalues of isotropic blade, baseline configuration. . . . .	287
9. 9	Effect of tip sweep on the imaginary part of hover eigenvalues of isotropic blade, modified torsional frequency. . . . .	288

9.10	Effect of tip sweep on the real part of hover eigenvalues of isotropic blade, modified torsional frequency. . . . .	289
9.11	Effect of tip anhedral on the imaginary part of hover eigenvalues of isotropic blade, baseline configuration. . . . .	290
9.12	Effect of tip anhedral on the real part of hover eigenvalues of isotropic blade, baseline configuration. . . . .	291
9.13	Effect of tip anhedral on the imaginary part of hover eigenvalues of isotropic blade, modified torsional frequency. . . . .	292
9.14	Effect of tip anhedral on the real part of hover eigenvalues of isotropic blade, modified torsional frequency. . . . .	293
9.15	Root locus of first lag mode eigenvalues as a function of ply angle in vertical wall for single-cell composite blade in hover. . . . .	294
9.16	Root locus of first flap mode eigenvalues as a function of ply angle in vertical wall for single-cell composite blade in hover. . . . .	295
9.17	Root locus of first torsion mode eigenvalues as a function of ply angle in vertical wall for single-cell composite blade in hover. . . . .	296
9.18	Root locus of first lag mode eigenvalues as a function of ply angle in horizontal wall for single-cell composite blade in hover. . . . .	297
9.19	Root locus of first flap mode eigenvalues as a function of ply angle in horizontal wall for single-cell composite blade in hover. . . . .	298
9.20	Root locus of first torsion mode eigenvalues as a function of ply angle in horizontal wall for single-cell composite blade in hover. . . . .	299
9.21	Effect of tip sweep on the imaginary part of hover eigenvalues of two-cell composite blade, baseline configuration. . . . .	300
9.22	Effect of tip sweep on the real part of hover eigenvalues of two-cell composite blade, baseline configuration. . . . .	301
9.23	Root locus of first lag mode eigenvalues as a function of ply angle in vertical wall for two-cell composite blade in hover. . . . .	302
9.24	Root locus of first flap mode eigenvalues as a function of ply angle in vertical wall for two-cell composite blade in hover. . . . .	303
9.25	Root locus of first torsion mode eigenvalues as a function of ply angle in vertical wall for two-cell composite blade in hover. . . . .	304

9.26	Root locus of first lag mode eigenvalues as a function of ply angle in horizontal wall for two-cell composite blade in hover. . . . .	305
9.27	Root locus of first flap mode eigenvalues as a function of ply angle in horizontal wall for two-cell composite blade in hover. . . . .	306
9.28	Root locus of first torsion mode eigenvalues as a function of ply angle in horizontal wall for two-cell composite blade in hover. . . . .	307
9.29	Root locus of second flap mode eigenvalues as a function of ply angle in horizontal wall for two-cell composite blade in hover. . . . .	308
10. 1	Effect of horizontal wall ply angle on blade tip response; lag mode ( $\mu = 0.30$ ). . . . .	309
10. 2	Effect of horizontal wall ply angle on blade tip response; flap mode ( $\mu = 0.30$ ). . . . .	310
10. 3	Effect of horizontal wall ply angle on blade tip response; torsion mode ( $\mu = 0.30$ ). . . . .	311
10. 4	Effect of vertical wall ply angle on blade tip response; lag mode ( $\mu = 0.30$ ). . . . .	312
10. 5	Effect of vertical wall ply angle on blade tip response; flap mode ( $\mu = 0.30$ ). . . . .	313
10. 6	Effect of vertical wall ply angle on blade tip response; torsion mode ( $\mu = 0.30$ ). . . . .	314
10. 7	Effect of tip sweep angle on blade tip response; lag mode ( $\mu = 0.30$ ). . . . .	315
10. 8	Effect of tip sweep angle on blade tip response; flap mode ( $\mu = 0.30$ ). . . . .	316
10. 9	Effect of tip sweep angle on blade tip response; torsion mode ( $\mu = 0.30$ ). . . . .	317
10.10	Effect of tip anhedral angle on blade tip response; lag mode ( $\mu = 0.30$ ). . . . .	318
10.11	Effect of tip anhedral angle on blade tip response; flap mode ( $\mu = 0.30$ ). . . . .	319
10.12	Effect of tip anhedral angle on blade tip response; torsion mode ( $\mu = 0.30$ ). . . . .	320

10.13	Effect of horizontal wall ply angle on trim variables; pitch setting ( $\mu = 0.30$ ). . . . .	321
10.14	Effect of horizontal wall ply angle on trim variables; inflow and rotor angle of attack ( $\mu = 0.30$ ). . . . .	322
10.15	Effect of vertical wall ply angle on trim variables; pitch setting ( $\mu = 0.30$ ). . . . .	323
10.16	Effect of vertical wall ply angle on trim variables; inflow and rotor angle of attack ( $\mu = 0.30$ ). . . . .	324
10.17	Effect of tip sweep angle on trim variables; pitch setting ( $\mu = 0.30$ ). . . . .	325
10.18	Effect of tip sweep angle on trim variables; inflow and rotor angle of attack ( $\mu = 0.30$ ). . . . .	326
10.19	Effect of tip anhedral angle on trim variables; pitch setting ( $\mu = 0.30$ ). . . . .	327
10.20	Effect of tip anhedral angle on trim variables; inflow and rotor angle of attack ( $\mu = 0.30$ ). . . . .	328
10.21	Effect of horizontal wall ply angle on 4/rev hub shears ( $\mu = 0.30$ ). . . . .	329
10.22	Effect of horizontal wall ply angle on 4/rev hub moments ( $\mu = 0.30$ ). . . . .	330
10.23	Effect of vertical wall ply angle on 4/rev hub shears ( $\mu = 0.30$ ). . . . .	331
10.24	Effect of vertical wall ply angle on 4/rev hub moments ( $\mu = 0.30$ ). . . . .	332
10.25	Effect of tip sweep angle on 4/rev hub shears ( $\mu = 0.30$ ). . . . .	333
10.26	Effect of tip sweep angle on 4/rev hub moments ( $\mu = 0.30$ ). . . . .	334
10.27	Effect of tip anhedral angle on 4/rev hub shears ( $\mu = 0.30$ ). . . . .	335
10.28	Effect of tip anhedral angle on 4/rev hub moments ( $\mu = 0.30$ ). . . . .	336
10.29	Effect of horizontal wall ply angle on blade stability; first lag mode ( $\mu = 0.30$ ). . . . .	337
10.30	Effect of horizontal wall ply angle on blade stability; first flap mode ( $\mu = 0.30$ ). . . . .	338

10.31	Effect of horizontal wall ply angle on blade stability; first torsion and second flap modes ( $\mu = 0.30$ ). . . . .	339
10.32	Effect of vertical wall ply angle on blade stability; first lag mode ( $\mu = 0.30$ ). . . . .	340
10.33	Effect of vertical wall ply angle on blade stability; first, second flap and first torsion modes ( $\mu = 0.30$ ). . . . .	341
10.34	Effect of tip sweep angle on blade stability for the first six modes ( $\mu = 0.30$ ). . . . .	342
10.35	Effect of tip anhedral angle on blade stability for the first six modes ( $\mu = 0.30$ ). . . . .	343
10.36	Effect of horizontal wall ply angle on stability of first torsion and second flap modes, modified torsional frequency ( $\mu = 0.30$ ). . . . .	344
10.37	Effect of tip sweep angle on blade stability for the first six modes, modified torsional frequency ( $\mu = 0.30$ ). . . . .	345
10.38	The 4/rev longitudinal hub shear as a function of tip sweep angle, combined effect with ply orientation ( $\mu = 0.30$ ). . . . .	346
10.39	The 4/rev lateral hub shear as a function of tip sweep angle, combined effect with ply orientation ( $\mu = 0.30$ ). . . . .	347
10.40	The 4/rev vertical hub shear as a function of tip sweep angle, combined effect with ply orientation ( $\mu = 0.30$ ). . . . .	348
10.41	The 4/rev hub rolling moment as a function of tip sweep angle, combined effect with ply orientation ( $\mu = 0.30$ ). . . . .	349
10.42	The 4/rev hub pitching moment as a function of tip sweep angle, combined effect with ply orientation ( $\mu = 0.30$ ). . . . .	350
10.43	The 4/rev hub yawing moment as a function of tip sweep angle, combined effect with ply orientation ( $\mu = 0.30$ ). . . . .	351
10.44	Real part of characteristic exponent of blade first lag mode as a function of tip sweep angle, combined effect with ply orientation ( $\mu = 0.30$ ). . . . .	352
11. 1	The 4/rev hub shears corresponding to first blade configuration (soft-in-plane) and first objective function ( $\mu = 0.30$ ). . . . .	353

11. 2	The 4/rev hub moments corresponding to first blade configuration (soft-in-plane) and first objective function ( $\mu = 0.30$ ). . . . .	354
11. 3	The 4/rev hub shears corresponding to first blade configuration (soft-in-plane) and second objective function ( $\mu = 0.30$ ). . . . .	355
11. 4	The 4/rev hub moments corresponding to first blade configuration (soft-in-plane) and second objective function ( $\mu = 0.30$ ). . . . .	356
11. 5	The 4/rev hub shears corresponding to second blade configuration (soft-in-plane) and first objective function ( $\mu = 0.30$ ). . . . .	357
11. 6	The 4/rev hub moments corresponding to second blade configuration (soft-in-plane) and first objective function ( $\mu = 0.30$ ). . . . .	358
11. 7	The 4/rev hub shears corresponding to second blade configuration (soft-in-plane) and second objective function ( $\mu = 0.30$ ). . . . .	359
11. 8	The 4/rev hub moments corresponding to second blade configuration (soft-in-plane) and second objective function ( $\mu = 0.30$ ). . . . .	360
11. 9	The 4/rev hub shears corresponding to third blade configuration (stiff-in-plane) and first objective function ( $\mu = 0.30$ ). . . . .	361
11.10	The 4/rev hub moments corresponding to third blade configuration (stiff-in-plane) and first objective function ( $\mu = 0.30$ ). . . . .	362
11.11	The 4/rev hub shears corresponding to third blade configuration (stiff-in-plane) and second objective function ( $\mu = 0.30$ ). . . . .	363
11.12	The 4/rev hub moments corresponding to third blade configuration (stiff-in-plane) and second objective function ( $\mu = 0.30$ ). . . . .	364

## LIST OF TABLES

<u>Table</u>	<u>page</u>
8. 1 Baseline configuration for isotropic rotor blade in hover . . . . .	172
8. 2 Baseline configuration for single-cell composite rotor blade . . . . .	175
8. 3 Baseline configuration for soft-in-plane isotropic rotor blade in forward flight . . . . .	179
8. 4 Baseline configuration for stiff-in-plane isotropic rotor blade in forward flight . . . . .	180
8. 5 Frequency comparison for isotropic rotor blade configurations used in forward flight analysis . . . . .	181
9. 1 Baseline configuration for the two-cell composite rotor blade . . .	191
9. 2 Baseline configuration for the isotropic rotor blade . . . . .	193
10. 1 Baseline configuration for the two-cell soft-in-plane composite rotor blade . . . . .	203
11. 1 Baseline configuration for the two-cell stiff-in-plane composite rotor blade . . . . .	213
11. 2 Summary of optimization results for the first configuration . . . . .	218
11. 3 Summary of optimization results for the second configuration . . .	220
11. 4 Summary of optimization results for the third configuration . . .	221

## NOMENCLATURE

$a$	lift curve slope
$A$	cross-sectional area of beam
$b$	blade semichord
$b(U), b(T), b(W_e)$	boundary terms in the variations of strain energy, kinetic energy and external work of beam
$B$	number of blades
$c$	blade chord, $c = 2b$
$C_{d0}$	blade profile drag coefficient
$C_{m0}$	blade moment coefficient
$C_{ij} (i, j = 1, \dots, 6)$	coefficients of material stiffness matrix
$C_T$	thrust coefficient of rotor
$C_w$	weight coefficient of helicopter
$[C]$	system damping matrix in modal space, Eq. (6.12)
$[\bar{C}]$	damping matrix of linearized system
$[C_{bb}], [C_{bs}], [C_{sb}], [C_{ss}]$	sub-matrices of the material stiffness matrix
$[C_i]$	damping matrix of $i$ -th element, Eq. (4.87)
$D$	profile drag of blade per unit span
$D_f$	parasite drag of the fuselage
$\mathbf{D}$	vector of design variables
$c_1$	blade root offset from center of rotation
$\hat{e}_x, \hat{e}_y, \hat{e}_z$	unit vectors associated with the undefromed element coordinate system

$\hat{\mathbf{e}}_x, \hat{\mathbf{e}}_\eta, \hat{\mathbf{e}}_\zeta$	unit vectors associated with the undeformed curvilinear coordinate system
$\hat{\mathbf{e}}'_x, \hat{\mathbf{e}}'_\eta, \hat{\mathbf{e}}'_\zeta$	unit vectors associated with the deformed curvilinear coordinate system
$\hat{\mathbf{c}}''_x, \hat{\mathbf{c}}''_\eta, \hat{\mathbf{c}}''_\zeta$	the triad $(\hat{\mathbf{c}}'_x, \hat{\mathbf{c}}'_\eta, \hat{\mathbf{c}}'_\zeta)$ after a virtual motion, Eqs. (4.68a-c)
$\mathbf{E}_x, \mathbf{E}_\eta, \mathbf{E}_\zeta$	base vectors associated with a point on the deformed elastic axis of the blade
$E_L$	longitudinal Young's modulus
$E_T$	transverse Young's modulus
$EA$	modulus weighted cross-sectional area of the beam, Eq. (4.13a)
$EAB_0 - EAB_{15},$ $EAB_{3'}, EAB_{8'}$	anisotropic material coupling constants of the beam cross section, Eqs. (4.15a-r)
$EAC_0 - EAC_3$	modulus weighted cross section integrals of the beam, Eqs. (4.13g-j)
$EAD_0 - EAD_7,$ $EAD_{0'} - EAD_{7'}$	modulus weighted warping constants of the beam cross section, Eqs. (4.14a-o)
$EA\eta_a, EA\zeta_a$	modulus weighted first moments of the beam cross section, Eqs. (4.13b-c)
$EI_{\eta\eta}, EI_{\zeta\zeta}, EI_{\eta\zeta}$	modulus weighted moments of inertia of the beam cross-section, Eqs. (4.13d-f)
$f$	symbol defined in Eq. (6.1)
$f_{ij}$	strain tensor in the curvilinear coordinate system
$fC_{df}$	parasite drag area of fuselage
$\mathbf{f}$	vector of blade equations, Eq. (6.25)
$\mathbf{f}_b$	vector of blade equations, Eq. (6.35)
$\mathbf{f}_t$	vector of trim equations, Eq. (6.37)
$\mathbf{f}_A$	distributed aerodynamic force vector, Eq. (6.61)

$\mathbf{f}_i$	distributed inertial force vector, Eq. (6.57)
$\mathbf{F}$	symbol defined in Eq. (6.5)
$\mathbf{F}$	system load vector in modal space, Eq. (6.14)
$\mathbf{F}_i$	load vector of i-th element, Eq. (4.87)
$\mathbf{F}^{II}$	vector of total hub shear force
$\mathbf{F}^{Rk}$	vector of root force for k-th blade
$\{\mathbf{F}^{CF}\}$	element centrifugal force vector, Eq. (4.85)
$\{\mathbf{F}^I\}$	element applied force vector, Eq. (4.86)
$g$	$\equiv \det[\mathbf{g}_i \cdot \mathbf{g}_j]$ , Eq. (4.4)
$g_q$	q-th constraint function
$\mathbf{g}_x, \mathbf{g}_\eta, \mathbf{g}_\zeta$	undeformed base vectors, Eq. (3.2a-c)
$\mathbf{G}_x, \mathbf{G}_\eta, \mathbf{G}_\zeta$	deformed base vectors, Eq. (3.12a-c)
$G_{LT}$	longitudinal shear modulus
$GJ, G_\eta A, G_\zeta A,$ $G_{\eta\eta} A, G_{\zeta\zeta} A, G_{\eta\zeta} A,$ $G_\eta A \eta_b, G_\eta A \zeta_b, G_\zeta A \eta_c,$ $G_\zeta A \zeta_c, G_\eta J, G_\zeta J$	modulus weighted cross section integrals of the beam, Eqs. (4.13k-v)
$\dot{h}$	airfoil plunging velocity
$h_e$	offset of beam element in-board node from blade root
$h_x, h_y, h_z$	components of $h_e$ in the $(\hat{\mathbf{e}}_x, \hat{\mathbf{e}}_y, \hat{\mathbf{e}}_z)$ system
$H_R$	total longitudinal hub force
$\hat{\mathbf{i}}_b, \hat{\mathbf{j}}_b, \hat{\mathbf{k}}_b$	unit vectors associated with the precone, pitched, blade-fixed coordinate system
$\hat{\mathbf{i}}_p, \hat{\mathbf{j}}_p, \hat{\mathbf{k}}_p$	unit vectors associated with the precone, blade-fixed coordinate system
$\hat{\mathbf{i}}_{nr}, \hat{\mathbf{j}}_{nr}, \hat{\mathbf{k}}_{nr}$	unit vectors associated with the nonrotating, hub-fixed

	coordinate system
$\hat{i}_r, \hat{j}_r, \hat{k}_r$	unit vectors associated with the rotating, hub-fixed coordinate system
$I_b$	blade flapping moment of inertia about blade root
$Im_{\eta\eta}, Im_{\zeta\zeta}, Im_{\eta\zeta}$	mass weighted moments of inertia of the beam cross-section, Eq. (4.56d-f)
$J$	objective function, Eq. (7.3)
$J_1$	objective function, Eq. (7.8)
$J_2$	objective function, Eq. (7.9)
$\tilde{J}$	objective function of approximate problem
$k_A$	polar radius of gyration of blade cross-section, $k_A^2 = (EI_{\eta\eta} + EI_{\zeta\zeta})/EA$
$k_m$	mass radius of gyration of blade cross-section, $k_m^2 = k_{m1}^2 + k_{m2}^2$
$k_{m1}, k_{m2}$	principal mass radii of gyration of blade cross-section
$[K]$	system stiffness matrix in modal space, Eq. (6.11)
$[\bar{K}]$	stiffness matrix of linearized system
$[K_i]$	stiffness matrix of i-th element, Eq. (4.87)
$[K^{CF}]$	element centrifugal stiffening matrix, Eq. (4.85)
$[K^I]$	element applied moment stiffening matrix, Eq. (4.86)
$[K^L]$	element linear stiffness matrix, Eq. (4.83)
$[K^{NL}]$	element nonlinear stiffness matrix, Eq. (4.83)
$l$	length of the elastic portion of the blade
$l_e$	length of beam element
$L$	aerodynamic lift per unit span
$m$	mass per unit length of the blade

$mD_0 - mD_3$	mass weighted warping constants of the beam cross-section, Eq. (4.56g-j)
$m\eta_m, m\zeta_m$	mass weighted first moments of the beam cross-section, Eq. (4.56b-c)
$\mathbf{m}_A$	distributed aerodynamic moment vector, Eq. (6.62)
$\mathbf{m}_I$	distributed inertial moment vector, Eq. (6.59)
$M$	aerodynamic moment per unit span
$\overline{M}_y, \overline{M}_z, \overline{M}'_y, \overline{M}'_z,$ $\overline{P}_x, \overline{P}'_x, \overline{T}_x, \overline{R}_x,$ $\overline{S}_x, \overline{S}'_x$	moment resultants of the beam cross-section, Eqs. (4.12a-j)
$\mathbf{M}^H$	vector of total hub moment
$\mathbf{M}^{Rk}$	vector of root moment for k-th blade
$[M]$	element mass matrix, Eq. (4.85); also system mass matrix in modal space, Eq. (6.13)
$[M^C]$	element Coriolis damping matrix, Eq. (4.85)
$[M_i]$	mass matrix of i-th element, Eq. (4.87)
$n$	number of elements in the finite element model
$n_x', n_\eta', n_\zeta'$	components of $\delta\bar{\Theta}$ in the $(\hat{e}'_x, \hat{e}'_\eta, \hat{e}'_\zeta)$ system
$N_m$	number of modes used in modal transformation
$N_H$	number of harmonics retained in Fourier series expansion
$P_x, P_y, P_z$	components of $\mathbf{P}$ in the $(\hat{e}_x, \hat{e}_y, \hat{e}_z)$ system
$P_\eta', P_\zeta'$	components of aerodynamic forces per unit span in the $\hat{e}'_\eta$ and $\hat{e}'_\zeta$ directions, respectively
$\mathbf{P}$	distributed force vector of the beam, Eq. (4.60)
$Q_x, Q_y, Q_z$	components of $\mathbf{Q}$ in the $(\hat{e}_x, \hat{e}_y, \hat{e}_z)$ system
$Q_x', Q_\eta', Q_\zeta'$	components of $\mathbf{Q}$ in the $(\hat{e}'_x, \hat{e}'_\eta, \hat{e}'_\zeta)$ system

$\mathbf{q}$	vector of finite element nodal degrees of freedom
$\mathbf{q}_i$	vector of nodal degrees of freedom for i-th element
$Q$	number of constraints
$\mathbf{Q}$	distributed moment vector of the beam, Eq. (4.79)
$[\mathbf{Q}]$	reduced beam material stiffness matrix, Eq. (3.50)
$[\mathbf{Q}_i]$	modal transformation matrix for i-th element
$Q_{ij}$	coefficients of $[\mathbf{Q}]$
$r$	radial position of a point on the blade with respect to center of rotation, Eq. (5.38)
$\mathbf{r}$	position vector of a point on the undeformed beam with respect to fixed point in inertial reference frame
$\mathbf{r}_0$	position vector of a point on the elastic axis of the undeformed beam
$R$	rotor radius
$\mathbf{R}$	position vector of a point on the deformed beam
$\mathbf{R}_0$	position vector of a point on the deformed elastic axis
$\mathbf{R}_B$	position vector of blade root with respect to axis of rotation, Eq. (4.21)
$\mathbf{R}_C$	position vector of a point on the deformed beam with respect to blade root, Eq. (4.22)
$R_{cx}, R_{cy}, R_{cz}$	components of $\mathbf{R}_C$ in the $(\hat{e}_x, \hat{e}_y, \hat{e}_z)$ system
$t$	time
$T$	kinetic energy
$T_R$	total thrust generated by the rotor
$[\mathbf{T}_{rn}], [\mathbf{T}_{br}], [\mathbf{T}_{eb}],$ $[\mathbf{T}_{ce}], [\mathbf{T}_{dc}], [\mathbf{T}_{pb}]$	transformation matrices between coordinate systems, Eqs. (2.2), (2.4), (2.7), (2.9), (2.13), (2.17)
$[\mathbf{T}_{de}]$	transformation matrix defined in Eqs. (2.15), (4.40)

$[T^C]$	transformation matrix defined in Eq. (4.105)
$[T^K]$	transformation matrix defined in Eq. (4.104)
$[T^M]$	transformation matrix defined in Eq. (4.106)
$u, v, w$	components of $\mathbf{u}$ in the $(\hat{e}_x, \hat{e}_y, \hat{e}_z)$ system
$\mathbf{u}$	displacement vector of a point on the elastic axis of the blade, Eq. (3.25)
$U_R$	resultant airfoil velocity relative to air, Eq. (5.3)
$U$	strain energy
$\mathbf{U}$	velocity vector of a point on the elastic axis of the blade relative to air, Eq. (5.12)
$U_x', U_\eta', U_\zeta'$	components of $\mathbf{U}$ in the $(\hat{e}'_x, \hat{e}'_\eta, \hat{e}'_\zeta)$ system
$V$	free-stream velocity of airfoil
$\mathbf{V}$	velocity vector of a point on the beam with respect to the inertial reference frame
$\{\mathbf{V}\}, \{\mathbf{W}\}, \{\phi\}, \{\mathbf{U}\}, \{\alpha\}, \{\Gamma_\eta\}, \{\Gamma_\zeta\}$	vectors of element nodal values for $v, w, \phi, u, \alpha, \bar{y}_{x\eta}$ and $\bar{y}_{x\zeta}$ , respectively, Eq. (4.79)
$\mathbf{V}_A$	velocity vector of air due to forward flight and inflow
$\mathbf{V}_B$	velocity vector of the blade root, Eq. (4.24)
$V_{bx}, V_{by}, V_{bz}$	components of $\mathbf{V}_B$ in the $(\hat{e}_x, \hat{e}_y, \hat{e}_z)$ system
$\mathbf{V}_C$	velocity vector of a point on the deformed beam relative to the velocity of blade root, Eq. (4.28)
$\mathbf{V}_{EA}$	velocity vector of a point on the blade elastic axis
$\mathbf{V}_F$	flight velocity vector of helicopter
$V_F$	magnitude of $\mathbf{V}_F$
$V_x^A, V_y^A, V_z^A$	components of $\mathbf{V}_A$ in the $(\hat{e}_x, \hat{e}_y, \hat{e}_z)$ system

$V_x^{EA}, V_y^{EA}, V_z^{EA}$	components of $V_{EA}$ in the $(\hat{e}_x, \hat{e}_y, \hat{e}_z)$ system
$\bar{V}_x, \bar{V}_\eta, \bar{V}_\zeta$	stress resultants of the beam cross-section, Eq. (4.11a-c)
$\tilde{V}_x$	total axial inertial force due to the portion of blade outboard of the element, Eq. (6.3)
$W$	weight of helicopter
$W_e$	work of external loads including the effects of the nonconservative loads
$x, \eta, \zeta$	curvilinear coordinates
$x_A$	aerodynamic center offset from elastic axis, positive for aerodynamic center ahead of elastic axis
$x_1, x_2, x_3$	indicial notations for $x, \eta$ and $\zeta$ , respectively
$X_{FA}$	offset of fuselage center of drag from hub center in the $\hat{i}_{nr}$ direction
$X_{FC}$	offset of helicopter center of gravity from hub center in the $-\hat{i}_{nr}$ direction
$y_1, y_2, y_3$	local cartesian coordinates
$\mathbf{y}$	vector of generalized coordinates
$\mathbf{y}_0$	blade static equilibrium position in hover
$\mathbf{y}_b$	vector of generalized blade degrees of freedom
$\mathbf{y}_t$	vector of trim variables
$Y_u, Y_v, Y_w, Y_\phi,$ $Y_\alpha, Y_\eta, Y_\zeta$	notation used for writing the beam strain energy expressions in concise form, Eqs. (4.17a-g)
$Z_u, Z_v, Z_w, Z_\phi,$ $Z_\alpha, Z_\eta, Z_\zeta, Z'_y,$ $Z'_w, Z'_u, Z'_v, Z'_w,$ $Z'_\phi, Z'_\alpha, Z'_\eta, Z'_\zeta,$ $Z'_v, Z'_w$	notation used for writing the beam kinetic energy expressions in concise form, Eqs. (4.51a-i) and Eqs. (4.55a-i)
$Z_{FA}$	offset of fuselage center of drag from hub center

in the  $-\hat{k}_{nr}$  direction

$Z_{FC}$  offset of helicopter center of gravity from hub center in the  $-\hat{k}_{nr}$  direction

### Greek Symbols

$\alpha(x)$	amplitude of warping
$\alpha_d$	multiplication factor of critical damping, indicating the amount of structural damping added to a mode
$\alpha_\Lambda$	effective local angle of attack for the blade
$\alpha_R$	angle of attack of the rotor disc
$\beta(x)$	pretwist angle at spanwise coordinate $x$
$\beta_p$	blade precone angle
$\beta_J$	blade pretwist angle at junction between straight portion and swept tip
$\beta_T$	pretwist angle of swept tip portion of the blade measured relative to $\beta_J$
$\gamma$	Lock number
$\gamma_{\eta\zeta}, \gamma_{x\zeta}, \gamma_{x\eta}$	engineering shear strain components
$\bar{\gamma}_{x\eta}, \bar{\gamma}_{x\zeta}$	transverse shears at the elastic axis of the blade
$\delta\mathbf{u}$	virtual displacement vector
$(\delta W_e)_p$	virtual work due to distributed forces, Eq. (4.64)
$(\delta W_e)_Q$	virtual work due to distributed moments, Eq. (4.66)
$\delta\bar{\Theta}$	virtual rotation vector, Eq. (4.63)
$\varepsilon$	non-dimensional parameter representing the order of magnitude of typical elastic blade bending slope
$\{\varepsilon_b\}, \{\varepsilon_s\}$	sub-arrays of engineering strain components

$\varepsilon_{ij}$	strain tensor in the local cartesian coordinate system
$\bar{\varepsilon}_{xx}$	axial strain at the elastic axis
$\theta$	blade pitch angle with respect to free stream
$\theta_G$	total geometric pitch angle, Eqs. (5.24), (5.27)
$\theta_p$	blade pitch angle due to pitch control setting, $\theta_p = \theta_0 + \theta_{1c} \cos \psi + \theta_{1s} \sin \psi$
$\theta_w$	rotation due to bending in Timoshenko beam
$\theta_x, \theta_\eta, \theta_\zeta$	Euler angles used to describe the transformation from the undeformed curvilinear coordinate system to the deformed curvilinear coordinate system
$\theta_0, \theta_{1c}, \theta_{1s}$	collective and cyclic pitch control inputs
$\kappa_\eta, \kappa_\zeta$	deformed curvature of the beam
$[\kappa]$	transformation matrix between the triad $(\hat{e}'_x, \hat{e}'_\eta, \hat{e}'_\zeta)$ and its derivatives, Eq. (3.34)
$[\kappa_0]$	transformation matrix between the triad $(\hat{e}_x, \hat{e}_\eta, \hat{e}_\zeta)$ and its derivatives, Eq. (3.33)
$\lambda$	inflow ratio, $\lambda = \frac{V_F \sin \alpha_R + v}{\Omega R}$
$\Lambda_a$	blade tip anhedral angle, positive upward
$\Lambda_h$	ply angle in horizontal walls of box beams
$\Lambda_s$	blade tip sweep angle, positive for sweep back
$\Lambda_v$	ply angle in vertical walls of box beams
$[\Lambda]$	local-to-global transformation matrix, Eq. (4.92)
$[\Lambda^c]$	local-to-global transformation matrix, Eq. (4.111)
$[\Lambda^k]$	local-to-global transformation matrix, Eq. (4.110)
$[\Lambda^l]$	local-to-global transformation matrix, Eq. (4.110)
$[\Lambda^m]$	local-to-global transformation matrix, Eq. (4.112)

$\mu$	advance ratio, $\mu = \frac{V_F \cos \alpha_R}{\Omega R}$
$v$	rotor induced velocity
$\nu_{LT}$	longitudinal Poisson's ratio
$\xi$	non-dimensional coordinate of beam element ( $= \frac{x}{l_e}$ )
$\rho$	mass density of the beam
$\rho_\Lambda$	density of air
$\sigma$	rotor solidity
$\sigma_{xx}, \sigma_{\eta\eta}, \sigma_{\zeta\zeta},$ $\sigma_{\eta\zeta}, \sigma_{x\zeta}, \sigma_{x\eta}$	components of stress tensor; also engineering stress components
$\{\sigma_b\}, \{\sigma_s\}$	sub-arrays of engineering stress components
$\tau$	twist of the deformed beam
$\tau_c'$	notation defined in Eq. (4.41)
$\tau_0$	initial twist of the beam ( $= \frac{d\beta}{dx}$ )
$\phi$	torsional elastic deformation of the blade
$\phi_0$	second order elastic twist effect of the beam, Eq. (3.41)
$\bar{\phi}$	$\equiv \beta + \phi$ , Eq. (4.109)
$\{\Phi_c\}, \{\Phi_q\}$	arrays of Hermite cubic and quadratic interpolation polynomials, respectively, for the beam element
$\{\Phi_c'\}, \{\Phi_q'\}$	first derivatives of $\{\Phi_c\}$ and $\{\Phi_q\}$ , respectively, with respect to $x$
$\{\Phi_c''\}, \{\Phi_q''\}$	second derivatives of $\{\Phi_c\}$ and $\{\Phi_q\}$ , respectively, with respect to $x$
$\psi$	blade azimuth; also non-dimensional time ( $\psi = \Omega t$ )
$\Psi$	out-of-plane warping function for the cross-section

$\omega_F, \omega_L, \omega_T$	rotating flap, lead-lag and torsional frequencies
$\omega_{F1}, \omega_{L1}, \omega_{T1}$	fundamental rotating flap, lead-lag and torsional frequencies, respectively
$\bar{\omega}$	angular velocity of the undeformed element coordinate system $(\hat{e}_x, \hat{e}_y, \hat{e}_z)$ , Eq. (4.29)
$\Omega$	speed of rotation of the rotor
$\Omega_x, \Omega_y, \Omega_z$	components of $\bar{\omega}$ in the $(\hat{e}_x, \hat{e}_y, \hat{e}_z)$ system, Eq. (4.32)

### Special Symbols

$( )_t$	quantity associated with the tip element, unless specifically defined
$( )_G, ( )^G$	quantity in the global coordinate system, unless specifically defined
$( )_L, ( )^L$	quantity in the local coordinate system, unless specifically defined
$( )_{,x}, ( )_{,\eta}, ( )_{,\zeta}$	derivative of $( )$ with respect to $x, \eta, \zeta$ , respectively
$d( )$	differential of $( )$
$\delta( )$	variation of $( )$
$( \dot{ } ), ( \ddot{ } )$	$\frac{\partial( )}{\partial t}, \frac{\partial^2( )}{\partial t^2}$
$\{ \}$	vector
$[ ]$	matrix
$[ ]^T$	transpose of $[ ]$

## SUMMARY

This report describes the development of an aeroelastic analysis capability for composite helicopter rotor blades with straight and swept tips, and its application to the simulation of helicopter vibration reduction through structural optimization. A new aeroelastic model is developed in this study which is suitable for composite rotor blades with swept tips in hover and in forward flight. The hingeless blade is modeled by beam type finite elements. A single finite element is used to model the swept tip. Arbitrary cross-sectional shape, generally anisotropic material behavior, transverse shears and out-of-plane warping are included in the blade model. The nonlinear equations of motion, derived using Hamilton's principle, are based on a moderate deflection theory. Composite blade cross-sectional properties are calculated by a separate linear, two-dimensional cross section analysis. The aerodynamic loads are obtained from quasi-steady, incompressible aerodynamics, based on an implicit formulation. The trim and steady state blade aeroelastic response are solved in a fully coupled manner. In forward flight, where the blade equations of motion are periodic, the coupled trim-aeroelastic response solution is obtained from the harmonic balance method. Subsequently, the periodic system is linearized about the steady state response, and its stability is determined from Floquet theory.

Numerical results illustrating the influence of composite ply orientation, tip sweep and anhedral on trim, vibratory hub loads, blade response and stability, are presented. It is found that composite ply orientation has a significant influence on blade stability. The flap-torsion coupling associated with tip sweep can induce aeroelastic instability due to frequency coalescence. This instability can be removed by appropriate ply orientation in the composite construction.

The structural optimization study is conducted by combining the aeroelastic analysis developed in this study with an optimization package (DOT) to minimize the vibratory hub loads in forward flight; subject to frequency and aeroelastic stability constraints. The design variables, during optimization, consist of the composite ply orientations, of the primary blade structure, and tip sweep and anhedral. A parametric study showing the effects of tip sweep, anhedral and composite ply orientation on blade aeroelastic behavior is used as a valuable precursor in selecting the initial design for the optimization studies. However, the most appropriate combination of the design variables, for vibration reduction, can only be selected by the optimizer. Optimization results show that remarkable reductions in vibration levels, at the hub, can be achieved by a judicious combination of design variables; and that tip sweep is the most dominant design variable for the cases considered.

## Chapter I

### INTRODUCTION AND LITERATURE REVIEW

#### 1.1 INTRODUCTION

Structural optimization of rotor blades for vibration reduction in forward flight has been recognized by industry, research organizations and academia as an important area of endeavor because vibrations generated by the rotor and their reduction represent a principal area of concern in the helicopter design process. During the last decade design criteria for vibration levels at typical locations in the fuselage, such as the pilot seat, have become increasingly more stringent. The problem is further complicated by the highly interdisciplinary nature of helicopter rotor blade design, where numerous disciplines interact with each other. The use of structural optimization for vibration reduction in forward flight is particularly effective because it is aimed at reducing the vibration levels at the source, i.e., the main rotor, before it propagates into the fuselage. Therefore it is not surprising that a considerable amount of research in this area has been performed during the last decade[28].

The majority of the structural optimization studies[28] have been restricted to straight isotropic blades. Modern helicopter rotor blades have been built of composite materials because such blades have better fatigue life and damage tolerance than comparable metal blades. Furthermore, current manufacturing processes for composite blades facilitate the incorporation of refined planforms

and airfoil geometries in the blade design process. Blade manufacturing costs are also lower because there are fewer machining operations. Composite rotor blades also offer the potential for aeroelastic tailoring using structural optimization, which can produce remarkable payoffs in the multidisciplinary design of rotorcraft.

Rotor blades with swept tips, shown schematically in Fig. 1.1, experience bending-torsion and bending-axial coupling effects due to sweep and anhedral. Swept tips influence blade dynamics because they are located at the regions of high dynamic pressure and relatively large elastic displacements. Thus, tip sweep and tip anhedral provide an alternative for the aeroelastic tailoring of rotor blades. Swept tips are also effective for reducing aerodynamic noise and blade vibrations.

The general objectives of this research are to develop a new aeroelastic analysis capability for composite helicopter rotor blades with swept tips and to conduct a structural optimization study combining this new analysis capability with a structural optimization package. In the next section, a review of the state of the art is given in the areas pertinent to these objectives. The specific objectives of this dissertation are then described in the last section of the chapter.

## 1.2 LITERATURE REVIEW

### 1.2.1 *Structural Modeling of Isotropic Rotor Blades*

During the last twenty five years, it has been established that aeroelastic stability of helicopter rotor blades is an inherently nonlinear phenomenon due to moderate blade deflections[23,24,25,26,32,70,71]. The overwhelming majority of studies dealing with the structural modeling of helicopter rotor blades use a beam type model. Nonlinear beam kinematics, incorporating small strains and finite (moderate or large) rotations, are being used to account for the coupling effects between axial, bending, and torsional deformations associated with the centrifugal forces. In the derivation of the strain-displacement relationships, a small strain assumption stating that strains are small as compared to unity is usually made. This is due to the requirement that helicopter rotor blades must be designed to operate at strain levels well below the elastic limit of the blade material due to fatigue life considerations.

A substantial number of the rotor blade models available have been restricted to isotropic material properties. Several typical isotropic blade models are discussed below.

The first analytical model for the flap-lag-torsion of pretwisted nonuniform rotor blades was developed by Houbolt and Brooks[51]. This model is based on a linear theory and nonlinear displacement terms in the derivation were neglected. As a result, the bending-torsion coupling effects due to the ge-

ometrical nonlinearities, which are important for the rotor blade analysis, were absent in this model.

In order to incorporate the geometrical nonlinearities due to the assumption of small strains and finite rotations, one should distinguish between the deformed and the undeformed configurations of the blade, and derive the transformation between the triad of unit vectors associated with the undeformed configuration of the blade and the triad of unit vectors associated with the deformed configuration of the blade. In the moderate deflection beam theories developed by Hodges and Dowell[40], and Rosen and Friedmann[76], the transformations between the deformed and the undeformed triad of unit vectors were derived which, together with the Euler-Bernoulli assumption that plane sections perpendicular to the undeformed elastic axis remain plane and perpendicular to the elastic axis after deformation, were used in the derivation of the nonlinear strain-displacement relationships. These beam theories were validated by comparing them to static tests performed in the moderate deflection regime[21,77]. Subsequently these beam theories[40,76] which provided the structural operators, were combined with the appropriate inertial and aerodynamic operators and used in the aeroelastic stability analyses of isolated rotor blades[41,81]. A moderate deflection beam theory, similar to those developed in Refs. 40 and 76, was also derived by Kaza and Kvaternik[54].

During the derivations of a moderate deflection beam theory, a large number of nonlinear terms are generated. Many of them are relatively small due to the assumption of small strains and moderate rotations. Therefore, ordering

schemes can be useful for identifying and neglecting higher order nonlinear terms in a consistent manner. Most ordering schemes[40,41,76,81] are based on assigning orders of magnitude to the non-dimensional physical parameters governing the aeroelastic problem in terms of the blade bending slopes, which are assumed to be of order  $\epsilon$ . A second order approximation implies that terms of order  $\epsilon^2$  are neglected compared to terms of order 1; and using such an approximation allows one to derive, conveniently, dynamic equations of equilibrium for the blade. A few latter studies[15,16,78,79] also used a third order approximation where terms of order  $\epsilon^3$  were neglected compared to terms of order 1. It is important to note that such ordering schemes are based on experience with actual blade configurations, and therefore a certain degree of flexibility is used in their implementation.

Hodges[43] developed a nonlinear beam kinematics in which the assumption of moderate rotation was removed. The only assumptions introduced on the magnitudes of the kinematical parameters were that the extensional strain was small (and negligible) compared to unity, and that the orientation angles were less than  $90^\circ$ . For rotations larger than  $90^\circ$ , Rodrigues parameters were used instead of orientation angles. This theory was used in the development of the nonlinear equations of motion of a straight pretwisted rotating isotropic beam, which was subsequently employed as the theoretical basis for the beam element used in the computer program GRASP[44]. This beam element served as a valuable tool for examining the effects of higher order nonlinear terms in the equations of motion.

### **1.2.2 *Structural Modeling of Composite Rotor Blades***

Modern helicopter rotor blades are frequently built of composite materials; therefore during the past few years, a substantial number of analytical studies have been aimed at the development of models which are suitable for the structural and aeroelastic analysis of composite rotor blades. The important attributes of such a structural model require the capability to represent transverse shear deformation, cross-sectional warping and elastic coupling, in addition to an adequate representation of geometric nonlinearities. A review of the existing structural models suitable for modeling composite rotor blades were presented by Friedmann[26], Hodges[45] and Friedmann and Hodges[32]. As mentioned earlier, rotor blades are typically modeled as beams. In a beam theory, the deformations of the cross-section, both in and out of the plane, are assumed to be either small or neglected. Therefore, an approach commonly used in the structural models for composite rotor blade analysis is to determine the cross section warping functions, shear center location, and cross sectional properties based on a linear theory. The linear two-dimensional analysis for the cross-section is decoupled from the nonlinear one-dimensional global analysis for the beam and it needs to be done once for each cross section of a nonuniform beam. The discussion of composite rotor blade structural modeling can, therefore, be divided into two categories: (1) Modeling approaches which lead to the determination of the stiffness properties of arbitrary blade cross sections. Anisotropic materials and the composite nature of the blade are taken into account in this category. (2) Structural models which use an one-dimensional beam kinematics suitable for composite rotor blade analysis.

A typical structural model of this category should include geometric nonlinearities, pretwist, transverse shear deformation and cross section warping. Many of the existing composite rotor blade models in category (I) were discussed in detail by Hodges[45].

Mansfield and Sobey[63] made the first attempt to the study of this subject by developing the stiffness properties of a fiber composite tube subjected to coupled bending, torsion and extension. Transverse shear and warping of the cross section were not included in the model. This model was too primitive for composite rotor blade aeroelastic analysis. Rehfield[75] used a similar approach but included out-of-plane warping and transverse shear deformation. This was a static theory for a single cell, thin-walled, closed cross-section composite, with arbitrary layup, undergoing small displacements. This relatively simple theory was subsequently correlated by Nixon[69] with experimental data. Hodges, Nixon and Rehfield[47] also conducted a comparison study of this model[75] with a NASTRAN finite element analysis for a beam having a single closed cell.

Wörndle[101] developed a linear, two-dimensional finite element model to calculate the cross sectional warping functions of a composite beam under transverse and torsional shear. With these warping functions, the shear center locations and the stiffness properties of the cross section could be calculated. In this theory arbitrary cross sectional shapes could be modeled but the material properties were restricted to monoclinic.

A more general model for calculating the shear center and the stiffness properties of an arbitrarily shaped composite cross section was developed by

Kosmatka[56]. He used a two-dimensional finite element model to obtain the St. Venent solution of the cross-section warping functions of a tip loaded composite cantilever beam with an arbitrary cross section. The beam was assumed to be prismatic (axially uniform) and nonhomogeneous. The blade consisted of generally anisotropic materials. Subsequently, this cross sectional analysis was combined with a moderate deflection beam theory suitable for the structural dynamic analysis of advanced propeller blades[56,57].

Giavotto, et al.[37] also formulated a two-dimensional finite element analysis for determining the cross sectional warping functions, shear center location and stiffness properties. A special aspect of this formulation was that the resulting equations had both extremity solutions and central solutions. The central solutions correspond to the warping displacements due to applied loads without considering end effects, while the extremity solutions correspond to the warping displacements due to end effects. Subsequently, this work was extended by Borri and Merlini[10] to include the so-called geometric section stiffness associated with large displacement formulations.

Bauchau[3] developed a beam theory for anisotropic materials based on the assumption that the cross section of the beam does not deform in its own plane. The out-of-plane cross section warping was expressed in terms of the so-called eigenwarpings. This theory is valid for thin-walled, closed, multi-celled beams with transversely isotropic material properties. Subsequently it was extended by Bauchau, Coffenberry and Rehfield[5] to allow for general orthotropic material properties.

The studies on composite blade structural modeling, described above, were based on a separate two-dimensional analysis to determine the cross-sectional warping functions and the stiffness properties, and as mentioned earlier for non-uniform beams, such a two-dimensional analysis has to be carried out once for each cross section. An alternate approach, developed by Lee and Kim[58] and Stemple and Lee[87], uses a finite element formulation which can represent thin-walled beams with arbitrary cross sections, general spanwise taper and planform distributions and allows arbitrary cross section warping. This was accomplished by distributing warping nodes over the cross section situated at the node of regular beam type finite element. Thus the treatment of the cross section warping is coupled with the treatment of the beam bending, torsion and extension. This formulation considers only the out-of-plane warping and linear problems. Subsequently it was partially extended by Stemple and Lee[88] and used in the preliminary study of large static deflections of beams as well as the free vibration analysis of rotating composite beams. This approach is much more expensive than those whose cross sectional analysis is decoupled from the nonlinear beam analysis, and therefore it was never used in the aeroelastic analysis of rotor blades.

The structural models for composite blade discussed so far emphasize the modeling approach associated with category (1), where the emphasis is on determining the shear center, warping and cross-sectional properties of the composite cross section. For category (2) structural modeling, where the emphasis is the one-dimensional beam kinematics suitable for the analysis of composite rotor blades, two types of theories are available depending on the level of ge-

ometric nonlinearity being retained in the one-dimensional beam kinematics. The first type is based on a moderate deflection theory while the second type is capable of modeling large deflections. Moderate deflection theories usually use an ordering scheme to limit the magnitude of blade displacements and rotations, thus enable the strain-displacement relations and the transformation between the deformed and undeformed coordinates be expressed in terms of blade displacement quantities ( $u$ ,  $v$ ,  $w$ ,  $\phi$ , and their derivatives with respect to the axial coordinate,  $x$ ) explicitly. While large deflection theories do not utilize an ordering scheme to limit the magnitude of blade displacements and rotations. For such theories the only assumption used to neglect higher order terms is that the strains are small.

For helicopter rotor blade aeroelastic analysis, moderate deflection theories are usually adequate provided that a consistent ordering scheme is used. Blade models based on large deflection theories are mathematically more elegant and more consistent than those using an ordering scheme; however, the incorporation of such models into general aeroelastic analyses involving forward flight could be complicated. The computational requirements associated with moderate deflection theories may also be more modest than those associated with large deflection theories.

The first aeroelastic model for a composite rotor blade in hover was presented in a comprehensive study by Hong and Chopra[48]. In this model, the blade was treated as a single-cell, laminated box beam composed of an arbitrary lay-up of composite plies. The strain-displacement relations for moderate deflections were taken from Hodges and Dowell[40], which do not include the

effect of transverse shear deformations. Each lamina of the laminate was assumed to have orthotropic material properties. The equations of motion were obtained using Hamilton's principle. A finite element model was used to discretize the equations of motion. Numerical results for the coupled flap-lag-torsional behavior of hingeless rotor blades showed that the coupling effects due to composite construction have a strong influence on blade stability boundaries in hover. Subsequently this analysis was extended to the modeling of composite bearingless rotor blades in hover[49]. The structural model presented in Ref. 48 was also used by Panda and Chopra[72] to study the aeroelastic stability and response of composite hingeless rotor blades in forward flight. In a more recent study, Smith and Chopra[84] modified the structural model presented in Ref. 48 to include the effect of transverse shear deformation, together with a more refined cross section analysis[85], to investigate the aeroelastic response, stability and loads of composite rotor blades in forward flight. The models used in Refs. 48, 72 and 84 were restricted to single-cell, rectangular box beams.

A comprehensive analysis for the structural dynamic modeling of advanced composite propeller blades, which, with some modifications, could be also suitable for the general modeling of curved, pretwisted composite rotor blades, was developed by Kosmatka[56,57]. In this model the blade cross sectional geometry was general. The cross-sectional stiffness properties and shear center location were obtained from a linear two-dimensional finite element model[56], which has been discussed briefly earlier in this section.

Bauchau and Hong[4,6,7] developed a series of large deflection composite beam models which were intended for rotor blade structural dynamic and aeroelastic analysis. Some shortcomings in the first two models[4,6] were noted by Hong in his dissertation[50]. The final version of their theory[7] was suitable for modeling naturally curved and twisted beams undergoing large displacements and rotations, while undergoing only small strains. The kinematics associated with this theory were based on an extension of the common approach, using the definition of Green strains, to incorporate effects such as small initial curvature, transverse shear deformations and out-of-plane warpings. The basic assumptions in the kinematics were the restriction that the cross-section is rigid in its own plane combined with a revised small strain assumption. In this revised small strain assumption, both axial and shear strains were neglected when compared to unity, however no assumption was made on the relative magnitude between the axial and shear strains. Therefore, the second order shear strain coupling terms in the axial strain expression were retained under this revised small strain assumption. A frequently used small strain assumption, which includes an additional assumption that the axial and shearing strains are of the same order of magnitude, was often used successfully in beam models with isotropic or slightly anisotropic materials. However, Bauchau and Hong[7] showed that it might be inadequate for beams having large amounts of anisotropy, by comparing analytical and experimental results obtained for a thin-walled kevlar beam. This model was used for free vibration studies[50], as well as studies on beams undergoing

large static deflections. However, an aeroelastic analysis of rotor blades based on this model is not available to date.

Minguet and Dugundji[66,67] also developed a large deflection composite blade model for static[66] and free vibration[67] analyses. Large deflections were accounted for by using the Euler angles to describe the transformation between a global and local coordinate system after deformation. However, transverse shear deformation and cross section warping were not incorporated in this model. Thus this model is more suitable for the study of flat composite strips than actual rotor blades.

Hodges[46] presented a general beam theory based on a nonlinear intrinsic formulation for the dynamics of initially curved and twisted beams in a moving frame. This beam model is valid for both isotropic and composite beams. The nonlinear beam kinematics was based on a theory developed by Danielson and Hodges[17,18]. The final set of equations of motion were derived using a mixed variational principle, which provided the basis for finite element formulation. Subsequently Fulton and Hodges[22] developed a finite element based stability analysis for a hingeless composite isolated rotor in hover.

### ***1.2.3 Structural Modeling of Swept-tip Blades***

Only a limited number of analytical studies have addressed the aeroelastic modeling of rotor blades with swept tips. An analytical study was conducted by Tarzanin and Vlamincck[90] to investigate the effect of tip sweep on the hub loads of an articulated rotor system. In this model, tip sweep was simu-

lated approximately by manipulating the relative positions of the shear center, aerodynamic center and mass center of the cross sections of a straight blade. The mathematical model consisted of coupled flap-torsion and uncoupled lag equations of motion. The numerical results obtained led them to conclude that tip sweep influences both blade vibrations and stability.

Celi and Friedmann[12] developed a comprehensive and consistent model which was capable of simulating the aeroelastic behavior of a hingeless rotor blade with a swept tip. The analysis was based on the equations of motion presented in Ref. [81]. The swept tip was modeled by developing the structural, inertia and aerodynamic operators for a special beam finite element representing the tip, while the straight portion of the blade was modeled using a number of Galerkin type finite elements[27,89]. This was the first detailed and systematic study of the effect of tip sweep on blade stability in both hover and forward flight. The most important conclusions obtained in Ref. 12 are briefly described next. Tip sweep has a powerful influence on the dynamic behavior of hingeless rotor blades. However, its effect depends on a number of blade design parameters, such as precone and the combination of blade fundamental frequencies. The aeroelastic instabilities induced by tip sweep are associated with frequency coalescence. Such instabilities are strong, and cannot be eliminated by the addition of small amounts of structural damping. When frequency coalescence does not occur, tip sweep is usually stabilizing. Despite its comprehensive nature, the model used in Ref. 12 had a number of limitations because it approximated the swept tip portion of the blade as axially rigid element, and it also employed a linear transformation at the

junction where the swept-tip element was combined with the straight portion of the blade. It was latter shown that such a transformation could be inaccurate for large sweep angles[73]. Furthermore, it should be noted that the studies presented in Refs. 90 and 12 were restricted in the sense that they could only represent tip sweep, but not anhedral (see Fig. 2.3).

Benquet and Chopra [8] developed an aeroelastic analysis to calculate the response and loads of an advanced tip hingeless blade in forward flight using finite element method. This model included both tip sweep and anhedral, however it was still based on a linear transformation for combining the swept tip with the straight portion of the blade. Subsequently, Kim and Chopra[55] extended the formulation given in Ref. 8 to include nonlinear transformation in the assembly between the swept tip and the straight portion of the blade, using the transformation and constraint relations developed by Panda[73]. Bir and Chopra[9] developed an aeroelastic formulation for advanced geometry blades with variable sweep, anhedral, pretwist and planform. The blade was modeled as a series of arbitrarily oriented elastic segments with each segment divided into finite elements. Fuselage dynamic interaction with the blades was included in the formulation.

All of the studies on swept tip blades mentioned above were restricted to isotropic blades.

#### 1.2.4 *Structural Optimization for Vibration Reduction*

A fairly recent survey describing research on helicopter vibration reduction using structural optimization, with aeroelastic and multidisciplinary constraints, was presented by Friedmann[28]. It was shown[28] that the integrated multidisciplinary optimization of rotorcraft offers the potential for substantial improvements, particularly in vibration levels, which can be achieved by careful preliminary design and analysis without requiring additional hardware such as rotor vibration absorbers or isolation systems.

To avoid duplicating the review presented in Ref. 28, only a few studies will be mentioned in this section. The majority of the structural optimization studies on helicopter rotor blades[28] have been restricted to straight isotropic blades. Friedmann and Shanthakumaran[29] applied mathematical programming methods and approximation concepts[80] to vibration reduction of helicopter rotor blades in forward flight. The objective function consisted of the oscillatory vertical hub shears or the hub rolling moments at an advance ratio  $\mu = 0.3$ . The behavior constraints included frequency placements of the blade and aeroelastic stability constraints in hover. Cross sectional dimensions and nonstructural tuning masses, located in the outboard portion of the blade, were used as design variables. Numerical results for typical soft-in-plane hingeless rotor configurations indicated that a 15%-40% reduction in vibration levels, as well as a 20% weight reduction were obtained.

Lim and Chopra[61,62] carried out a comprehensive study of vibration reduction in helicopter rotor blades with aeroelastic constraints. An important contribution made in Refs. 61 and 62 consisted of using a direct analytical

approach for the calculation of the derivatives of the hub loads[59] and blade stability[60], with respect to the design variables. These sensitivity derivatives were obtained at a fraction of the computational cost associated with the more conventional finite difference method, such as that used in Ref. 29. However this approach is applicable only when explicit analytical expressions are available, as a function of the design variables, in the calculation of the sensitivity derivatives.

Davis and Weller[19] developed a modal-based rotor blade optimization analysis which was applied to various rotor dynamics problems, such as blade natural frequency placement, minimization of hub shears and minimization of modal vibration indices. This modal-based analysis was an automated analysis capable of optimizing blade modal characteristics through tailoring of structural properties. They concluded that the modal-based optimization analysis can produce blade design with significantly lower vibration levels. Frequency placement alone was shown to be inadequate to achieve minimum vibration level. However minimization of modal vibration indices and modal hub shears lead to substantially lower vibratory hub loads, with the modal vibration indices minimization being the most effective criteria for rotor vibration reduction. Subsequently, these results were verified by fairly extensive wind-tunnel tests[99,20]. In these tests the baseline rotor vibration levels were compared with those measured for the optimum rotor, and reasonably good correlation between theory and experiments was obtained. It should be also mentioned that aeroelastic stability constraints were not considered in Ref. 19.

Young and Tarzanin[102] conducted a combined analytical-experimental study on the application of structural optimization to rotor design. In this study two different rotors: a reference rotor and a low vibration rotor; having identical planform, twist and airfoil, were tested in the wind tunnel. The reference rotor was designed using a conventional approach; while the low vibration rotor was designed using an analytical structural optimization procedure, in which the objective function consisted of the fixed system hub loads. The wind tunnel test results showed substantial reductions in the 4/rev vertical hub shear and overturning moment for the low vibration rotor at both low and high advance ratios. Thus, Ref. 102 provides a validation of the structural optimization procedure for the design of low vibration rotors in forward flight.

Adelman and Mantay[1] edited a comprehensive report on the current state of integrated multidisciplinary optimization of rotorcraft, which included an intelligent plan for future development towards the complete integration of various disciplines. It is evident from this document that helicopter vibration reduction is one of the areas where an integrated multidisciplinary design approach offers excellent potential for performance gains.

The improved modeling capability available for composite rotor blade aeroelastic response and stability analysis produced a few structural optimization studies on straight composite rotor blades[35,36]. In Ref. 35, the design variables were the ply angles of the laminated walls of the box beam, and the objective was the minimization of the 4/rev hub loads; both hub shears and moments. Reference 36 was an extension of the study performed in Ref. 35

by allowing the ply angles to vary from element to element in the spanwise direction, and performing a multi-objective optimization to minimize the 4/rev hub loads and the blade root moment simultaneously.

Only a limited number of structural optimization studies were conducted on swept-tip blades; with aeroelastic constraints[14,34]. While References 14 and 34 are both restricted to isotropic blades, they indicated that tip sweep can be used effectively as an important design variable for vibration reduction.

### **1.3 OBJECTIVES OF THE RESEARCH**

The present study has a number of important objectives which are listed below:

1. Development of an analysis capable of modeling the aeroelastic behavior of composite helicopter rotor blades with swept tips in hover and forward flight. The important features of this analysis include: (a) computational efficiency so that the analysis is suitable for the repetitive calculations required for structural optimization; (b) fully coupled trim/aeroelastic response analysis capability, since this feature was found to be critical for the accurate modeling of the dynamic behavior of rotor blades with swept tips; and (c) ability to represent arbitrary multi-cell blade cross-sections.
2. Conduct detailed studies on the aeroelastic behavior of composite rotor blades with straight and swept tips to determine the combined effect of

sweep, anhedral and composite ply orientation on blade response and aeroelastic stability in hover and in forward flight.

3. Conduct studies illustrating the effects of sweep, anhedral and ply orientation on the hub shears and moments of composite rotor blades in forward flight.
4. Combine the new aeroelastic analysis capability for swept tip composite blades with a structural optimization package, such as DOT[106].
5. Conduct a few basic structural optimization studies on two-cell, composite blade configurations to illustrate the potential benefits of using ply orientation, tip sweep and tip anhedral as design variables for reducing vibration levels in forward flight.

## Chapter II

### MODEL DESCRIPTION AND COORDINATE SYSTEMS

In this chapter, the assumptions used in the development of the aeroelastic analysis of a composite helicopter rotor blade with a swept tip are summarized. The ordering scheme used in the formulation of the moderate deflection theory is described next. Finally, the various coordinate systems and related coordinate transformations, used in the derivation of the equations of motion of the blade, are defined.

#### 2.1 BASIC ASSUMPTIONS

1. The hingeless blade is cantilevered at the hub, with a root offset  $e_1$  from the axis of rotation (see Fig. 2.2).
2. The blade has a precone angle  $\beta_p$  (see Fig. 2.2) and it has a built-in pretwist distribution  $\tau_0$  about the elastic axis (line of shear centers) of the blade.
3. The blade has no sweep, droop or torque offset.
4. The blade consists of a straight portion and a swept tip whose orientation relative to the straight portion is described by a sweep angle ( $\Lambda_s$ ) and an anedral angle ( $\Lambda_a$ ) (see Fig. 2.3).
5. The blade is modeled by beam type finite elements along the elastic axis of the blade.

6. A single finite element is used to model the swept tip.
7. The blade cross section can have arbitrary shape with distinct shear center, aerodynamic center, tension center and center of mass.
8. The stiffness and mass properties of the blade, and its chord and pre-twist, are allowed to vary along the span of the blade.
9. The blade feathering axis coincides with the line of shear centers of the straight portion of the blade, which is approximated by a straight line. Note that the blade stiffness distribution for a typical helicopter, such as the MBB BO-105[86], usually consists of a stiff, nonuniform inboard portion (approximately 25% of the blade length) in which large variations in stiffness can occur, and a flexible outboard portion (approximately 75% of the blade length) where the blade properties are relatively uniform. The elastic deformations of the blade occur primarily in the outboard portion; thus the line of shear centers associated with this blade segment is to a large extent representative of the behavior of the elastic axis of the whole blade.
10. The blade is built of generally orthotropic materials, and it is anisotropic.
11. The blade has completely coupled flap, lead-lag, torsional and axial dynamics.
12. The effects of transverse shear deformations and out-of-plane warping are included.
13. The blade undergoes moderate deflections, which imply small strains and moderate rotations.

14. Two-dimensional quasi-steady aerodynamics, based on Greenberg's theory, is used to obtain the distributed aerodynamic loads; this simple unsteady theory is justifiable because the principal objectives emphasize the structural modeling of the blade and its optimization for vibration reduction.
15. The induced inflow is assumed to be uniform and steady.
16. Stall and compressibility effects are neglected.
17. Reverse flow effects are included by setting the lift and moment equal to zero and by changing the sign of the drag force inside the reverse flow region (see Fig. 5.3).
18. The rotor shaft is assumed to be rigid and the speed of rotation ( $\Omega$ ) of the rotor is constant.
19. The helicopter is in trimmed, steady and straight flight.

The assumptions listed above are used in various stages of the formulation of the aeroelastic model. Additional assumptions needed for the structural modeling of the blade, such as the kinematical assumptions and the assumptions used in the development of the constitutive relations, are discussed in Chapter 3.

## 2.2 ORDERING SCHEME

An ordering scheme is defined and used to identify and delete higher order nonlinear terms, generated during the derivation of the equations of motion for a beam element undergoing moderate deflections, in a consistent manner. This ordering scheme is based on the assumption that the slopes of the deformed elastic blade are moderate, and of order  $\varepsilon$  (where  $\varepsilon$  is assumed to have a magnitude  $0.10 \leq \varepsilon \leq 0.20$ ). Orders of magnitude are then assigned to the various non-dimensional physical parameters governing the aeroclastic problem in terms of  $\varepsilon$ . In the derivation of the governing equations, it is assumed that terms of order  $\varepsilon^2$  are neglected with respect to terms of order 1, i.e.,

$$O(1) + O(\varepsilon^2) \simeq O(1)$$

The orders of magnitude for various non-dimensional parameters used in this study are listed below:

$$O(1) : \quad \frac{x}{l}, \frac{R}{l}, \frac{h_e}{l}, \frac{l_e}{l}, l \frac{\partial}{\partial x}, \psi, \frac{\partial}{\partial \psi} = \frac{1}{\Omega} \frac{\partial}{\partial t}, \sin \psi, \cos \psi, \\ \Lambda_s, \Lambda_a, \sin \Lambda_s, \cos \Lambda_s, \sin \Lambda_a, \cos \Lambda_a$$

$$O(\varepsilon^{1/2}) : \quad \theta_p, \beta$$

$$O(\varepsilon) : \quad \frac{\eta}{l}, \frac{\zeta}{l}, \frac{v}{l}, \frac{w}{l}, v_{,x}, w_{,x}, \phi, \alpha l, \frac{\Psi_{,\eta}}{l}, \frac{\Psi_{,\zeta}}{l}, \frac{e_1}{l}, \beta_p, \\ \theta_x, \theta_\eta, \theta_\zeta$$

$$O(\varepsilon^2) : \quad \frac{u}{l}, u_{,x}, \bar{\varepsilon}_{xx}, \bar{\gamma}_{x\eta}, \bar{\gamma}_{x\zeta}, \frac{\Psi}{l^2}, \frac{m\Omega^2 l^2}{EA}$$

In general, it is assumed that rotation terms such as  $v_{,x}$ ,  $w_{,x}$  and  $\phi$  are of order  $\varepsilon$ , while strain terms such as  $u_{,x}$ ,  $\bar{y}_{x\eta}$  and  $\bar{y}_{x\zeta}$  are of order  $\varepsilon^2$ . The warping amplitude  $\alpha$  is assumed to have the same order of magnitude as  $\phi_{,x}$ . This scheme is consistent with a moderate deflection theory (small strains and moderate rotations). Furthermore, it is assumed that the coefficients of the reduced material stiffness matrices,  $Q_{ij}$  ( $i, j = 1, 5, 6$ ), are of the same order of magnitude. It is important to note that, ordering schemes are not unique and are based on common sense and experience with actual blade configurations. Therefore, the application of the ordering scheme requires both care and a certain degree of flexibility.

### 2.3 COORDINATE SYSTEMS

Several coordinate systems are required to fully describe the geometry and deformation of the blade. Each coordinate system is symbolically represented by a triad of orthonormal unit vectors. The first three systems, namely, the nonrotating, hub-fixed system  $(\hat{i}_{nr}, \hat{j}_{nr}, \hat{k}_{nr})$ , the rotating, hub-fixed system  $(\hat{i}_r, \hat{j}_r, \hat{k}_r)$ , and the precone, pitched, blade-fixed system  $(\hat{i}_b, \hat{j}_b, \hat{k}_b)$ , respectively, are used to position and orient the blade relative to the hub through rigid-body motions, as shown in Figs. 2.1 and 2.2. The next two systems,  $(\hat{c}_x, \hat{c}_y, \hat{c}_z)$  and  $(\hat{c}_x, \hat{c}_\eta, \hat{c}_\zeta)$ , respectively, are used to position and orient each beam finite element relative to the  $(\hat{i}_b, \hat{j}_b, \hat{k}_b)$  system in the undeformed configuration of the blade, as shown in Figs. 2.3 and 2.4. A final system,  $(\hat{c}'_x, \hat{c}'_\eta, \hat{c}'_\zeta)$ , is used to represent the orientation of the local blade geometry after defor-

mation. An additional system, the precone, blade-fixed system  $(\hat{i}_p, \hat{j}_p, \hat{k}_p)$ , is used as explained in Subsection 2.3.7.

### 2.3.1 *Nonrotating, Hub-fixed Coordinate System*

The  $(\hat{i}_{nr}, \hat{j}_{nr}, \hat{k}_{nr})$  system, shown in Fig. 2.1, is an inertial reference frame and has its origin at the hub center. The vector  $\hat{i}_{nr}$  points toward the helicopter tail;  $\hat{j}_{nr}$  points to starboard; and  $\hat{k}_{nr}$  coincides with the rotation vector of the rotor.  $\hat{i}_{nr}$  and  $\hat{j}_{nr}$  are in the plane of rotation. Hub shears and moments are defined in this coordinate system.

### 2.3.2 *Rotating, Hub-fixed Coordinate System*

The  $(\hat{i}_r, \hat{j}_r, \hat{k}_r)$  system, shown in Fig. 2.1, also has its origin at the hub center but rotates with a constant angular velocity  $\Omega \hat{k}_r$ . The vector  $\hat{i}_r$  coincides with the azimuth position of the blade, while  $\hat{k}_r$  is coincident with the vector  $\hat{k}_{nr}$ ;  $\hat{i}_r$  and  $\hat{j}_r$  are also in the plane of rotation of the rotor.

### 2.3.3 *Precone, Pitched, Blade-fixed Coordinate System*

The  $(\hat{i}_b, \hat{j}_b, \hat{k}_b)$  system, shown in Fig. 2.2, rotates with the blade and has its origin at the blade root, offset from the hub center by  $e_1 \hat{i}_r$ . The vector  $\hat{i}_b$  coincides with the pitch axis, which is also the undeformed elastic axis of the straight portion of the blade. The  $(\hat{i}_b, \hat{j}_b, \hat{k}_b)$  system is oriented by rotating the  $(\hat{i}_r, \hat{j}_r, \hat{k}_r)$  system about  $-\hat{j}_r$  axis by the precone angle  $\beta_p$ , and subsequently in-

roducing a second rotation about the rotated  $\hat{i}_r$  axis by the geometric pitch angle  $\theta_p$ . In the finite element model of the blade, the  $(\hat{i}_b, \hat{j}_b, \hat{k}_b)$  system is the global coordinate system.

#### 2.3.4 Undeformed Element Coordinate System

The  $(\hat{e}_x, \hat{e}_y, \hat{e}_z)$  system, shown in Fig. 2.3, has its origin at the inboard node of the finite element. The vector  $\hat{e}_x$ , is aligned with the beam element elastic axis; while the vectors  $\hat{e}_y$  and  $\hat{e}_z$  are defined in the cross section of the beam. For the straight portion of the blade, the  $(\hat{e}_x, \hat{e}_y, \hat{e}_z)$  system has the same orientation as the  $(\hat{i}_b, \hat{j}_b, \hat{k}_b)$  system. For the swept-tip element, the  $(\hat{e}_x, \hat{e}_y, \hat{e}_z)$  system is oriented by rotating the  $(\hat{i}_b, \hat{j}_b, \hat{k}_b)$  system about  $-\hat{k}_b$  by the sweep angle  $\Lambda_s$ , and then about  $-\hat{j}_b$  by the anhedral angle  $\Lambda_a$ . The  $(\hat{e}_x, \hat{e}_y, \hat{e}_z)$  system is also the local coordinate system for the blade finite element model. The displacement components and the applied loads of the beam finite element are defined in this coordinate system.

#### 2.3.5 Undeformed Curvilinear Coordinate System

In the  $(\hat{e}_x, \hat{e}_\eta, \hat{e}_\zeta)$  system, the vectors  $\hat{e}_\eta$  and  $\hat{e}_\zeta$  are defined parallel to the modulus weighted principal axes of the cross section; and the pretwist angle  $\beta(x)$  is defined as the change in the orientation of  $\hat{e}_\eta, \hat{e}_\zeta$  with respect to  $\hat{e}_y, \hat{e}_z$ , respectively, at any location along the beam element, as shown in Fig. 2.4. Effects of blade pretwist are properly accounted for by deriving the beam element strain-displacement relations in the  $(\hat{e}_x, \hat{e}_\eta, \hat{e}_\zeta)$  system, which rotates with

the beam pretwist. The strain components, the material properties, and the cross section warping function are all derived in this coordinate system.

### 2.3.6 *Deformed Curvilinear Coordinate System*

The  $(\hat{c}'_x, \hat{c}'_\eta, \hat{c}'_\zeta)$  system, which will be discussed in more detail in chapter 3, represents the orientation of the local blade geometry after deformation. The orientation of the  $(\hat{c}'_x, \hat{c}'_\eta, \hat{c}'_\zeta)$  system is obtained by rotating the  $(\hat{c}_x, \hat{c}_\eta, \hat{c}_\zeta)$  system through three Euler angles in the order of  $\theta_\zeta$ ,  $\theta_\eta$  and  $\theta_x$  about  $\hat{c}_\zeta$ , rotated  $\hat{c}_\eta$  and rotated  $\hat{c}_x$ , respectively. This sequence was chosen following the work of previous authors[40,76] but other sequences are also possible. The vector  $\hat{c}'_x$  is chosen to be tangent to the local deformed elastic axis.

### 2.3.7 *Preconed, Blade-fixed Coordinate System*

The  $(\hat{i}_p, \hat{j}_p, \hat{k}_p)$  system is identical to the preconed, pitched, blade-fixed system  $(\hat{i}_b, \hat{j}_b, \hat{k}_b)$  when the pitch angle  $\theta_p$  is equal to zero. The  $(\hat{i}_p, \hat{j}_p, \hat{k}_p)$  system is oriented by rotating the  $(\hat{i}_b, \hat{j}_b, \hat{k}_b)$  system about  $-\hat{i}_b$  by the pitch angle  $\theta_p$ , thereby canceling the pitch rotation inherent in the definition of the  $(\hat{i}_b, \hat{j}_b, \hat{k}_b)$  system. Expressing the blade response and blade root loads in this coordinate system is convenient when comparing the results, for these quantities, with similar results available in the literature.

## 2.4 COORDINATE TRANSFORMATIONS

The coordinate transformations between the various coordinate systems described in the previous section, which are needed for the formulation of the equations of motion, are defined in this section.

### 2.4.1 *Rotating to Nonrotating Transformation*

The transformation between the rotating, hub-fixed coordinate system and the nonrotating, hub-fixed coordinate system is defined as:

$$\begin{Bmatrix} \hat{i}_r \\ \hat{j}_r \\ \hat{k}_r \end{Bmatrix} = [T_m] \begin{Bmatrix} \hat{i}_{nr} \\ \hat{j}_{nr} \\ \hat{k}_{nr} \end{Bmatrix} \quad (2.1)$$

and the transformation matrix  $[T_m]$  is given by

$$[T_m] = \begin{bmatrix} \cos \psi & \sin \psi & 0 \\ -\sin \psi & \cos \psi & 0 \\ 0 & 0 & 1 \end{bmatrix} \quad (2.2)$$

where,  $\psi$  is the blade azimuth,  $\psi = \Omega t$ .

### 2.4.2 Blade-fixed to Hub-fixed Transformation

The transformation between the precone, pitched, blade-fixed coordinate system and the rotating, hub-fixed coordinate system is defined as:

$$\begin{Bmatrix} \hat{i}_b \\ \hat{j}_b \\ \hat{k}_b \end{Bmatrix} = [T_{br}] \begin{Bmatrix} \hat{i}_r \\ \hat{j}_r \\ \hat{k}_r \end{Bmatrix} \quad (2.3)$$

and the transformation matrix  $[T_{br}]$  is given by

$$[T_{br}] = \begin{bmatrix} 1 & 0 & 0 \\ 0 & \cos \theta_p & \sin \theta_p \\ 0 & -\sin \theta_p & \cos \theta_p \end{bmatrix} \begin{bmatrix} \cos \beta_p & 0 & \sin \beta_p \\ 0 & 1 & 0 \\ -\sin \beta_p & 0 & \cos \beta_p \end{bmatrix} \quad (2.4)$$

where,  $\beta_p$  is the blade precone angle, and  $\theta_p$  is the blade pitch angle due to pitch control setting, expressed by:

$$\theta_p = \theta_0 + \theta_{1c} \cos \psi + \theta_{1s} \sin \psi \quad (2.5)$$

in which  $\theta_0$  is the collective pitch,  $\theta_{1c}$  and  $\theta_{1s}$  are the cyclic cosine pitch and cyclic sine pitch, respectively.

### 2.4.3 Element to Blade Transformation

The transformation between the undeformed element coordinate system and the precone, pitched, blade-fixed coordinate system is defined as:

$$\begin{Bmatrix} \hat{e}_x \\ \hat{e}_y \\ \hat{e}_z \end{Bmatrix} = [T_{eb}] \begin{Bmatrix} \hat{i}_b \\ \hat{j}_b \\ \hat{k}_b \end{Bmatrix} \quad (2.6)$$

*For the straight portion of the blade*

$$[T_{cb}] = \begin{bmatrix} 1 & 0 & 0 \\ 0 & 1 & 0 \\ 0 & 0 & 1 \end{bmatrix} \quad (2.7a)$$

*For the swept-tip element*

$$\begin{aligned} [T_{cb}] &= \begin{bmatrix} \cos \Lambda_s & -\sin \Lambda_s & 0 \\ \sin \Lambda_s & \cos \Lambda_s & 0 \\ 0 & 0 & 1 \end{bmatrix} \begin{bmatrix} \cos \Lambda_a & 0 & \sin \Lambda_a \\ 0 & 1 & 0 \\ -\sin \Lambda_a & 0 & \cos \Lambda_a \end{bmatrix} \\ &= \begin{bmatrix} \cos \Lambda_s \cos \Lambda_a & -\sin \Lambda_s & \cos \Lambda_s \sin \Lambda_a \\ \sin \Lambda_s \cos \Lambda_a & \cos \Lambda_s & \sin \Lambda_s \sin \Lambda_a \\ -\sin \Lambda_a & 0 & \cos \Lambda_a \end{bmatrix} \end{aligned} \quad (2.7b)$$

where,  $\Lambda_s$  is the blade tip sweep angle, positive for backward sweep, and  $\Lambda_a$  is the blade tip anhedral angle, positive upward.

#### 2.4.4 Undeformed Curvilinear to Undeformed Element Transformation

The transformation between the undeformed curvilinear coordinate system and the undeformed element coordinate system is defined as:

$$\begin{Bmatrix} \hat{e}_x \\ \hat{e}_\eta \\ \hat{e}_\zeta \end{Bmatrix} = [T_{ce}] \begin{Bmatrix} \hat{e}_x \\ \hat{e}_y \\ \hat{e}_z \end{Bmatrix} \quad (2.8)$$

and the transformation matrix  $[T_{ce}]$  is given by

$$[T_{ce}] = \begin{bmatrix} 1 & 0 & 0 \\ 0 & \cos \beta & \sin \beta \\ 0 & -\sin \beta & \cos \beta \end{bmatrix} \quad (2.9)$$

where,  $\beta$  is the blade local pretwist angle which varies along the blade elastic axis. Differentiating Eq. (2.8) with respect to  $x$  gives

$$\begin{Bmatrix} \hat{c}_{x,x} \\ \hat{c}_{\eta,x} \\ \hat{c}_{\zeta,x} \end{Bmatrix} = \begin{Bmatrix} 0 \\ \tau_0 \hat{e}_{\zeta} \\ -\tau_0 \hat{e}_{\eta} \end{Bmatrix} \quad (2.10)$$

where

$$\tau_0 = \beta_{,x} \quad (2.11)$$

#### 2.4.5 Deformed to Undeformed Curvilinear Transformation

The transformation between the deformed curvilinear coordinate system and the undeformed curvilinear coordinate system is defined as:

$$\begin{Bmatrix} \hat{e}'_x \\ \hat{e}'_{\eta} \\ \hat{e}'_{\zeta} \end{Bmatrix} = [T_{dc}] \begin{Bmatrix} \hat{e}_x \\ \hat{e}_{\eta} \\ \hat{e}_{\zeta} \end{Bmatrix} \quad (2.12)$$

and the transformation matrix  $[T_{dc}]$  is given by

$$[T_{dc}] =$$

$$\begin{bmatrix} 1 & 0 & 0 \\ 0 & \cos \theta_x & \sin \theta_x \\ 0 & -\sin \theta_x & \cos \theta_x \end{bmatrix} \begin{bmatrix} \cos \theta_{\eta} & 0 & -\sin \theta_{\eta} \\ 0 & 1 & 0 \\ \sin \theta_{\eta} & 0 & \cos \theta_{\eta} \end{bmatrix} \begin{bmatrix} \cos \theta_{\zeta} & \sin \theta_{\zeta} & 0 \\ -\sin \theta_{\zeta} & \cos \theta_{\zeta} & 0 \\ 0 & 0 & 1 \end{bmatrix} \quad (2.13)$$

where,  $\theta_{\zeta}$ ,  $\theta_{\eta}$ , and  $\theta_x$  are Euler angles about  $\hat{e}_{\zeta}$ , rotated  $\hat{e}_{\eta}$ , and rotated  $\hat{e}_x$ , respectively.

#### 2.4.6 Deformed Curvilinear to Undeformed Element Transformation

The transformation between the deformed curvilinear coordinate system and the undeformed element coordinate system is defined as:

$$\begin{Bmatrix} \hat{c}'_x \\ \hat{c}'_\eta \\ \hat{c}'_\zeta \end{Bmatrix} = [T_{de}] \begin{Bmatrix} \hat{e}_x \\ \hat{e}_y \\ \hat{e}_z \end{Bmatrix} \quad (2.14)$$

where the transformation matrix  $[T_{de}]$  is given by

$$[T_{de}] = [T_{dc}] [T_{ce}] \quad (2.15)$$

This transformation is discussed in greater detail in Chapter 4 and Appendix A.

#### 2.4.7 Preconed, Blade-fixed to Preconed, Pitched, Blade-fixed Transformation

The transformation between the preconed, blade-fixed coordinate system and the preconed, pitched, blade-fixed coordinate system, described in Subsection 2.3.7, is defined as:

$$\begin{Bmatrix} \hat{i}_p \\ \hat{j}_p \\ \hat{k}_p \end{Bmatrix} = [T_{pb}] \begin{Bmatrix} \hat{i}_b \\ \hat{j}_b \\ \hat{k}_b \end{Bmatrix} \quad (2.16)$$

where the transformation matrix  $[T_{pb}]$  is given by

$$[T_{pb}] = \begin{bmatrix} 1 & 0 & 0 \\ 0 & \cos \theta_p & -\sin \theta_p \\ 0 & \sin \theta_p & \cos \theta_p \end{bmatrix} \quad (2.17)$$

### **Chapter III**

#### **STRUCTURAL MODELING OF THE COMPOSITE ROTOR BLADE**

The derivation of the structural operator for the composite rotor blade model is presented in this chapter. Important features for a composite beam, such as transverse shear deformations and out-of-plane warping, are included. The nonlinear kinematics of deformation is based on the mechanics of curved rods (Ref. 97 and Ref. 100, Chap. 8), and the theory of elasticity in curvilinear coordinates (Ref. 98, Chap. 4). The strain components are first derived in a curvilinear coordinate system so that the effects of pretwist are properly accounted for. These strain components are then transformed to a local cartesian coordinate system. The stress-strain relations are assumed to be defined in this local cartesian coordinate system.

The kinematical assumptions used in the derivation of the structural operator are listed below:

1. The deformations of the cross section in its own plane are neglected.
2. The strain components are small compared to unity such that both axial and shear strain components are neglected with respect to unity. However, the relative magnitude between the axial and shear strains is not assumed due to material anisotropy, e.g., squares of shear strains cannot be neglected with respect to axial strains under this assumption[7].
3. Higher order warping terms are neglected.

The derivation of the strain components based on these assumptions is valid for small strains and large deflections. However, quantities such as displacement components (  $u, v, w$  ) and elastic twist angle (  $\phi$  ) do not appear explicitly in the resulting expressions of the strain components. Subsequently, explicit expressions for the strain-displacement relationship are obtained by considering the deformation procedure during the finite rotation from the undeformed to the deformed configuration and using an ordering scheme to systematically identify and neglect higher order nonlinear terms which are generated during the derivation[40,76]. Thus, the final strain-displacement relations are valid for small strains and moderate deflections.

### 3.1 KINEMATICS OF DEFORMATION

The position vector of a point P on the undeformed beam with respect to the hub center is:

$$\mathbf{r}(x, \eta, \zeta) = e_1 \hat{i}_r + h_e \hat{i}_b + x \hat{e}_x + \eta \hat{e}_\eta + \zeta \hat{e}_\zeta \quad (3.1)$$

where  $e_1$  is the blade root offset from the hub center, and  $h_e$  is the offset of the in-board node of the beam finite element from the blade root. The physical interpretation of this position vector is facilitated by considering the geometry described by the combination of Figs. 2.2-2.4. Equation (3.1) can be used to represent the undeformed position vector both for a point on the straight portion as well as a point on the swept tip portion. For a point on the swept tip

element,  $h_c$  equals the length of the straight portion of the blade. The corresponding undeformed based vectors at point P are

$$\mathbf{g}_x = \mathbf{r}_{,x} = \hat{\mathbf{c}}_x - \zeta \tau_0 \hat{\mathbf{e}}_\eta + \eta \tau_0 \hat{\mathbf{e}}_\zeta \quad (3.2a)$$

$$\mathbf{g}_\eta = \mathbf{r}_{,\eta} = \hat{\mathbf{e}}_\eta \quad (3.2b)$$

$$\mathbf{g}_\zeta = \mathbf{r}_{,\zeta} = \hat{\mathbf{e}}_\zeta \quad (3.2c)$$

where the derivatives of the orthonormal triad  $(\hat{\mathbf{e}}_x, \hat{\mathbf{e}}_\eta, \hat{\mathbf{e}}_\zeta)$  are related to the initial twist,  $\tau_0$ , of the undeformed beam by:

$$\begin{Bmatrix} \hat{\mathbf{c}}_{x,x} \\ \hat{\mathbf{c}}_{\eta,x} \\ \hat{\mathbf{c}}_{\zeta,x} \end{Bmatrix} = \begin{bmatrix} 0 & 0 & 0 \\ 0 & 0 & \tau_0 \\ 0 & -\tau_0 & 0 \end{bmatrix} \begin{Bmatrix} \hat{\mathbf{e}}_x \\ \hat{\mathbf{e}}_\eta \\ \hat{\mathbf{e}}_\zeta \end{Bmatrix} \quad (3.3)$$

which can be obtained from Eq. (2.10). Note that if point P is not on the elastic axis, and the initial twist  $\tau_0$  is nonzero, then the base vector  $\mathbf{g}_x$  is neither a unit vector nor orthogonal to the cross-sectional plane of  $\hat{\mathbf{e}}_\eta$  and  $\hat{\mathbf{e}}_\zeta$ , as is evident from Eq. (3.2a).

Since the in-plane deformations of the beam cross-section are neglected, the position vector of the point P in the deformed configuration can be written as:

$$\mathbf{R}(x, \eta, \zeta) = \mathbf{R}_0(x) + \eta \mathbf{E}_\eta + \zeta \mathbf{E}_\zeta + \alpha(x) \Psi(\eta, \zeta) \hat{\mathbf{e}}'_x \quad (3.4)$$

where

$$\mathbf{R}_0(x) = \mathbf{R}(x, 0, 0) \quad (3.5)$$

is the corresponding position vector of a point on the deformed elastic axis; and

$$\mathbf{E}_i(x) = \mathbf{R}_{,i}(x, 0, 0), \quad i = x, \eta, \zeta \quad (3.6)$$

are the base vectors of a point on the deformed elastic axis. In Eq. (3.4), the first three terms represent translations and rotations of the cross-section, while the last term is the out-of-plane warping of the cross-section;  $\alpha(x)$  is the unknown amplitude of warping;  $\Psi(\eta, \zeta)$  is the out-of-plane warping function of the cross-section, with

$$\Psi(0, 0) = \Psi_{, \eta}(0, 0) = \Psi_{, \zeta}(0, 0) = 0 \quad (3.7)$$

due to the definitions of  $\mathbf{R}_0$  and  $\mathbf{E}_i$ , Eqs. (3.5) and (3.6), respectively.

The orthonormal triad of the deformed curvilinear coordinate system,  $(\hat{\mathbf{c}}'_x, \hat{\mathbf{c}}'_\eta, \hat{\mathbf{c}}'_\zeta)$ , can be viewed as a rigidly translated and rotated version of the orthonormal triad of the undeformed curvilinear coordinate system,  $(\hat{\mathbf{c}}_x, \hat{\mathbf{c}}_\eta, \hat{\mathbf{c}}_\zeta)$ . Without loss of generality, the unit vector  $\hat{\mathbf{c}}'_x$  is assumed to be in the direction of  $\mathbf{E}_x$ , i.e., tangent to the deformed elastic axis of the beam; while the orientations of  $\hat{\mathbf{c}}'_\eta$  and  $\hat{\mathbf{c}}'_\zeta$  are nearly that of  $\mathbf{E}_\eta$  and  $\mathbf{E}_\zeta$  but differ on account of the strains[100]. The deformed base vectors of the elastic axis are expressed in terms of  $\hat{\mathbf{c}}'_x, \hat{\mathbf{c}}'_\eta$  and  $\hat{\mathbf{c}}'_\zeta$  by the following definition [Ref. 100, p.356] :

$$\mathbf{E}_x = (1 + \bar{\varepsilon}_{xx}) \hat{\mathbf{c}}'_x \quad (3.8a)$$

$$\mathbf{E}_\eta = 2 \bar{\varepsilon}_{x\eta} \hat{\mathbf{c}}'_x + (1 + \bar{\varepsilon}_{\eta\eta}) \hat{\mathbf{c}}'_\eta + \bar{\varepsilon}_{\eta\zeta} \hat{\mathbf{c}}'_\zeta \quad (3.8b)$$

$$\mathbf{E}_\zeta = 2 \bar{\varepsilon}_{x\zeta} \hat{\mathbf{c}}'_x + \bar{\varepsilon}_{\eta\zeta} \hat{\mathbf{c}}'_\eta + (1 + \bar{\varepsilon}_{\zeta\zeta}) \hat{\mathbf{c}}'_\zeta \quad (3.8c)$$

With the assumption that in-plane deformations of the beam cross-section are neglected, i.e.,

$$\bar{\epsilon}_{\eta\eta} = \bar{\epsilon}_{\zeta\zeta} = \bar{\epsilon}_{\eta\zeta} = 0 \quad (3.9)$$

the base vectors of the deformed elastic axis become:

$$\mathbf{E}_x = (1 + \bar{\epsilon}_{xx}) \hat{\mathbf{e}}'_x \quad (3.10a)$$

$$\mathbf{E}_\eta = 2 \bar{\epsilon}_{x\eta} \hat{\mathbf{e}}'_x + \hat{\mathbf{e}}'_\eta = \bar{\gamma}_{x\eta} \hat{\mathbf{e}}'_x + \hat{\mathbf{e}}'_\eta \quad (3.10b)$$

$$\mathbf{E}_\zeta = 2 \bar{\epsilon}_{x\zeta} \hat{\mathbf{e}}'_x + \hat{\mathbf{e}}'_\zeta = \bar{\gamma}_{x\zeta} \hat{\mathbf{e}}'_x + \hat{\mathbf{e}}'_\zeta \quad (3.10c)$$

where it will be shown later that  $\bar{\epsilon}_{xx}$ ,  $\bar{\gamma}_{x\eta}$  and  $\bar{\gamma}_{x\zeta}$  are the axial and the transverse shear strains, respectively, at the elastic axis. Equations (3.10) imply that cross sections which are normal to the elastic axis before deformation ( e.g.,  $\hat{\mathbf{e}}'_\eta$ - $\hat{\mathbf{e}}'_\zeta$  plane ) will no longer be normal to the elastic axis after deformation ( e.g.,  $\mathbf{E}_\eta$ - $\mathbf{E}_\zeta$  plane is not normal to  $\mathbf{E}_x$  ) due to the presence of transverse shear strains. The deformed base vectors at point P are:

$$\begin{aligned} \mathbf{G}_x = \mathbf{R}_{,x} &= \mathbf{E}_x + \eta \mathbf{E}_{\eta,x} + \zeta \mathbf{E}_{\zeta,x} + \alpha_{,x} \Psi \hat{\mathbf{e}}'_x + \alpha \Psi \hat{\mathbf{e}}'_{x,x} \\ &= [(1 + \bar{\epsilon}_{xx}) + \eta(2\bar{\epsilon}_{x\eta,x} - \kappa_\eta) + \zeta(2\bar{\epsilon}_{x\zeta,x} - \kappa_\zeta) + \alpha_{,x} \Psi] \hat{\mathbf{e}}'_x \\ &\quad + [2\eta\kappa_\eta \bar{\epsilon}_{x\eta} + \zeta(2\kappa_\eta \bar{\epsilon}_{x\zeta} - \tau) + \alpha \Psi \kappa_\eta] \hat{\mathbf{e}}'_\eta \\ &\quad + [\eta(2\kappa_\zeta \bar{\epsilon}_{x\eta} + \tau) + 2\zeta\kappa_\zeta \bar{\epsilon}_{x\zeta} + \alpha \Psi \kappa_\zeta] \hat{\mathbf{e}}'_\zeta \end{aligned} \quad (3.11a)$$

$$\begin{aligned} \mathbf{G}_\eta = \mathbf{R}_{,\eta} &= \mathbf{E}_\eta + \alpha \Psi_{,\eta} \hat{\mathbf{e}}'_x \\ &= (2\bar{\epsilon}_{x\eta} + \alpha \Psi_{,\eta}) \hat{\mathbf{e}}'_x + \hat{\mathbf{e}}'_\eta \end{aligned} \quad (3.11b)$$

$$\begin{aligned}
\mathbf{G}_\zeta &= \mathbf{R}_{,\zeta} = \mathbf{E}_\zeta + \alpha \Psi_{,\zeta} \hat{\mathbf{c}}'_x \\
&= (2\bar{\varepsilon}_{x\zeta} + \alpha \Psi_{,\zeta}) \hat{\mathbf{c}}'_x + \hat{\mathbf{c}}'_\zeta
\end{aligned} \tag{3.11c}$$

where the derivatives of the orthonormal triad  $(\hat{\mathbf{e}}'_x, \hat{\mathbf{e}}'_\eta, \hat{\mathbf{e}}'_\zeta)$  are related to the curvatures,  $\kappa_\eta$ ,  $\kappa_\zeta$ , and twist,  $\tau$ , of the deformed beam by:

$$\begin{Bmatrix} \hat{\mathbf{c}}'_{x,x} \\ \hat{\mathbf{c}}'_{\eta,x} \\ \hat{\mathbf{c}}'_{\zeta,x} \end{Bmatrix} = \begin{bmatrix} 0 & \kappa_\eta & \kappa_\zeta \\ -\kappa_\eta & 0 & \tau \\ -\kappa_\zeta & -\tau & 0 \end{bmatrix} \begin{Bmatrix} \hat{\mathbf{e}}'_x \\ \hat{\mathbf{e}}'_\eta \\ \hat{\mathbf{e}}'_\zeta \end{Bmatrix} \tag{3.12}$$

## 3.2 STRAIN COMPONENTS

The set of coordinates  $(x, \eta, \zeta)$  are, in general, non-orthogonal curvilinear coordinates since the base vector  $\mathbf{g}_x$ , expressed in Eq. (3.2a) is neither a unit vector nor orthogonal to the base vectors  $\mathbf{g}_\eta$  and  $\mathbf{g}_\zeta$  for an arbitrary point on the beam with nonzero initial twist  $\tau_0$ . In the derivation that follows, the notation  $(x_1, x_2, x_3)$  will be used in place of  $(x, \eta, \zeta)$  whenever convenient.

### 3.2.1 Strain Components in Curvilinear Coordinates

The components of the strain tensor in the curvilinear coordinates are defined by (Ref. 97 and Ref. 98, p. 113):

$$f_{ij} = \frac{1}{2} (\mathbf{G}_i \cdot \mathbf{G}_j) - (\mathbf{g}_i \cdot \mathbf{g}_j), \quad i, j = x, \eta, \zeta \tag{3.13}$$

Combining Eqs. (3.2) and (3.11) with Eq. (3.13) gives:

$$f_{xx} = \bar{\epsilon}_{xx} + \eta(2\bar{\epsilon}_{x\eta,x} - \kappa_\eta) + \zeta(2\bar{\epsilon}_{x\zeta,x} - \kappa_\zeta) + \alpha_{,x}\Psi + \frac{1}{2}(\eta^2 + \zeta^2)(\tau^2 - \tau_0^2) \quad (3.14a)$$

$$f_{x\eta} = f_{\eta x} = \bar{\epsilon}_{x\eta} + \frac{1}{2}[\alpha\Psi_{,\eta} - \zeta(\tau - \tau_0)] \quad (3.14b)$$

$$f_{x\zeta} = f_{\zeta x} = \bar{\epsilon}_{x\zeta} + \frac{1}{2}[\alpha\Psi_{,\zeta} + \eta(\tau - \tau_0)] \quad (3.14c)$$

$$f_{\eta\eta} \simeq 0 \quad (3.14d)$$

$$f_{\zeta\zeta} \simeq 0 \quad (3.14e)$$

$$f_{\eta\zeta} = f_{\zeta\eta} \simeq 0 \quad (3.14f)$$

In the derivation of Eqs. (3.14), both axial and shear strain components were neglected with respect to unity, but no assumption was made regarding the relative magnitude of axial and shear strains[7]. Higher order terms containing warping were also neglected in the derivation presented in this section.

### 3.2.2 Strain Components in Local Cartesian Coordinates

Define a system of local cartesian coordinates  $(y_1, y_2, y_3)$  at point P with its unit vectors parallel to the orthonormal triad  $(\hat{e}_x, \hat{e}_\eta, \hat{e}_\zeta)$  of the cross section, respectively. The stress-strain relations of the beam are assumed to be given in the local cartesian coordinate system. To find the transformation between the curvilinear coordinates  $(x_1, x_2, x_3)$  and the local cartesian coordinates  $(y_1, y_2, y_3)$ , consider

$$\hat{\mathbf{c}}_j = \frac{\partial \mathbf{r}}{\partial y_j} = \frac{\partial \mathbf{r}}{\partial x_i} \frac{\partial x_i}{\partial y_j} = \mathbf{g}_i \frac{\partial x_i}{\partial y_j} \quad (3.15)$$

$$\mathbf{g}_k \cdot \hat{\mathbf{c}}_j = (\mathbf{g}_k \cdot \mathbf{g}_i) \frac{\partial x_i}{\partial y_j} \quad (3.16)$$

Therefore, the transformation relation,  $\frac{\partial x_i}{\partial y_j}$ , can be expressed in matrix form

as:

$$\begin{aligned} \left[ \frac{\partial x_i}{\partial y_j} \right] &= [\mathbf{g}_k \cdot \mathbf{g}_i]^{-1} [\mathbf{g}_k \cdot \hat{\mathbf{c}}_j] \\ &= \begin{bmatrix} 1 & \zeta\tau_0 & -\eta\tau_0 \\ \zeta\tau_0 & 1 + \zeta^2\tau_0^2 & -\eta\zeta\tau_0^2 \\ -\eta\tau_0 & -\eta\zeta\tau_0^2 & 1 + \eta^2\tau_0^2 \end{bmatrix} \begin{bmatrix} 1 & -\zeta\tau_0 & \eta\tau_0 \\ 0 & 1 & 0 \\ 0 & 0 & 1 \end{bmatrix} \\ &= \begin{bmatrix} 1 & 0 & 0 \\ \zeta\tau_0 & 1 & 0 \\ -\eta\tau_0 & 0 & 1 \end{bmatrix} \end{aligned} \quad (3.17)$$

where

$$[\mathbf{g}_k \cdot \mathbf{g}_i] = \begin{bmatrix} 1 + (\eta^2 + \zeta^2)\tau_0^2 & -\zeta\tau_0 & \eta\tau_0 \\ -\zeta\tau_0 & 1 & 0 \\ \eta\tau_0 & 0 & 1 \end{bmatrix} \quad (3.18)$$

The strain tensor defined in the local cartesian coordinates,  $\varepsilon_{ij}$ , is obtained from (Ref. 97 and Ref. 98, p. 118):

$$\begin{aligned}
\varepsilon_{ij} &= \frac{1}{2} \left( \frac{\partial \mathbf{R}}{\partial y_i} \cdot \frac{\partial \mathbf{R}}{\partial y_j} - \frac{\partial \mathbf{r}}{\partial y_i} \cdot \frac{\partial \mathbf{r}}{\partial y_j} \right) \\
&= \frac{1}{2} \sum_{k=1}^3 \sum_{l=1}^3 \left( \frac{\partial \mathbf{R}}{\partial x_k} \cdot \frac{\partial \mathbf{R}}{\partial x_l} - \frac{\partial \mathbf{r}}{\partial x_k} \cdot \frac{\partial \mathbf{r}}{\partial x_l} \right) \frac{\partial x_k}{\partial y_i} \frac{\partial x_l}{\partial y_j} \\
&= \sum_{k=1}^3 \sum_{l=1}^3 \frac{\partial x_k}{\partial y_i} \frac{\partial x_l}{\partial y_j} f_{kl}
\end{aligned} \tag{3.19}$$

Substituting Eq. (3.17) into Eq. (3.19), the transformation between the strain components in the local cartesian coordinate system,  $\varepsilon_{ij}$ , and the strain components in the curvilinear coordinate system,  $f_{ij}$ , can be written as:

$$\varepsilon_{xx} = f_{xx} + 2\zeta\tau_0 f_{x\eta} - 2\eta\tau_0 f_{x\zeta} \tag{3.20a}$$

$$\varepsilon_{x\eta} = \varepsilon_{\eta x} = f_{x\eta} \tag{3.20b}$$

$$\varepsilon_{x\zeta} = \varepsilon_{\zeta x} = f_{x\zeta} \tag{3.20c}$$

$$\varepsilon_{\eta\eta} \simeq 0 \tag{3.20d}$$

$$\varepsilon_{\zeta\zeta} \simeq 0 \tag{3.20e}$$

$$\varepsilon_{\eta\zeta} = \varepsilon_{\zeta\eta} \simeq 0 \tag{3.20f}$$

Combining Eqs. (3.14) with Eqs. (3.20), the strain components in the local cartesian coordinates become:

$$\begin{aligned}
\varepsilon_{xx} &= \bar{\varepsilon}_{xx} - \eta\kappa_\eta - \zeta\kappa_\zeta + \alpha_{,x}\Psi + \alpha\tau_0(\zeta\Psi_{,\eta} - \eta\Psi_{,\zeta}) \\
&\quad + \frac{1}{2}(\eta^2 + \zeta^2)(\tau - \tau_0)^2 + \eta(\bar{v}_{x\eta,x} - \tau_0\bar{v}_{x\zeta}) \\
&\quad + \zeta(\bar{v}_{x\zeta,x} + \tau_0\bar{v}_{x\eta})
\end{aligned} \tag{3.21a}$$

$$\gamma_{x\eta} = \bar{\gamma}_{x\eta} + \alpha \Psi_{,\eta} - \zeta(\tau - \tau_0) \quad (3.21b)$$

$$\gamma_{x\zeta} = \bar{\gamma}_{x\zeta} + \alpha \Psi_{,\zeta} + \eta(\tau - \tau_0) \quad (3.21c)$$

$$\varepsilon_{\eta\eta} \simeq \varepsilon_{\zeta\zeta} \simeq \gamma_{\eta\zeta} \simeq 0 \quad (3.21d-f)$$

where

$$\gamma_{x\eta} \equiv 2 \varepsilon_{x\eta} \quad , \quad \gamma_{x\zeta} \equiv 2 \varepsilon_{x\zeta} \quad , \quad \gamma_{\eta\zeta} \equiv 2 \varepsilon_{\eta\zeta} \quad (3.22)$$

$$\bar{\gamma}_{x\eta} \equiv 2 \bar{\varepsilon}_{x\eta} \quad , \quad \bar{\gamma}_{x\zeta} \equiv 2 \bar{\varepsilon}_{x\zeta} \quad , \quad \bar{\gamma}_{\eta\zeta} \equiv 2 \bar{\varepsilon}_{\eta\zeta} \quad (3.23)$$

The strain components in Eqs. (3.21a-c) are valid for small strains and large deflections since the kinematical assumptions used in the derivation of Eqs. (3.21) are only on strains and warping, and not on displacements and rotations. These strain components are expressed in terms of seven unknown functions of the axial coordinate  $x$  :  $\bar{\varepsilon}_{xx}$ ,  $\bar{\gamma}_{x\eta}$ ,  $\bar{\gamma}_{x\zeta}$ ,  $\kappa_\eta$ ,  $\kappa_\zeta$ ,  $\tau$  and  $\alpha$ . The first three are the axial and transverse shear strains, respectively, at the elastic axis, since

$$\varepsilon_{xx}(x, 0, 0) = \bar{\varepsilon}_{xx} \quad (3.24a)$$

$$\gamma_{x\eta}(x, 0, 0) = \bar{\gamma}_{x\eta} \quad (3.24b)$$

$$\gamma_{x\zeta}(x, 0, 0) = \bar{\gamma}_{x\zeta} ; \quad (3.24c)$$

and the next three are the curvatures and twist, respectively, of the deformed beam; the last one,  $\alpha$ , is the amplitude of warping.

Equations (3.21) can be compared directly with the strain components derived by Hodges[43] and Bauchau and Hong[7]. The beam theories derived

by Hodges[43] and by Bauchau and Hong[7] are valid for small strains and large deflections, however the former is primarily for isotropic beams since transverse shears are not included, while the latter is a composite beam theory. When the warping amplitude,  $\alpha$ , is replaced by  $(\tau - \tau_0)$ , Eqs. (3.21) agree with Eqs. (5) of Hodges[43] except that Eqs. (3.21) have additional terms due to transverse shear. If bending related warpings ( $W_2, W_3$  in Ref. 7, Eqs. (29-31)) are excluded, then Eqs. (3.21) agree with Eqs. (29-31) of Bauchau and Hong[7] except the shear strain terms in the axial strain expression. This is due to a slight difference in the orientation of the orthonormal triad ( $\hat{e}'_x, \hat{e}'_\eta, \hat{e}'_\zeta$ ) in the deformed configuration. In this development,  $\hat{e}'_x$  is in the direction of  $\mathbf{E}_x$ , i.e., tangent to the deformed elastic axis, while  $\hat{e}'_\eta$  and  $\hat{e}'_\zeta$  are not in the directions of  $\mathbf{E}_\eta$  and  $\mathbf{E}_\zeta$ , respectively, because of the transverse shear strains. On the other hand, Bauchau and Hong chose to align  $\hat{e}'_\eta$  and  $\hat{e}'_\zeta$  with  $\mathbf{E}_\eta$  and  $\mathbf{E}_\zeta$ , respectively, due to the assumption that the cross section does not deform in its own plane, while  $\hat{e}'_x$  is not in the direction of  $\mathbf{E}_x$  due to transverse shear strains. When transverse shear strains of the elastic axis are set to zero, then both Eq. (3.21a) and Bauchau and Hong's Eq. (29) reduce to Eq. (5) of Hodges.

Note that the term  $\frac{1}{2}(\eta^2 + \zeta^2)(\tau - \tau_0)^2$ , which represents a nonlinear shear strain coupling term in the axial strain expression, is retained in this development due to an assumption associated with material anisotropy. However, this term has also been shown to be important for the analysis of pretwisted isotropic beams subjected to axial loads[51,40,42].

### 3.2.3 *Explicit Strain-Displacement Relations*

For aeroelastic applications, it is desirable to express the strain components in terms of the displacement components ( $u, v, w$ ) of the elastic axis and the elastic twist angle ( $\phi$ ) so that the structural model can be conveniently combined with the inertial and aerodynamic models. To accomplish this, four of the seven unknowns in Eqs. (3.21) have to be eliminated by relating them to  $u, v, w$ , and  $\phi$ .

The displacement vector of a point on the elastic axis is defined as:

$$\mathbf{u} = \mathbf{R}_0 - \mathbf{r}_0 \quad (3.25)$$

where

$$\mathbf{r}_0(x) = \mathbf{r}(x, 0, 0) \quad (3.26)$$

Writing the displacement vector,  $\mathbf{u}$ , in the undeformed element coordinate system as:

$$\mathbf{u} = u \hat{\mathbf{e}}_x + v \hat{\mathbf{e}}_y + w \hat{\mathbf{e}}_z \quad (3.27)$$

Combining Eq. (3.27) with Eq. (3.25) gives:

$$\mathbf{R}_0 = \mathbf{r}_0 + u \hat{\mathbf{e}}_x + v \hat{\mathbf{e}}_y + w \hat{\mathbf{e}}_z \quad (3.28)$$

Differentiating Eq. (3.28) with respect to  $x$  gives:

$$\mathbf{E}_x = (1 + u_{,x}) \hat{\mathbf{e}}_x + v_{,x} \hat{\mathbf{e}}_y + w_{,x} \hat{\mathbf{e}}_z \quad (3.29)$$

The magnitude of  $\mathbf{E}_x$  is, from Eq. (3.10a) and (3.29):

$$|\mathbf{E}_x|^2 = (1 + u_{,x})^2 + (v_{,x})^2 + (w_{,x})^2 = (1 + \bar{\epsilon}_{xx})^2 \quad (3.30)$$

The term  $\bar{\epsilon}_{xx}^2$  is neglected with respect to the term  $2\bar{\epsilon}_{xx}$  due to the small strain assumption. Also, the term  $(u_{,x})^2$  is neglected compared to the term  $2u_{,x}$  by applying the ordering scheme since  $u_{,x}$  is of order  $\epsilon^2$ . Therefore, Eq. (3.30) is reduced to

$$\bar{\epsilon}_{xx} = u_{,x} + \frac{1}{2}(v_{,x})^2 + \frac{1}{2}(w_{,x})^2 \quad (3.31)$$

The deformed curvatures and twist can be related to the Euler angles  $(\theta_x, \theta_\eta, \theta_\zeta)$  by differentiating Eq. (2.12) with respect to  $x$ , and combining the resulting expression with Eqs. (3.3) and (3.12):

$$\begin{aligned} \begin{Bmatrix} \hat{c}'_{x,x} \\ \hat{c}'_{\eta,x} \\ \hat{c}'_{\zeta,x} \end{Bmatrix} &= ([T_{dc}]_{,x} + [T_{dc}][\kappa_0]) \begin{Bmatrix} \hat{e}_x \\ \hat{e}_\eta \\ \hat{e}_\zeta \end{Bmatrix} \\ &= ([T_{dc}]_{,x} + [T_{dc}][\kappa_0])[T_{dc}]^T \begin{Bmatrix} \hat{e}'_x \\ \hat{e}'_\eta \\ \hat{e}'_\zeta \end{Bmatrix} \\ &= [\kappa] \begin{Bmatrix} \hat{e}'_x \\ \hat{e}'_\eta \\ \hat{e}'_\zeta \end{Bmatrix} \end{aligned} \quad (3.32)$$

where

$$[\kappa_0] \equiv \begin{bmatrix} 0 & 0 & 0 \\ 0 & 0 & \tau_0 \\ 0 & -\tau_0 & 0 \end{bmatrix} \quad (3.33)$$

$$[\kappa] \equiv \begin{bmatrix} 0 & \kappa_\eta & \kappa_\zeta \\ -\kappa_\eta & 0 & \tau \\ -\kappa_\zeta & -\tau & 0 \end{bmatrix} \quad (3.34)$$

It follows that,

$$[\kappa] = ([T_{dc}]_{,x} + [T_{dc}][\kappa_0])[T_{dc}]^T \quad (3.35)$$

Writing the deformed base vector of the elastic axis in the undeformed curvilinear coordinate system, using Eqs. (3.29), (2.8) and (2.9), yields:

$$\mathbf{E}_x = (1 + u_{,x})\hat{\mathbf{e}}_x + (v_{,x} \cos \beta + w_{,x} \sin \beta)\hat{\mathbf{e}}_\eta + (w_{,x} \cos \beta - v_{,x} \sin \beta)\hat{\mathbf{e}}_\zeta \quad (3.36)$$

Recall that the transformation between the triad  $(\hat{\mathbf{e}}'_x, \hat{\mathbf{e}}'_\eta, \hat{\mathbf{e}}'_\zeta)$  of the deformed curvilinear coordinate system and the triad  $(\hat{\mathbf{e}}_x, \hat{\mathbf{e}}_\eta, \hat{\mathbf{e}}_\zeta)$  of the undeformed curvilinear coordinate system is a rigid-body rotation, defined by:

$$\begin{Bmatrix} \hat{\mathbf{e}}'_x \\ \hat{\mathbf{e}}'_\eta \\ \hat{\mathbf{e}}'_\zeta \end{Bmatrix} = [T_{dc}] \begin{Bmatrix} \hat{\mathbf{e}}_x \\ \hat{\mathbf{e}}_\eta \\ \hat{\mathbf{e}}_\zeta \end{Bmatrix} \quad (2.12)$$

where the transformation matrix,  $[T_{dc}]$ , is given by:

$$[T_{dc}] = \begin{bmatrix} 1 & 0 & 0 \\ 0 & \cos \theta_x & \sin \theta_x \\ 0 & -\sin \theta_x & \cos \theta_x \end{bmatrix} \begin{bmatrix} \cos \theta_\eta & 0 & -\sin \theta_\eta \\ 0 & 1 & 0 \\ \sin \theta_\eta & 0 & \cos \theta_\eta \end{bmatrix} \begin{bmatrix} \cos \theta_\zeta & \sin \theta_\zeta & 0 \\ -\sin \theta_\zeta & \cos \theta_\zeta & 0 \\ 0 & 0 & 1 \end{bmatrix} \quad (2.13)$$

and the finite rotation is described by three Euler angles  $(\theta_x, \theta_\eta, \theta_\zeta)$ . The sequence of rotation is assumed to be  $\theta_\zeta, \theta_\eta$  and  $\theta_x$  about  $\hat{\mathbf{e}}_\zeta$ , rotated  $\hat{\mathbf{e}}_\eta$  and rotated  $\hat{\mathbf{e}}_x$ , respectively. It should be noted that other sequences of rotation are

also possible, and the form of the final set of equations is dependent on the choice of the sequence of rotations. Without loss of generality, assume that the unit vector  $\hat{e}'_x$  is carried to the direction of  $E_x$ , i.e., tangent to the deformed elastic axis of the beam. Based on these assumptions and Eq. (3.36), the deformation procedure can be described as follows (see Fig. 3.1). Consider an element  $dx$ , on the undeformed elastic axis of the beam. The triad  $(\hat{e}'_x, \hat{e}'_\eta, \hat{e}'_\zeta)$  is attached to the element and initially aligned with the triad  $(\hat{c}_x, \hat{c}_\eta, \hat{c}_\zeta)$  of the undeformed curvilinear coordinate system. First, the element is carried by a rigid-body translation, which does not appear in Fig. 3.1, and then stretched by an amount  $u_{,x}dx$ . Next, the element is rotated by  $\theta_\zeta$  about  $\hat{e}_\zeta$  while the tip of the element moves a distance  $(v_{,x} \cos \beta + w_{,x} \sin \beta)dx$  in the  $\hat{c}_\eta$  direction. Then, the element is rotated by  $\theta_\eta$  about the rotated  $\hat{e}_\eta$  while the tip of the element moves a distance  $(w_{,x} \cos \beta - v_{,x} \sin \beta)dx$  in the  $\hat{e}_\zeta$  direction. Finally, the element is rotated by  $\theta_x$  about the rotated  $\hat{e}_x$ , which is also its own axis. It is assumed that transverse shear deformations and out-of-plane warping occur after the deformation sequence described above.

The following trigonometric relations can be obtained from Fig. 3.1 :

$$\sin \theta_\eta = \frac{v_{,x} \sin \beta - w_{,x} \cos \beta}{\sqrt{(1 + u_{,x})^2 + (v_{,x} \cos \beta + w_{,x} \sin \beta)^2 + (w_{,x} \cos \beta - v_{,x} \sin \beta)^2}}$$

$$\cos \theta_\eta = \frac{\sqrt{(1 + u_{,x})^2 + (v_{,x} \cos \beta + w_{,x} \sin \beta)^2}}{\sqrt{(1 + u_{,x})^2 + (v_{,x} \cos \beta + w_{,x} \sin \beta)^2 + (w_{,x} \cos \beta - v_{,x} \sin \beta)^2}}$$

$$\sin \theta_{\zeta} = \frac{v_{,x} \cos \beta + w_{,x} \sin \beta}{\sqrt{(1 + u_{,x})^2 + (v_{,x} \cos \beta + w_{,x} \sin \beta)^2}} \quad (3.37)$$

$$\cos \theta_{\zeta} = \frac{1 + u_{,x}}{\sqrt{(1 + u_{,x})^2 + (v_{,x} \cos \beta + w_{,x} \sin \beta)^2}}$$

The expressions given in Eqs.(3.37) can be simplified to second order by using the ordering scheme described in Chapter 2:

$$\sin \theta_{\eta} \simeq v_{,x} \sin \beta - w_{,x} \cos \beta, \quad \cos \theta_{\eta} \simeq 1 \quad (3.38a)$$

$$\sin \theta_{\zeta} \simeq v_{,x} \cos \beta + w_{,x} \sin \beta, \quad \cos \theta_{\zeta} \simeq 1 \quad (3.38b)$$

Since the Euler angles  $\theta_x, \theta_{\eta}$  and  $\theta_{\zeta}$  are of order  $\varepsilon$  for moderate rotation, and the typical magnitude of the parameter  $\varepsilon$  is  $0.1 \leq \varepsilon \leq 0.2$ , therefore combining Eqs. (3.38) with the small angle assumption gives:

$$\sin \theta_x \simeq \theta_x \equiv \phi, \quad \cos \theta_x \simeq 1 \quad (3.39a)$$

$$\sin \theta_{\eta} \simeq \theta_{\eta} \simeq v_{,x} \sin \beta - w_{,x} \cos \beta, \quad \cos \theta_{\eta} \simeq 1 \quad (3.39b)$$

$$\sin \theta_{\zeta} \simeq \theta_{\zeta} \simeq v_{,x} \cos \beta + w_{,x} \sin \beta, \quad \cos \theta_{\zeta} \simeq 1 \quad (3.39c)$$

where the torsional twist angle  $\theta_x$  is replaced by  $\phi$ , in order to be consistent with the usual notation in the literature.

Equations (3.39) can be used in the derivation of the relationships between the curvature quantities  $(\kappa_{\eta}, \kappa_{\zeta}, \tau)$  of the deformed beam and the displacement variables  $(u, v, w, \phi)$ . Combining Eqs. (2.13), (3.33), (3.34) and (3.39) with

Eq. (3.35) and applying the ordering scheme, the explicit expressions for the deformed curvatures and twist are given by:

$$\kappa_\eta = v_{,xx} \cos(\beta + \phi) + w_{,xx} \sin(\beta + \phi) \quad (3.40a)$$

$$\kappa_\zeta = -v_{,xx} \sin(\beta + \phi) + w_{,xx} \cos(\beta + \phi) \quad (3.40b)$$

$$\tau = \tau_0 + \phi_{,x} + \phi_0 \quad (3.40c)$$

where

$$\phi_0 = (-v_{,x} \sin \beta + w_{,x} \cos \beta)(v_{,xx} \cos \beta + w_{,xx} \sin \beta) \quad (3.41)$$

The small angle assumption for  $\phi$ :

$$\cos(\beta + \phi) \simeq \cos \beta - \phi \sin \beta \quad (3.42a)$$

$$\sin(\beta + \phi) \simeq \sin \beta + \phi \cos \beta \quad (3.42b)$$

has also been used in the derivation of Eqs. (3.40).

The non-zero strain components in Eqs. (3.21) can now be expressed in terms of  $u, v, w$  and  $\phi$  by substituting Eqs. (3.31) and (3.40a-c) into Eqs. (3.21a-c) and applying the ordering scheme. The resulting expressions are:

$$\begin{aligned} \varepsilon_{xx} = & u_{,x} + \frac{1}{2}(v_{,x})^2 + \frac{1}{2}(w_{,x})^2 - v_{,xx} [\eta \cos(\beta + \phi) - \zeta \sin(\beta + \phi)] \\ & - w_{,xx} [\eta \sin(\beta + \phi) + \zeta \cos(\beta + \phi)] + \frac{1}{2}(\eta^2 + \zeta^2)(\phi_{,x})^2 \end{aligned} \quad (3.43a)$$

$$\begin{aligned} & + \alpha_{,x} \Psi + \alpha \tau_0 (\zeta \Psi_{,\eta} - \eta \Psi_{,\zeta}) \\ & + \eta (\bar{\gamma}_{x\eta,x} - \tau_0 \bar{\gamma}_{x\zeta}) + \zeta (\bar{\gamma}_{x\zeta,x} + \tau_0 \bar{\gamma}_{x\eta}) \end{aligned}$$

$$\gamma_{x\eta} = \bar{\gamma}_{x\eta} + \alpha \Psi_{,\eta} - \zeta (\phi_{,x} + \phi_0) \quad (3.43b)$$

$$\underline{\gamma_{x\zeta}} = \underline{\bar{\gamma}_{x\zeta}} + \alpha \Psi_{,\zeta} + \eta(\phi_{,x} + \phi_0) \quad (3.43c)$$

The underlined term in Eq. (3.43a) could have been neglected when using a strict interpretation of the ordering scheme. However, as mentioned in the previous subsection, this term represents a nonlinear shear strain coupling term in the axial strain expression, and is retained based on the kinematical assumption that the relative magnitude between the axial and shear strains is not assumed due to material anisotropy. Furthermore, this nonlinear tension-torsion coupling term has been shown to be important for the analysis of pre-twisted isotropic beam under axial loading[40,42]. In the derivation of the structural operator, presented in the next chapter, terms associated with this underlined term will be retained or neglected in the same way as the terms which are one order lower than these terms; when the ordering scheme is applied.

The seven unknown functions of the axial coordinate,  $x$ , in the strain-displacement relationships, Eqs. (3.43a-c), become:  $u, v, w, \phi, \alpha, \bar{\epsilon}_{x\eta}$ , and  $\bar{\epsilon}_{x\zeta}$ . It is important to note that, Eqs. (3.43) are now valid for small strains and moderate deflections because the ordering scheme has been used.

### 3.3 CONSTITUTIVE RELATIONS

The constitutive relations are defined based on the following assumptions:

1. The material properties of the beam are linearly elastic and generally orthotropic, i.e., orthotropic material whose material principal axes are not aligned with the coordinate axes.

2. The stress-strain relations for the beam are defined in the local cartesian coordinate system, which has been defined in the development of the strain-displacement relationships.
3. The stress components in the cross-section are equal to zero, i.e.,  $\sigma_{\eta\eta} = \sigma_{\zeta\zeta} = \sigma_{\eta\zeta} = 0$  . This assumption is commonly used in classical isotropic beam theory[94], as well as composite beam theories for thin-walled box beams[5,7]; it is also used here because helicopter rotor blades are typically thin-walled box beams.

For a generally orthotropic material, the stiffness and compliance matrices can be fully populated containing up to 21 different coefficients, and therefore the material behaves in an anisotropic manner. These coefficients are functions of the nine orthotropic material constants and three Euler angles, which are used to relate the material principal axes with the coordinate axes of the beam. Expressions for these coefficients in terms of the orthotropic material properties and the Euler angles are given in Refs. 53 and 95.

The anisotropic stress-strain relations for a linearly elastic body are written as:

$$\begin{bmatrix} \sigma_{xx} \\ \sigma_{\eta\eta} \\ \sigma_{\zeta\zeta} \\ \sigma_{\eta\zeta} \\ \sigma_{x\zeta} \\ \sigma_{x\eta} \end{bmatrix} = \begin{bmatrix} C_{11} & C_{12} & C_{13} & C_{14} & C_{15} & C_{16} \\ C_{12} & C_{22} & C_{23} & C_{24} & C_{25} & C_{26} \\ C_{13} & C_{23} & C_{33} & C_{34} & C_{35} & C_{36} \\ C_{14} & C_{24} & C_{34} & C_{44} & C_{45} & C_{46} \\ C_{15} & C_{25} & C_{35} & C_{45} & C_{55} & C_{56} \\ C_{16} & C_{26} & C_{36} & C_{46} & C_{56} & C_{66} \end{bmatrix} \begin{bmatrix} \varepsilon_{xx} \\ \varepsilon_{\eta\eta} \\ \varepsilon_{\zeta\zeta} \\ \gamma_{\eta\zeta} \\ \gamma_{x\zeta} \\ \gamma_{x\eta} \end{bmatrix} \quad (3.44)$$

where  $C_{ij}$  ( $i, j = 1, 2, 3, 4, 5, 6$ ) are the stiffness coefficients. It is important to note that the stress components,  $\sigma_{ij}$  , and the strain components,  $\varepsilon_{ij}$  , reduce to

the engineering stress and strain measures due to the small strain assumption used in the derivations (Ref. 2, p.381).

Equation (3.44) can be written in partitioned form as:

$$\begin{Bmatrix} \{\sigma_b\} \\ \{\sigma_s\} \end{Bmatrix} = \begin{bmatrix} [C_{bb}] & [C_{bs}] \\ [C_{sb}] & [C_{ss}] \end{bmatrix} \begin{Bmatrix} \{\varepsilon_b\} \\ \{\varepsilon_s\} \end{Bmatrix} \quad (3.45)$$

where

$$\{\sigma_b\} = \begin{Bmatrix} \sigma_{xx} \\ \sigma_{x\zeta} \\ \sigma_{x\eta} \end{Bmatrix} ; \quad \{\varepsilon_b\} = \begin{Bmatrix} \varepsilon_{xx} \\ \gamma_{x\zeta} \\ \gamma_{x\eta} \end{Bmatrix} \quad (3.46a, b)$$

$$\{\sigma_s\} = \begin{Bmatrix} \sigma_{\eta\eta} \\ \sigma_{\zeta\zeta} \\ \sigma_{\eta\zeta} \end{Bmatrix} ; \quad \{\varepsilon_s\} = \begin{Bmatrix} \varepsilon_{\eta\eta} \\ \varepsilon_{\zeta\zeta} \\ \gamma_{\eta\zeta} \end{Bmatrix} \quad (3.46c, d)$$

$$[C_{bb}] = \begin{bmatrix} C_{11} & C_{15} & C_{16} \\ C_{15} & C_{55} & C_{56} \\ C_{16} & C_{56} & C_{66} \end{bmatrix} ; \quad [C_{ss}] = \begin{bmatrix} C_{22} & C_{23} & C_{24} \\ C_{23} & C_{33} & C_{34} \\ C_{24} & C_{34} & C_{44} \end{bmatrix} \quad (3.46e, f)$$

$$[C_{bs}] = [C_{sb}]^T = \begin{bmatrix} C_{12} & C_{13} & C_{14} \\ C_{25} & C_{35} & C_{45} \\ C_{26} & C_{36} & C_{46} \end{bmatrix} \quad (3.46g)$$

Using the assumption that stresses in the cross-section are equal to zero ( $\sigma_{\eta\eta} = \sigma_{\zeta\zeta} = \sigma_{\eta\zeta} = 0$ ), Eq. (3.45) becomes:

$$\begin{Bmatrix} \{\sigma_b\} \\ \{0\} \end{Bmatrix} = \begin{bmatrix} [C_{bb}] & [C_{bs}] \\ [C_{sb}] & [C_{ss}] \end{bmatrix} \begin{Bmatrix} \{\varepsilon_b\} \\ \{\varepsilon_s\} \end{Bmatrix} \quad (3.47)$$

The column matrix  $\{\varepsilon_s\}$  can be obtained from the lower portion of Eq. (3.47) in terms of  $[C_{sb}]$ ,  $[C_{ss}]$ , and  $\{\varepsilon_b\}$ , thus

$$\{\varepsilon_s\} = - [C_{ss}]^{-1} [C_{sb}] \{\varepsilon_b\} \quad (3.48)$$

Substituting Eq. (3.48) into the upper half of Eq. (3.47), yields the constitutive relations for the beam:

$$\{\sigma_b\} = [Q] \{\varepsilon_b\} \quad (3.49)$$

where

$$\begin{aligned} [Q] &\equiv \begin{bmatrix} Q_{11} & Q_{15} & Q_{16} \\ Q_{15} & Q_{55} & Q_{56} \\ Q_{16} & Q_{56} & Q_{66} \end{bmatrix} \\ &= [C_{bb}] - [C_{bs}] [C_{ss}]^{-1} [C_{sb}] \end{aligned} \quad (3.50)$$

Combining Eqs. (3.46a-b) and (3.50) with Eq. (3.49), the expanded form of the constitutive relations is written as:

$$\begin{Bmatrix} \sigma_{xx} \\ \sigma_{x\zeta} \\ \sigma_{x\eta} \end{Bmatrix} = \begin{bmatrix} Q_{11} & Q_{15} & Q_{16} \\ Q_{15} & Q_{55} & Q_{56} \\ Q_{16} & Q_{56} & Q_{66} \end{bmatrix} \begin{Bmatrix} \varepsilon_{xx} \\ \gamma_{x\zeta} \\ \gamma_{x\eta} \end{Bmatrix} \quad (3.51)$$

## Chapter IV

### FORMULATION OF THE FINITE ELEMENT EQUATIONS OF MOTION

The nonlinear equations of motion and the corresponding finite element matrices are derived for each beam element using Hamilton's principle. These equations can be used for both the straight and the swept tip portion of the rotor blade in the finite element discretization. Both the geometric and mass properties of the beam (i.e. blade) such as: pretwist, mass, stiffness, mass center and tension (area) center offsets from the elastic axis; are allowed to vary in the spanwise direction. The external loads are represented by a set of generalized distributed forces and moments, which are defined in the undeformed element coordinate system  $(\hat{e}_x, \hat{e}_y, \hat{e}_z)$ . These generalized forces and moments will be replaced by the corresponding aerodynamic forces and moments in the aeroelastic analysis.

Hamilton's principle can be stated as

$$\int_{t_1}^{t_2} (\delta U - \delta T - \delta W_e) dt = 0 \quad (4.1)$$

where  $U$  is the strain energy;  $T$  is the kinetic energy;  $W_e$  is the work of external loads which includes the effects of the nonconservative loads. Equation (4.1) is an integral equation which states that the total dynamic potential,  $(U - T - W_e)$ , is an extremum over the time interval:  $t_1 \leq t \leq t_2$ .

#### 4.1 STRAIN ENERGY CONTRIBUTIONS

The total strain energy,  $U$ , is calculated using the strain components and the constitutive relations defined in the local cartesian coordinate system, Eqs. (3.43) and (3.51), respectively. Its complete form is written as[97,98] :

$$U = \frac{1}{2} \iiint_V \sigma_{ij} \varepsilon_{ij} dV \quad (4.2)$$

where

$$dV = \sqrt{g} dx d\eta d\zeta \quad (4.3)$$

with

$$g \equiv \det [ \mathbf{g}_i \cdot \mathbf{g}_j ] = 1 \quad (4.4)$$

The determinant of the undeformed metric tensor,  $[ \mathbf{g}_i \cdot \mathbf{g}_j ]$ , in Eq. (4.4) is calculated from Eq. (3.18).

Using the constitutive relations, Eq. (3.49), the strain energy of a beam element becomes:

$$\begin{aligned} U &= \frac{1}{2} \int_0^{l_e} \iint_A \{ \varepsilon_b \}^T \{ \sigma_b \} d\eta d\zeta dx \\ &= \frac{1}{2} \int_0^{l_e} \iint_A \{ \varepsilon_b \}^T [ Q ] \{ \varepsilon_b \} d\eta d\zeta dx \end{aligned} \quad (4.5)$$

or, in expanded form:

$$U = \frac{1}{2} \int_0^{l_e} \iint_A \begin{Bmatrix} \varepsilon_{xx} \\ \gamma_{x\zeta} \\ \gamma_{x\eta} \end{Bmatrix}^T \begin{bmatrix} Q_{11} & Q_{15} & Q_{16} \\ Q_{15} & Q_{55} & Q_{56} \\ Q_{16} & Q_{56} & Q_{66} \end{bmatrix} \begin{Bmatrix} \varepsilon_{xx} \\ \gamma_{x\zeta} \\ \gamma_{x\eta} \end{Bmatrix} d\eta d\zeta dx \quad (4.6)$$

and its variation is given by:

$$\begin{aligned}\delta U &= \int_0^{l_e} \iint_{\Lambda} \delta \{ \varepsilon_b \}^T [ Q_b ] \{ \varepsilon_b \} d\eta d\zeta dx \\ &= \int_0^{l_e} \iint_{\Lambda} \begin{Bmatrix} \delta \varepsilon_{xx} \\ \delta \gamma_{x\zeta} \\ \delta \gamma_{x\eta} \end{Bmatrix}^T \begin{bmatrix} Q_{11} & Q_{15} & Q_{16} \\ Q_{15} & Q_{55} & Q_{56} \\ Q_{16} & Q_{56} & Q_{66} \end{bmatrix} \begin{Bmatrix} \varepsilon_{xx} \\ \gamma_{x\zeta} \\ \gamma_{x\eta} \end{Bmatrix} d\eta d\zeta dx\end{aligned}\quad (4.7)$$

The variations of the strain components can be obtained from Eqs. (3.43) :

$$\begin{aligned}\delta \varepsilon_{xx} &= \delta u_{,x} + v_{,x} \delta v_{,x} + w_{,x} \delta w_{,x} + (\eta^2 + \zeta^2) \phi_{,x} \delta \phi_{,x} \\ &\quad - (\eta \cos \beta - \zeta \sin \beta) (\delta v_{,xx} + \phi \delta w_{,xx} + w_{,xx} \delta \phi) \\ &\quad - (\eta \sin \beta + \zeta \cos \beta) (\delta w_{,xx} - \phi \delta v_{,xx} - v_{,xx} \delta \phi) \\ &\quad + \delta \alpha_{,x} \Psi + \tau_0 (\zeta \Psi_{,\eta} - \eta \Psi_{,\zeta}) \delta \alpha \\ &\quad + \eta (\delta \bar{\gamma}_{x\eta,x} - \tau_0 \delta \bar{\gamma}_{x\zeta}) + \zeta (\delta \bar{\gamma}_{x\zeta,x} + \tau_0 \delta \bar{\gamma}_{x\eta})\end{aligned}\quad (4.8a)$$

$$\delta \gamma_{x\eta} = \delta \bar{\gamma}_{x\eta} + \Psi_{,\eta} \delta \alpha - \zeta (\delta \phi_{,x} + \delta \phi_0) \quad (4.8b)$$

$$\delta \gamma_{x\zeta} = \delta \bar{\gamma}_{x\zeta} + \Psi_{,\zeta} \delta \alpha + \eta (\delta \phi_{,x} + \delta \phi_0) \quad (4.8c)$$

where

$$\begin{aligned}\delta \phi_0 &= (-\delta v_{,x} \sin \beta + \delta w_{,x} \cos \beta) (v_{,xx} \cos \beta + w_{,xx} \sin \beta) + \\ &\quad (-v_{,x} \sin \beta + w_{,x} \cos \beta) (\delta v_{,xx} \cos \beta + \delta w_{,xx} \sin \beta)\end{aligned}\quad (4.9)$$

It is assumed that the variations of the strain components are of the same order as the corresponding strain components. The reduced material stiffness matrix,  $[ Q ]$ , is defined in a general form so that all of the coefficients can be of the same order. This is important for the analysis of fiber reinforced

composite materials, because varying the ply angle of the laminate will change the relative order of magnitude of the material stiffness properties.

Substituting Eqs. (4.8) into Eq. (4.7) and integrating over the cross-section, the variation of the strain energy for a beam element,  $\delta U$ , is expressed in terms of the stress and moment resultants as:

$$\begin{aligned}
 \delta U = \int_0^{l_e} \{ & \bar{V}_x (\delta u_{,x} + v_{,x} \delta v_{,x} + w_{,x} \delta w_{,x}) + (\bar{S}_x + \bar{T}_x \phi_{,x}) \delta \phi_{,x} + \bar{S}'_x \delta \phi_0 \\
 & + [(\bar{M}_y \sin \beta + \bar{M}_z \cos \beta) + \phi (\bar{M}'_y \cos \beta - \bar{M}'_z \sin \beta)] \delta v_{,xx} \\
 & + [(-\bar{M}_y \cos \beta + \bar{M}_z \sin \beta) + \phi (\bar{M}'_y \sin \beta + \bar{M}'_z \cos \beta)] \delta w_{,xx} \quad (4.10) \\
 & + [v_{,xx} (\bar{M}'_y \cos \beta - \bar{M}'_z \sin \beta) + w_{,xx} (\bar{M}'_y \sin \beta + \bar{M}'_z \cos \beta)] \delta \phi \\
 & + \bar{P}_x \delta \alpha_{,x} + (\tau_0 \bar{P}'_x + \bar{R}_x) \delta \alpha + \bar{M}'_y \delta \bar{y}_{x\zeta, x} - \bar{M}'_z \delta \bar{y}_{x\eta, x} \\
 & + (\bar{V}_\zeta + \tau_0 \bar{M}'_z) \delta \bar{y}_{x\zeta} + (\bar{V}_\eta + \tau_0 \bar{M}'_y) \delta \bar{y}_{x\eta} \} dx
 \end{aligned}$$

where the stress resultants are defined as:

$$\begin{aligned}
\bar{V}_x &\equiv \iint_A (Q_{11} \varepsilon_{xx} + Q_{15} \gamma_{x\zeta} + Q_{16} \gamma_{x\eta}) d\eta d\zeta \\
&= EA [u_{,x} + \frac{1}{2}(v_{,x})^2 + \frac{1}{2}(w_{,x})^2] + \frac{1}{2}EAC_0(\phi_{,x})^2 \\
&\quad - v_{,xx} [(EA\eta_a \cos \beta - EA\zeta_a \sin \beta) - \\
&\quad \quad \phi (EA\eta_a \sin \beta + EA\zeta_a \cos \beta)] \\
&\quad - w_{,xx} [(EA\eta_a \sin \beta + EA\zeta_a \cos \beta) + \\
&\quad \quad \phi (EA\eta_a \cos \beta - EA\zeta_a \sin \beta)] \\
&\quad + EAB_0(\phi_{,x} + \phi_0) + EAD_0\alpha_{,x} + (\tau_0 EAD_0' + EAB_5)\alpha \\
&\quad + EA\eta_a \bar{\gamma}_{x\eta,x} + EA\zeta_a \bar{\gamma}_{x\zeta,x} + (G_\eta A + \tau_0 EA\zeta_a) \bar{\gamma}_{x\eta} \\
&\quad + (G_\zeta A - \tau_0 EA\eta_a) \bar{\gamma}_{x\zeta}
\end{aligned} \tag{4.11a}$$

$$\begin{aligned}
\bar{V}_\eta &\equiv \iint_A (Q_{16} \varepsilon_{xx} + Q_{56} \gamma_{x\zeta} + Q_{66} \gamma_{x\eta}) d\eta d\zeta \\
&= G_\eta A [u_{,x} + \frac{1}{2}(v_{,x})^2 + \frac{1}{2}(w_{,x})^2] + \frac{1}{2}G_\eta J(\phi_{,x})^2 \\
&\quad - v_{,xx} [(G_\eta A\eta_b \cos \beta - G_\eta A\zeta_b \sin \beta) - \\
&\quad \quad \phi (G_\eta A\eta_b \sin \beta + G_\eta A\zeta_b \cos \beta)] \\
&\quad - w_{,xx} [(G_\eta A\eta_b \sin \beta + G_\eta A\zeta_b \cos \beta) + \\
&\quad \quad \phi (G_\eta A\eta_b \cos \beta - G_\eta A\zeta_b \sin \beta)] \\
&\quad + EAB_{12}(\phi_{,x} + \phi_0) + EAD_7\alpha_{,x} + (\tau_0 EAD_7' + EAB_{13})\alpha \\
&\quad + G_\eta A\eta_b \bar{\gamma}_{x\eta,x} + G_\eta A\zeta_b \bar{\gamma}_{x\zeta,x} + (G_\eta A + \tau_0 G_\eta A\zeta_b) \bar{\gamma}_{x\eta} \\
&\quad + (G_\eta \zeta A - \tau_0 G_\eta A\eta_b) \bar{\gamma}_{x\zeta}
\end{aligned} \tag{4.11b}$$

$$\begin{aligned}
\bar{V}_\zeta &\equiv \iint_{\Lambda} (Q_{15} \varepsilon_{xx} + Q_{55} \gamma_{x\zeta} + Q_{56} \gamma_{x\eta}) d\eta d\zeta \\
&= G_\zeta A [u_{,x} + \frac{1}{2}(v_{,x})^2 + \frac{1}{2}(w_{,x})^2] + \frac{1}{2}G_\zeta J(\phi_{,x})^2 \\
&\quad - v_{,xx} [(G_\zeta A \eta_c \cos \beta - G_\zeta A \zeta_c \sin \beta) - \\
&\quad \quad \phi (G_\zeta A \eta_c \sin \beta + G_\zeta A \zeta_c \cos \beta)] \\
&\quad - w_{,xx} [(G_\zeta A \eta_c \sin \beta + G_\zeta A \zeta_c \cos \beta) + \\
&\quad \quad \phi (G_\zeta A \eta_c \cos \beta - G_\zeta A \zeta_c \sin \beta)] \\
&\quad + EAB_{10}(\phi_{,x} + \phi_0) + EAD_6 \alpha_{,x} + (\tau_0 EAD_6' + EAB_{11}) \alpha \\
&\quad + G_\zeta A \eta_c \bar{\gamma}_{x\eta,x} + G_\zeta A \zeta_c \bar{\gamma}_{x\zeta,x} + (G_{\eta\zeta} A + \tau_0 G_\zeta A \zeta_c) \bar{\gamma}_{x\eta} \\
&\quad + (G_\zeta \zeta_c A - \tau_0 G_\zeta A \eta_c) \bar{\gamma}_{x\zeta}
\end{aligned} \tag{4.11c}$$

and the moment resultants are defined as:

$$\begin{aligned}
\bar{M}_y &\equiv \iint_{\Lambda} \zeta (Q_{11} \varepsilon_{xx} + Q_{15} \gamma_{x\zeta} + Q_{16} \gamma_{x\eta}) d\eta d\zeta \\
&= EA \zeta_a [u_{,x} + \frac{1}{2}(v_{,x})^2 + \frac{1}{2}(w_{,x})^2] + \frac{1}{2}EAC_2(\phi_{,x})^2 \\
&\quad - [(EI_{\eta\zeta} \cos \beta - EI_{\eta\eta} \sin \beta) - \phi (EI_{\eta\zeta} \sin \beta + EI_{\eta\eta} \cos \beta)] v_{,xx} \\
&\quad - [(EI_{\eta\zeta} \sin \beta + EI_{\eta\eta} \cos \beta) + \phi (EI_{\eta\zeta} \cos \beta - EI_{\eta\eta} \sin \beta)] w_{,xx} \\
&\quad + EAB_2(\phi_{,x} + \phi_0) + EAD_2 \alpha_{,x} + (\tau_0 EAD_2' + EAB_7) \alpha \\
&\quad + EI_{\eta\zeta} \bar{\gamma}_{x\eta,x} + EI_{\eta\eta} \bar{\gamma}_{x\zeta,x} + (G_\eta A \zeta_b + \tau_0 EI_{\eta\eta}) \bar{\gamma}_{x\eta} \\
&\quad + (G_\zeta A \zeta_c - \tau_0 EI_{\eta\zeta}) \bar{\gamma}_{x\zeta}
\end{aligned} \tag{4.12a}$$

$$\begin{aligned}
\bar{M}_z &\equiv \iint_A -\eta (Q_{11} \varepsilon_{xx} + Q_{15} \gamma_{x\zeta} + Q_{16} \gamma_{x\eta}) d\eta d\zeta \\
&= -EA\eta_a [u_{,x} + \frac{1}{2}(v_{,x})^2 + \frac{1}{2}(w_{,x})^2] - \frac{1}{2}EAC_1 (\phi_{,x})^2 \\
&\quad + [(EI_{\zeta\zeta} \cos \beta - EI_{\eta\zeta} \sin \beta) - \phi (EI_{\zeta\zeta} \sin \beta + EI_{\eta\zeta} \cos \beta)] v_{,xx} \\
&\quad + [(EI_{\zeta\zeta} \sin \beta + EI_{\eta\zeta} \cos \beta) + \phi (EI_{\zeta\zeta} \cos \beta - EI_{\eta\zeta} \sin \beta)] w_{,xx} \quad (4.12b) \\
&\quad - EAB_1 (\phi_{,x} + \phi_0) - EAD_1 \alpha_{,x} - (\tau_0 EAD_1' + EAB_6) \alpha \\
&\quad - EI_{\zeta\zeta} \bar{\gamma}_{x\eta,x} - EI_{\eta\zeta} \bar{\gamma}_{x\zeta,x} - (G_\eta A \eta_b + \tau_0 EI_{\eta\zeta}) \bar{\gamma}_{x\eta} \\
&\quad - (G_\zeta A \eta_c - \tau_0 EI_{\zeta\zeta}) \bar{\gamma}_{x\zeta}
\end{aligned}$$

$$\begin{aligned}
\bar{M}'_y &\equiv \iint_A \zeta (Q_{11} \varepsilon_{xx} + Q_{15} \gamma_{x\zeta} + Q_{16} \gamma_{x\eta}) d\eta d\zeta \\
&= EA\zeta_a [u_{,x} + \frac{1}{2}(v_{,x})^2 + \frac{1}{2}(w_{,x})^2] + EAB_2 \phi_{,x} \\
&\quad - (EI_{\eta\zeta} \cos \beta - EI_{\eta\eta} \sin \beta) v_{,xx} - (EI_{\eta\zeta} \sin \beta + EI_{\eta\eta} \cos \beta) w_{,xx} \quad (4.12c) \\
&\quad + EAD_2 \alpha_{,x} + (\tau_0 EAD_2' + EAB_7) \alpha + EI_{\eta\zeta} \bar{\gamma}_{x\eta,x} + EI_{\eta\eta} \bar{\gamma}_{x\zeta,x} \\
&\quad + (G_\eta A \zeta_b + \tau_0 EI_{\eta\eta}) \bar{\gamma}_{x\eta} + (G_\zeta A \zeta_c - \tau_0 EI_{\eta\zeta}) \bar{\gamma}_{x\zeta}
\end{aligned}$$

$$\begin{aligned}
\bar{M}'_z &\equiv \iint_A -\eta (Q_{11} \varepsilon_{xx} + Q_{15} \gamma_{x\zeta} + Q_{16} \gamma_{x\eta}) d\eta d\zeta \\
&= -EA\eta_a [u_{,x} + \frac{1}{2}(v_{,x})^2 + \frac{1}{2}(w_{,x})^2] - EAB_1 \phi_{,x} \\
&\quad + (EI_{\zeta\zeta} \cos \beta - EI_{\eta\zeta} \sin \beta) v_{,xx} + (EI_{\zeta\zeta} \sin \beta + EI_{\eta\zeta} \cos \beta) w_{,xx} \quad (4.12d) \\
&\quad - EAD_1 \alpha_{,x} - (\tau_0 EAD_1' + EAB_6) \alpha - EI_{\zeta\zeta} \bar{\gamma}_{x\eta,x} - EI_{\eta\zeta} \bar{\gamma}_{x\zeta,x} \\
&\quad - (G_\eta A \eta_b + \tau_0 EI_{\eta\zeta}) \bar{\gamma}_{x\eta} - (G_\zeta A \eta_c - \tau_0 EI_{\zeta\zeta}) \bar{\gamma}_{x\zeta}
\end{aligned}$$

$$\begin{aligned}
\bar{P}_x &\equiv \iint_{\Lambda} \Psi (Q_{11} \varepsilon_{xx} + Q_{15} \gamma_{x\zeta} + Q_{16} \gamma_{x\eta}) d\eta d\zeta \\
&= EAD_0 [u_{,x} + \frac{1}{2}(v_{,x})^2 + \frac{1}{2}(w_{,x})^2] + \frac{1}{2}EAD_4(\phi_{,x})^2 \\
&\quad - v_{,xx} [(EAD_1 \cos \beta - EAD_2 \sin \beta) - \\
&\quad \quad \phi (EAD_1 \sin \beta + EAD_2 \cos \beta)] \\
&\quad - w_{,xx} [(EAD_1 \sin \beta + EAD_2 \cos \beta) + \\
&\quad \quad \phi (EAD_1 \cos \beta - EAD_2 \sin \beta)] \\
&\quad + EAB_3 \phi_{,x} + EAD_3 \alpha_{,x} + (\tau_0 EAD_5 + EAB_8) \alpha \\
&\quad + EAD_1 \bar{\gamma}_{x\eta,x} + EAD_2 \bar{\gamma}_{x\zeta,x} + (EAD_7 + \tau_0 EAD_2) \bar{\gamma}_{x\eta} \\
&\quad + (EAD_6 - \tau_0 EAD_1) \bar{\gamma}_{x\zeta}
\end{aligned} \tag{4.12c}$$

$$\begin{aligned}
\bar{P}'_x &\equiv \iint_{\Lambda} (\zeta \Psi_{,\eta} - \eta \Psi_{,\zeta}) (Q_{11} \varepsilon_{xx} + Q_{15} \gamma_{x\zeta} + Q_{16} \gamma_{x\eta}) d\eta d\zeta \\
&= EAD'_0 [u_{,x} + \frac{1}{2}(v_{,x})^2 + \frac{1}{2}(w_{,x})^2] + \frac{1}{2}EAD'_4(\phi_{,x})^2 \\
&\quad - v_{,xx} [(EAD'_1 \cos \beta - EAD'_2 \sin \beta) - \\
&\quad \quad \phi (EAD'_1 \sin \beta + EAD'_2 \cos \beta)] \\
&\quad - w_{,xx} [(EAD'_1 \sin \beta + EAD'_2 \cos \beta) + \\
&\quad \quad \phi (EAD'_1 \cos \beta - EAD'_2 \sin \beta)] \\
&\quad + EAB'_3 \phi_{,x} + EAD'_5 \alpha_{,x} + (\tau_0 EAD'_3 + EAB'_8) \alpha \\
&\quad + EAD'_1 \bar{\gamma}_{x\eta,x} + EAD'_2 \bar{\gamma}_{x\zeta,x} + (EAD'_7 + \tau_0 EAD'_2) \bar{\gamma}_{x\eta} \\
&\quad + (EAD'_6 - \tau_0 EAD'_1) \bar{\gamma}_{x\zeta}
\end{aligned} \tag{4.12f}$$

$$\begin{aligned}
\bar{T}_x &\equiv \iint_A (\eta^2 + \zeta^2) (Q_{11} \varepsilon_{xx} + Q_{15} \gamma_{x\zeta} + Q_{16} \gamma_{x\eta}) d\eta d\zeta \\
&= EAC_0 [u_{,x} + \frac{1}{2} (v_{,x})^2 + \frac{1}{2} (w_{,x})^2] + \frac{1}{2} EAC_3 (\phi_{,x})^2 \\
&\quad - v_{,xx} [ (EAC_1 \cos \beta - EAC_2 \sin \beta) - \\
&\quad \quad \phi (EAC_1 \sin \beta + EAC_2 \cos \beta) ] \\
&\quad - w_{,xx} [ (EAC_1 \sin \beta + EAC_2 \cos \beta) + \\
&\quad \quad \phi (EAC_1 \cos \beta - EAC_2 \sin \beta) ] \\
&\quad + EAB_4 \phi_{,x} + EAD_4 \alpha_{,x} + (\tau_0 EAD_4' + EAB_9) \alpha \\
&\quad + EAC_1 \bar{\gamma}_{x\eta,x} + EAC_2 \bar{\gamma}_{x\zeta,x} + (G_\eta J + \tau_0 EAC_2) \bar{\gamma}_{x\eta} \\
&\quad + (G_\zeta J - \tau_0 EAC_1) \bar{\gamma}_{x\zeta}
\end{aligned} \tag{4.12g}$$

$$\begin{aligned}
\bar{R}_x &\equiv \iint_A [ \Psi_{, \zeta} (Q_{15} \varepsilon_{xx} + Q_{55} \gamma_{x\zeta} + Q_{56} \gamma_{x\eta}) + \\
&\quad \Psi_{, \eta} (Q_{16} \varepsilon_{xx} + Q_{56} \gamma_{x\zeta} + Q_{66} \gamma_{x\eta}) ] d\eta d\zeta \\
&= EAB_5 [u_{,x} + \frac{1}{2} (v_{,x})^2 + \frac{1}{2} (w_{,x})^2] + \frac{1}{2} EAB_9 (\phi_{,x})^2 \\
&\quad - v_{,xx} [ (EAB_6 \cos \beta - EAB_7 \sin \beta) - \\
&\quad \quad \phi (EAB_6 \sin \beta + EAB_7 \cos \beta) ] \\
&\quad - w_{,xx} [ (EAB_6 \sin \beta + EAB_7 \cos \beta) + \\
&\quad \quad \phi (EAB_6 \cos \beta - EAB_7 \sin \beta) ] \\
&\quad + EAB_{14} (\phi_{,x} + \phi_0) + EAB_8 \alpha_{,x} + (\tau_0 EAB_8' + EAB_{15}) \alpha \\
&\quad + EAB_6 \bar{\gamma}_{x\eta,x} + EAB_7 \bar{\gamma}_{x\zeta,x} + (EAB_{13} + \tau_0 EAB_7) \bar{\gamma}_{x\eta} \\
&\quad + (EAB_{11} - \tau_0 EAB_6) \bar{\gamma}_{x\zeta}
\end{aligned} \tag{4.12h}$$

$$\begin{aligned}
\bar{S}_x &\equiv \iint_A [\eta (Q_{15} \varepsilon_{xx} + Q_{55} \gamma_{x\zeta} + Q_{56} \gamma_{x\eta}) - \\
&\quad \zeta (Q_{16} \varepsilon_{xx} + Q_{56} \gamma_{x\zeta} + Q_{66} \gamma_{x\eta})] d\eta d\zeta \\
&= EAB_0 [u_{,x} + \frac{1}{2}(v_{,x})^2 + \frac{1}{2}(w_{,x})^2] + \frac{1}{2}EAB_4 (\phi_{,x})^2 \\
&\quad - v_{,xx} [(EAB_1 \cos \beta - EAB_2 \sin \beta) - \\
&\quad \phi (EAB_1 \sin \beta + EAB_2 \cos \beta)] \\
&\quad - w_{,xx} [(EAB_1 \sin \beta + EAB_2 \cos \beta) + \\
&\quad \phi (EAB_1 \cos \beta - EAB_2 \sin \beta)] \\
&\quad + GJ (\phi_{,x} + \phi_0) + EAB_3 \alpha_{,x} + (\tau_0 EAB_3' + EAB_{14}) \alpha \\
&\quad + EAB_1 \bar{\gamma}_{x\eta,x} + EAB_2 \bar{\gamma}_{x\zeta,x} + (EAB_{12} + \tau_0 EAB_2) \bar{\gamma}_{x\eta} \\
&\quad + (EAB_{10} - \tau_0 EAB_1) \bar{\gamma}_{x\zeta}
\end{aligned} \tag{4.12i}$$

$$\begin{aligned}
\bar{S}'_x &\equiv \iint_A [\eta (Q_{15} \varepsilon_{xx} + Q_{55} \gamma_{x\zeta} + Q_{56} \gamma_{x\eta}) - \\
&\quad \zeta (Q_{16} \varepsilon_{xx} + Q_{56} \gamma_{x\zeta} + Q_{66} \gamma_{x\eta})] d\eta d\zeta \\
&= EAB_0 [u_{,x} + \frac{1}{2}(v_{,x})^2 + \frac{1}{2}(w_{,x})^2] + GJ \phi_{,x} \\
&\quad - (EAB_1 \cos \beta - EAB_2 \sin \beta) v_{,xx} - (EAB_1 \sin \beta + EAB_2 \cos \beta) w_{,xx} \\
&\quad + EAB_3 \alpha_{,x} + (\tau_0 EAB_3' + EAB_{14}) \alpha + EAB_1 \bar{\gamma}_{x\eta,x} + EAB_2 \bar{\gamma}_{x\zeta,x} \\
&\quad + (EAB_{12} + \tau_0 EAB_2) \bar{\gamma}_{x\eta} + (EAB_{10} - \tau_0 EAB_1) \bar{\gamma}_{x\zeta}
\end{aligned} \tag{4.12j}$$

In the above expressions, the moment resultants  $\bar{M}'_y$ ,  $\bar{M}'_z$  and  $\bar{S}'_x$  have the same definitions as  $\bar{M}_y$ ,  $\bar{M}_z$  and  $\bar{S}_x$ , respectively. However the final expressions of  $\bar{M}_y$ ,  $\bar{M}_z$  and  $\bar{S}_x$ , include both terms of order  $\varepsilon^3$  and  $\varepsilon^4$ , while the final expressions of  $\bar{M}'_y$ ,  $\bar{M}'_z$  and  $\bar{S}'_x$  include only terms of order  $\varepsilon^3$  only. This is because

that  $\bar{M}_y, \bar{M}_z$  and  $\bar{S}_x$ , are coupled with terms of order  $\varepsilon$ , while  $\bar{M}'_y, \bar{M}'_z$  and  $\bar{S}'_x$  are coupled with terms of  $\varepsilon^2$ . Note that the integrals  $\bar{P}_x, \bar{P}'_x$  and  $\bar{T}_x$  have a unit of second moment of force, instead of moment; they are grouped with the moment resultants for convenience. The cross-sectional integrals associated with the strain energy variation in Eqs. (4.11) and (4.12) are defined as following:

*Modulus weighted area, first and second moments of inertia, and torsional integrals:*

$$EA = \iint_{\Lambda} Q_{11} d\eta d\zeta \quad (4.13a)$$

$$EA\eta_a = \iint_{\Lambda} Q_{11} \eta d\eta d\zeta \quad (4.13b)$$

$$EA\zeta_a = \iint_{\Lambda} Q_{11} \zeta d\eta d\zeta \quad (4.13c)$$

$$EI_{\eta\eta} = \iint_{\Lambda} Q_{11} \zeta^2 d\eta d\zeta \quad (4.13d)$$

$$EI_{\zeta\zeta} = \iint_{\Lambda} Q_{11} \eta^2 d\eta d\zeta \quad (4.13e)$$

$$EI_{\eta\zeta} = \iint_{\Lambda} Q_{11} \eta\zeta d\eta d\zeta \quad (4.13f)$$

$$EAC_0 = \iint_{\Lambda} Q_{11} (\eta^2 + \zeta^2) d\eta d\zeta \quad (4.13g)$$

$$EAC_1 = \iint_A Q_{11} \eta (\eta^2 + \zeta^2) d\eta d\zeta \quad (4.13h)$$

$$EAC_2 = \iint_A Q_{11} \zeta (\eta^2 + \zeta^2) d\eta d\zeta \quad (4.13i)$$

$$EAC_3 = \iint_A Q_{11} (\eta^2 + \zeta^2)^2 d\eta d\zeta \quad (4.13j)$$

$$G_{\eta A} = \iint_A Q_{16} d\eta d\zeta \quad (4.13k)$$

$$G_{\zeta A} = \iint_A Q_{15} d\eta d\zeta \quad (4.13l)$$

$$G_{\eta\eta A} = \iint_A Q_{66} d\eta d\zeta \quad (4.13m)$$

$$G_{\zeta\zeta A} = \iint_A Q_{55} d\eta d\zeta \quad (4.13n)$$

$$G_{\eta\zeta A} = \iint_A Q_{56} d\eta d\zeta \quad (4.13o)$$

$$G_{\eta A} \eta_b = \iint_A Q_{16} \eta d\eta d\zeta \quad (4.13p)$$

$$G_{\eta A} \zeta_b = \iint_A Q_{16} \zeta d\eta d\zeta \quad (4.13q)$$

$$G_{\zeta A} \eta_c = \iint_A Q_{15} \eta d\eta d\zeta \quad (4.13r)$$

$$G_{\zeta} A \zeta_c = \iint_{\Lambda} Q_{15} \zeta \, d\eta d\zeta \quad (4.13s)$$

$$G_{\eta} J = \iint_{\Lambda} Q_{16} (\eta^2 + \zeta^2) \, d\eta d\zeta \quad (4.13t)$$

$$G_{\zeta} J = \iint_{\Lambda} Q_{15} (\eta^2 + \zeta^2) \, d\eta d\zeta \quad (4.13u)$$

$$GJ = \iint_{\Lambda} (Q_{55} \eta^2 + Q_{66} \zeta^2 - 2Q_{56} \eta \zeta) \, d\eta d\zeta \quad (4.13v)$$

*Modulus weighted area, first and second moment warping integrals:*

$$EAD_0 = \iint_{\Lambda} Q_{11} \Psi \, d\eta d\zeta \quad (4.14a)$$

$$EAD_1 = \iint_{\Lambda} Q_{11} \eta \Psi \, d\eta d\zeta \quad (4.14b)$$

$$EAD_2 = \iint_{\Lambda} Q_{11} \zeta \Psi \, d\eta d\zeta \quad (4.14c)$$

$$EAD_3 = \iint_{\Lambda} Q_{11} \Psi^2 \, d\eta d\zeta \quad (4.14d)$$

$$EAD_4 = \iint_{\Lambda} Q_{11} (\eta^2 + \zeta^2) \Psi \, d\eta d\zeta \quad (4.14e)$$

$$EAD_5 = \iint_{\Lambda} Q_{11} \Psi (\zeta \Psi_{,\eta} - \eta \Psi_{,\zeta}) \, d\eta d\zeta \quad (4.14f)$$

$$\text{EAD}_6 = \iint_{\Lambda} Q_{15} \Psi \, d\eta d\zeta \quad (4.14g)$$

$$\text{EAD}_7 = \iint_{\Lambda} Q_{16} \Psi \, d\eta d\zeta \quad (4.14h)$$

$$\text{EAD}_{0'} = \iint_{\Lambda} Q_{11} (\zeta \Psi_{,\eta} - \eta \Psi_{,\zeta}) \, d\eta d\zeta \quad (4.14i)$$

$$\text{EAD}_{1'} = \iint_{\Lambda} Q_{11} \eta (\zeta \Psi_{,\eta} - \eta \Psi_{,\zeta}) \, d\eta d\zeta \quad (4.14j)$$

$$\text{EAD}_{2'} = \iint_{\Lambda} Q_{11} \zeta (\zeta \Psi_{,\eta} - \eta \Psi_{,\zeta}) \, d\eta d\zeta \quad (4.14k)$$

$$\text{EAD}_{3'} = \iint_{\Lambda} Q_{11} (\zeta \Psi_{,\eta} - \eta \Psi_{,\zeta})^2 \, d\eta d\zeta \quad (4.14l)$$

$$\text{EAD}_{4'} = \iint_{\Lambda} Q_{11} (\eta^2 + \zeta^2) (\zeta \Psi_{,\eta} - \eta \Psi_{,\zeta}) \, d\eta d\zeta \quad (4.14m)$$

$$\text{EAD}_{6'} = \iint_{\Lambda} Q_{15} (\zeta \Psi_{,\eta} - \eta \Psi_{,\zeta}) \, d\eta d\zeta \quad (4.14n)$$

$$\text{EAD}_{7'} = \iint_{\Lambda} Q_{16} (\zeta \Psi_{,\eta} - \eta \Psi_{,\zeta}) \, d\eta d\zeta \quad (4.14o)$$

*Anisotropic material stiffness coupling integrals:*

$$\text{EAB}_0 = \iint_{\Lambda} (Q_{15} \eta - Q_{16} \zeta) \, d\eta d\zeta \quad (4.15a)$$

$$EAB_1 = \iint_A (Q_{15}\eta - Q_{16}\zeta)\eta \, d\eta d\zeta \quad (4.15b)$$

$$EAB_2 = \iint_A (Q_{15}\eta - Q_{16}\zeta)\zeta \, d\eta d\zeta \quad (4.15c)$$

$$EAB_3 = \iint_A (Q_{15}\eta - Q_{16}\zeta)\Psi \, d\eta d\zeta \quad (4.15d)$$

$$EAB_4 = \iint_A (Q_{15}\eta - Q_{16}\zeta)(\eta^2 + \zeta^2) \, d\eta d\zeta \quad (4.15e)$$

$$EAB_5 = \iint_A (Q_{15}\Psi_{,\zeta} + Q_{16}\Psi_{,\eta}) \, d\eta d\zeta \quad (4.15f)$$

$$EAB_6 = \iint_A (Q_{15}\Psi_{,\zeta} + Q_{16}\Psi_{,\eta})\eta \, d\eta d\zeta \quad (4.15g)$$

$$EAB_7 = \iint_A (Q_{15}\Psi_{,\zeta} + Q_{16}\Psi_{,\eta})\zeta \, d\eta d\zeta \quad (4.15h)$$

$$EAB_8 = \iint_A (Q_{15}\Psi_{,\zeta} + Q_{16}\Psi_{,\eta})\Psi \, d\eta d\zeta \quad (4.15i)$$

$$EAB_9 = \iint_A (Q_{15}\Psi_{,\zeta} + Q_{16}\Psi_{,\eta})(\eta^2 + \zeta^2) \, d\eta d\zeta \quad (4.15j)$$

$$EAB_{10} = \iint_A (Q_{55}\eta - Q_{56}\zeta) \, d\eta d\zeta \quad (4.15k)$$

$$EAB_{11} = \iint_A (Q_{55}\Psi_{,\zeta} + Q_{56}\Psi_{,\eta}) \, d\eta d\zeta \quad (4.15l)$$

$$EAB_{12} = \iint_{\Lambda} (Q_{56} \eta - Q_{66} \zeta) d\eta d\zeta \quad (4.15m)$$

$$EAB_{13} = \iint_{\Lambda} (Q_{56} \Psi_{,\zeta} + Q_{66} \Psi_{,\eta}) d\eta d\zeta \quad (4.15n)$$

$$EAB_{14} = \iint_{\Lambda} [(Q_{55} \eta - Q_{56} \zeta) \Psi_{,\zeta} + (Q_{56} \eta - Q_{66} \zeta) \Psi_{,\eta}] d\eta d\zeta \quad (4.15o)$$

$$EAB_{15} = \iint_{\Lambda} [Q_{55} (\Psi_{,\zeta})^2 + Q_{66} (\Psi_{,\eta})^2 + 2 Q_{56} \Psi_{,\eta} \Psi_{,\zeta}] d\eta d\zeta \quad (4.15p)$$

$$EAB_{3'} = \iint_{\Lambda} (Q_{15} \eta - Q_{16} \zeta) (\zeta \Psi_{,\eta} - \eta \Psi_{,\zeta}) d\eta d\zeta \quad (4.15q)$$

$$EAB_{8'} = \iint_{\Lambda} (Q_{15} \Psi_{,\zeta} + Q_{16} \Psi_{,\eta}) (\zeta \Psi_{,\eta} - \eta \Psi_{,\zeta}) d\eta d\zeta \quad (4.15r)$$

The modulus weighted area, EA, represents the axial stiffness of the beam.  $EA\eta_a$  and  $EA\zeta_a$  are the modulus weighted offsets of the tension (area) center from the shear center along  $\hat{e}_\eta$  and  $\hat{e}_\zeta$ , respectively. The modulus weighted moments of inertia about the shear center,  $EI_{\eta\eta}$ ,  $EI_{\zeta\zeta}$  and  $EI_{\eta\zeta}$ , represent the bending stiffnesses of the beam.  $EAC_0$ ,  $EAC_1$ ,  $EAC_2$  and  $EAC_3$  are higher order section constants for modeling the axial-torsion coupling effects. The constant GJ represents the direct torsional stiffness. It is important to note that if the blade is isotropic and the warping amplitude  $\alpha$  is replaced by  $\phi_x$ , then the section constants GJ and  $EAB_{14}$  can be combined to become the torsional rigidity of the beam. The grouping of the modulus weighted section constants,

defined in Eqs. (4.13), (4.14) and (4.15) is based on convenience and should not be considered to be definitive.

The section constants defined in Eqs. (4.13)-(4.15) are calculated by a separate linear, two-dimensional analysis which is decoupled from the nonlinear, one-dimensional global analysis for the beam. In this study, a composite cross section analysis model, consisting of a suitably modified version of the analysis developed by Kosmatka[56], is used to calculate the shear center location and the modulus weighted section constants of an arbitrarily shaped composite cross section. This model is based on the Saint Venant solution of a tip loaded composite cantilever beam with a general prismatic cross section. It uses the principle of minimum potential energy and 2-D finite element analysis to calculate the cross-sectional warping functions and stress distribution. The shear center location is determined using moment equilibrium and the shear stress distribution. The modifications made in the computer code, implementing the cross section analysis model presented in Ref. 56, consist of the replacement of the modulus weighted section constants present in the code, associated with the one-dimensional global analysis described in Ref. 56, by the modulus weighted section constants defined in this study. Several other two-dimensional composite cross section analysis models are also available in the literature[101,37,75,5], among these Ref. 37, which is also capable of modeling cross sections with arbitrary shape and anisotropic and nonhomogeneous materials, is probably the most general.

Integrating the strain energy variation, Eq. (4.10), by parts gives:

$$\begin{aligned} \delta U = \int_0^{l_c} [ Y_u \delta u + Y_v \delta v + Y_w \delta w + Y_\phi \delta \phi \\ + Y_\alpha \delta \alpha + Y_\eta \delta \gamma_{\eta\eta} + Y_\zeta \delta \gamma_{\zeta\zeta} ] dx + b(U) \end{aligned} \quad (4.16)$$

where

$$Y_u = - \{ \bar{V}_x \}_{,x} \quad (4.17a)$$

$$\begin{aligned} Y_v = \{ \bar{M}_y \sin \beta + \bar{M}_z \cos \beta + \phi (\bar{M}'_y \cos \beta - \bar{M}'_z \sin \beta) + \\ \bar{S}'_x \cos \beta ( - v_{,x} \sin \beta + w_{,x} \cos \beta ) \}_{,xx} \\ - \{ \bar{V}_x v_{,x} - \bar{S}'_x \sin \beta ( v_{,xx} \cos \beta + w_{,xx} \sin \beta ) \}_{,x} \end{aligned} \quad (4.17b)$$

$$\begin{aligned} Y_w = \{ - \bar{M}_y \cos \beta + \bar{M}_z \sin \beta + \phi (\bar{M}'_y \sin \beta + \bar{M}'_z \cos \beta) + \\ \bar{S}'_x \sin \beta ( - v_{,x} \sin \beta + w_{,x} \cos \beta ) \}_{,xx} \\ - \{ \bar{V}_x w_{,x} + \bar{S}'_x \cos \beta ( v_{,xx} \cos \beta + w_{,xx} \sin \beta ) \}_{,x} \end{aligned} \quad (4.17c)$$

$$\begin{aligned} Y_\phi = v_{,xx} ( \bar{M}'_y \cos \beta - \bar{M}'_z \sin \beta ) + w_{,xx} ( \bar{M}'_y \sin \beta + \bar{M}'_z \cos \beta ) \\ - \{ \bar{S}_x + \bar{T}_x \phi_{,x} \}_{,x} \end{aligned} \quad (4.17d)$$

$$Y_\alpha = - \{ \bar{P}_x \}_{,x} + \bar{P}'_x + \bar{R}_x \quad (4.17e)$$

$$Y_\eta = \{ \bar{M}'_z \}_{,x} + \bar{V}_\eta + \tau_0 \bar{M}'_y \quad (4.17f)$$

$$Y_\zeta = - \{ \bar{M}'_y \}_{,x} + \bar{V}_\zeta + \tau_0 \bar{M}'_z \quad (4.17g)$$

and the associated boundary terms:

$$\begin{aligned}
b(U) = & \{ \bar{V}_x \} \delta u \Big|_0^{l_e} + \{ \bar{M}_y \sin \beta + \bar{M}_z \cos \beta + \phi (\bar{M}'_y \cos \beta - \bar{M}'_z \sin \beta) + \\
& \bar{S}'_x \cos \beta (-v_{,x} \sin \beta + w_{,x} \cos \beta) \} \delta v_{,x} \Big|_0^{l_e} \\
& + [ - \{ \bar{M}_y \sin \beta + \bar{M}_z \cos \beta + \phi (\bar{M}'_y \cos \beta - \bar{M}'_z \sin \beta) + \\
& \bar{S}'_x \cos \beta (-v_{,x} \sin \beta + w_{,x} \cos \beta) \}_{,x} + \bar{V}_x v_{,x} - \\
& \bar{S}'_x \sin \beta (v_{,xx} \cos \beta + w_{,xx} \sin \beta) ] \delta v \Big|_0^{l_e} \\
& + \{ - \bar{M}_y \cos \beta + \bar{M}_z \sin \beta + \phi (\bar{M}'_y \sin \beta + \bar{M}'_z \cos \beta) + \\
& \bar{S}'_x \sin \beta (-v_{,x} \sin \beta + w_{,x} \cos \beta) \} \delta w_{,x} \Big|_0^{l_e} \tag{4.18} \\
& + [ - \{ - \bar{M}_y \cos \beta + \bar{M}_z \sin \beta + \phi (\bar{M}'_y \sin \beta + \bar{M}'_z \cos \beta) + \\
& \bar{S}'_x \sin \beta (-v_{,x} \sin \beta + w_{,x} \cos \beta) \}_{,x} + \bar{V}_x w_{,x} + \\
& \bar{S}'_x \cos \beta (v_{,xx} \cos \beta + w_{,xx} \sin \beta) ] \delta w \Big|_0^{l_e} \\
& + \{ \bar{S}_x + \bar{T}_x \phi_{,x} \} \delta \phi \Big|_0^{l_e} + \{ \bar{P}_x \} \delta \alpha \Big|_0^{l_e} - \{ \bar{M}'_z \} \delta \bar{y}_{x\eta} \Big|_0^{l_e} \\
& + \{ \bar{M}'_y \} \delta \bar{y}_{x\zeta} \Big|_0^{l_e}
\end{aligned}$$

The boundary terms contained in Eq. (4.18) are latter combined with the boundary terms associated with the variations of kinetic energy and work of external loads to obtain the boundary conditions associated with the equations of motion.

## 4.2 KINETIC ENERGY CONTRIBUTIONS

The total kinetic energy of a beam element is defined as:

$$T = \frac{1}{2} \iiint_V \rho \mathbf{V} \cdot \mathbf{V} dV = \frac{1}{2} \int_0^{l_c} \iiint_{\Lambda} \rho \mathbf{V} \cdot \mathbf{V} d\eta d\zeta dx \quad (4.19)$$

where  $\mathbf{V}$  is the velocity vector of an arbitrary point on the beam with respect to the inertial reference frame.

The position vector,  $\mathbf{R}$ , of a point on the deformed beam is written, by combining Eqs. (3.28), (3.26), and (3.1) with Eq. (3.4), as:

$$\begin{aligned} \mathbf{R} &= c_1 \hat{i}_r + h_c \hat{i}_b + (x + u) \hat{e}_x + v \hat{e}_y + w \hat{e}_z \\ &\quad + \eta \mathbf{E}_\eta + \zeta \mathbf{E}_\zeta + \alpha \Psi \hat{e}'_x \\ &= \mathbf{R}_B + \mathbf{R}_C \end{aligned} \quad (4.20)$$

where

$$\mathbf{R}_B = c_1 \hat{i}_r \quad (4.21)$$

is the position vector of the blade root with respect to the hub center, and

$$\begin{aligned} \mathbf{R}_C &= h_c \hat{i}_b + (x + u) \hat{e}_x + v \hat{e}_y + w \hat{e}_z + \eta \mathbf{E}_\eta \\ &\quad + \zeta \mathbf{E}_\zeta + \alpha \Psi \hat{e}'_x \end{aligned} \quad (4.22)$$

is the position vector of an arbitrary point on the deformed beam with respect to the blade root.

The velocity vector,  $\mathbf{V}$ , is calculated by differentiating the deformed position vector,  $\mathbf{R}$ , with respect to time:

$$\mathbf{V} = \left\{ \frac{d\mathbf{R}}{dt} \right\}_{nr} = \mathbf{V}_B + \mathbf{V}_C \quad (4.23)$$

where  $\mathbf{V}_B$  and  $\mathbf{V}_C$  are the time derivatives of  $\mathbf{R}_B$  and  $\mathbf{R}_C$ , respectively. The notation  $\left\{ \frac{d}{dt} \right\}_{nr}$  denotes time derivative with respect to the nonrotating, hub-fixed coordinate system  $(\hat{i}_{nr}, \hat{j}_{nr}, \hat{k}_{nr})$ , which is an inertial reference frame. In this derivation, the velocity components are expressed in terms of the undeformed element coordinate system  $(\hat{e}_x, \hat{e}_y, \hat{e}_z)$ . It follows that, the velocity vector of the blade root,  $\mathbf{V}_B$  is:

$$\begin{aligned} \mathbf{V}_B &= \Omega \hat{k}_r \times \mathbf{R}_B = \Omega e_1 \hat{j}_r \\ &= V_{bx} \hat{e}_x + V_{by} \hat{e}_y + V_{bz} \hat{e}_z \end{aligned} \quad (4.24)$$

where

$$\begin{Bmatrix} V_{bx} \\ V_{by} \\ V_{bz} \end{Bmatrix} = \Omega e_1 [T_{eb}] [T_{br}] \begin{Bmatrix} 0 \\ 1 \\ 0 \end{Bmatrix} = \Omega e_1 [T_{eb}] \begin{Bmatrix} 0 \\ \cos \theta_p \\ -\sin \theta_p \end{Bmatrix} \quad (4.25)$$

*For the straight portion of the blade*

$$\begin{Bmatrix} V_{bx} \\ V_{by} \\ V_{bz} \end{Bmatrix} = \Omega e_1 \begin{Bmatrix} 0 \\ \cos \theta_p \\ -\sin \theta_p \end{Bmatrix} \quad (4.26)$$

*For the swept-tip element*

$$\begin{Bmatrix} V_{bx} \\ V_{by} \\ V_{bz} \end{Bmatrix} = \Omega e_1 \begin{Bmatrix} -\sin \Lambda_s \cos \theta_p - \cos \Lambda_s \sin \Lambda_a \sin \theta_p \\ \cos \Lambda_s \cos \theta_p - \sin \Lambda_s \sin \Lambda_a \sin \theta_p \\ -\cos \Lambda_a \sin \theta_p \end{Bmatrix} \quad (4.27)$$

The velocity vector,  $\mathbf{V}_C$ , which is the velocity of an arbitrary point on the deformed beam relative to the velocity of the blade root, is:

$$\mathbf{V}_C = \dot{\mathbf{R}}_C + \vec{\omega} \times \mathbf{R}_C \quad (4.28)$$

where  $\vec{\omega}$  is the angular velocity of the undeformed element coordinate system  $(\hat{\mathbf{e}}_x, \hat{\mathbf{e}}_y, \hat{\mathbf{e}}_z)$ :

$$\vec{\omega} = \Omega \hat{\mathbf{k}}_r + \dot{\theta}_p \hat{\mathbf{i}}_b = \Omega_x \hat{\mathbf{e}}_x + \Omega_y \hat{\mathbf{e}}_y + \Omega_z \hat{\mathbf{e}}_z \quad (4.29)$$

which is the sum of the constant angular velocity of the rotor and the angular velocity of the blade due to the harmonic components of the blade pitch settings. The notation  $\dot{(\ )}$  denotes the time derivative with respect to the  $(\hat{\mathbf{e}}_x, \hat{\mathbf{e}}_y, \hat{\mathbf{e}}_z)$  system when  $(\ )$  is a vector, and it is the usual time derivative when  $(\ )$  is a scalar. Recall that the pitch angle  $\theta_p$  is:

$$\theta_p = \theta_0 + \theta_{1c} \cos \psi + \theta_{1s} \sin \psi \quad (2.5)$$

Therefore,

$$\dot{\theta}_p = \Omega (-\theta_{1c} \sin \psi + \theta_{1s} \cos \psi) \quad (4.30)$$

$$\ddot{\theta}_p = -\Omega^2 (\theta_{1c} \cos \psi + \theta_{1s} \sin \psi) \quad (4.31)$$

In forward flight, the blade pitch angle  $\theta_p$  is a function of the blade azimuth angle  $\psi$ , therefore it contributes to the angular velocity of the blade. For the case of hover,  $\dot{\theta}_p$  and  $\ddot{\theta}_p$  vanish since the cyclic cosine  $\theta_{1c}$  and the cyclic sine

$\theta_{1s}$  are equal to zero. The angular velocity components in the  $(\hat{c}_x, \hat{c}_y, \hat{c}_z)$  system is obtained by:

$$\begin{aligned} \begin{Bmatrix} \Omega_x \\ \Omega_y \\ \Omega_z \end{Bmatrix} &= [T_{cb}] \left( [T_{br}] \begin{Bmatrix} 0 \\ 0 \\ \Omega \end{Bmatrix} + \begin{Bmatrix} \dot{\theta}_p \\ 0 \\ 0 \end{Bmatrix} \right) \\ &= [T_{eb}] \begin{Bmatrix} \Omega\beta_p + \dot{\theta}_p \\ \Omega \sin \theta_p \\ \Omega \cos \theta_p \end{Bmatrix} \end{aligned} \quad (4.32)$$

*For the straight portion of the blade*

$$\begin{Bmatrix} \Omega_x \\ \Omega_y \\ \Omega_z \end{Bmatrix} = \begin{Bmatrix} \Omega\beta_p + \dot{\theta}_p \\ \Omega \sin \theta_p \\ \Omega \cos \theta_p \end{Bmatrix} \quad (4.33)$$

*For the swept-tip element*

$$\begin{Bmatrix} \Omega_x \\ \Omega_y \\ \Omega_z \end{Bmatrix} = \begin{Bmatrix} (\Omega\beta_p + \dot{\theta}_p) \cos \Lambda_s \cos \Lambda_a - \Omega \sin \theta_p \sin \Lambda_s + \Omega \cos \theta_p \cos \Lambda_s \sin \Lambda_a \\ (\Omega\beta_p + \dot{\theta}_p) \sin \Lambda_s \cos \Lambda_a + \Omega \sin \theta_p \cos \Lambda_s + \Omega \cos \theta_p \sin \Lambda_s \sin \Lambda_a \\ - (\Omega\beta_p + \dot{\theta}_p) \sin \Lambda_a + \Omega \cos \theta_p \cos \Lambda_a \end{Bmatrix}$$

(4.34)

The position vector  $\mathbf{R}_C$  can be written in terms of the  $(\hat{c}_x, \hat{c}_y, \hat{c}_z)$  system by substituting Eqs. (3.10b,c) into Eq. (4.22):

$$\mathbf{R}_C = R_{cx} \hat{e}_x + R_{cy} \hat{e}_y + R_{cz} \hat{e}_z \quad (4.35)$$

where

$$\begin{Bmatrix} R_{cx} \\ R_{cy} \\ R_{cz} \end{Bmatrix} = \begin{Bmatrix} h_x + x + u \\ h_y + v \\ h_z + w \end{Bmatrix} + [T_{dc}]^T \begin{Bmatrix} \alpha\Psi + \eta\bar{\gamma}_{x\eta} + \zeta\bar{\gamma}_{x\zeta} \\ \eta \\ \zeta \end{Bmatrix} \quad (4.36)$$

In Eq. (4.36),  $h_x$ ,  $h_y$  and  $h_z$  are the components of  $h_e$ , which is the offset of the in-board node of the beam finite element from the blade root, in the  $(\hat{e}_x, \hat{e}_y, \hat{e}_z)$  system:

$$\begin{Bmatrix} h_x \\ h_y \\ h_z \end{Bmatrix} = [T_{cb}] \begin{Bmatrix} h_c \\ 0 \\ 0 \end{Bmatrix} \quad (4.37)$$

*For the straight portion of the blade*

$$\begin{Bmatrix} h_x \\ h_y \\ h_z \end{Bmatrix} = \begin{Bmatrix} h_c \\ 0 \\ 0 \end{Bmatrix} \quad (4.38)$$

*For the swept-tip element*

$$\begin{Bmatrix} h_x \\ h_y \\ h_z \end{Bmatrix} = h_e \begin{Bmatrix} \cos \Lambda_s \cos \Lambda_a \\ \sin \Lambda_s \cos \Lambda_a \\ -\sin \Lambda_a \end{Bmatrix} \quad (4.39)$$

The matrix  $[T_{dc}]$ , which is the transformation between the deformed curvilinear coordinate system  $(\hat{e}'_x, \hat{e}'_y, \hat{e}'_z)$  and the undeformed element coordinate system  $(\hat{e}_x, \hat{e}_y, \hat{e}_z)$ , is given by

$$[T_{dc}] = [T_{dc}] [T_{ce}] \quad (2.15)$$

Combining Eqs. (2.9), (2.13) and (3.39) with Eq. (2.15) and applying the ordering scheme, the transformation matrix  $[T_{de}]$  becomes:

$$[T_{de}] = \begin{bmatrix} 1 & v_{,x} & w_{,x} \\ -v_{,x} \cos(\beta + \phi) & \cos(\beta + \phi) & \sin(\beta + \phi) \\ -w_{,x} \sin(\beta + \phi) & & \\ v_{,x} \sin(\beta + \phi) & -\sin(\beta + \phi) & \cos(\beta + \phi) \\ -w_{,x} \cos(\beta + \phi) & +\tau_c' \cos \beta & +\tau_c' \sin \beta \end{bmatrix} \quad (4.40)$$

where

$$\tau_c' = (v_{,x} \sin \beta - w_{,x} \cos \beta)(v_{,x} \cos \beta + w_{,x} \sin \beta) \quad (4.41)$$

A comparison of the transformation matrix  $[T_{de}]$  with similar transformation matrices by other authors is presented in Appendix A.

Differentiating Eq. (4.36) with respect to time gives:

$$\begin{aligned} \begin{Bmatrix} \dot{R}_{cx} \\ \dot{R}_{cy} \\ \dot{R}_{cz} \end{Bmatrix} &= \begin{Bmatrix} \dot{u} \\ \dot{v} \\ \dot{w} \end{Bmatrix} + [T_{de}]^T \begin{Bmatrix} \dot{\alpha}\Psi + \eta \dot{\gamma}_{x\eta} + \zeta \dot{\gamma}_{x\zeta} \\ 0 \\ 0 \end{Bmatrix} \\ &+ [\dot{T}_{de}]^T \begin{Bmatrix} \alpha\Psi + \eta \bar{\gamma}_{x\eta} + \zeta \bar{\gamma}_{x\zeta} \\ \eta \\ \zeta \end{Bmatrix} \end{aligned} \quad (4.42)$$

where the matrix  $[\dot{T}_{de}]$  is:

$$[\dot{T}_{de}] = \begin{bmatrix} 0 & \dot{v}_{,x} & \dot{w}_{,x} \\ -\dot{v}_{,x} \cos(\beta + \phi) - \dot{w}_{,x} \sin(\beta + \phi) & -\dot{\phi} \sin(\beta + \phi) & \dot{\phi} \cos(\beta + \phi) \\ +\dot{\phi} \{v_{,x} \sin(\beta + \phi) - w_{,x} \cos(\beta + \phi)\} & & \\ \dot{v}_{,x} \sin(\beta + \phi) - \dot{w}_{,x} \cos(\beta + \phi) & -\dot{\phi} \cos(\beta + \phi) & -\dot{\phi} \sin(\beta + \phi) \\ +\dot{\phi} \{v_{,x} \cos(\beta + \phi) + w_{,x} \sin(\beta + \phi)\} & +\dot{\tau}_c' \cos \beta & +\dot{\tau}_c' \sin \beta \end{bmatrix}$$

(4.43)

with

$$\begin{aligned} \dot{\tau}_c' &= (\dot{v}_{,x} \sin \beta - \dot{w}_{,x} \cos \beta)(v_{,x} \cos \beta + w_{,x} \sin \beta) + \\ & \quad (v_{,x} \sin \beta - w_{,x} \cos \beta)(\dot{v}_{,x} \cos \beta + \dot{w}_{,x} \sin \beta) \end{aligned} \quad (4.44)$$

Therefore, the time derivative of  $\mathbf{R}_C$  is:

$$\begin{aligned} \dot{\mathbf{R}}_C &= \dot{R}_{cx} \hat{e}_x + \dot{R}_{cy} \hat{e}_y + \dot{R}_{cz} \hat{e}_z \\ &= [(\eta \sin \beta + \zeta \cos \beta)(-\dot{w}_{,x} + \dot{\phi} v_{,x} + \phi \dot{v}_{,x}) - (\eta \cos \beta - \zeta \sin \beta) \\ & \quad (\dot{v}_{,x} + \dot{\phi} w_{,x} + \phi \dot{w}_{,x}) + \dot{u} + \dot{\alpha} \Psi + \eta \dot{\gamma}_{x\eta} + \zeta \dot{\gamma}_{x\zeta}] \hat{e}_x \\ & \quad + [\dot{v} - \dot{\phi}(\eta \sin \beta + \zeta \cos \beta) - \zeta \cos^3 \beta (\dot{v}_{,x} w_{,x} + v_{,x} \dot{w}_{,x})] \hat{e}_y \\ & \quad + [\dot{w} + \dot{\phi}(\eta \cos \beta - \zeta \sin \beta)] \hat{e}_z \end{aligned} \quad (4.45)$$

where the expressions of  $\dot{R}_{cx}$ ,  $\dot{R}_{cy}$  and  $\dot{R}_{cz}$  have been obtained by combining Eqs. (4.40), (4.41), (4.43) and (4.44) with (4.42) and applying the ordering scheme.

The term  $\bar{\omega} \times \mathbf{R}_C$  is obtained by combining Eqs. (4.29), (4.35), (4.36) and (4.40):

$$\begin{aligned}
\vec{\omega} \times \mathbf{R}_C &= (\Omega_y R_{cz} - \Omega_z R_{cy}) \hat{e}_x + (\Omega_z R_{cx} - \Omega_x R_{cz}) \hat{e}_y + \\
&\quad (\Omega_x R_{cy} - \Omega_y R_{cx}) \hat{e}_z \\
&= \{ (\eta \sin \beta + \zeta \cos \beta) (\Omega_y + \Omega_z \phi) - \\
&\quad (\eta \cos \beta - \zeta \sin \beta) (\Omega_z - \Omega_y \phi) + \\
&\quad \Omega_y (h_z + w) - \Omega_z (h_y + v) + \zeta \cos^3 \beta \Omega_z v_{,x} w_{,x} \} \hat{e}_x \\
&+ \{ (\eta \sin \beta + \zeta \cos \beta) [ -\Omega_x + \Omega_z (\phi v_{,x} - w_{,x}) ] - \\
&\quad (\eta \cos \beta - \zeta \sin \beta) [ \Omega_x \phi + \Omega_z (v_{,x} + \phi w_{,x}) ] + \\
&\quad \Omega_z (h_x + x + u + \alpha \Psi + \eta \bar{y}_{x\eta} + \zeta \bar{y}_{x\zeta}) - \Omega_x (h_z + w) \} \hat{e}_y \\
&+ \{ (\eta \cos \beta - \zeta \sin \beta) [ \Omega_x + \Omega_y (v_{,x} + \phi w_{,x}) ] - \\
&\quad (\eta \sin \beta + \zeta \cos \beta) [ \Omega_x \phi + \Omega_y (\phi v_{,x} - w_{,x}) ] - \\
&\quad \Omega_y (h_x + x + u + \alpha \Psi + \eta \bar{y}_{x\eta} + \zeta \bar{y}_{x\zeta}) + \Omega_x (h_y + v) - \\
&\quad \zeta \cos^3 \beta \Omega_x v_{,x} w_{,x} \} \hat{e}_z
\end{aligned} \tag{4.46}$$

Terms up to order  $\varepsilon^3$  have been retained in Eqs. (4.45) and (4.46) since some terms of order  $\varepsilon^3$  can not be neglected in the derivation of the kinetic energy variation,  $\delta T$ , when the dot product of the velocity vector,  $\mathbf{V}$ , and its variation,  $\delta \mathbf{V}$ , is carried out.

The total velocity vector,  $\mathbf{V}$ , is obtained by substituting Eqs. (4.45) and (4.46) into Eq. (4.28) and combining Eqs. (4.24) and (4.28) with Eq. (4.23):

$$\begin{aligned}
\mathbf{V} = & \{ (\eta \sin \beta + \zeta \cos \beta) (-\dot{w}_{,x} + \dot{\phi}v_{,x} + \phi\dot{v}_{,x} + \Omega_y + \Omega_z\phi) - \\
& (\eta \cos \beta - \zeta \sin \beta) (\dot{v}_{,x} + \dot{\phi}w_{,x} + \phi\dot{w}_{,x} + \Omega_z - \Omega_y\phi) + \\
& \dot{u} + \dot{\alpha}\Psi + \eta\dot{\bar{\gamma}}_{x\eta} + \zeta\dot{\bar{\gamma}}_{x\zeta} + \Omega_y(h_z + w) - \\
& \Omega_z(h_y + v) + \zeta \cos^3\beta \Omega_z v_{,x} w_{,x} + V_{bx} \} \hat{\mathbf{e}}_x \\
+ & \{ (\eta \sin \beta + \zeta \cos \beta) [ -\Omega_x + \Omega_z(\phi v_{,x} - w_{,x}) - \dot{\phi} ] - \\
& (\eta \cos \beta - \zeta \sin \beta) [ \Omega_x\phi + \Omega_z(v_{,x} + \phi w_{,x}) ] + \\
& \Omega_z(h_x + x + u + \alpha\Psi + \eta\bar{\gamma}_{x\eta} + \zeta\bar{\gamma}_{x\zeta}) - \Omega_x(h_z + w) + \\
& \dot{v} - \zeta \cos^3\beta (\dot{v}_{,x}w_{,x} + v_{,x}\dot{w}_{,x}) + V_{by} \} \hat{\mathbf{e}}_y \\
+ & \{ (\eta \cos \beta - \zeta \sin \beta) [ \Omega_x + \Omega_y(v_{,x} + \phi w_{,x}) + \dot{\phi} ] - \\
& (\eta \sin \beta + \zeta \cos \beta) [ \Omega_x\phi + \Omega_y(\phi v_{,x} - w_{,x}) ] - \\
& \Omega_y(h_x + x + u + \alpha\Psi + \eta\bar{\gamma}_{x\eta} + \zeta\bar{\gamma}_{x\zeta}) + \Omega_x(h_y + v) + \\
& \dot{w} - \zeta \cos^3\beta \Omega_x v_{,x} w_{,x} + V_{bz} \} \hat{\mathbf{e}}_z
\end{aligned} \tag{4.47}$$

The variation of the velocity vector,  $\delta\mathbf{V}$ , is:

$$\begin{aligned}
\delta \mathbf{V} = & \{ (\eta \sin \beta + \zeta \cos \beta) [ - \delta \dot{w}_{,x} + \dot{\phi} \delta v_{,x} + \phi \delta \dot{v}_{,x} + v_{,x} \delta \dot{\phi} + \\
& (\Omega_z + \dot{v}_{,x}) \delta \phi ] - (\eta \cos \beta - \zeta \sin \beta) [ \delta \dot{v}_{,x} + \dot{\phi} \delta w_{,x} + \\
& \phi \delta \dot{w}_{,x} + w_{,x} \delta \dot{\phi} - (\Omega_y - \dot{w}_{,x}) \delta \phi ] + \\
& \delta \dot{u} + \delta \dot{\alpha} \Psi + \eta \delta \ddot{\bar{\gamma}}_{x\eta} + \zeta \delta \ddot{\bar{\gamma}}_{x\zeta} + \Omega_y \delta w - \Omega_z \delta v + \\
& \zeta \cos^3 \beta \Omega_z (v_{,x} \delta w_{,x} + w_{,x} \delta v_{,x}) \} \hat{e}_x \\
+ & \{ (\eta \sin \beta + \zeta \cos \beta) [ \Omega_z (\phi \delta v_{,x} + v_{,x} \delta \phi - \delta w_{,x}) - \delta \dot{\phi} ] - \\
& (\eta \cos \beta - \zeta \sin \beta) [ (\Omega_x + \Omega_z w_{,x}) \delta \phi + \\
& \Omega_z (\delta v_{,x} + \phi \delta w_{,x}) ] + \Omega_z (\delta u + \Psi \delta \alpha + \eta \delta \bar{\gamma}_{x\eta} + \zeta \delta \bar{\gamma}_{x\zeta}) - \\
& \Omega_x \delta w + \delta \dot{v} - \zeta \cos^3 \beta (\dot{v}_{,x} \delta w_{,x} + v_{,x} \delta \dot{w}_{,x} + \\
& \dot{w}_{,x} \delta v_{,x} + w_{,x} \delta \dot{v}_{,x}) \} \hat{e}_y \\
+ & \{ (\eta \cos \beta - \zeta \sin \beta) [ \Omega_y (\delta v_{,x} + \phi \delta w_{,x} + w_{,x} \delta \phi) + \delta \dot{\phi} ] - \\
& (\eta \sin \beta + \zeta \cos \beta) [ (\Omega_x + \Omega_y v_{,x}) \delta \phi - \Omega_y (\delta w_{,x} - \phi \delta v_{,x}) ] - \\
& \Omega_y (\delta u + \Psi \delta \alpha + \eta \delta \bar{\gamma}_{x\eta} + \zeta \delta \bar{\gamma}_{x\zeta}) + \Omega_x \delta v + \delta \dot{w} - \\
& \zeta \cos^3 \beta \Omega_x (v_{,x} \delta w_{,x} + w_{,x} \delta v_{,x}) \} \hat{e}_z
\end{aligned} \tag{4.48}$$

The variation of the kinetic energy,  $\delta T$ , for a beam element is, from Eq. (4.19):

$$\delta T = \int_0^{l_e} \iiint_A \rho \mathbf{V} \cdot \delta \mathbf{V} \, d\eta d\zeta dx \tag{4.49}$$

Substituting Eqs. (4.47) and (4.48) into Eq. (4.49) and integrating  $\delta T$  by parts with respect to time between two arbitrarily specified configurations at times  $t_1$  and  $t_2$  give:

$$\delta T = \int_0^1 \int \int_A \rho [ Z_u \delta u + Z_v \delta v + Z'_v \delta v_{,x} + Z_w \delta w + Z'_w \delta w_{,x} + Z_\phi \delta \phi + Z_\alpha \delta \alpha + Z_\eta \delta \bar{\gamma}_{x\eta} + Z_\zeta \delta \bar{\gamma}_{x\zeta} ] d\eta d\zeta dx \quad (4.50)$$

where

$$\begin{aligned} Z_u = & (\eta \sin \beta + \zeta \cos \beta) [ -\Omega_x \Omega_z - \dot{\Omega}_y + \ddot{w}_{,x} - 2\Omega_z \dot{\phi} + (\Omega_x \Omega_y - \dot{\Omega}_z) \phi - \\ & (\Omega_y^2 + \Omega_z^2) w_{,x} ] + (\eta \cos \beta - \zeta \sin \beta) [ -\Omega_x \Omega_y + \dot{\Omega}_z + \ddot{v}_{,x} - \\ & 2\Omega_y \dot{\phi} - (\Omega_x \Omega_z + \dot{\Omega}_y) \phi - (\Omega_y^2 + \Omega_z^2) v_{,x} ] . \\ & - \ddot{u} - \Psi \ddot{\alpha} - \eta \ddot{\bar{\gamma}}_{x\eta} - \zeta \ddot{\bar{\gamma}}_{x\zeta} + 2\Omega_z \dot{v} - 2\Omega_y \dot{w} \end{aligned} \quad (4.51a)$$

$$\begin{aligned} & + (\Omega_y^2 + \Omega_z^2) (h_x + x + u + \Psi \alpha + \eta \bar{\gamma}_{x\eta} + \zeta \bar{\gamma}_{x\zeta}) \\ & - (\Omega_x \Omega_y - \dot{\Omega}_z) (h_y + v) - (\Omega_x \Omega_z + \dot{\Omega}_y) (h_z + w) \\ & + \Omega_z V_{by} - \Omega_y V_{bz} - \dot{V}_{bx} \end{aligned}$$

$$\begin{aligned} Z_v = & (\eta \sin \beta + \zeta \cos \beta) [ -\Omega_y \Omega_z + \dot{\Omega}_x + \ddot{\phi} + 2\Omega_z \dot{w}_{,x} + (\Omega_x \Omega_y + \dot{\Omega}_z) w_{,x} - \\ & (\Omega_x^2 + \Omega_z^2) \phi ] + (\eta \cos \beta - \zeta \sin \beta) [ \Omega_x^2 + \Omega_z^2 + \\ & 2\Omega_z \dot{v}_{,x} + 2\Omega_x \dot{\phi} + (\Omega_x \Omega_y + \dot{\Omega}_z) v_{,x} - (\Omega_y \Omega_z - \dot{\Omega}_x) \phi ] \\ & - \ddot{v} - 2\Omega_z (\dot{u} + \Psi \dot{\alpha} + \eta \dot{\bar{\gamma}}_{x\eta} + \zeta \dot{\bar{\gamma}}_{x\zeta}) + 2\Omega_x \dot{w} \end{aligned} \quad (4.51b)$$

$$\begin{aligned} & - (\Omega_x \Omega_y + \dot{\Omega}_z) (h_x + x + u + \Psi \alpha + \eta \bar{\gamma}_{x\eta} + \zeta \bar{\gamma}_{x\zeta}) \\ & + (\Omega_x^2 + \Omega_z^2) (h_y + v) - (\Omega_y \Omega_z - \dot{\Omega}_x) (h_z + w) \\ & + \Omega_x V_{bz} - \Omega_z V_{bx} - \dot{V}_{by} \end{aligned}$$

$$\begin{aligned}
Z'_v = & (\eta \sin \beta + \zeta \cos \beta) [(\Omega_y^2 + \Omega_z^2)(h_x + x) - (\Omega_x \Omega_y - \dot{\Omega}_z)h_y - \\
& (\Omega_x \Omega_z + \dot{\Omega}_y)h_z + \Omega_z V_{by} - \Omega_y V_{bz} - \dot{V}_{bx}] \phi \\
& + (\eta \cos \beta - \zeta \sin \beta) \{ \ddot{u} + \Psi \ddot{\alpha} + \eta \ddot{\gamma}_{x\eta} + \zeta \ddot{\gamma}_{x\zeta} - 2\Omega_z \dot{v} + \\
& 2\Omega_y \dot{w} - (\Omega_y^2 + \Omega_z^2)(h_x + x + u + \Psi \alpha + \eta \bar{\gamma}_{x\eta} + \zeta \bar{\gamma}_{x\zeta}) + \\
& (\Omega_x \Omega_y - \dot{\Omega}_z)(h_y + v) + (\Omega_x \Omega_z + \dot{\Omega}_y)(h_z + w) - \\
& \Omega_z V_{by} + \Omega_y V_{bz} + \dot{V}_{bx} \} \\
& + (\Omega_x \Omega_y - \dot{\Omega}_z)(\eta^2 \cos^2 \beta + \zeta^2 \sin^2 \beta - 2\eta \zeta \sin \beta \cos \beta) \\
& + (\Omega_x \Omega_z + \dot{\Omega}_y) [(\eta^2 - \zeta^2) \sin \beta \cos \beta + \eta \zeta (\cos^2 \beta - \sin^2 \beta)] \\
& + \zeta \cos^3 \beta [(\Omega_x \Omega_y + \dot{\Omega}_z)(h_x + x) - (\Omega_x^2 + \Omega_z^2)h_y + (\Omega_y \Omega_z - \dot{\Omega}_x)h_z \\
& + \Omega_z V_{bx} - \Omega_x V_{bz} + \dot{V}_{by}] w_{,x}
\end{aligned} \tag{4.51c}$$

$$\begin{aligned}
Z_w = & (\eta \sin \beta + \zeta \cos \beta) [\Omega_x^2 + \Omega_y^2 - 2\Omega_y \dot{w}_{,x} + 2\Omega_x \dot{\phi} + \\
& (\Omega_x \Omega_z - \dot{\Omega}_y)w_{,x} + (\Omega_y \Omega_z + \dot{\Omega}_x)\phi] - (\eta \cos \beta - \zeta \sin \beta) \\
& [\Omega_y \Omega_z + \dot{\Omega}_x + \ddot{\phi} + 2\Omega_y \dot{v}_{,x} - (\Omega_x \Omega_z - \dot{\Omega}_y)v_{,x} - (\Omega_x^2 + \Omega_y^2)\phi] \\
& - \ddot{w} + 2\Omega_y (\dot{u} + \Psi \dot{\alpha} + \eta \dot{\gamma}_{x\eta} + \zeta \dot{\gamma}_{x\zeta}) - 2\Omega_x \dot{v} \\
& - (\Omega_x \Omega_z - \dot{\Omega}_y)(h_x + x + u + \Psi \alpha + \eta \bar{\gamma}_{x\eta} + \zeta \bar{\gamma}_{x\zeta}) \\
& + (\Omega_x^2 + \Omega_y^2)(h_z + w) - (\Omega_y \Omega_z + \dot{\Omega}_x)(h_y + v) \\
& + \Omega_y V_{bx} - \Omega_x V_{by} - \dot{V}_{bz}
\end{aligned} \tag{4.51d}$$

$$\begin{aligned}
Z'_w = & (\eta \sin \beta + \zeta \cos \beta) \{ \ddot{u} + \Psi \ddot{\alpha} + \eta \ddot{\bar{y}}_{x\eta} + \zeta \ddot{\bar{y}}_{x\zeta} - 2\Omega_z \dot{v} + 2\Omega_y \dot{w} - \\
& (\Omega_y^2 + \Omega_z^2)(h_x + x + u + \Psi \alpha + \eta \bar{y}_{x\eta} + \zeta \bar{y}_{x\zeta}) + \\
& (\Omega_x \Omega_y - \dot{\Omega}_z)(h_y + v) + (\Omega_x \Omega_z + \dot{\Omega}_y)(h_z + w) - \Omega_z V_{by} + \Omega_y V_{bz} + \dot{V}_{bx} \} \\
& - (\eta \cos \beta - \zeta \sin \beta) [(\Omega_y^2 + \Omega_z^2)(h_x + x) - \\
& (\Omega_x \Omega_y - \dot{\Omega}_z)h_y - (\Omega_x \Omega_z + \dot{\Omega}_y)h_z + \Omega_z V_{by} - \Omega_y V_{bz} - \dot{V}_{bx}] \phi \quad (4.51c) . \\
& + (\Omega_x \Omega_y - \dot{\Omega}_z) [(\eta^2 - \zeta^2) \sin \beta \cos \beta + \eta \zeta (\cos^2 \beta - \sin^2 \beta)] \\
& + (\Omega_x \Omega_z + \dot{\Omega}_y)(\eta^2 \sin^2 \beta + \zeta^2 \cos^2 \beta + 2\eta \zeta \sin \beta \cos \beta) \\
& + \zeta \cos^3 \beta [(\Omega_x \Omega_y + \dot{\Omega}_z)(h_x + x) - (\Omega_x^2 + \Omega_z^2)h_y + (\Omega_y \Omega_z - \dot{\Omega}_x)h_z \\
& + \Omega_z V_{bx} - \Omega_x V_{bz} + \dot{V}_{by}] v_{,x}
\end{aligned}$$

$$\begin{aligned}
Z_\phi = & (\eta \sin \beta + \zeta \cos \beta) \{ \ddot{v} + 2\Omega_z (\dot{u} + \Psi \dot{\alpha} + \eta \ddot{\gamma}_{x\eta} + \zeta \ddot{\gamma}_{x\zeta}) - \\
& 2\Omega_x \dot{w} + (\Omega_x \Omega_y + \dot{\Omega}_z) (h_x + x + u + \Psi \alpha + \eta \gamma_{x\eta} + \zeta \gamma_{x\zeta}) - \\
& (\Omega_x^2 + \Omega_z^2) (h_y + v) + (\Omega_y \Omega_z - \dot{\Omega}_x) (h_z + w) + \Omega_z V_{bx} - \Omega_x V_{bz} + \dot{V}_{by} \\
& + [(\Omega_y^2 + \Omega_z^2) (h_x + x) - (\Omega_x \Omega_y - \dot{\Omega}_z) h_y - (\Omega_x \Omega_z + \dot{\Omega}_y) h_z + \\
& \Omega_z V_{by} - \Omega_y V_{bz} - \dot{V}_{bx}] v_{,x} \} - (\eta \cos \beta - \zeta \sin \beta) \\
& \{ \ddot{w} - 2\Omega_y (\dot{u} + \Psi \dot{\alpha} + \eta \ddot{\gamma}_{x\eta} + \zeta \ddot{\gamma}_{x\zeta}) + 2\Omega_x \dot{v} + \\
& (\Omega_x \Omega_z - \dot{\Omega}_y) (h_x + x + u + \Psi \alpha + \eta \gamma_{x\eta} + \zeta \gamma_{x\zeta}) + \\
& (\Omega_y \Omega_z + \dot{\Omega}_x) (h_y + v) - (\Omega_x^2 + \Omega_y^2) (h_z + w) - \Omega_y V_{bx} + \Omega_x V_{by} + \dot{V}_{bz} \\
& + [(\Omega_y^2 + \Omega_z^2) (h_x + x) - (\Omega_x \Omega_y - \dot{\Omega}_z) h_y - (\Omega_x \Omega_z + \dot{\Omega}_y) h_z + \\
& \Omega_z V_{by} - \Omega_y V_{bz} - \dot{V}_{bx}] w_{,x} \} - (\eta^2 + \zeta^2) (\ddot{\phi} + \dot{\Omega}_x) \\
& + (\Omega_y^2 - \Omega_z^2) [(\eta^2 - \zeta^2) \sin \beta \cos \beta + \eta \zeta (\cos^2 \beta - \sin^2 \beta)] \\
& - \Omega_y \Omega_z [(\eta^2 - \zeta^2) (\cos^2 \beta - \sin^2 \beta) - 4\eta \zeta \sin \beta \cos \beta] - \\
& \{ (\Omega_z^2 - \Omega_y^2) [(\eta^2 - \zeta^2) (\cos^2 \beta - \sin^2 \beta) - 4\eta \zeta \sin \beta \cos \beta] - \\
& 4\Omega_y \Omega_z [(\eta^2 - \zeta^2) \sin \beta \cos \beta + \eta \zeta (\cos^2 \beta - \sin^2 \beta)] \} \phi
\end{aligned} \tag{4.51f}$$

$$\begin{aligned}
Z_x = & \Psi \{ (\eta \sin \beta + \zeta \cos \beta) [ -\Omega_x \Omega_z - \dot{\Omega}_y + \ddot{w}_{,x} - 2\Omega_z \dot{\phi} + (\Omega_x \Omega_y - \dot{\Omega}_z) \phi \\
& - (\Omega_y^2 + \Omega_z^2) w_{,x} ] + (\eta \cos \beta - \zeta \sin \beta) [ -\Omega_x \Omega_y + \dot{\Omega}_z + \ddot{v}_{,x} \\
& - 2\Omega_y \dot{\phi} - (\Omega_x \Omega_z + \dot{\Omega}_y) \phi - (\Omega_y^2 + \Omega_z^2) v_{,x} ] \\
& - \ddot{u} - \Psi \ddot{\alpha} - \eta \ddot{\gamma}_{x\eta} - \zeta \ddot{\gamma}_{x\zeta} + 2\Omega_z \dot{v} - 2\Omega_y \dot{w} \\
& + (\Omega_y^2 + \Omega_z^2) (h_x + x + u + \Psi \alpha + \eta \bar{\gamma}_{x\eta} + \zeta \bar{\gamma}_{x\zeta}) \\
& - (\Omega_x \Omega_y - \dot{\Omega}_z) (h_y + v) - (\Omega_x \Omega_z + \dot{\Omega}_y) (h_z + w) \\
& + \Omega_z V_{by} - \Omega_y V_{bz} - \dot{V}_{bx} \} \tag{4.51g}
\end{aligned}$$

$$\begin{aligned}
Z_\eta = & \eta \{ (\eta \sin \beta + \zeta \cos \beta) [ -\Omega_x \Omega_z - \dot{\Omega}_y + \ddot{w}_{,x} - 2\Omega_z \dot{\phi} + (\Omega_x \Omega_y - \dot{\Omega}_z) \phi \\
& - (\Omega_y^2 + \Omega_z^2) w_{,x} ] + (\eta \cos \beta - \zeta \sin \beta) [ -\Omega_x \Omega_y + \dot{\Omega}_z + \ddot{v}_{,x} \\
& - 2\Omega_y \dot{\phi} - (\Omega_x \Omega_z + \dot{\Omega}_y) \phi - (\Omega_y^2 + \Omega_z^2) v_{,x} ] \\
& - \ddot{u} - \Psi \ddot{\alpha} - \eta \ddot{\gamma}_{x\eta} - \zeta \ddot{\gamma}_{x\zeta} + 2\Omega_z \dot{v} - 2\Omega_y \dot{w} \\
& + (\Omega_y^2 + \Omega_z^2) (h_x + x + u + \Psi \alpha + \eta \bar{\gamma}_{x\eta} + \zeta \bar{\gamma}_{x\zeta}) \\
& - (\Omega_x \Omega_y - \dot{\Omega}_z) (h_y + v) - (\Omega_x \Omega_z + \dot{\Omega}_y) (h_z + w) \\
& + \Omega_z V_{by} - \Omega_y V_{bz} - \dot{V}_{bx} \} \tag{4.51h}
\end{aligned}$$

$$\begin{aligned}
Z_\zeta = & \zeta \{ (\eta \sin \beta + \zeta \cos \beta) [ -\Omega_x \Omega_z - \dot{\Omega}_y + \ddot{w}_{,x} - 2\Omega_z \dot{\phi} + (\Omega_x \Omega_y - \dot{\Omega}_z) \phi \\
& - (\Omega_y^2 + \Omega_z^2) w_{,x} ] + (\eta \cos \beta - \zeta \sin \beta) [ -\Omega_x \Omega_y + \dot{\Omega}_z + \ddot{v}_{,x} \\
& - 2\Omega_y \dot{\phi} - (\Omega_x \Omega_z + \dot{\Omega}_y) \phi - (\Omega_y^2 + \Omega_z^2) v_{,x} ] \\
& - \ddot{u} - \Psi \ddot{\alpha} - \eta \ddot{\gamma}_{x\eta} - \zeta \ddot{\gamma}_{x\zeta} + 2\Omega_z \dot{v} - 2\Omega_y \dot{w} \\
& + (\Omega_y^2 + \Omega_z^2) (h_x + x + u + \Psi \alpha + \eta \bar{\gamma}_{x\eta} + \zeta \bar{\gamma}_{x\zeta}) \\
& - (\Omega_x \Omega_y - \dot{\Omega}_z) (h_y + v) - (\Omega_x \Omega_z + \dot{\Omega}_y) (h_z + w) \\
& + \Omega_z V_{by} - \Omega_y V_{bz} - \dot{V}_{bx} \}
\end{aligned} \tag{4.51i}$$

In Eqs. (4.51), the expressions of  $(\dot{V}_{bx}, \dot{V}_{by}, \dot{V}_{bz})$  and  $(\dot{\Omega}_x, \dot{\Omega}_y, \dot{\Omega}_z)$  are obtained by differentiating Eqs. (4.25) and (4.32), respectively, with respect to time:

$$\begin{Bmatrix} \dot{V}_{bx} \\ \dot{V}_{by} \\ \dot{V}_{bz} \end{Bmatrix} = -\Omega \dot{\theta}_p e_1 [T_{cb}] \begin{Bmatrix} 0 \\ \sin \theta_p \\ \cos \theta_p \end{Bmatrix} \tag{4.52}$$

$$\begin{Bmatrix} \dot{\Omega}_x \\ \dot{\Omega}_y \\ \dot{\Omega}_z \end{Bmatrix} = [T_{cb}] \begin{Bmatrix} \ddot{\theta}_p \\ \Omega \dot{\theta}_p \cos \theta_p \\ -\Omega \dot{\theta}_p \sin \theta_p \end{Bmatrix} \tag{4.53}$$

Integrating Eq. (4.50) over the cross section gives:

$$\begin{aligned}
\delta T = & \int_0^{l_c} [ \bar{Z}_u \delta u + \bar{Z}_v \delta v + \bar{Z}'_v \delta v_{,x} + \bar{Z}_w \delta w + \bar{Z}'_w \delta w_{,x} \\
& + \bar{Z}_\phi \delta \phi + \bar{Z}_\alpha \delta \alpha + \bar{Z}_\eta \delta \bar{\gamma}_{x\eta} + \bar{Z}_\zeta \delta \bar{\gamma}_{x\zeta} ] dx
\end{aligned} \tag{4.54}$$

where

$$\begin{aligned}
\bar{Z}_u = & (m\eta_m \sin \beta + m\zeta_m \cos \beta) [ -\Omega_x \Omega_z - \dot{\Omega}_y + \ddot{w}_{,x} - 2\Omega_z \dot{\phi} \\
& + (\Omega_x \Omega_y - \dot{\Omega}_z) \phi - (\Omega_y^2 + \Omega_z^2) w_{,x} ] + (m\eta_m \cos \beta - m\zeta_m \sin \beta) \\
& [ -\Omega_x \Omega_y + \dot{\Omega}_z + \ddot{v}_{,x} - 2\Omega_y \dot{\phi} - (\Omega_x \Omega_z + \dot{\Omega}_y) \phi - (\Omega_y^2 + \Omega_z^2) v_{,x} ] \\
& - m[\ddot{u} - 2\Omega_z \dot{v} + 2\Omega_y \dot{w} - (\Omega_y^2 + \Omega_z^2)(h_x + x + u) + \quad (4.55a) \\
& (\Omega_x \Omega_y - \dot{\Omega}_z)(h_y + v) + (\Omega_x \Omega_z + \dot{\Omega}_y)(h_z + w) - \Omega_z V_{by} + \Omega_y V_{bz} + \dot{V}_{bx}] \\
& - mD_0[\ddot{\alpha} - (\Omega_y^2 + \Omega_z^2)\alpha] - m\eta_m[\ddot{\gamma}_{x\eta} - (\Omega_y^2 + \Omega_z^2)\bar{\gamma}_{x\eta}] \\
& - m\zeta_m[\ddot{\gamma}_{x\zeta} - (\Omega_y^2 + \Omega_z^2)\bar{\gamma}_{x\zeta}]
\end{aligned}$$

$$\begin{aligned}
\bar{Z}_v = & (m\eta_m \sin \beta + m\zeta_m \cos \beta) [ -\Omega_y \Omega_z + \dot{\Omega}_x + \ddot{\phi} + 2\Omega_z \dot{w}_{,x} + \\
& (\Omega_x \Omega_y + \dot{\Omega}_z) w_{,x} - (\Omega_x^2 + \Omega_z^2) \phi ] + (m\eta_m \cos \beta - m\zeta_m \sin \beta) \\
& [ \Omega_x^2 + \Omega_z^2 + 2\Omega_z \dot{v}_{,x} + 2\Omega_x \dot{\phi} + (\Omega_x \Omega_y + \dot{\Omega}_z) v_{,x} - (\Omega_y \Omega_z - \dot{\Omega}_x) \phi ] \\
& - m[\ddot{v} + 2\Omega_z \dot{u} - 2\Omega_x \dot{w} + (\Omega_x \Omega_y + \dot{\Omega}_z)(h_x + x + u) - \quad (4.55b) \\
& (\Omega_x^2 + \Omega_z^2)(h_y + v) + (\Omega_y \Omega_z - \dot{\Omega}_x)(h_z + w) - \Omega_x V_{bz} + \Omega_z V_{bx} + \dot{V}_{by}] \\
& - mD_0[2\Omega_z \dot{\alpha} + (\Omega_x \Omega_y + \dot{\Omega}_z)\alpha] - m\eta_m [2\Omega_z \dot{\gamma}_{x\eta} + (\Omega_x \Omega_y + \dot{\Omega}_z)\bar{\gamma}_{x\eta}] \\
& - m\zeta_m [2\Omega_z \dot{\gamma}_{x\zeta} + (\Omega_x \Omega_y + \dot{\Omega}_z)\bar{\gamma}_{x\zeta}]
\end{aligned}$$

$$\begin{aligned}
\bar{Z}'_v = & (m\eta_m \sin \beta + m\zeta_m \cos \beta) [(\Omega_y^2 + \Omega_z^2)(h_x + x) - \\
& (\Omega_x \Omega_y - \dot{\Omega}_z)h_y - (\Omega_x \Omega_z + \dot{\Omega}_y)h_z + \Omega_z V_{by} - \Omega_y V_{bz} - \dot{V}_{bx}] \phi \\
& + (m\eta_m \cos \beta - m\zeta_m \sin \beta) \{ \ddot{u} - 2\Omega_z \dot{v} + 2\Omega_y \dot{w} - (\Omega_y^2 + \Omega_z^2) \\
& (h_x + x + u) + (\Omega_x \Omega_y - \dot{\Omega}_z)(h_y + v) + (\Omega_x \Omega_z + \dot{\Omega}_y)(h_z + w) \\
& - \Omega_z V_{by} + \Omega_y V_{bz} + \dot{V}_{bx} \} \\
& + (mD_1 \cos \beta - mD_2 \sin \beta) [\ddot{\alpha} - (\Omega_y^2 + \Omega_z^2) \alpha] \\
& + (Im_{\zeta\zeta} \cos \beta - Im_{\eta\zeta} \sin \beta) [\ddot{\bar{y}}_{x\eta} - (\Omega_y^2 + \Omega_z^2) \bar{y}_{x\eta}] \\
& + (Im_{\eta\zeta} \cos \beta - Im_{\eta\eta} \sin \beta) [\ddot{\bar{y}}_{x\zeta} - (\Omega_y^2 + \Omega_z^2) \bar{y}_{x\zeta}] \\
& + (\Omega_x \Omega_y - \dot{\Omega}_z)(Im_{\zeta\zeta} \cos^2 \beta + Im_{\eta\eta} \sin^2 \beta - 2Im_{\eta\zeta} \sin \beta \cos \beta) \\
& + (\Omega_x \Omega_z + \dot{\Omega}_y) [(Im_{\zeta\zeta} - Im_{\eta\eta}) \sin \beta \cos \beta + Im_{\eta\zeta} (\cos^2 \beta - \sin^2 \beta)] \\
& + m\zeta_m \cos^3 \beta [(\Omega_x \Omega_y + \dot{\Omega}_z)(h_x + x) - (\Omega_x^2 + \Omega_z^2) h_y + (\Omega_y \Omega_z - \dot{\Omega}_x) h_z \\
& + \Omega_z V_{bx} - \Omega_x V_{bz} + \dot{V}_{by}] w_{,x}
\end{aligned} \tag{4.55c}$$

$$\begin{aligned}
\bar{Z}_w = & (m\eta_m \sin \beta + m\zeta_m \cos \beta) [\Omega_x^2 + \Omega_y^2 - 2\Omega_y \dot{w}_{,x} + 2\Omega_x \dot{\phi} + \\
& (\Omega_x \Omega_z - \dot{\Omega}_y)w_{,x} + (\Omega_y \Omega_z + \dot{\Omega}_x)\phi] - (m\eta_m \cos \beta - m\zeta_m \sin \beta) \\
& [\Omega_y \Omega_z + \dot{\Omega}_x + \ddot{\phi} + 2\Omega_y \dot{v}_{,x} - (\Omega_x \Omega_z - \dot{\Omega}_y)v_{,x} - (\Omega_x^2 + \Omega_y^2) \phi] \\
& - m[\ddot{w} - 2\Omega_y \dot{u} + 2\Omega_x \dot{v} + (\Omega_x \Omega_z - \dot{\Omega}_y)(h_x + x + u) - \\
& (\Omega_x^2 + \Omega_y^2)(h_z + w) + (\Omega_y \Omega_z + \dot{\Omega}_x)(h_y + v) - \Omega_y V_{bx} + \Omega_x V_{by} + \dot{V}_{bz}] \\
& + mD_0 [2\Omega_y \dot{\alpha} - (\Omega_x \Omega_z - \dot{\Omega}_y)\alpha] + m\eta_m [2\Omega_y \dot{\bar{y}}_{x\eta} - (\Omega_x \Omega_z - \dot{\Omega}_y)\bar{y}_{x\eta}] \\
& + m\zeta_m [2\Omega_y \dot{\bar{y}}_{x\zeta} - (\Omega_x \Omega_z - \dot{\Omega}_y)\bar{y}_{x\zeta}]
\end{aligned} \tag{4.55d}$$

$$\begin{aligned}
\bar{Z}'_w = & (m\eta_m \sin \beta + m\zeta_m \cos \beta) \{ \ddot{u} - 2\Omega_z \dot{v} + 2\Omega_y \dot{w} - (\Omega_y^2 + \Omega_z^2) \\
& (h_x + x + u) + (\Omega_x \Omega_y - \dot{\Omega}_z)(h_y + v) + (\Omega_x \Omega_z + \dot{\Omega}_y)(h_z + w) \\
& - \Omega_z V_{by} + \Omega_y V_{bz} + \dot{V}_{bx} \} \\
& - (m\eta_m \cos \beta - m\zeta_m \sin \beta) [(\Omega_y^2 + \Omega_z^2)(h_x + x) - \\
& (\Omega_x \Omega_y - \dot{\Omega}_z)h_y - (\Omega_x \Omega_z + \dot{\Omega}_y)h_z + \Omega_z V_{by} - \Omega_y V_{bz} - \dot{V}_{bx}] \phi \\
& + (mD_1 \sin \beta + mD_2 \cos \beta) [\ddot{\alpha} - (\Omega_y^2 + \Omega_z^2) \alpha] \\
& + (\text{Im}_{\zeta\zeta} \sin \beta + \text{Im}_{\eta\zeta} \cos \beta) [\ddot{\bar{\gamma}}_{x\eta} - (\Omega_y^2 + \Omega_z^2) \bar{\gamma}_{x\eta}] \\
& + (\text{Im}_{\eta\zeta} \sin \beta + \text{Im}_{\eta\eta} \cos \beta) [\ddot{\bar{\gamma}}_{x\zeta} - (\Omega_y^2 + \Omega_z^2) \bar{\gamma}_{x\zeta}] \\
& + (\Omega_x \Omega_y - \dot{\Omega}_z)[(\text{Im}_{\zeta\zeta} - \text{Im}_{\eta\eta}) \sin \beta \cos \beta + \text{Im}_{\eta\zeta}(\cos^2 \beta - \sin^2 \beta)] \\
& + (\Omega_x \Omega_z + \dot{\Omega}_y)(\text{Im}_{\zeta\zeta} \sin^2 \beta + \text{Im}_{\eta\eta} \cos^2 \beta + 2\text{Im}_{\eta\zeta} \sin \beta \cos \beta) \\
& + m\zeta_m \cos^3 \beta [(\Omega_x \Omega_y + \dot{\Omega}_z)(h_x + x) - (\Omega_x^2 + \Omega_z^2)h_y + (\Omega_y \Omega_z - \dot{\Omega}_x)h_z \\
& + \Omega_z V_{bx} - \Omega_x V_{bz} + \dot{V}_{by}] v_{,x}
\end{aligned} \tag{4.55e}$$

$$\begin{aligned}
\bar{Z}_\phi = & (m\eta_m \sin \beta + m\zeta_m \cos \beta) \{ \ddot{v} + 2\Omega_z \dot{u} - 2\Omega_x \dot{w} + (\Omega_x \Omega_y + \dot{\Omega}_z) \\
& (h_x + x + u) - (\Omega_x^2 + \Omega_z^2)(h_y + v) + (\Omega_y \Omega_z - \dot{\Omega}_x)(h_z + w) + \\
& \Omega_z V_{bx} - \Omega_x V_{bz} + \dot{V}_{by} + \\
& [(\Omega_y^2 + \Omega_z^2)(h_x + x) - (\Omega_x \Omega_y - \dot{\Omega}_z)h_y - (\Omega_x \Omega_z + \dot{\Omega}_y)h_z + \\
& \Omega_z V_{by} - \Omega_y V_{bz} - \dot{V}_{bx}] v_{,x} \} - (m\eta_m \cos \beta - m\zeta_m \sin \beta) \\
& \{ \ddot{w} - 2\Omega_y \dot{u} + 2\Omega_x \dot{v} + (\Omega_x \Omega_z - \dot{\Omega}_y)(h_x + x + u) + \\
& (\Omega_y \Omega_z + \dot{\Omega}_x)(h_y + v) - (\Omega_x^2 + \Omega_y^2)(h_z + w) - \Omega_y V_{bx} + \Omega_x V_{by} + \dot{V}_{bz} \\
& + [(\Omega_y^2 + \Omega_z^2)(h_x + x) - (\Omega_x \Omega_y - \dot{\Omega}_z)h_y - (\Omega_x \Omega_z + \dot{\Omega}_y)h_z + \\
& \Omega_z V_{by} - \Omega_y V_{bz} - \dot{V}_{bx}] w_{,x} \} - (\text{Im}_{\eta\eta} + \text{Im}_{\zeta\zeta})(\ddot{\phi} + \dot{\Omega}_x) \\
& + (\Omega_y^2 - \Omega_z^2) [(\text{Im}_{\zeta\zeta} - \text{Im}_{\eta\eta}) \sin \beta \cos \beta + \text{Im}_{\eta\zeta} (\cos^2 \beta - \sin^2 \beta)] \quad (4.55f) \\
& - \Omega_y \Omega_z [(\text{Im}_{\zeta\zeta} - \text{Im}_{\eta\eta})(\cos^2 \beta - \sin^2 \beta) - 4\text{Im}_{\eta\zeta} \sin \beta \cos \beta] \\
& + (mD_1 \sin \beta + mD_2 \cos \beta) [2\Omega_z \dot{\alpha} + (\Omega_x \Omega_y + \dot{\Omega}_z)\alpha] \\
& + (mD_1 \cos \beta - mD_2 \sin \beta) [2\Omega_y \dot{\alpha} - (\Omega_x \Omega_z - \dot{\Omega}_y)\alpha] \\
& + (\text{Im}_{\zeta\zeta} \sin \beta + \text{Im}_{\eta\zeta} \cos \beta) [2\Omega_z \dot{\bar{y}}_{x\eta} + (\Omega_x \Omega_y + \dot{\Omega}_z)\bar{y}_{x\eta}] \\
& + (\text{Im}_{\zeta\zeta} \cos \beta - \text{Im}_{\eta\zeta} \sin \beta) [2\Omega_y \dot{\bar{y}}_{x\eta} - (\Omega_x \Omega_z - \dot{\Omega}_y)\bar{y}_{x\eta}] \\
& + (\text{Im}_{\eta\zeta} \sin \beta + \text{Im}_{\eta\eta} \cos \beta) [2\Omega_z \dot{\bar{y}}_{x\zeta} + (\Omega_x \Omega_y + \dot{\Omega}_z)\bar{y}_{x\zeta}] \\
& + (\text{Im}_{\eta\zeta} \cos \beta - \text{Im}_{\eta\eta} \sin \beta) [2\Omega_y \dot{\bar{y}}_{x\zeta} - (\Omega_x \Omega_z - \dot{\Omega}_y)\bar{y}_{x\zeta}] \\
& - \{(\Omega_z^2 - \Omega_y^2)[(\text{Im}_{\zeta\zeta} - \text{Im}_{\eta\eta})(\cos^2 \beta - \sin^2 \beta) - 4\text{Im}_{\eta\zeta} \sin \beta \cos \beta] - \\
& 4\Omega_y \Omega_z [(\text{Im}_{\zeta\zeta} - \text{Im}_{\eta\eta}) \sin \beta \cos \beta + \text{Im}_{\eta\zeta} (\cos^2 \beta - \sin^2 \beta)]\} \phi
\end{aligned}$$

$$\begin{aligned}
\bar{Z}_x = & (mD_1 \sin \beta + mD_2 \cos \beta) [ - \Omega_x \Omega_z - \dot{\Omega}_y + \ddot{w}_{,x} - 2\Omega_z \dot{\phi} \\
& + (\Omega_x \Omega_y - \dot{\Omega}_z) \phi - (\Omega_y^2 + \Omega_z^2) w_{,x} ] + (mD_1 \cos \beta - mD_2 \sin \beta) \\
& [ - \Omega_x \Omega_y + \dot{\Omega}_z + \ddot{v}_{,x} - 2\Omega_y \dot{\phi} - (\Omega_x \Omega_z + \dot{\Omega}_y) \phi - (\Omega_y^2 + \Omega_z^2) v_{,x} ] \\
& - mD_0 [ \ddot{u} - 2\Omega_z \dot{v} + 2\Omega_y \dot{w} - (\Omega_y^2 + \Omega_z^2) (h_x + x + u) + \\
& (\Omega_x \Omega_y - \dot{\Omega}_z) (h_y + v) + (\Omega_x \Omega_z + \dot{\Omega}_y) (h_z + w) - \Omega_z V_{by} + \Omega_y V_{bz} + \dot{V}_{bx} ] \\
& - mD_3 [ \ddot{\alpha} - (\Omega_y^2 + \Omega_z^2) \alpha ] - mD_1 [ \ddot{\bar{y}}_{x\eta} - (\Omega_y^2 + \Omega_z^2) \bar{y}_{x\eta} ] \\
& - mD_2 [ \ddot{\bar{y}}_{x\zeta} - (\Omega_y^2 + \Omega_z^2) \bar{y}_{x\zeta} ]
\end{aligned} \tag{4.55g}$$

$$\begin{aligned}
\bar{Z}_\eta = & (Im_{\zeta\zeta} \sin \beta + Im_{\eta\zeta} \cos \beta) [ - \Omega_x \Omega_z - \dot{\Omega}_y + \ddot{w}_{,x} - 2\Omega_z \dot{\phi} \\
& + (\Omega_x \Omega_y - \dot{\Omega}_z) \phi - (\Omega_y^2 + \Omega_z^2) w_{,x} ] + (Im_{\zeta\zeta} \cos \beta - Im_{\eta\zeta} \sin \beta) \\
& [ - \Omega_x \Omega_y + \dot{\Omega}_z + \ddot{v}_{,x} - 2\Omega_y \dot{\phi} - (\Omega_x \Omega_z + \dot{\Omega}_y) \phi - (\Omega_y^2 + \Omega_z^2) v_{,x} ] \\
& - m\eta_m [ \ddot{u} - 2\Omega_z \dot{v} + 2\Omega_y \dot{w} - (\Omega_y^2 + \Omega_z^2) (h_x + x + u) + \\
& (\Omega_x \Omega_y - \dot{\Omega}_z) (h_y + v) + (\Omega_x \Omega_z + \dot{\Omega}_y) (h_z + w) - \Omega_z V_{by} + \Omega_y V_{bz} + \dot{V}_{bx} ] \\
& - mD_1 [ \ddot{\alpha} - (\Omega_y^2 + \Omega_z^2) \alpha ] - Im_{\zeta\zeta} [ \ddot{\bar{y}}_{x\eta} - (\Omega_y^2 + \Omega_z^2) \bar{y}_{x\eta} ] \\
& - Im_{\eta\zeta} [ \ddot{\bar{y}}_{x\zeta} - (\Omega_y^2 + \Omega_z^2) \bar{y}_{x\zeta} ]
\end{aligned} \tag{4.55h}$$

$$\begin{aligned}
\bar{Z}_\zeta = & (\text{Im}_{\eta\zeta} \sin \beta + \text{Im}_{\eta\eta} \cos \beta) [ - \Omega_x \Omega_z - \dot{\Omega}_y + \ddot{w}_{,x} - 2\Omega_z \dot{\phi} \\
& + (\Omega_x \Omega_y - \dot{\Omega}_z) \phi - (\Omega_y^2 + \Omega_z^2) w_{,x} ] + (\text{Im}_{\eta\zeta} \cos \beta - \text{Im}_{\eta\eta} \sin \beta) \\
& [ - \Omega_x \Omega_y + \dot{\Omega}_z + \ddot{v}_{,x} - 2\Omega_y \dot{\phi} - (\Omega_x \Omega_z + \dot{\Omega}_y) \phi - (\Omega_y^2 + \Omega_z^2) v_{,x} ] \\
& - m\zeta_m [ \ddot{u} - 2\Omega_z \dot{v} + 2\Omega_y \dot{w} - (\Omega_y^2 + \Omega_z^2) (h_x + x + u) + \\
& (\Omega_x \Omega_y - \dot{\Omega}_z) (h_y + v) + (\Omega_x \Omega_z + \dot{\Omega}_y) (h_z + w) - \Omega_z V_{by} + \Omega_y V_{bz} + \dot{V}_{bx} ] \\
& - mD_2 [ \ddot{\alpha} - (\Omega_y^2 + \Omega_z^2) \alpha ] - \text{Im}_{\eta\zeta} [ \ddot{\bar{y}}_{x\eta} - (\Omega_y^2 + \Omega_z^2) \bar{y}_{x\eta} ] \\
& - \text{Im}_{\eta\eta} [ \ddot{\bar{y}}_{x\zeta} - (\Omega_y^2 + \Omega_z^2) \bar{y}_{x\zeta} ]
\end{aligned} \tag{4.55i}$$

The section integrals associated with the kinetic energy variation in Eqs. (4.55) are defined in the following manner:

$$m = \iint_A \rho \, d\eta d\zeta \tag{4.56a}$$

$$m\eta_m = \iint_A \rho\eta \, d\eta d\zeta \tag{4.56b}$$

$$m\zeta_m = \iint_A \rho\zeta \, d\eta d\zeta \tag{4.56c}$$

$$\text{Im}_{\eta\eta} = \iint_A \rho\zeta^2 \, d\eta d\zeta \tag{4.56d}$$

$$\text{Im}_{\zeta\zeta} = \iint_A \rho\eta^2 \, d\eta d\zeta \tag{4.56e}$$

$$\text{Im}_{\eta\zeta} = \iint_A \rho\eta\zeta \, d\eta d\zeta \tag{4.56f}$$

$$mD_0 = \iint_{\Lambda} \rho \Psi \, d\eta d\zeta \quad (4.56g)$$

$$mD_1 = \iint_{\Lambda} \rho \Psi \eta \, d\eta d\zeta \quad (4.56h)$$

$$mD_2 = \iint_{\Lambda} \rho \Psi \zeta \, d\eta d\zeta \quad (4.56i)$$

$$mD_3 = \iint_{\Lambda} \rho \Psi^2 \, d\eta d\zeta \quad (4.56j)$$

In Eqs. (4.56),  $m$  is the mass per unit length of the beam;  $m\eta_m$  and  $m\zeta_m$  are the mass weighted offsets of the mass center from the shear center along  $\hat{e}_\eta$  and  $\hat{e}_\zeta$ , respectively;  $Im_{\eta\eta}$ ,  $Im_{\zeta\zeta}$  and  $Im_{\eta\zeta}$  are the mass moments of inertia per unit length of the beam about the shear center;  $mD_0$ ,  $mD_1$ ,  $mD_2$  and  $mD_3$  are the mass weighted warping integrals.

Integrating the kinetic energy variation, Eq. (4.54), by parts gives:

$$\begin{aligned} \delta T = \int_0^{l_e} \{ & \bar{Z}_u \delta u + [\bar{Z}_v - (\bar{Z}'_v)_{,x}] \delta v + [\bar{Z}_w - (\bar{Z}'_w)_{,x}] \delta w \\ & + \bar{Z}_\phi \delta \phi + \bar{Z}_\alpha \delta \alpha + \bar{Z}_\eta \delta \bar{y}_{x\eta} + \bar{Z}_\zeta \delta \bar{y}_{x\zeta} \} dx + b(T) \end{aligned} \quad (4.57)$$

where the associated boundary terms are:

$$b(T) = \bar{Z}'_v \delta v \Big|_0^{l_e} + \bar{Z}'_w \delta w \Big|_0^{l_e} \quad (4.58)$$

The boundary terms contained in Eq. (4.58) are latter combined with the boundary terms associated with the variations of strain energy and work of

external loads to obtain the boundary conditions associated with the equations of motion.

### 4.3 EXTERNAL WORK CONTRIBUTIONS

The effects of the generalized (nonconservative) distributed forces and moments are included based on the principle of virtual work. In the aeroelastic analysis of rotor blades, these generalized forces and moments will be replaced by the corresponding aerodynamic forces and moments based on the aerodynamic model being used.

Virtual work is the work done by the distributed forces and moments acting through the corresponding virtual displacements and virtual rotations, respectively, about the deformed equilibrium position. The mathematical form of the virtual work done on a beam element is given by:

$$\begin{aligned}\delta W_c &= (\delta W_c)_P + (\delta W_c)_Q \\ &= \int_0^{l_c} (\mathbf{P} \cdot \delta \mathbf{u}) dx + \int_0^{l_c} (\mathbf{Q} \cdot \delta \bar{\Theta}) dx\end{aligned}\quad (4.59)$$

where  $\mathbf{P}$  and  $\mathbf{Q}$  are the distributed force and moment vectors, respectively, along the elastic axis;  $\delta \mathbf{u}$  and  $\delta \bar{\Theta}$  are the virtual displacement and virtual rotation vectors, respectively, of a point on the deformed elastic axis. The distributed forces and moments are defined in the undeformed element coordinate system  $(\hat{e}_x, \hat{e}_y, \hat{e}_z)$  as:

$$\mathbf{P} = p_x \hat{e}_x + p_y \hat{e}_y + p_z \hat{e}_z \quad (4.60)$$

$$\mathbf{Q} = q_x \hat{\mathbf{c}}_x + q_y \hat{\mathbf{c}}_y + q_z \hat{\mathbf{c}}_z \quad (4.61)$$

For convenience, the virtual displacement  $\delta \mathbf{u}$  is also defined in the  $(\hat{\mathbf{c}}_x, \hat{\mathbf{c}}_y, \hat{\mathbf{c}}_z)$  system:

$$\delta \mathbf{u} = \delta u \hat{\mathbf{c}}_x + \delta v \hat{\mathbf{c}}_y + \delta w \hat{\mathbf{c}}_z \quad (4.62)$$

The virtual rotation,  $\delta \bar{\Theta}$ , is defined in the deformed curvilinear coordinate system  $(\hat{\mathbf{c}}'_x, \hat{\mathbf{c}}'_\eta, \hat{\mathbf{c}}'_\zeta)$  because the compatibility condition associated with it, presented latter in this section, is also derived in this system. Thus, the virtual rotation is given by

$$\delta \bar{\Theta} = n_x' \hat{\mathbf{c}}'_x + n_\eta' \hat{\mathbf{c}}'_\eta + n_\zeta' \hat{\mathbf{c}}'_\zeta \quad (4.63)$$

The virtual work done on a beam element due to the distributed forces is given by:

$$(\delta W_c)_P = \int_0^{l_e} (\mathbf{P} \cdot \delta \mathbf{u}) dx = \int_0^{l_e} (p_x \delta u + p_y \delta v + p_z \delta w) dx \quad (4.64)$$

Expressing the distributed moment vector in terms of the  $(\hat{\mathbf{c}}'_x, \hat{\mathbf{c}}'_\eta, \hat{\mathbf{c}}'_\zeta)$  system as:

$$\mathbf{Q} = q_x' \hat{\mathbf{c}}'_x + q_\eta' \hat{\mathbf{c}}'_\eta + q_\zeta' \hat{\mathbf{c}}'_\zeta \quad (4.65)$$

then the virtual work done on a beam element due to the distributed moments is given by:

$$(\delta W_c)_Q = \int_0^{l_e} (\mathbf{Q} \cdot \delta \bar{\Theta}) dx = \int_0^{l_e} (q_x' n_x' + q_\eta' n_\eta' + q_\zeta' n_\zeta') dx \quad (4.66)$$

The transformation between the components of the distributed moment vector,  $\mathbf{Q}$ , is:

$$\begin{Bmatrix} q_{x'} \\ q_{\eta'} \\ q_{\zeta'} \end{Bmatrix} = [T_{dc}] \begin{Bmatrix} q_x \\ q_y \\ q_z \end{Bmatrix} \quad (4.67)$$

After the virtual displacement,  $\delta\mathbf{u}$ , and the virtual rotation,  $\delta\bar{\Theta}$ , the triad  $(\hat{\mathbf{c}}'_x, \hat{\mathbf{c}}'_\eta, \hat{\mathbf{c}}'_\zeta)$  of the deformed curvilinear coordinate system is rotated to a new triad  $(\hat{\mathbf{c}}''_x, \hat{\mathbf{c}}''_\eta, \hat{\mathbf{c}}''_\zeta)$ , given by:

$$\hat{\mathbf{c}}''_x = \hat{\mathbf{c}}'_x + \delta\bar{\Theta} \times \hat{\mathbf{c}}'_x = \hat{\mathbf{c}}'_x + n_{\zeta'} \hat{\mathbf{c}}'_\eta - n_{\eta'} \hat{\mathbf{c}}'_\zeta \quad (4.68a)$$

$$\hat{\mathbf{c}}''_\eta = \hat{\mathbf{c}}'_\eta + \delta\bar{\Theta} \times \hat{\mathbf{c}}'_\eta = \hat{\mathbf{c}}'_\eta + n_{x'} \hat{\mathbf{c}}'_\zeta - n_{\zeta'} \hat{\mathbf{c}}'_x \quad (4.68b)$$

$$\hat{\mathbf{c}}''_\zeta = \hat{\mathbf{c}}'_\zeta + \delta\bar{\Theta} \times \hat{\mathbf{c}}'_\zeta = \hat{\mathbf{c}}'_\zeta + n_{\eta'} \hat{\mathbf{c}}'_x - n_{x'} \hat{\mathbf{c}}'_\eta \quad (4.68c)$$

The virtual rotation about the deformed elastic axis,  $n_{x'}$ , is identified as:

$$n_{x'} \equiv \delta\phi \quad (4.69)$$

In order to determine  $n_{\eta'}$  and  $n_{\zeta'}$ , consider an element,  $dx$ , of the deformed elastic axis as it goes through a virtual displacement,  $\delta\mathbf{u}$  ( Fig. 4.1 ). Before the virtual displacement, the element is at position  $AB$ . After the virtual displacement, the element moves to position  $A'B'$  given by:

$$\begin{aligned} \vec{A'B'} &= (\mathbf{R}_0 + dx \hat{\mathbf{c}}'_x + \delta\mathbf{u} + \delta\mathbf{u}_{,x} dx) - (\mathbf{R}_0 + \delta\mathbf{u}) \\ &= dx (\hat{\mathbf{c}}'_x + \delta\mathbf{u}_{,x}) \end{aligned} \quad (4.70)$$

where

$$\begin{aligned}\delta \mathbf{u}_{,x} &= \delta u_{,x} \hat{\mathbf{e}}_x + \delta v_{,x} \hat{\mathbf{e}}_y + \delta w_{,x} \hat{\mathbf{e}}_z \\ &= [\delta u_{,x} \quad \delta v_{,x} \quad \delta w_{,x}] [\mathbf{T}_{dc}]^T \begin{Bmatrix} \hat{\mathbf{e}}'_x \\ \hat{\mathbf{e}}'_y \\ \hat{\mathbf{e}}'_z \end{Bmatrix}\end{aligned}\quad (4.71)$$

The vector  $\vec{A}'B'$  is in the  $\hat{\mathbf{e}}'_x$  direction, therefore, the virtual rotation components  $n_{\eta}'$  and  $n_{\zeta}'$  are obtained by substituting Eqs. (4.40) and (4.71) into Eq. (4.70) and comparing with Eq. (4.68a):

$$\begin{aligned}n_{\eta}' &= -[v_{,x} \sin(\beta + \phi) - w_{,x} \cos(\beta + \phi)] \delta u_{,x} + [\sin(\beta + \phi) - \\ &\quad \tau_c' \cos \beta] \delta v_{,x} - [\cos(\beta + \phi) + \tau_c' \sin \beta] \delta w_{,x}\end{aligned}\quad (4.72a)$$

$$\begin{aligned}n_{\zeta}' &= -[v_{,x} \cos(\beta + \phi) + w_{,x} \sin(\beta + \phi)] \delta u_{,x} \\ &\quad + [\cos(\beta + \phi)] \delta v_{,x} + [\sin(\beta + \phi)] \delta w_{,x}\end{aligned}\quad (4.72b)$$

Combining Eqs. (4.67), (4.69), (4.72) and (4.40) with Eq. (4.66), the virtual work done on a beam element due to the distributed moments,  $(\delta W_e)_Q$ , becomes:

$$\begin{aligned}(\delta W_e)_Q &= \int_0^{l_c} [(q_y w_{,x} - q_z v_{,x}) \delta u_{,x} + (q_z - q_x w_{,x}) \delta v_{,x} + \\ &\quad (q_x v_{,x} - q_y) \delta w_{,x} + (q_x + q_y v_{,x} + q_z w_{,x}) \delta \phi] dx\end{aligned}\quad (4.73)$$

In the derivation of Eq. (4.73), the terms associated with  $\tau_c'$  are order  $\varepsilon^2$  higher than the other terms in the same group, and therefore are neglected according to the ordering scheme.

The total virtual work done on a beam element,  $\delta W_e$ , is obtained by combining the virtual work due to distributed forces, Eq. (4.64), and the virtual work due to distributed moments, Eq. (4.73), and integrating by parts:

$$\begin{aligned} \delta W_e = \int_0^{l_c} \{ [p_x - (q_y w_{,x} - q_z v_{,x})_{,x}] \delta u + [p_y - (q_z - q_x w_{,x})_{,x}] \delta v \\ + [p_z - (q_x v_{,x} - q_y)_{,x}] \delta w + (q_x + q_y v_{,x} + q_z w_{,x}) \delta \phi \} dx \\ + b(W_e) \end{aligned} \quad (4.74)$$

where the associated boundary terms are:

$$\begin{aligned} b(W_e) = (q_y w_{,x} - q_z v_{,x}) \delta u \Big|_0^{l_c} + (q_z - q_x w_{,x}) \delta v \Big|_0^{l_c} \\ + (q_x v_{,x} - q_y) \delta w \Big|_0^{l_c} \end{aligned} \quad (4.75)$$

The boundary terms contained in Eq. (4.75) are latter combined with the boundary terms associated with the variations of strain energy and kinetic energy to obtain the boundary conditions associated with the equations of motion. It is evident, from Eqs. (4.74) and (4.75), that the pretwist does not appear explicitly in the virtual work expressions.

#### 4.4 SUMMARY OF THE PARTIAL DIFFERENTIAL EQUATIONS OF MOTION

The partial differential equations of motion and the associated boundary conditions for an element of the beam (blade) are obtained by substituting the variation of the strain energy,  $\delta U$  ( Eq. (4.16) ), the variation of the kinetic energy,  $\delta T$  ( Eq. (4.57) ), and the virtual work of the external

loads,  $\delta W_e$  ( Eq. (4.74) ), into Hamilton's principle, Eq. (4.1). Since the variations of the generalized coordinates  $\delta u$ ,  $\delta v$ ,  $\delta w$ ,  $\delta \phi$ ,  $\delta \alpha$ ,  $\delta \bar{\gamma}_{x\eta}$ ,  $\delta \bar{\gamma}_{x\xi}$ , are arbitrary over the length of the beam element, the partial differential equations of motion are obtained by requiring that the coefficient of each variation of a generalized coordinate be equal to zero. At the boundary ( $x = 0, l_e$ ), it is required that either a generalized coordinate be specified (kinematic boundary condition) or the coefficient of its variation be equal to zero (natural boundary condition). Note, that if the boundary node of an element is not at the boundary of the blade (either root or tip); then the kinematic boundary condition at this node, which is shared by this element and its neighbor, becomes the inter-element compatibility condition.

The seven partial differential equations of motion are:

**$\delta u$  equation**

$$\{ -\bar{V}_x + q_y w_{,x} - q_z v_{,x} \}_{,x} - \bar{Z}_u - p_x = 0 \quad (4.76a)$$

**$\delta v$  equation**

$$\begin{aligned} & \{ \bar{M}_y \sin \beta + \bar{M}_z \cos \beta + \phi (\bar{M}'_y \cos \beta - \bar{M}'_z \sin \beta) + \\ & \bar{S}'_x \cos \beta ( -v_{,x} \sin \beta + w_{,x} \cos \beta ) \}_{,xx} - \\ & \{ \bar{V}_x v_{,x} - \bar{S}'_x \sin \beta (v_{,xx} \cos \beta + w_{,xx} \sin \beta) - \bar{Z}'_v + q_x w_{,x} - q_z \}_{,x} \\ & - \bar{Z}_v - p_y = 0 \end{aligned} \quad (4.76b)$$

*δw equation*

$$\begin{aligned}
 & \{ -\bar{M}_y \cos \beta + \bar{M}_z \sin \beta + \phi (\bar{M}'_y \sin \beta + \bar{M}'_z \cos \beta) + \\
 & \bar{S}'_x \sin \beta (-v_{,x} \sin \beta + w_{,x} \cos \beta) \}_{,xx} - \\
 & \{ \bar{V}_x w_{,x} + \bar{S}'_x \cos \beta (v_{,xx} \cos \beta + w_{,xx} \sin \beta) - \bar{Z}'_w - q_x x_{,x} + q_y \}_{,x} \\
 & - \bar{Z}_w - p_z = 0
 \end{aligned} \tag{4.76c}$$

*δφ equation*

$$\begin{aligned}
 & v_{,xx} (\bar{M}'_y \cos \beta - \bar{M}'_z \sin \beta) + w_{,xx} (\bar{M}'_y \sin \beta + \bar{M}'_z \cos \beta) \\
 & - \{ \bar{S}_x + \bar{T}_x \phi_{,x} \}_{,x} - \bar{Z}_\phi - q_x - q_y v_{,x} - q_z w_{,x} = 0
 \end{aligned} \tag{4.76d}$$

*δα equation*

$$- \{ \bar{P}_x \}_{,x} + \bar{P}'_x + \bar{R}_x - \bar{Z}_\alpha = 0 \tag{4.76e}$$

*δ $\bar{v}_{\eta}$  equation*

$$\{ \bar{M}'_z \}_{,x} + \bar{V}_\eta + \tau_0 \bar{M}'_y - \bar{Z}_\eta = 0 \tag{4.76f}$$

*δ $\bar{v}_{\zeta}$  equation*

$$- \{ \bar{M}'_y \}_{,x} + \bar{V}_\zeta + \tau_0 \bar{M}'_z - \bar{Z}_\zeta = 0 \tag{4.76g}$$

and the associated boundary conditions are:

$$\{ \bar{V}_x - q_y w_{,x} + q_z v_{,x} \} \delta u \Big|_0^{l_c} = 0 \quad (4.77a)$$

$$\{ \bar{M}_y \sin \beta + \bar{M}_z \cos \beta + \phi (\bar{M}'_y \cos \beta - \bar{M}'_z \sin \beta) + \bar{S}'_x \cos \beta ( - v_{,x} \sin \beta + w_{,x} \cos \beta ) \} \delta v_{,x} \Big|_0^{l_c} = 0 \quad (4.77b)$$

$$\{ [ \bar{M}_y \sin \beta + \bar{M}_z \cos \beta + \phi (\bar{M}'_y \cos \beta - \bar{M}'_z \sin \beta) + \bar{S}'_x \cos \beta ( - v_{,x} \sin \beta + w_{,x} \cos \beta ) ]_{,x} - \bar{V}_x v_{,x} + \bar{S}'_x \sin \beta ( v_{,xx} \cos \beta + w_{,xx} \sin \beta ) + \bar{Z}'_v - q_x w_{,x} + q_z \} \delta v \Big|_0^{l_c} = 0 \quad (4.77c)$$

$$\{ - \bar{M}_y \cos \beta + \bar{M}_z \sin \beta + \phi (\bar{M}'_y \sin \beta + \bar{M}'_z \cos \beta) + \bar{S}'_x \sin \beta ( - v_{,x} \sin \beta + w_{,x} \cos \beta ) \} \delta w_{,x} \Big|_0^{l_c} = 0 \quad (4.77d)$$

$$\{ [ - \bar{M}_y \cos \beta + \bar{M}_z \sin \beta + \phi (\bar{M}'_y \sin \beta + \bar{M}'_z \cos \beta) + \bar{S}'_x \sin \beta ( - v_{,x} \sin \beta + w_{,x} \cos \beta ) ]_{,x} - \bar{V}_x w_{,x} - \bar{S}'_x \cos \beta ( v_{,xx} \cos \beta + w_{,xx} \sin \beta ) + \bar{Z}'_w + q_x v_{,x} - q_y \} \delta w \Big|_0^{l_c} = 0 \quad (4.77e)$$

$$\{ \bar{S}_x + \bar{T}_x \phi_{,x} \} \delta \phi \Big|_0^{l_c} = 0 \quad (4.77f)$$

$$\{ \bar{P}_x \} \delta \alpha \Big|_0^{l_c} = 0 \quad (4.77g)$$

$$\{ \bar{M}'_z \} \delta \bar{y}_{xj} \Big|_0^{l_c} = 0 \quad (4.77h)$$

$$\{ \bar{M}'_y \} \delta \bar{y}_{xi} \Big|_0^{l_c} = 0 \quad (4.77i)$$

where, the stress and moment resultants have been defined in Eqs. (4.11) and (4.12); the inertial forces and moments are defined in Eqs. (4.55). All the algebraic derivations associated with the structural and inertial operators which are lengthy, have been verified using the symbolic manipulation program MACSYMA[108].

#### **4.5 FINITE ELEMENT DISCRETIZATION OF THE EQUATIONS OF MOTION**

The nonlinear partial differential equations of motion, and related boundary conditions, which have been derived in the previous section, depend on both space and time. The spatial discretization of these equations is obtained by using the finite element method[105]. It is important to mention that, it is possible to obtain the element properties, required for the finite element method, without the prior explicit derivation of the equations of motion. However, for the fairly complicated problem treated here, and the treatment of the axial degree of freedom which will be discussed latter, it is convenient to have the complete formulation of the problem in partial differential equation form.

The element properties, for a beam type finite element, can be obtained by representing the blade as a combination of beam type finite elements, and using Hamilton's principle on the local level to generate the element matrices and load vector. In carrying out this discretization process, the straight portion of the blade is divided into several elements, while the swept tip portion is modeled as a single element.

The discretized form of Hamilton's principle is written as:

$$\int_{t_1}^{t_2} \sum_{i=1}^n (\delta U_i - \delta T_i - \delta W_{ei}) dt = 0 \quad (4.78)$$

In Eq. (4.78),  $n$  is the number of finite elements in the model,  $\delta U_i$  is the variation of strain energy in the  $i$ -th element,  $\delta T_i$  is the variation of kinetic energy in the  $i$ -th element, and  $\delta W_{ei}$  is the virtual work of external loads in the  $i$ -th element.

Assume that the seven unknown generalized coordinates of the beam finite element are expressed in the following form

$$\begin{bmatrix} v \\ w \\ \phi \\ u \\ \alpha \\ \bar{\gamma}_{x\eta} \\ \bar{\gamma}_{x\zeta} \end{bmatrix} = \begin{bmatrix} \{\Phi_v\}^T & 0 & 0 & 0 & 0 & 0 & 0 \\ 0 & \{\Phi_w\}^T & 0 & 0 & 0 & 0 & 0 \\ 0 & 0 & \{\Phi_\phi\}^T & 0 & 0 & 0 & 0 \\ 0 & 0 & 0 & \{\Phi_u\}^T & 0 & 0 & 0 \\ 0 & 0 & 0 & 0 & \{\Phi_\alpha\}^T & 0 & 0 \\ 0 & 0 & 0 & 0 & 0 & \{\Phi_\eta\}^T & 0 \\ 0 & 0 & 0 & 0 & 0 & 0 & \{\Phi_\zeta\}^T \end{bmatrix} \begin{bmatrix} \{V\} \\ \{W\} \\ \{\phi\} \\ \{U\} \\ \{\alpha\} \\ \{\Gamma_\eta\} \\ \{\Gamma_\zeta\} \end{bmatrix} \quad (4.79)$$

where  $\{\Phi_v\}, \{\Phi_w\}, \{\Phi_\phi\}, \{\Phi_u\}, \{\Phi_\alpha\}, \{\Phi_\eta\}, \{\Phi_\zeta\}$  are space dependent interpolation functions ;  $\{V\}, \{W\}, \{\phi\}, \{U\}, \{\alpha\}, \{\Gamma_\eta\}, \{\Gamma_\zeta\}$  are time dependent nodal parameters of the generalized degrees of freedom  $v, w, \phi, u, \alpha, \bar{\gamma}_{x\eta}, \bar{\gamma}_{x\zeta}$ , respectively, for the beam element.

The variations of the generalized coordinates for the beam element are:

$$\begin{bmatrix} \delta v \\ \delta w \\ \delta \phi \\ \delta u \\ \delta \alpha \\ \delta \bar{y}_{x\eta} \\ \delta \bar{y}_{x\zeta} \end{bmatrix} = \begin{bmatrix} \{\Phi_v\}^T & 0 & 0 & 0 & 0 & 0 & 0 \\ 0 & \{\Phi_w\}^T & 0 & 0 & 0 & 0 & 0 \\ 0 & 0 & \{\Phi_\phi\}^T & 0 & 0 & 0 & 0 \\ 0 & 0 & 0 & \{\Phi_u\}^T & 0 & 0 & 0 \\ 0 & 0 & 0 & 0 & \{\Phi_\alpha\}^T & 0 & 0 \\ 0 & 0 & 0 & 0 & 0 & \{\Phi_\eta\}^T & 0 \\ 0 & 0 & 0 & 0 & 0 & 0 & \{\Phi_\zeta\}^T \end{bmatrix} \begin{bmatrix} \{\delta V\} \\ \{\delta W\} \\ \{\delta \phi\} \\ \{\delta U\} \\ \{\delta \alpha\} \\ \{\delta \Gamma_\eta\} \\ \{\delta \Gamma_\zeta\} \end{bmatrix} \quad (4.80)$$

In this study, Hermite interpolation polynomials are used to discretize the space dependence. Cubic polynomials are used for the transverse deflections  $v$  and  $w$ , with the displacements and slopes at the end nodes as the nodal parameters. Quadratic polynomials are used for the torsional rotation  $\phi$ , the axial deflection  $u$ , the warping amplitude  $\alpha$ , and the transverse shears at the elastic axis  $\bar{y}_{x\eta}$ ,  $\bar{y}_{x\zeta}$ ; for these quantities the nodal parameters are the values of the displacement function at the two end nodes and at the internal node of the element. The mathematical expressions for the interpolation polynomials are:

$$\{\Phi_v\} = \{\Phi_w\} = \begin{bmatrix} 1 - 3\xi^2 + 2\xi^3 \\ l_e(\xi - 2\xi^2 + \xi^3) \\ 3\xi^2 - 2\xi^3 \\ l_e(-\xi^2 + \xi^3) \end{bmatrix} = \{\Phi_c\} \quad (4.81a)$$

$$\{\Phi_\phi\} = \{\Phi_u\} = \{\Phi_\alpha\} = \{\Phi_\eta\} = \{\Phi_\zeta\} = \begin{bmatrix} 1 - 3\xi + 2\xi^2 \\ 4\xi - 4\xi^2 \\ -\xi + 2\xi^2 \end{bmatrix} = \{\Phi_q\} \quad (4.81b)$$

where:  $\xi = x/l_e$ ,  $x$  is the spanwise (axial) coordinate of the beam element, and  $l_e$  is the length of the beam element. Each beam element consists of two end nodes and one internal node at its mid-point, resulting in a total of 23 nodal degrees of freedom, as shown in Fig. 4.2. The quadratic polynomial has the

capability of modeling a linear variation of strains along the element length, thus being compatible with the cubic polynomial for transverse deflections. These polynomials also satisfy all inter-element compatibility requirements associated with the variational principle in this formulation.

Note that when the problem is restricted to bending and shear in the vertical plane, Eqs. (3.43a-c) reduce to the strain-displacement relations of Timoshenko beam where a constraint relation, such as

$$w_{,x} = \theta_w + \bar{\gamma}_{x\zeta} \quad (4.82)$$

exists, and  $\theta_w$  is the rotation due to bending. In this special case the boundary terms for  $\delta w_{,x}$  and  $\delta \bar{\gamma}_{x\zeta}$  in the  $\delta U$  expression will have the same coefficient with opposite sign, and thus can be combined into a boundary term containing only  $\delta \theta_w$ . This also agrees with Timoshenko beam theory and implies that  $w_{,x}$  and  $\bar{\gamma}_{x\zeta}$  are not required to have inter-element continuity[91]. For a beam with built-in twist, undergoing moderate deflections in two mutually perpendicular planes, combined with torsion and transverse shears, the boundary terms for  $\delta w_{,x}$  and  $\delta \bar{\gamma}_{x\zeta}$  have different coefficients which contain coupling terms such as  $v_{,x}$ ,  $\phi$  and  $\beta$ , and Eq. (4.82) is no longer valid. The corresponding variational principle thus requires inter-element continuity on both  $w_{,x}$  and  $\bar{\gamma}_{x\zeta}$ , and for the same reason also on  $v_{,x}$  and  $\bar{\gamma}_{x\eta}$ . In the literature of Timoshenko beam finite elements, there is a group of higher order elements[68,92,93] which also enforced inter-element continuity on  $w_{,x}$  and  $\bar{\gamma}_{x\zeta}$  either directly or indirectly through Eq. (82); and they produced excellent agreement with exact solutions. For more complex structures such as swept-tip blades, the actual behavior of

$\bar{\gamma}_{x\eta}$  and  $\bar{\gamma}_{x\zeta}$  at the junction of the swept tip and the straight portion of the blade is complicated. Therefore, the enforcement of inter-element continuity on  $\bar{\gamma}_{x\eta}$  and  $\bar{\gamma}_{x\zeta}$  at the junction node should be treated as an assumption.

#### 4.5.1 *Element Matrices Associated with the Strain Energy Variation*

The beam element matrices associated with the strain energy variation are derived by substituting the expressions for the generalized coordinates, Eq. (4.79), and their variations, Eq. (4.80), into the strain energy variation, Eq. (4.10). Using the interpolation functions given by Eqs. (4.81), and carrying out the integration over the length of the beam element; the resulting variation of the strain energy has the form:

$$\delta U = \delta \mathbf{q}^T ( [\mathbf{K}^L] + [\mathbf{K}^{NL}(\mathbf{q})] ) \mathbf{q} \quad (4.83)$$

where

$$\mathbf{q} = [ \{\mathbf{V}\}^T, \{\mathbf{W}\}^T, \{\phi\}^T, \{\mathbf{U}\}^T, \{\alpha\}^T, \{\Gamma_\eta\}^T, \{\Gamma_\zeta\}^T ]^T \quad (4.84)$$

and  $[\mathbf{K}^L]$  and  $[\mathbf{K}^{NL}]$  are the linear stiffness matrix (symmetric) and nonlinear stiffness matrix, respectively. Detailed expressions for these stiffness matrices are presented in Appendix B.1 .

#### 4.5.2 *Element Matrices Associated with the Kinetic Energy Variation*

The beam element matrices associated with the kinetic energy variation are obtained by substituting Eqs. (4.79) and (4.80) into the kinetic energy variation, Eq. (4.54). Using the interpolation functions given by Eqs. (4.81), and carrying out the integration over the length of the beam element; the resulting variation of the kinetic energy has the form:

$$\delta T = -\delta \mathbf{q}^T ( [\mathbf{M}] \ddot{\mathbf{q}} + [\mathbf{M}^C] \dot{\mathbf{q}} + [\mathbf{K}^{CF}] \mathbf{q} + \{\mathbf{F}^{CF}\} ) \quad (4.85)$$

where

$[\mathbf{M}]$  is the mass matrix (symmetric),  $[\mathbf{M}^C]$  is a Coriolis damping matrix (anti-symmetric),  $[\mathbf{K}^{CF}]$  is a centrifugal stiffening matrix (symmetric when  $\bar{\omega}$  is constant), and  $\{\mathbf{F}^{CF}\}$  is a centrifugal force vector. Detailed expressions for  $[\mathbf{M}]$ ,  $[\mathbf{M}^C]$ ,  $[\mathbf{K}^{CF}]$  and  $\{\mathbf{F}^{CF}\}$  are presented in Appendix B.2 .

#### 4.5.3 *Element Matrices Associated with the Virtual Work of External Loads*

The beam element matrices associated with the external virtual work are derived by substituting Eqs. (4.79) and (4.80) into the virtual work of external loads, Eq. (4.74). Using the interpolation functions given by Eqs. (4.81), and carrying out the integration over the length of the beam element; the resulting virtual work of external loads has the form:

$$\delta W_e = -\delta \mathbf{q}^T ( [\mathbf{K}^I] \mathbf{q} + \{\mathbf{F}^I\} ) \quad (4.86)$$

where  $[K^I]$  is a stiffness type matrix associated with applied distributed torques acting on the blade (beam), and  $\{F^I\}$  is an applied force vector. Detailed expressions for  $[K^I]$  and  $\{F^I\}$  are presented in Appendix B.3 .

#### 4.5.4 Summary of the Beam Finite Element Equations of Motion

The finite element equations of motion for a single beam element are obtained by substituting the strain energy variation, Eq. (4.83), the kinetic energy variation, Eq. (4.85), and the virtual work of external loads, Eq. (4.86), into the discretized form of Hamilton's principle, Eq. (4.78). Since the variation of the generalized coordinates  $(\delta v, \delta w, \delta \phi, \delta u, \delta \alpha, \delta \bar{y}_{x\eta}, \delta \bar{y}_{x\zeta})$  are arbitrary over the time interval, therefore  $\delta \mathbf{q}$  is also arbitrary; and this results in the finite element equations of motion for the  $i$ -th beam element, written as:

$$[M_i] \ddot{\mathbf{q}} + [C_i] \dot{\mathbf{q}} + [K_i] \mathbf{q} + \mathbf{F}_i = \mathbf{0} \quad (4.87)$$

where:

$$[M_i] = [M]_i \quad (4.88)$$

$$[C_i] = [M^C]_i \quad (4.89)$$

$$[K_i] = [K^L]_i + [K^{CF}]_i + [K^I]_i + [K^{NL}(\mathbf{q})]_i \quad (4.90)$$

$$\mathbf{F}_i = \{\mathbf{F}^{CF}\}_i + \{\mathbf{F}^I\}_i \quad (4.91)$$

The reason for defining the element mass, damping and stiffness matrices  $[M_i]$ ,  $[C_i]$ ,  $[K_i]$  and the load vector  $F_i$ , is to define the notation which is subsequently used in the assembly process described in Chapter 6.

#### 4.5.5 *Local-to-global Coordinate Transformation*

The local-to-global coordinate transformation for the swept-tip element can be written in the form

$$\mathbf{q}_t^L = [\Lambda] \mathbf{q}_t^G \quad (4.92)$$

where the subscript  $t$  denotes quantities associated with the tip element; the superscripts  $L$  and  $G$  denote the local and global coordinate system, respectively;  $\mathbf{q}$  is the vector of element nodal degrees of freedom, defined in Eq. (4.84). The transformation matrix,  $[\Lambda]$ , is derived with the constraint that the angular relationship between the swept-tip and the straight portion of the blade at the junction is preserved after deformation[73]. For the translational degrees of freedom, the transformation is linear, as indicated by:

$$\begin{Bmatrix} u \\ v \\ w \end{Bmatrix}_t^L = [T_{eb}]_t \begin{Bmatrix} u \\ v \\ w \end{Bmatrix}_t^G \quad (4.93)$$

where the transformation matrix  $[T_{eb}]_t$  is given by Eq. (2.7b):

$$\begin{aligned}
[T_{cb}]_t &= \begin{bmatrix} \cos \Lambda_s & -\sin \Lambda_s & 0 \\ \sin \Lambda_s & \cos \Lambda_s & 0 \\ 0 & 0 & 1 \end{bmatrix} \begin{bmatrix} \cos \Lambda_a & 0 & \sin \Lambda_a \\ 0 & 1 & 0 \\ -\sin \Lambda_a & 0 & \cos \Lambda_a \end{bmatrix} \\
&= \begin{bmatrix} \cos \Lambda_s \cos \Lambda_a & -\sin \Lambda_s & \cos \Lambda_s \sin \Lambda_a \\ \sin \Lambda_s \cos \Lambda_a & \cos \Lambda_s & \sin \Lambda_s \sin \Lambda_a \\ -\sin \Lambda_a & 0 & \cos \Lambda_a \end{bmatrix} \quad (4.94)
\end{aligned}$$

The transformation for the warping and transverse shear degrees of freedom is also linear:

$$(\alpha)_t^L = \cos \Lambda_s \cos \Lambda_a (\alpha)_t^G \quad (4.95)$$

$$(\bar{v}_{xy})_t^L = \cos \Lambda_a (\bar{v}_{xy})_t^G \quad (4.96)$$

$$(\bar{v}_{xz})_t^L = \cos \Lambda_a (\bar{v}_{xz})_t^G - \sin \Lambda_s \sin \Lambda_a (\bar{v}_{xy})_t^G \quad (4.97)$$

However, the transformation corresponding to the rotational degrees of freedom of the junction node, derived below, is nonlinear due to moderate rotation[73].

The transformation between the  $(\hat{e}'_x, \hat{e}'_\eta, \hat{e}'_z)$  system and the  $(\hat{e}_x, \hat{e}_y, \hat{e}_z)$  system is:

For the straight portion of the blade (global system)

$$\begin{Bmatrix} \hat{e}'_x \\ \hat{e}'_\eta \\ \hat{e}'_z \end{Bmatrix}_G = [T_{de}]_G \begin{Bmatrix} \hat{e}_x \\ \hat{e}_y \\ \hat{e}_z \end{Bmatrix}_G \quad (4.98)$$

For the swept tip element (local system)

$$\begin{Bmatrix} \hat{c}'_x \\ \hat{c}'_\eta \\ \hat{c}'_\zeta \end{Bmatrix}_L = [T_{de}]_L \begin{Bmatrix} \hat{e}_x \\ \hat{c}_y \\ \hat{e}_z \end{Bmatrix}_L \quad (4.99)$$

The transformation between the local and global coordinate systems before deformation is:

$$\begin{Bmatrix} \hat{c}_x \\ \hat{c}_y \\ \hat{c}_z \end{Bmatrix}_L = [T_{cb}]_t \begin{Bmatrix} \hat{e}_x \\ \hat{e}_y \\ \hat{e}_z \end{Bmatrix}_G \quad (4.100)$$

The constraint that the angular relationship between the swept tip and the straight portion of the blade at the junction is preserved after deformation can be written as:

$$\begin{Bmatrix} \hat{c}'_x \\ \hat{c}'_\eta \\ \hat{c}'_\zeta \end{Bmatrix}_L = [T_{cb}]_t \begin{Bmatrix} \hat{e}'_x \\ \hat{e}'_\eta \\ \hat{e}'_\zeta \end{Bmatrix}_G \quad (4.101)$$

Combining Eqs. (4.98) and (4.100) with Eq. (4.101) and comparing with Eq. (4.99) gives:

$$[T_{de}]_L = [T_{eb}]_t [T_{de}]_G [T_{eb}]_t^T \quad (4.102)$$

If the general second order expression of  $[T_{de}]$ , Eq. (4.40), is used, an explicit form of the constraint relations for the rotational degrees of freedom cannot be obtained because of the mathematical complexity. When the effect of pretwist at the junction is not included, the matrix  $[T_{de}]$  becomes

$$[T_{dc}] = \begin{bmatrix} 1 & v_{,x} & w_{,x} \\ -(v_{,x} + \phi w_{,x}) & 1 & \phi \\ -w_{,x} + \phi v_{,x} & -(\phi + v_{,x} w_{,x}) & 1 \end{bmatrix} \quad (4.103)$$

where the small angle assumption, Eq. (3.39), is used for  $\phi$ . Substituting Eq. (4.103) into Eq. (4.102) and equating elements (1,2), (1,3) and (2,3) of both sides, yields the following constraint relations:

$$\begin{Bmatrix} \phi^L \\ -w_{,x}^L \\ v_{,x}^L \end{Bmatrix} = ([T_{cb}]_t + [T^K]) \begin{Bmatrix} \phi^G \\ -w_{,x}^G \\ v_{,x}^G \end{Bmatrix} \quad (4.104)$$

where the elements of the matrix  $[T^K]$  are presented in Appendix C.1. For the velocity and acceleration of the rotational degrees of freedom, the constraint relations are obtained by differentiating Eq. (4.104) with respect to time:

$$\begin{Bmatrix} \dot{\phi}^L \\ -\dot{w}_{,x}^L \\ \dot{v}_{,x}^L \end{Bmatrix} = ([T_{cb}]_t + [T^C]) \begin{Bmatrix} \dot{\phi}^G \\ -\dot{w}_{,x}^G \\ \dot{v}_{,x}^G \end{Bmatrix} \quad (4.105)$$

$$\begin{Bmatrix} \ddot{\phi}^L \\ -\ddot{w}_{,x}^L \\ \ddot{v}_{,x}^L \end{Bmatrix} = ([T_{cb}]_t + [T^C]) \begin{Bmatrix} \ddot{\phi}^G \\ -\ddot{w}_{,x}^G \\ \ddot{v}_{,x}^G \end{Bmatrix} + [T^M] \begin{Bmatrix} \dot{\phi}^G \\ -\dot{w}_{,x}^G \\ \dot{v}_{,x}^G \end{Bmatrix} \quad (4.106)$$

where

$$[T^M] = [\dot{T}^C] \quad (4.107)$$

The elements of the matrices  $[T^C]$  and  $[T^M]$  are also presented in Appendix C.1. It is evident from Appendix C.1 that the transformation matrices

$[T^K]$ ,  $[T^C]$  and  $[T^M]$  are nonlinear in the generalized coordinates or their derivatives. If the pretwist angle at the junction,  $\beta_j$ , is nonzero but it can be approximated as of order  $\varepsilon$ , instead of  $\varepsilon^{1/2}$ , then the matrix  $[T_{de}]$ , Eq. (4.40) can be written as:

$$[T_{de}] = \begin{bmatrix} 1 & v_{,x} & w_{,x} \\ -v_{,x} - (\beta + \phi)w_{,x} & 1 & \beta + \phi \\ -w_{,x} + (\beta + \phi)v_{,x} & -(\beta + \phi + v_{,x}w_{,x}) & 1 \end{bmatrix} \quad (4.108)$$

where the small angle assumption is used for both  $\beta$  and  $\phi$ . This form of Eq. (4.108) is essential in order to be able to derive transformation of the type given in Eqs. (4.104)-(4.106). Furthermore, it is also important to note that assuming the pretwist angle at the blade tip junction to be of order  $\varepsilon$  is very reasonable. In practical blade configurations most of the pretwist is in the in-board section, and the outermost 10% portion of the blade has only small amount of pretwist. Using an approach similar to the case when  $\beta_j = 0$  (see above), a set of constraint relations can be obtained which has the same form as that given in Eqs. (4.104), (4.105), (4.106) and in Appendix C.1, except that the variable  $\phi$  is replaced by  $\bar{\phi}$ , where

$$\bar{\phi} \equiv \beta + \phi \quad (4.109)$$

The local-to-global coordinate transformation, for the vector of nodal degrees of freedom, Eq. (4.92), can be rewritten as:

$$\mathbf{q}_t^L = ([\Lambda^L] + [\Lambda^K]) \mathbf{q}_t^G \quad (4.110)$$

where  $[\Lambda^L]$  and  $[\Lambda^K]$  are the linear and nonlinear parts of the transformation matrix  $[\Lambda]$ , respectively. The nodal vectors for velocity and acceleration are:

$$\dot{\mathbf{q}}_t^L = ([\Lambda^L] + [\Lambda^C])\dot{\mathbf{q}}_t^G \quad (4.111)$$

$$\ddot{\mathbf{q}}_t^L = ([\Lambda^L] + [\Lambda^C])\ddot{\mathbf{q}}_t^G + [\Lambda^M]\dot{\mathbf{q}}_t^G \quad (4.112)$$

Equations (4.110)-(4.112) are employed in the assembly process, which is described in Chapter 6. In Eqs. (4.110)-(4.112), the matrices  $[\Lambda^K]$ ,  $[\Lambda^C]$  and  $[\Lambda^M]$  are nonlinear in the nodal value of the generalized coordinates or their derivatives at the tip junction. The elements of the matrices  $[\Lambda^L]$ ,  $[\Lambda^K]$ ,  $[\Lambda^C]$  and  $[\Lambda^M]$  are presented in Appendix C.2.

## Chapter V

### INCORPORATION OF AERODYNAMICS IN THE EQUATIONS OF MOTION

In the equations of motion given in Chapter 4, the nonconservative distributed forces and moments associated with the external work contributions were written in general symbolic form. These generalized forces and moments are replaced by the aerodynamic forces and moments described in this chapter to complete the aeroelastic analysis. The expressions used in the derivation of the aerodynamic loads in this chapter are not combined algebraically. Instead, they are coded separately in the computer program implementing this study, and assembled numerically during the solution process[13]. Since the explicit algebraic form of the aerodynamic loads as a function of the blade displacement variables is not required in this implicit aerodynamic formulation, therefore the ordering scheme is not used in this chapter.

#### 5.1 AERODYNAMIC LIFT AND PITCHING MOMENT

The expressions used for the aerodynamic lift and pitching moment acting on the blade are based on Greenberg's extension of Theodorsen's theory [38] for a two-dimensional airfoil undergoing sinusoidal motion in pulsating incompressible flow. A quasi-steady approximation of the unsteady theory is used where Theodorsen's lift deficiency function  $C(k)$  is taken to be unity. This approximation is quite reasonable because it was shown in an earlier

paper[33] that a completely unsteady time domain representation of Greenberg's theory has a fairly small effect on the coupled flap-lag-torsional blade response, stability and loads. Thus the neglect of this particular unsteady aerodynamic effect is not expected to have a significant influence on the validity of the numerical results generated in this study. With the quasi-steady assumption, the aerodynamic lift  $L$  and pitching moment  $M$  per unit span are given by:

$$L = \frac{1}{2}a\rho_{\Lambda}b^2\left[\frac{d}{dt}(\dot{h} + V\theta) - (x_{\Lambda} - \frac{1}{2}b)\ddot{\theta}\right] + a\rho_{\Lambda}bV[\dot{h} + V\theta + (b - x_{\Lambda})\dot{\theta}] \quad (5.1)$$

$$M = \frac{1}{2}a\rho_{\Lambda}b^2\left\{(x_{\Lambda} - \frac{1}{2}b)\frac{d}{dt}(\dot{h} + V\theta) - \frac{1}{2}bV\dot{\theta} - \left[\frac{1}{8}b^2 + (x_{\Lambda} - \frac{1}{2}b)^2\right]\ddot{\theta}\right\} + a\rho_{\Lambda}bx_{\Lambda}V[\dot{h} + V\theta + (b - x_{\Lambda})\dot{\theta}] \quad (5.2)$$

where  $a$  is the two-dimensional airfoil lift curve slope;  $b$  is the semi-chord;  $\rho_{\Lambda}$  is the density of air;  $\dot{h}$  is the plunging velocity;  $V$  is the free-stream velocity component of the two-dimensional airfoil;  $\theta$  is the pitch angle with respect to free-stream;  $x_{\Lambda}$  is the blade airfoil cross-sectional aerodynamic center offset from the elastic axis, positive for aerodynamic center before elastic axis. The aerodynamic lift  $L$  is defined positive up and the pitching moment  $M$  is defined positive nose up.

The resultant airfoil velocity relative to the air is:

$$U_R = \sqrt{V^2 + \dot{h}^2} \quad (5.3)$$

The components of  $U_R$  in the deformed curvilinear coordinate system  $(\hat{c}'_x, \hat{c}'_\eta, \hat{c}'_\zeta)$  are, from Fig. 5.1:

$$U_\eta' = V \cos \theta - \dot{h} \sin \theta \quad (5.4a)$$

$$U_\zeta' = -V \sin \theta - \dot{h} \cos \theta \quad (5.4b)$$

Inverse relations corresponding to Eqs. (5.4) can be also written as:

$$V = U_\eta' \cos \theta - U_\zeta' \sin \theta \quad (5.5)$$

$$\dot{h} = -U_\eta' \sin \theta - U_\zeta' \cos \theta \quad (5.6)$$

Due to the small oscillation assumption, which is an inherent assumption in Greenberg's theory [38], the expressions for  $(\dot{h} + V\theta)$  and  $V$  in Eqs. (5.1) and (5.2) can be approximated, from Eqs. (5.4b) and (5.5), respectively, as:

$$\dot{h} + V\theta \simeq -U_\zeta' \quad (5.7)$$

$$V \simeq U_\eta' - U_\zeta'\theta \quad (5.8)$$

Substituting Eqs. (5.7) and (5.8) into Eqs. (5.1) and (5.2), the aerodynamic lift and pitching moment per unit span are written in terms of  $U_\eta'$  and  $U_\zeta'$  as:

$$L = \frac{1}{2} a \rho_A b^2 \left[ -\dot{U}_\zeta' - (x_A - \frac{1}{2}b) \ddot{\theta} \right] + a \rho_A b (U_\eta' - U_\zeta'\theta) \left[ -U_\zeta' + (b - x_A) \dot{\theta} \right] \quad (5.9)$$

$$\begin{aligned}
M = & -\frac{1}{2}a\rho_{\Lambda}b^2\left\{(x_{\Lambda} - \frac{1}{2}b)\dot{U}_{\zeta}' + \frac{1}{2}b(U_{\eta}' - U_{\zeta}'\theta)\dot{\theta} + \right. \\
& \left. [\frac{1}{8}b^2 + (x_{\Lambda} - \frac{1}{2}b)^2]\ddot{\theta}\right\} \\
& + a\rho_{\Lambda}bx_{\Lambda}(U_{\eta}' - U_{\zeta}'\theta)[-U_{\zeta}' + (b - x_{\Lambda})\dot{\theta}]
\end{aligned} \tag{5.10}$$

The profile drag per unit span is:

$$D = C_{d_0}\rho_{\Lambda}bU_R^2 = C_{d_0}\rho_{\Lambda}b(U_{\eta}'^2 + U_{\zeta}'^2) \tag{5.11}$$

## 5.2 BLADE VELOCITY RELATIVE TO AIR

The velocity vector of a point on the elastic axis of the blade relative to the air is:

$$\mathbf{U} = \mathbf{V}_{EA} - \mathbf{V}_A = U_x' \hat{\mathbf{e}}_x' + U_{\eta}' \hat{\mathbf{e}}_{\eta}' + U_{\zeta}' \hat{\mathbf{e}}_{\zeta}' \tag{5.12}$$

where  $\mathbf{V}_{EA}$  is the velocity vector of a point on the elastic axis of the blade and  $\mathbf{V}_A$  is the velocity vector of air due to forward flight and inflow.

The velocity vector of a point on the elastic axis of the blade,  $\mathbf{V}_{EA}$ , can be obtained from Eq. (4.47) as:

$$\mathbf{V}_{EA} = (\mathbf{V})_{\eta=\zeta=0} = V_x^{EA} \hat{\mathbf{e}}_x + V_y^{EA} \hat{\mathbf{e}}_y + V_z^{EA} \hat{\mathbf{e}}_z \tag{5.13}$$

where

$$\begin{Bmatrix} V_x^{EA} \\ V_y^{EA} \\ V_z^{EA} \end{Bmatrix} = \begin{Bmatrix} \dot{u} + \Omega_y(h_z + w) - \Omega_z(h_y + v) + V_{bx} \\ \dot{v} + \Omega_z(h_x + x + u) - \Omega_x(h_z + w) + V_{by} \\ \dot{w} + \Omega_x(h_y + v) - \Omega_y(h_x + x + u) + V_{bz} \end{Bmatrix} \tag{5.14}$$

The velocity vector of air due to forward flight and inflow,  $V_\Lambda$ , is:

$$\begin{aligned} V_\Lambda &= \Omega R (\mu \cos \psi \hat{i}_r - \mu \sin \psi \hat{j}_r - \lambda \hat{k}_r) \\ &= V_x^\Lambda \hat{e}_x + V_y^\Lambda \hat{e}_y + V_z^\Lambda \hat{e}_z \end{aligned} \quad (5.15)$$

where

$$\begin{aligned} \begin{Bmatrix} V_x^\Lambda \\ V_y^\Lambda \\ V_z^\Lambda \end{Bmatrix} &= \Omega R [T_{eb}] [T_{br}] \begin{Bmatrix} \mu \cos \psi \\ -\mu \sin \psi \\ -\lambda \end{Bmatrix} \\ &= \Omega R [T_{eb}] \begin{Bmatrix} \mu \cos \psi - \beta_p \lambda \\ -\mu \beta_p \cos \psi \sin \theta_p - \mu \sin \psi \cos \theta_p - \lambda \sin \theta_p \\ -\mu \beta_p \cos \psi \cos \theta_p + \mu \sin \psi \sin \theta_p - \lambda \cos \theta_p \end{Bmatrix} \end{aligned} \quad (5.16)$$

In Eqs. (5.14) and (5.16), the explicit expressions for  $(\Omega_x, \Omega_y, \Omega_z)$ ,  $(h_x, h_y, h_z)$ ,  $(V_{bx}, V_{by}, V_{bz})$  and  $[T_{eb}]$  can be found in Eqs. (4.33), (4.38), (4.26) and (2.7a), respectively, for the straight portion of the blade, and in Eqs. (4.34), (4.39), (4.27) and (2.7b), respectively, for the swept-tip element.

The velocity component  $U_\eta'$  and  $U_\zeta'$  can be obtained by combining Eqs. (5.12), (5.13) and (5.15) as:

$$\begin{Bmatrix} U_x' \\ U_\eta' \\ U_\zeta' \end{Bmatrix} = [T_{de}] \begin{Bmatrix} V_x^{EA} - V_x^A \\ V_y^{EA} - V_y^A \\ V_z^{EA} - V_z^A \end{Bmatrix} \quad (5.17)$$

where the transformation matrix,  $[T_{de}]$ , between the deformed curvilinear coordinate system  $(\hat{e}'_x, \hat{e}'_\eta, \hat{e}'_\zeta)$  and the undeformed element coordinate system

$(\hat{c}_x, \hat{c}_y, \hat{c}_z)$ , has been defined in Eq. (2.15) and the second order expression for  $[T_{de}]$  is given by Eq. (4.40).

The acceleration component  $\ddot{U}_{\zeta}'$  can be obtained by differentiating Eq. (5.17) with respect to time:

$$\begin{Bmatrix} \dot{U}_x' \\ \dot{U}_y' \\ \dot{U}_z' \end{Bmatrix} = [T_{de}] \begin{Bmatrix} \dot{V}_x^{EA} - \dot{V}_x^A \\ \dot{V}_y^{EA} - \dot{V}_y^A \\ \dot{V}_z^{EA} - \dot{V}_z^A \end{Bmatrix} + [\dot{T}_{de}] \begin{Bmatrix} V_x^{EA} - V_x^A \\ V_y^{EA} - V_y^A \\ V_z^{EA} - V_z^A \end{Bmatrix} \quad (5.18)$$

where

$$\begin{Bmatrix} \dot{V}_x^{EA} \\ \dot{V}_y^{EA} \\ \dot{V}_z^{EA} \end{Bmatrix} = \begin{Bmatrix} \ddot{u} + \Omega_y \dot{w} - \Omega_z \dot{v} + \dot{\Omega}_y (h_z + w) - \dot{\Omega}_z (h_y + v) + \dot{V}_{bx} \\ \ddot{v} + \Omega_z \dot{u} - \Omega_x \dot{w} + \dot{\Omega}_z (h_x + x + u) - \dot{\Omega}_x (h_z + w) + \dot{V}_{by} \\ \ddot{w} + \Omega_x \dot{v} - \Omega_y \dot{u} + \dot{\Omega}_x (h_y + v) - \dot{\Omega}_y (h_x + x + u) + \dot{V}_{bz} \end{Bmatrix} \quad (5.19)$$

$$\begin{Bmatrix} \dot{V}_x^A \\ \dot{V}_y^A \\ \dot{V}_z^A \end{Bmatrix} = \Omega R [T_{eb}] \begin{Bmatrix} -\Omega \mu \sin \psi \\ \{\Omega \mu (\beta_p \sin \psi \sin \theta_p - \cos \psi \cos \theta_p) - \dot{\theta}_p\} \\ (\mu \beta_p \cos \psi \cos \theta_p - \mu \sin \psi \sin \theta_p + \lambda \cos \theta_p) \\ \{\Omega \mu (\beta_p \sin \psi \cos \theta_p + \cos \psi \sin \theta_p) + \dot{\theta}_p\} \\ (\mu \beta_p \cos \psi \sin \theta_p + \mu \sin \psi \cos \theta_p + \lambda \sin \theta_p) \end{Bmatrix} \quad (5.20)$$

The matrix  $[T_{de}]$  is given in Eq. (4.43); while the expressions of  $(\dot{V}_{bx}, \dot{V}_{by}, \dot{V}_{bz})$  and  $(\dot{\Omega}_x, \dot{\Omega}_y, \dot{\Omega}_z)$  are given in Eqs. (4.52) and (4.53), respectively. Equations (5.19) and (5.20) are obtained by differentiating Eqs. (5.14) and (5.16), respectively, with respect to time.

### 5.3 BLADE PITCH ANGLE WITH RESPECT TO FREE STREAM

The blade pitch angle with respect to the free stream is:

$$\theta = \theta_G + \phi \quad (5.21)$$

where  $\theta_G$  is the total geometric pitch angle. The time derivatives of  $\theta$  are:

$$\dot{\theta} = \dot{\theta}_G + \dot{\phi} \quad (5.22)$$

$$\ddot{\theta} = \ddot{\theta}_G + \ddot{\phi} \quad (5.23)$$

*For the straight portion of the blade*

$$\theta_G = \theta_p(\psi) + \beta(x) \quad (5.24)$$

$$\dot{\theta}_G = \dot{\theta}_p \quad (5.25)$$

$$\ddot{\theta}_G = \ddot{\theta}_p \quad (5.26)$$

*For the swept-tip element*

$$\theta_G = [\theta_p(\psi) + \beta_J] \cos \Lambda_s \cos \Lambda_a + \beta_T(x) \quad (5.27)$$

$$\dot{\theta}_G = \dot{\theta}_p \cos \Lambda_s \cos \Lambda_a \quad (5.28)$$

$$\ddot{\theta}_G = \ddot{\theta}_p \cos \Lambda_s \cos \Lambda_a \quad (5.29)$$

where  $\beta_J$  is the blade pretwist angle at the junction between the straight portion of the blade and the swept tip, and  $\beta_T(x)$  is the pretwist angle of the swept tip with respect to the junction.

#### 5.4 AERODYNAMIC FORCES AND MOMENTS IN THE UNDEFORMED ELEMENT COORDINATE SYSTEM

The components of the aerodynamic forces and moments per unit span in the deformed curvilinear coordinate system  $(\hat{e}'_x, \hat{e}'_\eta, \hat{e}'_\zeta)$  are related to the aerodynamic lift and pitching moment per unit span by (see Fig. 5.2):

$$p_\eta' = L \sin \alpha_A - D \cos \alpha_A \quad (5.30)$$

$$p_\zeta' = L \cos \alpha_A + D \sin \alpha_A \quad (5.31)$$

$$q_x' = M \quad (5.32)$$

where the blade local angle of attack,  $\alpha_A$ , and its sine and cosine can be written in terms of  $U_\eta'$  and  $U_\zeta'$  (see Fig. 5.1) as:

$$\alpha_A = -\tan^{-1}\left(\frac{U_\zeta'}{U_\eta'}\right) \quad (5.33)$$

$$\sin \alpha_A = -\frac{U_\zeta'}{U_R} = \frac{-U_\zeta'}{\sqrt{U_\eta'^2 + U_\zeta'^2}} \quad (5.34)$$

$$\cos \alpha_A = \frac{U_\eta'}{U_R} = \frac{U_\eta'}{\sqrt{U_\eta'^2 + U_\zeta'^2}} \quad (5.35)$$

The aerodynamic forces and moments per unit span in the undeformed element coordinate system  $(\hat{e}_x, \hat{e}_y, \hat{e}_z)$  are obtained from Eqs. (5.30), (5.31) and (5.32); and can be written as:

$$\begin{Bmatrix} p_x \\ p_y \\ p_z \end{Bmatrix} = [T_{dc}]^T \begin{Bmatrix} 0 \\ p_{\eta'} \\ p_{\zeta'} \end{Bmatrix} \quad (5.36)$$

$$\begin{Bmatrix} q_x \\ q_y \\ q_z \end{Bmatrix} = [T_{dc}]^T \begin{Bmatrix} q_{x'} \\ 0 \\ 0 \end{Bmatrix} \quad (5.37)$$

## 5.5 TREATMENT OF REVERSE FLOW

Reverse flow is a phenomenon due to forward flight[52] and it is characterized by the existence of a reverse flow region on the retreating blade ( $180^\circ \leq \psi \leq 360^\circ$ ), where the relative air velocity sensed by the blade cross-section is from the trailing edge to the leading edge. At the boundary of the reverse flow region, the tangential velocity of the blade with respect to air is equal to zero. It should be noted that an exact solution of the boundary of the reverse flow region requires knowledge of the blade motion, which is not known a-priori. A commonly used approximate solution for the boundary of the reverse flow region is obtained[52] by neglecting the blade deformations; i.e.:

$$\Omega r + \mu \Omega R \sin \psi = 0$$

or

$$r = -\mu R \sin \psi \quad (5.38)$$

which represents a circle of diameter  $\mu R$ , and centered at  $r = \mu R/2$  on the  $\psi = 270^\circ$  azimuth station of the retreating side of the rotor disk, as shown in

Fig. 5.3. Since the diameter of the reverse flow region is directly proportional to the advance ratio,  $\mu$ , the size of the reverse flow region increases with the forward speed.

In this study, it is assumed that the aerodynamic lift and moment per unit span are equal to zero, while the sign of the profile drag per unit span is reversed inside the reverse flow region. The reverse flow region can have an influence on rotor aerodynamic loads at high advance ratios and it should be taken into account in the calculation of the aerodynamic loads.

## Chapter VI

### METHOD OF SOLUTION

The finite element discretization of the blade equations of motion has been described in Chapter 4. This chapter describes the treatment of the blade axial degree of freedom. This is an important step required for the appropriate representation of the centrifugal force and Coriolis damping effects, before the blade equations of motion can be solved. Subsequently, the various solution procedures needed for determining the aeroelastic stability in hover, as well as the response and stability in forward flight are described.

#### 6.1 TREATMENT OF THE AXIAL DEGREE OF FREEDOM

A careful treatment of the blade axial degree of freedom is required so as to properly account for the centrifugal force and Coriolis damping effects. In the past, two basic approaches have emerged for the treatment of this problem: (1) the elimination approach and (2) the substitution approach. The elimination approach aims at eliminating the axial degree of freedom from the blade equations of motion. Historically, this has been done through mathematical manipulations[41,83,12] described below. The blade axial equation of motion, derived previously, is given by:

$$\{ -\bar{V}_x + q_y w_{,x} - q_z v_{,x} \}_{,x} - \bar{Z}_u - p_x = 0 \quad (4.76a)$$

where the axial stress resultant  $\bar{V}_x$  is written, from Eq. (4.11a), as

$$\begin{aligned}\bar{V}_x &\equiv \iint_{\Lambda} (Q_{11}\varepsilon_{xx} + Q_{15}\gamma_{xz} + Q_{16}\gamma_{xy}) d\eta d\zeta \\ &= EA[u_{,x} + \frac{1}{2}(v_{,x})^2 + \frac{1}{2}(w_{,x})^2] + f\end{aligned}\quad (6.1)$$

where  $f$  represents the additional terms which do not depend on the axial degree of freedom,  $u$ . The axial component of the distributed inertia force,  $\bar{Z}_u$ , is given in Eq. (4.55a). In Eq. (4.76a), the distributed external force and moment terms  $p_x, q_y$  and  $q_z$  are often neglected. Using three equations, Eqs. (4.76a), (6.1) and (4.55a), the elimination procedure is carried out in two stages. In the first stage, a new expression for the axial strain at the elastic axis in terms of the axial inertia force is obtained after some mathematical manipulation. Rewrite Eq. (6.1) as

$$u_{,x} + \frac{1}{2}(v_{,x})^2 + \frac{1}{2}(w_{,x})^2 = \frac{\bar{V}_x}{EA} - \frac{f}{EA}\quad (6.2)$$

where the term on the left hand side of Eq. (6.2) is, from Eq. (3.31), the axial strain at the elastic axis,  $\bar{\varepsilon}_{xx}$ . The axial stress resultant  $\bar{V}_x$  is also the total axial force on the blade due to inertial and external loads at the spanwise station  $x$  of the blade element, and can be calculated by integrating Eq. (4.76a), while neglecting the distributed external force and moment terms

$$\bar{V}_x = \int_x^l \bar{Z}_u dx + \tilde{V}_x\quad (6.3)$$

where  $\tilde{V}_x$  is the total inertial force in the axial direction due to the portion of the blade outboard of the element. Combining Eqs. (6.2) and (6.3), the new expression for the axial strain at the elastic axis is given by

$$\bar{\epsilon}_{xx} = u_{,x} + \frac{1}{2} (v_{,x})^2 + \frac{1}{2} (w_{,x})^2 = F \quad (6.4)$$

where

$$F = \frac{1}{EA} \left( \int_x^{l_c} \bar{Z}_u dx + \tilde{V}_x - f \right) \quad (6.5)$$

Using Eqs. (6.4) and (6.5), all the terms involving  $\bar{\epsilon}_{xx}$  in flap, lag and torsion equations are replaced by the function  $F$ , which is equivalent to the proper representation of the centrifugal force effects in these equations.

In the second stage, terms involving  $u$  and its time derivatives are eliminated from the flap, lag and torsion equations. Integrating Eq. (6.4) with respect to  $x$  yields

$$u = \int_0^x F dx - \int_0^x \frac{1}{2} (v_{,x}^2 + w_{,x}^2) dx \quad (6.6)$$

This expression for  $u$ , Eq. (6.6), and its time derivatives are then used to replace the corresponding terms in the flap, lag and torsion equations. The Coriolis damping effect is retained in this process of eliminating  $u$  and its time derivatives. It is worthwhile mentioning that in the past, additional simplification was often introduced in the second stage by imposing the axial inextensionality condition; which is equivalent to the requirement  $\bar{\epsilon}_{xx} = 0$ , in Eq. (6.4), and it also implies that  $F = 0$ , in Eq. (6.6). In the two-stage elimi-

nation process described above, the axial degree of freedom is completely eliminated from the system of equations. Subsequently these modified system of equations, with reduced degrees of freedom, can be used in the aeroelastic analysis. Such an elimination procedure becomes algebraically tedious in the case of composite blade model or when higher order terms are retained in the blade model[15].

The substitution approach , which is used in this study, has also been employed by Chopra and his associates since the mid 80's (e.g., Ref. 48). It represents a somewhat more general alternative to elimination. In this approach, Eqs. (6.4) and (6.5) are used to substitute for the axial strain at the elastic axis so as to properly account for the centrifugal force effects. However, both the axial degree of freedom  $u$  and the axial equation of motion are retained in the aeroelastic calculations. In the nonlinear equilibrium position calculation, the nonlinear terms encountered in the substitution procedure are treated as known quantities and are substituted using the approximate solution from the previous iteration. For linearized stability analysis, these nonlinear terms are substituted using the converged equilibrium values. It is important to note that when using the substitution procedure in an aeroelastic analysis, the modal coordinate transformation should include an axial mode in order to properly account for the Coriolis damping effect. Without this axial mode, the flap and lag damping obtained from the linearized stability analysis can be inaccurate at high pitch angles, as will be shown latter in this study. A more concise description of the approaches for the treatment of the axial degree of freedom, presented in this section, has been included in Ref. 104.

## 6.2 FREE VIBRATION ANALYSIS

The first step in the solution procedure is the calculation of the natural frequencies and mode shapes of the blade. The coupled equations of motion representing the free vibrations of the rotating composite blade are a set of nonlinear ordinary differential equations obtained from the finite element discretization described in Chapter 4. These nonlinear equations of motion are converted into a set of linear equations by replacing the nonlinear terms associated with the axial strain at the elastic axis by a linear term representing the inertial force in the axial direction, and neglecting all other nonlinear terms associated with the substitution procedure described in the previous section. The computation of the natural frequencies and mode shapes of the blade is based on the linear, undamped equations of motion of the blade in vacuum. The equations of motion for the typical element used to model the straight portion of the blade are:

$$[M_i^F] \ddot{q}_i + [K_i^F] q_i = \mathbf{0}, \quad i = 1, \dots, n - 1 \quad (6.7)$$

and for the swept tip element, the equations of motion are given by

$$[\Lambda^L]^T [M_t^F] [\Lambda^L] \ddot{q}_t^G + [\Lambda^L]^T [K_t^F] [\Lambda^L] q_t^G = \mathbf{0} \quad (6.8)$$

where the linear transformation matrix  $[\Lambda^L]$  is used in the local-to-global coordinate transformation.

The  $n - 1$  equations, Eq. (6.7), and Eq. (6.8) are then assembled using the standard finite element assembly procedure. The assembled finite element equations of motion for the free vibrations of the blade are written as

$$[M^F] \ddot{\mathbf{q}} + [K^F] \mathbf{q} = \mathbf{0} \quad (6.9)$$

In Eqs. (6.7)-(6.9), the superscript F denotes matrices used in the free vibration analysis. The boundary conditions at the root are imposed by deleting the appropriate rows and columns of the system mass and stiffness matrices that correspond to the constrained degrees of freedom at the blade root.

For the baseline configuration of the blade, the free vibration modes are calculated with zero pitch angle. In an aeroelastic analysis where a modal coordinate transformation is used to reduce the number of degrees of freedom, the free vibration modes of the blade are calculated for a root pitch angle that corresponds to the collective pitch setting of the blade. The coupled modes of the blade are identified using a procedure[11] which is described next. The eigenvector representing the mode shape of a particular mode is normalized by dividing it by the largest tip displacement among its seven component modes. The identification of the mode is based on the component mode with the largest participation in the tip displacement, i.e., having a normalized tip displacement of one.

### **6.3 MODAL COORDINATE TRANSFORMATION AND ASSEMBLY PROCEDURE**

A preliminary step in the solution of the aeroelastic response and stability in hover and in forward flight consists of a modal coordinate transformation performed on the blade equations so as to reduce the number of degrees of freedom of the problem, and to assemble the various element matrices into

global system mass, damping and stiffness matrices and generate the system load vector. For the  $i$ -th element, the modal coordinate transformation has the form:

$$\mathbf{q}_i = [\mathbf{Q}_i] \mathbf{y} \quad (6.10)$$

where  $\mathbf{y}$  is the vector of generalized modal coordinates, which become the new unknowns of the problem. If  $N_m$  modes are used to perform the modal coordinate transformation, then  $\mathbf{y}$  is a vector of size  $N_m$ . The transformation matrix  $[\mathbf{Q}_i]$  for the  $i$ -th element has a size of 23 by  $N_m$ ; the columns of  $[\mathbf{Q}_i]$  contain the portions of the normal mode eigenvectors corresponding to the modal degrees of freedom for the  $i$ -th element.

The assembled stiffness matrix of the blade is obtained by summing the stiffness matrices of the individual elements after the modal coordinate transformation has been performed on each of these elements:

$$[\mathbf{K}] = \sum_{i=1}^{n-1} [\mathbf{Q}_i]^T [\mathbf{K}_i] [\mathbf{Q}_i] + [\mathbf{Q}_t]^T [\mathbf{\Lambda}^L]^T [\mathbf{K}_t] ([\mathbf{\Lambda}^L] + [\mathbf{\Lambda}^K]) [\mathbf{Q}_t] \quad (6.11)$$

Similarly, the assembled damping and mass matrices are written, respectively, as:

$$[\mathbf{C}] = \sum_{i=1}^{n-1} [\mathbf{Q}_i]^T [\mathbf{C}_i] [\mathbf{Q}_i] + [\mathbf{Q}_t]^T [\mathbf{\Lambda}^L]^T \{ [\mathbf{C}_t] ([\mathbf{\Lambda}^L] + [\mathbf{\Lambda}^C]) + [\mathbf{M}_t] [\mathbf{\Lambda}^M] \} [\mathbf{Q}_t] \quad (6.12)$$

$$[\mathbf{M}] = \sum_{i=1}^{n-1} [\mathbf{Q}_i]^T [\mathbf{M}_i] [\mathbf{Q}_i] + [\mathbf{Q}_t]^T [\mathbf{\Lambda}^L]^T [\mathbf{M}_t] ([\mathbf{\Lambda}^L] + [\mathbf{\Lambda}^C]) [\mathbf{Q}_t] \quad (6.13)$$

and the assembled load vector is given by:

$$\mathbf{F} = \sum_{i=1}^{n-1} [\mathbf{Q}_i]^T \mathbf{F}_i + [\mathbf{Q}_t]^T [\mathbf{\Lambda}^L]^T \mathbf{F}_t \quad (6.14)$$

In Eqs. (6.11), (6.12) and (6.13), the local-to-global transformations for the swept tip element, Eqs. (4.110), (4.111) and (4.112) have been applied before implementing the modal transformation.

The assembled blade equations of motion in the modal space are a set of nonlinear, coupled, ordinary differential equations written as:

$$[\mathbf{M}(\mathbf{y})]\ddot{\mathbf{y}} + [\mathbf{C}(\mathbf{y}, \dot{\mathbf{y}})]\dot{\mathbf{y}} + [\mathbf{K}(\mathbf{y}, \dot{\mathbf{y}}, \ddot{\mathbf{y}})]\mathbf{y} + \mathbf{F}(\mathbf{y}, \dot{\mathbf{y}}, \ddot{\mathbf{y}}) = \mathbf{0} \quad (6.15)$$

For the case of forward flight, these equations also have periodic coefficients. In Eq. (6.15) the nonlinearity of the mass and damping matrices comes from the local-to-global transformation associated with the swept tip element. The dependence of the stiffness matrix on  $\dot{\mathbf{y}}$  and  $\ddot{\mathbf{y}}$ , on the other hand, is due to the substitution procedure in the treatment of the axial degree of freedom.

#### 6.4 HOVER ANALYSIS

For the case of hover, the nonlinear equations of motion, Eq. (6.15), have constant coefficients. The blade static equilibrium position,  $\mathbf{y}_0$ , is obtained from Eq. (6.15) by setting  $\dot{\mathbf{y}} = \ddot{\mathbf{y}} = \mathbf{0}$  and solving the resulting nonlinear algebraic equations:

$$[\mathbf{K}(\mathbf{y}_0, \mathbf{0}, \mathbf{0})]\mathbf{y}_0 + \mathbf{F}(\mathbf{y}_0, \mathbf{0}, \mathbf{0}) = \mathbf{0} \quad (6.16)$$

using a Newton-Raphson iteration procedure.

In this study, the blade response analysis is coupled with the calculation of the trim variables such that the overall equilibrium of the helicopter is maintained:

$$C_T = C_W \quad (6.17)$$

The trim variables in hover consist of the collective pitch angle  $\theta_0$  and the inflow ratio  $\lambda$ . A brief description of the coupled trim-aeroelastic response solution process is given below. At the beginning of the analysis, an initial estimate of the equilibrium position  $\mathbf{y}_0$  and the trim variables is assumed. The approximate solution of Eq. (6.16),  $\tilde{\mathbf{y}}_0$ , is obtained while keeping the estimated trim variables constant. The error in the collective pitch angle is calculated from

$$\Delta\theta_0 = \frac{C_W - \tilde{C}_T}{\frac{\partial C_T}{\partial \theta_0}} \quad (6.18)$$

where  $\tilde{C}_T$  is the thrust coefficient corresponding to the approximate equilibrium solution  $\tilde{\mathbf{y}}_0$ . Details of the calculation of the thrust coefficient will be described later in this chapter. The derivative of  $C_T$  with respect to  $\theta_0$  is approximated by

$$\frac{\partial C_T}{\partial \theta_0} = \frac{a\sigma}{6} \quad (6.19)$$

which is based on the approximate relation

$$C_T = \frac{a\sigma}{2} \left( \frac{\theta_{0.75}}{3} - \frac{\lambda}{2} \right) \quad (6.20)$$

obtained from the blade element theory[52], where

$$\theta_{0.75} = \theta_0 + (\beta + \phi)_{0.75} \quad (6.21)$$

is the total pitch angle at the 3/4 span of the blade. The absolute value of  $\Delta\theta_0$  is compared with its convergence criterion; where a value of 0.0001 radian is used as the convergence criterion in this study. If convergence is not achieved, then a new estimate of the collective pitch is calculated from:

$$(\tilde{\theta}_0)_{\text{new}} = (\tilde{\theta}_0)_{\text{old}} + \Delta\theta_0 \quad (6.22)$$

Corresponding to the new pitch angle, a new estimate of the inflow ratio is also obtained from

$$(\tilde{\lambda})_{\text{new}} = \frac{a\sigma}{16} \left( \sqrt{1 + \frac{24\tilde{\theta}_{0.75}}{a\sigma}} - 1 \right) \quad (6.23)$$

where

$$\tilde{\theta}_{0.75} = (\tilde{\theta}_0)_{\text{new}} + (\beta + \phi)_{0.75} \quad (6.24)$$

is the total pitch angle at the 3/4 span of the blade based on the current approximation of equilibrium position,  $\tilde{y}_0$ . Equation (6.23) is based on the extended blade element theory[52]. With  $(\tilde{\theta}_0)_{\text{new}}$ ,  $(\tilde{\lambda})_{\text{new}}$  and  $\tilde{y}_0$  as the new estimate of  $\theta_0$ ,  $\lambda$  and  $y_0$ , respectively, for the next solution pass, the process described above is repeated until this fairly simple coupled trim-aeroelastic response problem converges, to produce final converged values for  $\theta_0$ ,  $\lambda$  and  $y_0$ .

The blade equations of motion in the modal space, Eq. (6.15), can be written as:

$$\mathbf{f}(\mathbf{y}, \dot{\mathbf{y}}, \ddot{\mathbf{y}}) = \mathbf{0} \quad (6.25)$$

For the hover case, Eq. (6.25) can be linearized about the nonlinear static equilibrium position  $\mathbf{y}_0$ , to yield:

$$\mathbf{f} = [\bar{\mathbf{M}}(\mathbf{y}_0)]\Delta\ddot{\mathbf{y}} + [\bar{\mathbf{C}}(\mathbf{y}_0)]\Delta\dot{\mathbf{y}} + [\bar{\mathbf{K}}(\mathbf{y}_0)]\Delta\mathbf{y} + \text{H.O.T.} = \mathbf{0} \quad (6.26)$$

where

$$[\bar{\mathbf{M}}] = \left[ \frac{\partial \mathbf{f}}{\partial \ddot{\mathbf{y}}} \right]_{\mathbf{y}_0, \mathbf{0}, \mathbf{0}} \quad (6.27)$$

$$[\bar{\mathbf{C}}] = \left[ \frac{\partial \mathbf{f}}{\partial \dot{\mathbf{y}}} \right]_{\mathbf{y}_0, \mathbf{0}, \mathbf{0}} \quad (6.28)$$

$$[\bar{\mathbf{K}}] = \left[ \frac{\partial \mathbf{f}}{\partial \mathbf{y}} \right]_{\mathbf{y}_0, \mathbf{0}, \mathbf{0}} \quad (6.29)$$

are the mass, damping and stiffness matrices, respectively, of the linearized system. In the linearization process, the generalized modal coordinate vector  $\mathbf{y}$  has been written as

$$\mathbf{y} = \mathbf{y}_0 + \Delta\mathbf{y} \quad (6.30)$$

where  $\Delta\mathbf{y}$  is a time dependent small perturbation vector of  $\mathbf{y}$ ; and the fact that  $\mathbf{f}(\mathbf{y}_0, \mathbf{0}, \mathbf{0}) = \mathbf{0}$  has been used. Neglecting the higher order terms, the linearized system, Eq. (6.26), can be expressed in the first order state variable form by

$$\dot{\mathbf{z}} = [\mathbf{A}] \mathbf{z} \quad (6.31)$$

where the state vector  $\mathbf{z}$  is defined as

$$\mathbf{z} = \begin{Bmatrix} \Delta \mathbf{y} \\ \Delta \dot{\mathbf{y}} \end{Bmatrix} \quad (6.32)$$

and the system matrix  $[\mathbf{A}]$  has the form

$$[\mathbf{A}] = \begin{bmatrix} [0] & [1] \\ -[\bar{\mathbf{M}}]^{-1}[\bar{\mathbf{K}}] & -[\bar{\mathbf{M}}]^{-1}[\bar{\mathbf{C}}] \end{bmatrix} \quad (6.33)$$

The linearized stability of the system is determined by the eigenvalues of  $[\mathbf{A}]$ .

These eigenvalues are in complex conjugate pairs

$$\lambda_j = \zeta_j \pm i\omega_j, \quad j = 1, \dots, N_m \quad (6.34)$$

The blade is stable if  $\zeta_j < 0$  for all  $j$ .

## 6.5 FORWARD FLIGHT ANALYSIS

In forward flight the nonlinear equations of motion of the isolated blade are periodic and can be written symbolically as

$$\mathbf{f}_b(\mathbf{y}_b, \dot{\mathbf{y}}_b, \ddot{\mathbf{y}}_b, \mathbf{y}_t; \psi) = \mathbf{0} \quad (6.35)$$

where  $\mathbf{y}_b$  is the vector of generalized blade degrees of freedom. The vector  $\mathbf{y}_t$  in Eq. (6.35) contains the parameters governing the trim state of the helicopter, including the collective pitch angle  $\theta_0$ , the cyclic cosine pitch input  $\theta_{1c}$ , the cyclic sine pitch input  $\theta_{1s}$ , the inflow ratio  $\lambda$ , and the rotor angle of attack  $\alpha_R$ ; thus the vector  $\mathbf{y}_t$  is given by

$$\mathbf{y}_t = [\theta_0, \theta_{1c}, \theta_{1s}, \lambda, \alpha_R]^T \quad (6.36)$$

These five trim variables appear explicitly in the blade equations of motion. Obviously the blade equations cannot be solved without knowledge of the trim state represented by Eq. (6.36), because the aeroelastic problem in forward flight is inherently coupled to the flight mechanics of the helicopter as represented by trim. The trim vector  $y_t$  is obtained from the solution of a set of nonlinear trim equations

$$\mathbf{f}_t(y_b, \dot{y}_b, \ddot{y}_b, y_t; \psi) = \mathbf{0} \quad (6.37)$$

which are based on the overall force and moment equilibrium of the helicopter in steady, level forward flight. The procedure used to determine the trim state of the helicopter is referred to as the "trim analysis".

### 6.5.1 *Trim Analysis*

The trim analysis employed in this study is called "propulsive trim"[24], which enforces longitudinal and vertical force equilibrium, as well as pitch and roll moment equilibrium of the helicopter in steady, level flight. A helicopter (Fig. 6.1) in free flight has a total of six degrees of freedom, including three translational and three rotational. Therefore three force and three moment equilibrium equations have to be satisfied in order to maintain the overall equilibrium of the helicopter. For simplified propulsive trim employed here, the yawing moment equilibrium and the lateral force equilibrium are not enforced; thus the tail rotor pitch setting and the main rotor shaft angle in the lateral plane are not included in the vector of trim variables given in Eq. (6.36).

This implies that one assumes that the yawing moment equilibrium and the lateral force equilibrium are satisfied.

The four equilibrium equations, together with an inflow equation, constitute a total of five trim equations which must be solved for the five trim variables defined in Eq. (6.36). These trim equations are collectively represented in a vector form by Eq. (6.37). The equilibrium equations are formulated in the nonrotating, hub-fixed system  $(\hat{i}_{nr}, \hat{j}_{nr}, \hat{k}_{nr})$  with the hub center  $O_H$  as the moment center for moment equilibrium equations, as shown schematically in Fig. 6.2.

The five trim equations are:

1. The inflow equation. This equation governs the relation between the inflow ratio  $\lambda$ , advance ratio  $\mu$ , rotor angle of attack  $\alpha_R$  and thrust coefficient  $C_T$ , based on the momentum theory[52]:

$$f_i(1) = \lambda - \mu \tan(\alpha_R) - \frac{C_T}{2\sqrt{\lambda^2 + \mu^2}} = 0 \quad (6.38)$$

The thrust coefficient is defined as:

$$C_T = \frac{T_R}{\rho_A (\pi R^2) (\Omega R)^2} \quad (6.39)$$

where  $T_R$  is the total thrust generated by the rotor.

2. The pitching moment equation. This equation is obtained by enforcing pitching moment equilibrium about the hub center. Summing the pitching moments due to hub loads, helicopter weight and fuselage drag gives (see Fig. 6.2):

$$\begin{aligned}
M_{pt} + W(-X_{FC} \cos \alpha_R + Z_{FC} \sin \alpha_R) \\
+ D_f(X_{FA} \sin \alpha_R - Z_{FA} \cos \alpha_R) = 0
\end{aligned} \tag{6.40}$$

where  $M_{pt}$  is the pitching moment due to hub loads;  $W$  is the weight of the helicopter;  $D_f$  is the parasite drag of the fuselage. The weight  $W$  acts at the center of gravity of the helicopter, offset from the hub center  $O_H$  by the distances  $X_{FC}$  and  $Z_{FC}$  in the  $-\hat{i}_{nr}$  and  $-\hat{k}_{nr}$  directions, respectively, as shown in Fig. 6.2. The parasite drag  $D_f$  acting on the fuselage is given by[52]:

$$D_f = \frac{1}{2} \rho_A V_F^2 fC_{df} \tag{6.41}$$

where  $V_F$  is the forward flight speed with respect to the air; and  $fC_{df}$  is the parasite drag area. The typical value of the parasite drag area is approximately  $fC_{df} \simeq 0.01\pi R^2$ . The velocity vector  $V_F$  of the helicopter with respect to the air can be written as:

$$V_F = V_F \cos \alpha_R \hat{i}_{nr} - V_F \sin \alpha_R \hat{k}_{nr} \tag{6.42}$$

It is assumed that the drag force  $D_f$  acts parallel to  $V_F$ , at the center of drag, which is offset from the hub center  $O_H$  by the distances  $X_{FA}$  and  $Z_{FA}$  in the  $\hat{i}_{nr}$  and  $-\hat{k}_{nr}$  directions, respectively, as shown in Fig. 6.2. Nondimensionalizing Eq. (6.40) by the factor  $\rho_A(\pi R^2)(\Omega R)^2 R$  yields:

$$\begin{aligned}
f_t(2) = \bar{M}_{pt} + C_W(-\bar{X}_{FC} \cos \alpha_R + \bar{Z}_{FC} \sin \alpha_R) \\
+ C_{Df}(\bar{X}_{FA} \sin \alpha_R - \bar{Z}_{FA} \cos \alpha_R) = 0
\end{aligned} \tag{6.43}$$

where

$$\bar{M}_{pt} = \frac{M_{pt}}{\rho_{\Lambda} (\pi R^2) (\Omega R)^2 R} \quad (6.44)$$

$$C_W = \frac{W}{\rho_{\Lambda} (\pi R^2) (\Omega R)^2} \quad (6.45)$$

$$C_{Df} = \frac{D_f}{\rho_{\Lambda} (\pi R^2) (\Omega R)^2} \quad (6.46)$$

$$\bar{X}_{FC} = \frac{X_{FC}}{R}, \quad \bar{Z}_{FC} = \frac{Z_{FC}}{R} \quad (6.47)$$

$$\bar{X}_{FA} = \frac{X_{FA}}{R}, \quad \bar{Z}_{FA} = \frac{Z_{FA}}{R} \quad (6.48)$$

Substituting Eq. (6.41) into Eq. (6.46), the nondimensional parasite drag coefficient  $C_{Df}$  can be written as:

$$C_{Df} = \frac{\frac{1}{2} \rho_{\Lambda} V_F^2 f C_{df}}{\rho_{\Lambda} (\pi R^2) (\Omega R)^2} = \frac{1}{2} \left( \frac{\mu}{\cos \alpha_R} \right)^2 \left( \frac{f C_{df}}{\pi R^2} \right) \quad (6.49)$$

where  $f C_{df} / (\pi R^2) \simeq 0.01$ .

3. The rolling moment equation. Since the tail rotor and the main rotor tilt angle in the lateral plane are not modeled, the rolling moment equation is obtained by simply setting the rolling moment due to hub loads equal to zero:

$$f_i(3) = M_{rl} = \bar{M}_{rl} = 0 \quad (6.50)$$

where

$$\bar{M}_{rl} = \frac{M_{rl}}{\rho_A (\pi R^2) (\Omega R)^2 R} \quad (6.51)$$

4. The vertical force equation. This equation is obtained by enforcing the force equilibrium in the  $\hat{k}_{nr}$  direction (see Fig. 6.2):

$$T_R - W \cos \alpha_R - D_f \sin \alpha_R = 0 \quad (6.52)$$

Nondimensionalizing Eq. (6.52) by the factor  $\rho_A (\pi R^2) (\Omega R)^2$  yields:

$$f_t(4) = C_T - C_W \cos \alpha_R - C_{Df} \sin \alpha_R = 0 \quad (6.53)$$

5. The longitudinal force equation. This equation is obtained by enforcing the force equilibrium in the  $\hat{i}_{nr}$  direction (see Fig. 6.2):

$$H_R - W \sin \alpha_R + D_f \cos \alpha_R = 0 \quad (6.54)$$

where  $H_R$  is the total longitudinal hub force. Nondimensionalizing Eq. (6.54) by  $\rho_A (\pi R^2) (\Omega R)^2$  yields:

$$f_t(5) = C_H - C_W \sin \alpha_R + C_{Df} \cos \alpha_R = 0 \quad (6.55)$$

where

$$C_H = \frac{H_R}{\rho_A (\pi R^2) (\Omega R)^2} \quad (6.56)$$

### 6.5.2 Distributed Loads on the blade

The distributed loads on the blade are due to inertial and aerodynamic sources described below.

#### 6.5.2.1 Inertial Loads

The inertial loads on the blade are derived using the variation of the kinetic energy expression shown in Eq. (4.54):

$$\begin{aligned} \delta T = \int_0^{l_c} [ & \bar{Z}_u \delta u + \bar{Z}_v \delta v + \bar{Z}'_v \delta v_{,x} + \bar{Z}_w \delta w + \bar{Z}'_w \delta w_{,x} \\ & + \bar{Z}_\phi \delta \phi + \bar{Z}_\alpha \delta \alpha + \bar{Z}_\eta \delta \bar{\gamma}_{x\eta} + \bar{Z}_\zeta \delta \bar{\gamma}_{x\zeta} ] dx \end{aligned} \quad (4.54)$$

The expression inside the brackets in Eq. (4.54) is the virtual work done by the distributed inertial loads on the blade. The quantities  $\delta u$ ,  $\delta v$  and  $\delta w$  are virtual displacements in the  $\hat{e}_x$ ,  $\hat{e}_y$  and  $\hat{e}_z$  directions, respectively, therefore  $\bar{Z}_u$ ,  $\bar{Z}_v$  and  $\bar{Z}_w$  represent inertial forces per unit span in the  $\hat{e}_x$ ,  $\hat{e}_y$  and  $\hat{e}_z$  directions, respectively. Similarly,  $\bar{Z}'_v$  and  $\bar{Z}'_w$  are inertial moments per unit span in the  $\hat{e}_z$  and  $-\hat{e}_y$  directions, respectively, since  $\delta v_{,x}$  and  $\delta w_{,x}$  are the corresponding virtual rotations. The virtual rotations  $\delta \phi$ ,  $\delta \bar{\gamma}_{x\eta}$  and  $\delta \bar{\gamma}_{x\zeta}$  are in the  $\hat{e}'_x$ ,  $-\hat{e}'_\zeta$  and  $\hat{e}'_\eta$  directions, respectively; thus  $\bar{Z}_\phi$ ,  $\bar{Z}_\eta$  and  $\bar{Z}_\zeta$  are inertial moments per unit span in the  $\hat{e}'_x$ ,  $-\hat{e}'_\zeta$  and  $\hat{e}'_\eta$  directions, respectively. Note that the orientations of  $\delta \bar{\gamma}_{x\eta}$  and  $\delta \bar{\gamma}_{x\zeta}$  are obtained from Eqs. (3.10b-c) which define the base vectors  $\mathbf{E}_\eta$  and  $\mathbf{E}_\zeta$  of the deformed elastic axis. The inertial loads due to warping are assumed to be small and are neglected in the calculation of blade root and hub

loads. Similar assumption regarding the inertial warping loads has been used by other researchers (e.g., Ref. 22).

The distributed inertial force vector at a point on the blade is written as:

$$\mathbf{f}_I = f_{xI} \hat{\mathbf{e}}_x + f_{yI} \hat{\mathbf{e}}_y + f_{zI} \hat{\mathbf{e}}_z \quad (6.57)$$

where the components of  $\mathbf{f}_I$  in the  $(\hat{\mathbf{e}}_x, \hat{\mathbf{e}}_y, \hat{\mathbf{e}}_z)$  system are obtained from

$$\begin{Bmatrix} f_{xI} \\ f_{yI} \\ f_{zI} \end{Bmatrix} = \begin{Bmatrix} \bar{Z}_u \\ \bar{Z}_v \\ \bar{Z}_w \end{Bmatrix} \quad (6.58)$$

The distributed inertial moment vector at a point on the blade is written as:

$$\mathbf{m}_I = m_{xI} \hat{\mathbf{e}}_x + m_{yI} \hat{\mathbf{e}}_y + m_{zI} \hat{\mathbf{e}}_z \quad (6.59)$$

where the components of  $\mathbf{m}_I$  in the  $(\hat{\mathbf{e}}_x, \hat{\mathbf{e}}_y, \hat{\mathbf{e}}_z)$  system are obtained from

$$\begin{Bmatrix} m_{xI} \\ m_{yI} \\ m_{zI} \end{Bmatrix} = \begin{Bmatrix} 0 \\ -\bar{Z}'_w \\ \bar{Z}'_v \end{Bmatrix} + [\mathbf{T}_{de}]^T \begin{Bmatrix} \bar{Z}_\phi \\ \bar{Z}_\zeta \\ -\bar{Z}_\eta \end{Bmatrix} \quad (6.60)$$

### 6.5.2.2 Aerodynamic Loads

The distributed aerodynamic force and moment vectors at a point on the blade are written as:

$$\mathbf{f}_A = p_x \hat{\mathbf{e}}_x + p_y \hat{\mathbf{e}}_y + p_z \hat{\mathbf{e}}_z \quad (6.61)$$

and

$$\mathbf{m}_A = q_x \hat{\mathbf{e}}_x + q_y \hat{\mathbf{e}}_y + q_z \hat{\mathbf{e}}_z \quad (6.62)$$

, respectively, where the components of  $\mathbf{f}_A$  and  $\mathbf{m}_A$  in the  $(\hat{\mathbf{e}}_x, \hat{\mathbf{e}}_y, \hat{\mathbf{e}}_z)$  system are obtained from Eqs. (5.36) and (5.37), respectively.

### 6.5.3 Rotor Hub Loads

The rotor hub loads are obtained by integrating the distributed loads along the span of the isolated blade in the rotating frame, then transforming these loads to the hub-fixed nonrotating reference frame, and summing the contribution from the individual blades.

The distributed forces and moments are due to the inertial and aerodynamic loads on each blade. The combined distributed force and moment vectors,  $\mathbf{f}^L$ , and  $\mathbf{m}^L$ , respectively, at a point on the blade are given by

$$\mathbf{f}^L = \mathbf{f}_I + \mathbf{f}_A = f_x^L \hat{\mathbf{e}}_x + f_y^L \hat{\mathbf{e}}_y + f_z^L \hat{\mathbf{e}}_z \quad (6.63)$$

and

$$\mathbf{m}^L = \mathbf{m}_I + \mathbf{m}_A = m_x^L \hat{\mathbf{e}}_x + m_y^L \hat{\mathbf{e}}_y + m_z^L \hat{\mathbf{e}}_z \quad (6.64)$$

where the components of  $\mathbf{f}_I$  and  $\mathbf{m}_I$  in the  $(\hat{\mathbf{e}}_x, \hat{\mathbf{e}}_y, \hat{\mathbf{e}}_z)$  system are obtained from

$$\begin{Bmatrix} f_x^L \\ f_y^L \\ f_z^L \end{Bmatrix} = \begin{Bmatrix} f_{xI} + p_x \\ f_{yI} + p_y \\ f_{zI} + p_z \end{Bmatrix} \quad (6.65)$$

and

$$\begin{Bmatrix} m_x^L \\ m_y^L \\ m_z^L \end{Bmatrix} = \begin{Bmatrix} m_{xI} + q_x \\ m_{yI} + q_y \\ m_{zI} + q_z \end{Bmatrix} \quad (6.66)$$

, respectively. These local force and moment distributions, after suitable integration, produce blade root force and moment at the axis of rotation which is expressed in the rotating, hub-fixed system  $(\hat{i}_r, \hat{j}_r, \hat{k}_r)$ .

Since a finite element formulation is employed in this study, the integration of the distributed loads simply implies a summation of the element contributions over the blade. To carry out these summations the local loads have to be transformed to the rotating, hub-fixed system in which the total rotating hub loads are obtained. The contribution to the blade root force, due to local force distribution, is obtained by

$$\mathbf{f}^R = \mathbf{f}^L = f_x^R \hat{i}_r + f_y^R \hat{j}_r + f_z^R \hat{k}_r \quad (6.67)$$

where

$$\begin{Bmatrix} f_x^R \\ f_y^R \\ f_z^R \end{Bmatrix} = [T_{er}]^T \begin{Bmatrix} f_x^L \\ f_y^L \\ f_z^L \end{Bmatrix} \quad (6.68)$$

and the transformation matrix  $[T_{er}]$  is defined as:

$$[T_{er}] = [T_{eb}] [T_{br}] \quad (6.69)$$

where  $[T_{eb}]$  and  $[T_{br}]$  are given by Eqs. (2.7) and (2.4), respectively.

The blade root moment, in the rotating system, consists of contributions from both the local moment distribution and the local force distribution. The contribution due to the local distributed moment is

$$\mathbf{m}^{R1} = \mathbf{m}^L = m_x^{R1} \hat{i}_r + m_y^{R1} \hat{j}_r + m_z^{R1} \hat{k}_r \quad (6.70)$$

where

$$\begin{Bmatrix} m_x^{R1} \\ m_y^{R1} \\ m_z^{R1} \end{Bmatrix} = [T_{cr}]^T \begin{Bmatrix} m_x^L \\ m_y^L \\ m_z^L \end{Bmatrix} \quad (6.71)$$

and the contribution due to the local distributed force is given by

$$\begin{aligned} \mathbf{m}^{R2} &= \mathbf{R}_0 \times \mathbf{f}^L \\ &= m_x^{R2} \hat{i}_r + m_y^{R2} \hat{j}_r + m_z^{R2} \hat{k}_r \end{aligned} \quad (6.72)$$

where the vector  $\mathbf{R}_0$  is the position vector of a point on the deformed elastic axis, given by combining Eqs. (3.5) and (4.20)

$$\begin{aligned} \mathbf{R}_0 &= c_1 \hat{i}_r + h_c \hat{i}_b + (x + u) \hat{e}_x + v \hat{e}_y + w \hat{e}_z \\ &= R_{x0}^R \hat{i}_r + R_{y0}^R \hat{j}_r + R_{z0}^R \hat{k}_r \end{aligned} \quad (6.73)$$

with

$$\begin{Bmatrix} R_{x0}^R \\ R_{y0}^R \\ R_{z0}^R \end{Bmatrix} = \begin{Bmatrix} c_1 + h_c \cos \beta_p \\ 0 \\ h_c \sin \beta_p \end{Bmatrix} + [T_{cr}]^T \begin{Bmatrix} x + u \\ v \\ w \end{Bmatrix} \quad (6.74)$$

Therefore the components of  $\mathbf{m}^{R2}$  in the  $(\hat{i}_r, \hat{j}_r, \hat{k}_r)$  system can be obtained by combining Eqs. (6.73), (6.63) and (6.67) with Eq. (6.72):

$$\begin{Bmatrix} m_x^{R2} \\ m_y^{R2} \\ m_z^{R2} \end{Bmatrix} = \begin{Bmatrix} R_{y0}^R f_z^R - R_{z0}^R f_y^R \\ R_{z0}^R f_x^R - R_{x0}^R f_z^R \\ R_{x0}^R f_y^R - R_{y0}^R f_x^R \end{Bmatrix} \quad (6.75)$$

The total contribution to the blade root moment due to the moment and force distribution at a point on the blade,  $\mathbf{m}^R$ , is given in by:

$$\begin{aligned} \mathbf{m}^R &= \mathbf{m}^{R1} + \mathbf{m}^{R2} \\ &= m_x^R \hat{i}_r + m_y^R \hat{j}_r + m_z^R \hat{k}_r \end{aligned} \quad (6.76)$$

where

$$\begin{Bmatrix} m_x^R \\ m_y^R \\ m_z^R \end{Bmatrix} = \begin{Bmatrix} m_x^{R1} + m_x^{R2} \\ m_y^{R1} + m_y^{R2} \\ m_z^{R1} + m_z^{R2} \end{Bmatrix} \quad (6.77)$$

The total blade root force and moment at the axis of rotation are obtained by integrating the contributions to the blade root force and moment,  $\mathbf{f}^R$  and  $\mathbf{m}^R$ , respectively, due to local distributed loads, over the span of the blade. For the k-th blade, the total blade root force and moment vectors have the form:

$$\mathbf{F}^{Rk}(\psi_k) = F_x^{Rk}(\psi_k) \hat{i}_r + F_y^{Rk}(\psi_k) \hat{j}_r + F_z^{Rk}(\psi_k) \hat{k}_r \quad (6.78)$$

$$\mathbf{M}^{Rk}(\psi_k) = M_x^{Rk}(\psi_k) \hat{i}_r + M_y^{Rk}(\psi_k) \hat{j}_r + M_z^{Rk}(\psi_k) \hat{k}_r \quad (6.79)$$

where

$$\psi_k = \psi + \frac{2\pi(k-1)}{B} \quad (6.80)$$

is the azimuth angle of the k-th blade for a B-bladed rotor.

Transforming the root force  $\mathbf{F}^{\text{Rk}}$  and the root moment  $\mathbf{M}^{\text{Rk}}$  to the nonrotating, hub-fixed system  $(\hat{i}_{\text{nr}}, \hat{j}_{\text{nr}}, \hat{k}_{\text{nr}})$  and summing the contribution due to each blade, yields the total hub force and hub moment vectors

$$\mathbf{F}^{\text{H}}(\psi) = F_x^{\text{H}}(\psi)\hat{i}_{\text{nr}} + F_y^{\text{H}}(\psi)\hat{j}_{\text{nr}} + F_z^{\text{H}}(\psi)\hat{k}_{\text{nr}} \quad (6.81)$$

and

$$\mathbf{M}^{\text{H}}(\psi) = M_x^{\text{H}}(\psi)\hat{i}_{\text{nr}} + M_y^{\text{H}}(\psi)\hat{j}_{\text{nr}} + M_z^{\text{H}}(\psi)\hat{k}_{\text{nr}} \quad (6.82)$$

, respectively, where

$$F_x^{\text{H}}(\psi) = \sum_{k=1}^B [ F_x^{\text{Rk}}(\psi_k) \cos \psi_k - F_y^{\text{Rk}}(\psi_k) \sin \psi_k ] \quad (6.83a)$$

$$F_y^{\text{H}}(\psi) = \sum_{k=1}^B [ F_x^{\text{Rk}}(\psi_k) \sin \psi_k + F_y^{\text{Rk}}(\psi_k) \cos \psi_k ] \quad (6.83b)$$

$$F_z^{\text{H}}(\psi) = \sum_{k=1}^B F_z^{\text{Rk}}(\psi_k) \quad (6.83c)$$

$$M_x^{\text{H}}(\psi) = \sum_{k=1}^B [ M_x^{\text{Rk}}(\psi_k) \cos \psi_k - M_y^{\text{Rk}}(\psi_k) \sin \psi_k ] \quad (6.84a)$$

$$M_y^H(\psi) = \sum_{k=1}^B [ M_x^{Rk}(\psi_k) \sin \psi_k + M_y^{Rk}(\psi_k) \cos \psi_k ] \quad (6.84b)$$

$$M_z^H(\psi) = \sum_{k=1}^B M_z^{Rk}(\psi_k) \quad (6.84c)$$

In Eqs. (6.83) and (6.84), the transformation between the rotating, hub-fixed system  $(\hat{i}_r, \hat{j}_r, \hat{k}_r)$  and the nonrotating, hub-fixed system  $(\hat{i}_{nr}, \hat{j}_{nr}, \hat{k}_{nr})$  has been defined in Eqs. (2.1) and (2.2).

In the trim analysis, described the previous subsection, the total thrust generated by the rotor,  $T_R$ , and the longitudinal hub force,  $H_R$ , are given by:

$$T_R = F_z^H(\psi) \quad (6.85)$$

and

$$H_R = F_x^H(\psi) \quad (6.86)$$

respectively; while the pitching moment  $M_{pt}$  and the rolling moment  $M_{rl}$  due to hub loads are given by:

$$M_{pt} = M_y^H(\psi) \quad (6.87)$$

and

$$M_{rl} = M_x^H(\psi) \quad (6.88)$$

respectively.

#### **6.5.4 *Coupled Trim and Aeroelastic Response Solution Using Harmonic Balance***

The trim equations depends upon the blade degrees of freedom through the rotor forces and moments, which are functions of the blade response. Therefore the helicopter trim and blade aeroelastic response problems are inherently coupled, and cannot be solved independently. One possible approach uses an iterative procedure in which an approximation of the blade response is used to solve for an approximate trim solution, which is then substituted back into the blade equations to obtain an improved approximation of the blade response. This procedure is continued until the trim and response solutions converge. If the number of unknowns in the blade equations is small, then this iterative procedure for solving the coupled trim-aeroelastic response problem is convenient, such as in the case of hover. However this procedure can be computationally inefficient for the case of forward flight since the number of unknowns involved in the blade equations for forward flight is usually at least one order of magnitude larger than that for the case of hover.

In this study, the coupled helicopter trim and blade aeroelastic response problem in forward flight is solved by an alternate procedure in which the trim and response solutions are obtained simultaneously using the harmonic balance technique.

The equations of motion of an isolated blade in steady, level forward flight, Eq. (6.35), are periodic. The response of the blade is also periodic with a fundamental frequency of 1/rev (i.e.  $y_b(\psi) = y_b(\psi + 2\pi)$ ), and thus it can be

approximated by a truncated Fourier series expansion containing  $N_H$  harmonics

$$\mathbf{y}_b \simeq \mathbf{y}_{b0} + \sum_{n=1}^{N_H} [\mathbf{y}_{bnc} \cos(n\psi) + \mathbf{y}_{bns} \sin(n\psi)] \quad (6.89)$$

where  $\mathbf{y}_{b0}$  represents the constant part, or the average value of  $\mathbf{y}_b$  over one rotor revolution;  $\mathbf{y}_{bnc}$  and  $\mathbf{y}_{bns}$  represent the cosine and sine amplitudes, respectively, of the  $n/\text{rev}$  harmonics. Collectively  $\mathbf{y}_{b0}$ ,  $\mathbf{y}_{bnc}$  and  $\mathbf{y}_{bns}$  represent a total of  $(1 + 2N_H)$  vectors, each containing  $N_m$  coefficients where  $N_m$  is the number of modes used in the modal coordinate transformation, or the size of the vector of generalized coordinates of the blade. The number of harmonics  $N_H$  retained in the Fourier series expansion of the blade degrees of freedom determines the accuracy of the response solution. For a B-bladed rotor the vibratory hub loads, which are calculated based on the response solution, are predominantly  $B/\text{rev}$ , thus at least  $B$  harmonics must be retained. In this study, the number of harmonics retained is obtained by

$$N_H = B + 1 \quad (6.90)$$

The blade equations and the trim equations, represented by Eqs. (6.35) and (6.37), respectively, can also be approximated by truncated Fourier series expansions containing  $N_H$  harmonics

$$\mathbf{f}_b \simeq \mathbf{f}_{b0} + \sum_{n=1}^{N_H} [\mathbf{f}_{bnc} \cos(n\psi) + \mathbf{f}_{bns} \sin(n\psi)] \quad (6.91)$$

$$\mathbf{f}_t \simeq \mathbf{f}_{t0} + \sum_{n=1}^{N_H} [\mathbf{f}_{tnc} \cos(n\psi) + \mathbf{f}_{tns} \sin(n\psi)] \quad (6.92)$$

An approximate solution to the blade equations can be obtained by setting the constant part, and the first  $N_H$  harmonics, in Eq. (6.91) to zero:

$$\mathbf{f}_{b0} = \frac{1}{2\pi} \int_0^{2\pi} \mathbf{f}_b(\mathbf{y}_b, \dot{\mathbf{y}}_b, \ddot{\mathbf{y}}_b, \mathbf{y}_t; \psi) d\psi = \mathbf{0} \quad (6.93)$$

and for  $1 \leq n \leq N_H$

$$\mathbf{f}_{bnc} = \frac{1}{\pi} \int_0^{2\pi} \mathbf{f}_b(\mathbf{y}_b, \dot{\mathbf{y}}_b, \ddot{\mathbf{y}}_b, \mathbf{y}_t; \psi) \cos(n\psi) d\psi = \mathbf{0} \quad (6.94)$$

$$\mathbf{f}_{bns} = \frac{1}{\pi} \int_0^{2\pi} \mathbf{f}_b(\mathbf{y}_b, \dot{\mathbf{y}}_b, \ddot{\mathbf{y}}_b, \mathbf{y}_t; \psi) \sin(n\psi) d\psi = \mathbf{0} \quad (6.95)$$

The trim state requires enforcing the equilibrium condition only on the average value of the forces and moments acting on the helicopter over one revolution, thus only the constant portion of Eq. (6.92) needs to be set to zero:

$$\mathbf{f}_{t0} = \frac{1}{2\pi} \int_0^{2\pi} \mathbf{f}_t(\mathbf{y}_b, \dot{\mathbf{y}}_b, \ddot{\mathbf{y}}_b, \mathbf{y}_t; \psi) d\psi = \mathbf{0} \quad (6.96)$$

The harmonic balance approach to the coupled trim-aeroelastic response solution requires the simultaneous solution of the nonlinear algebraic system represented by Eqs. (6.93)-(6.95) and (6.96) for the vector of trim parameters  $\mathbf{y}_t$  and the coefficient vectors denoted by  $\mathbf{y}_{b0}$ ,  $\mathbf{y}_{bnc}$ , and  $\mathbf{y}_{bns}$  ( $1 \leq n \leq N_H$ ). There are  $[5 + N_m(1 + 2N_H)]$  algebraic equations in terms of 5 trim variables and  $N_m(1 + 2N_H)$  blade expansion coefficients. In this study, Gaussian

quadrature with 30 integration points is used to evaluate the integrals in Eqs. (6.93)-(6.95) and (6.96); and the nonlinear algebraic equations solver DNEQNF of the IMSL[107] subroutine library is used to obtain the coupled trim and aeroelastic response solution.

### 6.5.5 Vibratory Hub shears and Moments

For a B-bladed rotor in steady, level flight, the vibratory hub loads are predominantly B/rev in the nonrotating, hub-fixed system (Ref. 52, p. 696). The amplitude of the B/rev hub shears and moments are obtained from a harmonic analysis of the hub loads. The cosine and sine components of the B/rev hub shear are

$$\begin{aligned} (\mathbf{F}_{\text{II}}^{\text{BP}})_c &= \frac{1}{\pi} \int_0^{2\pi} \mathbf{F}^{\text{H}}(\psi) \cos(B\psi) d\psi \\ &= (\mathbf{F}_{\text{xIH}}^{\text{BP}})_c \hat{i}_{\text{nr}} + (\mathbf{F}_{\text{yIH}}^{\text{BP}})_c \hat{j}_{\text{nr}} + (\mathbf{F}_{\text{zIH}}^{\text{BP}})_c \hat{k}_{\text{nr}} \end{aligned} \quad (6.97a)$$

$$\begin{aligned} (\mathbf{F}_{\text{II}}^{\text{BP}})_s &= \frac{1}{\pi} \int_0^{2\pi} \mathbf{F}^{\text{H}}(\psi) \sin(B\psi) d\psi \\ &= (\mathbf{F}_{\text{xIH}}^{\text{BP}})_s \hat{i}_{\text{nr}} + (\mathbf{F}_{\text{yIH}}^{\text{BP}})_s \hat{j}_{\text{nr}} + (\mathbf{F}_{\text{zIH}}^{\text{BP}})_s \hat{k}_{\text{nr}} \end{aligned} \quad (6.97b)$$

, respectively. Similarly, the cosine and sine components of the B/rev hub moment are

$$\begin{aligned} (\mathbf{M}_{\text{II}}^{\text{BP}})_c &= \frac{1}{\pi} \int_0^{2\pi} \mathbf{M}^{\text{H}}(\psi) \cos(B\psi) d\psi \\ &= (\mathbf{M}_{\text{xIH}}^{\text{BP}})_c \hat{i}_{\text{nr}} + (\mathbf{M}_{\text{yIH}}^{\text{BP}})_c \hat{j}_{\text{nr}} + (\mathbf{M}_{\text{zIH}}^{\text{BP}})_c \hat{k}_{\text{nr}} \end{aligned} \quad (6.98a)$$

$$\begin{aligned}
(M_{II}^{BP})_s &= \frac{1}{\pi} \int_0^{2\pi} M^{II}(\psi) \sin(B\psi) d\psi \\
&= (M_{xII}^{BP})_s \hat{i}_{nr} + (M_{yII}^{BP})_s \hat{j}_{nr} + (M_{zII}^{BP})_s \hat{k}_{nr}
\end{aligned} \tag{6.98b}$$

, respectively. The amplitudes of the B/rev hub shear and moment components are calculated by

$$F_{xII}^{BP} = \sqrt{(F_{xII}^{BP})_c^2 + (F_{xH}^{BP})_s^2} \tag{6.99a}$$

$$F_{yH}^{BP} = \sqrt{(F_{yH}^{BP})_c^2 + (F_{yH}^{BP})_s^2} \tag{6.99b}$$

$$F_{zH}^{BP} = \sqrt{(F_{zH}^{BP})_c^2 + (F_{zH}^{BP})_s^2} \tag{6.99c}$$

and

$$M_{xII}^{BP} = \sqrt{(M_{xII}^{BP})_c^2 + (M_{xH}^{BP})_s^2} \tag{6.100a}$$

$$M_{yII}^{BP} = \sqrt{(M_{yII}^{BP})_c^2 + (M_{yH}^{BP})_s^2} \tag{6.100b}$$

$$M_{zII}^{BP} = \sqrt{(M_{zII}^{BP})_c^2 + (M_{zH}^{BP})_s^2} \tag{6.100c}$$

, respectively. The B/rev hub shears and moments obtained from Eqs. (6.99) and (6.100) are a measure of the vibration levels of a helicopter in forward flight; and they will be used in the study for vibration reduction using structural optimization, described in the next chapter.

### 6.5.6 Stability in Forward Flight

The nonlinear periodic system, Eq. (6.35), is first linearized about the steady state, time-dependent equilibrium position. Subsequently, the stability of the resulting linear periodic system is determined from Floquet theory[30]. The procedure used for linearizing the equations is similar to the hover case, except that the equilibrium position is now time-dependent. Linearizing Eq. (6.35) about the nonlinear equilibrium position  $\mathbf{y}_b$ , at given azimuth position  $\psi$ , yields:

$$\mathbf{f}_b = [\bar{\mathbf{M}}(\mathbf{y}_b)]\Delta\ddot{\mathbf{y}}_b + [\bar{\mathbf{C}}(\mathbf{y}_b)]\Delta\dot{\mathbf{y}}_b + [\bar{\mathbf{K}}(\mathbf{y}_b)]\Delta\mathbf{y}_b + \text{H.O.T.} = \mathbf{0} \quad (6.101)$$

where

$$[\bar{\mathbf{M}}] = \frac{\partial \mathbf{f}_b}{\partial \ddot{\mathbf{y}}_b} \quad (6.102)$$

$$[\bar{\mathbf{C}}] = \frac{\partial \mathbf{f}_b}{\partial \dot{\mathbf{y}}_b} \quad (6.103)$$

$$[\bar{\mathbf{K}}] = \frac{\partial \mathbf{f}_b}{\partial \mathbf{y}_b} \quad (6.104)$$

are the mass, damping and stiffness matrices, respectively, of the linearized system.

Expressing the linearized system, Eq. (6.101), in the first order state variable form

$$\dot{\mathbf{z}} = [\mathbf{A}(\psi)] \mathbf{z} \quad (6.105)$$

where the state vector  $\mathbf{z}$  is defined as

$$\mathbf{z} = \begin{Bmatrix} \Delta \mathbf{y}_b \\ \Delta \dot{\mathbf{y}}_b \end{Bmatrix} \quad (6.106)$$

and the system matrix  $[\mathbf{A}]$  has the form

$$[\mathbf{A}] = \begin{bmatrix} [0] & [1] \\ -[\bar{\mathbf{M}}]^{-1}[\bar{\mathbf{K}}] & -[\bar{\mathbf{M}}]^{-1}[\bar{\mathbf{C}}] \end{bmatrix} \quad (6.107)$$

For the case of hover, matrix  $[\mathbf{A}]$  is constant and the stability of the system is determined by the eigenvalues of  $[\mathbf{A}]$ . However in forward flight, the system matrix  $[\mathbf{A}]$  is periodic with a period of one rotor revolution (i.e.  $[\mathbf{A}(\psi)] = [\mathbf{A}(\psi + 2\pi)]$ ). Therefore the stability of the periodic system is determined from the eigenvalues of the state transition matrix at the end of one period, using Floquet theory[30]. The characteristic multipliers, which are the eigenvalues of the state transition matrix for the periodic system at the end of one period,  $[\Phi(2\pi, 0)]$ , are given by

$$\Lambda_j = Z_j \pm i \Omega_j, \quad j = 1, \dots, N_m \quad (6.108)$$

The characteristic exponents

$$\lambda_j = \zeta_j \pm i \omega_j, \quad j = 1, \dots, N_m \quad (6.109)$$

of the periodic system are related to the characteristic multipliers by[30]:

$$\zeta_j = \frac{1}{2\tau} \ln(Z_j^2 + \Omega_j^2) \quad (6.110a)$$

$$\omega_j = \frac{1}{\tau} \tan^{-1} \left( \frac{\Omega_j}{Z_j} \right) \quad (6.110b)$$

where  $\tau = 2\pi$  is the nondimensional period of rotor. From Eqs. (6.110a,b), it is evident that the real part of the characteristic exponent is associated with the damping present in a particular mode. However, the imaginary part, which represents the frequency, is determined only within an integer multiple of the common period  $\tau$ . The linearized system is stable if the real part of the characteristic exponents  $\zeta_j < 0$  for all  $j$ .

The state transition matrix at the end of one period,  $[\Phi(2\pi, 0)]$ , is calculated by integrating the linearized system from 0 to  $2\pi$  using DE/STEP, a general purpose Adams-Bashforth ODE solver[82]. In this study, all  $2N_m$  columns of the state transition matrix are calculated in a single pass using the method described in Ref. 13.

## Chapter VII

### STRUCTURAL OPTIMIZATION FOR VIBRATION REDUCTION

This chapter describes the optimum structural design of composite helicopter rotor blades, with swept tips, for vibration reduction in forward flight, subject to frequency and aeroelastic stability constraints. The aeroelastic analysis, needed for optimization, consists of the finite element analysis described in the previous chapters of this study. Approximation concepts[80] are used in the optimization process to reduce the computational requirements. The optimization study is applied to composite blades with two-cell, hingeless configuration. Ply orientations in the horizontal and vertical walls of the blade cross section and tip sweep and anhedral angles are selected as design variables.

#### 7.1 STATEMENT OF THE OPTIMIZATION PROBLEM

The optimum design problem, solved using mathematical programming methods, can be stated in the following mathematical form[31]. Find the vector of design variables  $\mathbf{D}$  such that

$$g_q(\mathbf{D}) \leq 0, \quad q = 1, 2, \dots, Q \quad (7.1)$$

$$D_i^L \leq D_i \leq D_i^U, \quad i = 1, 2, \dots, ND \quad (7.2)$$

and

$$J(\mathbf{D}) \rightarrow \min \quad (7.3)$$

where  $g_q(\mathbf{D})$  is the  $q$ -th constraint function;  $D_i$  is the  $i$ -th design variable; and  $J(\mathbf{D})$  is the objective function. The superscripts  $L$  and  $U$  denote lower and upper bounds, respectively.

### 7.1.1 *Design Variables*

Previous studies[28,29,14] on rotor blade optimization for vibration reduction in forward flight have emphasized the effect of design variables representing the dimensions of the main spar of the blade, together with the influence of non-structural tuning masses. Changing the structural dimensions of the main spar, would require recalculation of the numerous constants computed by the two-dimensional section analysis used for the composite cross-section, and this would not provide a clear picture on the influence of the new elements associated with the current aeroelastic analysis, such as blade sweep and ply orientation angles of the composite blade. Therefore it was decided to restrict the design variables used in this study to four. These are the ply orientation in the horizontal and vertical walls of the composite cross section,  $\Lambda_h$  and  $\Lambda_v$ , together with the sweep and anhedral angles,  $\Lambda_s$  and  $\Lambda_a$ , which characterize the swept tip. Thus the vector of design variables is given by

$$\mathbf{D} = [\Lambda_h, \Lambda_v, \Lambda_s, \Lambda_a]^T \quad (7.4)$$

In this study, composite blades having a two-cell configuration, shown schematically in Fig. 7.1, are used as the basis of structural optimization. The ply

angle  $\Lambda_h$  is positive when the fibers in the horizontal walls are oriented toward the leading edge of the blade; while a positive  $\Lambda_v$  implies that the fibers in the vertical walls are oriented toward the top wall of the blade. Detailed layout of the two-cell composite cross sections will be described in the chapters dealing with the results obtained in this study.

### 7.1.2 Constraints

Two types of behavior constraints are used.

1. *Frequency placement constraints.* The fundamental frequencies in flap, lag and torsion are required to be between preassigned upper and lower bounds. A typical frequency placement constraint is expressed mathematically in the form

$$g(\mathbf{D}) = \frac{\omega}{\omega_U} - 1 \leq 0, \quad (7.5)$$

$$g(\mathbf{D}) = 1 - \frac{\omega}{\omega_L} \leq 0, \quad (7.6)$$

Equations (7.5) and (7.6) are written for each of the three fundamental frequencies of the blade in flap, lag and torsion, respectively, providing a total of six behavior constraints. The higher frequencies are also constrained to avoid  $B/\text{rev}$  resonances in a  $B$ -bladed composite hingeless rotor system.

2. *Aeroelastic stability constraints.* The blade is required to be aeroelastically stable and retain adequate aeroelastic stability margins in hover. These constraints are expressed mathematically as

$$g(\mathbf{D}) = \zeta_k + \varepsilon_k \leq 0, \quad k = 1, \dots, N_m \quad (7.7)$$

where  $N_m$  is the number of modes used in the modal coordinate transformation during the solution of the equations of motion;  $\zeta_k$  is the real part of the eigenvalue in hover for the  $k$ -th mode;  $\varepsilon_k$  represents the minimum acceptable damping level in hover for the  $k$ -th mode. Although no constraints are placed on the stability in forward flight, an aeroelastic stability analysis in forward flight is always performed at the end of the optimization process in order to ensure that the rotor blade configuration corresponding to the final optimum design is aeroelastically stable. Furthermore, it should be noted that for many soft-in-plane blade configurations the most critical condition for aeroelastic stability, is the hover condition. Thus, using this constraint, instead of an aeroelastic stability constraint in forward flight, is quite reasonable.

Side constraints, shown mathematically in Eq. (7.2), are also placed on the design variables in the form of upper and lower bounds to prevent the variables from reaching impractical values during the optimization process.

### 7.1.3 Objective Function

The objective function to be minimized is a mathematical expression representing the weighted sum of the B/rev oscillatory hub shear resultant and the B/rev oscillatory hub moment resultant, in the hub-fixed nonrotating frame; for a B-bladed rotor system, at an advance ratio of  $\mu = 0.30$ . It should be noted that the choice of this particular advance ratio as a representative value has been justified in previous studies[28]. This expression can be written symbolically as

$$J_1(\mathbf{D}) = K_F \sqrt{(F_{xH}^{BP})^2 + (F_{yH}^{BP})^2 + (F_{zH}^{BP})^2} + K_M \sqrt{(M_{xH}^{BP})^2 + (M_{yH}^{BP})^2 + (M_{zH}^{BP})^2} \quad (7.8)$$

where  $K_F$  and  $K_M$  are weighting factors. The hub shears and moments are nondimensionalized by  $m_0 \Omega^2 l^2$  and  $m_0 \Omega^2 l^3$ , respectively.

A second objective function is defined as the weighted sum of the B/rev oscillatory hub shear and hub moment components in the hub-fixed nonrotating frame

$$J_2(\mathbf{D}) = K_{Fx} F_{xH}^{BP} + K_{Fy} F_{yH}^{BP} + K_{Fz} F_{zH}^{BP} + K_{Mx} M_{xH}^{BP} + K_{My} M_{yH}^{BP} + K_{Mz} M_{zH}^{BP} \quad (7.9)$$

where  $K_{Fx}$ ,  $K_{Fy}$ ,  $K_{Fz}$ ,  $K_{Mx}$ ,  $K_{My}$  and  $K_{Mz}$  are weighting factors. All weighting factors used in this study were selected to be either 0 or 1.

## 7.2 FORMULATION OF APPROXIMATE PROBLEM

The calculation of the B/rev vibratory hub loads in forward flight is a fairly complicated and computationally expensive task, because it requires the solution of a complete aeroelastic response problem. Therefore, it is important to use optimization procedures which require the smallest possible number of aeroelastic response analyses and the associated hub loads computations. To meet this requirement, approximation concepts[80] are used to reduce the number of analysis required in the optimization process. Thus, the computer program which performs the aeroelastic response and stability analysis is not linked directly to the optimizer. Instead, the optimization is conducted on an approximate problem which possesses the characteristics of the actual problem in a neighborhood of the current design. This approximate problem is continuously updated as the optimization progresses.

In this study, a linear approximation for the objective function and a conservative approximation for the behavior constraints are used in the generation of the approximate problem. The linear approximation for the objective function is based on the Taylor series expansion

$$\tilde{J}(\mathbf{D}) = J(\mathbf{D}_0) + \sum_{i=1}^{ND} \left( \frac{\partial J}{\partial D_i} \right)_{\mathbf{D}_0} (D_i - D_{0i}) \quad (7.10)$$

The conservative approximation[39], used for the behavior constraints, is a hybrid form of the linear and reciprocal approximation which is more conservative than either; it is expressed mathematically as

$$\tilde{g}(\mathbf{D}) = g(\mathbf{D}_0) + \sum_{i=1}^{ND} G_i \left( \frac{\partial g}{\partial D_i} \right)_{\mathbf{D}_0} (D_i - D_{0i}) \quad (7.11)$$

where

$$G_i = \begin{cases} 1 & D_i \left( \frac{\partial g}{\partial D_i} \right)_{\mathbf{D}_0} \geq 0 \\ D_{0i}/D_i & D_i \left( \frac{\partial g}{\partial D_i} \right)_{\mathbf{D}_0} < 0 \end{cases} \quad (7.12)$$

The approximate problem described above is solved using a general purpose optimization package DOT[106], which is based on the modified method of feasible directions. A detailed description of the optimization process is provided next.

### 7.3 DETAILED DESCRIPTION OF THE OPTIMIZATION PROCESS

The organization of the optimization process used in this study is depicted in Fig. 7.2, and it consists of the steps provided below.

1. Select an initial trial design  $\bar{\mathbf{D}}_0$ .
2. Perform the two-dimensional cross sectional analysis to calculate the section constants based on the current design.
3. Calculate the natural frequencies and mode shapes.
4. Perform the aeroelastic analysis in hover.
5. Perform the aeroelastic analysis in forward flight, including calculation of hub loads.

6. Calculate the objective function, behavior constraints and the sensitivity derivatives of the objective function and constraints with respect to the design variables; where the sensitivity derivatives are calculated using the finite difference approach.
7. The exact problem represented by Eqs. (7.1-3) is replaced by an approximate problem where the objective function  $J(\mathbf{D})$  is expressed by its linear approximation about the current design, Eq. (7.10), and the constraints are expressed by a conservative approximation about the current design, Eq. (7.11).
8. Solve the approximate optimization problem, using the DOT optimizer, to obtain a new, improved design.
9. The optimization process is repeated with the improved design as the new starting point until the sequence of vectors  $\mathbf{D}$  converges to a solution  $\mathbf{D}^*$  where all constraints are satisfied and  $J(\mathbf{D}^*)$  is at least a local minimum.

It should be noted that in the formulation of the sensitivity derivatives, an analytical approach using chain rule differentiation[59-62] is computationally more efficient if it is applicable to the aeroelastic model being used. The implicit formulation[13] for the aerodynamic modeling, used in this study, has distinct advantages over the explicit approach. However, the implicit formulation does not lend itself to generating explicit analytical expressions for the sensitivity derivatives which have been found to be useful in structural optimization[59-62].

A semi-analytical approach[96] which employs a combination of analytical and finite difference approaches, compatible with the aeroelastic model used in this study, was recently developed with the intent of gaining some of the computational efficiency provided by the analytical approach. As shown in Ref. 96, frequency sensitivity with respect to ply orientation correlates well with the finite difference approach, when the ply angles are sufficiently far away from zero ply angles. However, the stability sensitivity analysis in hover was only partially successful because all second derivative terms in the formulation had to be neglected, so as to achieve computational efficiencies in excess of the finite difference approach. Furthermore, this approach also exhibits limited reliability when the design variables include tip sweep and anhedral angles. Therefore, it was decided to abandon the semi-analytical approach for the formulation of the sensitivity derivatives[96] and instead the sensitivity derivatives were calculated using the finite difference approach with carefully selected increment size for the design variables.

## **Chapter VIII**

### **MODEL VERIFICATION**

It is essential to validate the computer program implementing the analytical model and solution procedures developed in this study before using it for various analytical studies. Although the analytical model developed in this study is intended for composite blade analysis, validating the model for isotropic blades was an essential prerequisite. This is because the isotropic blade results obtained in previous studies can be used directly to validate the one-dimensional global analysis of the blade. For the case of composite blade, the blade sectional properties are generated by a separate two-dimensional cross sectional analysis and thus the comparison for these results is affected simultaneously by both the one-dimensional global analysis, as well as the two-dimensional cross sectional analysis, and it does provide direct comparisons for the one-dimensional global analysis.

In the present study, comparison of the trim and blade response results can be used to test both the validity of the equations of motion as well as the solution procedure for the coupled trim-acroelastic response analysis. The blade stability results are more sensitive to small differences in the equations of motion than the trim and response results. Therefore comparison of the blade stability results can also be used as a reliable test of the accuracy of the equations of motion. Finally, it should be emphasized that the vibratory hub loads can be very sensitive to small differences in the equations of motion, thus

comparison of the vibratory hub loads should be made after the stability comparisons have been carried out.

## **8.1 VALIDATION FOR THE CASE OF HOVER**

Two different blade configurations are used for the validation of the hover analysis computer program. The first is an isotropic stiff-in-plane blade configuration; and the results are compared with those presented in Ref. 41. The importance of the treatment of the axial degree of freedom is also illustrated in this validation. The second is a single-cell stiff-in-plane composite blade configuration; where the results are compared with those presented in Refs. 22 and 48.

### **8.1.1 *Isotropic Blade***

The isotropic stiff-in-plane blade configuration has fundamental rotating frequencies of 1.15/rev, 1.5/rev and 5.0/rev in flap, lag and torsion, respectively. The data for the baseline configuration of the blade is taken from Hodges and Ormiston[41] and is given in Table 8.1. Results from the present analysis are compared with those obtained in Ref. 41.

The isotropic blade model used in Ref. 41 is based on the equations of motion derived in Ref. 40 and specialized to the case of uniform, untwisted, hingeless rotor blades without chordwise offsets between the elastic, mass, tension and aerodynamic center axes. Quasi-steady aerodynamics based on Greenberg's theory were used to calculate the blade aerodynamic loads. The

elimination approach , described in Chapter 6, was used in the treatment of the axial degree of freedom. The equations of motion were solved by Galerkin's method using six coupled, rotating modes.

---

TABLE 8.1

Baseline configuration for isotropic rotor blade in hover

Fundamental, uncoupled rotating natural frequencies:

$$\omega_{L1} = 1.5$$

$$\omega_{F1} = 1.15$$

$$\omega_{T1} = 5.0$$

$$\gamma = 5.0$$

$$\sigma = 0.1$$

$$k_{m1}/R = 0.0$$

$$k_{m2}/R = 0.025$$

$$(k_A/k_m)^2 = 1.5$$

$$c/R = \pi/40$$

$$\beta_p = 0.0$$

$$a = 2\pi$$

$$C_{d0} = 0.01$$

$$B = 4$$

Offsets of center of mass, tension center and aerodynamic center from elastic axis are zero.

---

The results of the aeroelastic analysis are presented in Figs. 8.1 through 8.3, which were generated using seven coupled rotating modes, including three flap, two lag, one torsion and one axial. In the figures, the solid lines correspond to results from the present study, which uses the substitution approach in the treatment of the axial degree of freedom; while the symbols correspond to the results found in Hodges and Ormiston[41]. Figure 8.1 shows the equilibrium tip deflection of the blade as a function of blade collective pitch angle. It is evident that the results of the present analysis show an excellent correlation in the lag and torsion modes and very good correlation in the flap mode with those obtained in Ref. 41. The results of the stability analysis are shown in

Figs. 8.2 and 8.3. Figure 8.2 presents the variation of modal frequency as a function of collective pitch of the blade; while the variation in modal damping as a function of collective pitch angle is shown in Fig. 8.3. The results corresponding to the present study provide an excellent correlation in modal frequency and very good correlation in modal damping with the results of Ref. 41.

The effect of retaining or deleting the axial mode in the present study, which uses the substitution approach, on the results obtained from the aeroelastic analysis has been also examined. The aeroelastic stability analysis was performed for two cases; one with seven modes (having 3 flap, 2 lag, 1 torsion and 1 axial modes) and the other with six modes (having 3 flap, 2 lag and 1 torsion modes). The results are shown in Figs. 8.4 through 8.6. The solid lines represent results obtained when the axial mode is retained and the dotted lines correspond to the results without the axial mode. Figure 8.4 shows the variation of equilibrium tip deflection of the blade with collective pitch setting. It is evident, from these results that the equilibrium position of the blade in hover is not influenced by the presence or absence of the axial mode. Figure 8.5 shows the variation of modal frequencies with pitch angle, obtained in the stability analysis. The results indicate that the deletion of axial mode has a negligible effect on the modal frequencies when compared to the results obtained with the axial mode. At high pitch angles, the analysis without axial mode slightly over-estimates the frequency in the flap mode. The variation of modal damping with pitch angle is shown in Fig. 8.6. At low pitch angles ( $\theta_0 \leq 0.1$  rad), the inclusion or deletion of axial mode does not influence the

modal damping. However, at high collective pitch angles, the analysis without axial mode over-estimates the lag damping and under-estimates the damping in flap mode when compared to the damping levels predicted by the analysis which includes the axial mode. The difference in the damping levels predicted increases significantly with pitch angle. The damping in torsional mode is only slightly affected by the presence or absence of the axial mode, at high pitch angles.

### **8.1.2 *Single-cell Composite Blade***

The stability results for a stiff-in-plane, single-cell, composite hingeless blade configuration are compared with results obtained for a similar case from two different analyses described in Refs. 22 and 48. The blade structure is assumed to consist of a laminated rectangular box beam with uniform spanwise properties, as depicted in Fig. 8.7. The cross-section of the beam has a width of 7" and a height of 2", with a uniform thickness of 0.35". The baseline configuration is assumed to have zero ply angles, i.e., all laminates of the beam consists of laminae with fibers parallel to the blade length. The basic parameters describing this configuration are given in Table 8.2 where the material constants correspond to a graphite/epoxy type composite material.

The blade cross-sectional dimensions and rotor configuration shown in Table 8.2 are based on Hong and Chopra[48]. The rotor radius ( $R$ ), the rotor speed ( $\Omega$ ), and the principal mass radii of gyration of the cross section ( $k_{m1}, k_{m2}$ ) were not given in Ref. 48, but were selected for this study such that

---

TABLE 8.2

Baseline configuration for single-cell composite rotor blade

Fundamental, coupled rotating natural frequencies:

$$\omega_{L1} = 1.533$$

$$\omega_{F1} = 1.187$$

$$\omega_{T1} = 5.186$$

$$\gamma = 5.0$$

$$\sigma = 0.1$$

$$a = 5.7$$

$$C_{d0} = 0.01$$

$$k_{m1}/R = 0.0$$

$$k_{m2}/R = 0.01609$$

$$c/R = 0.08$$

$$\beta_p = 0.0$$

$$C_w = 0.005$$

$$B = 4$$

$$R = 255.45''$$

$$\Omega = 360 \text{ rpm}$$

Offsets of center of mass, tension center and aerodynamic center from elastic axis are zero.

Material constants:

$$E_L = 30. \times 10^6 \text{ psi}$$

$$E_T = 3. \times 10^6 \text{ psi}$$

$$G_{LT} = 1.2 \times 10^6 \text{ psi}$$

$$\nu_{LT} = 0.3$$


---

the nondimensional rotating natural frequencies match those given in Ref. 48 as closely as possible. The fundamental rotating natural frequencies obtained for this set of parameters are:  $\omega_{F1} = 1.187/\text{rev}$  ,  $\omega_{L1} = 1.533/\text{rev}$  , and  $\omega_{T1} = 5.186/\text{rev}$  ; which should be compared to  $\omega_{F1} = 1.15/\text{rev}$  ,  $\omega_{L1} = 1.5/\text{rev}$  , and  $\omega_{T1} = 5.0/\text{rev}$  from Ref. 48. Similar calculations were also carried out by Fulton and Hodges[22], who obtained a blade configuration with  $\omega_{F1} = 1.17/\text{rev}$  ,  $\omega_{L1} = 1.45/\text{rev}$  , and  $\omega_{T1} = 5.06/\text{rev}$  .

The composite blade model used in Ref. 48 was based on a moderate deflection theory, where the strain-displacement relations were taken from

Hodges and Dowell[40], and therefore the effect of transverse shear deformations was not included. Quasi-steady aerodynamics was used to calculate the aerodynamic loads. The solution of the equations of motion was based on a finite element approach.

The analysis presented in Ref. 22 used the nonlinear intrinsic formulation of Ref. 46, where the nonlinear beam kinematics was based on the large deflection theory developed in Refs. 17 and 18. Aerodynamic loads were calculated from quasi-steady aerodynamics. The solution of the equations of motion was obtained from the finite element approach.

The stability results obtained from the aeroelastic model developed in this study were compared with Ref. 22 and 48 for a symmetric ply configuration where the ply lay-ups on opposite walls were identical. The horizontal walls have zero ply angles ( $\Lambda_h \equiv 0$ ). For vertical walls the laminae in the outer half thickness have zero ply angles while the laminae in the inner half thickness are all oriented at the same ply angle  $\Lambda_v$ . A positive  $\Lambda_v$  implies that fibers are oriented toward the top wall of the blade. This configuration was referred to as Case I in Ref. 48.

The stability results, depicted in Fig. 8.8, are presented in terms of the real part of the hover eigenvalues, as a function of the rotor thrust level  $C_T/\sigma$ ; for  $\Lambda_v = 0^\circ, 30^\circ$  and  $-30^\circ$ . The lines in Fig. 8.8 are the results from the present analysis. The results from Ref. 22 are depicted by the bullet symbols for values of  $C_T/\sigma = 0.25, 0.5$  and  $0.1$ ; while the results from Ref. 48 are represented by the solid triangle symbols, for values of  $C_T/\sigma = 0.1$ . It is evident from Fig. 8.8 that the correlation with Ref. 22 is very good, but the correlation with Ref.

48 is poor except for the case  $\Lambda_v = 0^\circ$ . The discrepancy of the stability results from Ref. 48 with those from the present analysis and from Ref. 22 may be attributed to the fact that the blade model used in Ref. 48 does not contain the effect of transverse shear deformations, which is known to be important for composite blades.

It should be emphasized that the correlation presented in Ref. 22 was not as good as the comparison displayed in Fig. 8.8, especially for  $C_T/\sigma = 0.05$ . In Ref. 22, the correlation of Fulton and Hodges[22] with Yuan, et al.[103], which was based on the blade model of this study, was characterized as "fairly good", for  $C_T/\sigma = 0.05$  and 0.1. However, an input error in the results presented in Ref. 103 for the single-cell composite blade case had been found soon after those results were published. The results in Ref. 103 were based on an incorrect value of longitudinal Poisson's ratio equal to  $\nu_{LT} = 0.03$  which was an order of magnitude smaller than the correct value of  $\nu_{LT} = 0.3$ , listed in Table 8.2. This error had been corrected in all subsequent studies involving this single-cell blade configuration.

## **8.2 VALIDATION FOR THE CASE OF FORWARD FLIGHT**

To validate the forward flight analysis and the computer program which implements the analytical model and solution procedure, a correlation study with a completely different model, developed in Ref. 64 (a slightly modified version of Ref. 64 is available as a recent low number NASA CR report, Ref.

65), was conducted. Careful comparisons for trim, blade aeroelastic response and stability, and vibratory hub shears and moments, were carried out.

The model described in Ref. 64 was developed for isotropic rotor blades undergoing moderate deflections, and the primary objective of the study was vibration reduction in hingeless rotors using an actively controlled trailing edge flap located on the blade. A fully flexible blade cantilevered at the root, with fully coupled flap-lag-torsional dynamics, was selected to represent the hingeless blade. The structural operator was taken from Ref. 76 where equations of equilibrium for an isotropic blade, with coupled flap-lag-torsional dynamics, undergoing moderate deflections were presented in detail. The inertial loads were derived in a straightforward manner using D'Alembert's principle. Quasi-steady aerodynamics based on Greenberg's theory was used to approximate the aerodynamic loads in forward flight. Treatment of the axial degree of freedom was based on the elimination approach, with an additional simplifying assumption that the blade is inextensible. The inertial and aerodynamic loads were formulated explicitly using the symbolic manipulation program MACSYMA[108]. The equations of motion were solved using a global Galerkin approach based on six uncoupled free vibration modes of a rotating cantilevered blade, including three flap, two lead-lag, and one torsion. These rotating mode shapes and frequencies were generated from the first nine exact nonrotating modes of a uniform cantilevered beam.

It is important to note that although the two aeroelastic models use similar aerodynamic theories and assumptions, however, the aerodynamic loads were

formulated explicitly in Ref. 64; while an implicit formulation was used to calculate the aerodynamic loads used in this study.

The validation studies were carried out for an isotropic hingeless rotor blade, with uniform spanwise properties. Two blade configurations were considered; the first configuration was a soft-in-plane rotor blade with the properties given in Table 8.3, and the second configuration was a stiff-in-plane rotor blade with the properties shown in Table 8.4. The two baseline configurations are identical except for the lead-lag bending stiffnesses.

---

TABLE 8.3

Baseline configuration for soft-in-plane isotropic rotor blade in forward flight

$$\begin{aligned}
 EI_{\eta\eta}/m\Omega^2R^4 &= 0.0106 \\
 EI_{\zeta\zeta}/m\Omega^2R^4 &= 0.0301 \\
 GJ/m\Omega^2R^4 &= 0.001473 \\
 (k_A/k_m)^2 &= 0.5259 & a &= 2\pi \\
 k_{m1}/R &= 0.0 & C_{d0} &= 0.01 \\
 k_{m2}/R &= 0.02 & C_w &= 0.005 \\
 \gamma &= 5.5 & X_{FC}/R &= 0.0 \\
 \sigma &= 0.07 & Z_{FC}/R &= 0.50 \\
 c/R &= 0.055 & X_{FA}/R &= 0.0 \\
 \beta_p &= 0.0 & Z_{FA}/R &= 0.25 \\
 B &= 4 & fC_{df}/\pi R^2 &= 0.01
 \end{aligned}$$

Offsets of center of mass, tension center and aerodynamic center from elastic axis are zero.

---

The nondimensional, uncoupled, rotating natural frequencies calculated by the two different formulations are summarized in Table 8.5 for both soft-in-plane and stiff-in-plane configurations. The two formulations yield the same flap and lead-lag frequencies in both cases, but slightly different torsional fre-

---

TABLE 8.4

Baseline configuration for stiff-in-plane isotropic rotor blade in forward flight

$$\begin{array}{ll}
 EI_{\eta\eta}/m\Omega^2R^4 = 0.0106 & \\
 EI_{\zeta\zeta}/m\Omega^2R^4 = 0.1474 & \\
 GJ/m\Omega^2R^4 = 0.001473 & \\
 \\
 (k_A/k_m)^2 = 2.0415 & a = 2\pi \\
 k_{m1}/R = 0.0 & C_{d0} = 0.01 \\
 k_{m2}/R = 0.02 & C_w = 0.005 \\
 \gamma = 5.5 & X_{FC}/R = 0.0 \\
 \sigma = 0.07 & Z_{FC}/R = 0.50 \\
 c/R = 0.055 & X_{FA}/R = 0.0 \\
 \beta_p = 0.0 & Z_{FA}/R = 0.25 \\
 B = 4 & fC_{df}/\pi R^2 = 0.01
 \end{array}$$

Offsets of center of mass, tension center and aerodynamic center from elastic axis are zero.

---

quencies. The small discrepancies in torsional frequencies can be attributed to the difference in the treatment of the axial degree of freedom, which is retained in this formulation but eliminated in the formulation presented in Ref. 64. The presence of a finite axial stiffness in this formulation introduces a torsional stiffening effect proportional to  $k_A^2 = (EI_{\eta\eta} + EI_{\zeta\zeta})/EA$ . However when the blade is assumed to be inextensible, which is done in the formulation presented in Ref. 64, the axial stiffness  $EA$  is treated as infinite and thus  $k_A = 0$ .

A comparison of trim, blade response, stability, and 4/rev hub loads in forward flight was conducted for the two formulations. The results were obtained using three flap, two lead-lag, and one torsion modes for both approaches, but with an additional axial mode used in the present formulation. The results

---

TABLE 8.5

Frequency comparison for isotropic rotor blade configurations used in forward flight analysis

Soft-in-plane blade:

	<u>This study</u>	<u>Ref. 64</u>
$\omega_{F1} =$	1.125	1.125
$\omega_{L1} =$	0.732	0.732
$\omega_{T1} =$	3.263	3.176

Stiff-in-plane blade:

	<u>This study</u>	<u>Ref. 64</u>
$\omega_{F1} =$	1.125	1.125
$\omega_{L1} =$	1.417	1.417
$\omega_{T1} =$	3.501	3.176

---

were calculated for a weight coefficient of  $C_w = 0.005$  and for advance ratios up to  $\mu = 0.4$ . Results from this comparison study are presented next.

### 8.2.1 Trim Results

Figures 8.9 and 8.10 show a comparison of trim results obtained using the two formulations for the soft-in-plane blade configuration. The blade collective and cyclic pitch angles at various advance ratios are presented in Fig. 8.9, and the rotor inflow and angle of attack are shown in Fig. 8.10. The solid lines represent results obtained from the model presented in this study and the bullet symbols depict the results obtained in Ref. 64. The correlation between the two sets of results is excellent and there are only slight deviations at high ad-

vance ratios, (i.e.,  $\mu = 0.4$ ) in the collective pitch, cyclic sine and rotor angle of attack.

Similar comparisons of trim results are presented in Figs. 8.11 and 8.12 for the stiff-in-plane blade configuration. Once again the agreement is excellent, with only very minor deviations at high advance ratios. However, these differences are even smaller than those present in the soft-in-plane blade results.

Excellent agreement between the trim results is to be expected, since the trim solution is relatively insensitive to the higher order terms, which determine the accuracy of a particular formulation. The minor differences observed in the trim results at high advance ratios can probably be attributed to the difference in aerodynamic formulations; the model in Ref. 64 employs an explicit approach based on an ordering scheme, while the model in this study employs an implicit approach. Some of the higher order terms neglected in Ref. 64, but retained in this study, may influence the results at higher advance ratios.

Overall, the correlation between the trim results is excellent, and the minor differences present at high advance ratios are expected to have only a small influence on the blade response, stability, and vibratory loads.

### **8.2.2 *Blade Response***

Blade aeroelastic response obtained from the two formulations is compared by considering the tip deflections around the azimuth. The flap, lag and torsional tip deflections of the blade at an advance ratio of  $\mu = 0.3$  are compared in Fig. 8.13 for the soft-in-plane blade configuration. The correlation is

excellent for the flap and lag modes. There is a mild discrepancy in the torsional tip deflection which can be attributed to the differences in: (1) the treatment of the axial degree of freedom, which influenced the torsional frequency slightly; and (2) the formulation of the aerodynamic loads, which is explicit in Ref. 64 but implicit in this study.

The comparison of the tip deflections at  $\mu = 0.3$  for the stiff-in-plane blade configuration is presented in Fig. 8.14. Excellent agreement is again evident for the flap and lag modes, while minor discrepancy in the torsional tip deflection still exists for the same reasons that were stated above for the soft-in-plane blade configuration. The larger offset present in a portion of the torsional tip deflection near  $\psi = 120^\circ$  is probably due to the fact that the difference in torsional frequency between the two formulations is larger for the stiff-in-plane case.

### 8.2.3 *Blade Stability*

A comparison of blade aeroelastic stability for the soft-in plane configuration, using the two formulations, is presented in Figures 8.15 through 8.17. The real part of the characteristic exponent, which is a measure of blade damping or stability in forward flight, is shown as a function of advance ratio. The symbols L, F and T denote lag, flap and torsional modes, respectively. The first and second lag modes are shown in Fig. 8.15, which exhibits good correlation between the two approaches for the first lag mode. The discrepancy is quite small and it varies between 4% - 7%. The damping in the first

lag mode decreases initially between  $\mu = 0$  and 0.1, then remains relatively unchanged between  $\mu = 0.1$  and 0.2 and it finally increases for  $\mu > 0.2$ . The agreement between the results associated with the second lag mode is not as good as that associated with the first lag mode. The primary reason for these differences is attributed to the fact that the second lag mode has inherently low damping, and for soft-in-plane blade configurations it is sensitive to small differences in the blade models, such as the treatment of the axial degree of freedom. The results for the second lag mode, shown in Fig. 8.15, still display similar trends since the damping increases with advance ratio. The mild instability present in the second lag mode in the lower advance ratio range can be removed by a small amount of structural damping. The damping associated with the first flap and first torsion modes is depicted in Fig. 8.16, while damping in the second and third flap modes is displayed in Fig. 8.17. The correlation between the two sets of results is excellent for all the four modes considered in Figs. 8.16 and 8.17. The damping levels in these four modes are insensitive to variations in advance ratio  $\mu$ ; the characteristic exponent associated with the first flap mode exhibit a typical "split" between  $\mu = 0.3$  and  $\mu = 0.4$ , as shown in Fig. 8.16.

Similar comparisons of the aeroelastic stability results for the stiff-in-plane configuration are presented in Figs. 8.18 through 8.20. The correlation between the two sets of results is very good for both lag modes throughout the range of advance ratio (up to  $\mu = 0.4$ ), and for the first and third flap modes except that mild deviations are present at high advance ratios near  $\mu = 0.4$  for these two modes. The comparison of the damping in the first torsion and sec-

ond flap modes is fairly good; with discrepancies under 10% for most part of the range of advance ratios, as evident from Fig. 8.20. The damping level of the first lag mode is considerably higher for the stiff-in-plane blade than for the soft-in-plane blade, as evident from Figs. 8.15 and 8.18.

#### **8.2.4 *Vibratory Hub Loads***

The 4/rev hub loads calculated using the two formulations are compared in Figs. 8.21 through 8.23 for the soft-in-plane blade configuration. The longitudinal shear and rolling moment are plotted in Fig. 8.21, the lateral shear and pitching moment are shown in Fig. 8.22, and the vertical shear and yawing moment are depicted in Fig. 8.23. The comparisons are quite good over the entire range of advance ratios considered, though the results of the two formulations diverge slightly at the higher advance ratios. The comparison between the 4/rev hub moments is best with a difference of less than 5% at  $\mu = 0.4$ . The greatest discrepancy between the two sets of results obtained for the hub loads is evident in the 4/rev lateral hub shears, which differ by 20% at  $\mu = 0.4$ .

The 4/rev hub loads for the stiff-in-plane blade configuration are compared in Figs. 8.24 through 8.26. The comparisons are not as good as those obtained for the soft-in-plane case. All but the vertical shear component compare very well up to  $\mu = 0.3$ , and then begin to diverge at the higher advance ratios. At the highest advance ratio considered,  $\mu = 0.4$ , the two sets of hub moments differ by about 20%-50%, which is much larger than observed in the soft-in-

plane case. However, the disagreement in the inplane shears at high advance ratio is only slightly worse, differing by 30% at  $\mu = 0.4$ . The best agreement at high advance ratio for the stiff-in-plane configuration is observed in the vertical hub shears calculated by the two formulations, which are almost identical at  $\mu = 0.4$ .

The disagreement in the vibratory hub loads can be attributed to the differences between the two formulations already cited, i.e., the difference in the modeling of the axial degree of freedom, and the difference in the aerodynamic formulations. The results seem to indicate that the vibratory hub loads are most sensitive to the small differences in the formulations. Therefore good correlation in vibratory hub loads is more difficult to achieve than similar correlations for trim values, blade tip response, or aeroelastic stability.

## **Chapter IX**

### **FREE VIBRATION AND AEROELASTIC BEHAVIOR IN HOVER**

In this chapter, the free vibration and the hover stability characteristics of composite hingeless rotor blades with straight and swept tips are investigated. Numerical results illustrating the effects of tip sweep, anhedral and composite ply orientation on blade natural frequencies and aeroelastic stability in hover are presented.

#### **9.1 FREE VIBRATION ANALYSIS**

The results in this section are divided into two parts : (1) results illustrating the influence of ply orientation on the natural frequencies for both single-cell and two-cell composite rotor blades; and (2) influence of tip sweep and tip anhedral on the natural frequencies of a two-cell composite blade.

##### **9.1.1 *Influence of Ply Orientation***

The influence of composite ply orientation on the natural frequencies is studied for two rotor blade configurations; these are: (1) a stiff-in-plane blade having a single-cell composite construction, and (2) a soft-in-plane blade with two-cell construction. In the presentation of the results, the identification of the modes is based on the baseline configuration of the blade which has zero ply angles. The natural frequencies are then traced as the ply orientation is

varied from a zero ply angle. Since the modes are coupled at non-zero ply orientations, the designation of the modes as flap, lag or torsion is for identification purposes only. In the figures, the notation L, F and T is used to represent lag, flap and torsional modes, respectively. The blade is modeled with five elements for both configurations.

#### **9.1.1.1 Single-cell Composite Blade**

The behavior of a hingeless, single-cell, stiff-in-plane composite blade configuration is considered first. The blade structure is assumed to be represented by a laminated rectangular box beam with uniform spanwise properties, depicted in Figure 8.7. The cross-section of the beam has a width of 7" and a height of 2", with a uniform thickness of 0.35". The baseline configuration is assumed to have zero ply angles, i.e., all laminates of the beam consist of laminae with fibers parallel to the blade length, and its basic parameters are given in Table 8.2. Natural frequencies are computed for two cases, with symmetric configurations, where the ply lay-ups on opposite walls are identical. In the first case, the horizontal walls have zero ply angles. For vertical walls the laminae in the outer half thickness have zero ply angles while the laminae in the inner half thickness are all oriented at the same ply angle  $\Lambda_v$ . A positive  $\Lambda_v$  implies that fibers are oriented toward the top wall of the blade. In the second case, the vertical walls have zero ply angles. For horizontal walls the laminae in the outer half thickness have zero ply angles while the laminae in the inner half thickness are all oriented at the same ply angle  $\Lambda_h$ . A positive  $\Lambda_h$  implies that fibers are oriented toward the leading edge of the blade.

Note that varying the ply angles  $\Lambda_v$  and  $\Lambda_h$  influences the direct stiffness terms, as well as a number of coupling terms associated with the modulus weighted sectional constants. When  $\Lambda_v$  is varied, some of the coupling terms influenced are associated with the sectional constants  $EAB_1$ ,  $EAB_0$  and  $G_\zeta A$  which represent the effects of lag-torsion, torsion-shear, axial-torsion and axial-shear couplings. The variation of  $\Lambda_h$  influences coupling terms associated with sectional constants such as  $EAB_2$  and  $G_\eta A$  which represent the effects of flap-torsion, torsion-shear and axial-shear couplings.

Figure 9.1 shows the natural frequencies of the first six modes as a function of  $\Lambda_v$  for variations in  $\Lambda_v$  from  $0^\circ$  to  $90^\circ$ . The results indicate that the lowest three frequencies (first flap, first lag and second flap) are not very sensitive to the variations in the ply orientation. The torsional frequency increases initially and reaches a maximum value of 5.5/rev around  $30^\circ$  ply angle and then decreases with further increase in the angle of ply orientation. The second lag and the third flap frequencies decrease initially and reach asymptotic values beyond  $45^\circ$  ply orientation. A similar trend is evident for variation of natural frequencies with ply-orientation in horizontal wall, as shown in Fig. 9.2. In this case, the variation in frequencies is more pronounced than that observed in Fig. 9.1. The torsional frequency reaches a maximum value of 6.5/rev at  $30^\circ$  ply angle in horizontal wall.

#### **9.1.1.2 Two-cell Composite Blade.**

Results illustrating the behavior of a soft-in-plane, hingeless composite blade having a two-cell type cross section are presented next. The two-cell

cross-section was selected such that the fundamental natural frequencies for the baseline configuration are similar to those associated with a typical helicopter blade. Figure 7.1 shows the two-dimensional finite element model employed for the composite cross-section analysis from which the sectional properties of the cross-section were obtained. The leading edge has a semi-circular shape with a radius of 1.2" ; and the straight portion has a total length of 6". The internal wall is located 2.8" behind the leading edge; and all wall thicknesses are 0.1". The baseline configuration parameters for this blade are shown in Table 9.1 where the material constants correspond to glass/epoxy type composite material. For convenience, it is assumed that the blade has uniform spanwise properties, however, the analysis developed can represent blades with arbitrary mass and stiffness variation.

Natural frequencies are calculated for two cases. In the first case, the laminae in the middle vertical wall and the inner half of the rear vertical wall are oriented at ply angle  $\Lambda_v$  while the remaining walls have zero ply angles. In the second case, the laminae in the inner half of the horizontal walls are oriented at ply angle  $\Lambda_h$  while the remaining walls have zero ply angles.

The variation of natural frequencies of the two-cell composite blade as a function of  $\Lambda_v$  and  $\Lambda_h$  are depicted in Figures 9.3 and 9.4, respectively. It is evident from these figures that the lowest three natural frequencies are not influenced by variations in ply orientation; the first torsional frequency increases initially and then decreases with increase in the angle of ply orientation. In general, for the two-cell configuration, the natural frequencies remain virtually unchanged during the variation of the ply-orientation in either the vertical wall

---

TABLE 9.1

Baseline configuration for the two-cell composite rotor blade

Fundamental, coupled rotating natural frequencies:

$$\omega_{L1} = 0.765$$

$$\omega_{T1} = 1.096$$

$$\omega_{T1} = 3.356$$

$$\gamma = 5.0$$

$$\sigma = 0.076$$

$$a = 5.7$$

$$C_{d0} = 0.01$$

$$k_{m1}/R = 0.004$$

$$k_{m2}/R = 0.02439$$

$$c/R = 0.06$$

$$\beta_p = 0.0$$

$$C_w = 0.005$$

$$B = 4$$

$$R = 250''$$

$$\Omega = 360 \text{ rpm}$$

Tip length = 10% of the blade length.

Material constants:

$$E_L = 6.2 \times 10^6 \text{ psi}$$

$$E_T = 1.6 \times 10^6 \text{ psi}$$

$$G_{LT} = 0.8 \times 10^6 \text{ psi}$$

$$\nu_{LT} = 0.25$$

---

or the horizontal wall. But on a relative scale, the variation of ply orientation in the horizontal wall influences the natural frequencies more than that in the vertical wall.

### 9.1.2 *Effects of Tip Sweep and Anhedral*

The influence of tip sweep and tip anhedral on the natural frequencies of the two-cell composite blade is shown in Figs. 9.5 and 9.6, respectively. The swept tip, representing 10% of the blade length, is modeled with one element, while the straight portion is modeled using four elements having equal length.

It can be seen from Fig. 9.5 that tip sweep does not significantly influence the natural frequencies of the rotor blade. Only the first torsional frequency shows an increase with increasing sweep angle. Tip sweep can either increase (this study and Ref. 8) or decrease (Ref. 12) the natural frequency of the rotor blade in torsion. The physical reason for such behavior is due to the fact that tip sweep increases both the torsional stiffness (tennis racquet effect) and the torsional inertia. Depending on the relative increments in the stiffness and in the inertia effects, torsional frequency can increase or decrease with variation in sweep angle of the rotor blade.

Figure 9.6 presents the effects of tip anhedral on the rotating natural frequencies of the two-cell composite rotor blade. The influence of anhedral on the natural frequencies is negligible.

## **9.2 AEROELASTIC STABILITY IN HOVER**

The results in this section are divided into three parts: (1) results illustrating the influence of tip sweep and anhedral for isotropic blades; (2) results for single-cell composite blades emphasizing the influence of ply orientation on aeroelastic stability; and (3) results for two-cell composite blades, emphasizing the influence of ply orientation as well as the combined effect of sweep and ply orientation on aeroelastic stability.

### 9.2.1 Effects of Swept Tip

The effects of tip sweep and tip anhedral are presented for a soft-in-plane, isotropic hingeless blade configuration. The blade is modeled using a total of five finite elements. The swept tip, representing 10% of the blade length, is modeled with one element, while the straight portion is modeled using four elements having equal length. Seven coupled rotating modes, including three flap, two lag, one torsion and one axial mode, are used. The baseline configuration for the straight blade is given in Table 9.2.

---

TABLE 9.2

Baseline configuration for the isotropic rotor blade

Coupled rotating natural frequencies:

$$\omega_F = 1.125, 3.406, 7.622$$

$$\omega_L = 0.731, 4.465$$

$$\omega_{T1} = 4.875$$

$$(k_A/k_m)^2 = 0.5259$$

$$k_{m1}/R = 0.0$$

$$k_{m2}/R = 0.02$$

$$\gamma = 5.5$$

$$\sigma = 0.07$$

$$c/R = 0.055$$

$$a = 2\pi$$

$$C_{\alpha 0} = 0.01$$

$$C_w = 0.005$$

$$\beta_p = 0.0$$

$$B = 4$$

Tip length = 10% of the blade length.

Offsets of center of mass, tension center and aerodynamic center from elastic axis are zero.

---

The tip sweep angle,  $\Lambda_1$ , is varied between  $0^\circ$  and  $40^\circ$  in increments of  $10^\circ$  each; similarly, the tip anhedral angle,  $\Lambda_2$ , is varied between  $-20^\circ$  and  $20^\circ$  in increments of  $10^\circ$  each. The thrust coefficient of the rotor,  $C_T$ , is maintained

at a constant value of 0.005 which is equal to the weight coefficient,  $C_w$ , by using a coupled trim-aeroelastic response analysis.

Figures 9.7 through 9.10 illustrate the effect of tip sweep on the aeroelastic stability of the blade. Figures 9.7 and 9.8 show the imaginary and real parts, respectively, of the complex eigenvalues for hover as a function of  $\Lambda_s$ , for the baseline configuration. The notation L, F and T is used to denote lag, flap and torsion modes, respectively. The imaginary part of the eigenvalue represents the frequency while the real part of the eigenvalue represents damping of the mode. Tip sweep introduces flap-torsion coupling in the blade. However, for this baseline configuration, the frequencies of the flap and torsion modes are well separated, therefore varying the tip sweep angle does not have a significant influence on the blade stability. Figure 9.7 shows that the frequencies of the first five modes are insensitive to  $\Lambda_s$ , while the frequency of the third flap mode increases slightly with  $\Lambda_s$ . The damping in the first flap, first lag and first torsion modes decrease slightly with  $\Lambda_s$ , but no instability is induced by tip sweep, as shown in Fig. 9.8. Figures 9.9 and 9.10 show the imaginary and real parts, respectively, of the eigenvalues as a function of  $\Lambda_s$ , for a configuration with a torsional frequency of  $\omega_{T1} = 3.263/\text{rev}$  which is close to the second flap frequency of  $\omega_{F2} = 3.406/\text{rev}$ . Figure 9.9 shows that frequency coalescence has occurred between the first torsion and second flap modes over a large portion of the tip sweep range being investigated (approximately between  $5^\circ$  and  $30^\circ$ ). The effect of this frequency coalescence on the stability is evident in Figure 9.10 where one of the modes is stabilized while the other mode is destabilized. The second flap mode becomes unstable for  $\Lambda_s$  between

9° and 34°. The second lag mode also exhibits a slight instability. This instability is not associated with frequency coalescence and can be removed by a small amount of structural damping.

Figures 9.11 through 9.14 illustrate the effect of tip anhedral on the aeroelastic stability of the blade. Figures 9.11 and 9.12 show the imaginary and real parts, respectively, of the eigenvalues for hover as a function of the anhedral angle,  $\Lambda_a$ , for the baseline configuration. Tip anhedral introduces lag-torsion coupling in the blade. The frequencies of the first torsion and second lag modes for the baseline configuration are  $\omega_{T1} = 4.875/\text{rev}$  and  $\omega_{L2} = 4.465/\text{rev}$ , respectively, which are reasonably separated from each other. These two modes exhibit a mild frequency coalescence near  $\Lambda_a = 0$  in Fig. 9.11. This frequency coalescence has some destabilizing effect on the first torsion mode when  $\Lambda_a > 0^\circ$  or  $\Lambda_a < -9^\circ$  and some stabilizing effect on the second lag mode when  $\Lambda_a > 0^\circ$ , which is evident in Fig. 9.12. Figures 9.13 and 9.14 show the imaginary and real parts, respectively, of the eigenvalues as a function of  $\Lambda_a$ , for a configuration with a torsional frequency of  $\omega_{T1} = 4.340/\text{rev}$  which is close to  $\omega_{L2} (= 4.465/\text{rev})$ . The effect of lag-torsion coupling due to tip anhedral is more pronounced for this blade configuration since Fig. 9.13 exhibits some apparent frequency coalescence over a wider range, while Fig. 9.14 exhibits a more significant stabilizing effect on the second lag mode and destabilizing effect on the first torsion mode for  $\Lambda_a \neq 0^\circ$ . The first torsion mode remains stable within the range of anhedral angles considered.

### 9.2.2 *Single-cell Composite Blade*

The aeroelastic behavior of a hingeless, single-cell, stiff-in-plane, composite blade configuration is considered next. This configuration has also been described in detail in the last section. Eigenvalues of the stability problem are computed for two cases, having symmetric configurations, where the ply lay-ups on opposite walls are identical. In the first case, the horizontal walls have zero ply angles. For vertical walls the laminae in the outer half thickness have zero ply angles while the laminae in the inner half thickness are all oriented at ply angle  $\Lambda_v$ . In the second case, the vertical walls have zero ply angles. For horizontal walls the laminae in the outer half thickness have zero ply angles while the laminae in the inner half thickness are all oriented at ply angle  $\Lambda_h$ .

Figures 9.15 through 9.17 show the root locus plots of the complex eigenvalues as a function of  $\Lambda_v$  for first lag, first flap and first torsion modes, respectively, at thrust levels  $C_T = 0.005$  (solid lines) and  $C_T = 0.0025$  (dotted lines). The ply angle  $\Lambda_v$ , which is the parameter given on the plots, is varied from  $0^\circ$  to  $90^\circ$  in both positive and negative directions. Note that the ply angles  $\Lambda_v$  for  $90^\circ$  and  $-90^\circ$  have the same configuration with fibers oriented vertically, perpendicular to the blade axis, for the inner half of the vertical walls. Figure 9.15 shows that a positive ply angle  $\Lambda_v$  destabilizes the first lag mode, while a negative  $\Lambda_v$  stabilizes the first lag mode. Since the first lag mode is not heavily damped, the destabilizing effect on this mode due to positive  $\Lambda_v$  can be significant for certain ply angles. The combined effect of having a positive ply angle  $\Lambda_v$  between  $10^\circ$  and  $28^\circ$ , with a low thrust level  $C_T = 0.0025$  causes

instability in the first lag mode, as illustrated in Fig. 9.15. Figure 9.16 shows that a positive  $\Lambda_v$ , up to approximately  $45^\circ$ , stabilizes the first flap mode slightly. A positive  $\Lambda_v$  greater than  $45^\circ$  or a negative  $\Lambda_v$ , can destabilize the first flap mode slightly. Variation of  $\Lambda_v$  has little influence on the stability of the first torsional mode, as can be seen from Figure 9.17. Since the flap and torsion modes are heavily damped, the effect of  $\Lambda_v$  on the stability of these two modes is less significant.

Figures 9.18 through 9.20 show the root locus plots of the eigenvalues as a function of  $\Lambda_h$  for the first lag, first flap and first torsion modes, respectively, at a constant thrust coefficient  $C_T = 0.005$ . Figure 9.18 shows that a negative  $\Lambda_h$ , up to approximately  $-60^\circ$ , destabilizes the first lag mode, while a negative  $\Lambda_h$  beyond  $-60^\circ$  or a positive  $\Lambda_h$  stabilizes the first lag mode. For the first flap and first torsion modes, the variation of ply angle  $\Lambda_h$  has more influence on the frequency than on the stability, as evident from Figs. 9.19 and 9.20.

### **9.2.3 Two-cell Composite Blade**

Results illustrating the aeroelastic behavior of a composite soft-in-plane blade having a two-cell type cross section are presented next. The configuration of the blade has been described in detail in the last section. Stability results are first calculated for a swept-tip blade with zero ply angles and for a straight blade with ply angle variation in either the vertical walls or the horizontal walls. Subsequently, the combined effects of tip sweep and ply orien-

tation on blade stability are determined. The thrust coefficient  $C_T$  is maintained at a constant value of 0.005 for all cases.

Figures 9.21 and 9.22 illustrate the behavior of the imaginary and real parts, respectively, of the eigenvalues associated with the various modes used in the analysis as a function of the tip sweep angle  $\Lambda_s$ , for the baseline configuration which has zero ply angles. For this case, the blade exhibits a frequency coalescence induced by sweep between the second flap and first torsion modes that is evident in Figure 9.21. This produces a stabilizing effect on the second flap mode while destabilizing the first torsion mode, as depicted in Figure 9.22. Figure 9.22 shows that the frequency coalescence for this two-cell case induces a mild instability in the first torsion mode for sweep angles between  $14^\circ$  and  $22^\circ$ .

For the straight blade with ply angle variations, two cases are analyzed. In the first case, the laminae in the middle vertical wall and the inner half of the rear vertical wall are oriented at ply angle  $\Lambda_v$  while the remaining walls have zero ply angles. In the second case, the laminae in the inner half of the horizontal walls are oriented at ply angle  $\Lambda_h$  while the remaining walls have zero ply angles. Figures 9.23 through 9.25 show the root-locus plots of the eigenvalues as a function of the ply angle  $\Lambda_v$  for first lag, first flap and first torsion modes, respectively. Figure 9.23 indicates that a positive  $\Lambda_v$ , or a negative  $\Lambda_v$  beyond  $-60^\circ$ , destabilizes the first lag mode, while a negative  $\Lambda_v$  up to  $-60^\circ$  stabilizes the mode. The effects of the ply angle  $\Lambda_v$  variation on the first flap and first torsion modes are less significant, as illustrated in Figs. 9.24 and 9.25.

Figures 9.26 through 9.29 show the root locus plots of the eigenvalues as a function of the ply angle  $\Lambda_h$  for the first lag, first flap, first torsion and second flap modes, respectively, for the straight blade case (solid lines) and for the swept tip case with  $\Lambda_s = 20^\circ$  (dotted lines). Figure 9.26 shows that a positive  $\Lambda_h$  or a negative  $\Lambda_h$  beyond  $-50^\circ$  destabilizes the first lag mode, while a negative  $\Lambda_h$  up to  $-50^\circ$  stabilizes the mode. The first flap mode stability is only slightly influenced by the variation of  $\Lambda_h$ , as illustrated in Fig. 9.27. A tip sweep of  $20^\circ$  has a destabilizing effect on both the first lag and first flap modes, but no instability is induced in these modes, as depicted in Figs. 9.26 and 9.27. Figure 9.28 shows that for the straight blade case, the damping in the first torsion mode decreases for positive  $\Lambda_h$ , however, the mode remains stable. For the case of  $20^\circ$  sweep, the blade has a mild instability in the first torsion mode at zero ply angle, which has also been shown in Fig. 9.22. The first torsion mode is further destabilized for ply angle  $\Lambda_h$  between  $0^\circ$  and  $12^\circ$ , however, it becomes stable for  $\Lambda_h$  greater than  $13^\circ$  or for a negative ply angle  $\Lambda_h$  beyond  $-1^\circ$ , as illustrated in Fig. 9.28. Therefore, the instability caused by tip sweep can be removed by selecting an appropriate ply orientation in composite blades. Introducing a tip sweep of  $20^\circ$  destabilizes the first torsion mode and stabilizes the second flap mode for all ply angles, when compared to the case of a straight blade, as shown in Figs. 9.28 and 9.29, respectively.

## **Chapter X**

### **AEROELASTIC BEHAVIOR IN FORWARD FLIGHT**

This chapter explores the aeroelastic response, stability and loads in forward flight of composite rotor blades with straight and swept tips. Numerical results illustrating the influence of composite ply orientation, tip sweep and anhedral on trim, hub loads, blade response and stability are presented. The purpose of these calculations is twofold. First, to gain a better physical understanding on the aeroelastic stability and response of composite blades with swept tips. Second, these results serve as a necessary precursor for the blade optimization studies which are conducted in the following chapter.

The results presented in this chapter are for a four bladed hingeless rotor, in which each blade is assumed to be of composite construction, with uniform spanwise properties. Note, that uniform properties are assumed here only for convenience, the analysis and associated computer program are capable of representing configurations with arbitrary cross sectional variations in the spanwise direction. For completeness a concise description of the treatment of a nonuniform blade configuration is provided next. The nonuniform portion of the blade is divided into several sub-segments, such that approximately linear variation of the spanwise properties in each sub-segment can be assumed. A two-dimensional cross sectional analysis is then performed for each cross section corresponding to an end point of a sub-segment. At a beam element Gaussian point which is in a sub-segment of this portion of the blade, the

sectional properties are obtained from that of the end cross sections of the sub-segment by linear interpolation. Despite the variations inside the element, the assembly process of the various elements assumes that the elastic axis is a straight line for the straight portion of the blade. This is justifiable because the nonuniform inboard segment of the blade (approximately 25% of the blade length; see Sec. 2.1, Assumption 9) is relatively rigid; its deflections will be relatively small, and the inertial and aerodynamic loads in this blade segment are also low; and therefore approximations introduced for this blade portion will have a negligible effect on the global blade behavior.

The composite blade cross-sectional structure is represented by a two-cell laminated box beam, as shown in Figure 7.1. The leading edge has a semi-circular shape with a radius of 1.2" while the straight portion has a total length of 6". The internal vertical wall is located 2.8" behind the leading edge. All the walls have a thickness of 0.1".

It should be noted that, throughout this study, the term "swept tip" is used to denote a combination of sweep and anhedral. A parametric study of the influence of ply orientation and swept tip on the trim, hub loads, blade response and stability was conducted by considering four cases. The first two cases are for a straight blade with varying ply orientations in either the horizontal or vertical walls; while for the last two cases the ply angles are assumed to be zero and 10% outboard portion of the blade experiences varying amounts of tip sweep or anhedral. In the first case, the laminate associated with the inner half of the horizontal walls is oriented at ply angle  $\Lambda_h$ , while the remaining walls have zero ply angles. In the second case, the laminate in the

internal vertical wall and the inner half of the rear vertical wall is oriented at ply angle  $\Lambda_v$  while the remaining walls have zero ply angles. The ply angle in the leading edge semi-circle is always set at zero value. The principal reason for this assumption is convenience. Otherwise, the two-dimensional cross sectional analysis has to be used in an unwieldy manner to account for changes in the ply orientation in the semi-circular leading edge portion of the blade cross-section. A positive  $\Lambda_v$  implies that the fibers are oriented toward the top wall of the blade and for positive  $\Lambda_h$  the fibers are oriented toward the leading edge of the blade. In the third case , the blade has a tip sweep with sweep angle  $\Lambda_s$  , positive for backward sweep. In the fourth case , the blade has a tip anhedral with anhedral angle  $\Lambda_a$  , positive upward. The baseline configuration represents the case where  $\Lambda_h, \Lambda_v, \Lambda_s$  and  $\Lambda_a$  are all equal to zero. The properties of the baseline blade configuration are given in Table 10.1.

The aeroelastic response and stability calculations were performed using three flap, two lag, one torsional and one axial modes. Five elements, four for the straight portion and one for the swept tip, were used to model the blade. Five harmonics ( $N_H = 5$ ) were used in the harmonic balance solutions so as to accurately capture the 4/rev hub loads. The influence of composite ply orientation and swept tip on trim, hub loads, blade aeroelastic response and stability were all computed for an advance ratio  $\mu = 0.3$  .

---

TABLE 10.1

Baseline configuration for the two-cell soft-in-plane composite rotor blade

Coupled rotating natural frequencies:

$$\omega_L = 0.765, 4.666$$

$$\omega_F = 1.096, 3.110, 6.554$$

$$\omega_{T1} = 3.821$$

$$\gamma = 5.0$$

$$\sigma = 0.076$$

$$a = 5.7$$

$$C_{d0} = 0.01$$

$$k_{m1}/R = 0.004$$

$$k_{m2}/R = 0.0211$$

$$X_{FC}/R = 0.0$$

$$X_{FA}/R = 0.0$$

$$fC_{df}/\pi R^2 = 0.01$$

$$c/R = 0.06$$

$$\beta_p = 0.0$$

$$C_w = 0.005$$

$$B = 4$$

$$R = 250''$$

$$\Omega = 360 \text{ rpm}$$

$$Z_{FC}/R = 0.50$$

$$Z_{FA}/R = 0.25$$

Tip length = 10% of the blade length.

Material constants:

$$E_L = 6.2 \times 10^6 \text{ psi}$$

$$E_T = 1.6 \times 10^6 \text{ psi}$$

$$G_{LT} = 0.8 \times 10^6 \text{ psi}$$

$$\nu_{LT} = 0.25$$


---

## 10.1 BLADE RESPONSE

Figures 10.1 through 10.12 show the effects of  $\Lambda_h$ ,  $\Lambda_v$ ,  $\Lambda_s$ , and  $\Lambda_a$ , on blade tip deflection in lag, flap and torsion, respectively, during one revolution. In each figure, nondimensional tip deflections corresponding to three representative values of the parameter being studied are shown as a function of the blade azimuth. The selected ply angles are  $0^\circ$ ,  $15^\circ$  and  $-15^\circ$  for both  $\Lambda_h$  and  $\Lambda_v$ . For sweep the values of  $\Lambda_s$  are  $0^\circ$ ,  $10^\circ$  and  $20^\circ$ ; and for anhedral angle the values  $0^\circ$ ,  $10^\circ$  and  $-10^\circ$  are used. For swept tip cases, where either  $\Lambda_s$  or  $\Lambda_a$  is

the parameter, the nondimensional tip deflections shown in the figures are the values at the junction between the straight and the swept tip portions, which is located at 90% of the blade span, when measured from the root.

It is evident from Figs. 10.1 and 10.4 that variation of ply angles  $\Lambda_h$  and  $\Lambda_v$  has only a slight influence on lag deflection. The flap deflection is insensitive to variation in  $\Lambda_h$  and  $\Lambda_v$ , as depicted in Figs. 10.2 and 10.5. Figure 10.3 shows that a positive ply angle in the horizontal wall,  $\Lambda_h = 15^\circ$ , decreases the torsional tip deflection (makes it more negative), while a negative ply angle,  $\Lambda_h = -15^\circ$ , increases the torsional tip deflection (makes it more positive). On the other hand, Figure 10.6 shows that a positive ply angle in the vertical wall,  $\Lambda_v = 15^\circ$ , increases the torsional tip deflection, while a negative ply angle,  $\Lambda_v = -15^\circ$ , decreases the torsional tip deflection.

Figures 10.7 through 10.9 show the effect of sweep on blade tip deflection in lag, flap and torsion, respectively. It is evident that positive tip sweep, e.g.,  $\Lambda_s = 10^\circ, 20^\circ$ , increases (make it less negative) the lag deflection, but decreases (make it more negative) the torsional deflection. The flap deflection is not influenced by  $\Lambda_s$ . The influence of the anhedral angle  $\Lambda_a$  on the lag deflection varies along the blade azimuth, as shown in Fig. 10.10. A positive anhedral angle  $\Lambda_a = 10^\circ$  increases (makes it less negative) the lag deflection for azimuth angles  $0^\circ \leq \psi \leq 90^\circ$  and  $250^\circ \leq \psi \leq 360^\circ$ , while decreases (makes it more negative) the lag deflection for azimuth region  $90^\circ \leq \psi \leq 250^\circ$ . A negative anhedral angle  $\Lambda_a = -10^\circ$  has the opposite effect on the lag deflection when compared to the case for  $\Lambda_a = 10^\circ$ . Figure 10.11 shows that a positive

anhedral angle  $\Lambda_a = 10^\circ$  decreases the flap deflection around the azimuth, while a negative anhedral angle  $\Lambda_a = -10^\circ$  increases the flap deflection.

## 10.2 TRIM VARIABLES

Figures 10.13 through 10.20 show the trim variables as a function of one of the parameters  $\Lambda_h$ ,  $\Lambda_v$ ,  $\Lambda_s$ , or  $\Lambda_a$ . Blade pitch input angles, including collective pitch, cyclic cosine and cyclic sine, are presented in Figs. 10.13, 10.15, 10.17 and 10.19. While rotor inflow ratio and angle of attack are presented in Figs. 10.14, 10.16, 10.18 and 10.20. The ply angles  $\Lambda_h$  and  $\Lambda_v$  are varied from  $-90^\circ$  to  $+90^\circ$ . The tip sweep angle  $\Lambda_s$  is varied between  $0^\circ$  and  $40^\circ$  while the tip anhedral angle  $\Lambda_a$  is varied between  $-20^\circ$  and  $20^\circ$ . Figures 10.13 and 10.14 show the effect of  $\Lambda_h$  on the trim variables. It is evident that only collective pitch angle is significantly influenced by the variation in the ply angle  $\Lambda_h$ , with the most pronounced effect evident between  $-30^\circ$  and  $+30^\circ$ . The reason for the sensitivity of the collective pitch angle can be easily understood by simultaneously examining the torsional response of the blade and the collective pitch angle. As discussed in the previous section, Fig. 10.3 shows that a positive ply angle,  $\Lambda_h = 15^\circ$ , decreases the mean value of torsional response (makes it more negative) relative to the baseline case. In order to maintain a fixed thrust level, this decrease in the mean value of the torsional deformation of the blade must be accompanied by a corresponding increase in the collective pitch angle, as shown in Fig. 10.13. Similarly, for the case  $\Lambda_h = -15^\circ$  the mean value of the torsional response increases (less negative or

more positive) relative to the baseline case (Fig. 10.3) and the corresponding collective pitch angle shows a reduction from the baseline case (Fig. 10.13). Figures 10.15 and 10.16 show the effect of  $\Lambda_v$  on the trim variables. Again, only the collective pitch is influenced by the variation in  $\Lambda_v$ , and the physical explanations provided for variations due to  $\Lambda_h$  are also applicable to this case. Figures 10.17 and 10.18 show the effect of tip sweep on the trim variables. The collective pitch angle increases with sweep and the absolute value of the cyclic pitch angles, as well as the rotor angle of attack, also show slight increases with sweep. Figures 10.19 and 10.20 show the effect of tip anhedral on the trim variables. The collective pitch angle, rotor angle of attack and inflow ratio increase with both tip anhedral and dihedral; with rotor angle of attack,  $\alpha_R$ , being particularly sensitive to variation in  $\Lambda_a$  (Fig. 10.20). The cyclic cosine increases with tip anhedral and decreases with tip dihedral.

### 10.3 VIBRATORY HUB LOADS

Figures 10.21 through 10.28 show the absolute value of the 4/rev vibratory hub shears and moments as a function of one of the parameters  $\Lambda_h$ ,  $\Lambda_v$ ,  $\Lambda_s$  or  $\Lambda_a$ . Results illustrating the influence of ply orientation  $\Lambda_h$  on the 4/rev vibratory hub shears and moments are shown in Figs. 10.21 and 10.22, respectively. The variation in longitudinal and lateral shears is about 17% to 24%, from the baseline configuration, while the vertical shear is less sensitive to the variation in  $\Lambda_h$  (about 12% from the baseline). The roll and pitch moments decrease with  $\Lambda_h$  up to 28% relative to the baseline around  $\Lambda_h = 90^\circ$ .

The maximum variation in yaw moment consists of an increase of about 34% for  $\Lambda_h > 60^\circ$ . Results illustrating the influence of ply orientation  $\Lambda_v$  on the 4/rev vibratory hub shears and moments are shown in Figs. 10.23 and 10.24, respectively. The hub shears are less sensitive to  $\Lambda_v$  than to  $\Lambda_h$ . The roll and pitch moments are insensitive to  $\Lambda_v$  while the maximum variation in yaw moment is represented by an increase of about 21%, for  $\Lambda_v$  near  $90^\circ$ . Results illustrating the influence of tip sweep  $\Lambda_s$  on the 4/rev vibratory hub shears and moments are shown in Figs. 10.25 and 10.26, respectively. Tip sweep reduces both hub shears and moments, with the hub shears being more sensitive to the variation in tip sweep angle. Results depicting the influence of tip anhedral  $\Lambda_a$  on the 4/rev vibratory hub shears and moments are shown in Figs. 10.27 and 10.28, respectively. Most components of hub shears and moments increase with both anhedral and dihedral. The only exception is the vertical shear, which increases with dihedral but is relatively insensitive to anhedral.

#### 10.4 BLADE STABILITY

Figures 10.29 through 10.35 show the real part of the characteristic exponents, which represent a measure of blade modal damping, or stability, as a function of one of the parameters  $\Lambda_h$ ,  $\Lambda_v$ ,  $\Lambda_s$ , or  $\Lambda_a$ . The effect of varying the ply orientation  $\Lambda_h$  on the aeroelastic stability of the lag mode is shown first in Fig. 10.29, because lag is usually the critical mode in hingeless rotor stability studies. It is evident from Fig. 10.29 that the stability of the lag mode is significantly influenced by the ply angle variation. For  $\Lambda_h$  between  $-20^\circ$  and

+20°, the positive ply angles decrease amount of damping associated with the lag mode, whereas the negative ply angles substantially increase the level of damping in lag. Figure 10.30 indicates that the first flap mode stability is insensitive to  $\Lambda_h$ . Results illustrating the effect of  $\Lambda_h$  on the aeroelastic stability of the first torsion and second flap modes are presented in Fig. 10.31. It is evident that the stability of the first torsion and second flap modes is virtually unaffected by the variation in  $\Lambda_h$ . The effect of varying the ply orientation  $\Lambda_v$  on the aeroelastic stability of the lag mode is shown in Fig. 10.32. It is evident from Fig. 10.32 that the stability of the lag mode is significantly influenced by the ply angle variation. For  $\Lambda_v$  between -20° and +20°, the positive ply angles decrease the lag mode damping, whereas the negative ply angles increase the lag mode damping substantially. The stability of the first two flap modes and the torsion mode is insensitive to the ply angle  $\Lambda_v$ , as depicted in Fig. 10.33. Results illustrating the influence of the tip sweep angle  $\Lambda_s$  on the aeroelastic stability of the first six modes are shown in Fig. 10.34. The notation L, F and T is used to denote lag, flap and torsion modes, respectively. The real part of the characteristic exponent associated with the first lag and first torsion modes decreases while it increases for the second lag mode with tip sweep, but is fairly insensitive to the variation of  $\Lambda_s$ , in the flap modes, as evident from Fig. 10.34. It should be emphasized that while the curves representing the real part of the characteristic exponent associated with the first and second lag modes, in Fig. 10.34, appear to be flat, the level of damping for these two modes is at least an order of magnitude smaller than that of the other modes shown in Fig. 10.34, and thus the variation of the damping level

in these modes is quite significant. Results depicting the influence of the tip anhedral angle  $\Lambda_a$  on the aeroelastic stability of the first six modes are presented in Fig. 10.35. The real part of the characteristic exponent associated with the first lag mode increases with anhedral and decreases with dihedral. The level of damping for the second lag mode increases while that for the first torsion mode decreases with both anhedral and dihedral. The mild instability in the second lag mode, present in Figs. 10.34 and 10.35, can be removed by introducing a small amount of structural damping, in this particular mode.

The baseline blade configuration given in Table 10.1 has a rotating natural torsional frequency of 3.821/rev, which is well separated from the second flap frequency of 3.110/rev. By increasing the mass moment of inertia  $k_{m2}/R$  to 0.02439, the torsional frequency becomes 3.356/rev which is now close to the second flap frequency. Results for blade stability were also calculated for this modified configuration. The results illustrating the influence of  $\Lambda_h$  on the aeroelastic stability of the first torsion and second flap modes are presented in Fig. 10.36. The real part of the characteristic exponents indicate that the torsional mode undergoes a significant reduction in damping levels, while the second flap mode displays a significant increase in damping levels, around  $\Lambda_h = 15^\circ$ . This is a frequency coalescence phenomenon due to the flap-torsion coupling introduced by  $\Lambda_h$ . Results presented in Fig. 10.37 illustrate the influence of the tip sweep angle  $\Lambda_s$  on the aeroelastic stability of the first six modes. The frequency coalescence phenomenon between the first torsion and second flap modes is present over a wide range of sweep angle  $\Lambda_s$ , primarily

due to the flap-torsion coupling introduced by tip sweep. The first torsion mode becomes marginally stable around  $\Lambda_s \simeq 15^\circ$  to  $20^\circ$ .

## 10.5 COMBINED EFFECT OF SWEEP AND PLY ORIENTATION

Results showing the combined effect of tip sweep and composite construction of blade were calculated for  $\Lambda_h = 0^\circ, 15^\circ$  and  $-15^\circ$  at various tip sweep angles,  $\Lambda_s$ , between  $0^\circ$  and  $40^\circ$ . The ply angle in the vertical wall,  $\Lambda_v$ , and the anedral angle,  $\Lambda_a$ , were set to zero in these calculations. The selection of this particular combination of parameters was influenced by results for the 4/rev hub loads and blade stability described in previous sections of this chapter. Tip sweep reduces most vibratory hub load components, as previously illustrated in Figs. 10.25 and 10.26. A value of  $\Lambda_h = 15^\circ$  produces a modest reduction in the 4/rev hub loads at the expense of some lag damping levels; while a  $\Lambda_h = -15^\circ$  produces an increase in lag damping levels; with slightly increased 4/rev hub loads; as can be seen from Figs. 10.21, 10.22 and 10.29.

Figures 10.38 through 10.40 show the 4/rev longitudinal, lateral and vertical shears, respectively, as a function of  $\Lambda_s$ , for  $\Lambda_h = 0^\circ$  (baseline),  $15^\circ$  and  $-15^\circ$ . The baseline cases in Figs. 10.38 through 10.40 undergo a reduction in 4/rev hub shears with increasing tip sweep, as was indicated in Fig. 10.25. For longitudinal and vertical shears, the additional effect due to the presence of  $\Lambda_h = 15^\circ$  or  $-15^\circ$  with increasing  $\Lambda_s$  is not favorable compared to the baseline case, as evident from Figs. 10.38 and 10.39. For vertical shears the additional

effect due to  $\Lambda_h = 15^\circ$  or  $-15^\circ$  compared to the baseline case is unfavorable for lower sweep angles, but becomes beneficial for sweep angle  $\Lambda_s$  greater than  $35^\circ$ , as can be seen from Fig. 10.40. Figures 10.41 through 10.43 show the 4/rev rolling, pitching and yawing moments, respectively, as a function of  $\Lambda_s$ , for  $\Lambda_h = 0^\circ$ ,  $15^\circ$  and  $-15^\circ$ . The baseline cases in Figs. 10.41 through 10.43 undergo a slight to moderate reduction in 4/rev hub moments with increasing tip sweep, up to  $\Lambda_s = 25^\circ$ , as was indicated in Fig. 10.26. The additional effect due to  $\Lambda_h = 15^\circ$  or  $-15^\circ$ , compared to the baseline case, is generally unfavorable for all 4/rev hub moment components. Figure 10.44 shows the real part of the characteristic exponents for the first lag mode as a function of  $\Lambda_s$  for  $\Lambda_h = 0^\circ$  (baseline),  $15^\circ$  and  $-15^\circ$ . The first lag mode damping level decreases with increasing tip sweep angle for all three cases, as evident from Fig. 10.44. For the straight blade case,  $\Lambda_h = 15^\circ$  reduces the first lag mode damping level by 25%, while  $\Lambda_h = -15^\circ$  increases the first lag mode damping level by approximately 25%. When sweep is introduced, these effects diminish with increasing tip sweep angle  $\Lambda_s$ . It is obvious, from the results presented in Figs. 10.38 through 10.44, that the combined effect of swept tip and composite construction of the blade cannot be predicted by superposition of the respective individual effects; because the problem is inherently nonlinear. The mechanism associated with the combined effect is subtle and difficult to quantify precisely based on the results generated so far. However the parametric study presented in this chapter provides a valuable precursor to structural optimization studies where the proper combination among these parameters, for vibration reduction, is selected by an optimizer.

## Chapter XI

### STRUCTURAL OPTIMIZATION RESULTS

This chapter presents a structural optimization study conducted by combining the aeroelastic analysis capability developed in this study with the DOT structural optimization package[106]; to design composite rotor blades with swept tips for low vibration levels in forward flight, using composite ply orientation in the horizontal and vertical walls, and tip sweep and anhedral angles as design variables.

Three hingeless blade configurations with a two-cell cross section are investigated. The first configuration is a soft-in-plane blade with its baseline configuration shown in Table 10.1. Details of this blade configuration has been described in Chapter 10. The second configuration is the same as the first configuration except that its torsional frequency is modified from 3.821/rev to 3.356/rev and it was also described in Chapter 10. The third configuration is a stiff-in-plane blade with a cross sectional shape similar to that of the soft-in-plane blades (Fig. 7.1). For the stiff-in-plane blade, the leading edge semi-circle has a radius of 0.8" while the straight portion has a total length of 6.2". The internal vertical wall is located 3.6" behind the leading edge; and All walls have a thickness of 0.2". The composite ply orientation is defined in the same way as that of the soft-in-plane blade. The baseline configuration parameters for this blade are shown in Table 11.1, where the material constants correspond to graphite/epoxy type composite material.

---

TABLE 11.1

Baseline configuration for the two-cell stiff-in-plane composite rotor blade

Coupled rotating natural frequencies:

$$\begin{aligned}\omega_L &= 1.454, 8.817 \\ \omega_F &= 1.148, 3.654, 8.471 \\ \omega_{T1} &= 4.408\end{aligned}$$

$$\begin{array}{ll}\gamma = 5.0 & c/R = 0.06 \\ \sigma = 0.076 & \beta_p = 0.0 \\ a = 5.7 & C_w = 0.005 \\ C_{d0} = 0.01 & B = 4 \\ k_{m1}/R = 0.0 & R = 250'' \\ k_{m2}/R = 0.0155 & \Omega = 360 \text{ rpm} \\ X_{FC}/R = 0.0 & Z_{FC}/R = 0.50 \\ X_{FA}/R = 0.0 & Z_{FA}/R = 0.25 \\ fC_{df}/\pi R^2 = 0.01 & \end{array}$$

Tip length = 10% of the blade length.

Material constants:

$$\begin{aligned}E_L &= 28.0 \times 10^6 \text{ psi} \\ E_T &= 2.5 \times 10^6 \text{ psi} \\ G_{LT} &= 1.0 \times 10^6 \text{ psi} \\ \nu_{LT} &= 0.30\end{aligned}$$


---

The aeroelastic response and stability calculations were performed using three flap, two lag, one torsional and one axial modes. Five elements, four for the straight portion and one for the swept tip, were used to model the blade. Five harmonics ( $N_H = 5$ ) were used in the harmonic balance solutions so as to accurately capture the 4/rev hub loads. All the computations involving forward flight were carried out for an advance ratio  $\mu = 0.3$ .

The two objective functions  $J_1$  and  $J_2$  defined by Eqs. (7.8) and (7.9), respectively, are used for each of the three blade configurations and the values of the various weighting factors, used in the calculations, are specified below:

$$K_F = K_M = 1.0$$

$$K_{Fz} = 1.0; \quad K_{Fx} = K_{Fy} = K_{Mx} = K_{My} = K_{Mz} = 0.0$$

In the aeroelastic stability constraints, a 0.5% structural damping is added to the damping level associated with the second lag mode, so as to eliminate the slight instability which can occur in the second lag mode. This is accomplished by an approximate approach described below, where the subscript  $j$ , used to denote the  $j$ -th mode, is dropped for convenience. The eigenvalue obtained from the stability calculation for the  $j$ -th mode is

$$\lambda = \zeta \pm i\omega$$

where the real part is approximated by

$$\zeta = -\xi_d \omega_n$$

with  $\xi_d, \omega_n$  being the damping ratio and natural frequency, respectively, for the  $j$ -th mode ( $\xi_d = c/c_c$ ). When using a viscous type structural damping the additional damping,  $\alpha_d c_c$ , added to the mode, can be expressed as a small percentage of the critical damping  $c_c$ ; and the modified damping coefficient can be written as

$$c' = c + \alpha_d c_c = (\xi_d + \alpha_d) c_c$$

where  $c$  represents the damping initially present in the mode, and the modified damping ratio is given by

$$\zeta_d' = c'/c_c = \zeta_d + \alpha_d$$

The real part of the eigenvalue becomes

$$\zeta' = -\zeta_d' \omega_n = -(\zeta_d + \alpha_d) \omega_n$$

and the change in the real part of the eigenvalue which is indicative of the stability associated with the mode is:

$$\Delta\zeta = \zeta' - \zeta = -\alpha_d \omega_n$$

Since both  $\alpha_d$  and  $\omega_n$  are known quantities, a small amount of structural damping can be conveniently added to a particular mode, by modifying the real part of the eigenvalue associated with that mode.

The minimum acceptable damping level  $\varepsilon_k$ , defined in Eq. (7.7), is set to 0.01 for all modes, used in this study; for convenience. However one can specify different values of  $\varepsilon_k$ , for the various modes, as needed.

Initial designs for the two soft-in-plane blade configurations are chosen based upon the experience gained from the parametric studies conducted for these blade configurations, described in Chapters 9 and 10. For the first blade configuration, the initial design was selected to have the following values of the design variables:  $\Lambda_h = 15^\circ$ ,  $\Lambda_s = 20^\circ$ ,  $\Lambda_v = \Lambda_a = 0^\circ$ ; which represents a design with fairly low hub loads, and no significant reduction in aeroelastic stability margins (see Figs. 10.21, 10.22, 10.25 and 10.26). Note, that while parametric studies cannot be used to determine the optimum design, they can provide

useful information for selecting a reasonable initial design; so that the number of iterations required in the optimization process is reduced. Furthermore, the baseline design has zero values for the four design variables, while the initial design is characterized by preassigned (usually nonzero) values of these design variables.

The increment size (or step size) for the design variables, during the calculation of sensitivity derivatives based upon the finite difference approach, is set to  $0.1^\circ$  for all four design variables,  $\Lambda_h$ ,  $\Lambda_v$ ,  $\Lambda_s$  and  $\Lambda_a$ . This choice is a result of a study in which a variety of increment sizes ranging from  $0.001^\circ$  to  $1^\circ$  for each design variable were explored. It was found that the  $0.1^\circ$  increment size produced the most consistent and stable behavior in the computation of the sensitivity derivatives, among all increment sizes tested.

Figures 11.1 and 11.2 show the vibratory hub shears and moments, respectively, corresponding to the first configuration with  $J_1$  as the objective function. The objective function  $J_1$  is the sum of the 4/rev hub shear resultant and 4/rev hub moment resultant for the four-bladed rotors considered in this study. The results presented in Figs. 11.1 and 11.2 were obtained from the optimization process after eight iterations. It is evident from Fig. 11.1 that the 4/rev hub shears are reduced by 9% to 18% compared to the initial design, and by 32% to 37% compared to the baseline case. The 4/rev hub moments are reduced by 0.1% to 6% compared to the initial design, and by 25% to 28% compared to the baseline, as illustrated in Fig. 11.2. The reduction in the objective function  $J_1$  is 9% from the initial design and 33% from the baseline case (see Table 11.2).

Figures 11.3 and 11.4 show the vibratory hub shears and moments, respectively, corresponding to the first configuration when  $J_2$  is the objective function in the optimization process. The objective function  $J_2$  consists of the 4/rev vertical hub shear for the cases considered in this study. The 4/rev vertical shear is reduced by a remarkable 53% from the initial design; however, there is no reduction in 4/rev longitudinal and lateral shears. Furthermore, the reduction in vertical hub shear is accompanied by a 1% to 12% increase of 4/rev hub moments compared to the initial design as depicted in Figs. 11.3 and 11.4. When comparing the final design to the baseline configuration, one can identify a reduction of 26% to 63% for 4/rev hub shears and 13% to 20% for 4/rev hub moments; as is evident from Figs. 11.3 and 11.4.

The objective functions and the corresponding design variables in the baseline, initial and optimum designs for the first configuration are summarized in Table 11.2.

The second blade configuration has a torsional frequency of 3.356/rev, which is close to the second flap frequency of 3.110/rev.. The frequency coalescence phenomenon caused by either  $\Lambda_h$  or  $\Lambda_s$  can reduce the damping level in first torsion mode significantly, as has been shown in Fig. 9.28, for the case of hover; and in Figs. 10.36 and 10.37 for the case of forward flight. For  $\Lambda_s = 20^\circ$  and  $\Lambda_h$  between  $-1^\circ$  and  $13^\circ$ , the first torsion mode exhibits a mild instability in hover, as is evident from Fig. 9.28. The initial design for the structural optimization of this blade configuration was chosen as  $\Lambda_h = 5^\circ$ ,  $\Lambda_s = 20^\circ$ , and  $\Lambda_v = \Lambda_a = 0^\circ$ ; so that it violates the constraint on torsional stability and causes the design to be in the infeasible region. Since

---

**TABLE 11.2**

Summary of optimization results for the first configuration

	Baseline	Initial	Optimum
$J_1$ (E-3)	1.600	1.184	1.084
$\Lambda_h$	0.0	15.0	5.55
$\Lambda_v$	0.0	0.0	0.99
$\Lambda_s$	0.0	20.0	29.4
$\Lambda_a$	0.0	0.0	0.36
$J_2$ (E-4)	5.015	4.021	1.876
$\Lambda_h$	0.0	15.0	-7.41
$\Lambda_v$	0.0	0.0	3.74
$\Lambda_s$	0.0	20.0	39.5
$\Lambda_a$	0.0	0.0	0.81

All angles are in degrees.

---

the optimization problem includes aeroelastic stability constraints which have to be satisfied before convergence, the final optimum design for this blade configuration, determined by the optimization process and shown in Table 11.3, is aeroelastically stable.

Figures 11.5 and 11.6 show the vibratory hub shears and moments, respectively, corresponding to the second configuration, with  $J_1$  as the objective function. Compared to the initial design, the 4/rev hub shears are reduced by only 2% to 5% while the 4/rev hub moments are even increased by 0% to 2%, resulting in a mere 2% reduction in  $J_1$ . The reduction in the hub loads from the baseline case is still significant: 39% to 44% for 4/rev hub shears and 27%

to 33% for 4/rev hub moments, as illustrated in Figs. 11.5 and 11.6. The objective function  $J_1$  is reduced by 39% from the baseline case (see Table 11.3).

Figures 11.7 and 11.8 show the vibratory hub shears and moments, respectively, corresponding to the second configuration when  $J_2$  is used as the objective function. The 4/rev vertical shear is reduced by 6%, however the 4/rev longitudinal and lateral shears are increased by 3% and 12%, respectively. The 4/rev hub moments are only slightly reduced by 1% to 3% compared to the initial design. The reduction from the baseline is 34% to 40% for 4/rev hub shears and 29% to 35% for 4/rev hub moments, as is evident from Figs. 11.7 and 11.8. Therefore, the 4/rev hub loads for the initial design of the second configuration are already near their minimum. Thus, the primary function of the optimizer was to steer the initial design out of the infeasible region while maintaining the objective function as low as possible.

The objective functions and the corresponding design variables in the baseline, initial and optimum designs for the second configuration are summarized in Table 11.3.

The structural optimization studies for the third blade configuration, which is a stiff-in-plane blade, were conducted without the benefit of the parametric studies which were available for the first two blade configurations. Therefore the initial design was chosen to be identical to the baseline case, i.e.,  $\Lambda_h = \Lambda_v = \Lambda_s = \Lambda_a = 0^\circ$ .

Figures 11.9 and 11.10 show the vibratory hub shears and moments, respectively, corresponding to the third configuration with  $J_1$  as the objective function. The 4/rev hub shears are significantly reduced, by 46% to 67%;

---

**TABLE 11.3**

**Summary of optimization results for the second configuration**

	Baseline	Initial	Optimum
$J_1$ (E-3)	1.546	0.968	0.948
$\Lambda_h$	0.0	5.0	3.85
$\Lambda_v$	0.0	0.0	1.01
$\Lambda_s$	0.0	20.0	27.0
$\Lambda_a$	0.0	0.0	-0.10
$J_2$ (E-4)	4.822	3.047	2.873
$\Lambda_h$	0.0	5.0	0.11
$\Lambda_v$	0.0	0.0	8.54
$\Lambda_s$	0.0	20.0	25.7
$\Lambda_a$	0.0	0.0	3.49

All angles are in degrees.

---

however, the reduction in 4/rev hub moments is only 0% to 5% when compared to the baseline case. The objective function  $J_1$  is reduced by 31% from the baseline case (see Table 11.4). Figures 11.11 and 11.12 depict the vibratory hub shears and moments, respectively, corresponding to the third configuration with  $J_2$  as the objective function. The 4/rev vertical shear achieves an incredible 99.4% reduction from the baseline case, however the 4/rev longitudinal and lateral shears are increased significantly by 119% and 106%, respectively. The 4/rev hub moments are also increased by 17%, 17% and 121% from the baseline case for rolling, pitching and yawing moments, respectively.

The objective functions and the corresponding design variables in the baseline and optimum designs for the third configuration are summarized in Table 11.4.

---

TABLE 11.4

Summary of optimization results for the third configuration

	Initial	Optimum
$J_1$ (E-4)	9.515	6.544
$\Lambda_h$	0.0	-4.67
$\Lambda_v$	0.0	-2.96
$\Lambda_s$	0.0	15.1
$\Lambda_a$	0.0	14.1
$J_2$ (E-4)	4.091	0.026
$\Lambda_h$	0.0	0.75
$\Lambda_v$	0.0	-0.27
$\Lambda_s$	0.0	27.4
$\Lambda_a$	0.0	-5.52

All angles are in degrees.

---

From the three configurations considered in this study, one concludes that in general the combined objective function  $J_1$ , is a better choice than the second objective function  $J_2$ ; for vibration reduction studies for helicopter rotors. One could construct a variety of objective functions by assigning proper weighting factors in Eqs. (7.8) and (7.9). For most cases considered in this study, a typical case of optimization cycle converges in eight to fifteen iterations. The final optimum designs, listed in Tables 11.2-11.4, show that the sweep angle has the most important role among the four design variables considered in the optimization process. Since the combined effect of ply orientation and swept tip

is nonlinear, using the optimizer to select the proper combination of ply orientation, sweep and anhedral angles represents a cost effective approach to avoiding excessively large sweep angles, while enhancing the aeroelastic stability and frequency placement of the blade.

## Chapter XII

### CONCLUDING REMARKS

The aeroelasticity and structural optimization of composite helicopter rotor blades with swept tips has been studied analytically. The aeroelastic behavior was explored using a new analytical model developed in this study, which is capable of predicting the aeroelastic behavior of composite rotor blades with straight and swept tips in hover and in forward flight. This model is based on a moderate deflection theory and is particularly suitable for structural optimization studies due to its computational efficiency.

The hingeless blade was modeled by beam type finite elements. A single finite element was used to model the swept tip. The nonlinear equations of motion for the finite element model were derived using Hamilton's principle. Arbitrary cross-sectional shape, generally anisotropic material behavior, transverse shears and out-of-plane warping were included in the blade model. The cross-sectional properties of the composite blade were calculated by a separate linear, two-dimensional analysis using a suitably modified version of the analysis developed by Kosmatka[56], which is capable of calculating the shear center location and the modulus weighted section constants of an arbitrarily shaped composite cross section. The aerodynamic loads were obtained using Greenberg's theory with a quasi-steady assumption. Implementation of the aerodynamic model into the computer code was based on an implicit formulation such that more refined aerodynamic models can be incorporated in

the analysis to replace the simple theory used in this study without an excessive amount of additional effort. The trim and blade aeroelastic response were solved in a fully coupled manner, which is essential for the accurate modeling of the dynamic behavior of swept-tip rotor blades. In forward flight, the coupled trim-aeroelastic response solution was obtained using the harmonic balance technique, and the linearized stability was determined from Floquet theory.

Detailed studies were conducted on selected single-cell and two-cell composite rotor blades with straight and swept tips to investigate the individual and the combined effect of sweep, anhedral and composite ply orientation on blade response and aeroelastic stability in hover and in forward flight, as well as on the vibratory hub shears and moments in forward flight.

The structural optimization study was conducted by combining the aeroelastic analysis capability developed in this study with the DOT structural optimization package[106] to design composite rotor blades with swept tips for low vibration levels in forward flight, using composite ply orientations in the horizontal and vertical walls, and tip sweep and anhedral angles as design variables. Numerical results for four-bladed hingeless rotors with either a soft-in-plane or a stiff-in-plane configuration and a two-cell composite cross-section were presented.

The main conclusions obtained in this study are summarized below. They should be considered to be indicative of trends within the framework of the assumptions upon which the aeroelastic analysis was based. Also, they are valid primarily for the limited number of configurations studied.

1. The axial degree of freedom in the blade equations of motion must be treated such that the centrifugal force and Coriolis damping effects are properly included.
2. The fundamental rotating frequencies in flap and lag are not sensitive to the ply angle variation. The torsional frequency increases with ply angle initially; but after reaching a maximum value (around  $30^\circ$  in this study), it decreases with further increase in the ply angle. Tip sweep and tip anhedral have negligible influence on the fundamental flap and lag frequencies; while the torsional frequency may increase or decrease with tip sweep.
3. Tip sweep can cause aeroelastic instability due to frequency coalescence between the first torsion and second flap modes. This instability can be removed by appropriate modification of the torsional stiffness of the blade. When frequency coalescence occurs between the first torsion and second lag modes, both tip anhedral and dihedral have a stabilizing effect on the second lag mode.
4. Ply angle variation in composite blades has a significant influence on the stability of the first lag mode both in hover and in forward flight. The combined effect of low thrust condition and certain ply orientations can cause blade instability in the first lag mode in hover.
5. Composite ply orientation has a significant influence on blade torsional response, while flap and lag response of the blade are fairly insensitive to ply angle variation.

6. Variation of composite ply orientation has a pronounced influence on the collective pitch setting while the other trim parameters remain virtually unaffected.
7. Tip anhedral has significant influence on lag response, cyclic cosine and rotor angle of attack.
8. The damping in flap and torsion modes is insensitive to composite ply angle variation if frequency coalescence due to flap-torsion coupling is avoided.
9. The variation of the vibratory hub loads due to changes in composite ply orientation is fairly modest and is less than 30% in most cases. Tip sweep reduces most vibratory hub load components while tip anhedral causes them to increase.
10. The combined effect of swept tip and composite ply orientation cannot be accurately predicted by superposition of the respective individual effects because the problem is inherently nonlinear. However a parametric study is useful for selecting the initial design for the optimization process.
11. Blade instability due to frequency coalescence introduced by swept tip and composite ply orientation can be removed through structural optimization with aeroelastic constraints.
12. The combined sum of the hub shear resultant and hub moment resultant is a better objective function than the 4/rev vertical shear alone for the purpose of helicopter vibration reduction. Selecting 4/rev vertical shear as the objective function can result in remarkable reduction in this

4/rev hub load component, but at the expense of higher vibration level in the other components.

13. Tip sweep has a significant influence on vibratory hub loads and plays an important role in the optimization for vibration reduction. Proper combination of composite ply orientation and tip sweep and anhedral angles, however, can be employed to reduce the need for excessive sweep angles for vibration reduction, while simultaneously improving the aeroelastic stability and frequency placement of the blade.

These conclusions indicate that aeroelastic tailoring of swept tip composite blades, for stability enhancement and vibration reduction, is an area of research which holds remarkable promise.

## REFERENCES

1. Adelman, H.M. and Mantay, W.R., Editors, "Integrated Multidisciplinary Optimization of Rotorcraft: A Plan for Development," NASA TM 101617, May 1989.
2. Bathe, K., Finite Element Procedures in Engineering Analysis , first edition, Prentice-Hall Inc., 1982.
3. Bauchau, O.A., "A Beam Theory for Anisotropic Materials," Journal of Applied Mechanics , Vol. 52, June 1985, pp. 416-422.
4. Bauchau, O.A. and Hong, C.H., "Finite Element Approach to Rotor Blade Modeling," Journal of the American Helicopter Society , Vol. 32, No. 1, Jan. 1987, pp. 60-67.
5. Bauchau, O.A., Coffenberry, B.S. and Rehfield, L.W., "Composite Box Beam Analysis: Theory and Experiments," Journal of Reinforced Plastics and composites , Vol. 6, 1987, pp. 25-35.
6. Bauchau, O.A. and Hong, C.H., "Large Displacement Analysis of Naturally Curved and Twisted Composite Beams," AIAA Journal , Vol. 25, No. 11, November 1987, pp. 1469-1475.
7. Bauchau, O.A. and Hong, C.H., "Nonlinear composite Beam Theory," Journal of Applied Mechanics , Vol. 55, March 1988, pp. 156-163.
8. Benquet, P. and Chopra, I., "Calculated Dynamic Response and Loads for an Advanced Tip Rotor in Forward Flight," Proc. 15th European Rotorcraft Forum, Amsterdam, 1989, pp. 50.1-50.25.
9. Bir, G.S. and Chopra, I., "Aeromechanical Stability of Rotorcraft with Advanced Geometry Blades," AIAA Paper No. 93-1304, Proc. 34th AIAA/ASME/ASCE/AHS/ASC Structures, Structural Dynamics and Materials Conf., La Jolla, CA, April 1993, pp. 38-62.
10. Borri, M. and Merlini, T., "A Large Displacement Formulation for Anisotropic Beam analysis," Meccanica , Vol. 21, 1986, pp. 30-37.
11. Celi, R., "Aeroelasticity and Structural Optimization of Helicopter Rotor Blades with Swept Tips," Ph.D. Dissertation, Mechanical, Aerospace and Nuclear Engineering Department, University of California, Los Angeles, 1987.

12. Celi, R. and Friedmann, P.P., "Aeroelastic Modeling of Swept Tip Rotor Blades Using Finite Elements," Journal of the American Helicopter Society , Vol. 33, No. 2, April 1988, pp. 43-52.
13. Celi, R. and Friedmann, P.P., "Rotor Blade Aeroelasticity in Forward Flight with an Implicit Aerodynamic Formulation," AIAA Journal , Vol. 26, No. 12, 1988, pp. 1425-1433.
14. Celi, R. and Friedmann, P.P., "Structural Optimization with Aeroelastic Constraints of Rotor Blades with Straight and swept Tips," AIAA Journal , Vol. 28, No. 5, 1990, pp. 928-936.
15. Crespo DaSilva, M.R.M. and Hodges, D.H., "Nonlinear Flexure and Torsion of Rotating Beams, with Application to Helicopter Blades - I. Formulation," Vertica , Vol. 10, 1986, pp. 151-169.
16. Crespo DaSilva, M.R.M. and Hodges, D.H., "Nonlinear Flexure and Torsion of Rotating Beams, with Application to Helicopter Blades - II. Results for Hover," Vertica , Vol. 10, 1986, pp. 171-186.
17. Danielson, D.A. and Hodges, D.H., "Nonlinear Beam Kinematics by Decomposition of the Rotation Tensor," Journal of Applied Mechanics , Vol. 54, No. 2, 1987, pp. 258-262.
18. Danielson, D.A. and Hodges, D.H., "A Beam theory for Large Global Rotation, Moderate Local Rotation, and Small Strains," Journal of Applied Mechanics , Vol. 55, March 1988, pp. 179-184.
19. Davis, M.W. and Weller, W.H., "Application of Design Optimization Techniques to Rotor Dynamics Problems," Journal of the American Helicopter Society , Vol 33, No. 3, 1988, pp. 42-50.
20. Davis, M.W. and Weller, W.H., "Helicopter Rotor Dynamics Optimization with Experimental Verification," Journal of Aircraft , Vol 28, No. 1, 1991, pp. 38-48.
21. Dowell, E.H., Traybar, J., And Hodges, D.H., "An Experimental Theoretical Correlation Study of Non-linear Bending and Torsion Deformations of a Cantilever Beam," Journal of Sound and Vibrations , Vol. 50, 1977, pp. 533-544.
22. Fulton, M.V. and Hodges, D.H., "Aeroelastic Stability of Hingeless, Elastically Tailored Rotor Blades in Hover," in Recent Advances in the Structural Dynamic Modeling of Composite Rotor Blades and Thick Composites , ASME AD-Vol. 30, pp. 9-23, ASME Winter Annual Meeting, Nov. 1992.

23. Friedmann, P.P., "Recent Developments in Rotary-Wing Aeroelasticity," Journal of Aircraft , Vol. 14, No. 11, 1977, pp. 1027-1041.
24. Friedmann, P.P., "Formulation and Solution of Rotary-Wing Aeroelastic Stability and Response Problems," Vertica , Vol. 7, No. 2, 1983, pp.101-141.
25. Friedmann, P.P., "Recent Trends in Rotary-Wing Aeroelasticity," Vertica , Vol. 11, No. 1, 1987, pp.139-170.
26. Friedmann, P.P., "Helicopter Rotor Dynamics and Aeroelasticity: Some Key Ideas and Insights," Vertica , Vol. 14, No. 1, 1990, pp. 101-121.
27. Friedmann, P.P. and Straub, F.K., "Application of the Finite Element Method to Rotary-Wing Aeroelasticity," Journal of the American Helicopter Society , Vol. 25, No. 1, 1980, pp. 36-44.
28. Friedmann, P.P., "Helicopter Vibration Reduction Using Structural Optimization with Aeroelastic/Multidisciplinary Constraints - A Survey," Journal of Aircraft , Vol. 28, No. 1, 1991, pp. 8-21.
29. Friedmann, P.P. and Shanthakumaran, P., "Optimum Design of Rotor Blades for Vibration Reduction in Forward Flight," Journal of the American Helicopter Society , Vol. 29, No. 4, 1984, pp. 70-80.
30. Friedmann, P.P., Hammond, C.E. and Woo, T., "Efficient Numerical Treatment of Periodic Systems with Application to Stability Problems," The International Journal of Numerical Methods in Engineering , Vol. 11, July 1977, pp. 1117-1136.
31. Friedmann, P.P., Venkatesan, C. and Yuan, K.A., "Development of a Structural Optimization Capability for the Aeroelastic Tailoring of Composite Rotor Blades with Straight and Swept Tips," AIAA Paper No. 92-4779, Proc. 4th AIAA/USAF/NASA/OAI Symposium on Multidisciplinary Analysis and Optimization, Cleveland, OH, September 1992, pp. 722-748.
32. Friedmann, P.P. and Hodges, D.H., "Rotary-Wing Aeroelasticity with Application to VTOL Vehicles," Chapter 6, in Flight-Vehicle Materials, Structures and Dynamics, Vol. 5 - Structural Dynamics and Aeroelasticity , edited by A.K. Noor and S.L. Venneri, Published by ASME, 1993, pp. 299-391.

33. Friedmann, P.P. and Robinson, L.H., "Influence of Unsteady Aerodynamics on Rotor Blade Aeroelastic Stability and Response," AIAA Journal , Vol. 28, No. 10, 1990, pp. 1806-1812.
34. Ganguli, R. and Chopra, I., "Aeroelastic Optimization of an Advanced Geometry Helicopter Rotor," AIAA Paper No. 92-2360, Proc. 33rd AIAA/ASME/ASCE/AHS/ASC Structures, Structural Dynamics and Materials Conf., Dallas, TX, April 1992, pp. 3072-3085.
35. Ganguli, R. and Chopra, I., "Aeroelastic Optimization of a Helicopter Rotor with Composite Tailoring," Proc. 49th AHS Forum, St. Louis, Missouri, May 1993, pp. 1335-1368.
36. Ganguli, R. and Chopra, I., "Multi-Objective Optimization of a Composite Helicopter Rotor," AIAA Paper No. 94-1420, Proc. 35th AIAA/ASME/ASCE/AHS/ASC Structures, Structural Dynamics and Materials Conf., Hilton Head, SC, April 1994, pp. 892-912.
37. Giavotto, V., Borri, M., Mantegazza, P., Ghiringhelli, G., Carmaschi, V., Maffioli, G.C. and Mussi, F., "Anisotropic Beam Theory and Applications," Computers and Structures , Vol. 16, 1983, pp. 403-413.
38. Greenberg, J.M., "Airfoil in Sinusoidal Motion in a Pulsating Stream," NACA TN-1326, 1947.
39. Haftka, R.T. and Gurdal, Z., Elements of Structural Optimization , 3rd Edition, Kluwer Academic Publishers, 1992.
40. Hodges, D.H. and Dowell, E.H., "Nonlinear Equations of Motion for the Elastic Bending and Torsion of Twisted Nonuniform Rotor Blades," NASA TN D-7818, December 1974.
41. Hodges, D.H. and Ormiston, R.A., "Stability of Elastic Bending and Torsion of Uniform Cantilever Rotor Blades in Hover with Variable Structural Coupling," NASA TN D-8192, 1976.
42. Hodges, D.H., "Torsion of Pretwisted Beams Due to Axial Loading," Journal of Applied Mechanics , Vol. 47, June 1980, pp. 393-397.
43. Hodges, D.H., "Nonlinear Equations for Dynamics of Pretwisted Beams Undergoing Small Strains and Large Rotations," NASA TP-2470, May 1985.

44. Hodges, D.H., Hopkins, A.K., Kunz, D.L. and Hinnant, H.E., "Introduction to GRASP - General Rotorcraft Aeromechanical Stability Program - A Modern Approach to Rotorcraft Modeling," Proc. 42nd Annual Forum of the American Helicopter Society, Washington D.C., June 2-4, 1986, pp. 739-756.
45. Hodges, D.H., "Review of Composite Rotor Blade Modeling," AIAA Journal , Vol. 28, No. 3, 1990, pp. 561-564.
46. Hodges, D.H., "A Mixed Variational Formulation Based on Exact Intrinsic Equations for Dynamics of Moving Beams," International Journal of Solids and Structures , Vol. 26, No. 11, 1990, pp. 1253-1273.
47. Hodges, R.V., Nixon, M.W. and Rehfield, L.W., "Comparison of Composite Rotor Blade Models: A Coupled-Beam Analysis and An MSC/NASTRAN Finite Element Model," NASA TM 89024, 1987.
48. Hong, C.H., and Chopra, I., "Aeroelastic Stability Analysis of a Composite Rotor Blade," Journal of the American Helicopter Society , Vol. 30, No. 2, 1985, pp. 57-67.
49. Hong, C.H., and Chopra, I., "Aeroelastic Stability of a Composite Bearingless Rotor Blade," Journal of the American Helicopter Society , Vol. 31, No. 4, 1986, pp. 29-35.
50. Hong, C.H., "Finite Element Approach to the Dynamic Analysis of Composite Helicopter Blades," Ph.D. Dissertation, Rensselaer Polytechnic Institute, Troy, New York, 1987.
51. Houbolt, J.C., and Brooks, G.W., "Differential Equations of Motion for Combined Flapwise Bending, Chordwise Bending, and Torsion of Twisted Nonuniform Rotor Blades," NACA Report 1346, 1958.
52. Johnson, W., Helicopter Theory , Princeton University Press, 1980.
53. Jones, R.M., Mechanics of Composite Materials , first edition, McGraw-Hill Book Co., New York, N.Y., 1975.
54. Kaza, K.R. and Kvaternik, R.G., "Nonlinear Aeroelastic Equations for Combined Flapwise Bending, Chordwise Bending, Torsion and Extension of Twisted Non-Uniform Rotor Blades in Forward Flight," NASA TM-74059, 1977.
55. Kim, K.C., and Chopra, I., "Aeroelastic Analysis of Swept, Anhedral, and Tapered Tip Rotor Blades," Journal of the American Helicopter Society , Vol. 37, No. 1, 1992, pp. 15-30.

56. Kosmatka, J.B., "Structural Dynamic Modeling of Advanced Composite Propellers by the Finite Element Method," Ph.D. Dissertation, Mechanical, Aerospace and Nuclear Engineering Department, University of California, Los Angeles, 1986.
57. Kosmatka, J.B. and Friedmann, P.P., "Vibration Analysis of Composite Turbopropellers Using a Nonlinear Beam-Type Finite Element Approach," AIAA Journal , Vol. 27, No. 11, 1989, pp. 1606-1614.
58. Lee, S.W. and Kim, Y.H., "A New Approach to the Finite Element Modeling of Beams," International Journal for Numerical Methods in Engineering , Vol.24, 1987, pp. 2327-2341.
59. Lim, J.W. and Chopra, I., "Response and Hub Loads Sensitivity Analysis of a Helicopter Rotor," AIAA Journal , Vol. 28, No. 1, 1990, pp. 75-82.
60. Lim, J.W. and Chopra, I., "Stability Sensitivity Analysis of a Helicopter Rotor," AIAA Journal , Vol. 28, No. 6, 1990, pp. 1089-1097.
61. Lim, J.W. and Chopra, I., "Aceroelastic Optimization of a Helicopter Rotor," Journal of the American Helicopter Society , Vol. 34, No. 1, 1989, pp. 52-62.
62. Lim, J.W. and Chopra, I., "Aceroelastic Optimization of a Helicopter Rotor Using an Efficient Sensitivity Analysis," Journal of Aircraft , Vol. 28, No. 1, 1991, pp. 29-37.
63. Mansfield, E.H. and Sobey, A.J., "The fiber Composite Helicopter Blade - Part I: Stiffness Properties - Part II: Prospects for Aeroelastic Tailoring," Aeronautical Quarterly , Vol. 30, 1979, pp. 413-449.
64. Millott, T.A., "Vibration Reduction in Helicopter Rotors Using an Actively Controlled Partial Span Trailing Edge Flap Located on the Blade," Ph.D. Dissertation, Mechanical, Aerospace and Nuclear Engineering Department, University of California, Los Angeles, 1993.
65. Millott, T.A. and Friedmann, P.P., "Vibration Reduction in Helicopter Rotors Using an Actively Controlled Partial Span Trailing Edge Flap Located on the Blade," NASA CR-4611, June 1994.
66. Minguet, P. and Dugundji, J., "Experiments and Analysis for Composite Blades Under Large Deflections: Part I - Static Behavior," AIAA Journal , Vol. 28, No. 9, 1990, pp. 1573-1579.

67. Minguet, P. and Dugundji, J., "Experiments and Analysis for Composite Blades Under Large Deflections: Part 2 - Dynamic Behavior," AIAA Journal , Vol. 28, No. 9, 1990, pp. 1580-1588.
68. Nickell, R.E., and Secor, G.A., "Convergence of Consistently Derived Timoshenko Beam Finite Elements," International Journal for Numerical Methods in Engineering , Vol. 5, 1972, pp. 243-253.
69. Nixon, M.W., "Extension-Twist Coupling of Composite Circular Tubes with Application to Tilt Rotor Blade Design," AIAA Paper No. 87-0772, Proc. 28th AIAA/ASME/ASCE/AHS Structures, Structural Dynamics and Materials Conf., Monterey, CA, 1987, pp. 295-303.
70. Ormiston, R.A., "Investigation of Hingeless Rotor Stability," Vertica , Vol. 7, 1983, pp.143-181.
71. Ormiston, R.A., Warmbrodt, W.G., Hodges, D.H., and Peters, D.A., "Survey of Army/NASA Rotorcraft Aeroelastic Stability Research," NASA TM-101026, October 1988.
72. Panda, B. and Chopra, I., "Dynamics of Composite Rotor Blades in Forward Flight," Vertica , Vol. 11, No. 1/2, 1987, pp 187-209.
73. Panda, B., "Technical Note: Assembly of Moderate-Rotation Finite Elements Used in Helicopter Rotor Dynamics," Journal of the American Helicopter Society , Vol. 32, No. 4, 1987, pp. 63-69.
74. Peters, D.A., Rossow, M.P., Korn, A. and Ko, T., "Design of Helicopter Rotor Blades for Optimum Dynamic Characteristics," Computers and Mathematics with Applications , Vol. 12A, No. 1, 1986, pp. 85-109.
75. Rehfield, L.W., "Design Analysis Methodology for Composite Rotor Blades," Presented at the 7th DoD/NASA Conf. on Fibrous Composites in Structural Design, Denver, CO, June 17-20, 1985, AFWAL-TR-85-3094, pp. (V(a)-1)-(V(a)-15).
76. Rosen, A., and Friedmann, P.P., "Nonlinear Equations of Equilibrium for Elastic Helicopter or Wind Turbine Blades Undergoing Moderate Deflection," NASA CR-159478, October 1978.
77. Rosen, A., and Friedmann, P.P., "The Nonlinear Behavior of Elastic Slender Straight Beams Undergoing Small Strains and Moderate Rotations," Journal of Applied Mechanics , Vol. 46, March 1979, pp. 161-168.

78. Rosen, A., Loewy, R.G. and Mathew, M.B., "Nonlinear Analysis of Pretwisted Rods Using Principal Curvature Transformation - Part I: Theoretical derivation," AIAA Journal , Vol.25, No. 3, 1987, pp. 470-478.
79. Rosen, A., Loewy, R.G. and Mathew, M.B., "Nonlinear Dynamics of Slender Rods," AIAA Journal , Vol.25, No. 4, 1987, pp. 611-619.
80. Schmit, L.A. and Miura, H., "Approximation Concepts for Efficient Structural Synthesis," NASA CR-2552, 1976.
81. Shamie, J., and Friedmann, P.P., "Effect of Moderate Deflections on the Aeroelastic Stability of a Rotor Blade in Forward Flight," Proc. 3rd European Rotorcraft and Powered Lift Aircraft Forum ", Aix-en-Provence, 1977, pp. 24.1-24.37.
82. Shampine, L.F. and Gordon, M.K., Computer Solution of Ordinary differential Equations-The Initial Value Problem , W.H. Freeman and Co., San Francisco, CA, 1975.
83. Sivaneri, N.T., and Chopra, I., "Dynamic Stability of a Rotor Blade Using Finite Element Analysis," AIAA Journal , Vol. 20, No. 5, 1982, pp. 716-723.
84. Smith, E.C. and Chopra, I., "Aeroelastic Response and Blade Loads of a Composite Rotor in Forward Flight," AIAA Paper No. 92-2466, Proc. 33rd AIAA/ASME/ASCE/AHS/ASC Structures, Structural Dynamics and Materials Conf., Dallas, TX, April 1992, pp. 1996-2014.
85. Smith, E.C. and Chopra, I., "Formulation and Evaluation of an Analytical Model for Composite Box Beams," Journal of the American Helicopter Society , Vol. 36, No. 3, 1991, pp. 23-35.
86. Staley, J.A., "Validation of Rotorcraft Flight Simulation Program Through Correlation with Flight Data for Soft-in-plane Hingeless Rotors," USAAMRDL-TR-75-50, January 1976.
87. Stemple, A.D. and Lee, S.W., "Finite Element Model for Composite Beams with Arbitrary Cross-Sectional Warping," AIAA Journal , Vol. 26, No. 12, 1988, pp. 1512-1520.
88. Stemple, A.D. and Lee, S.W., "Large Deflection Static and Dynamic Finite Element Analysis of Composite Beams with Arbitrary Cross-Sectional Warping," AIAA Paper 89-1363-CP, Proc. 30th AIAA/ASME/ASCE/AHS/ASC Structures, Structural Dynamics and Materials Conf., Mobile, AL, April 1989, pp.1788-1798.

89. Straub, F.K., and Friedmann, P.P., "A Galerkin Type Finite Element for Rotary-Wing Aeroelasticity in Hover and Forward Flight," Vertica , Vol. 5, 1981, pp. 75-98.
90. Tarzanin, F.J. Jr., and Vlaminck, R.R., "Investigation of the Effect of Blade Sweep on Rotor Vibratory Loads," NASA CR-166526, October 1983.
91. Tessler, A., and Dong, S.B., "On a Hierarchy of Conforming Timoshenko Beam Elements," Computers & Structures , Vol. 14, No. 3-4, 1981, pp. 335-344.
92. Thomas, D.L., Wilson, J.M., and Wilson, R.R., "Timoshenko Beam Finite Elements," Journal of Sound and Vibrations , Vol. 31, 1973, pp. 315-330.
93. Thomas, J., and Abbas, B.A.H., "Finite Element Model for Dynamic Analysis of Timoshenko Beam," Journal of Sound and Vibrations , Vol. 41, 1975, pp. 291-299.
94. Timoshenko, S.P. and Goodier, J.N., Theory of Elasticity , 3rd edition, McGraw-Hill Book Co., 1970.
95. Tsai, S.W. and Hahn, H.T., Introduction to Composite Materials , Technomic Publishing Co., 1980.
96. Venkatesan, C., Friedmann, P.P. and Yuan, K.A., "A New Sensitivity Analysis for Structural Optimization of Composite Rotor Blades," Mathematical & Computer Modelling , Vol. 19, No. 3/4, 1994, pp. 1-25.
97. Washizu, K., "Considerations on a Naturally Curved and Twisted Slender Beam," Journal of Mathematics and Physics , Vol. 43, No. 2, June 1964, pp. 111-116.
98. Washizu, K., Variational Methods in Elasticity and Plasticity , 3rd edition, Pergamon Press, 1980.
99. Weller, W.H. and Davis, M.W., "Wind Tunnel Tests of Helicopter Blade Designs Optimized for Minimum Vibration," Journal of the American Helicopter Society , Vol. 34, No. 3, 1989, pp. 40-50.
100. Wempner, G., Mechanics of Solids with Application to Thin Bodies , Sijthoff & Noordhoff, 1981.

101. Wörndle, R., "Calculation of the Cross Section Properties and the Shear Stresses of Composite Rotor Blades," Vertica , Vol. 6, 1982, pp. 111-129.
102. Young, D.K. and Tarzanin, F.J., "Structural Optimization and Mach Scale Test Validation of a Low Vibration Rotor," Proc. 47th Annual Forum of the American Helicopter Society, Phoenix, AZ, May 1991, pp.955-968.
103. Yuan, K.A., Friedmann, P.P. and Venkatesan, C., "A New Aeroelastic Model for Composite Rotor Blades with Straight and Swept Tips," AIAA Paper No. 92-2259, Proc. 33rd AIAA/ASME/ASCE/AHS/ASC Structures, Structural Dynamics and Materials Conf., Dallas, TX, April 1992, pp. 1371-1390.
104. Yuan, K.A., Venkatesan, C., and Friedmann, P.P., "Structural Dynamic Model of Composite Rotor Blades Undergoing Moderate Deflections," in Recent Advances in the Structural Dynamic Modeling of Composite Rotor Blades and Thick Composites , ASME AD-Vol. 30, pp. 127-155, ASME Winter Annual Meeting, November 1992.
105. Zienkiewicz, O.C., The Finite Element Method , McGraw-Hill Book Co., New York, N.Y., 1977.
106. \_\_\_\_\_ , "DOT: User's Manual," , version 4.0, VMA Engineering, 1993.
107. \_\_\_\_\_ , "IMSL Math/Library : User's Manual," IMSL Inc., Houston, Texas, 1987.
108. \_\_\_\_\_ , "MACSYMA: Reference Manual," Symbolics Inc., June 1986.

## **FIGURES**

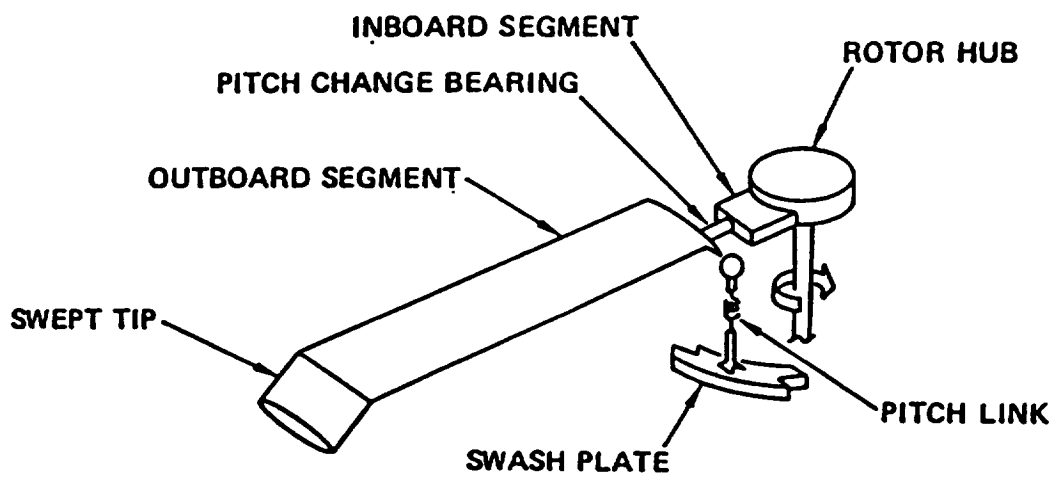


Figure 1.1: Rotor blade with tip sweep and anhedral

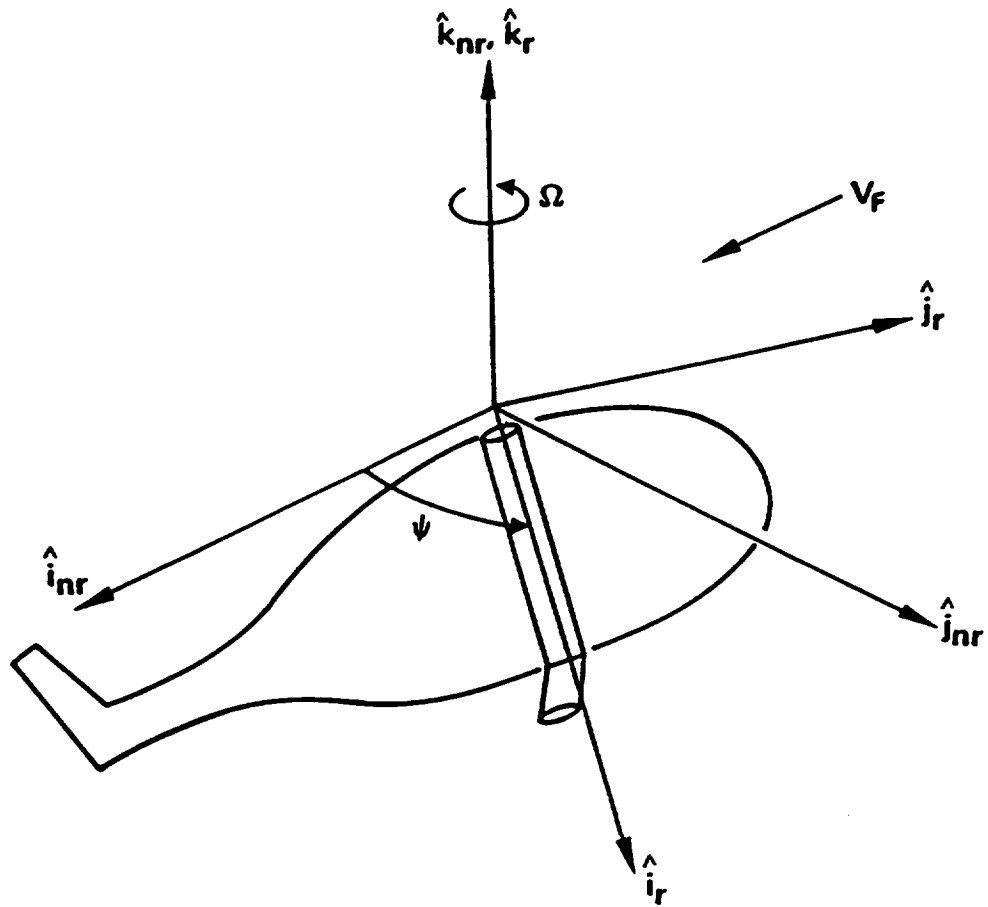


Figure 2.1: Nonrotating, hub-fixed coordinate system and rotating, hub-fixed coordinate system

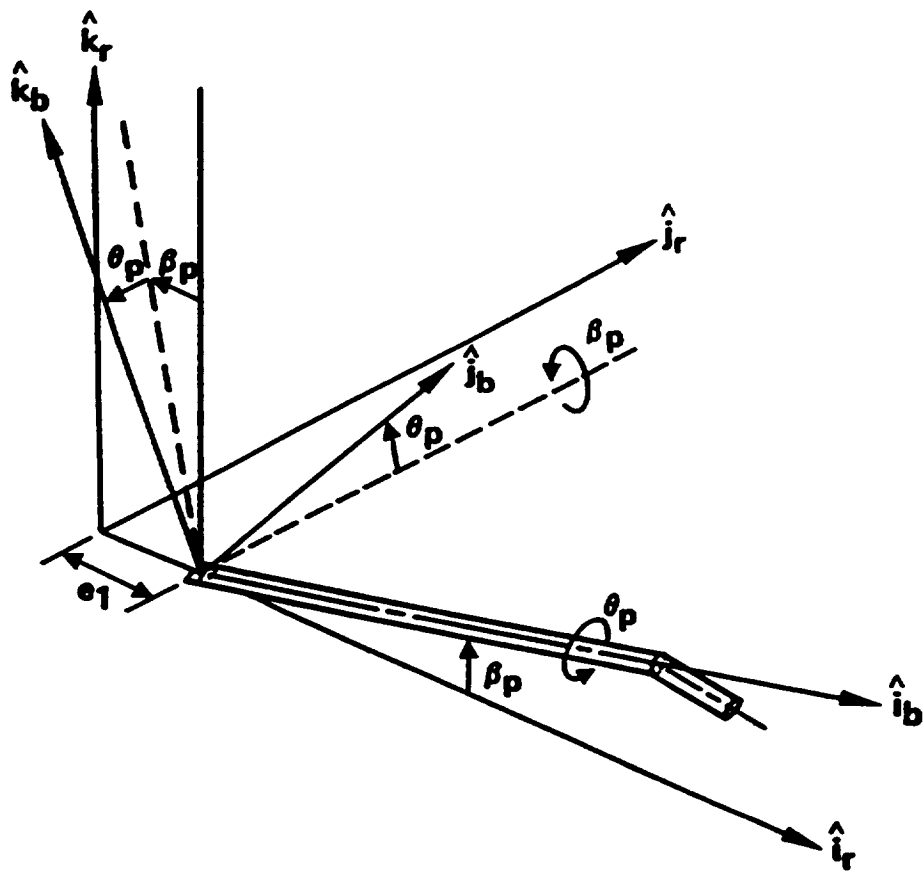


Figure 2.2: Precone, pitched, blade-fixed coordinate system

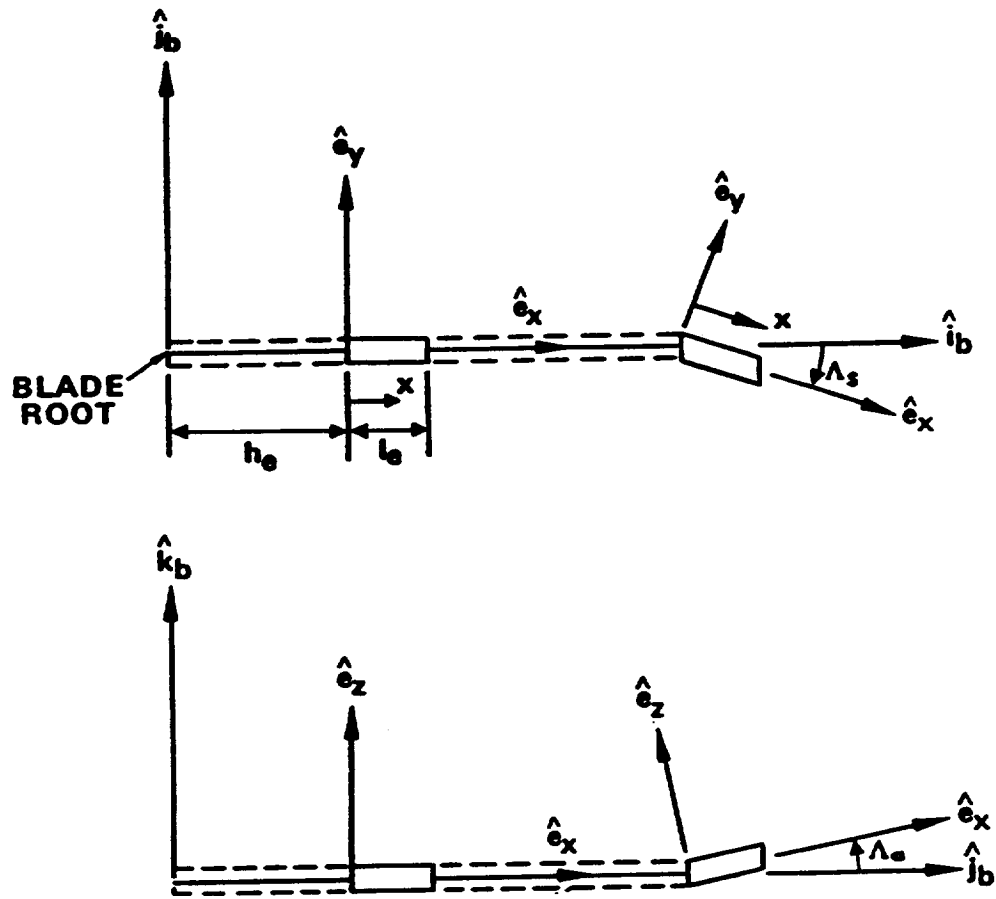


Figure 2.3: Undeformed element coordinate system

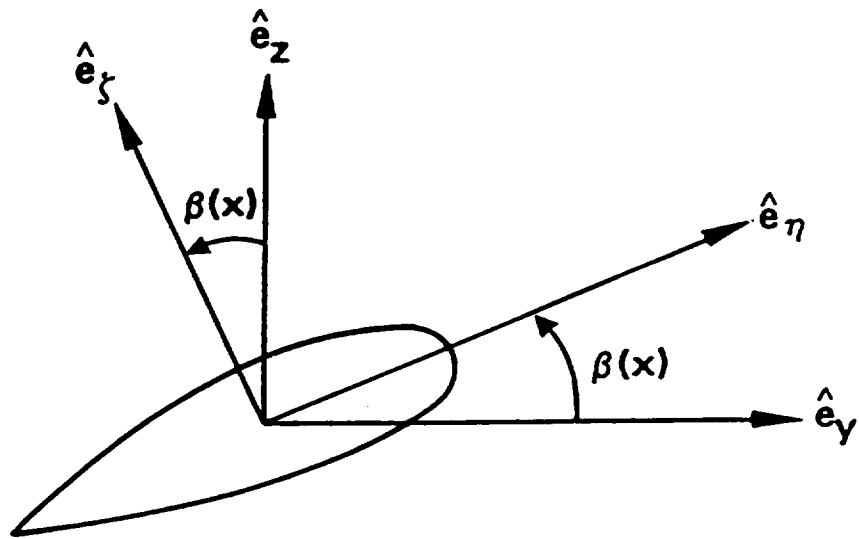


Figure 2.4: Undeformed curvilinear coordinate system

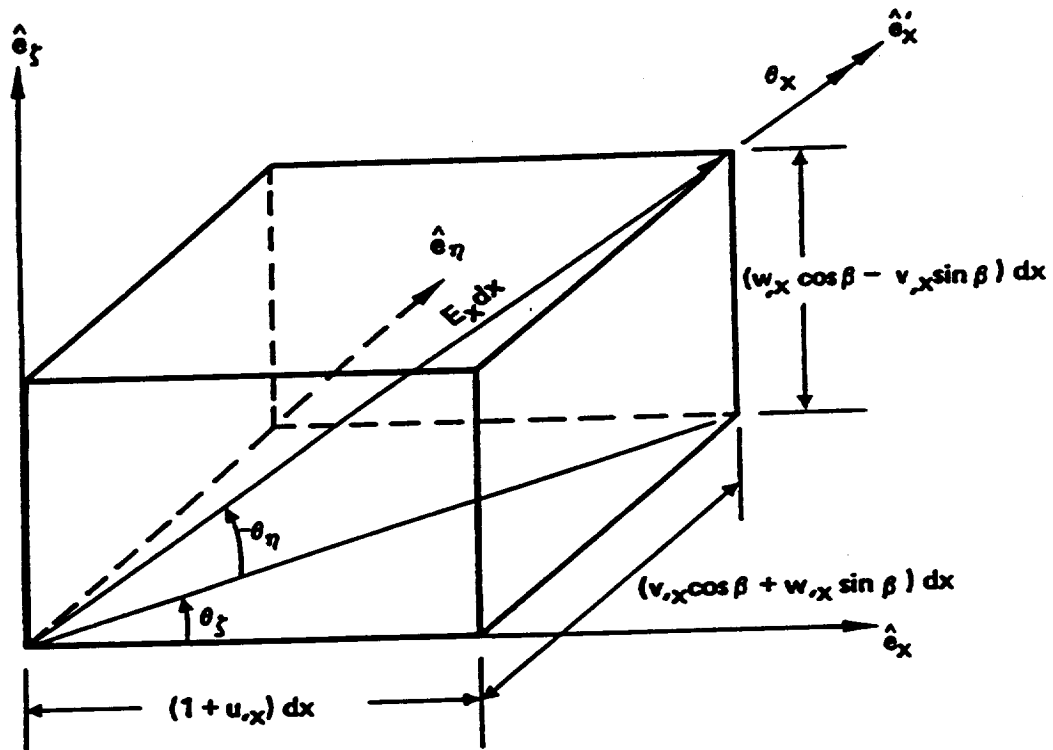


Figure 3.1: Deformation sequence and Euler angles

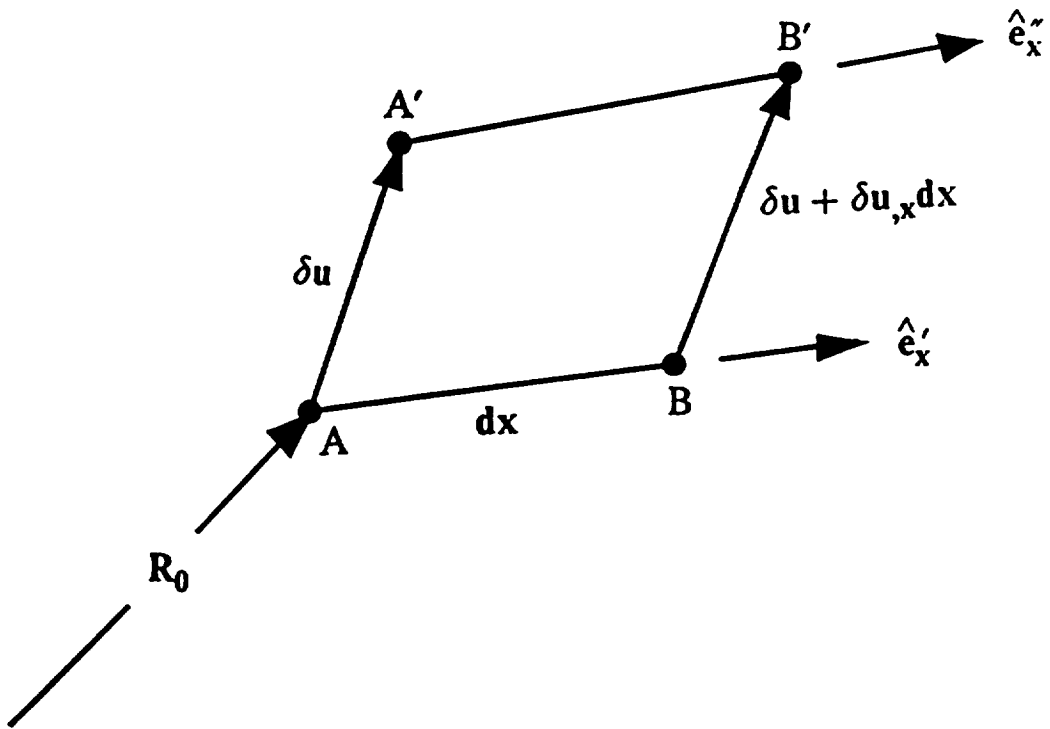


Figure 4.1: Motion of an element on the deformed elastic axis during the virtual displacement

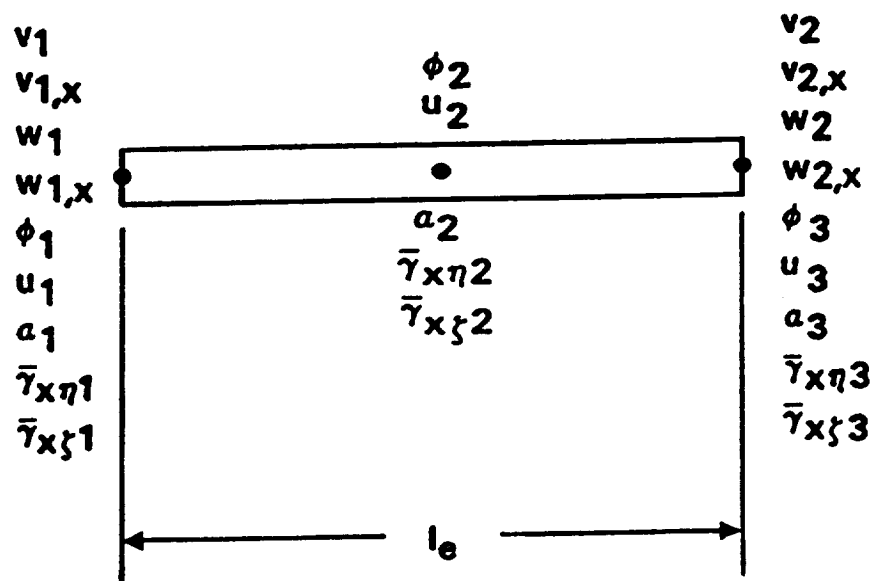


Figure 4.2: Finite element nodal degrees of freedom

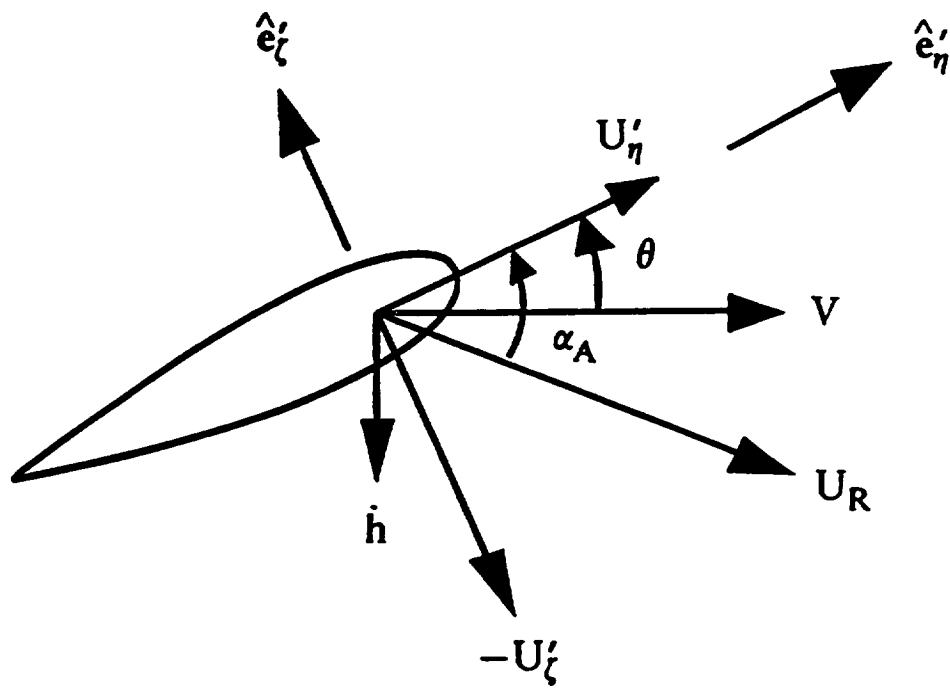


Figure 5.1: Components of blade velocity relative to the air

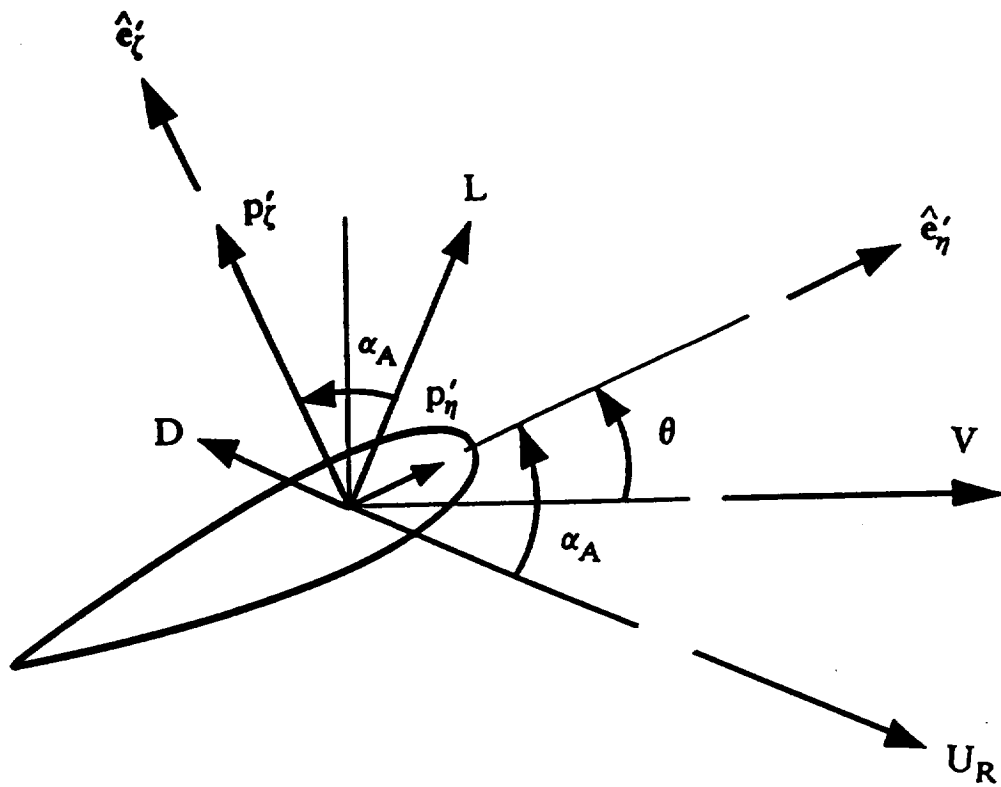


Figure 5.2: Components of aerodynamic force acting on the blade

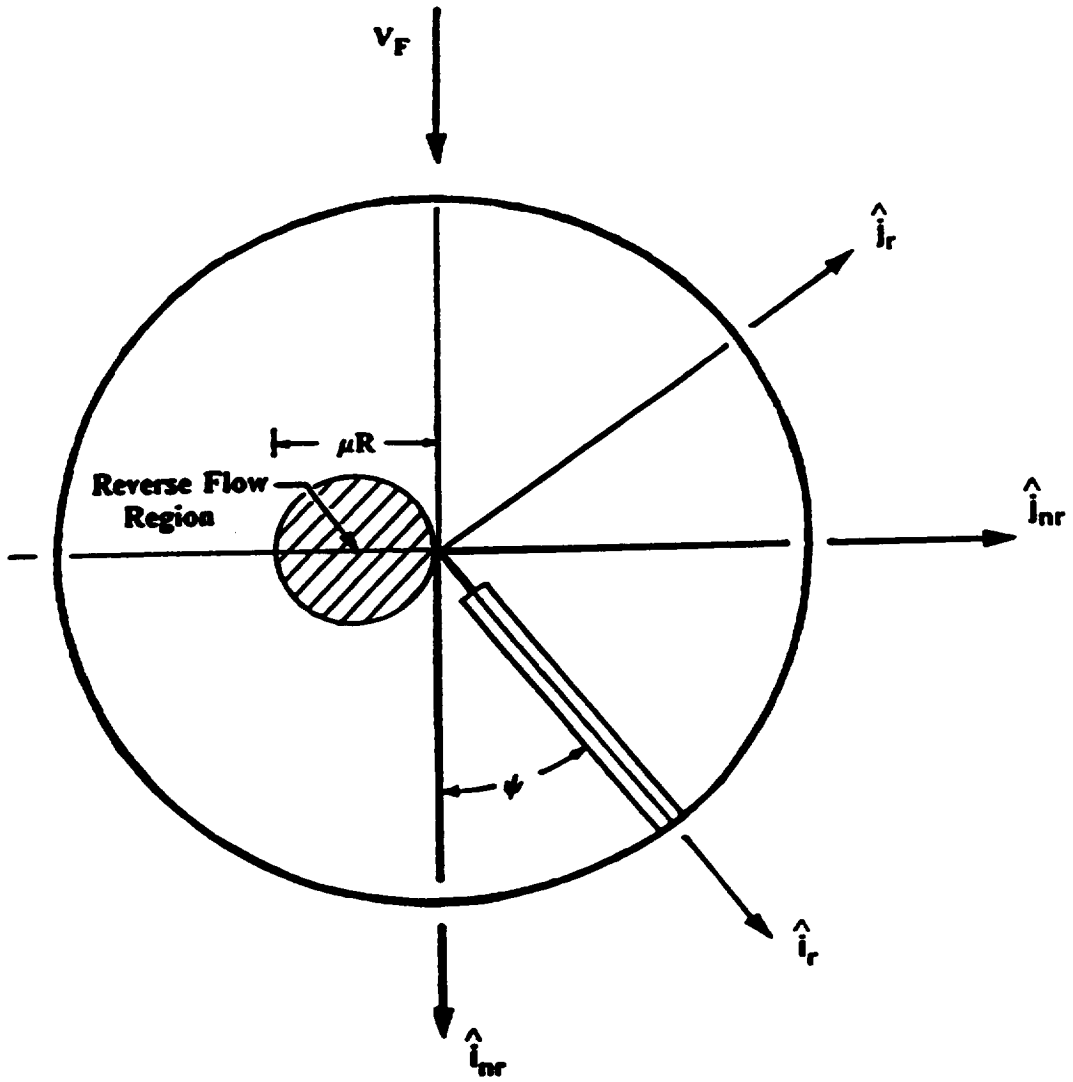


Figure 5.3: Reverse flow region

$O_H$ - Hub Center

C.G.- Fuselage Center of Mass

A.C.- Aerodynamic Drag Center of the Fuselage

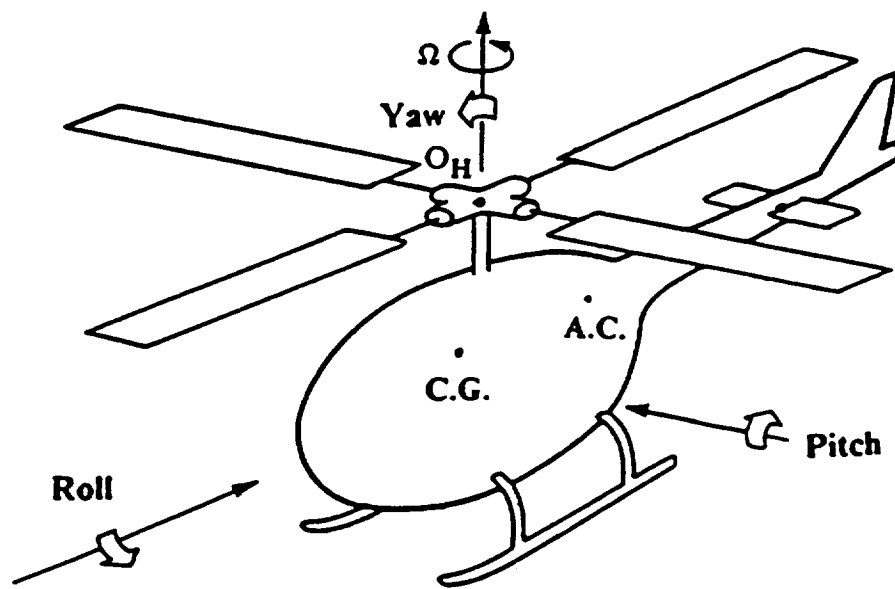


Figure 6.1: Schematic of a four-bladed helicopter

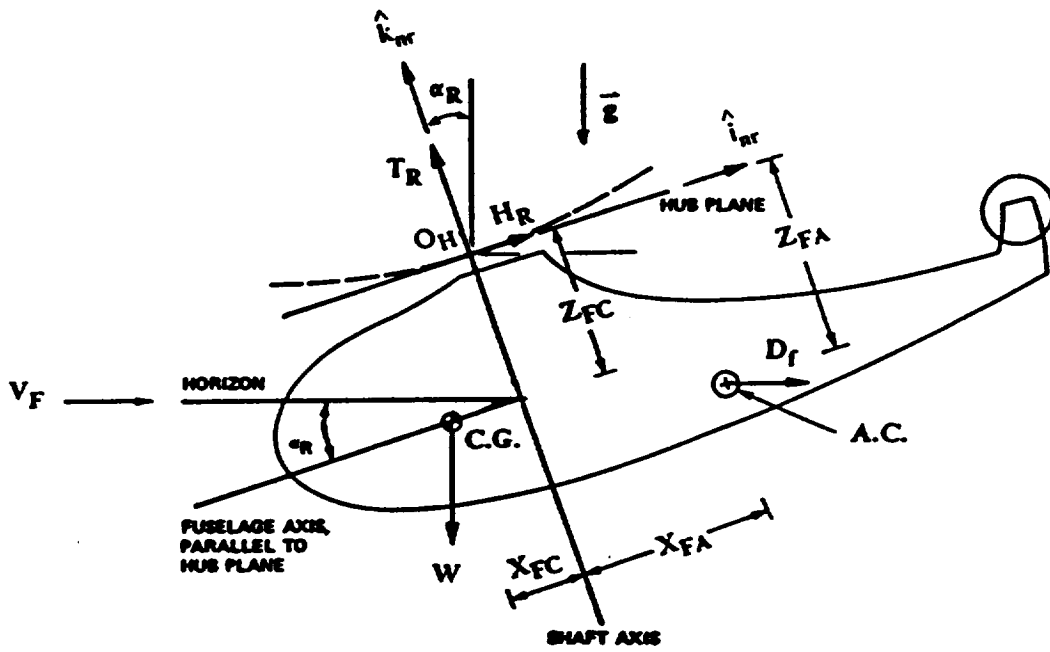


Figure 6.2: Forces on the helicopter in steady, level flight

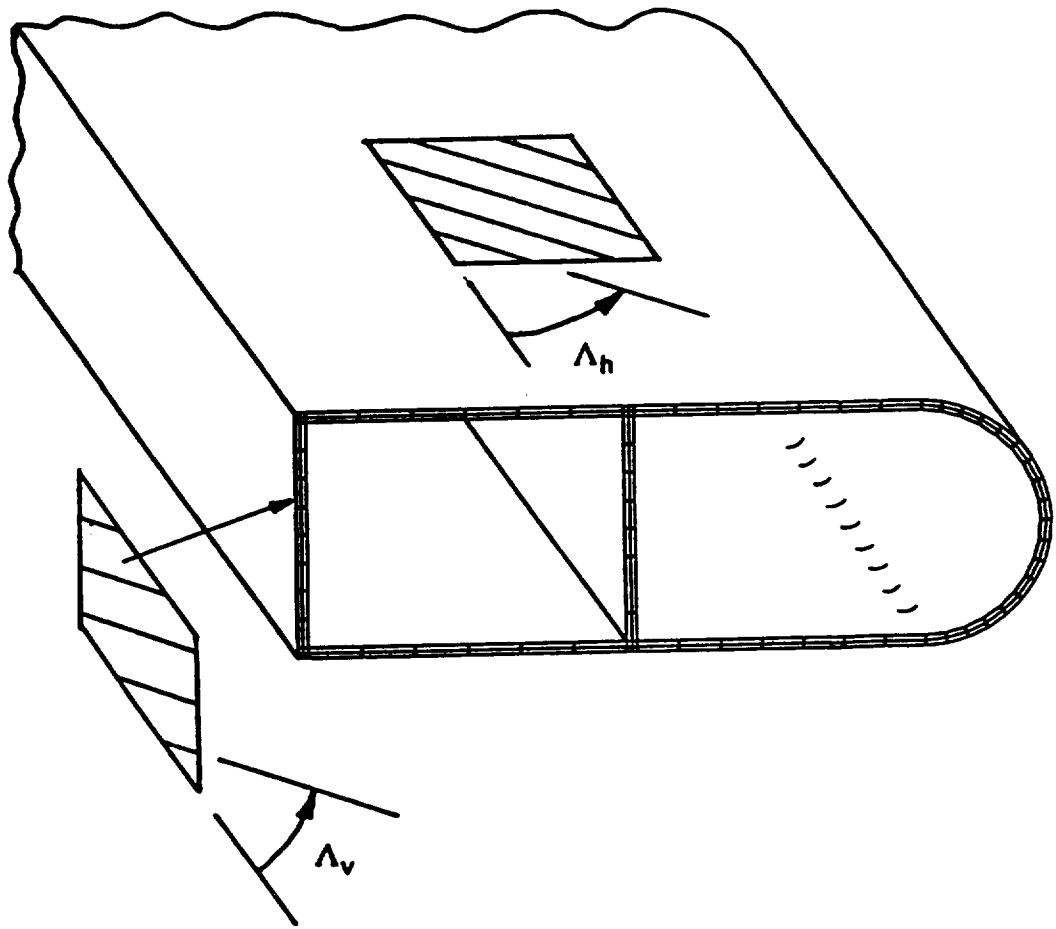


Figure 7.1: Finite element model for two-cell composite cross section

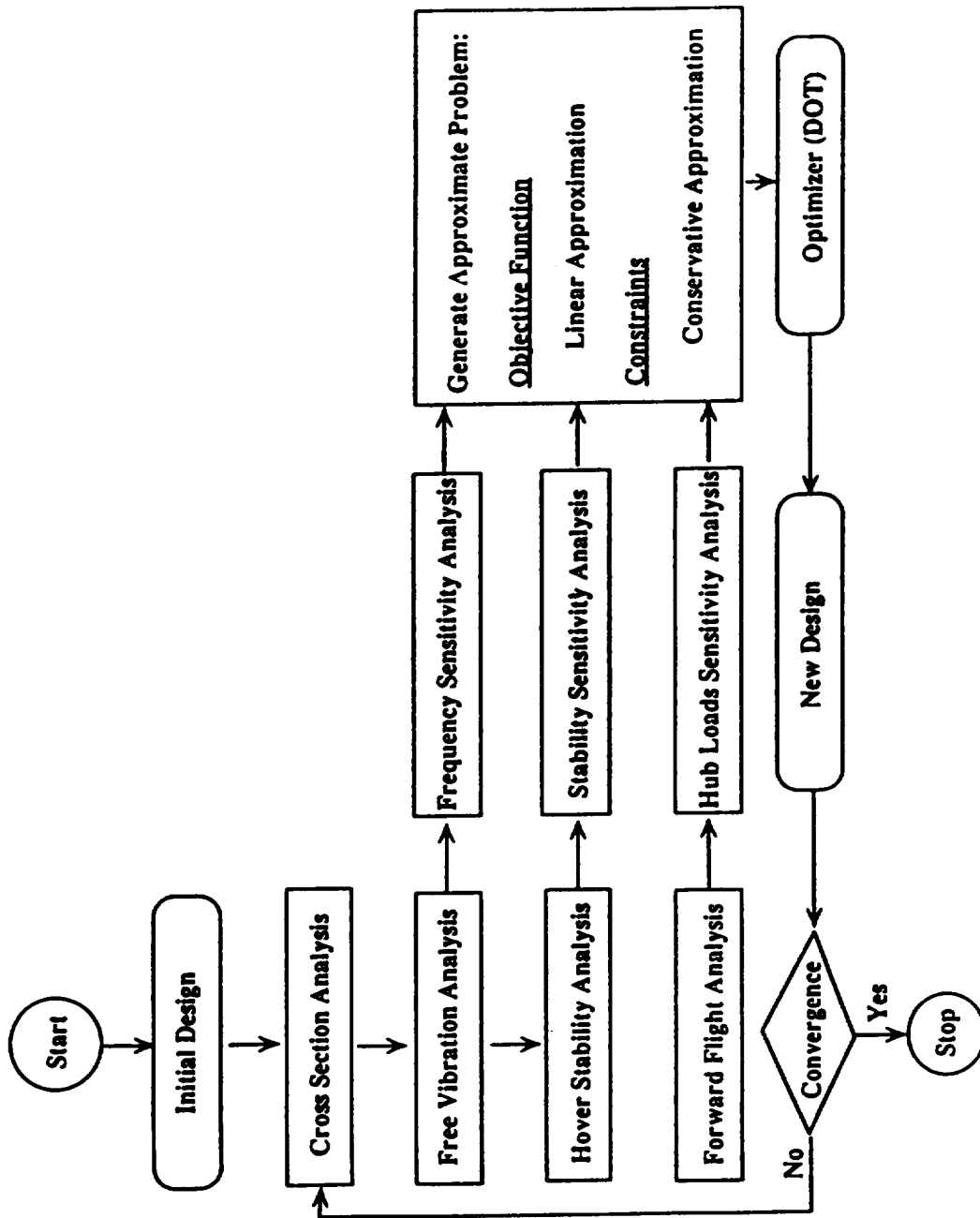


Figure 7.2: Organization of the optimization process

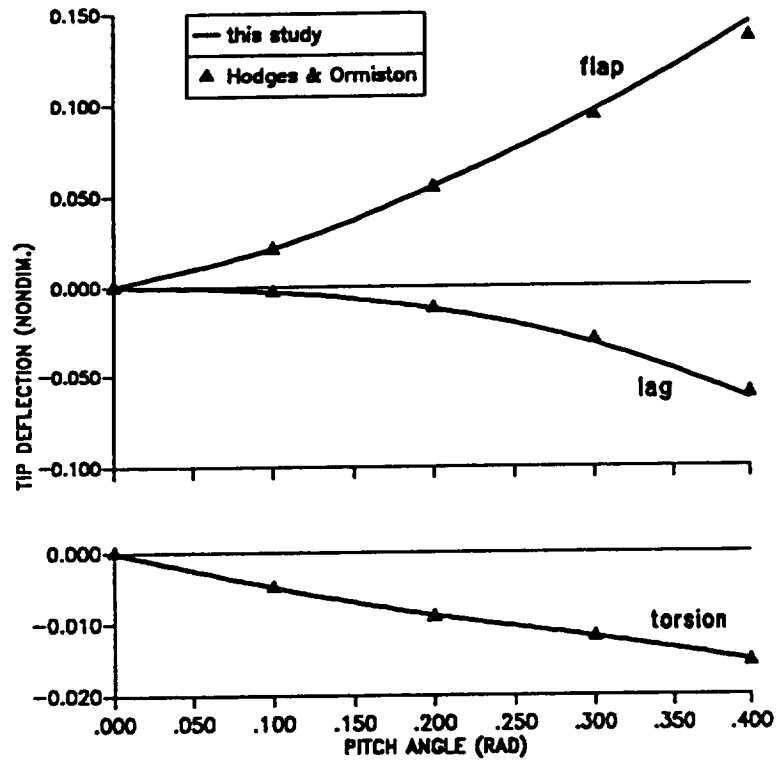


Figure 8.1: Nonlinear equilibrium position of isotropic blade in hover, as a function of blade collective pitch.

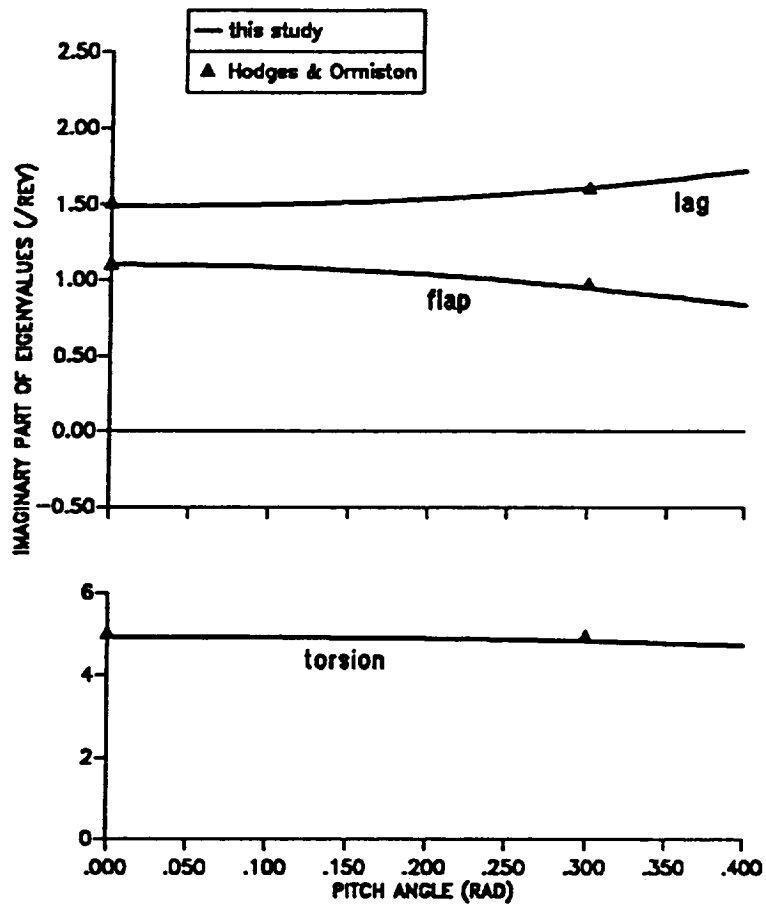


Figure 8.2: Imaginary part of hover eigenvalues of isotropic blade, as a function of blade collective pitch.

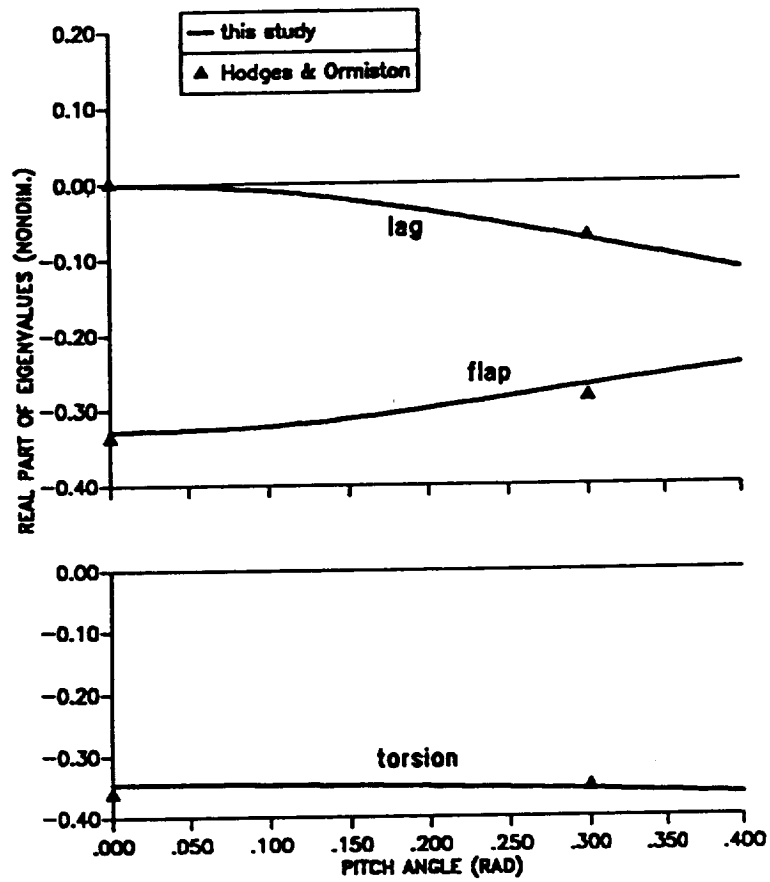


Figure 8.3: Real part of hover eigenvalues of isotropic blade, as a function of blade collective pitch.

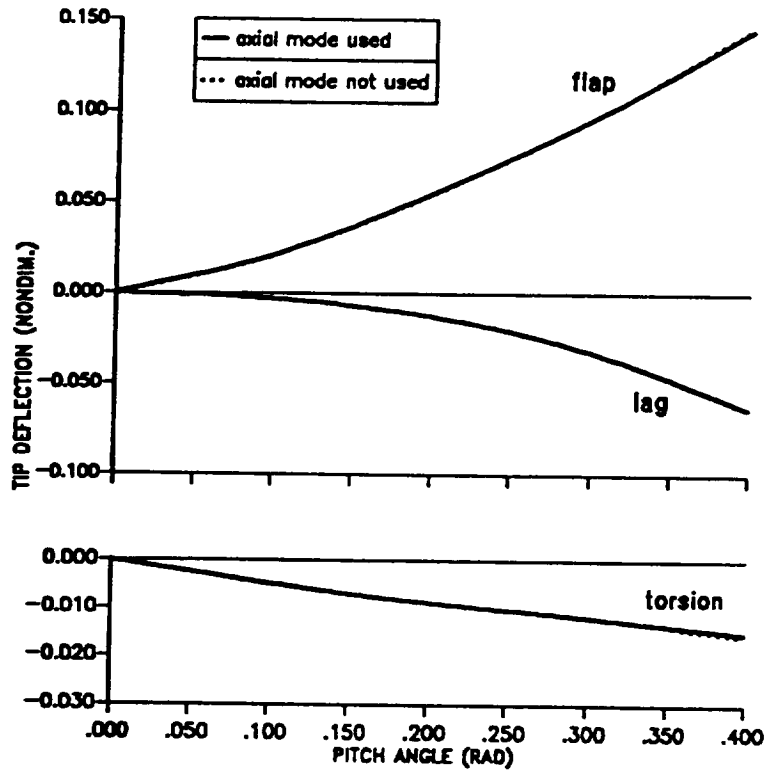


Figure 8.4: Effect of axial mode on the nonlinear equilibrium position of isotropic blade in hover. Analysis with substitution.

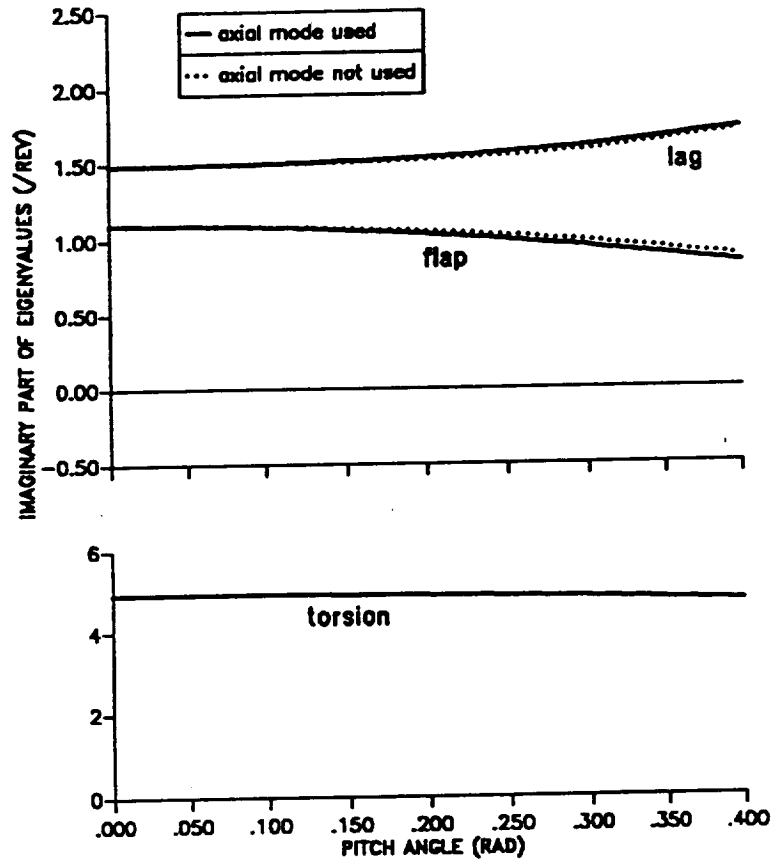


Figure 8.5: Effect of axial mode on the imaginary part of hover eigenvalues of isotropic blade. Analysis with substitution.

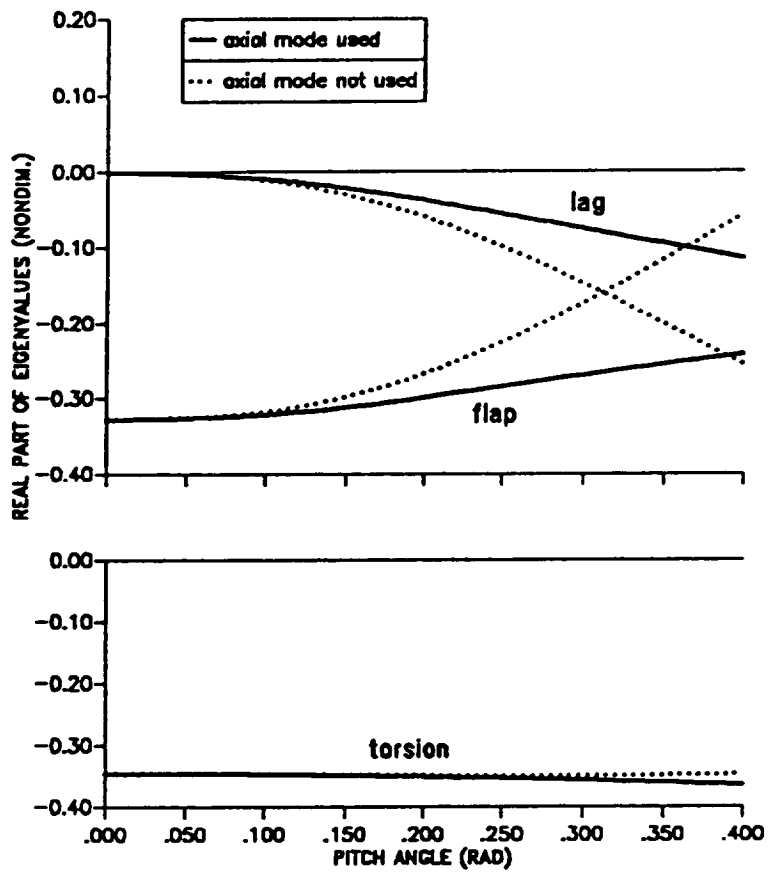


Figure 8.6: Effect of axial mode on the real part of hover eigenvalues of isotropic blade. Analysis with substitution.

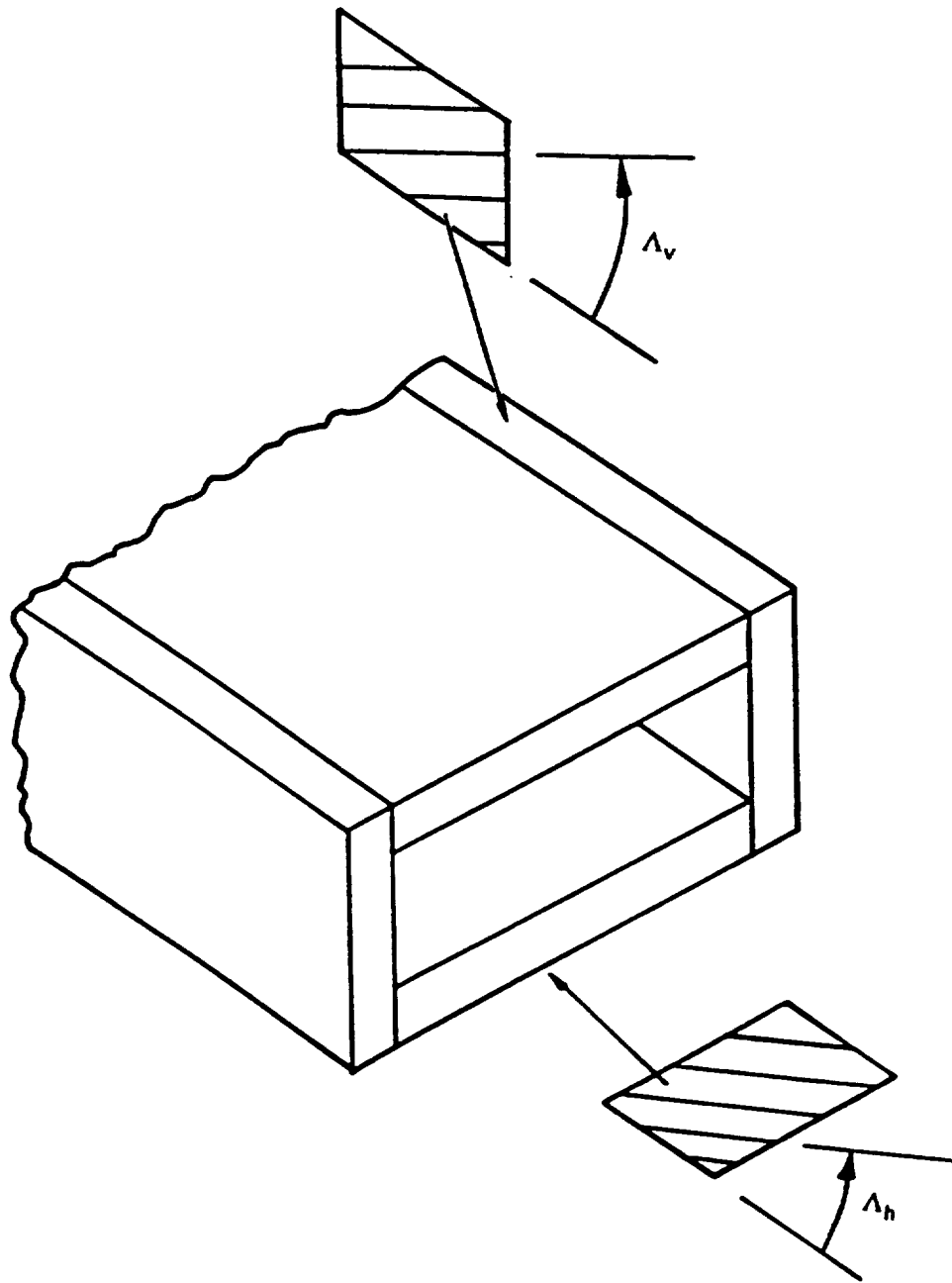


Figure 8.7: Single-cell composite rectangular box beam

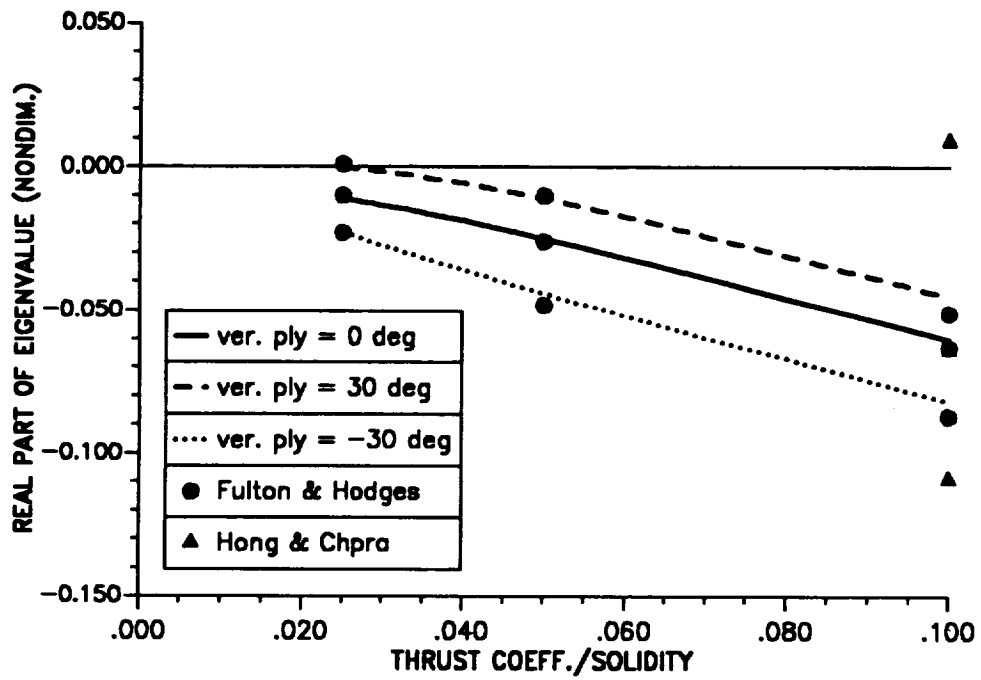


Figure 8.8: Real part of hover eigenvalues for single-cell composite blade as a function of (thrust coefficient/solidity).

## ISOTROPIC BLADE, SOFT-IN-PLANE

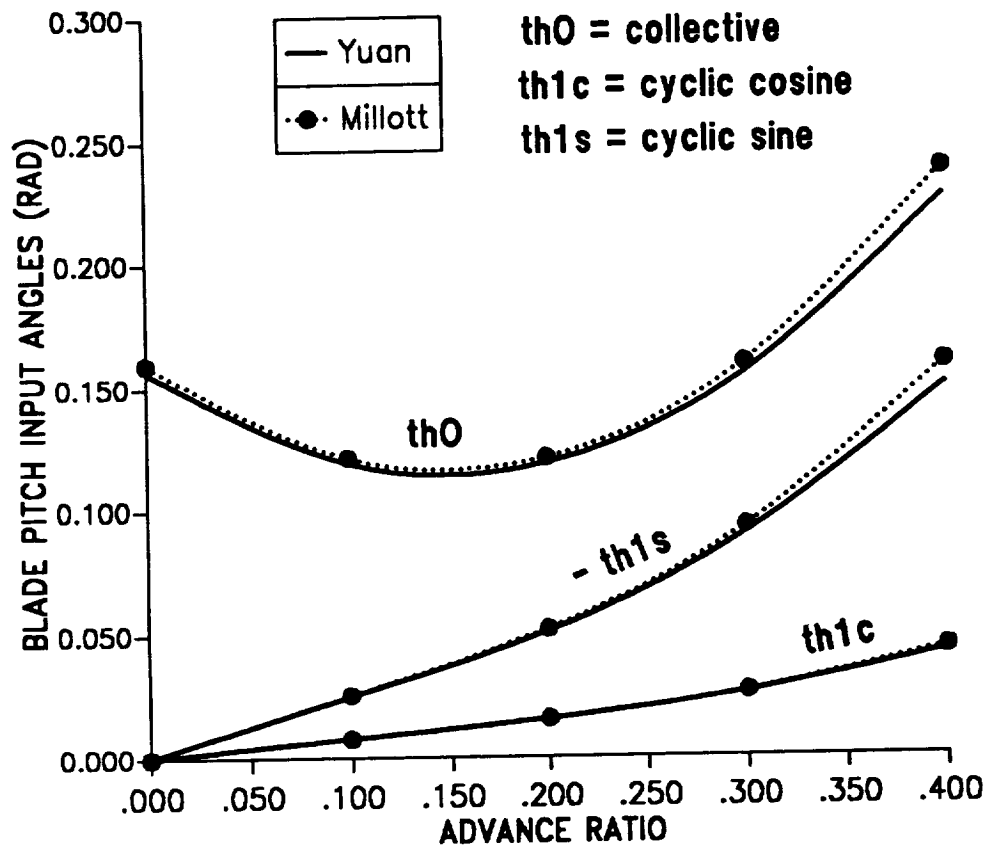


Figure 8.9: Trim variables for soft-in-plane isotropic blade in forward flight; pitch setting.

### ISOTROPIC BLADE, SOFT-IN-PLANE

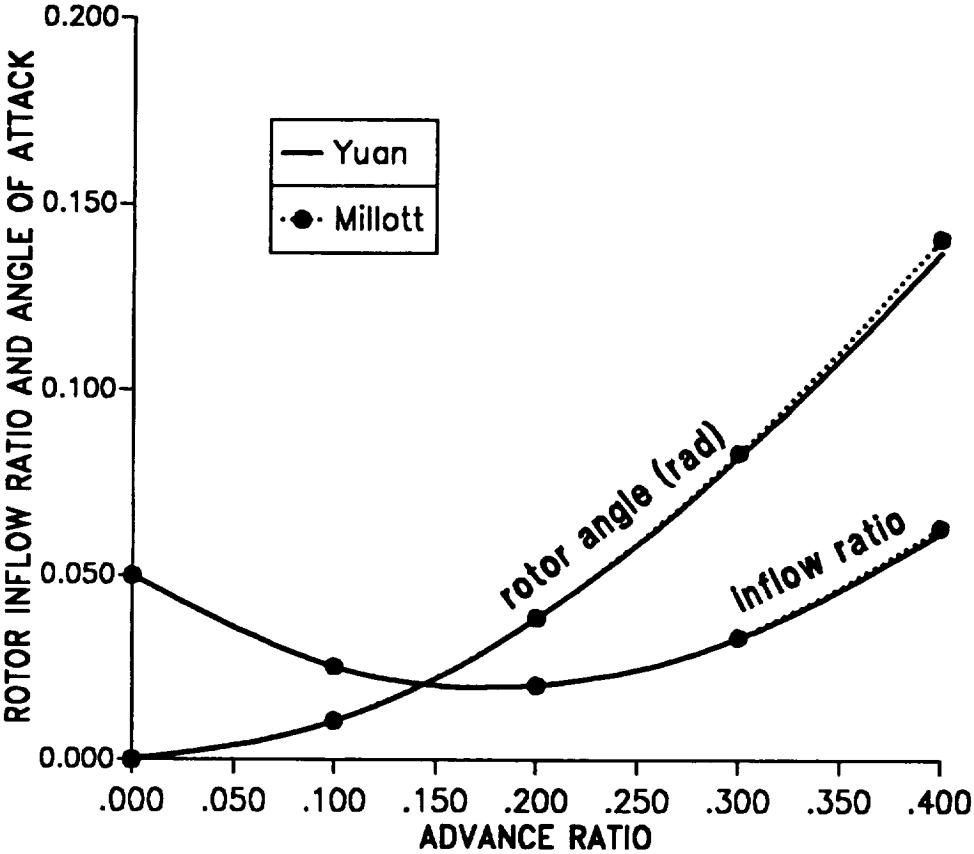


Figure 8.10: Trim variables for soft-in-plane isotropic blade in forward flight; inflow and rotor angle of attack.

## ISOTROPIC BLADE, STIFF-IN-PLANE

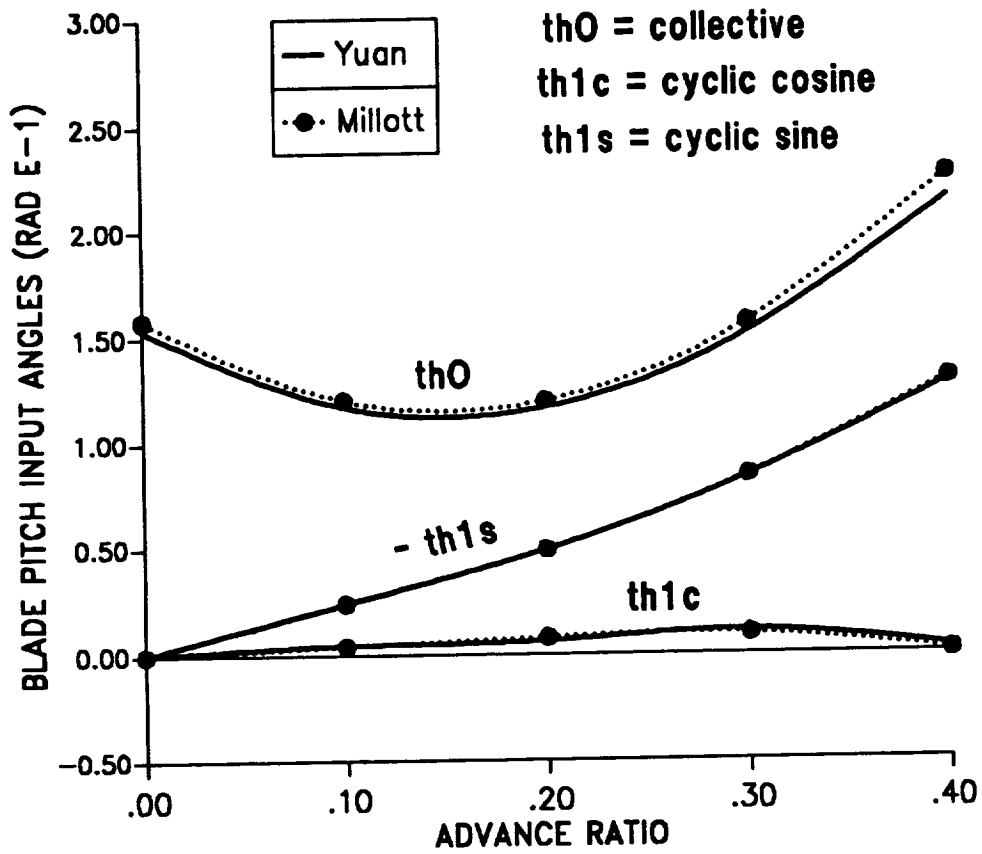


Figure 8.11: Trim variables for stiff-in-plane isotropic blade in forward flight; pitch setting.

## ISOTROPIC BLADE, STIFF-IN-PLANE

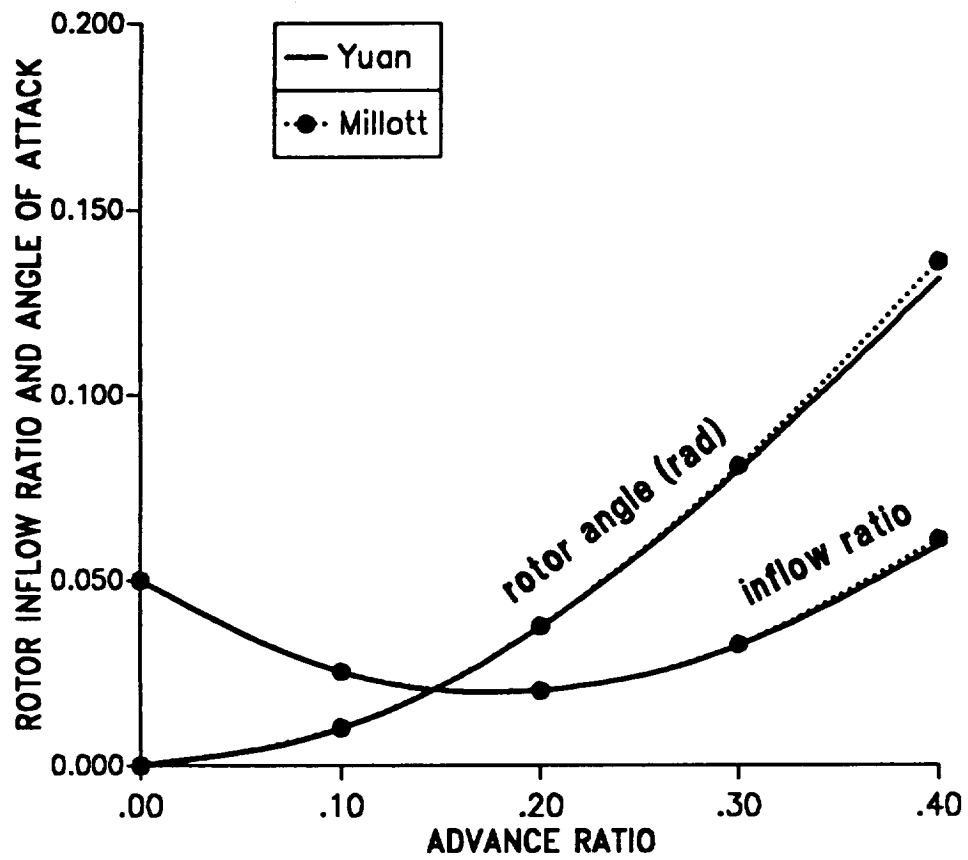


Figure 8.12: Trim variables for stiff-in-plane isotropic blade in forward flight; inflow and rotor angle of attack.

### ISOTROPIC BLADE, SOFT-IN-PLANE ( $\mu=0.3$ )

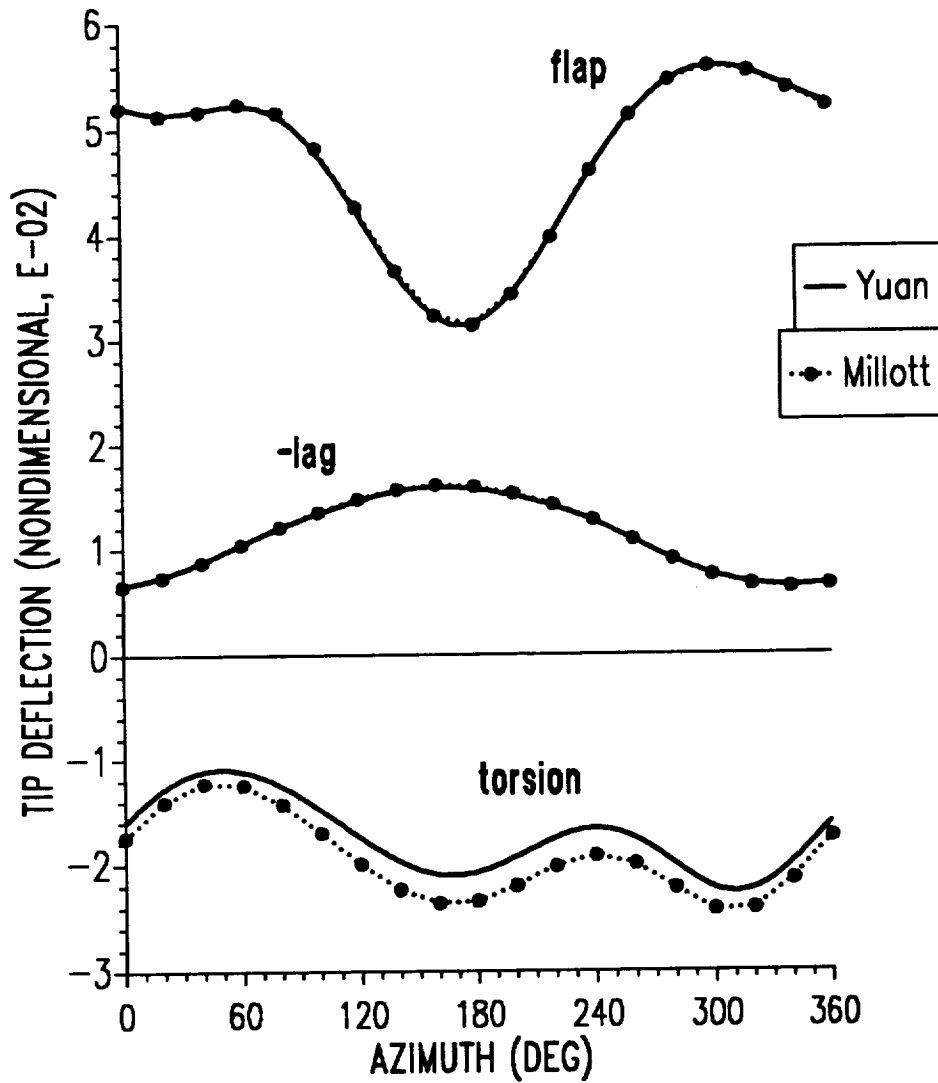


Figure 8.13: Blade tip response for soft-in-plane isotropic blade ( $\mu = 0.30$ ).

### ISOTROPIC BLADE, STIFF-IN-PLANE ( $\mu=0.3$ )

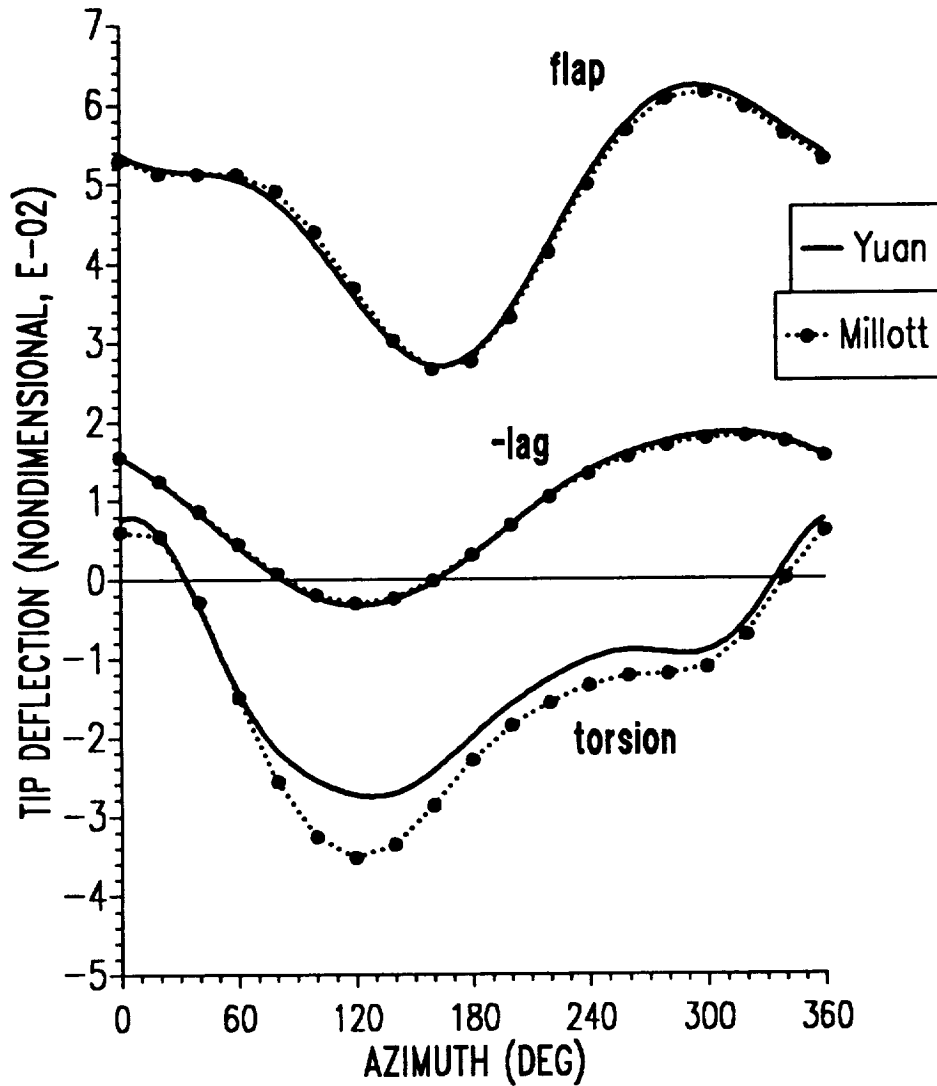


Figure 8.14: Blade tip response for stiff-in-plane isotropic blade ( $\mu = 0.30$ ).

### ISOTROPIC BLADE, SOFT-IN-PLANE

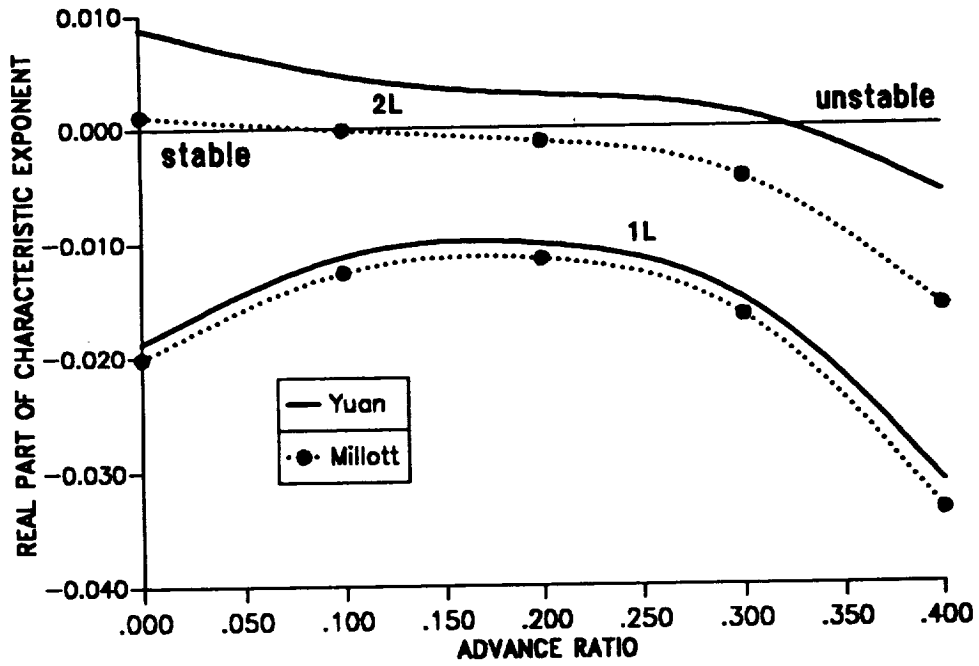


Figure 8.15: Blade damping for soft-in-plane isotropic blade in forward flight; first and second lag modes.

### ISOTROPIC BLADE, SOFT-IN-PLANE

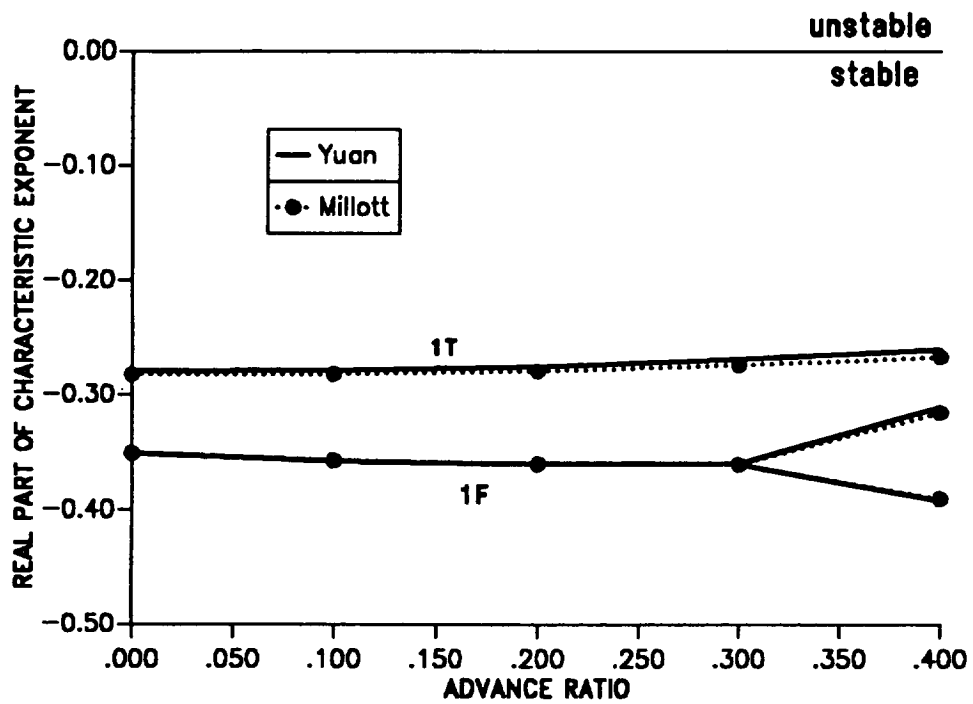


Figure 8.16: Blade damping for soft-in-plane isotropic blade in forward flight; first flap and torsion modes.

### ISOTROPIC BLADE, SOFT-IN-PLANE

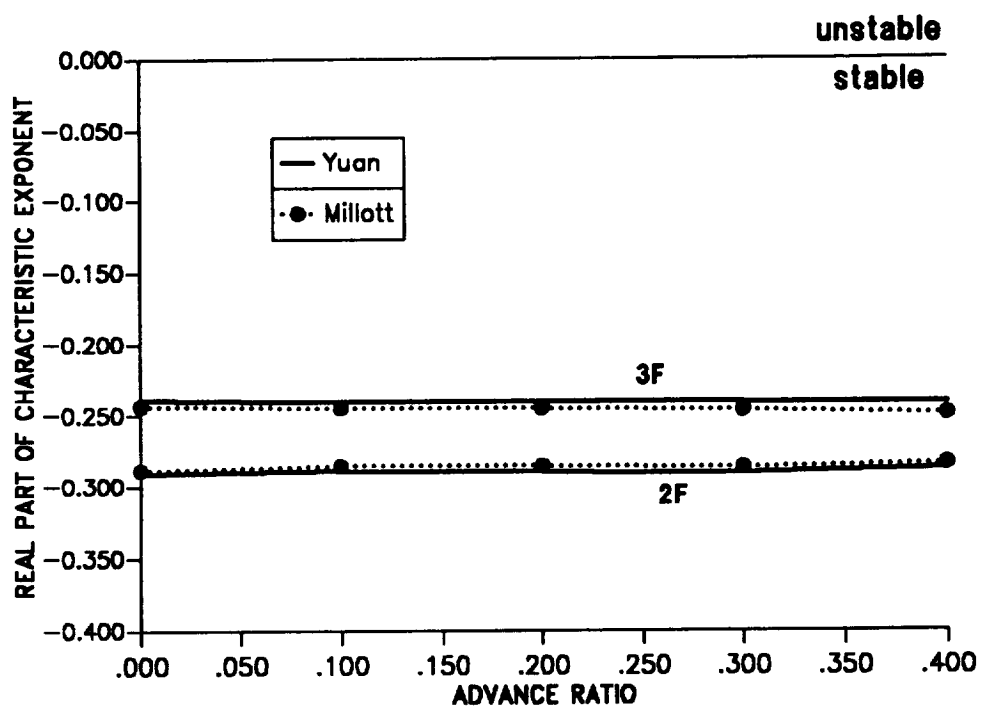


Figure 8.17: Blade damping for soft-in-plane isotropic blade in forward flight; second and third flap modes.

### ISOTROPIC BLADE, STIFF-IN-PLANE

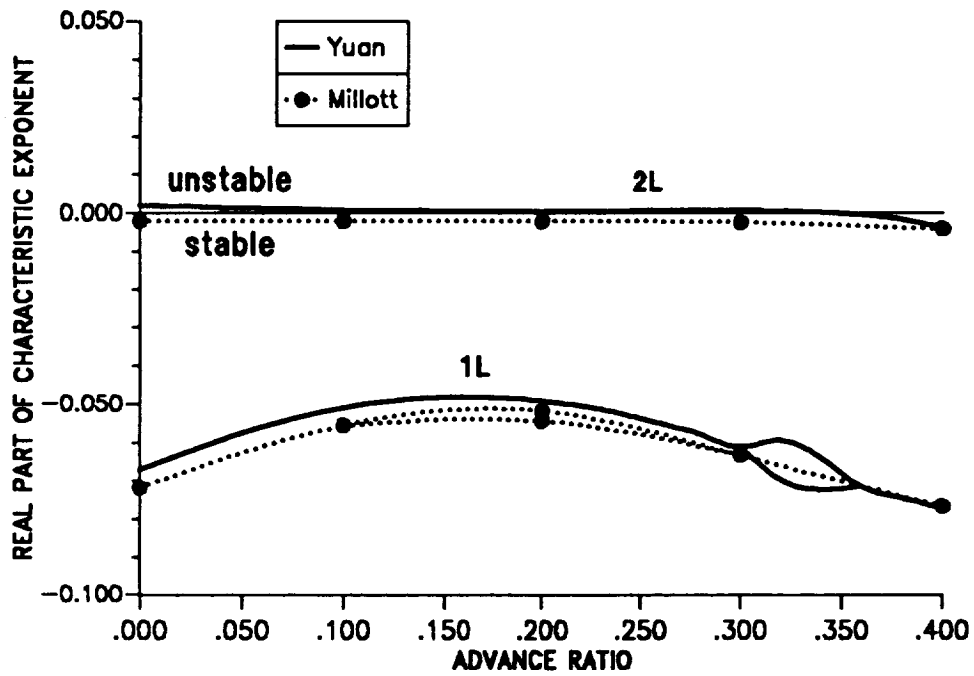


Figure 8.18: Blade damping for stiff-in-plane isotropic blade in forward flight; first and second lag modes.

### ISOTROPIC BLADE, STIFF-IN-PLANE

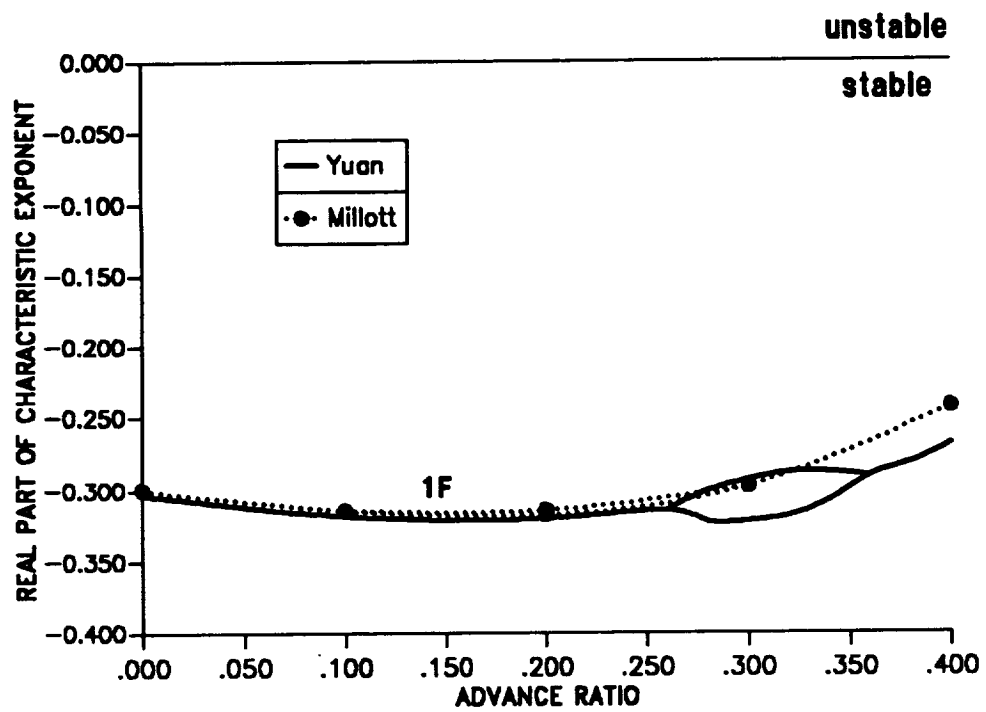


Figure 8.19: Blade damping for stiff-in-plane isotropic blade in forward flight; first flap mode.

### ISOTROPIC BLADE, STIFF-IN-PLANE

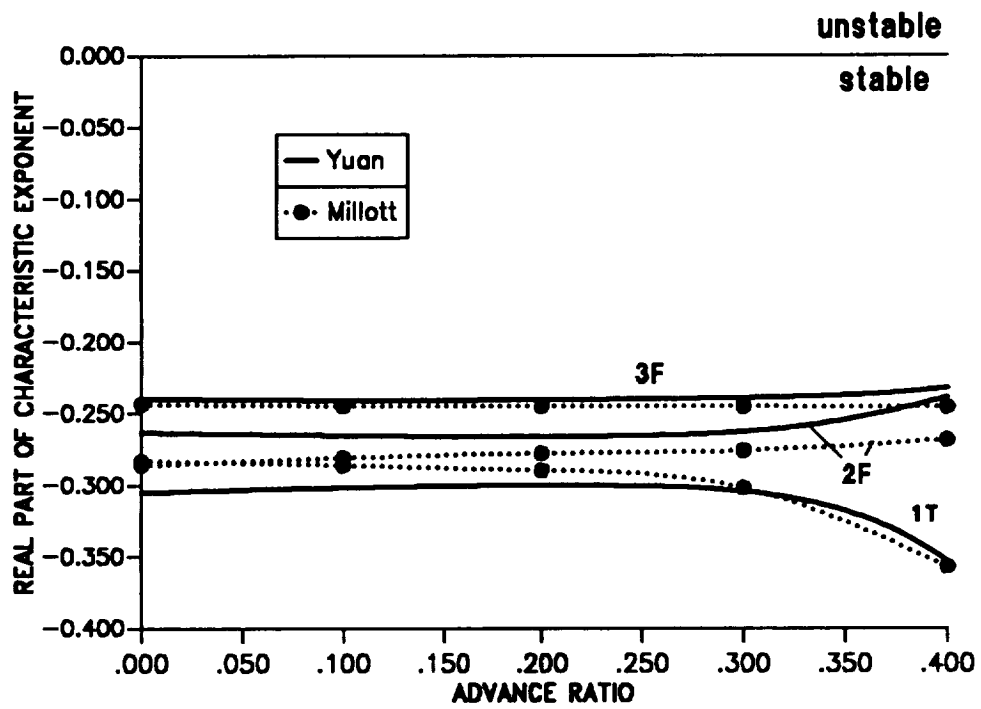


Figure 8.20: Blade damping for stiff-in-plane isotropic blade in forward flight; first torsion, second and third flap modes.

### ISOTROPIC BLADE, SOFT-IN-PLANE

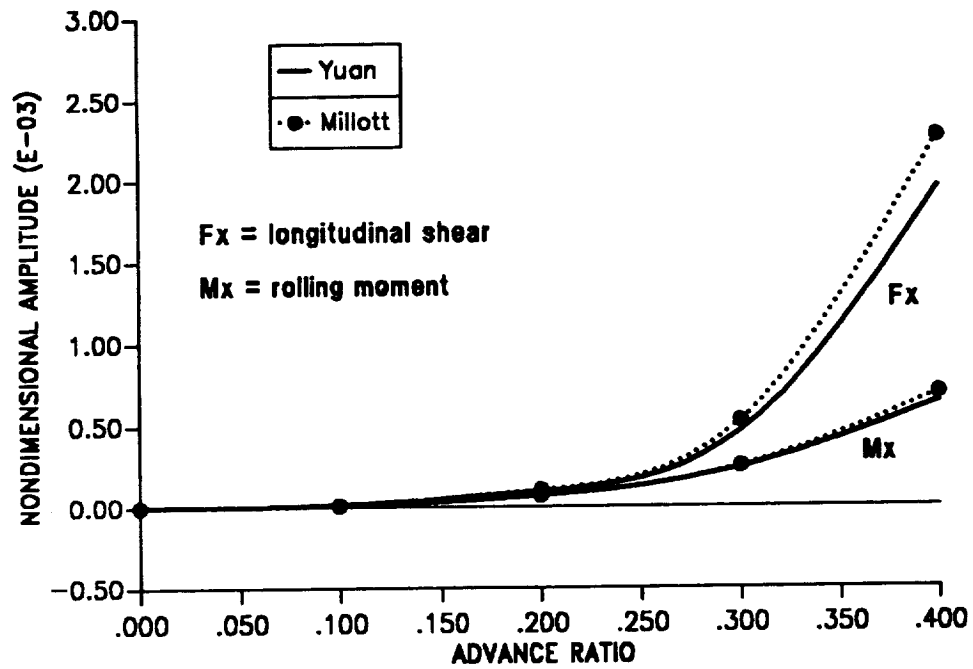


Figure 8.21: The 4/rev hub loads for soft-in-plane isotropic blade in forward flight; longitudinal shear and rolling moment.

### ISOTROPIC BLADE, SOFT-IN-PLANE

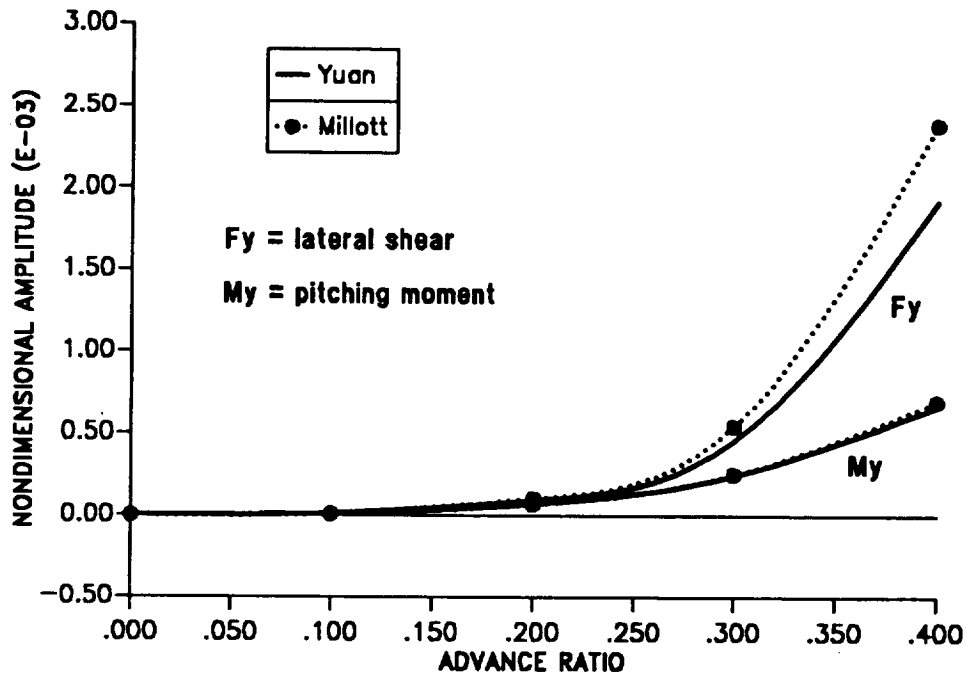


Figure 8.22: The 4/rev hub loads for soft-in-plane isotropic blade in forward flight; lateral shear and pitching moment.

### ISOTROPIC BLADE, SOFT-IN-PLANE

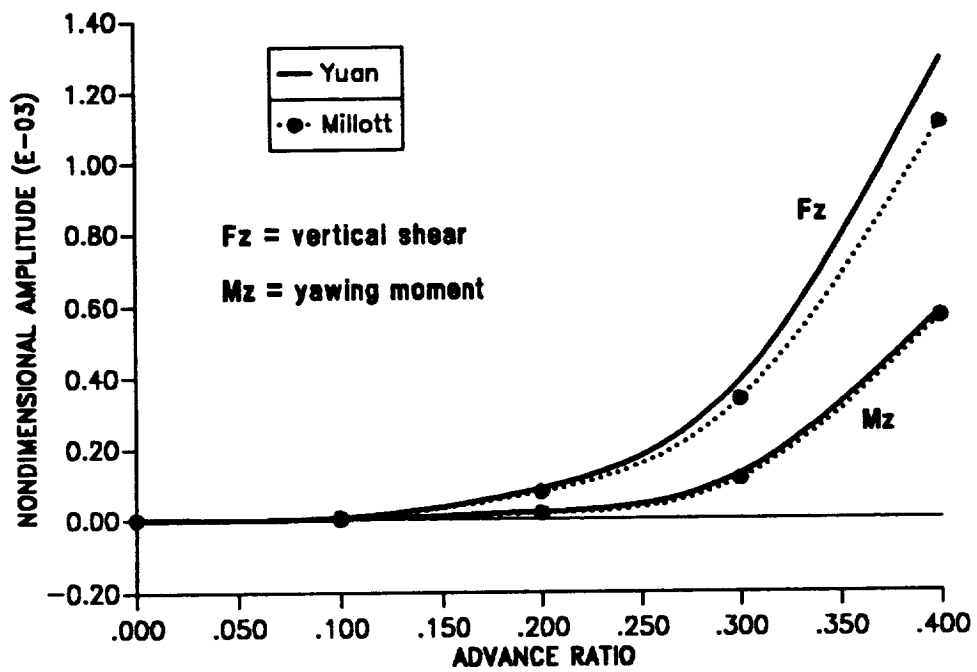


Figure 8.23: The 4/rev hub loads for soft-in-plane isotropic blade in forward flight; vertical shear and yawing moment.

### ISOTROPIC BLADE, STIFF-IN-PLANE

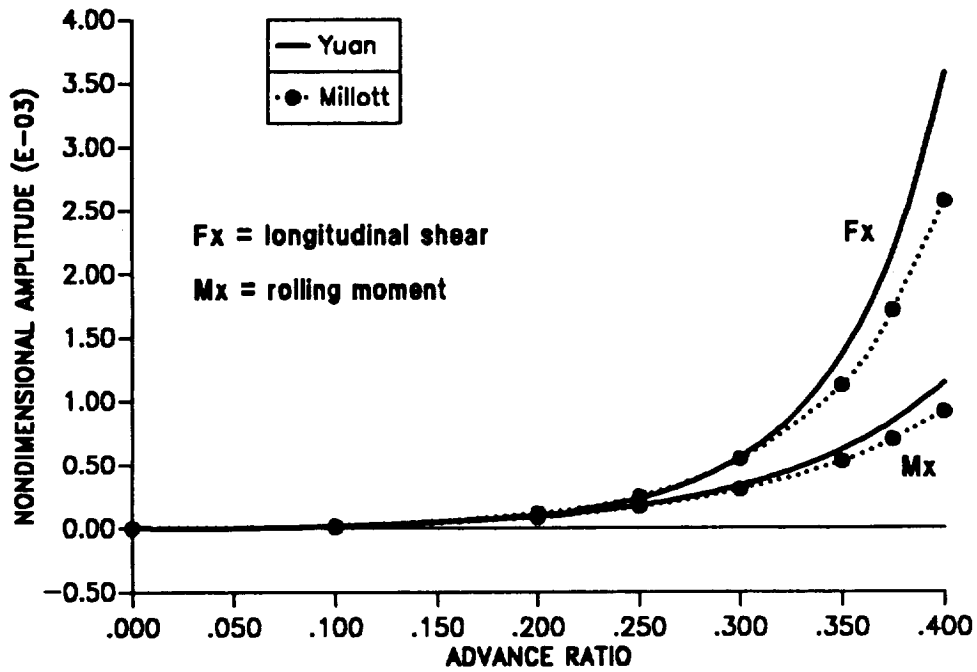


Figure 8.24: The 4/rev hub loads for stiff-in-plane isotropic blade in forward flight; longitudinal shear and rolling moment.

### ISOTROPIC BLADE, STIFF-IN-PLANE

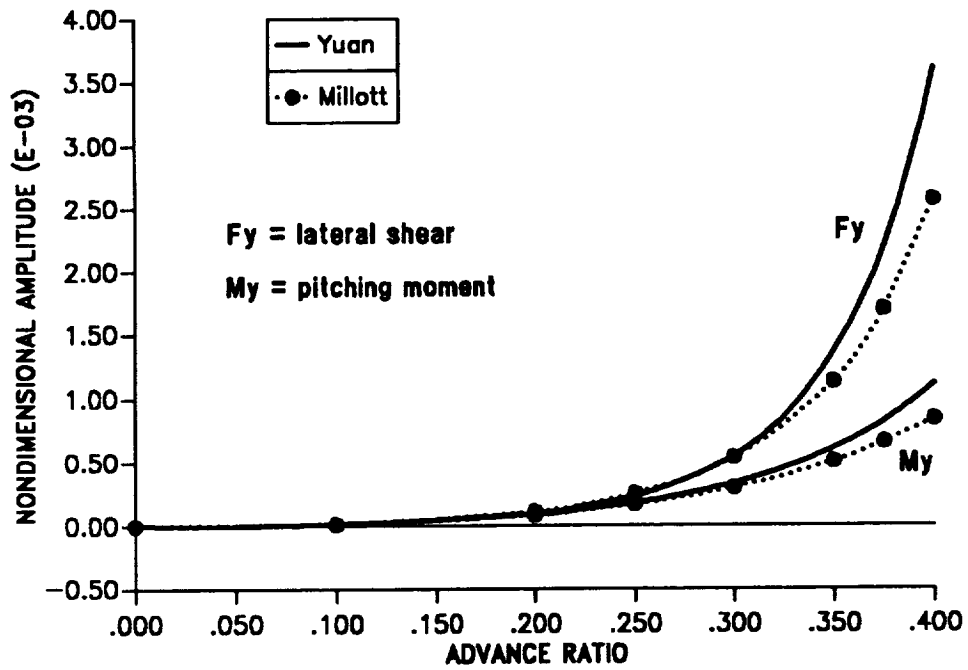


Figure 8.25: The 4/rev hub loads for stiff-in-plane isotropic blade in forward flight; lateral shear and pitching moment.

### ISOTROPIC BLADE, STIFF-IN-PLANE

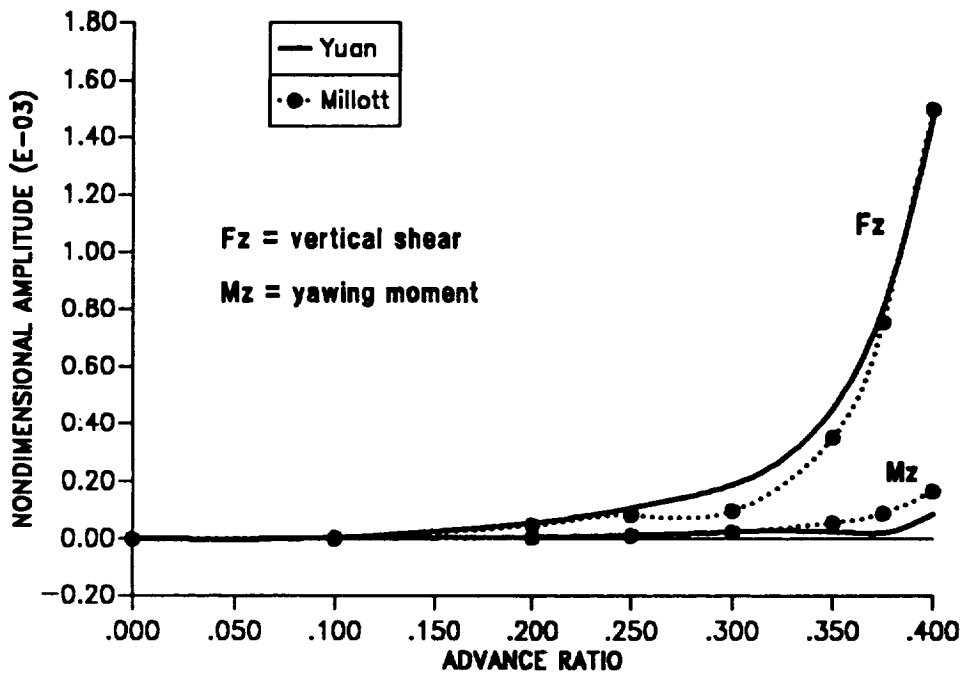


Figure 8.26: The 4/rev hub loads for stiff-in-plane isotropic blade in forward flight; vertical shear and yawing moment.

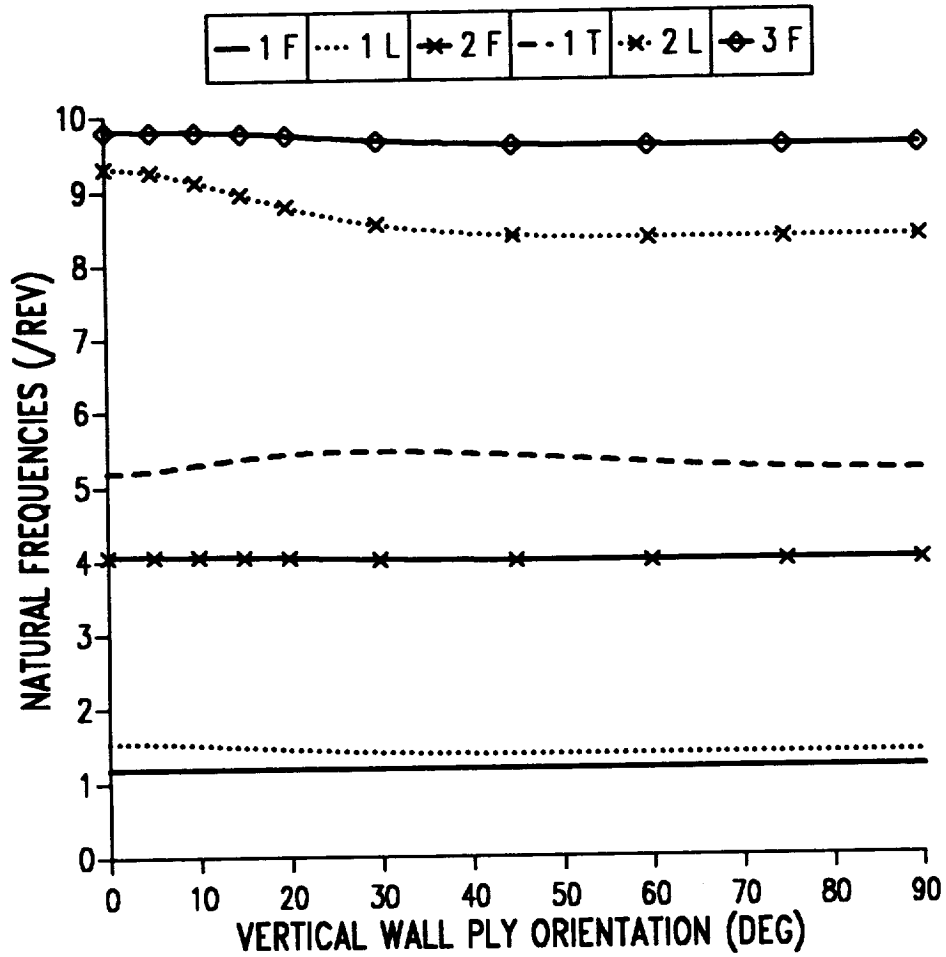


Figure 9.1: Natural frequencies as a function of ply angle in vertical wall for single-cell composite blade.

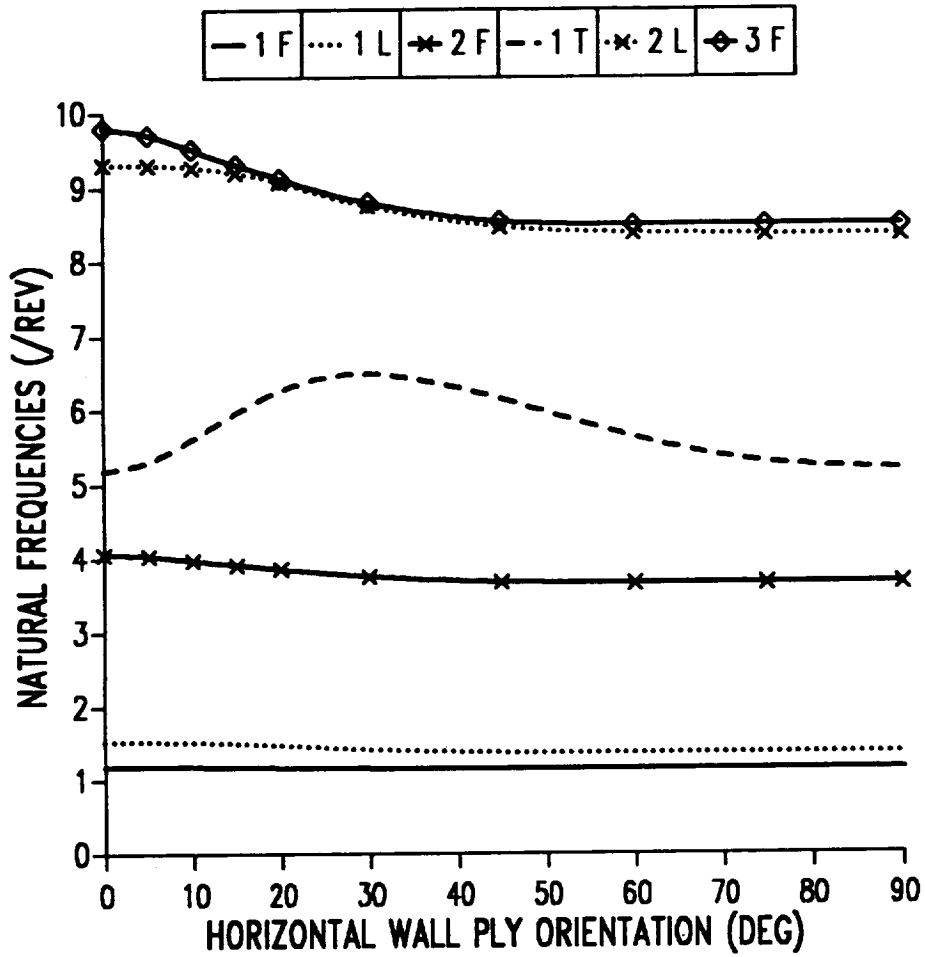


Figure 9.2: Natural frequencies as a function of ply angle in horizontal wall for single-cell composite blade.

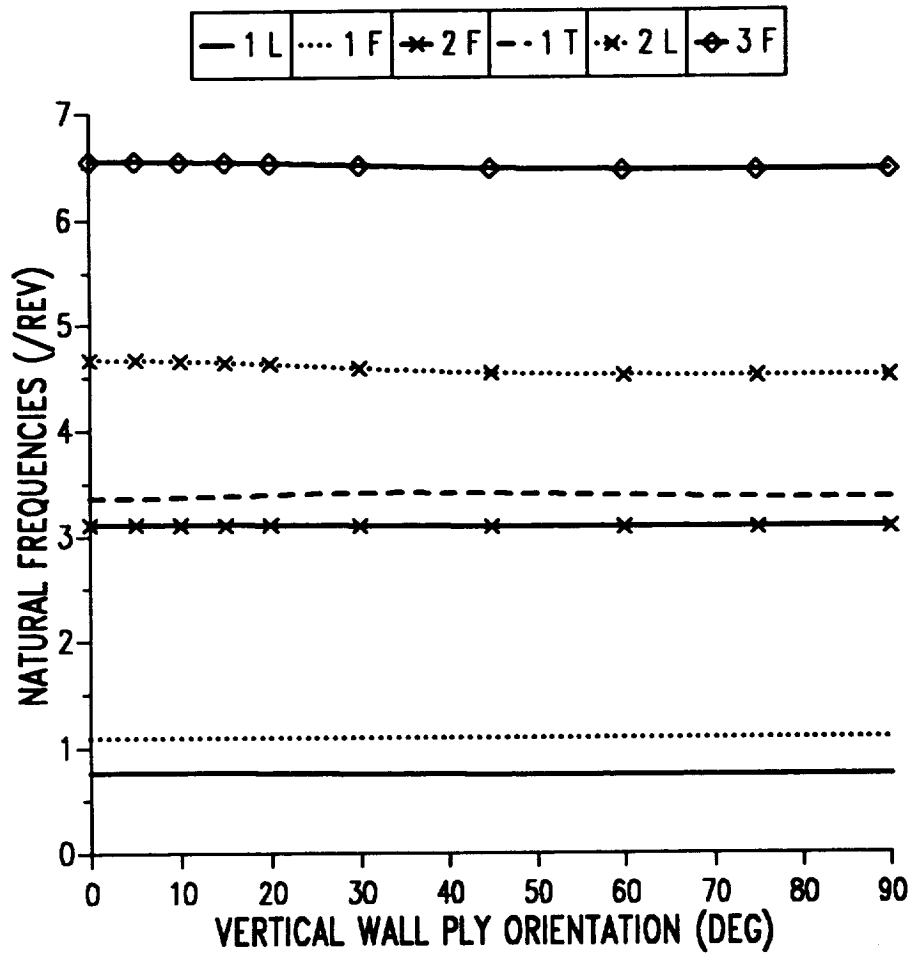


Figure 9.3: Natural frequencies as a function of ply angle in vertical wall for two-cell composite blade.

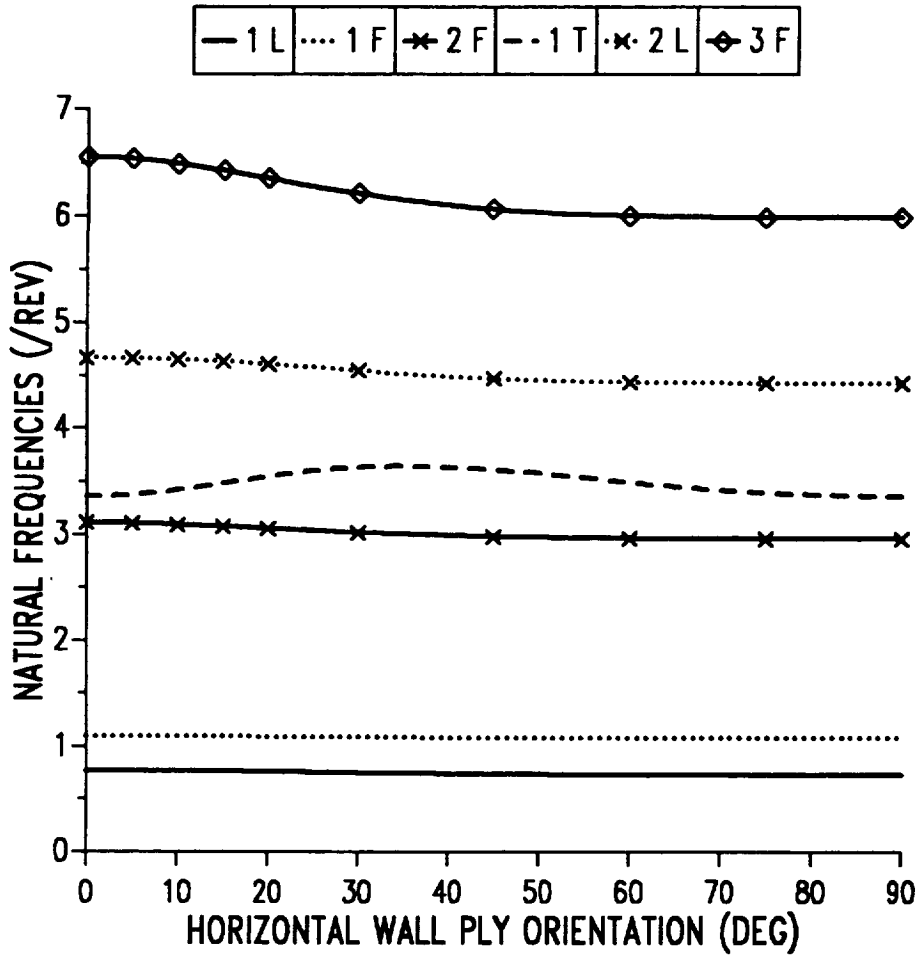


Figure 9.4: Natural frequencies as a function of ply angle in horizontal wall for two-cell composite blade.

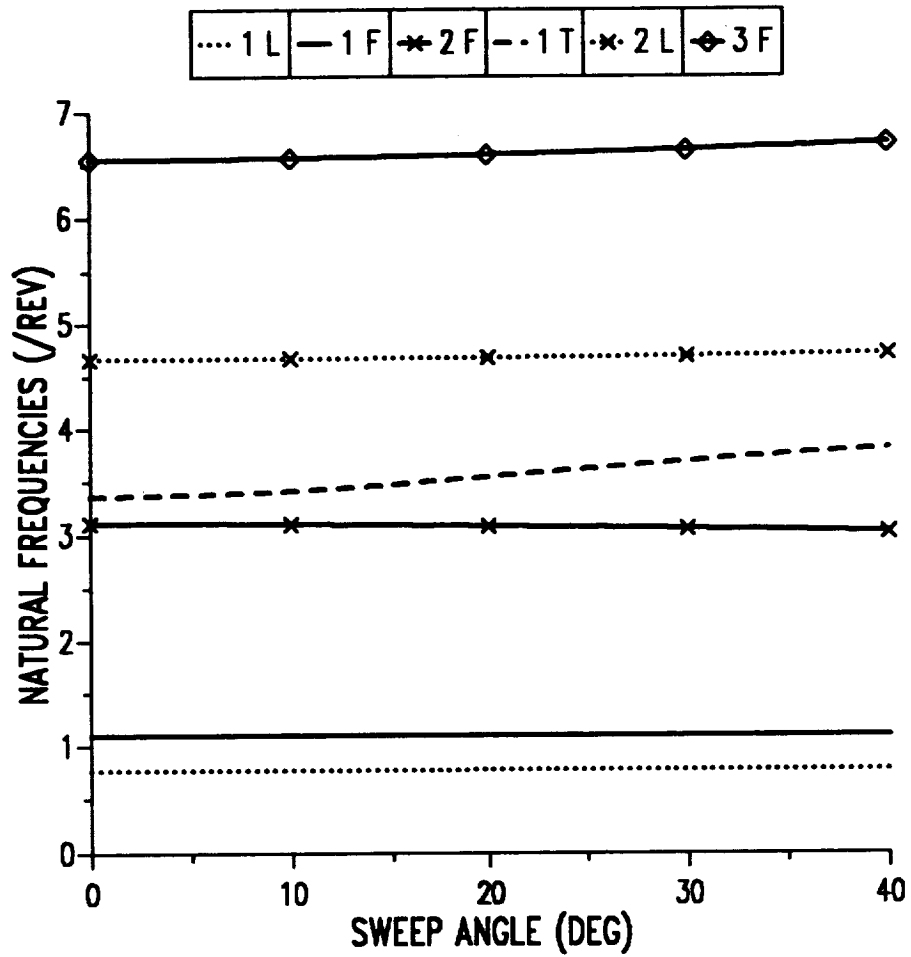


Figure 9.5: Natural frequencies as a function of tip sweep angle for two-cell composite blade with zero ply angle.

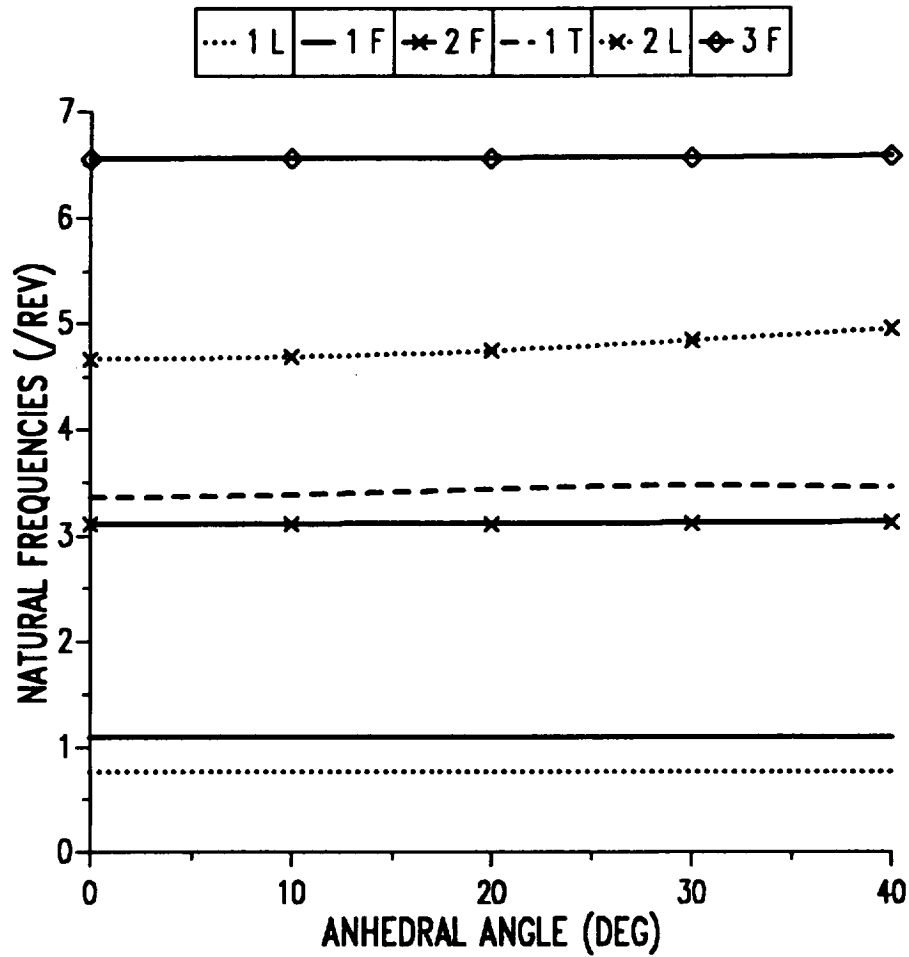


Figure 9.6: Natural frequencies as a function of tip anedral angle for two-cell composite blade with zero ply angle.

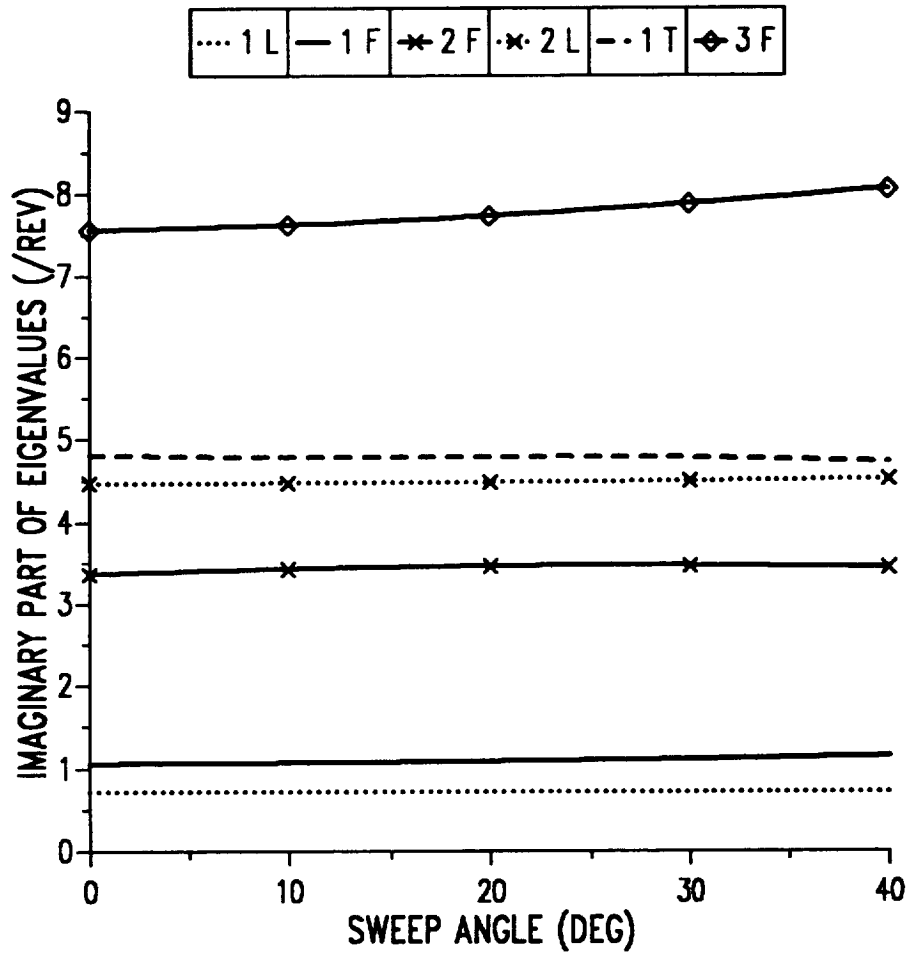


Figure 9.7: Effect of tip sweep on the imaginary part of hover eigenvalues of isotropic blade, baseline configuration.

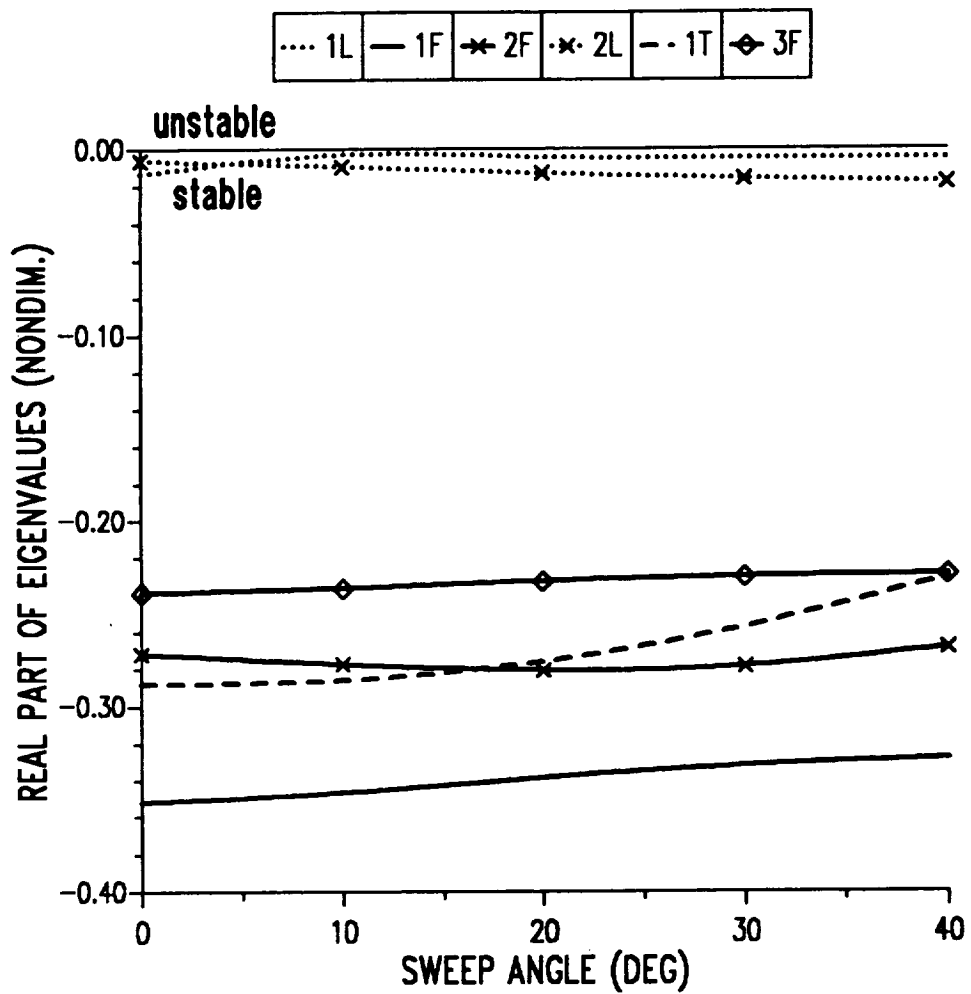


Figure 9.8: Effect of tip sweep on the real part of hover eigenvalues of isotropic blade, baseline configuration.

TORSIONAL FREQUENCY=3.263/REV

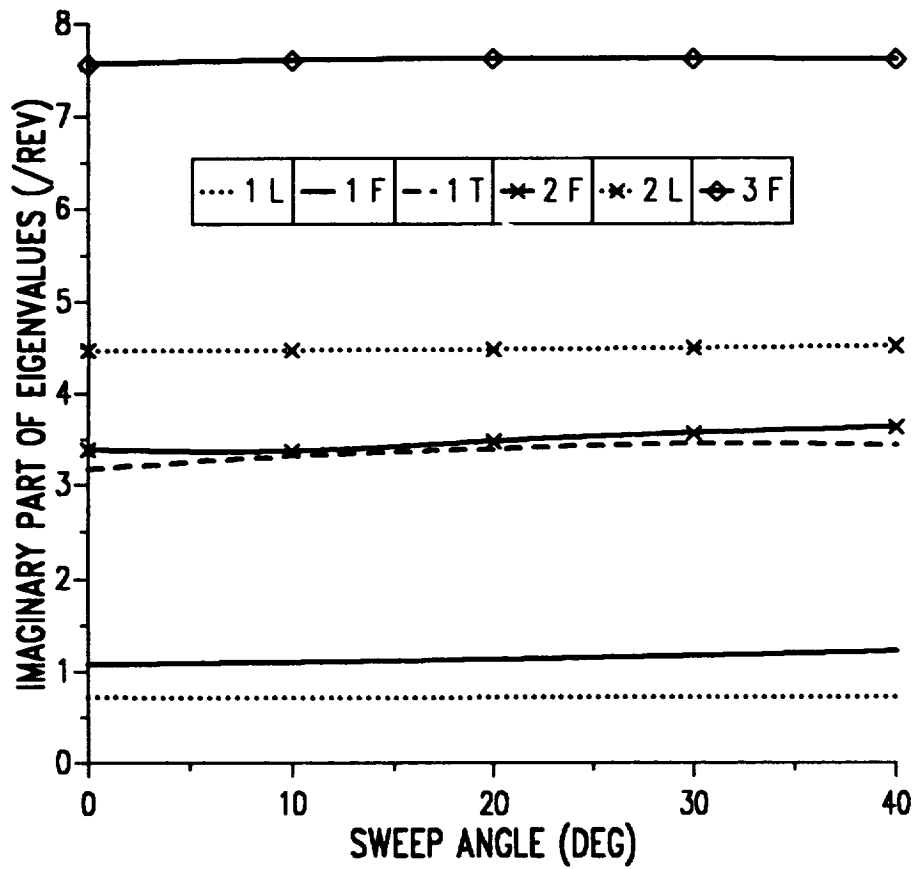


Figure 9.9: Effect of tip sweep on the imaginary part of hover eigenvalues of isotropic blade, modified torsional frequency.

TORSIONAL FREQUENCY=3.263/REV

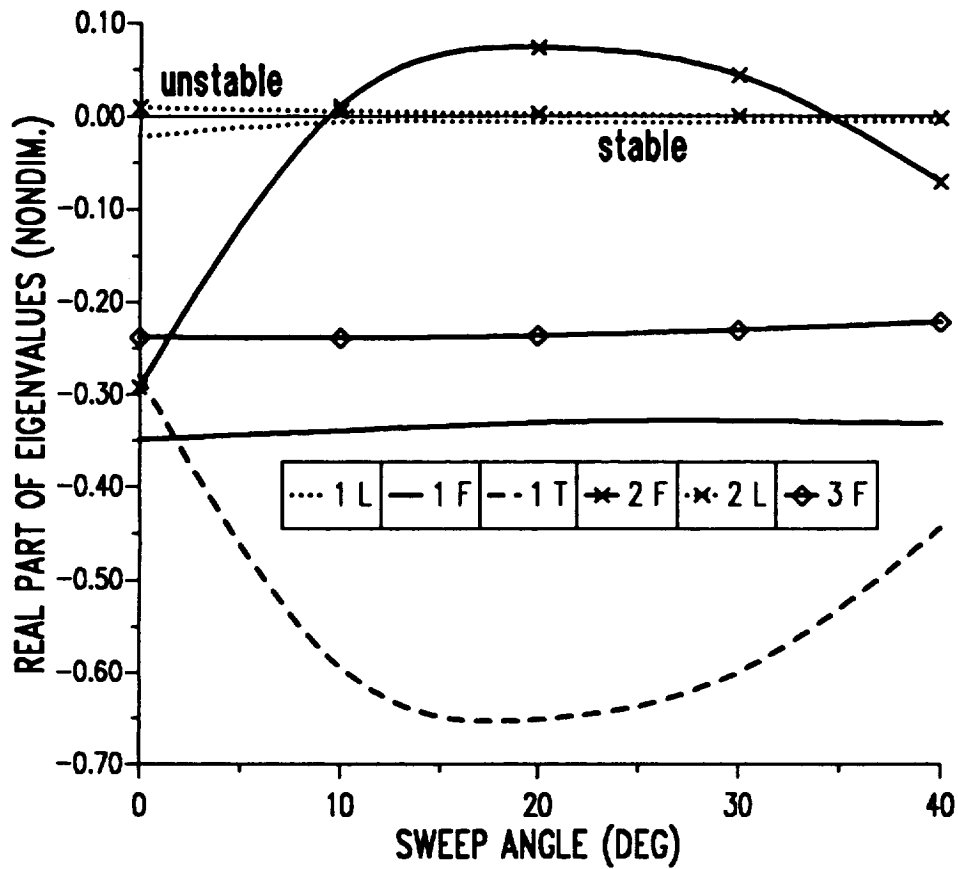


Figure 9.10: Effect of tip sweep on the real part of hover eigenvalues of isotropic blade, modified torsional frequency.

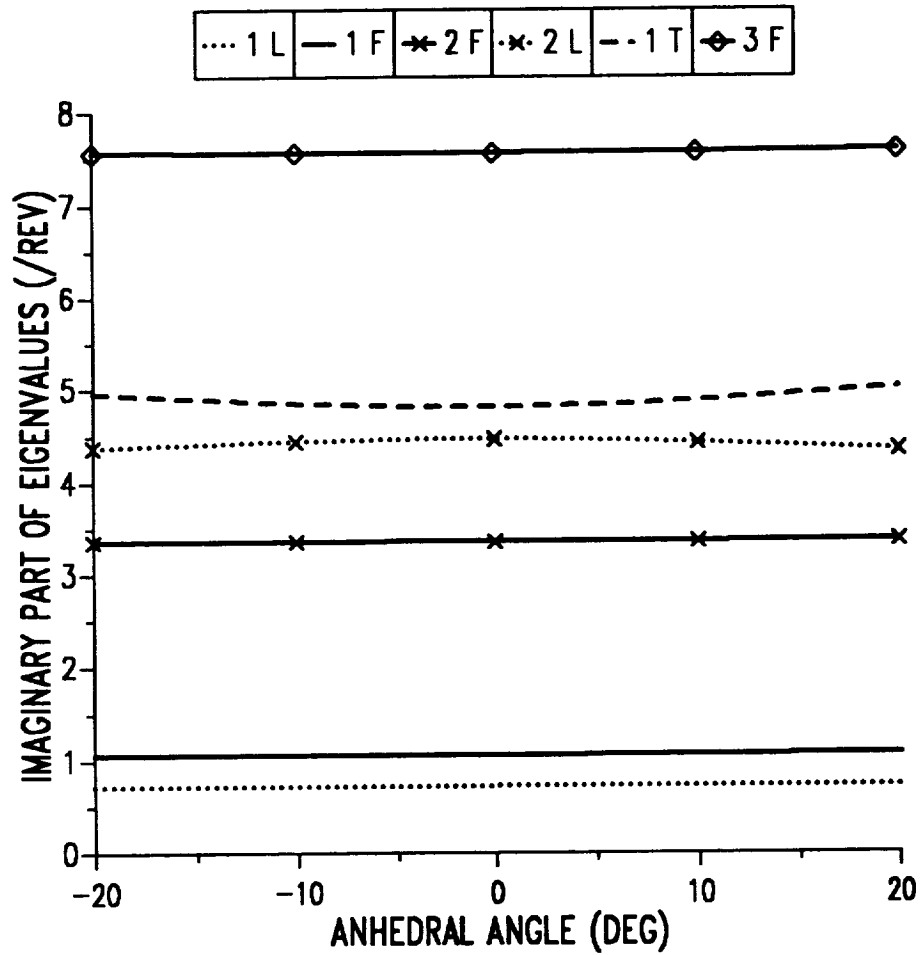


Figure 9.11: Effect of tip anhedral on the imaginary part of hover eigenvalues of isotropic blade, baseline configuration.

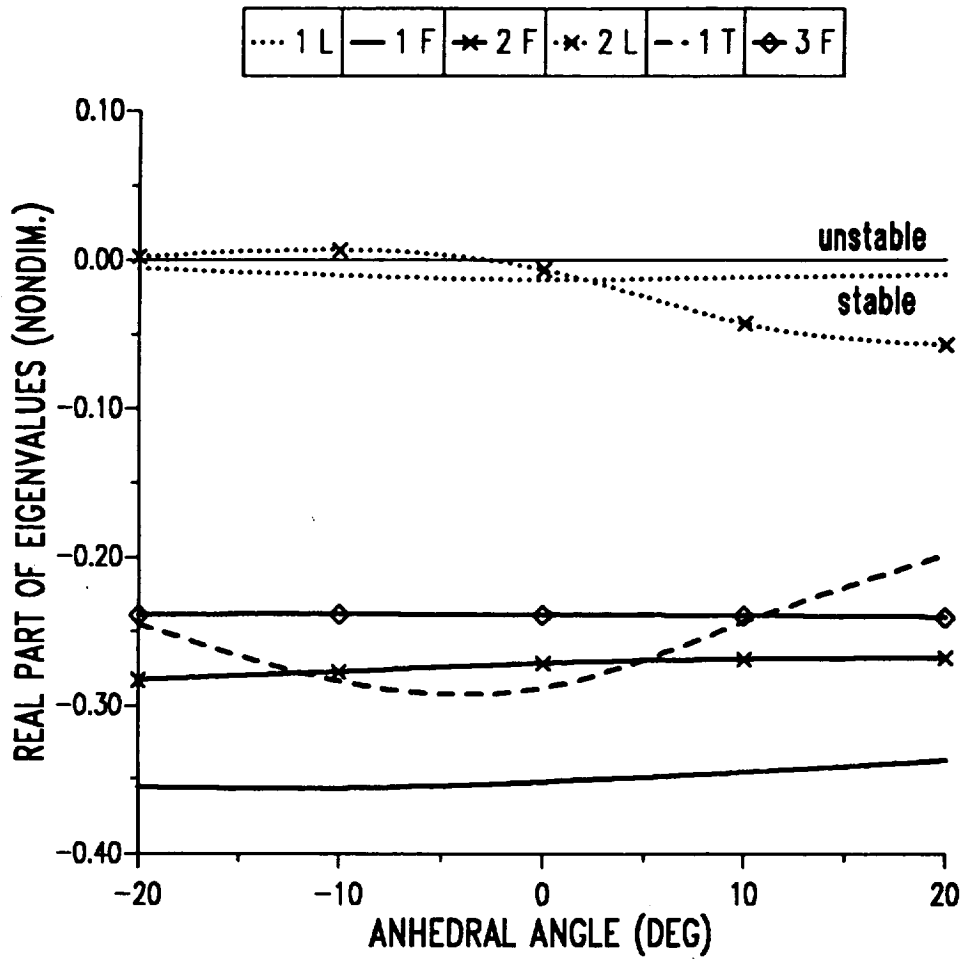


Figure 9.12: Effect of tip anhedral on the real part of hover eigenvalues of isotropic blade, baseline configuration.

TORSIONAL FREQUENCY=4.340/REV

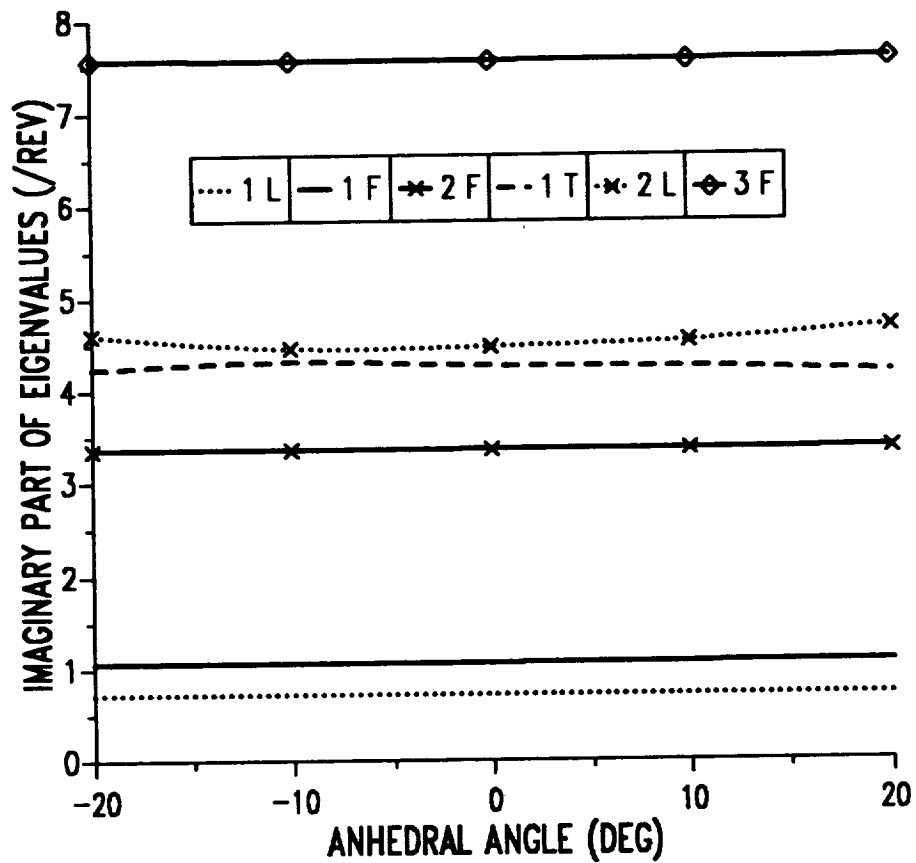


Figure 9.13: Effect of tip anhedral on the imaginary part of hover eigenvalues of isotropic blade, modified torsional frequency.

TORSIONAL FREQUENCY=4.340/REV

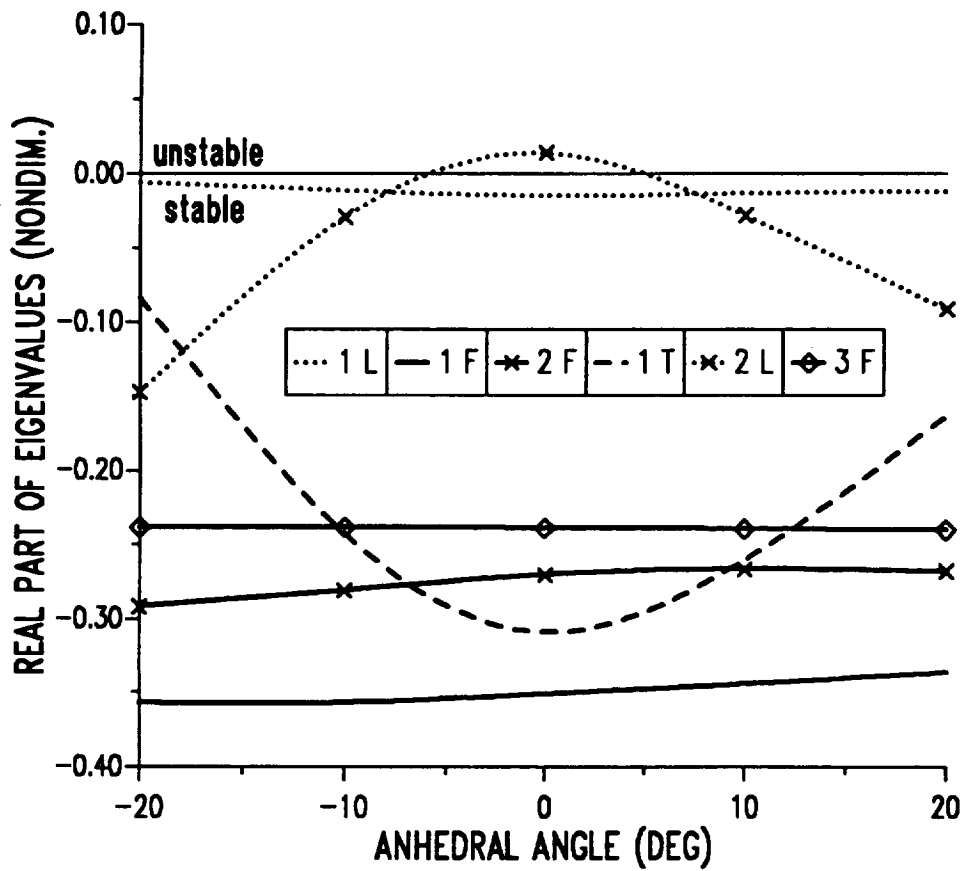


Figure 9.14: Effect of tip anhedral on the real part of hover eigenvalues of isotropic blade, modified torsional frequency.

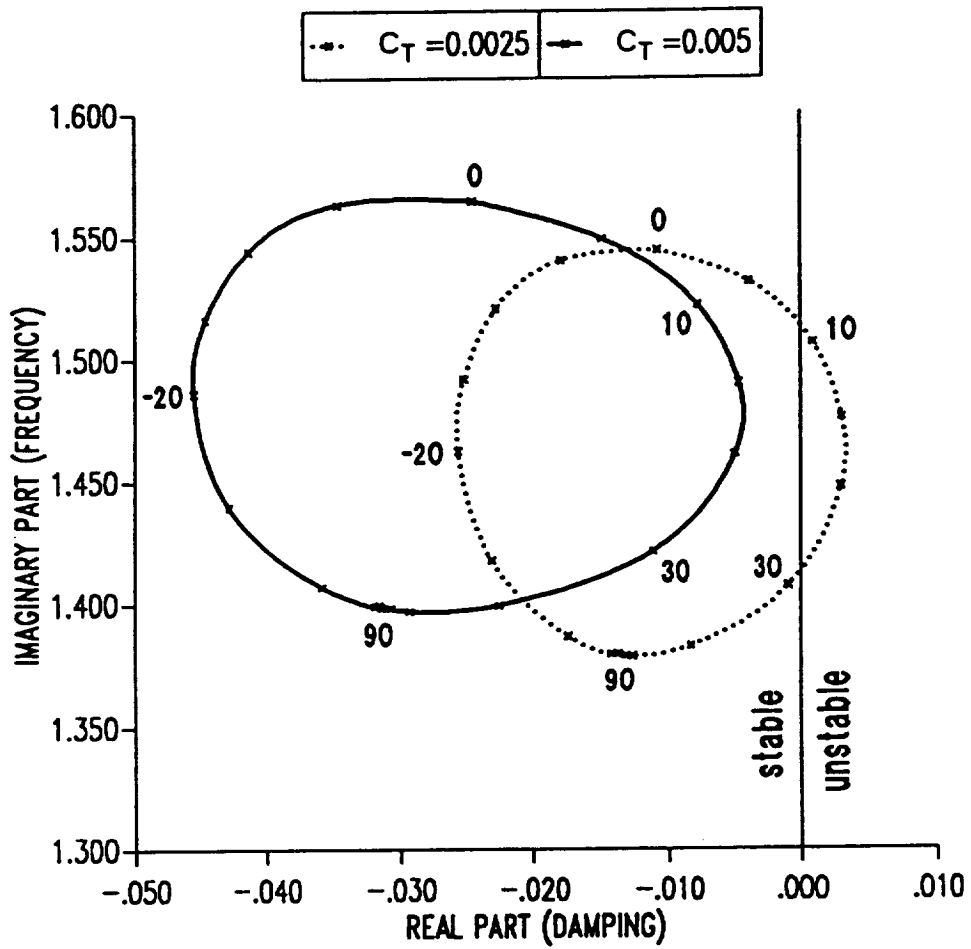


Figure 9.15: Root locus of first lag mode eigenvalues as a function of ply angle in vertical wall for single-cell composite blade in hover.

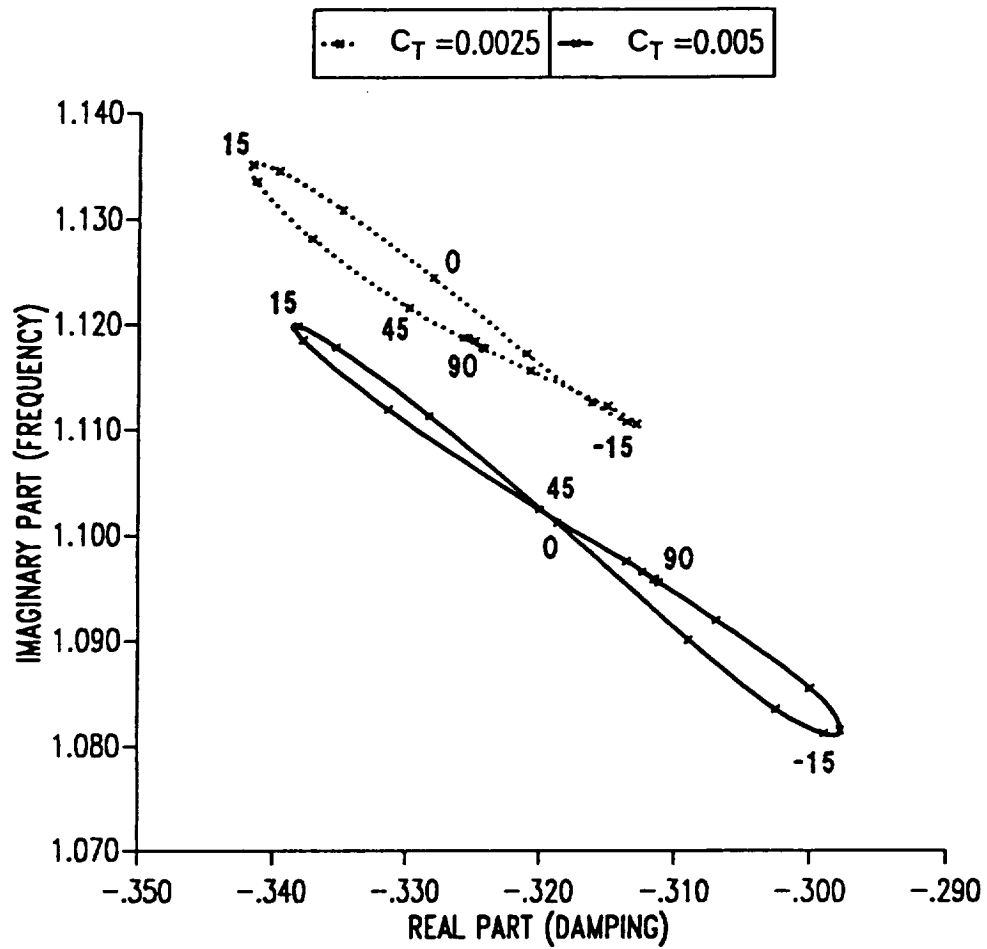


Figure 9.16: Root locus of first flap mode eigenvalues as a function of ply angle in vertical wall for single-cell composite blade in hover.

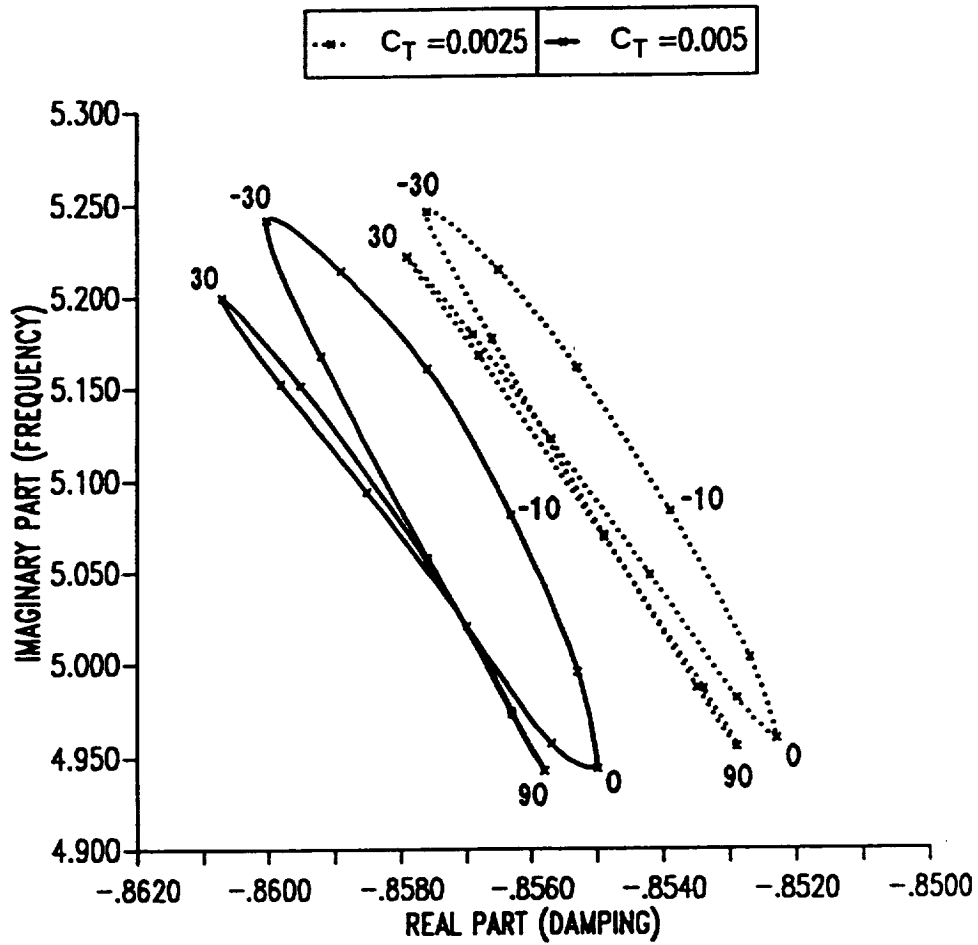


Figure 9.17: Root locus of first torsion mode eigenvalues as a function of ply angle in vertical wall for single-cell composite blade in hover.

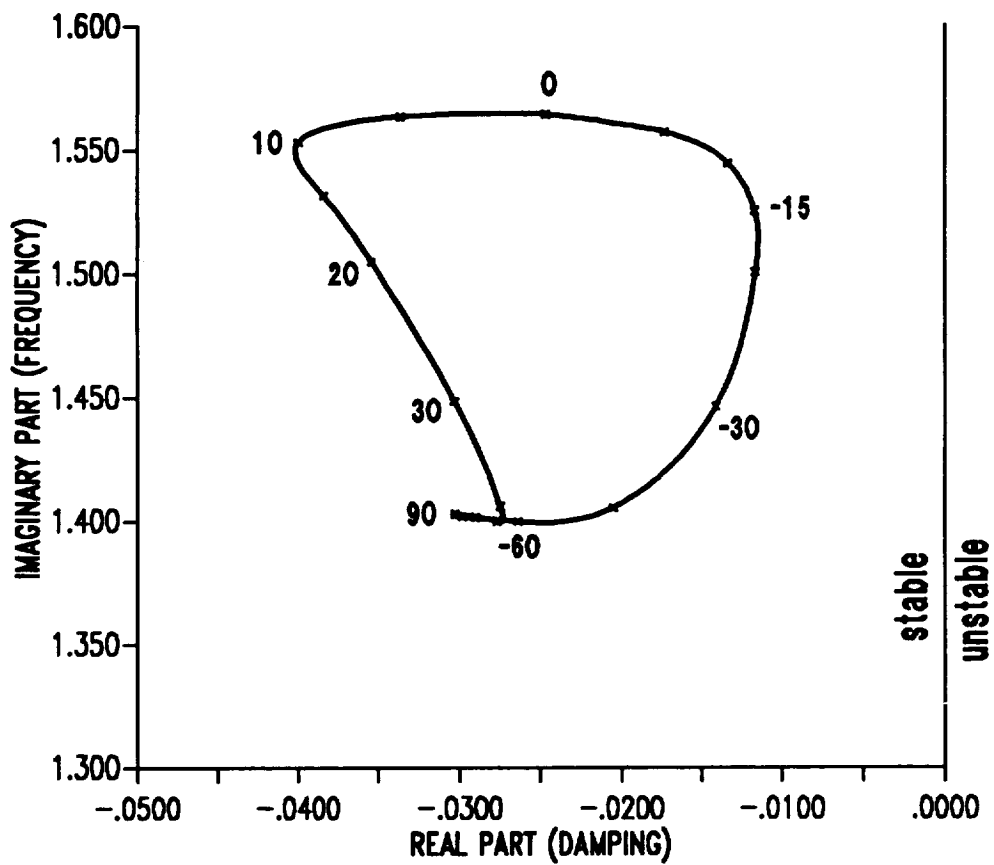


Figure 9.18: Root locus of first lag mode eigenvalues as a function of ply angle in horizontal wall for single-cell composite blade in hover.

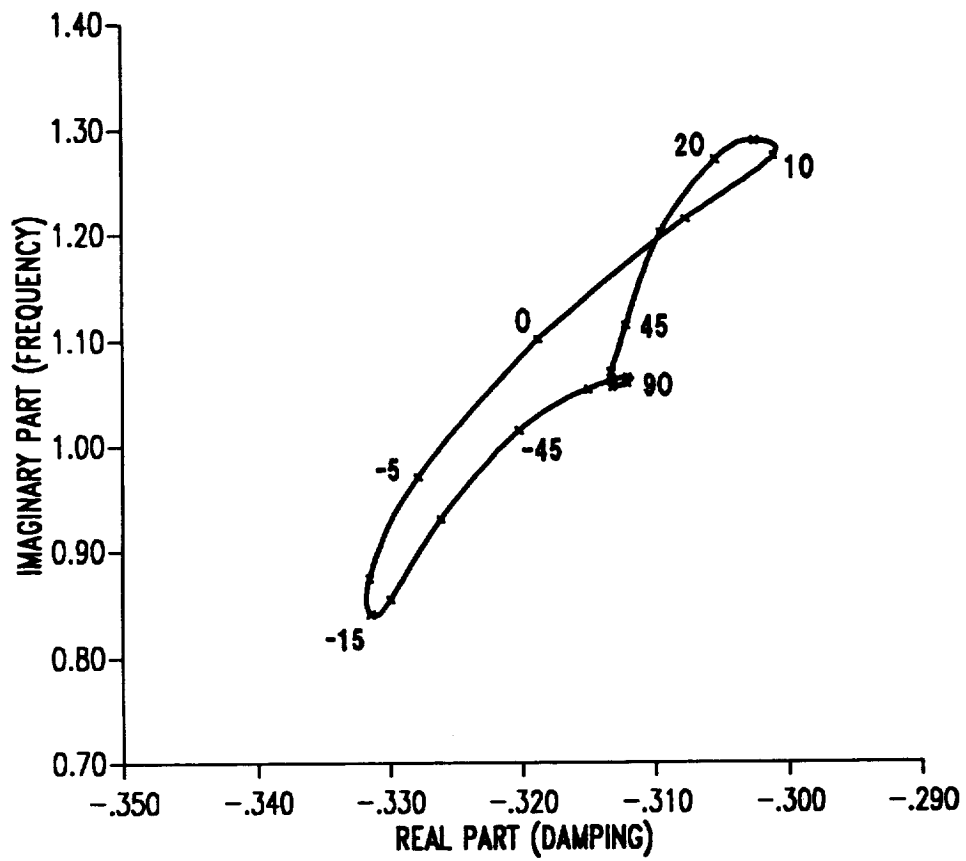


Figure 9.19: Root locus of first flap mode eigenvalues as a function of ply angle in horizontal wall for single-cell composite blade in hover.

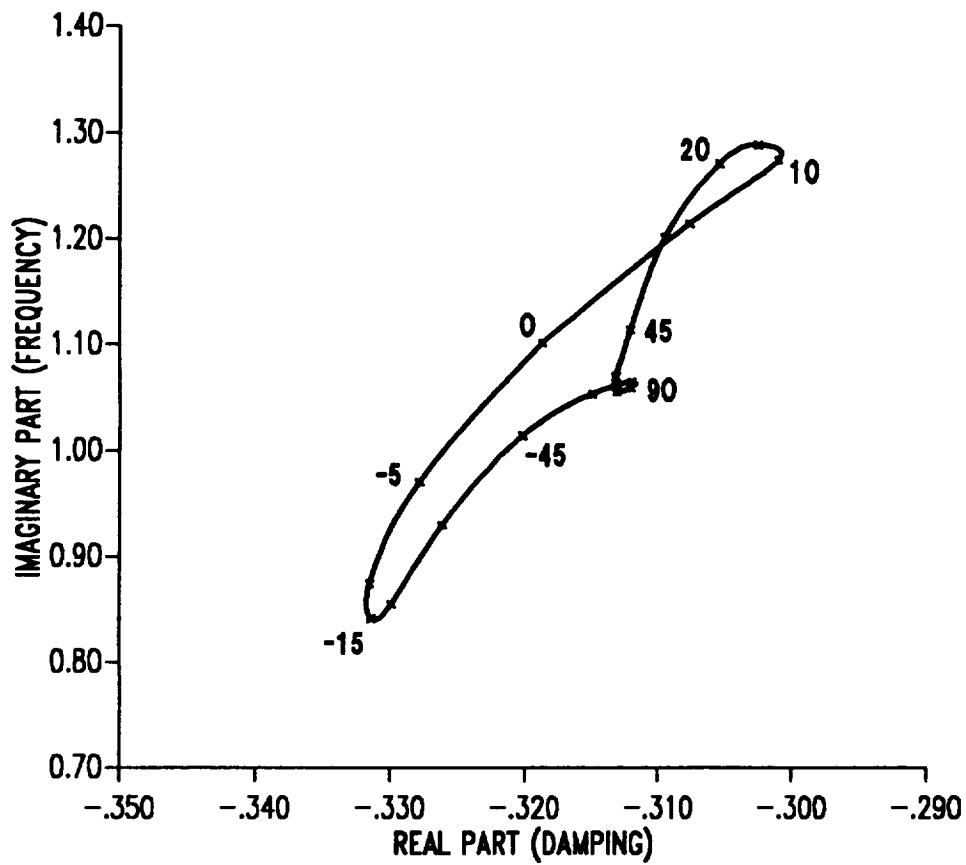


Figure 9.20: Root locus of first torsion mode eigenvalues as a function of ply angle in horizontal wall for single-cell composite blade in hover.

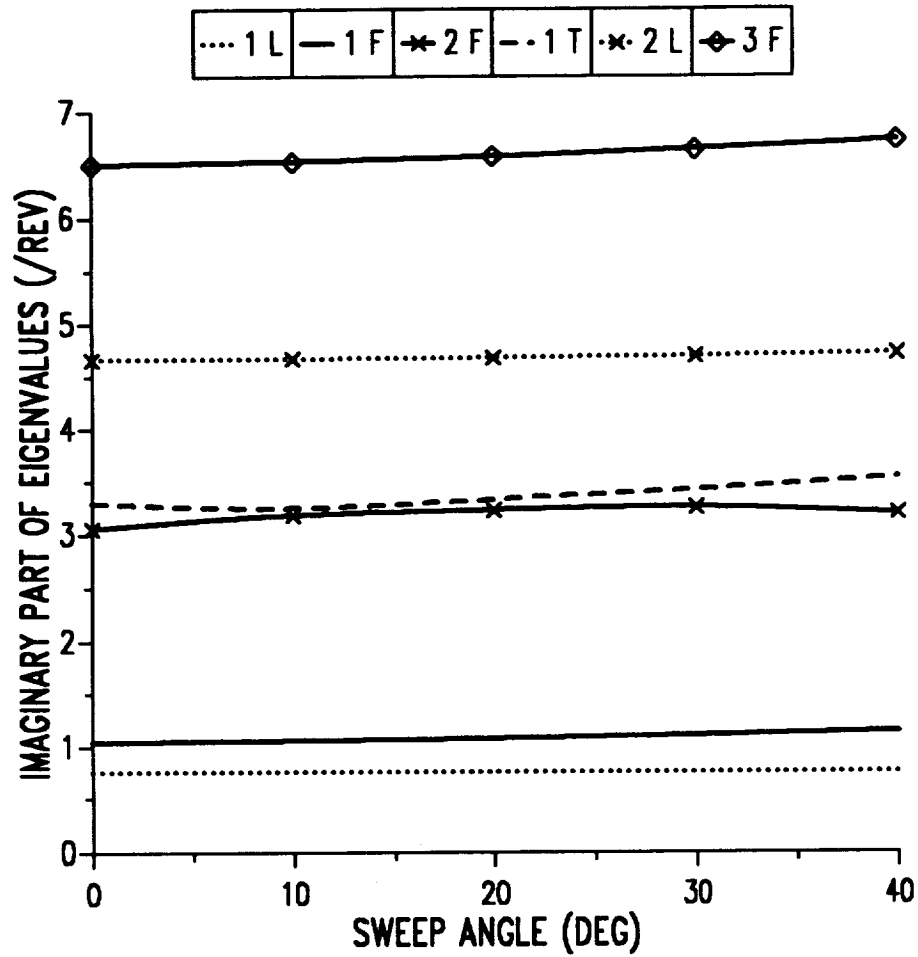


Figure 9.21: Effect of tip sweep on the imaginary part of hover eigenvalues of two-cell composite blade, baseline configuration.

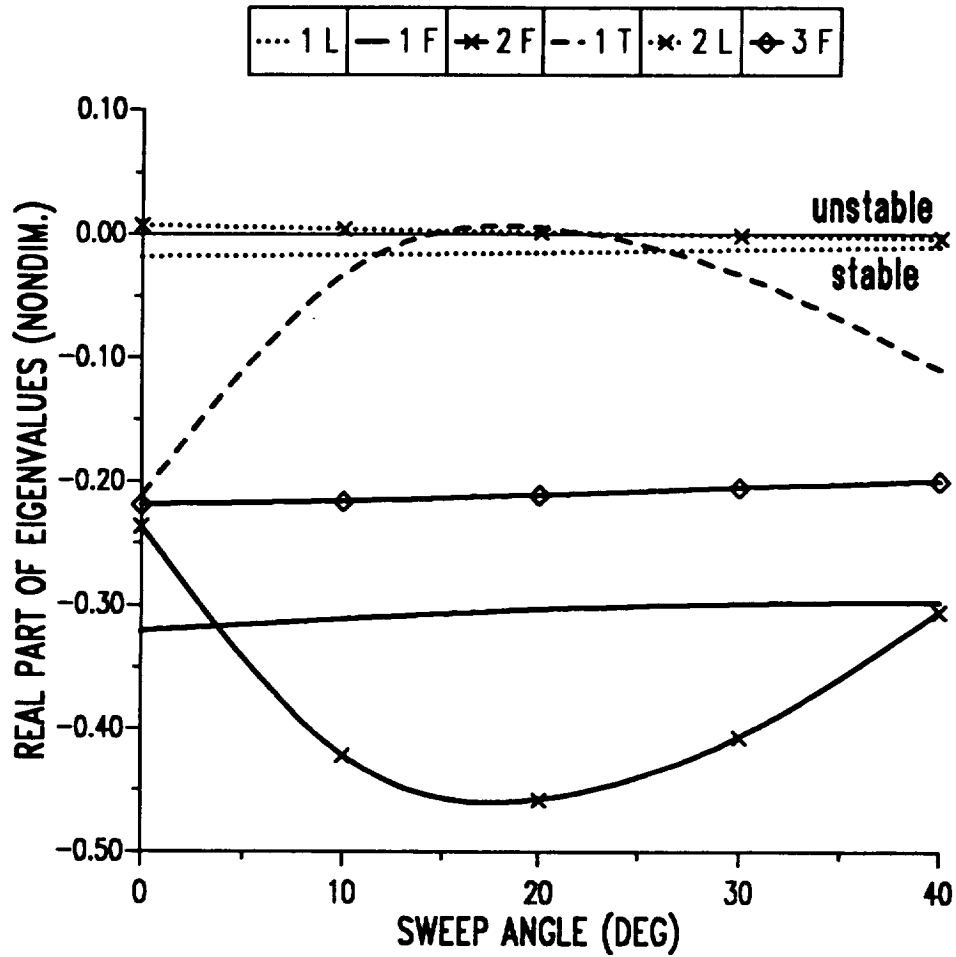


Figure 9.22: Effect of tip sweep on the real part of hover eigenvalues of two-cell composite blade, baseline configuration.

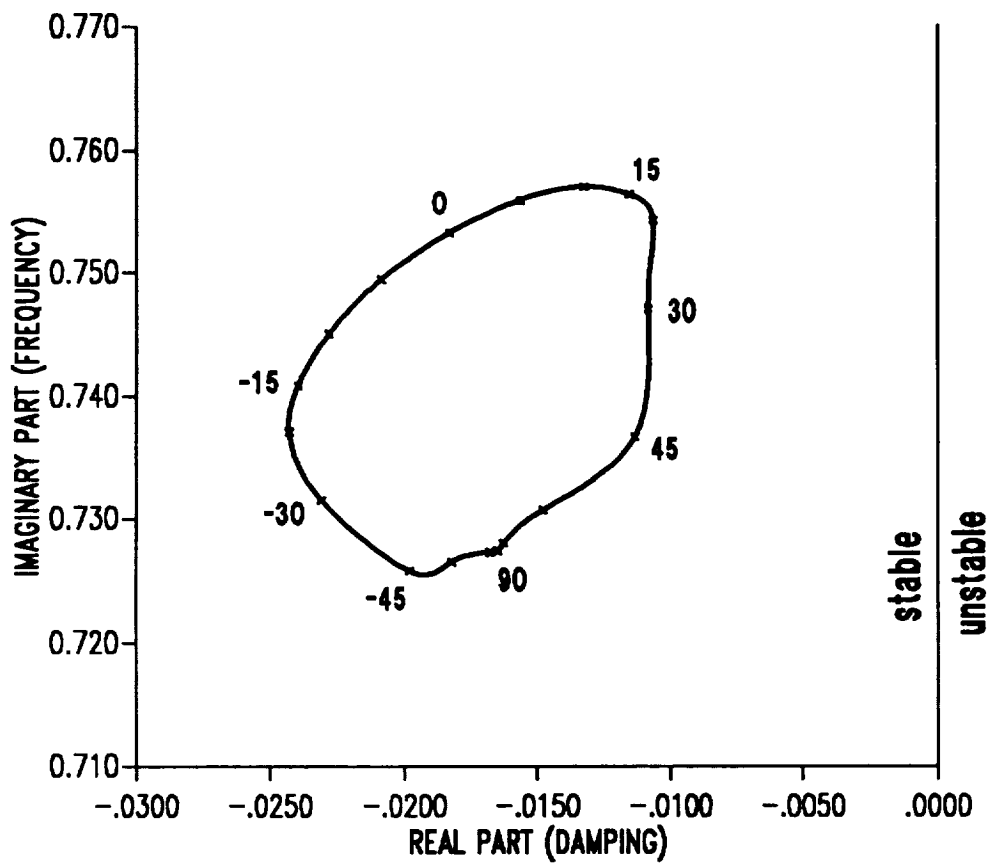


Figure 9.23: Root locus of first lag mode eigenvalues as a function of ply angle in vertical wall for two-cell composite blade in hover.

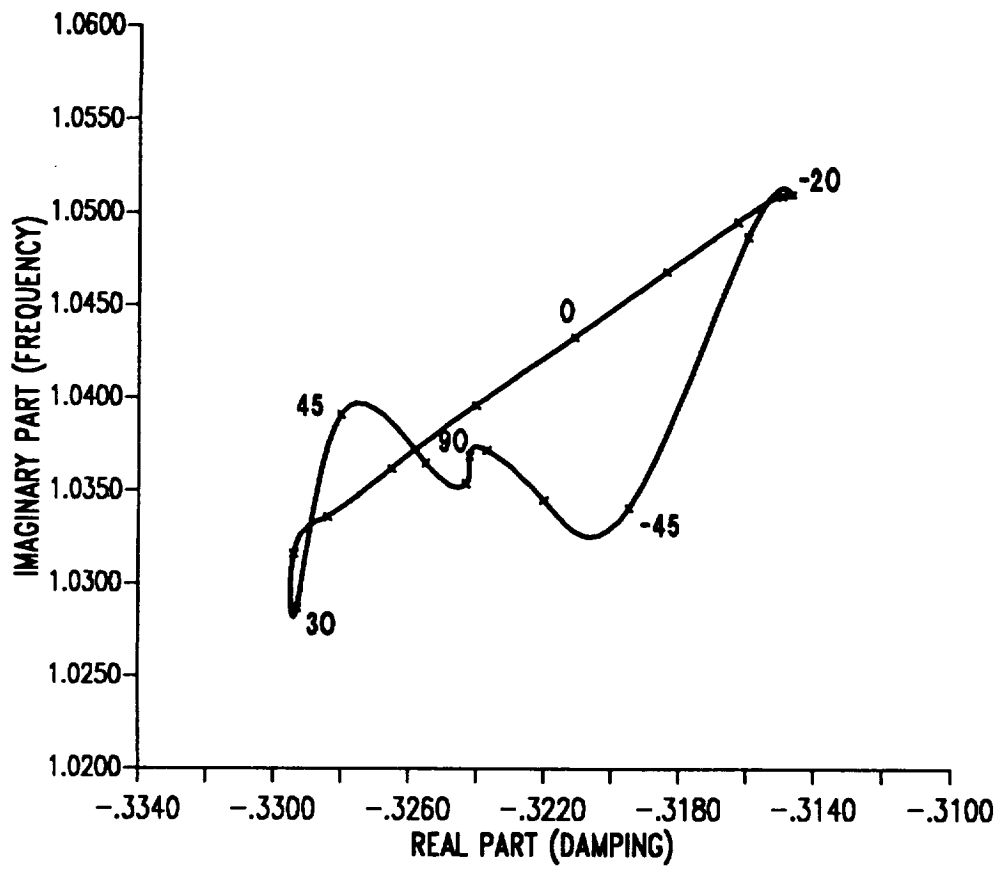


Figure 9.24: Root locus of first flap mode eigenvalues as a function of ply angle in vertical wall for two-cell composite blade in hover.

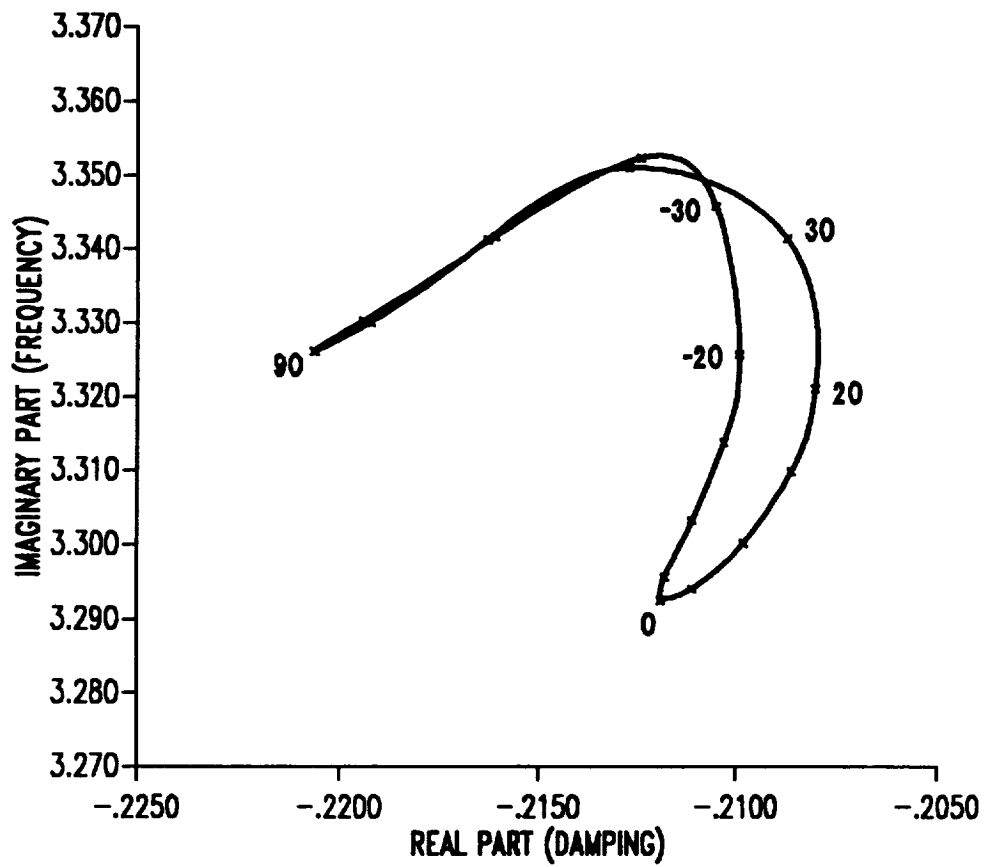


Figure 9.25: Root locus of first torsion mode eigenvalues as a function of ply angle in vertical wall for two-cell composite blade in hover.

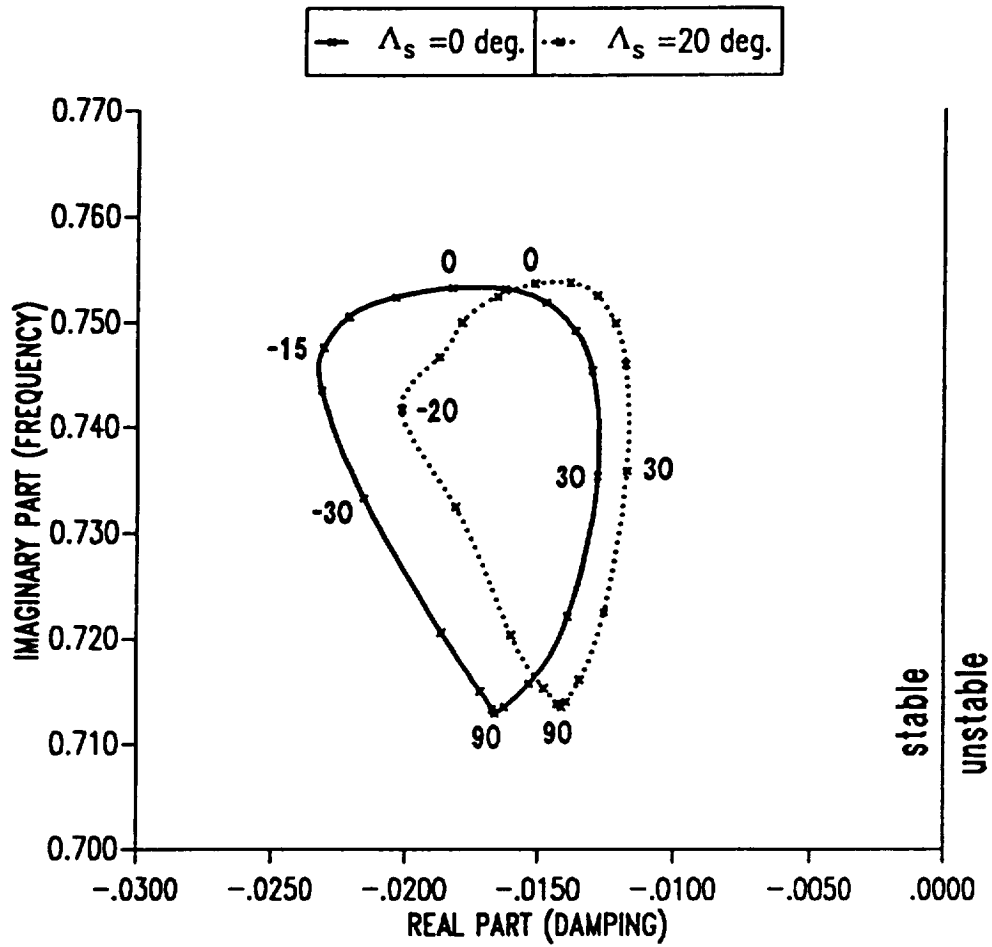


Figure 9.26: Root locus of first lag mode eigenvalues as a function of ply angle in horizontal wall for two-cell composite blade in hover.

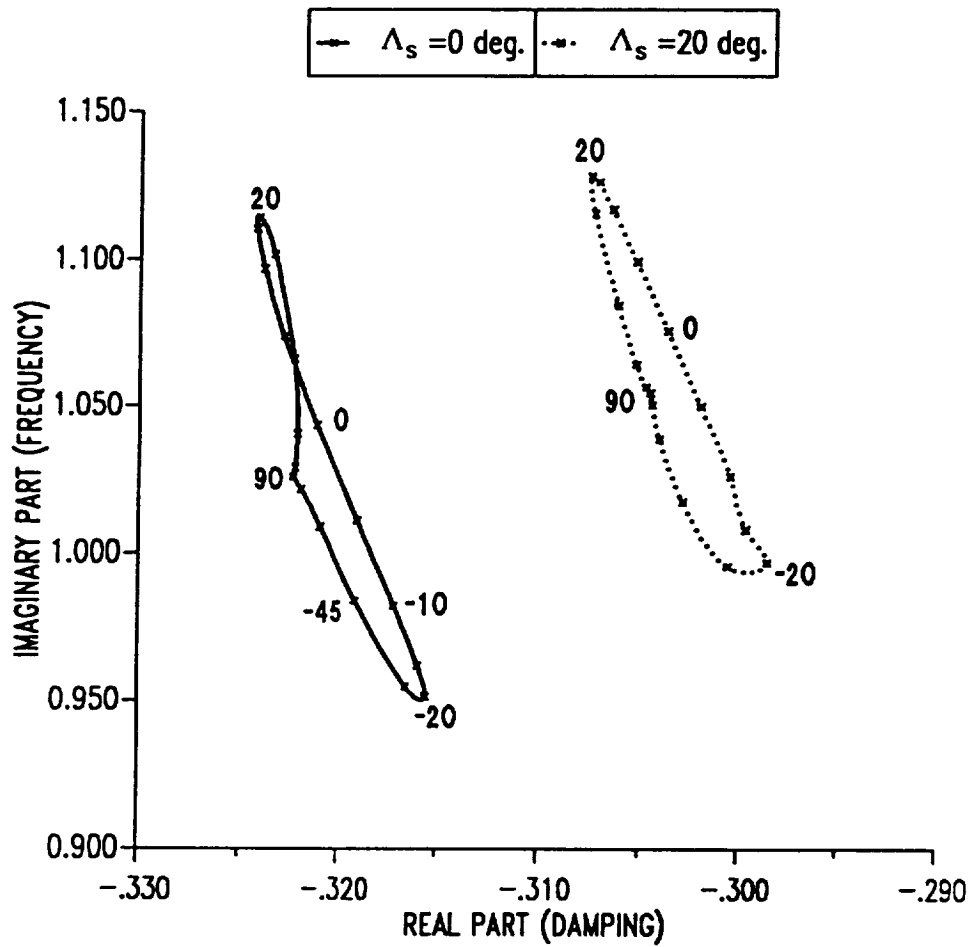


Figure 9.27: Root locus of first flap mode eigenvalues as a function of ply angle in horizontal wall for two-cell composite blade in hover.

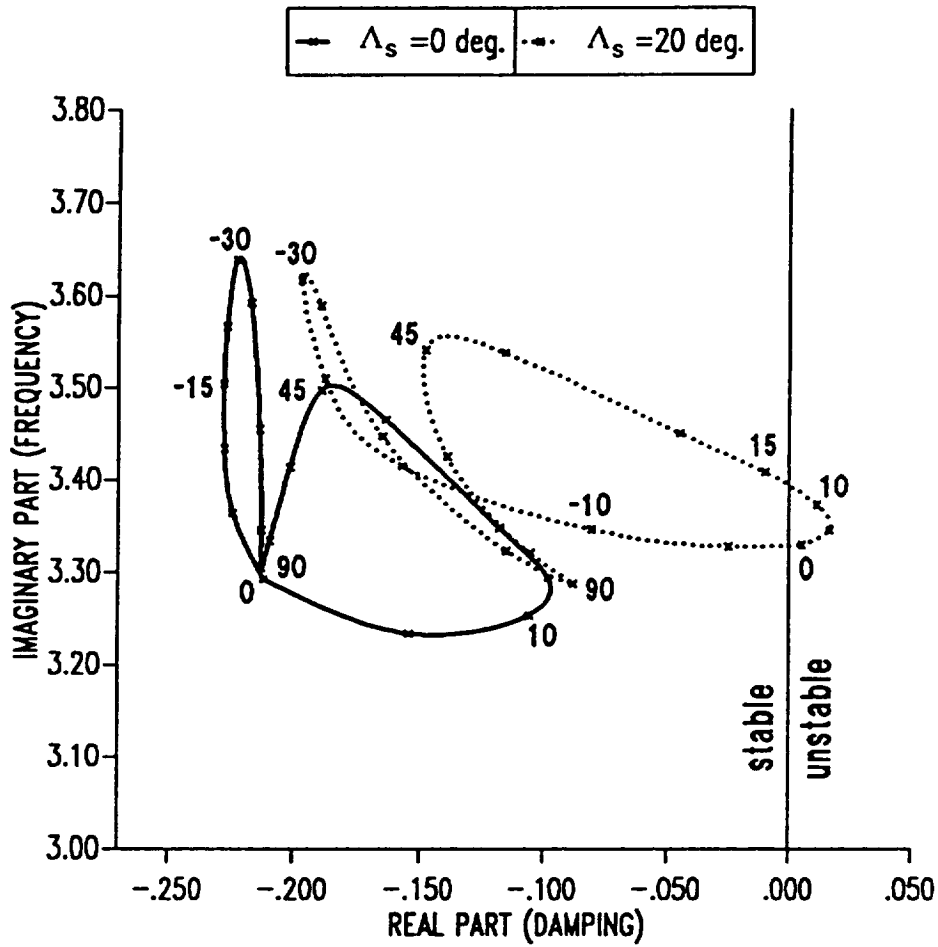


Figure 9.28: Root locus of first torsion mode eigenvalues as a function of ply angle in horizontal wall for two-cell composite blade in hover.

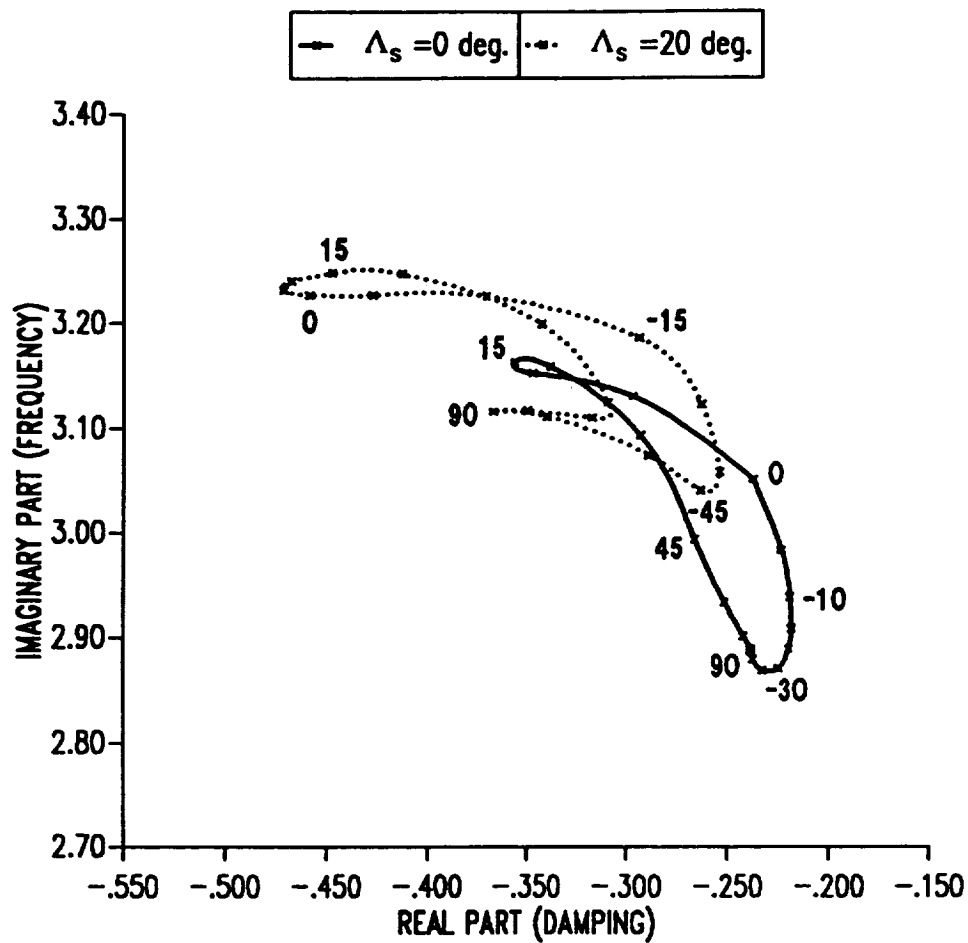


Figure 9.29: Root locus of second flap mode eigenvalues as a function of ply angle in horizontal wall for two-cell composite blade in hover.

**TWO-CELL COMPOSITE BLADE  
TIP RESPONSE, LAG MODE ( $\mu=0.3$ )**

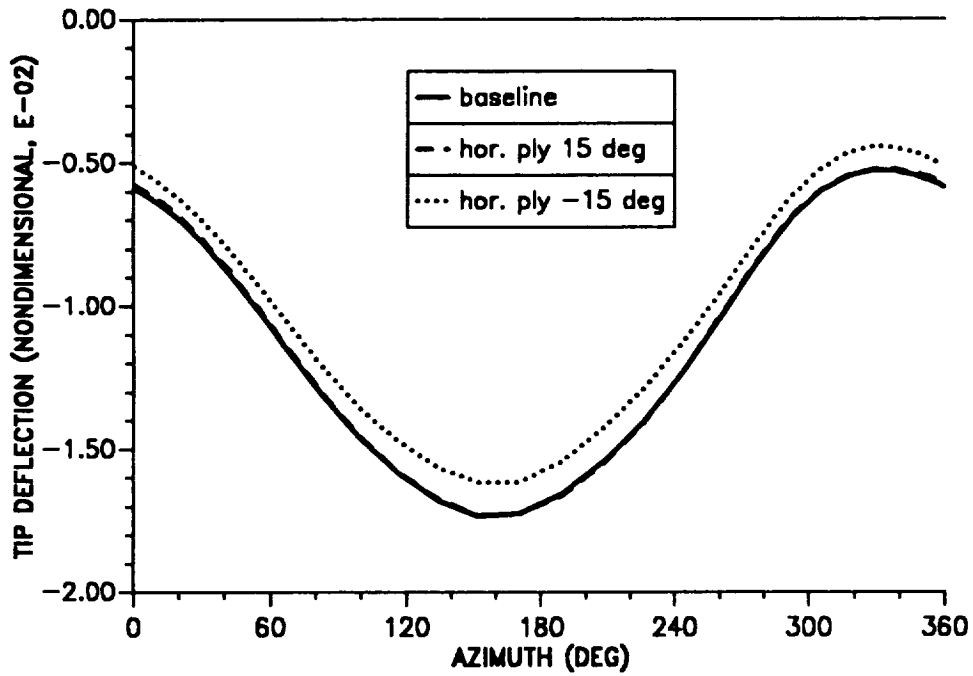


Figure 10.1: Effect of horizontal wall ply angle on blade tip response; lag mode ( $\mu = 0.30$ ).

**TWO-CELL COMPOSITE BLADE  
TIP RESPONSE, FLAP MODE ( $\mu=0.3$ )**

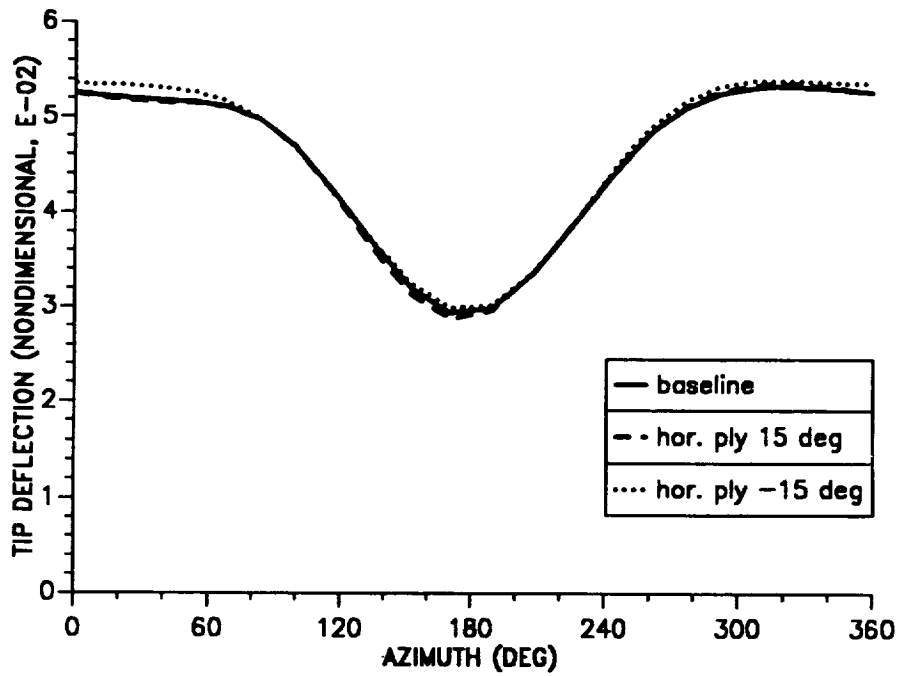


Figure 10.2: Effect of horizontal wall ply angle on blade tip response; flap mode ( $\mu = 0.30$ ).

**TWO-CELL COMPOSITE BLADE  
TIP RESPONSE, TORSION MODE (MU=0.3)**

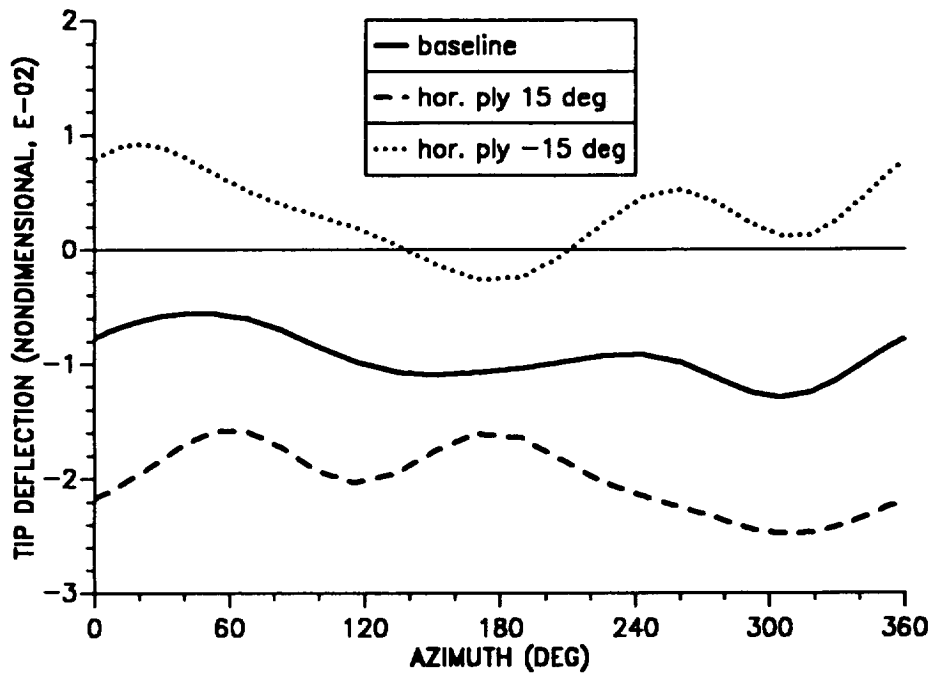


Figure 10.3: Effect of horizontal wall ply angle on blade tip response; torsion mode ( $\mu = 0.30$ ).

**TWO-CELL COMPOSITE BLADE  
TIP RESPONSE, LAG MODE ( $\mu=0.3$ )**

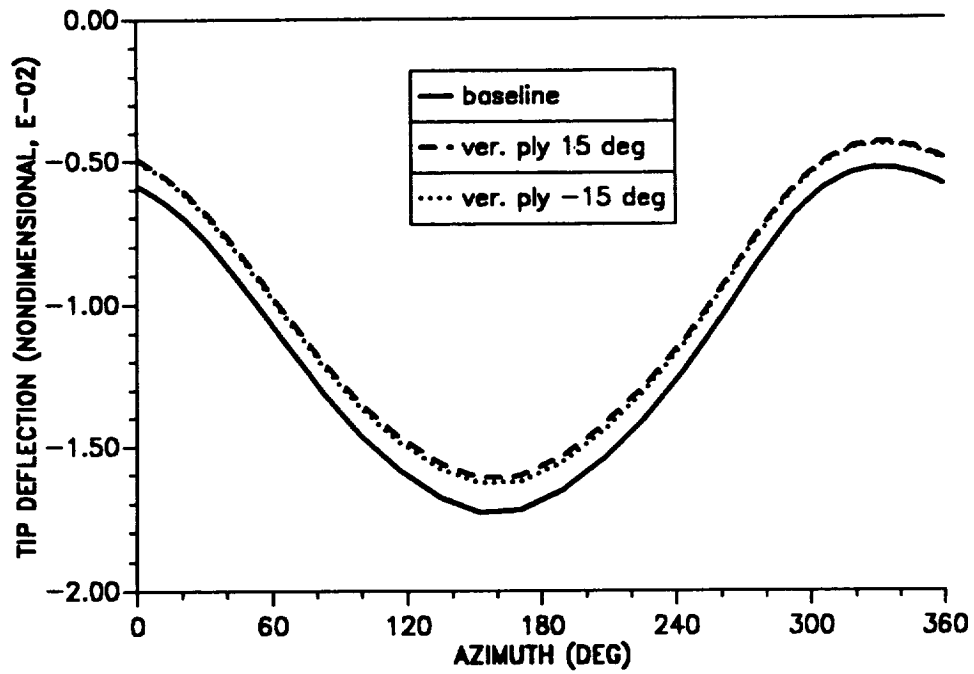


Figure 10.4: Effect of vertical wall ply angle on blade tip response; lag mode ( $\mu = 0.30$ ).

**TWO-CELL COMPOSITE BLADE  
TIP RESPONSE, FLAP MODE ( $\mu=0.3$ )**

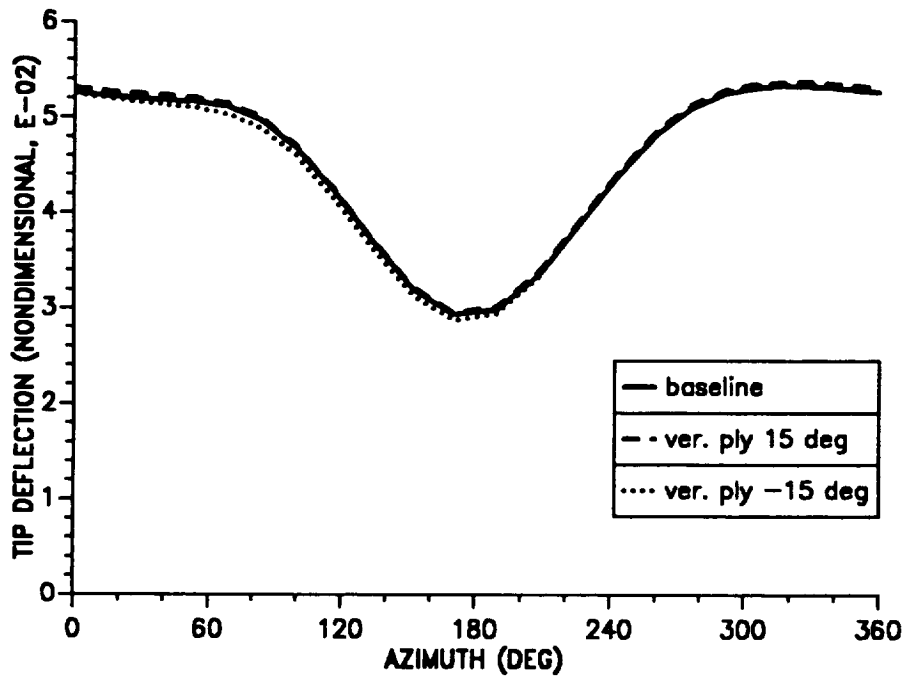


Figure 10.5: Effect of vertical wall ply angle on blade tip response; flap mode ( $\mu = 0.30$ ).

**TWO-CELL COMPOSITE BLADE  
TIP RESPONSE, TORSION MODE ( $\mu=0.3$ )**

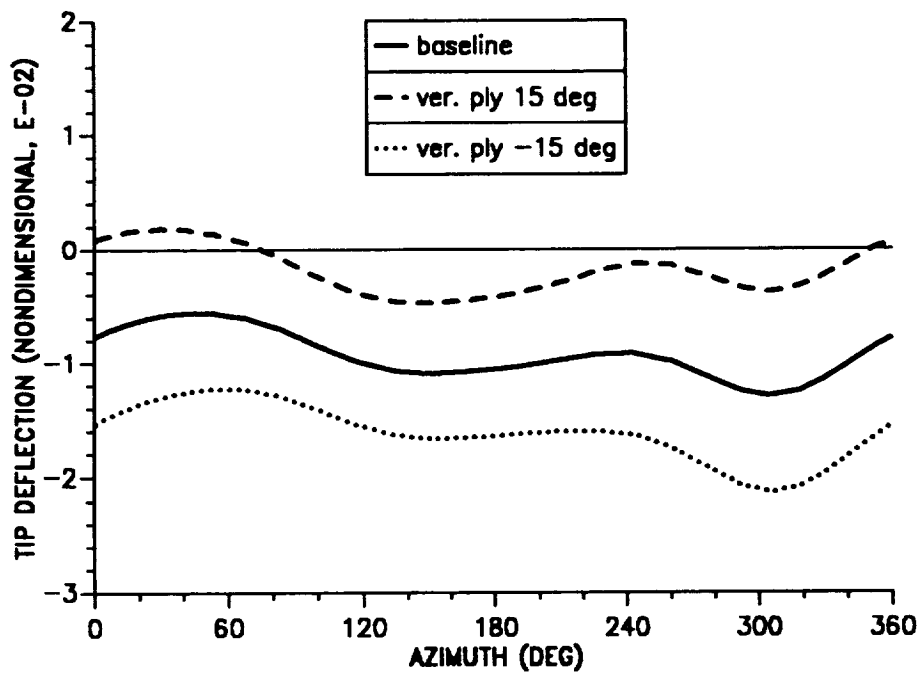


Figure 10.6: Effect of vertical wall ply angle on blade tip response; torsion mode ( $\mu = 0.30$ ).

**TWO-CELL COMPOSITE BLADE  
TIP RESPONSE, LAG MODE ( $\mu=0.3$ )**

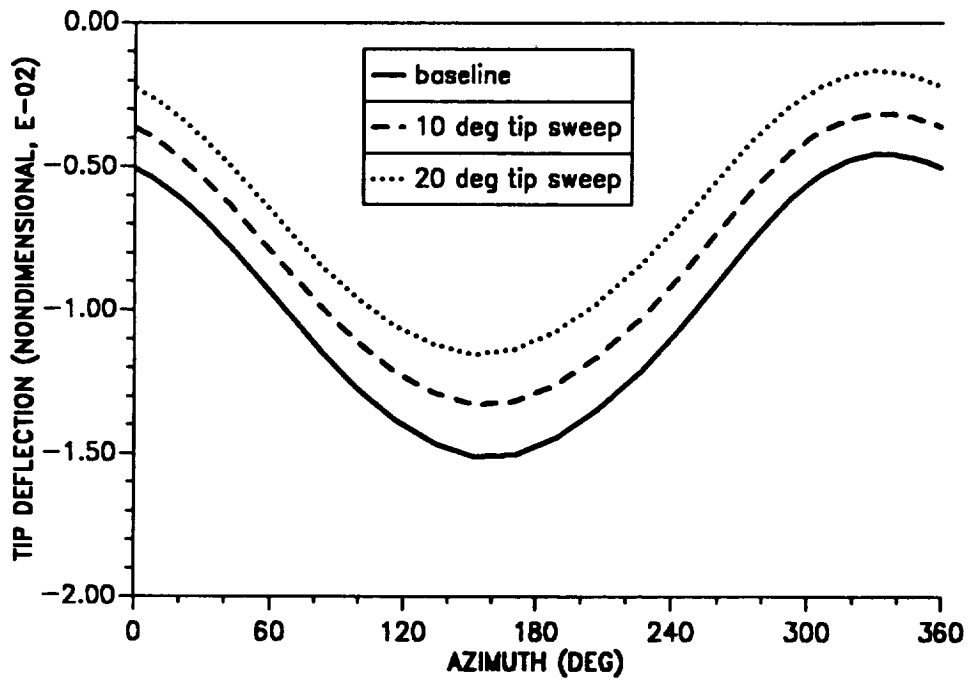


Figure 10.7: Effect of tip sweep angle on blade tip response; lag mode ( $\mu=0.30$ ).

**TWO-CELL COMPOSITE BLADE  
TIP RESPONSE, FLAP MODE ( $\mu=0.3$ )**

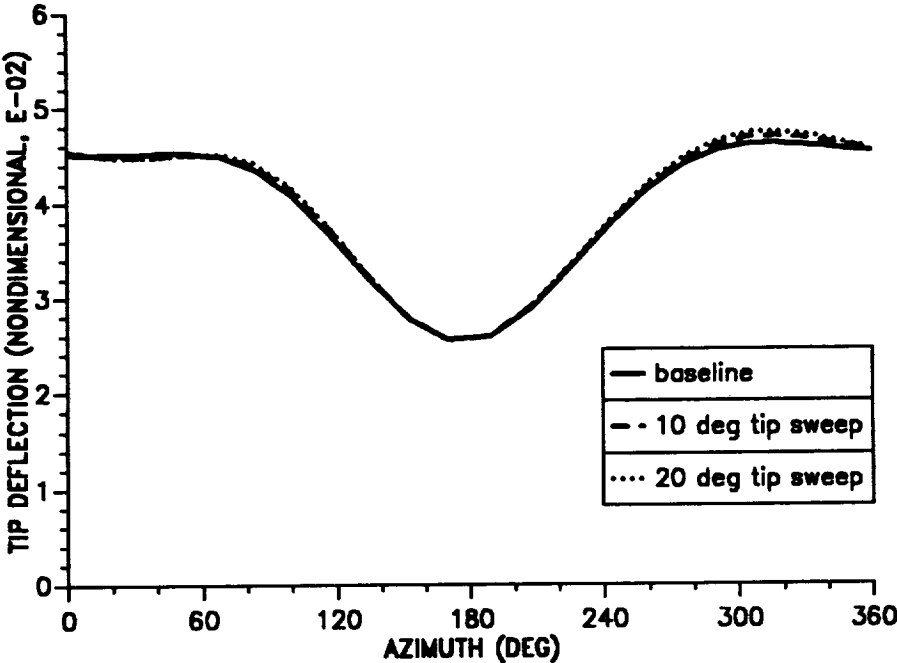


Figure 10.8: Effect of tip sweep angle on blade tip response; flap mode ( $\mu = 0.30$ ).

**TWO-CELL COMPOSITE BLADE  
TIP RESPONSE, TORSION MODE ( $\mu=0.3$ )**

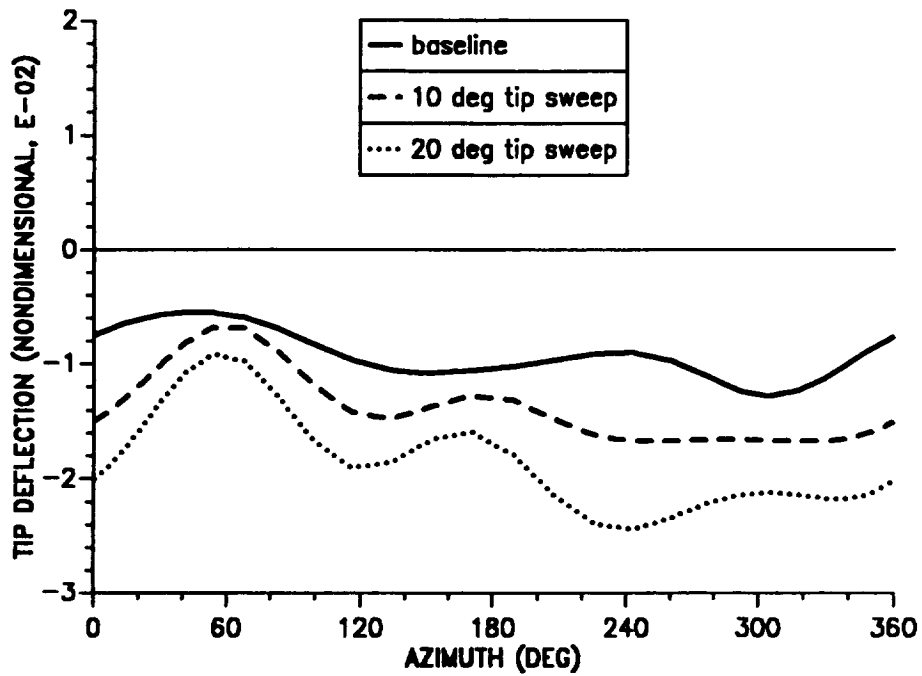


Figure 10.9: Effect of tip sweep angle on blade tip response; torsion mode ( $\mu=0.30$ ).

**TWO-CELL COMPOSITE BLADE  
TIP RESPONSE, LAG MODE ( $\mu=0.3$ )**

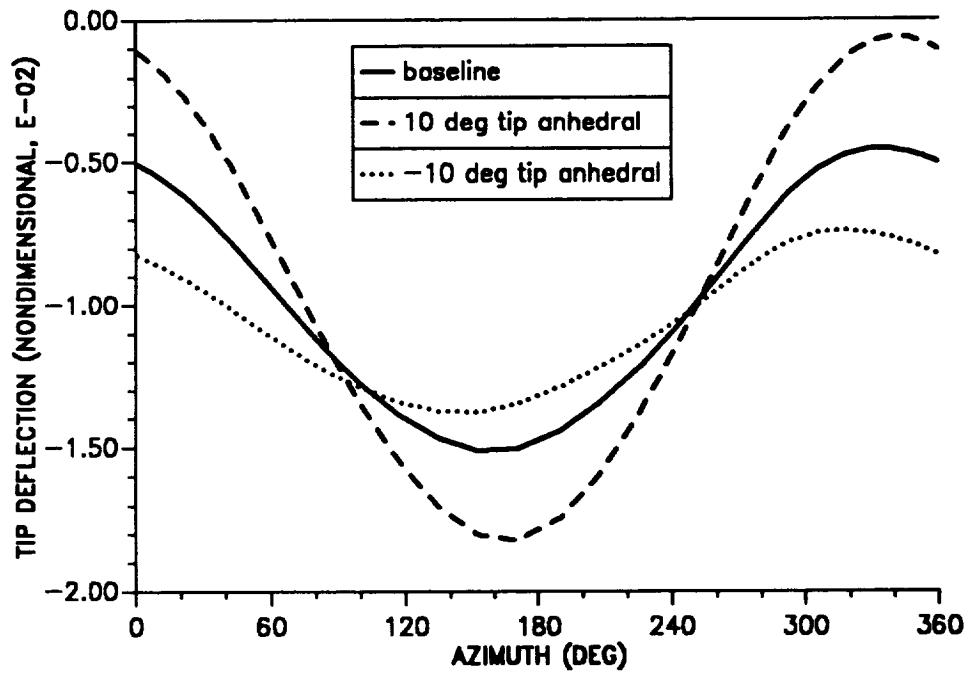


Figure 10.10: Effect of tip anhedral angle on blade tip response; lag mode ( $\mu = 0.30$ ).

**TWO-CELL COMPOSITE BLADE  
TIP RESPONSE, FLAP MODE ( $\mu=0.3$ )**

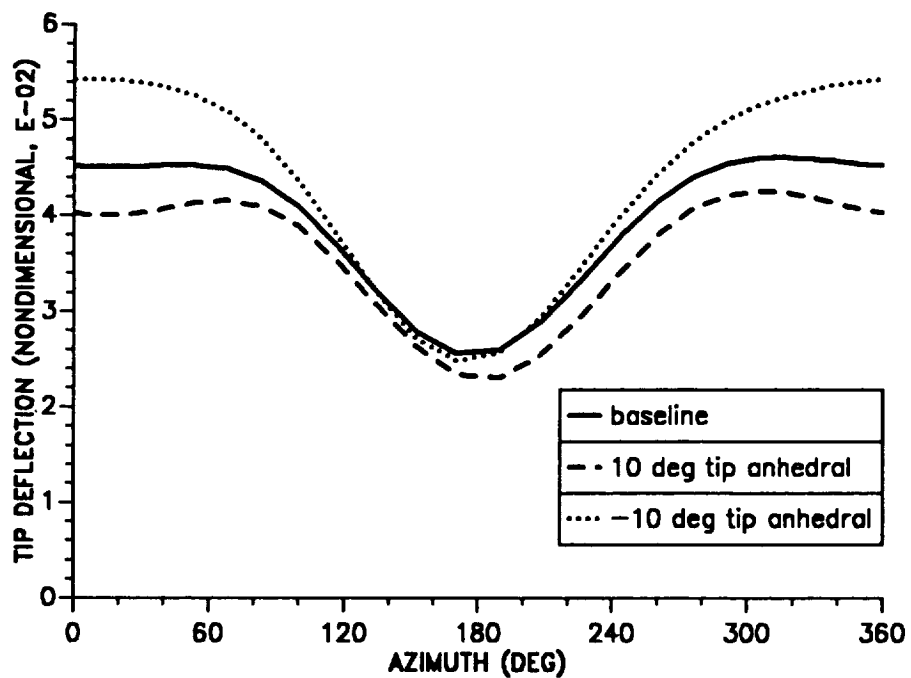


Figure 10.11: Effect of tip anhedral angle on blade tip response; flap mode ( $\mu = 0.30$ ).

**TWO-CELL COMPOSITE BLADE  
TIP RESPONSE, TORSION MODE (MU=0.3)**

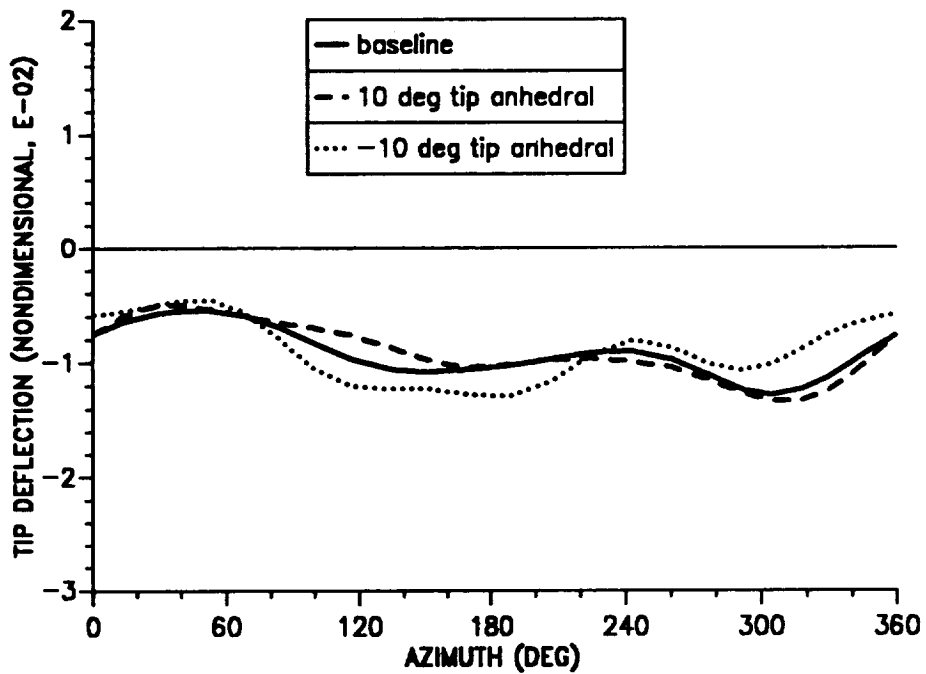


Figure 10.12: Effect of tip anhedral angle on blade tip response; torsion mode ( $\mu = 0.30$ ).

**TWO-CELL COMPOSITE BLADE  
TRIM VARIABLES ( $\mu=0.3$ )**

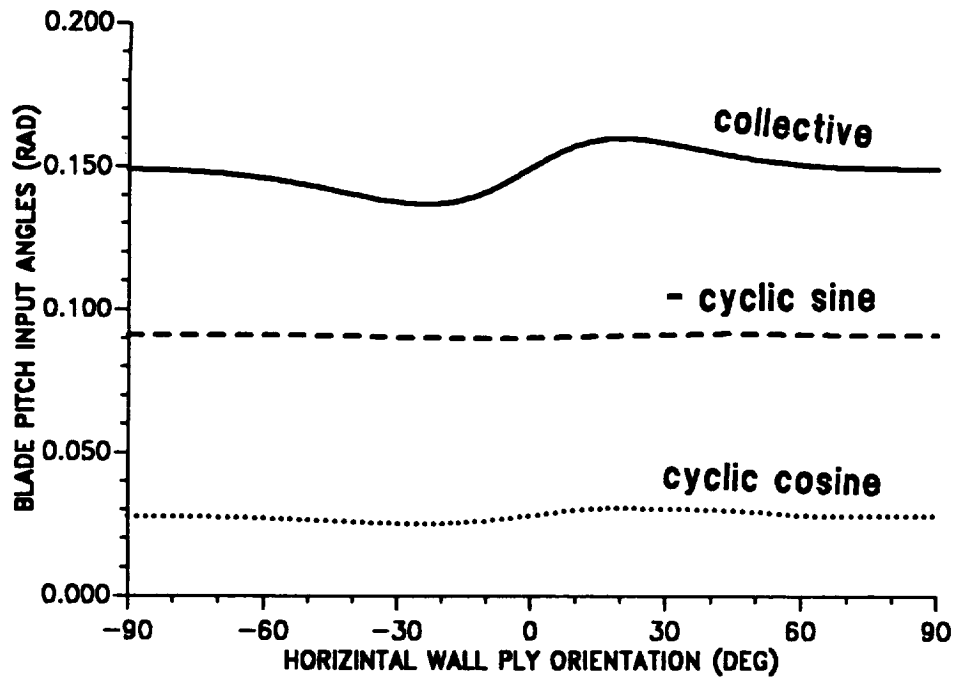


Figure 10.13: Effect of horizontal wall ply angle on trim variables; pitch setting ( $\mu = 0.30$ ).

**TWO-CELL COMPOSITE BLADE  
TRIM VARIABLES ( $\mu=0.3$ )**

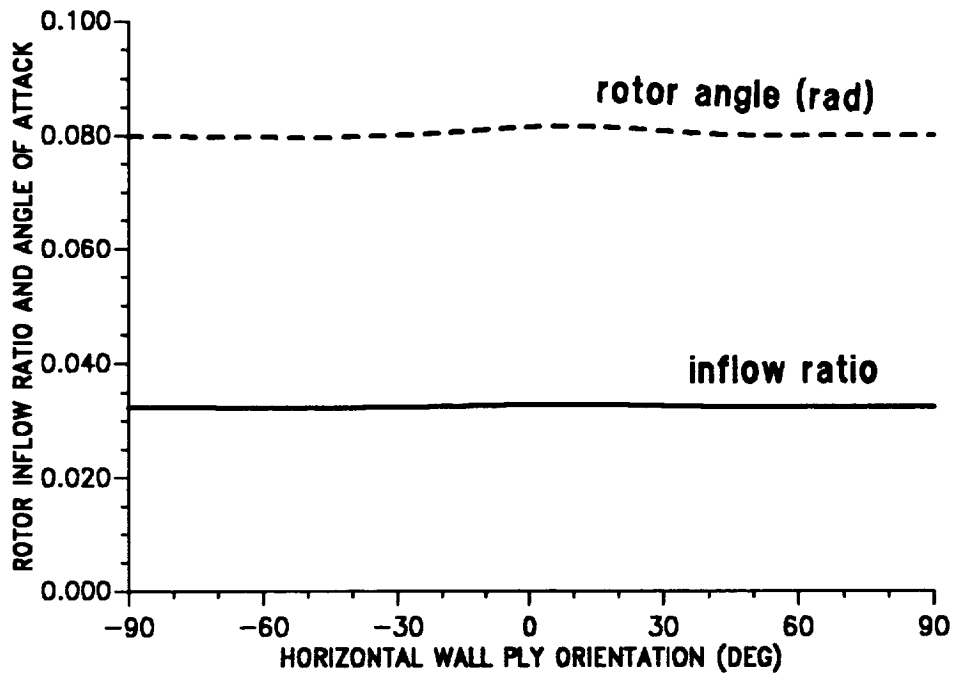


Figure 10.14: Effect of horizontal wall ply angle on trim variables; inflow and rotor angle of attack ( $\mu = 0.30$ ).

**TWO-CELL COMPOSITE BLADE  
TRIM VARIABLES ( $\mu=0.3$ )**

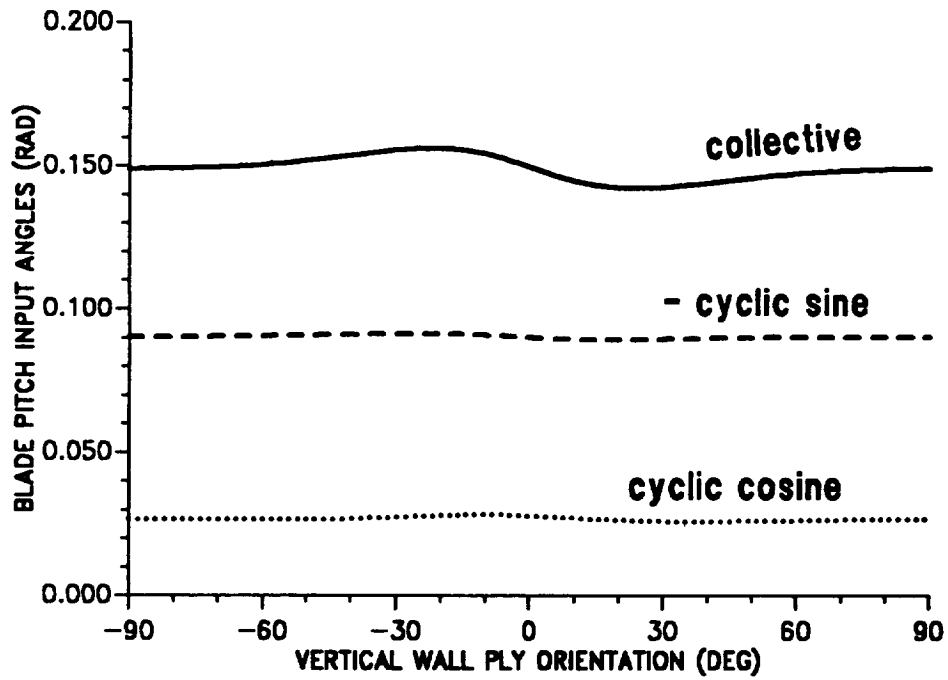


Figure 10.15: Effect of vertical wall ply angle on trim variables; pitch setting ( $\mu = 0.30$ ).

**TWO-CELL COMPOSITE BLADE  
TRIM VARIABLES ( $\mu=0.3$ )**

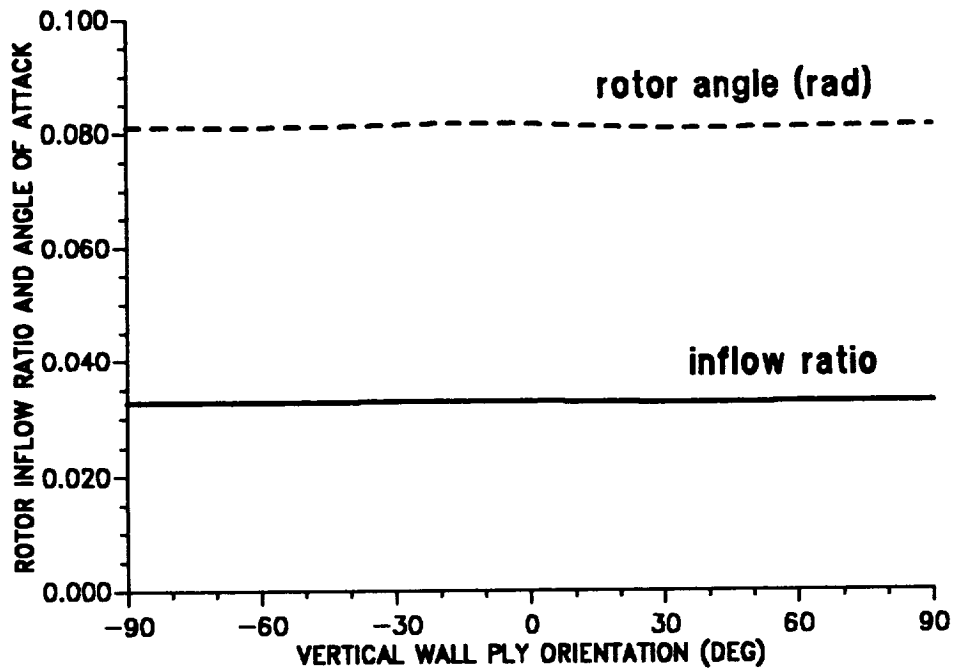


Figure 10.16: Effect of vertical wall ply angle on trim variables; inflow and rotor angle of attack ( $\mu = 0.30$ ).

**TWO-CELL COMPOSITE BLADE  
TRIM VARIABLES ( $\mu=0.3$ )**

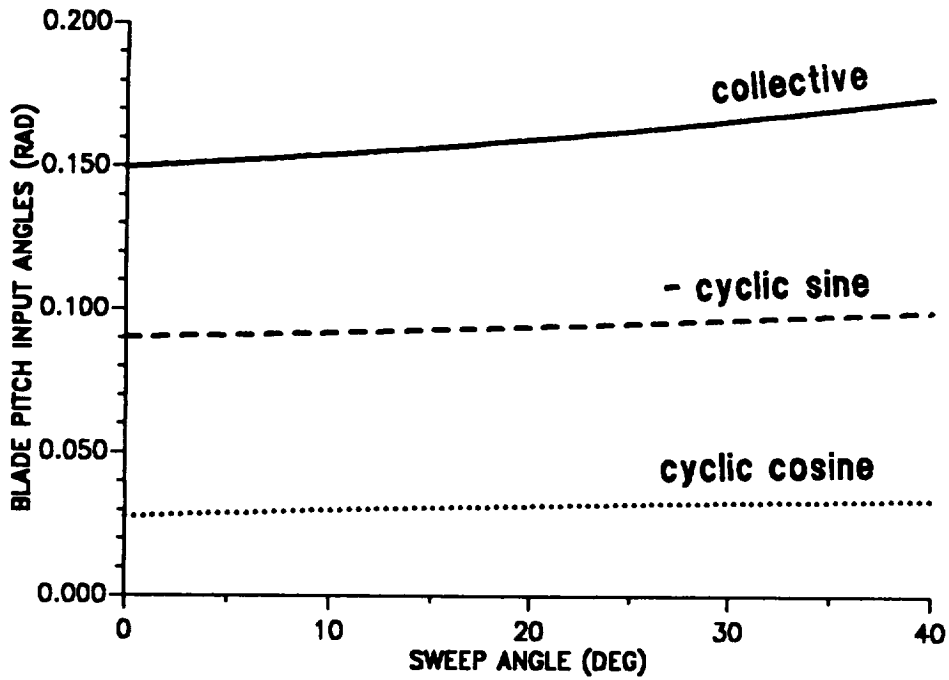


Figure 10.17: Effect of tip sweep angle on trim variables; pitch setting ( $\mu = 0.30$ ).

**TWO-CELL COMPOSITE BLADE  
TRIM VARIABLES ( $\mu=0.3$ )**

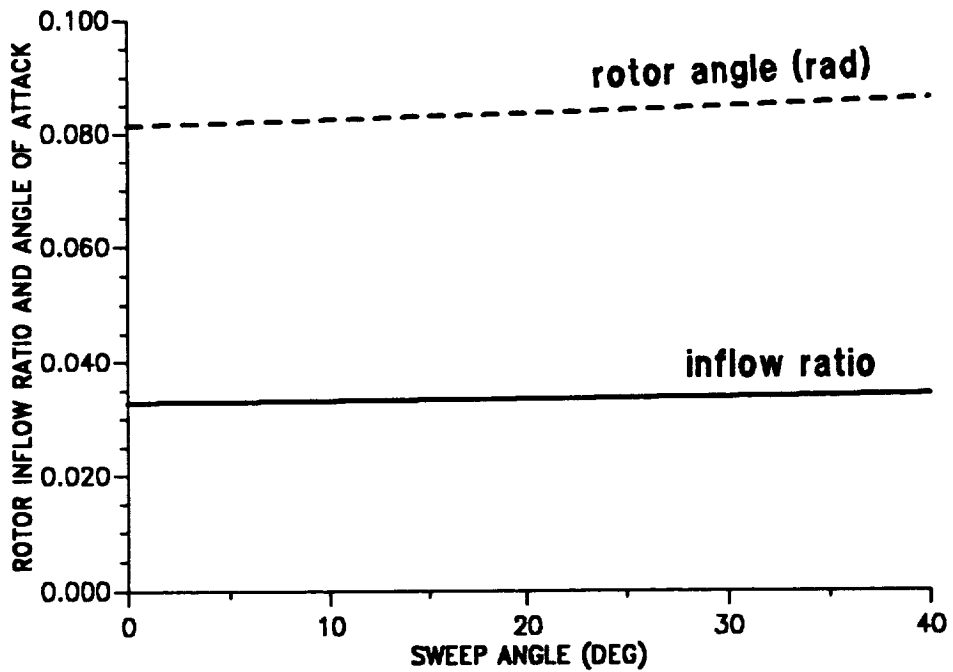


Figure 10.18: Effect of tip sweep angle on trim variables; inflow and rotor angle of attack ( $\mu=0.30$ ).

**TWO-CELL COMPOSITE BLADE  
TRIM VARIABLES ( $\mu=0.3$ )**

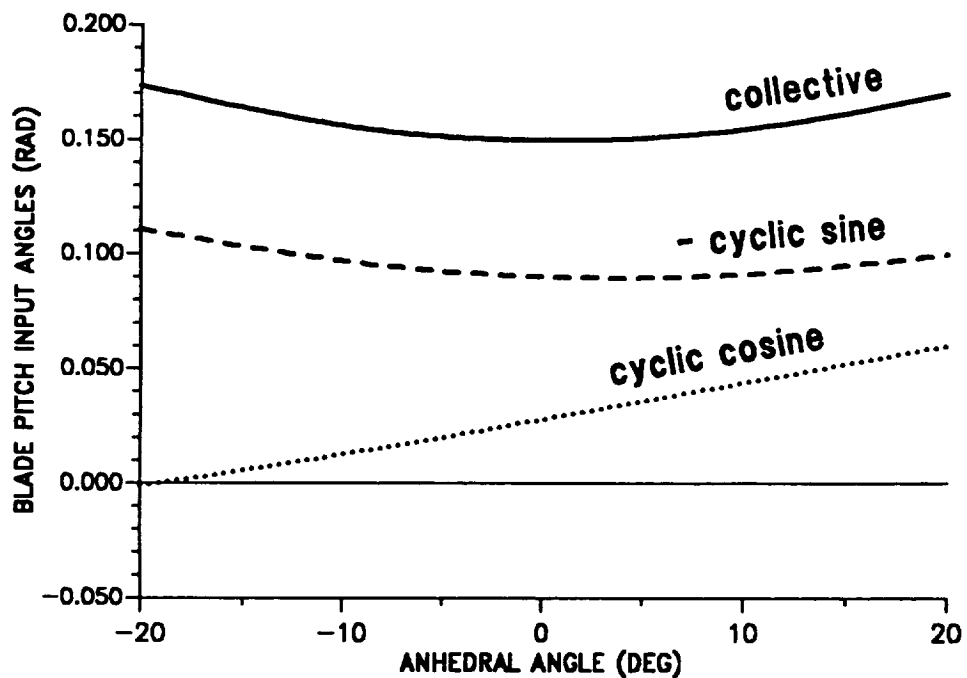


Figure 10.19: Effect of tip anedral angle on trim variables; pitch setting ( $\mu = 0.30$ ).

**TWO-CELL COMPOSITE BLADE  
TRIM VARIABLES ( $\mu=0.3$ )**

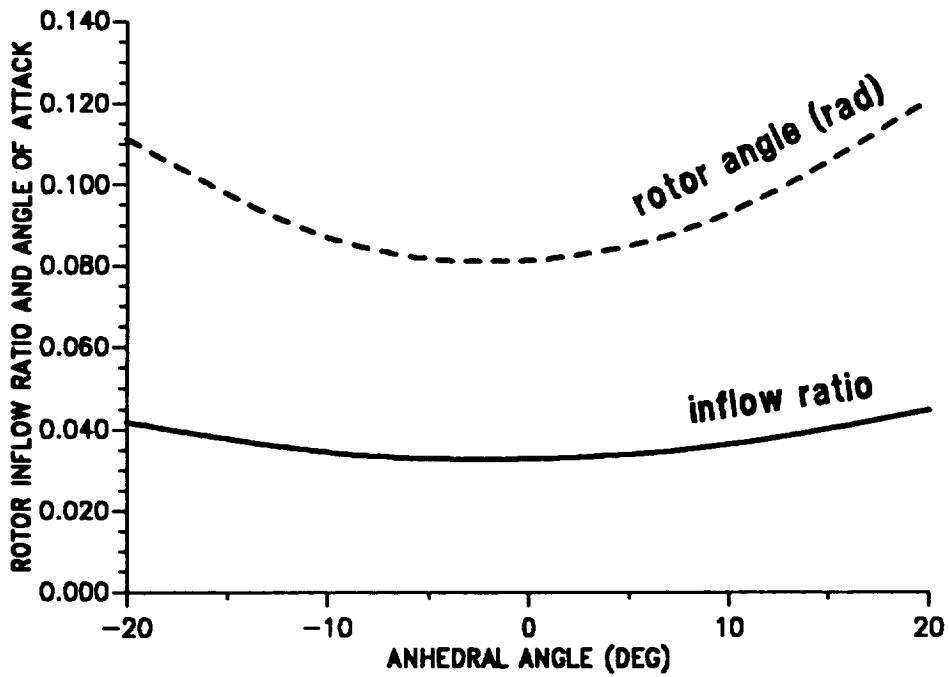


Figure 10.20: Effect of tip anhedral angle on trim variables; inflow and rotor angle of attack ( $\mu = 0.30$ ).

**TWO-CELL COMPOSITE BLADE  
VIBRATORY HUB SHEARS ( $\mu=0.3$ )**

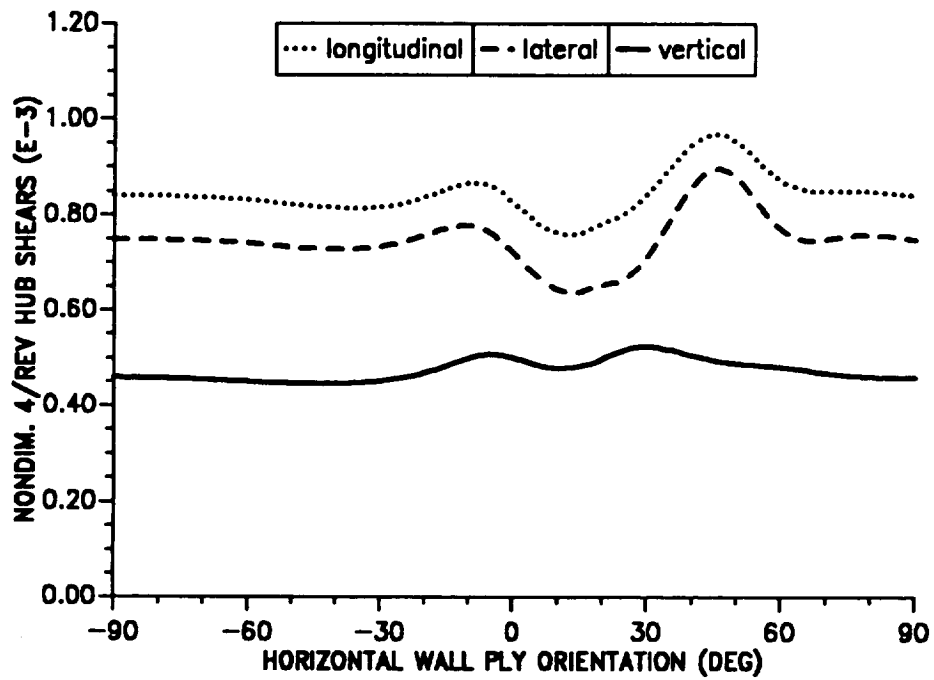


Figure 10.21: Effect of horizontal wall ply angle on 4/rev hub shears ( $\mu = 0.30$ ).

**TWO-CELL COMPOSITE BLADE  
VIBRATORY HUB MOMENTS ( $\mu=0.3$ )**

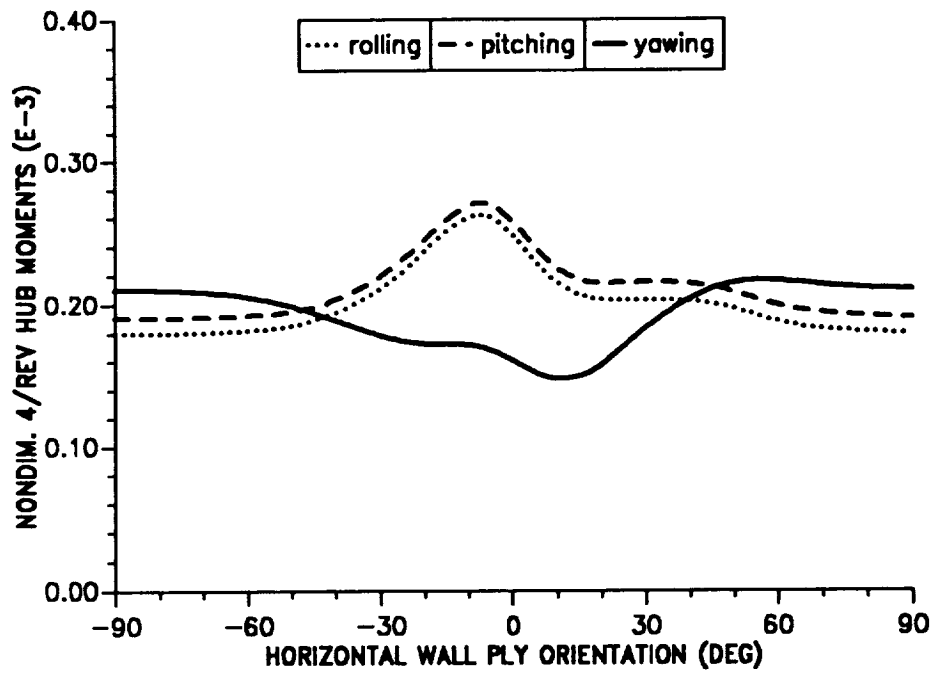


Figure 10.22: Effect of horizontal wall ply angle on 4/rev hub moments ( $\mu = 0.30$ ).

**TWO-CELL COMPOSITE BLADE  
VIBRATORY HUB SHEARS ( $\mu=0.3$ )**

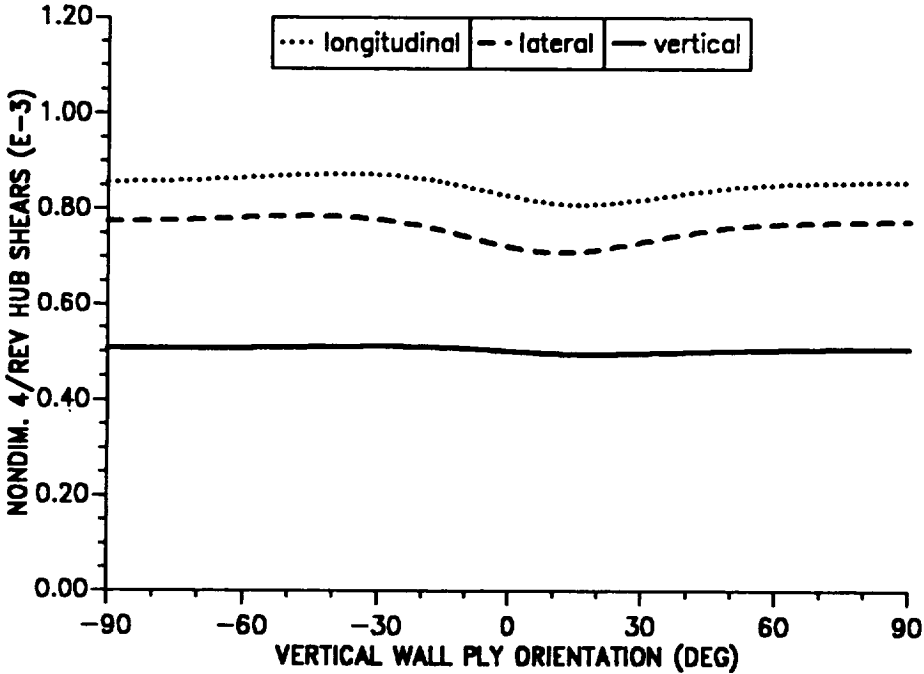


Figure 10.23: Effect of vertical wall ply angle on 4/rev hub shears ( $\mu = 0.30$ ).

**TWO-CELL COMPOSITE BLADE  
VIBRATORY HUB MOMENTS ( $\mu=0.3$ )**

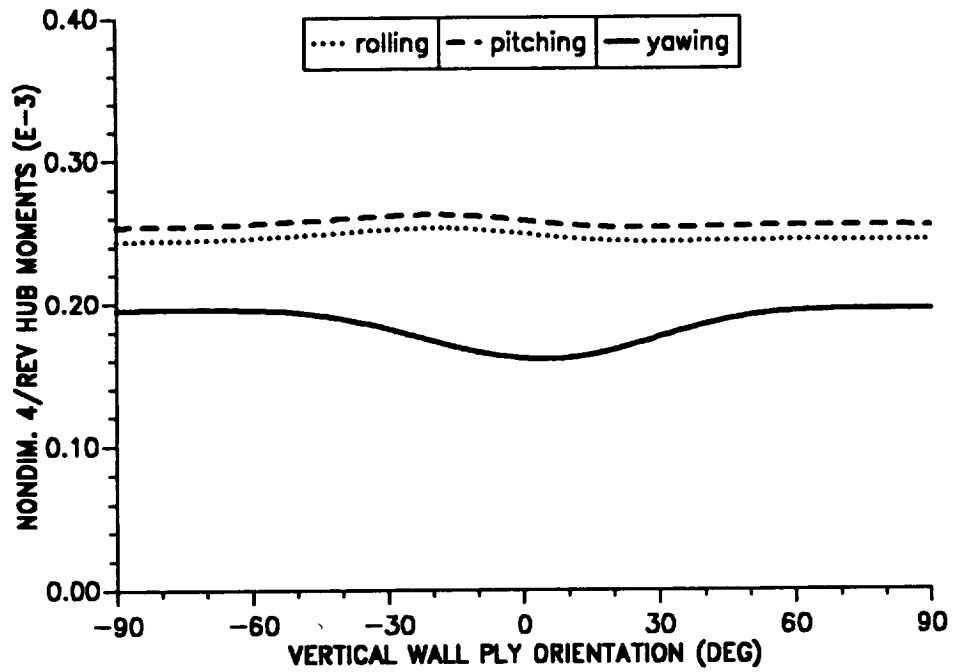


Figure 10.24: Effect of vertical wall ply angle on 4/rev hub moments ( $\mu = 0.30$ ).

**TWO-CELL COMPOSITE BLADE  
VIBRATORY HUB SHEARS ( $\mu=0.3$ )**

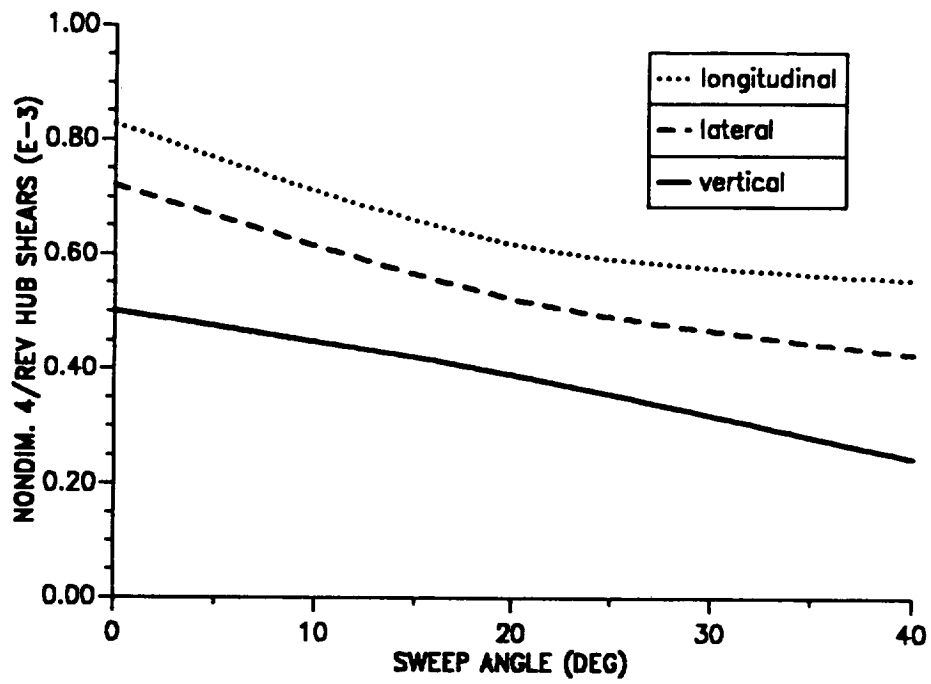


Figure 10.25: Effect of tip sweep angle on 4/rev hub shears ( $\mu = 0.30$ ).

**TWO-CELL COMPOSITE BLADE  
VIBRATORY HUB MOMENTS ( $\mu=0.3$ )**

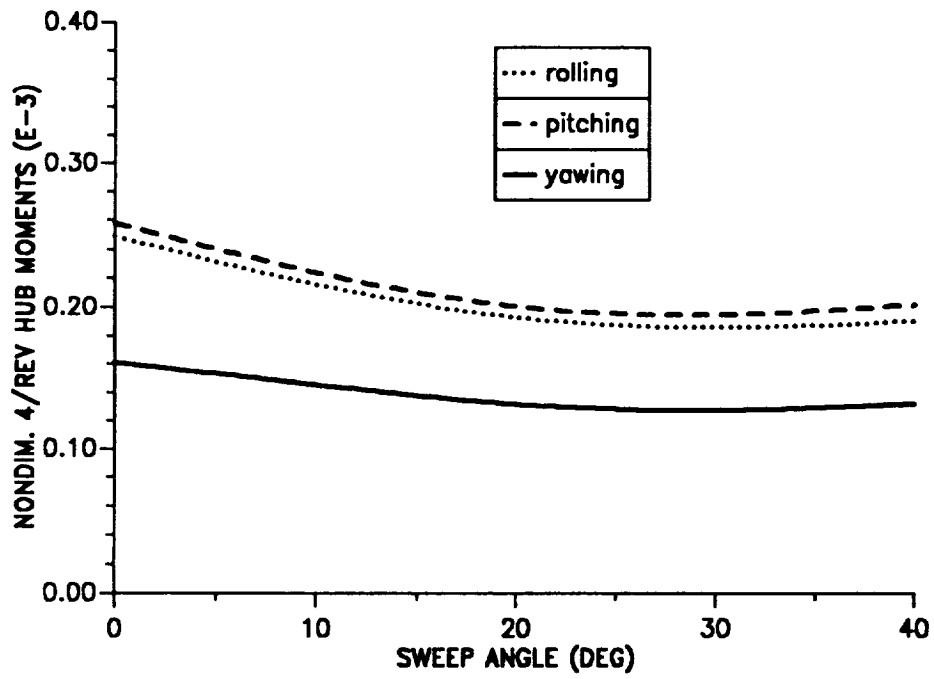


Figure 10.26: Effect of tip sweep angle on 4/rev hub moments ( $\mu = 0.30$ ).

**TWO-CELL COMPOSITE BLADE  
VIBRATORY HUB SHEARS ( $\mu=0.3$ )**

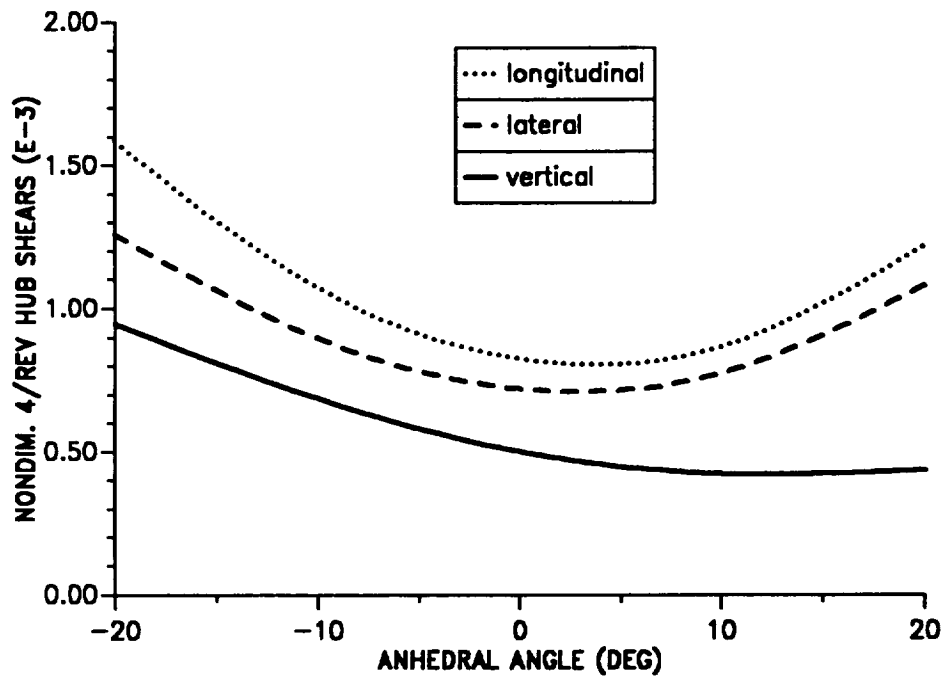


Figure 10.27: Effect of tip anedral angle on 4/rev hub shears ( $\mu = 0.30$ ).

**TWO-CELL COMPOSITE BLADE  
VIBRATORY HUB MOMENTS ( $\mu=0.3$ )**

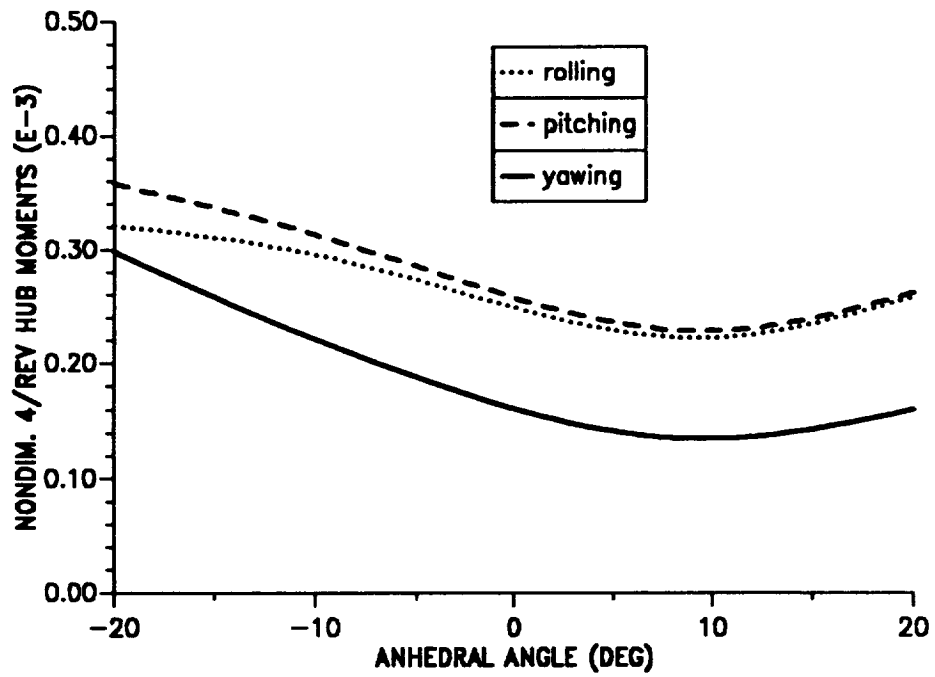


Figure 10.28: Effect of tip anhedral angle on 4/rev hub moments ( $\mu = 0.30$ ).

**TWO-CELL COMPOSITE BLADE  
AEROELASTIC STABILITY ( $\mu=0.3$ )**

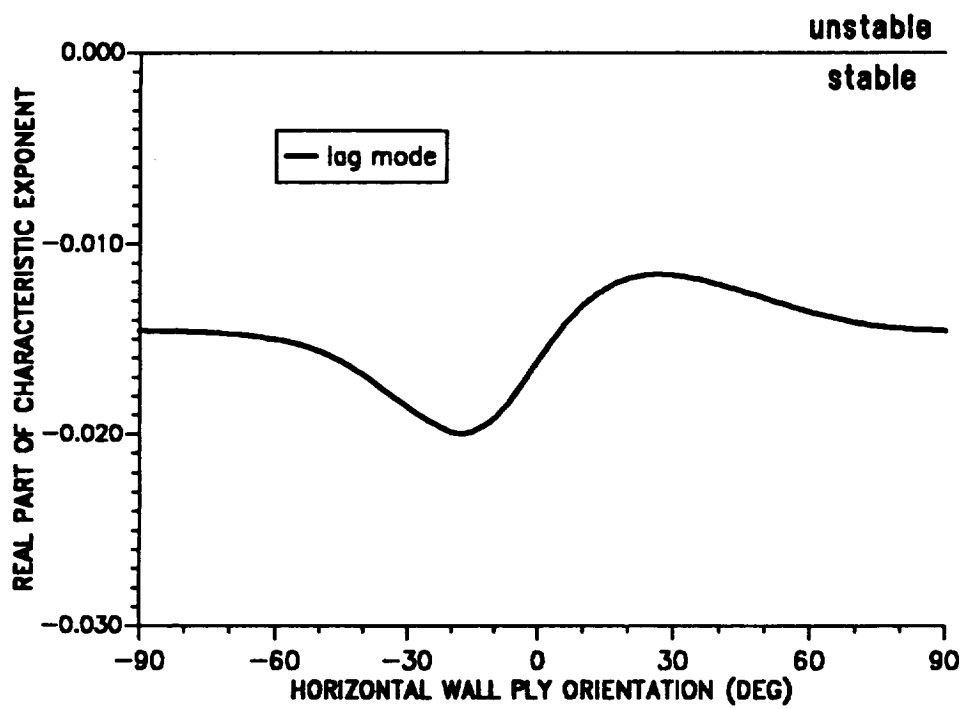


Figure 10.29: Effect of horizontal wall ply angle on blade stability; first lag mode ( $\mu = 0.30$ ).

**TWO-CELL COMPOSITE BLADE  
AEROELASTIC STABILITY ( $\mu=0.3$ )**

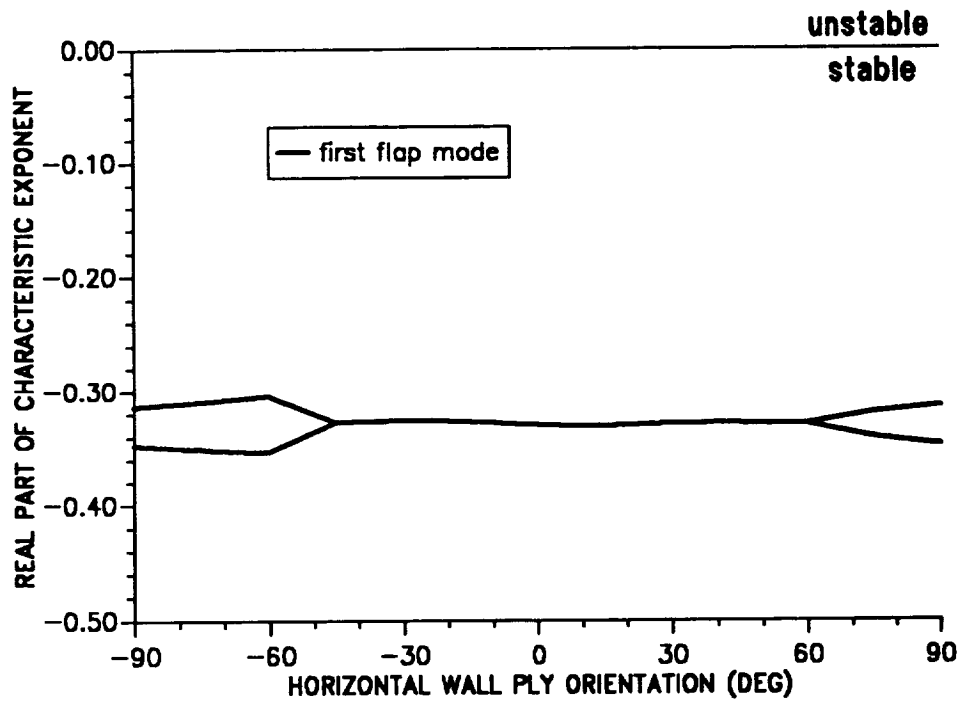


Figure 10.30: Effect of horizontal wall ply angle on blade stability; first flap mode ( $\mu = 0.30$ ).

**TWO-CELL COMPOSITE BLADE  
AEROELASTIC STABILITY ( $\mu=0.3$ )**

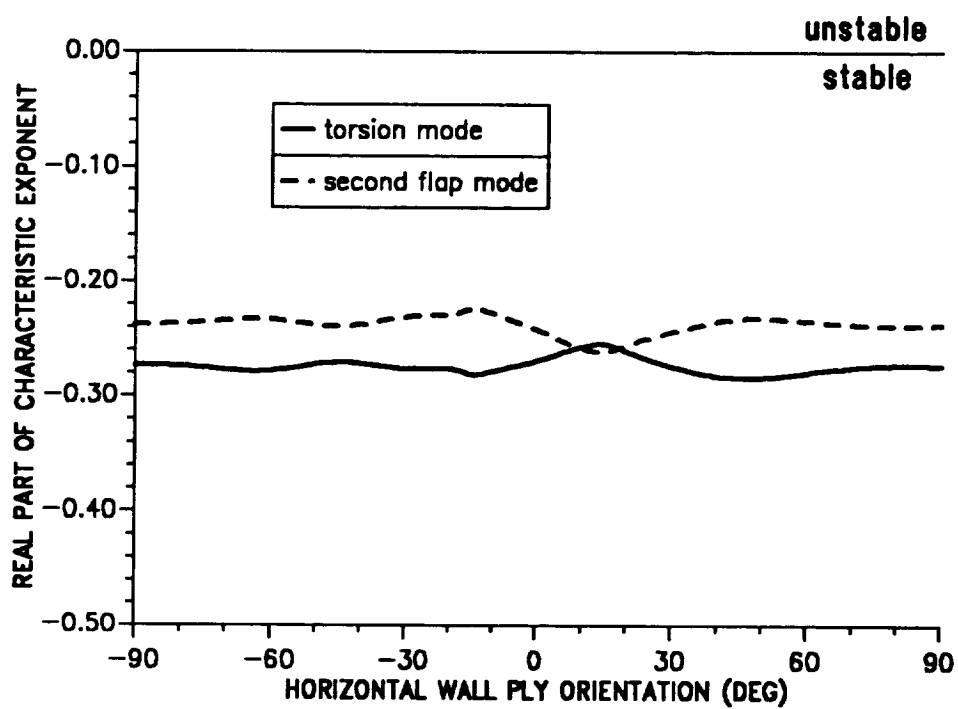


Figure 10.31: Effect of horizontal wall ply angle on blade stability; first torsion and second flap modes ( $\mu = 0.30$ ).

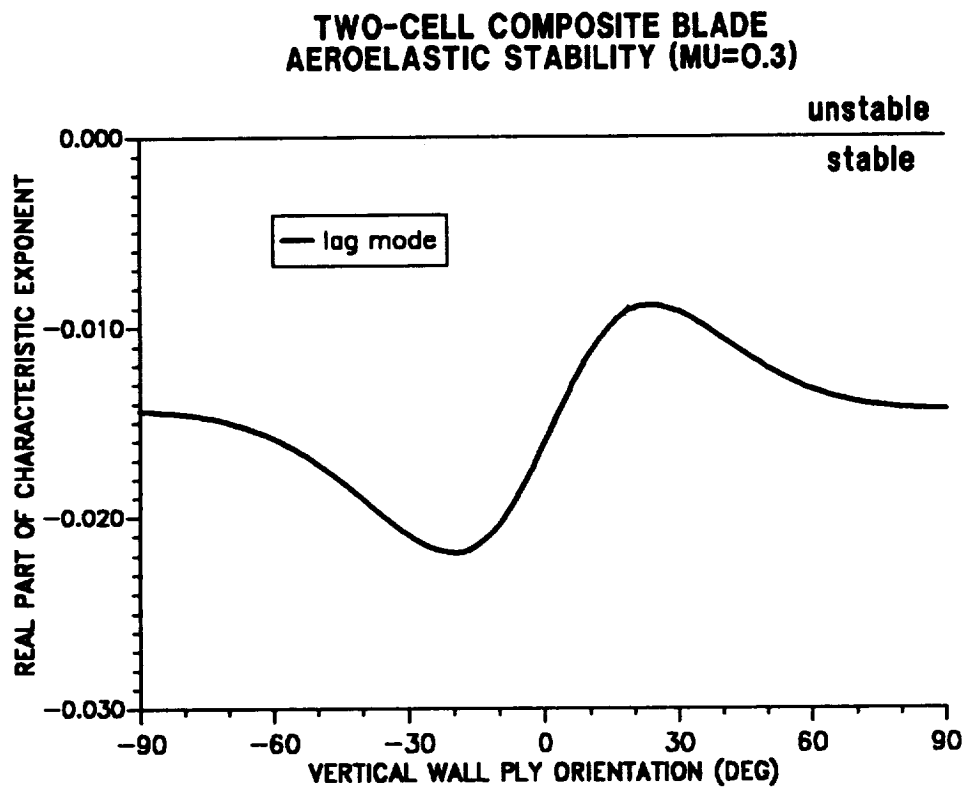


Figure 10.32: Effect of vertical wall ply angle on blade stability; first lag mode ( $\mu = 0.30$ ).

**TWO-CELL COMPOSITE BLADE  
AEROELASTIC STABILITY ( $\mu=0.3$ )**

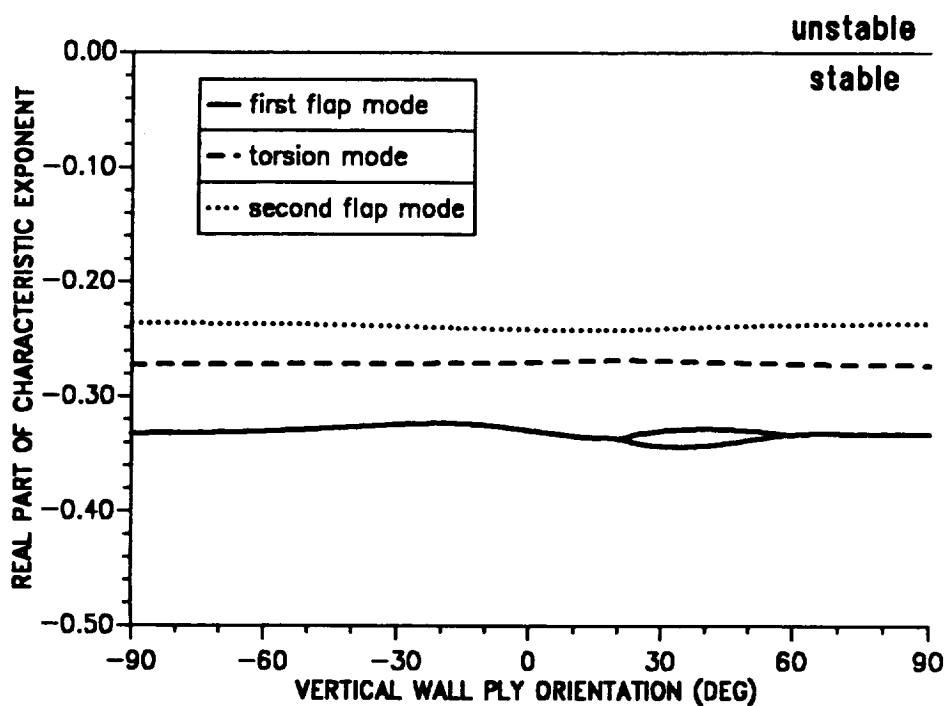


Figure 10.33: Effect of vertical wall ply angle on blade stability; first, second flap and first torsion modes ( $\mu = 0.30$ ).

**TWO-CELL COMPOSITE BLADE  
AEROELASTIC STABILITY ( $\mu=0.3$ )**

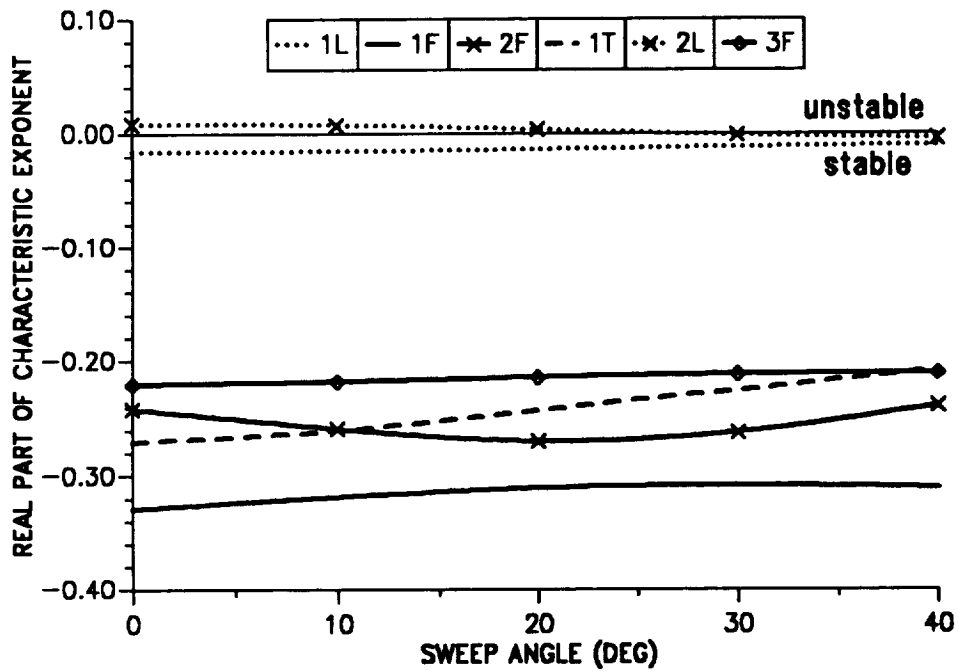


Figure 10.34: Effect of tip sweep angle on blade stability for the first six modes ( $\mu = 0.30$ ).

**TWO-CELL COMPOSITE BLADE  
AEROELASTIC STABILITY ( $\mu=0.3$ )**

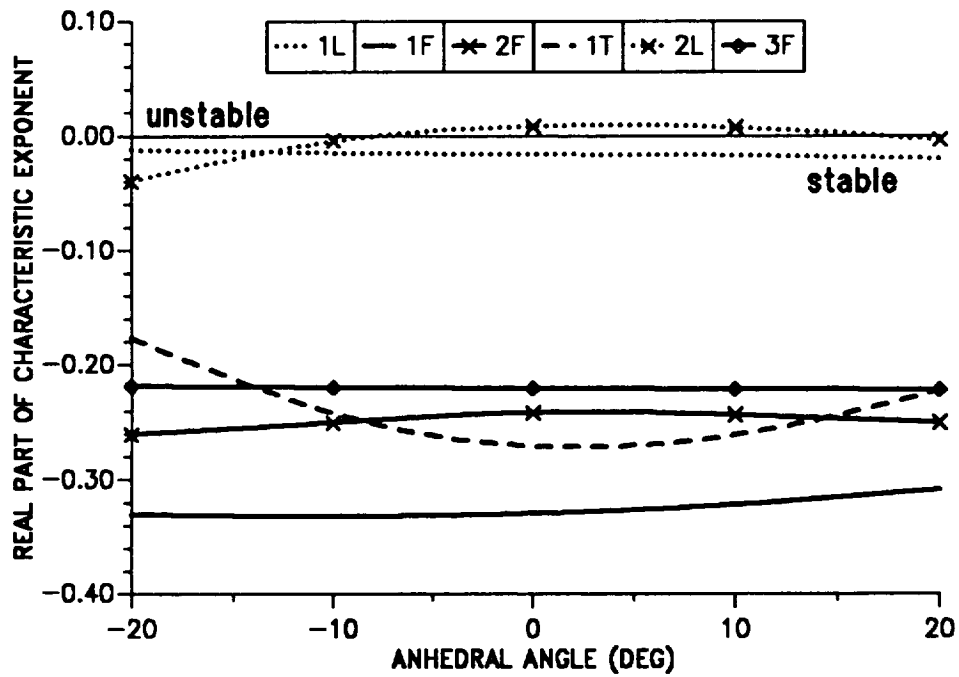


Figure 10.35: Effect of tip anhedral angle on blade stability for the first six modes ( $\mu = 0.30$ ).

**TWO-CELL COMPOSITE BLADE (MODIFIED)  
AEROELASTIC STABILITY ( $\mu=0.3$ )**

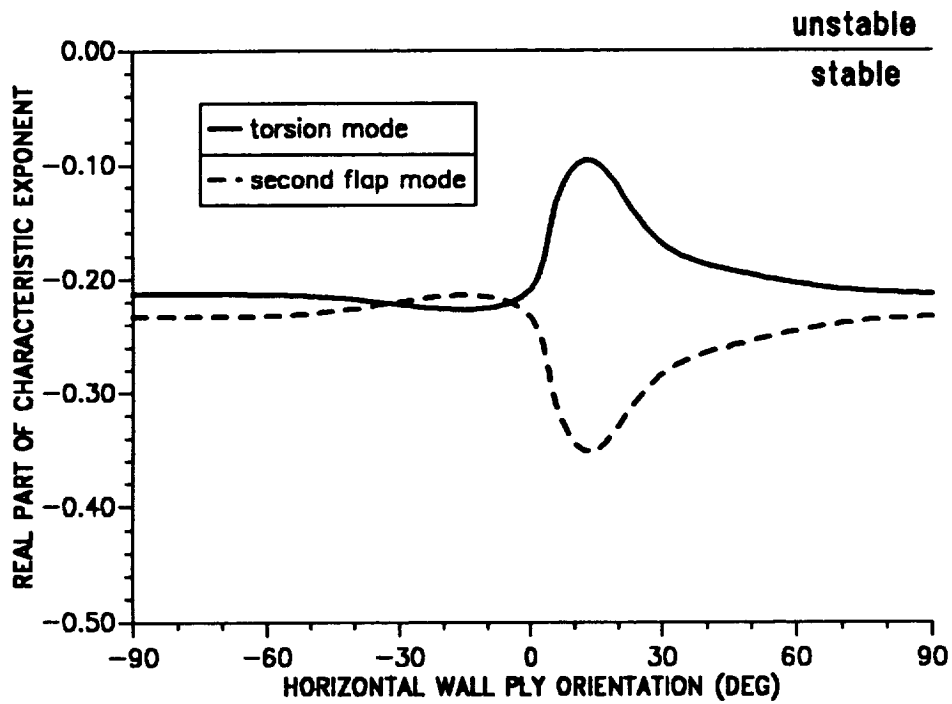


Figure 10.36: Effect of horizontal wall ply angle on stability of first torsion and second flap modes, modified torsional frequency ( $\mu = 0.30$ ).

**TWO-CELL COMPOSITE BLADE (MODIFIED)  
AEROELASTIC STABILITY (MU=0.3)**

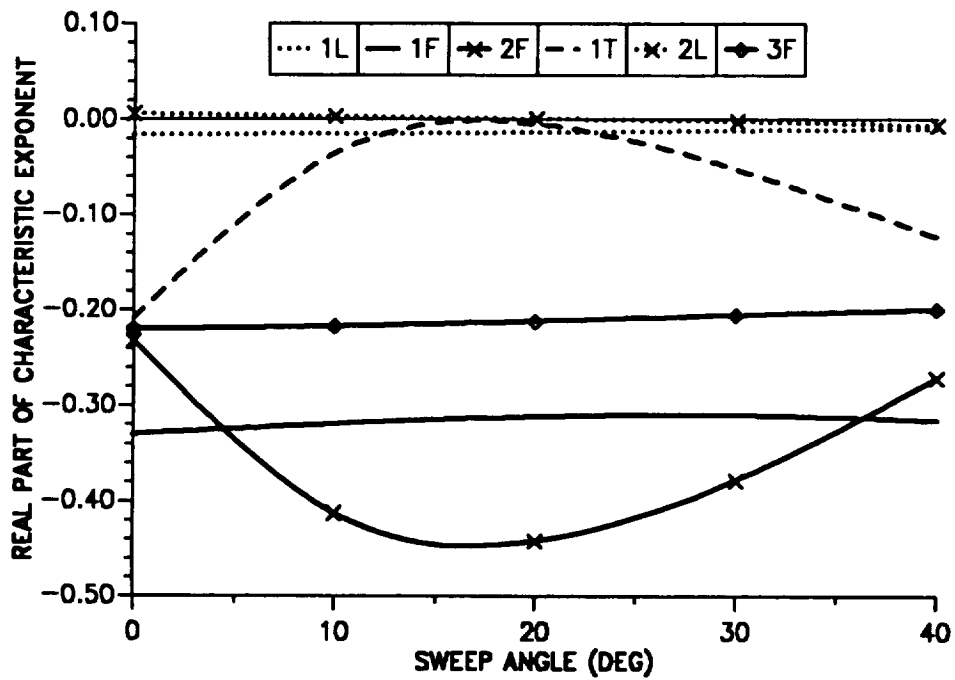


Figure 10.37: Effect of tip sweep angle on blade stability for the first six modes, modified torsional frequency ( $\mu = 0.30$ ).

**TWO-CELL COMPOSITE BLADE  
VIBRATORY LONGITUDINAL SHEAR ( $\mu=0.3$ )**

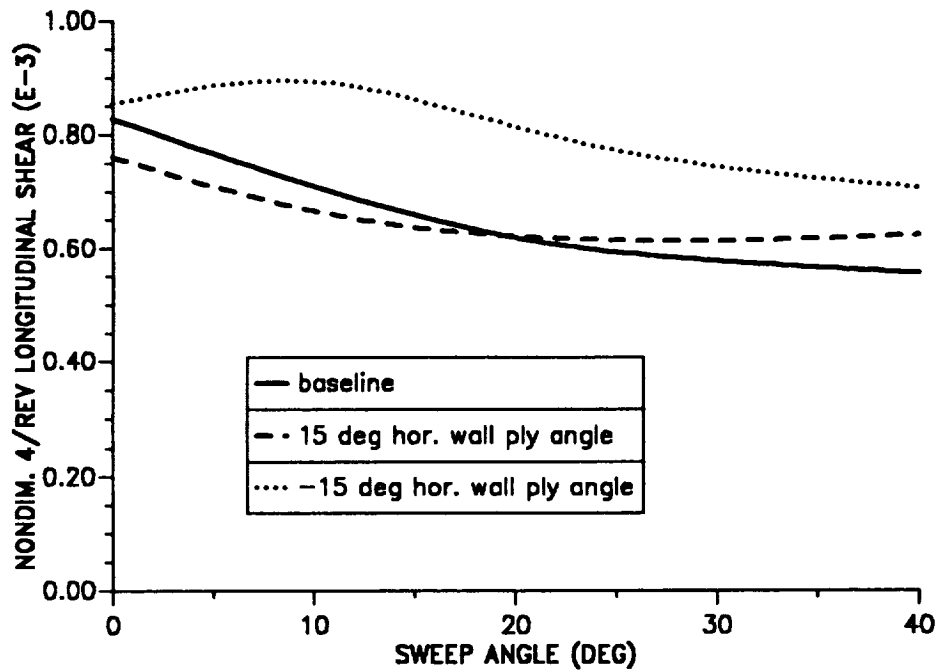


Figure 10.38: The 4/rev longitudinal hub shear as a function of tip sweep angle, combined effect with ply orientation ( $\mu = 0.30$ ).

**TWO-CELL COMPOSITE BLADE  
VIBRATORY LATERAL SHEAR ( $\mu=0.3$ )**

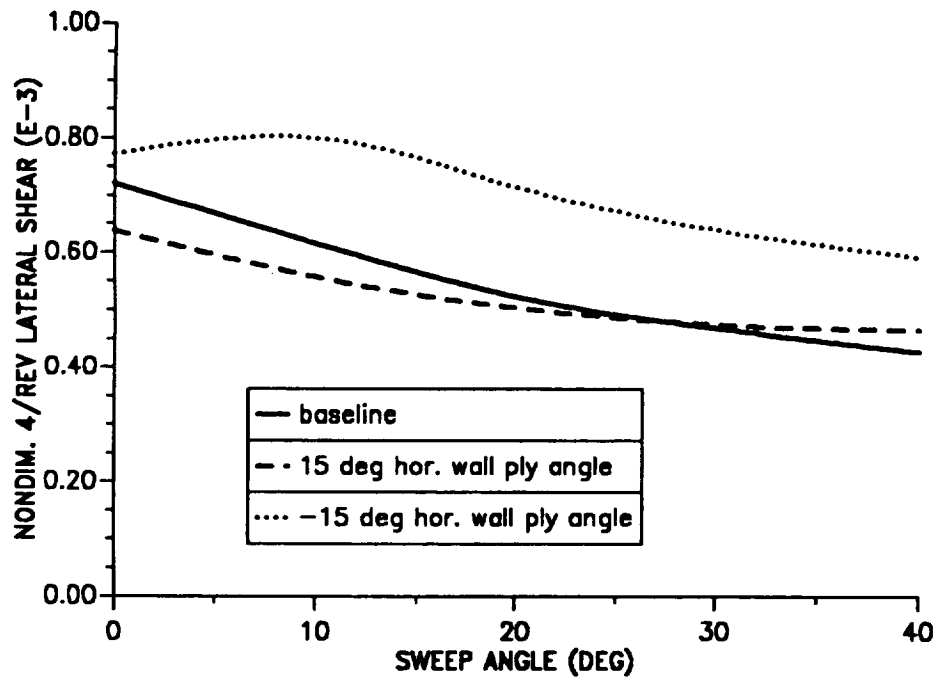


Figure 10.39: The 4/rev lateral hub shear as a function of tip sweep angle, combined effect with ply orientation ( $\mu = 0.30$ ).

**TWO-CELL COMPOSITE BLADE  
VIBRATORY VERTICAL SHEAR ( $\mu=0.3$ )**

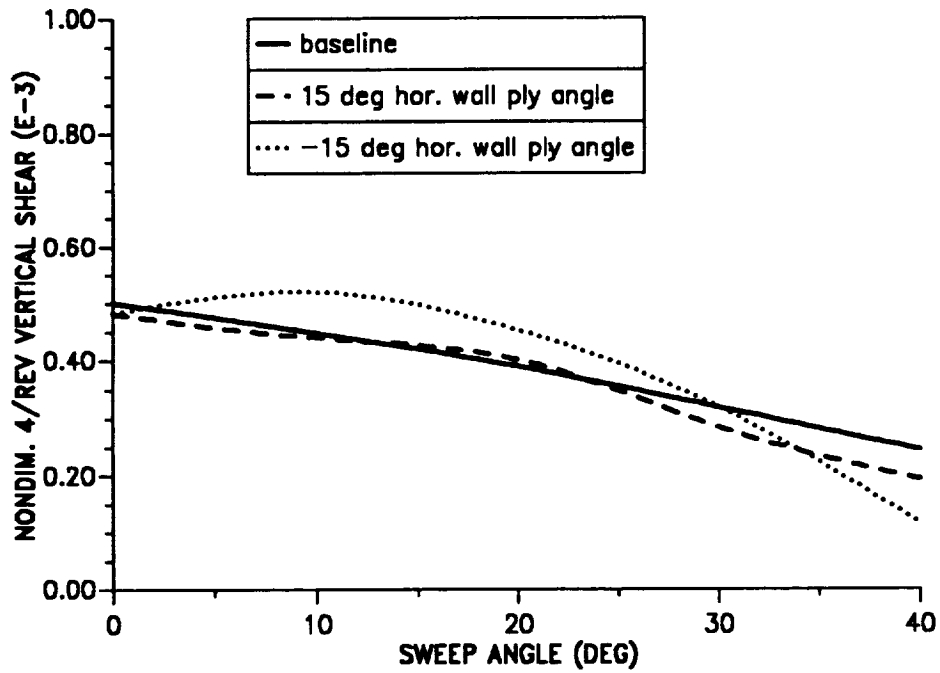


Figure 10.40: The 4/rev vertical hub shear as a function of tip sweep angle, combined effect with ply orientation ( $\mu = 0.30$ ).

**TWO-CELL COMPOSITE BLADE  
VIBRATORY ROLLING MOMENT ( $\mu=0.3$ )**

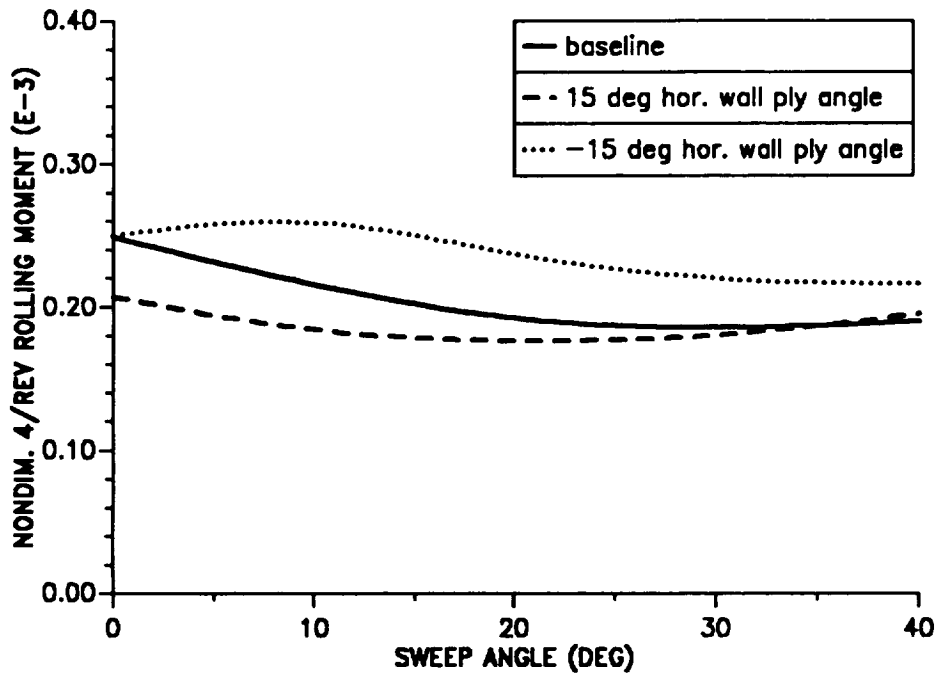


Figure 10.41: The 4/rev hub rolling moment as a function of tip sweep angle, combined effect with ply orientation ( $\mu = 0.30$ ).

**TWO-CELL COMPOSITE BLADE  
VIBRATORY PITCHING MOMENT ( $\mu=0.3$ )**

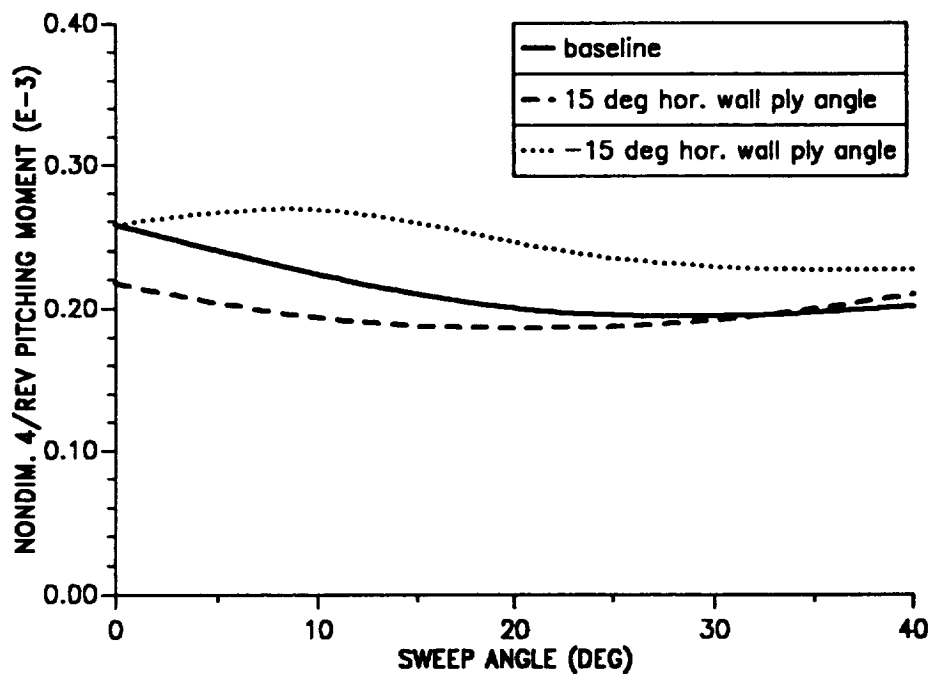


Figure 10.42: The 4/rev hub pitching moment as a function of tip sweep angle, combined effect with ply orientation ( $\mu = 0.30$ ).

**TWO-CELL COMPOSITE BLADE  
VIBRATORY YAWING MOMENT ( $\mu=0.3$ )**

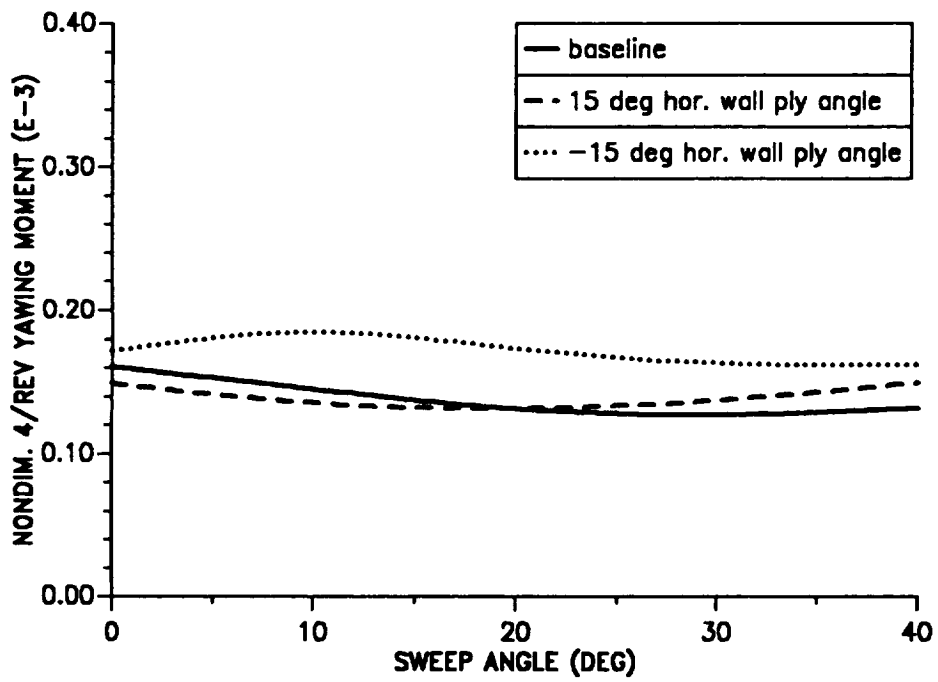


Figure 10.43: The 4/rev hub yawing moment as a function of tip sweep angle, combined effect with ply orientation ( $\mu = 0.30$ ).

**TWO-CELL COMPOSITE BLADE  
LAG MODE STABILITY ( $\mu=0.3$ )**

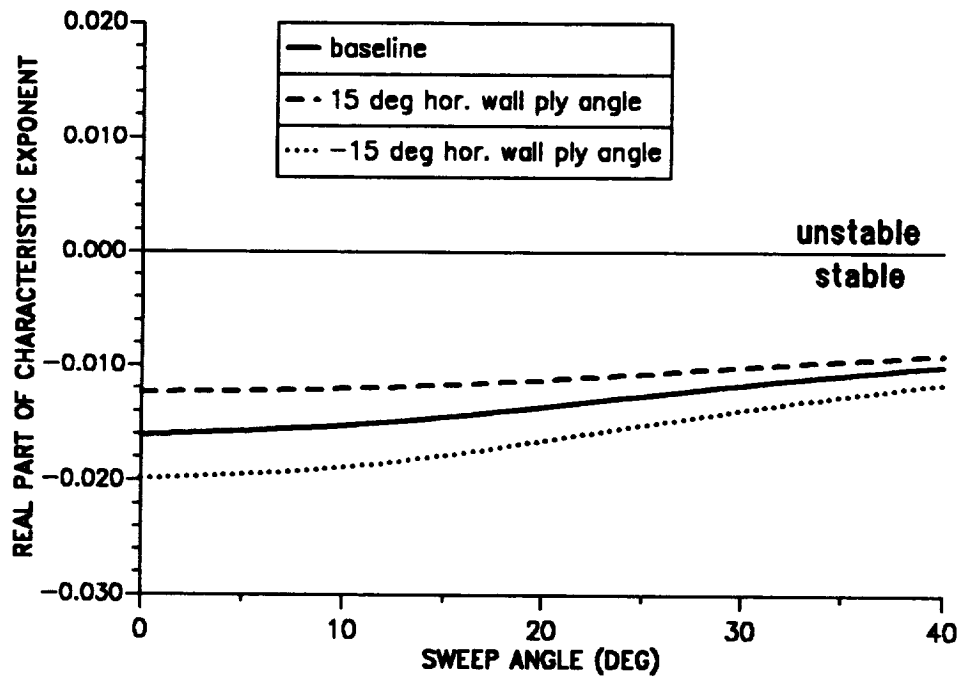


Figure 10.44: Real part of characteristic exponent of blade first lag mode as a function of tip sweep angle, combined effect with ply orientation ( $\mu = 0.30$ ).

**TWO-CELL COMPOSITE BLADE, FIRST CONFIGURATION  
OBJECTIVE FUNCTION J1 (MU=0.3)**

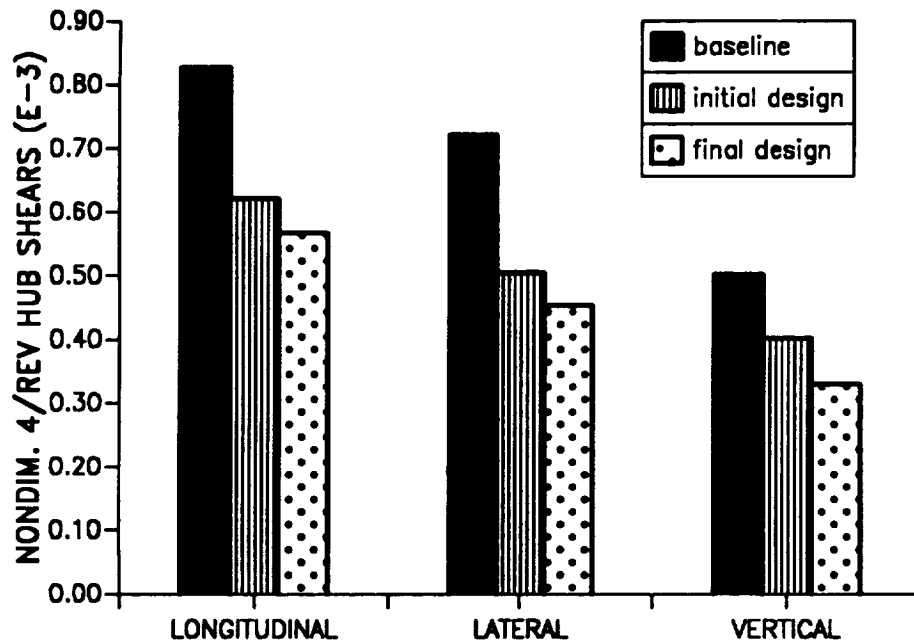


Figure 11.1: The 4/rev hub shears corresponding to first blade configuration (soft-in-plane) and first objective function ( $\mu = 0.30$ ).

**TWO-CELL COMPOSITE BLADE, FIRST CONFIGURATION  
OBJECTIVE FUNCTION J1 (MU=0.3)**

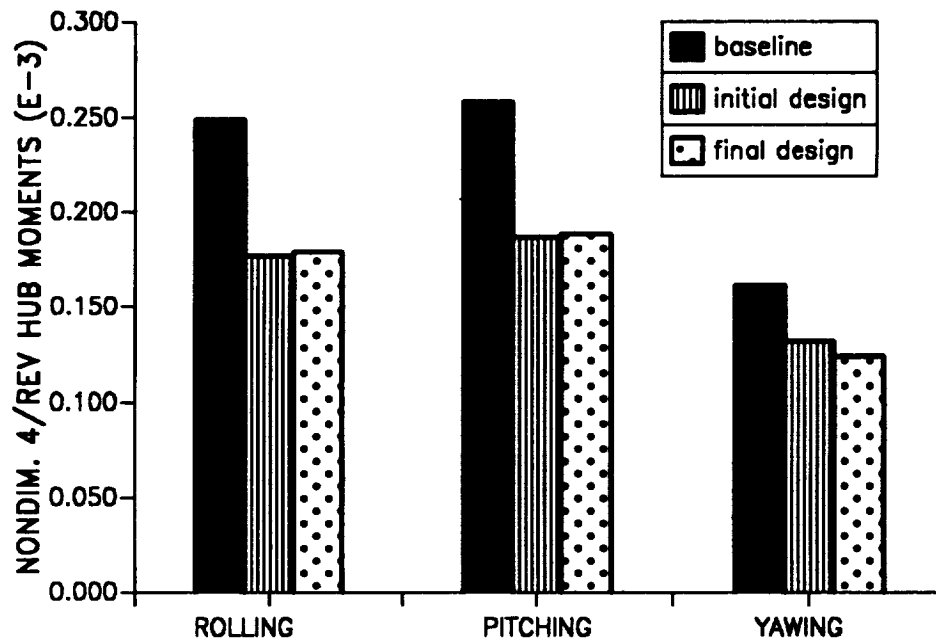


Figure 11.2: The 4/rev hub moments corresponding to first blade configuration (soft-in-plane) and first objective function ( $\mu = 0.30$ ).

**TWO-CELL COMPOSITE BLADE, FIRST CONFIGURATION  
OBJECTIVE FUNCTION J2 ( $\mu=0.3$ )**

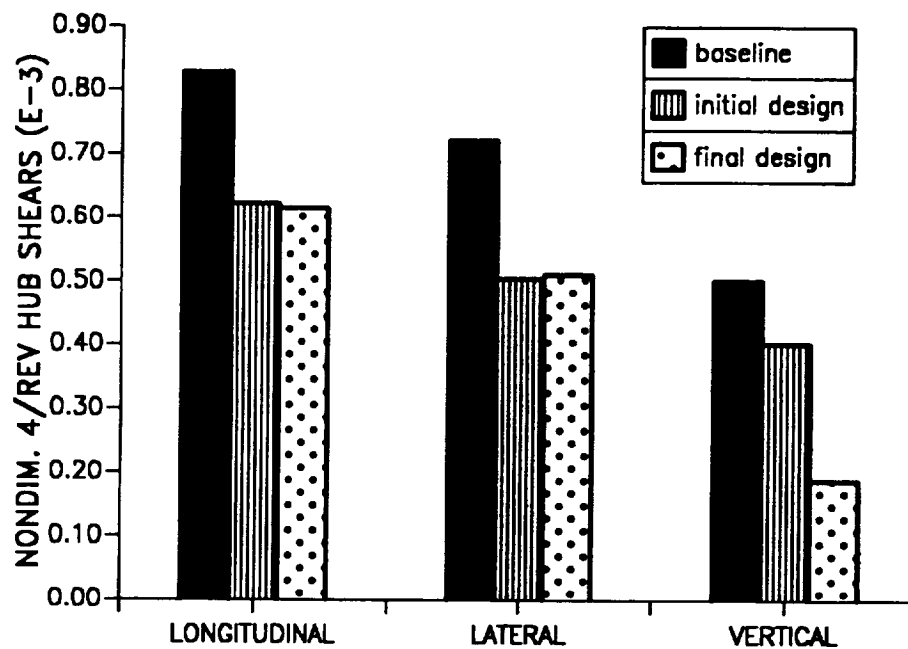


Figure 11.3: The 4/rev hub shears corresponding to first blade configuration (soft-in-plane) and second objective function ( $\mu = 0.30$ ).

**TWO-CELL COMPOSITE BLADE, FIRST CONFIGURATION  
OBJECTIVE FUNCTION J2 (MU=0.3)**

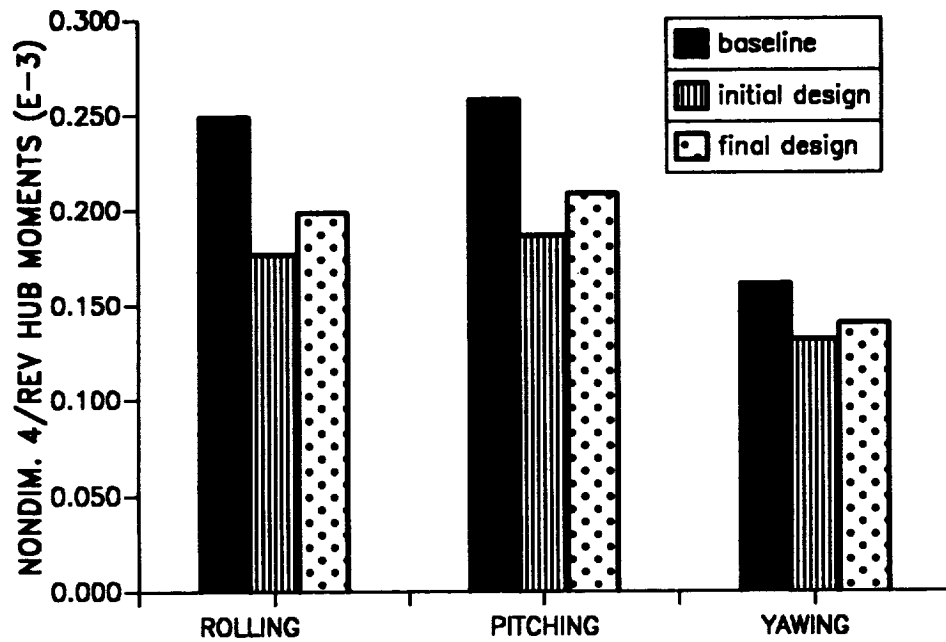


Figure 11.4: The 4/rev hub moments corresponding to first blade configuration (soft-in-plane) and second objective function ( $\mu = 0.30$ ).

**TWO-CELL COMPOSITE BLADE, SECOND CONFIGURATION  
OBJECTIVE FUNCTION J1 (MU=0.3)**

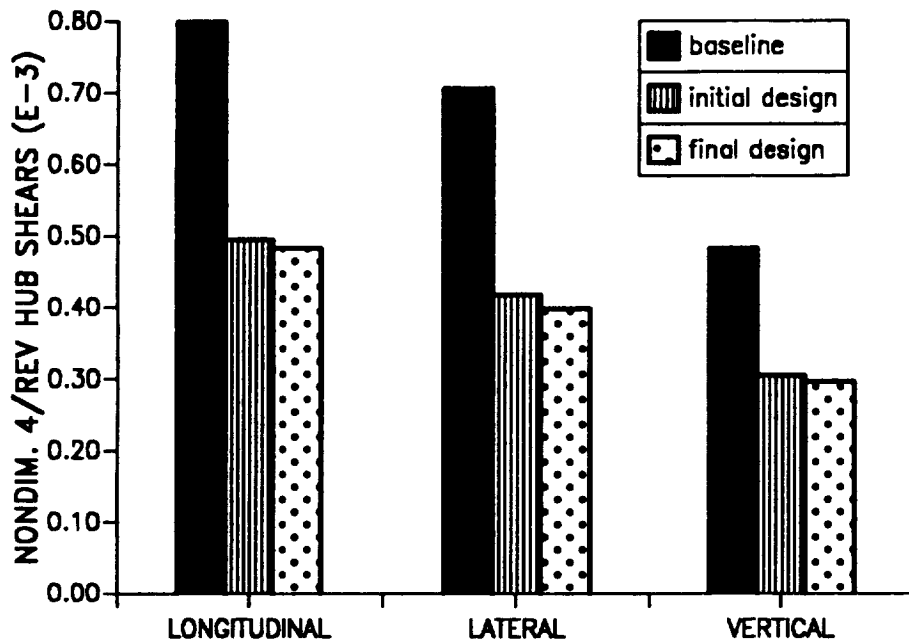


Figure 11.5: The 4/rev hub shears corresponding to second blade configuration (soft-in-plane) and first objective function ( $\mu = 0.30$ ).

**TWO-CELL COMPOSITE BLADE, SECOND CONFIGURATION  
OBJECTIVE FUNCTION J1 (MU=0.3)**

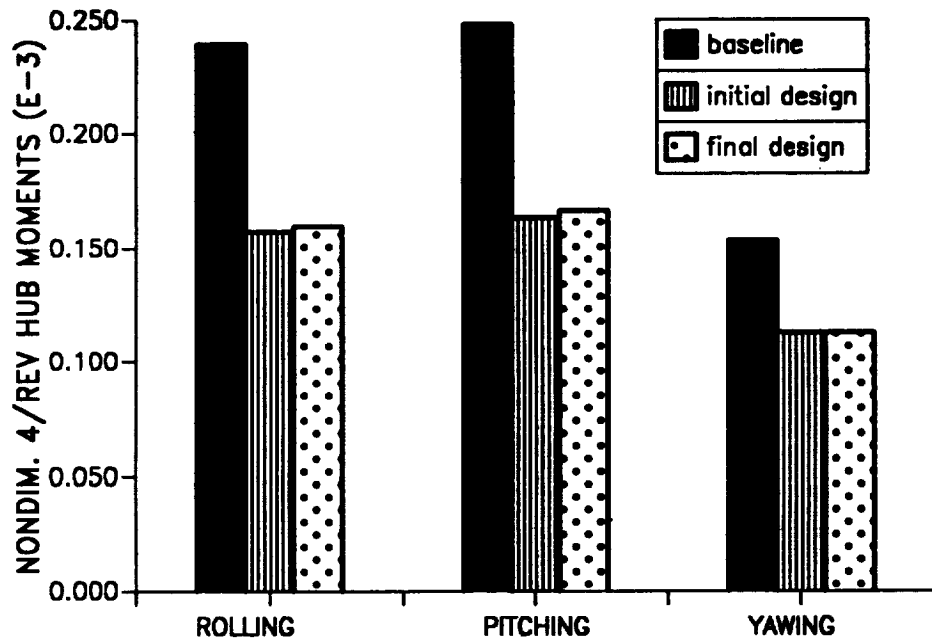


Figure 11.6: The 4/rev hub moments corresponding to second blade configuration (soft-in-plane) and first objective function ( $\mu = 0.30$ ).

0-5.

**TWO-CELL COMPOSITE BLADE, SECOND CONFIGURATION  
OBJECTIVE FUNCTION J2 (MU=0.3)**

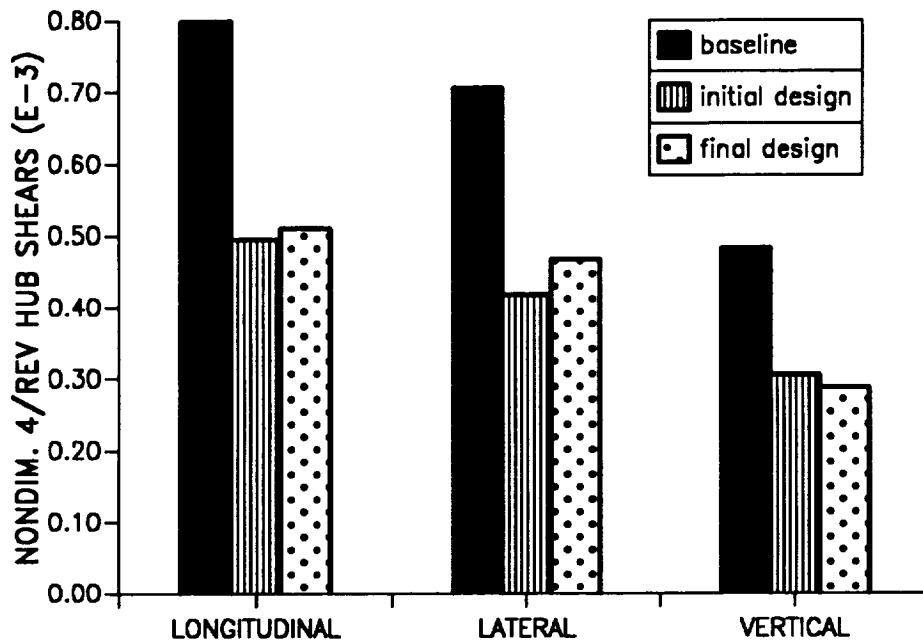


Figure 11.7: The 4/rev hub shears corresponding to second blade configuration (soft-in-plane) and second objective function ( $\mu = 0.30$ ).

**TWO-CELL COMPOSITE BLADE, SECOND CONFIGURATION  
OBJECTIVE FUNCTION J2 (MU=0.3)**

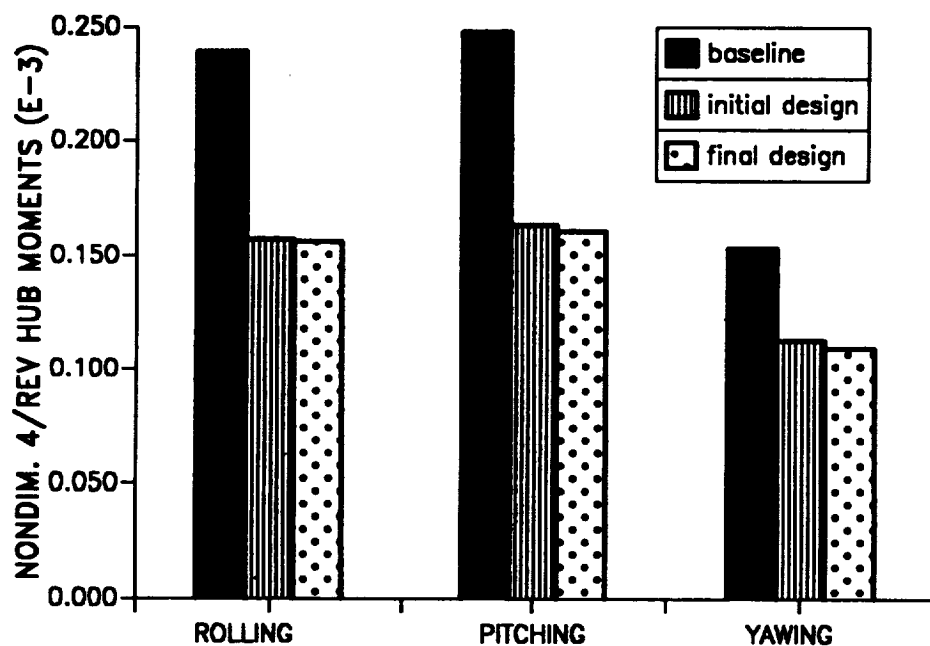


Figure 11.8: The 4/rev hub moments corresponding to second blade configuration (soft-in-plane) and second objective function ( $\mu = 0.30$ ).

**TWO-CELL COMPOSITE BLADE, THIRD CONFIGURATION  
OBJECTIVE FUNCTION J1 (MU=0.3)**

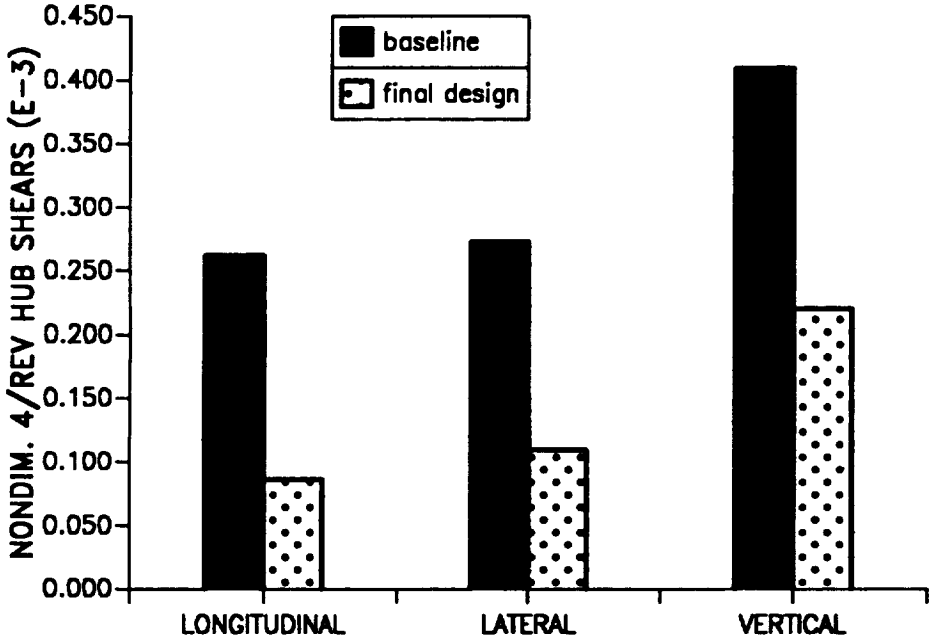


Figure 11.9: The 4/rev hub shears corresponding to third blade configuration (stiff-in-plane) and first objective function ( $\mu = 0.30$ ).

**TWO-CELL COMPOSITE BLADE, THIRD CONFIGURATION  
OBJECTIVE FUNCTION J1 (MU=0.3)**

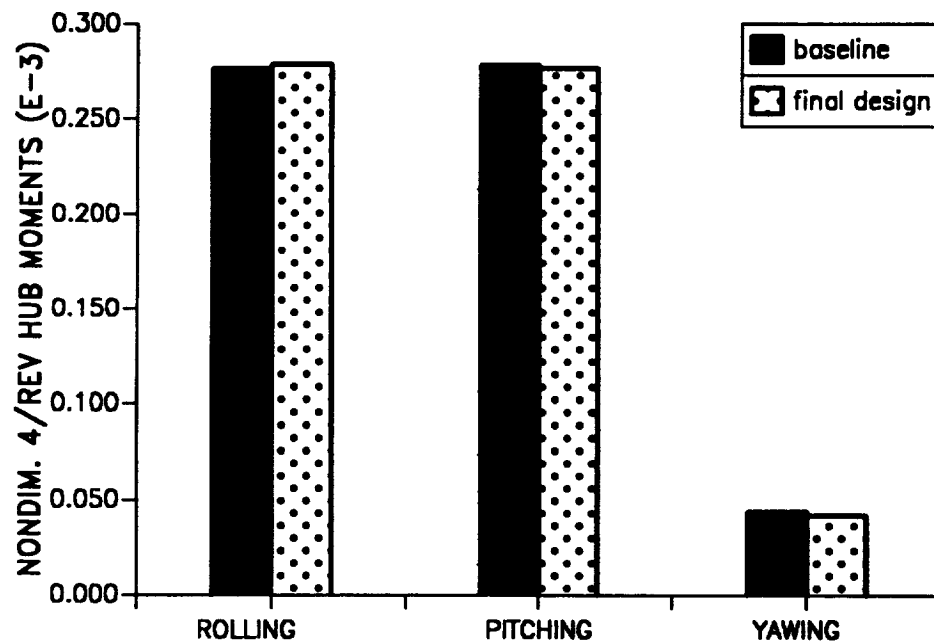


Figure 11.10: The 4/rev hub moments corresponding to third blade configuration (stiff-in-plane) and first objective function ( $\mu = 0.30$ ).

**TWO-CELL COMPOSITE BLADE, THIRD CONFIGURATION  
OBJECTIVE FUNCTION J2 ( $\mu=0.3$ )**

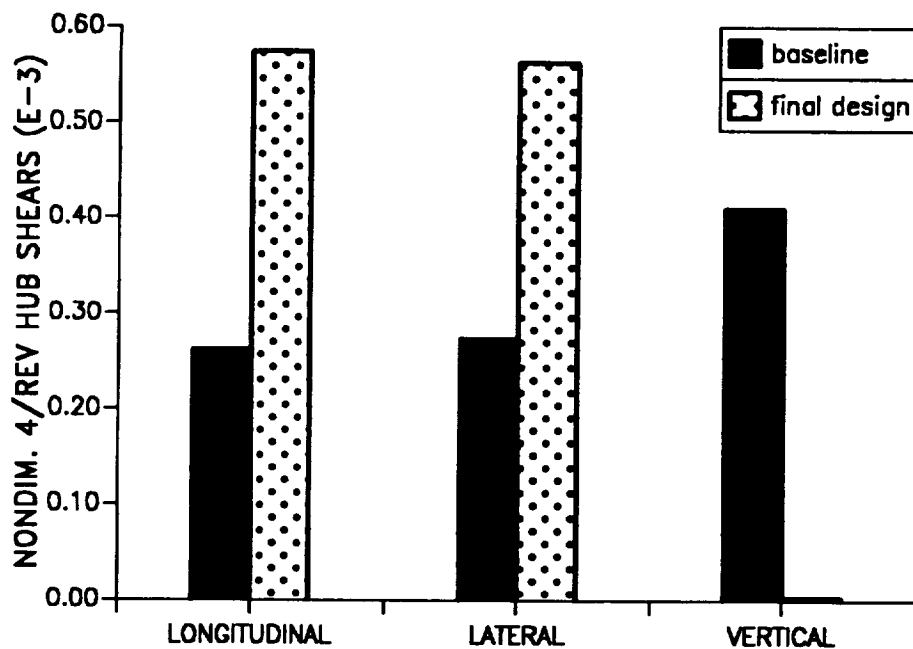


Figure 11.11: The 4/rev hub shears corresponding to third blade configuration (stiff-in-plane) and second objective function ( $\mu = 0.30$ ).

**TWO-CELL COMPOSITE BLADE, THIRD CONFIGURATION  
OBJECTIVE FUNCTION J2 (MU=0.3)**

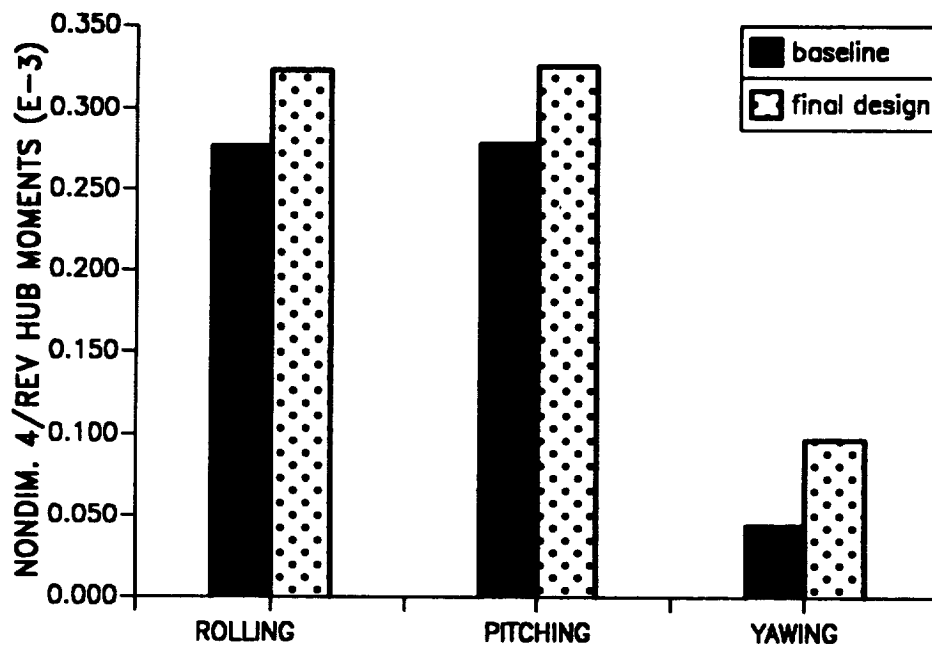


Figure 11.12: The 4/rev hub moments corresponding to third blade configuration (stiff-in-plane) and second objective function ( $\mu = 0.30$ ).

## Appendix A

### COMPARISON OF THE TRANSFORMATION MATRICES BETWEEN DEFORMED AND UNDEFORMED COORDINATE SYSTEMS

In this appendix, the transformation matrix,  $[T_{de}]$ , between the deformed curvilinear coordinate system and the undeformed element coordinate system is compared with similar transformations by other authors.

The matrix  $[T_{de}]$  is defined as:

$$\begin{aligned}
 [T_{de}] = & \begin{bmatrix} 1 & 0 & 0 \\ 0 & \cos \theta_x & \sin \theta_x \\ 0 & -\sin \theta_x & \cos \theta_x \end{bmatrix} \begin{bmatrix} \cos \theta_\eta & 0 & -\sin \theta_\eta \\ 0 & 1 & 0 \\ \sin \theta_\eta & 0 & \cos \theta_\eta \end{bmatrix} \\
 & \begin{bmatrix} \cos \theta_\zeta & \sin \theta_\zeta & 0 \\ -\sin \theta_\zeta & \cos \theta_\zeta & 0 \\ 0 & 0 & 1 \end{bmatrix} \begin{bmatrix} 1 & 0 & 0 \\ 0 & \cos \beta & \sin \beta \\ 0 & -\sin \beta & \cos \beta \end{bmatrix} \quad (A.1)
 \end{aligned}$$

where  $\theta_x, \theta_\eta, \theta_\zeta$  are Euler angles, and  $\beta$  is the pretwist angle. The relationships between the Euler angles and the displacement variables are:

$$\theta_x \equiv \phi$$

$$\sin \theta_\eta = \frac{v_{,x} \sin \beta - w_{,x} \cos \beta}{\sqrt{(1 + u_{,x})^2 + (v_{,x} \cos \beta + w_{,x} \sin \beta)^2 + (w_{,x} \cos \beta - v_{,x} \sin \beta)^2}}$$

$$\cos \theta_\eta = \frac{\sqrt{(1 + u_{,x})^2 + (v_{,x} \cos \beta + w_{,x} \sin \beta)^2}}{\sqrt{(1 + u_{,x})^2 + (v_{,x} \cos \beta + w_{,x} \sin \beta)^2 + (w_{,x} \cos \beta - v_{,x} \sin \beta)^2}}$$

$$\sin \theta_{\zeta} = \frac{v_{,x} \cos \beta + w_{,x} \sin \beta}{\sqrt{(1 + u_{,x})^2 + (v_{,x} \cos \beta + w_{,x} \sin \beta)^2}} \quad (\text{A.2})$$

$$\cos \theta_{\zeta} = \frac{1 + u_{,x}}{\sqrt{(1 + u_{,x})^2 + (v_{,x} \cos \beta + w_{,x} \sin \beta)^2}}$$

When  $[T_{de}]$  is simplified to second order using the ordering scheme and the small angle assumption for  $\phi$ , it becomes:

$$[T_{de}] = \begin{bmatrix} 1 & v_{,x} & w_{,x} \\ -v_{,x} \cos(\beta + \phi) & \cos(\beta + \phi) & \sin(\beta + \phi) \\ -w_{,x} \sin(\beta + \phi) & & \\ v_{,x} \sin(\beta + \phi) & -\sin(\beta + \phi) & \cos(\beta + \phi) \\ -w_{,x} \cos(\beta + \phi) & +\tau_c' \cos \beta & +\tau_c' \sin \beta \end{bmatrix} \quad (\text{A.3})$$

where

$$\tau_c' = (v_{,x} \sin \beta - w_{,x} \cos \beta)(v_{,x} \cos \beta + w_{,x} \sin \beta) \quad (\text{A.4})$$

Eqs. (A.2), (A.3) and (A.4) are taken from Eqs. (3.37), (4.40) and (4.41), respectively. These expressions are identical to the expressions used by Kosmatka [56] except for a minor difference in the second order simplification of  $[T_{de}]$  where Kosmatka's expression (Ref. 56, p. 78, Eq. (2.81b)) is:

$$[T_{de}] =$$

$$\begin{bmatrix} 1 & v_{,x} & w_{,x} \\ -v_{,x} \cos(\beta + \phi) - w_{,x} \sin(\beta + \phi) & \cos(\beta + \phi) & \sin(\beta + \phi) \\ v_{,x} \sin(\beta + \phi) - w_{,x} \cos(\beta + \phi) & -\sin(\beta + \phi - \tau_c') & \cos(\beta + \phi) \end{bmatrix} \quad (\text{A.5})$$

The slight difference in elements (3,2) and (3,3) is probably due to the ordering scheme being applied at different stages during the simplifying process.

A similar transformation between deformed and undeformed coordinate systems obtained by Hodges and Dowell[40], and by Crespo DaSilva and Hodges[15] is defined as:

$$[T_1] = \begin{bmatrix} 1 & 0 & 0 \\ 0 & \cos \theta_1 & \sin \theta_1 \\ 0 & -\sin \theta_1 & \cos \theta_1 \end{bmatrix} \begin{bmatrix} \cos \theta_y & 0 & \sin \theta_y \\ 0 & 1 & 0 \\ -\sin \theta_y & 0 & \cos \theta_y \end{bmatrix} \begin{bmatrix} \cos \theta_z & \sin \theta_z & 0 \\ -\sin \theta_z & \cos \theta_z & 0 \\ 0 & 0 & 1 \end{bmatrix} \quad (A.6)$$

where

$$\theta_1 = \beta + \theta_x$$

$$\sin \theta_y = \frac{w_{,x}}{\sqrt{(1 + u_{,x})^2 + (v_{,x})^2 + (w_{,x})^2}}$$

$$\cos \theta_y = \frac{\sqrt{(1 + u_{,x})^2 + (v_{,x})^2}}{\sqrt{(1 + u_{,x})^2 + (v_{,x})^2 + (w_{,x})^2}} \quad (A.7)$$

$$\sin \theta_z = \frac{v_{,x}}{\sqrt{(1 + u_{,x})^2 + (v_{,x})^2}}$$

$$\cos \theta_z = \frac{1 + u_{,x}}{\sqrt{(1 + u_{,x})^2 + (v_{,x})^2}}$$

The expressions for  $\sin \theta_y$ ,  $\cos \theta_y$ ,  $\sin \theta_z$  and  $\cos \theta_z$  in Hodges and Dowell[40] have a different appearance from Eq. (A.7), but can be rewritten in more suitable form resembling Eq. (A.7) by substituting

$$\frac{\partial x}{\partial r} = [(1 + u_{,x})^2 + (v_{,x})^2 + (w_{,x})^2]^{-1/2} \quad (\text{A.8})$$

into Eq. (A.3) of Ref. 40. Although Hodges and Dowell[40] have a slightly different interpretation for the third Euler angle  $\theta_x$ , which differs from the identity shown in Eq. (A.2); for convenience in this comparison, this difference is ignored. A second order simplification of the transformation matrix  $[T_1]$  can be obtained by assuming

$$\begin{aligned} \sin \theta_y &\simeq w_{,x} \quad , \quad \sin \theta_z \simeq v_{,x} \quad , \quad \theta_1 \simeq \beta + \phi \\ \cos \theta_y &\simeq 1 \quad , \quad \cos \theta_z \simeq 1 \end{aligned} \quad (\text{A.9})$$

and substituting into Eq. (A.6). The resulting expression is:

$$[T_1] = \begin{bmatrix} 1 & v_{,x} & w_{,x} \\ -v_{,x} \cos(\beta + \phi) & \cos(\beta + \phi) - v_{,x} w_{,x} \sin(\beta + \phi) & \sin(\beta + \phi) \\ v_{,x} \sin(\beta + \phi) & -\sin(\beta + \phi) - v_{,x} w_{,x} \cos(\beta + \phi) & \cos(\beta + \phi) \end{bmatrix} \quad (\text{A.10})$$

The transformation matrix  $[T_1]$  was derived based on the assumption that the pretwist angle ( $\beta$ ) is an additive term to the third Euler angle ( $\theta_x$ ). This assumption was used simply for mathematical convenience. On the other hand, the transformation matrix  $[T_{de}]$  was derived assuming that the pretwist angle is present before deformation. Therefore, the expression for  $[T_1]$  looks

different from  $[T_{de}]$  in their original form, before simplifications. However, when  $[T_1]$  and  $[T_{de}]$  are simplified to second order, they have identical expressions for  $T_{11}, T_{12}, T_{13}, T_{21}, T_{23}, T_{31}$  and identical first order terms for  $T_{22}, T_{32}, T_{33}$ ; where  $T_{ij}$  denotes the element (i, j) of  $[T_1]$  or  $[T_{de}]$ .

If the effect of pretwist on the transformation matrix is ignored, i.e.,  $\beta \equiv 0$ , and the small angle assumption is used for  $\phi$ , then both second order expressions for  $[T_1]$  and  $[T_{de}]$  reduce to the second order expression by Rosen and Friedmann[76]:

$$[T_2] = \begin{bmatrix} 1 & v_{,x} & w_{,x} \\ -(v_{,x} + \phi w_{,x}) & 1 & \phi \\ -(w_{,x} - \phi v_{,x}) & -(\phi + v_{,x} w_{,x}) & 1 \end{bmatrix} \quad (A.11)$$

## Appendix B

### FINITE ELEMENT MATRICES FOR THE COMPOSITE BEAM MODEL

The finite element matrices for the composite beam model are obtained by using a cubic Hermite interpolation polynomial,  $\{\Phi_c\}$ , for the transverse deflections ( $v, w$ ) and a quadratic Hermite interpolation polynomial,  $\{\Phi_q\}$ , for the torsional rotation ( $\phi$ ), the axial deflection ( $u$ ), the warping amplitude ( $\alpha$ ), and the transverse shears at the elastic axis ( $\bar{v}_{xy}, \bar{v}_{xz}$ ). Each of the element matrices can be written in the partitioned form as follows:

$$[A] = \begin{bmatrix} [A_{11}] & [A_{12}] & [A_{13}] & [A_{14}] & [A_{15}] & [A_{16}] & [A_{17}] \\ [A_{21}] & [A_{22}] & [A_{23}] & [A_{24}] & [A_{25}] & [A_{26}] & [A_{27}] \\ [A_{31}] & [A_{32}] & [A_{33}] & [A_{34}] & [A_{35}] & [A_{36}] & [A_{37}] \\ [A_{41}] & [A_{42}] & [A_{43}] & [A_{44}] & [A_{45}] & [A_{46}] & [A_{47}] \\ [A_{51}] & [A_{52}] & [A_{53}] & [A_{54}] & [A_{55}] & [A_{56}] & [A_{57}] \\ [A_{61}] & [A_{62}] & [A_{63}] & [A_{64}] & [A_{65}] & [A_{66}] & [A_{67}] \\ [A_{71}] & [A_{72}] & [A_{73}] & [A_{74}] & [A_{75}] & [A_{76}] & [A_{77}] \end{bmatrix} \quad (B.1)$$

#### B.1 FINITE ELEMENT MATRICES ASSOCIATED WITH THE STRAIN ENERGY VARIATION

The finite element matrices which are associated with the strain energy variation include the linear stiffness matrix,  $[K^L]$ , and the nonlinear stiffness matrix,  $[K^{NL}]$ . In order to conveniently express these finite element matrices in terms of their sub-matrices, the following constants are defined:

$$\overline{EA\eta_a} = EA\eta_a \cos \beta - EA\zeta_a \sin \beta$$

$$\overline{EA\zeta_a} = EA\eta_a \sin \beta + EA\zeta_a \cos \beta$$

$$\overline{G_\eta A\eta_b} = G_\eta A\eta_b \cos \beta - G_\eta A\zeta_b \sin \beta$$

$$\overline{G_\eta A\zeta_b} = G_\eta A\eta_b \sin \beta + G_\eta A\zeta_b \cos \beta$$

$$\overline{G_\zeta A\eta_c} = G_\zeta A\eta_c \cos \beta - G_\zeta A\zeta_c \sin \beta$$

$$\overline{G_\zeta A\zeta_c} = G_\zeta A\eta_c \sin \beta + G_\zeta A\zeta_c \cos \beta$$

$$\overline{EAB_1} = EAB_1 \cos \beta - EAB_2 \sin \beta$$

$$\overline{EAB_2} = EAB_1 \sin \beta + EAB_2 \cos \beta$$

$$\overline{EAB_6} = EAB_6 \cos \beta - EAB_7 \sin \beta$$

$$\overline{EAB_7} = EAB_6 \sin \beta + EAB_7 \cos \beta$$

$$\overline{EAC_1} = EAC_1 \cos \beta - EAC_2 \sin \beta$$

$$\overline{EAC_2} = EAC_1 \sin \beta + EAC_2 \cos \beta$$

$$\overline{EAD_1} = EAD_1 \cos \beta - EAD_2 \sin \beta$$

$$\overline{EAD_2} = EAD_1 \sin \beta + EAD_2 \cos \beta$$

$$\overline{EAD_1'} = EAD_1' \cos \beta - EAD_2' \sin \beta$$

$$\overline{EAD_2'} = EAD_1' \sin \beta + EAD_2' \cos \beta$$

$$\overline{EI_{\eta\zeta}} = EI_{\eta\zeta} \cos \beta - EI_{\eta\eta} \sin \beta$$

$$\overline{EI}_{\eta\eta} = EI_{\eta\zeta} \sin \beta + EI_{\eta\eta} \cos \beta$$

$$\overline{EI}_{\zeta\zeta} = EI_{\zeta\zeta} \cos \beta - EI_{\eta\zeta} \sin \beta$$

$$\overline{EI}_{\zeta\eta} = EI_{\zeta\zeta} \sin \beta + EI_{\eta\zeta} \cos \beta$$

The linear stiffness matrix,  $[K^L]$ , is defined by the following sub-matrices:

$$[K_{11}^L] = \int_0^{l_e} (\overline{EI}_{\zeta\zeta} \cos \beta - \overline{EI}_{\eta\zeta} \sin \beta) \{\Phi_c''\} \{\Phi_c''\}^T dx$$

$$[K_{12}^L] = \int_0^{l_e} (\overline{EI}_{\zeta\eta} \cos \beta - \overline{EI}_{\eta\eta} \sin \beta) \{\Phi_c''\} \{\Phi_c''\}^T dx$$

$$[K_{13}^L] = \int_0^{l_e} -\overline{EAB}_1 \{\Phi_c''\} \{\Phi_q'\}^T dx$$

$$[K_{14}^L] = \int_0^{l_e} -\overline{EA}\eta_a \{\Phi_c''\} \{\Phi_q'\}^T dx$$

$$[K_{15}^L] = \int_0^{l_e} (-\overline{EAD}_1 \{\Phi_c''\} \{\Phi_q'\}^T - (\overline{EAD}_1' + \overline{EAB}_6) \{\Phi_c''\} \{\Phi_q'\}^T) dx$$

$$[K_{16}^L] = \int_0^{l_e} (-\overline{EI}_{\zeta\zeta} \{\Phi_c''\} \{\Phi_q'\}^T - (\overline{G}_\eta A \eta_b + \tau_0 \overline{EI}_{\eta\zeta}) \{\Phi_c''\} \{\Phi_q'\}^T) dx$$

$$[K_{17}^L] = \int_0^{l_e} (-\overline{EI}_{\eta\zeta} \{\Phi_c''\} \{\Phi_q'\}^T - (\overline{G}_\zeta A \eta_c - \tau_0 \overline{EI}_{\zeta\zeta}) \{\Phi_c''\} \{\Phi_q'\}^T) dx$$

$$[K_{21}^L] = \int_0^{l_e} (\overline{EI}_{\eta\zeta} \cos \beta + \overline{EI}_{\zeta\zeta} \sin \beta) \{\Phi_c''\} \{\Phi_c''\}^T dx = [K_{12}^L]^T$$

$$[K_{22}^L] = \int_0^{l_e} (\overline{EI}_{\eta\eta} \cos \beta + \overline{EI}_{\zeta\eta} \sin \beta) \{\Phi_c''\} \{\Phi_c''\}^T dx$$

$$[K_{23}^L] = \int_0^{l_e} -\overline{EAB}_2 \{\Phi_c''\} \{\Phi_q'\}^T dx$$

$$[K_{24}^L] = \int_0^{l_e} -\overline{EA}\zeta_a \{\Phi_c''\} \{\Phi_q'\}^T dx$$

$$[K_{25}^L] = \int_0^{l_e} (-\overline{EAD}_2 \{\Phi_c''\} \{\Phi_q'\}^T - (\overline{EAD}_2' + \overline{EAB}_7) \{\Phi_c''\} \{\Phi_q'\}^T) dx$$

$$[K_{26}^L] = \int_0^{l_e} (-\overline{EI}_{\zeta\eta} \{\Phi_c''\} \{\Phi_q'\}^T - (\overline{G}_\eta \overline{A}\zeta_b + \tau_0 \overline{EI}_{\eta\eta}) \{\Phi_c''\} \{\Phi_q'\}^T) dx$$

$$[K_{27}^L] = \int_0^{l_e} (-\overline{EI}_{\eta\eta} \{\Phi_c''\} \{\Phi_q'\}^T - (\overline{G}_\zeta \overline{A}\zeta_c - \tau_0 \overline{EI}_{\zeta\eta}) \{\Phi_c''\} \{\Phi_q'\}^T) dx$$

$$[K_{31}^L] = [K_{13}^L]^T$$

$$[K_{32}^L] = [K_{23}^L]^T$$

$$[K_{33}^L] = \int_0^{l_e} GJ \{\Phi_q'\} \{\Phi_q'\}^T dx$$

$$[K_{34}^L] = \int_0^{l_e} \overline{EAB}_0 \{\Phi_q'\} \{\Phi_q'\}^T dx$$

$$[K_{35}^L] = \int_0^{l_e} (\overline{EAB}_3 \{\Phi_q'\} \{\Phi_q'\}^T + (\overline{EAB}_3' + \overline{EAB}_{14}) \{\Phi_q'\} \{\Phi_q'\}^T) dx$$

$$[K_{36}^L] = \int_0^{l_e} (\overline{EAB}_1 \{\Phi_q'\} \{\Phi_q'\}^T + (\overline{EAB}_{12} + \tau_0 \overline{EAB}_2) \{\Phi_q'\} \{\Phi_q'\}^T) dx$$

$$[K_{37}^L] = \int_0^{l_e} (EAB_2 \{\Phi_q'\} \{\Phi_q'\}^T + (EAB_{10} - \tau_0 EAB_1) \{\Phi_q'\} \{\Phi_q\}^T) dx$$

$$[K_{41}^L] = [K_{14}^L]^T$$

$$[K_{42}^L] = [K_{24}^L]^T$$

$$[K_{43}^L] = [K_{34}^L]^T$$

$$[K_{44}^L] = \int_0^{l_e} EA \{\Phi_q'\} \{\Phi_q'\}^T dx$$

$$[K_{45}^L] = \int_0^{l_e} (EAD_0 \{\Phi_q'\} \{\Phi_q'\}^T + (EAD_0' + EAB_5) \{\Phi_q'\} \{\Phi_q\}^T) dx$$

$$[K_{46}^L] = \int_0^{l_e} (EA\eta_a \{\Phi_q'\} \{\Phi_q'\}^T + (G_\eta A + \tau_0 EA\zeta_a) \{\Phi_q'\} \{\Phi_q\}^T) dx$$

$$[K_{47}^L] = \int_0^{l_e} (EA\zeta_a \{\Phi_q'\} \{\Phi_q'\}^T + (G_\zeta A - \tau_0 EA\eta_a) \{\Phi_q'\} \{\Phi_q\}^T) dx$$

$$[K_{51}^L] = [K_{15}^L]^T$$

$$[K_{52}^L] = [K_{25}^L]^T$$

$$[K_{53}^L] = [K_{35}^L]^T$$

$$[K_{54}^L] = [K_{45}^L]^T$$

$$[K_{55}^L] = \int_0^{l_e} (EAD_3 \{\Phi_q'\} \{\Phi_q'\}^T + (EAB_8 + EAD_5) (\{\Phi_q'\} \{\Phi_q\}^T + \{\Phi_q\} \{\Phi_q'\}^T) + (EAB_{15} + 2EAB_{8'} + EAD_{3'}) \{\Phi_q\} \{\Phi_q\}^T) dx$$

$$[K_{56}^L] = \int_0^{l_e} (EAD_1 \{\Phi_q'\} \{\Phi_q'\}^T + (EAD_7 + \tau_0 EAD_2) \{\Phi_q'\} \{\Phi_q\}^T + (EAB_6 + EAD_{1'}) \{\Phi_q\} \{\Phi_q'\}^T + (EAB_{13} + EAD_{7'} + \tau_0 EAB_7 + \tau_0 EAD_{2'}) \{\Phi_q\} \{\Phi_q\}^T) dx$$

$$[K_{57}^L] = \int_0^{l_e} (EAD_2 \{\Phi_q'\} \{\Phi_q'\}^T + (EAD_6 - \tau_0 EAD_1) \{\Phi_q'\} \{\Phi_q\}^T + (EAB_7 + EAD_{2'}) \{\Phi_q\} \{\Phi_q'\}^T + (EAB_{11} + EAD_{6'} - \tau_0 EAB_6 - \tau_0 EAD_{1'}) \{\Phi_q\} \{\Phi_q\}^T) dx$$

$$[K_{61}^L] = [K_{16}^L]^T$$

$$[K_{62}^L] = [K_{26}^L]^T$$

$$[K_{63}^L] = [K_{36}^L]^T$$

$$[K_{64}^L] = [K_{46}^L]^T$$

$$[K_{65}^L] = [K_{56}^L]^T$$

$$[K_{66}^L] = \int_0^{l_e} (EI_{\zeta\zeta} \{\Phi_q'\} \{\Phi_q'\}^T + (G_\eta A \eta_b + \tau_0 EI_{\eta\zeta}) (\{\Phi_q'\} \{\Phi_q\}^T + \{\Phi_q\} \{\Phi_q'\}^T) + (G_{\eta\eta} A + 2\tau_0 G_\eta A \zeta_b + \tau_0^2 EI_{\eta\eta}) \{\Phi_q\} \{\Phi_q\}^T) dx$$

$$\begin{aligned}
[K_{67}^L] = & \int_0^{l_e} (EI_{\eta\zeta} \{\Phi_q'\} \{\Phi_q'\}^T + (G_\zeta A \eta_c - \tau_0 EI_{\zeta\zeta}) \{\Phi_q'\} \{\Phi_q\}^T + \\
& (G_\eta A \zeta_b + \tau_0 EI_{\eta\eta}) \{\Phi_q\} \{\Phi_q'\}^T + (G_{\eta\zeta} A + \tau_0 G_\zeta A \zeta_c - \\
& \tau_0 G_\eta A \eta_b - \tau_0^2 EI_{\eta\zeta}) \{\Phi_q\} \{\Phi_q\}^T) dx
\end{aligned}$$

$$[K_{71}^L] = [K_{17}^L]^T$$

$$[K_{72}^L] = [K_{27}^L]^T$$

$$[K_{73}^L] = [K_{37}^L]^T$$

$$[K_{74}^L] = [K_{47}^L]^T$$

$$[K_{75}^L] = [K_{57}^L]^T$$

$$[K_{76}^L] = [K_{67}^L]^T$$

$$\begin{aligned}
[K_{77}^L] = & \int_0^{l_e} (EI_{\eta\eta} \{\Phi_q'\} \{\Phi_q'\}^T + (G_\zeta A \zeta_c - \tau_0 EI_{\eta\zeta}) \{\Phi_q'\} \{\Phi_q\}^T + \\
& \{\Phi_q\} \{\Phi_q'\}^T) + (G_{\zeta\zeta} A - 2\tau_0 G_\zeta A \eta_c + \tau_0^2 EI_{\zeta\zeta}) \{\Phi_q\} \{\Phi_q\}^T) dx
\end{aligned}$$

The nonlinear stiffness matrix,  $[K^{NL}]$ , is defined by the following non-zero sub-matrices:

$$\begin{aligned}
[K_{11}^{NL}] = & \int_0^{l_e} ((\bar{V}_x) \{\Phi_c'\} \{\Phi_c'\}^T + [\bar{EAB}_1 \cos \beta (v_{,x} \sin \beta - w_{,x} \cos \beta) + \\
& (\bar{EI}_{\eta\eta} \sin \beta - \bar{EI}_{\zeta\eta} \cos \beta) \phi] \{\Phi_c''\} \{\Phi_c''\}^T - \\
& [\frac{1}{2} \bar{EA}\eta_a v_{,x} + (\sin \beta \cos \beta) (\bar{S}'_x)] \{\Phi_c''\} \{\Phi_c'\}^T - \\
& (\sin \beta \cos \beta) (\bar{S}'_x) \{\Phi_c'\} \{\Phi_c''\}^T) dx
\end{aligned}$$

$$\begin{aligned}
[K_{12}^{NL}] = & \int_0^{l_e} ([\bar{EAB}_1 \sin \beta (v_{,x} \sin \beta - w_{,x} \cos \beta) + \\
& (\bar{EI}_{\zeta\zeta} \cos \beta - \bar{EI}_{\eta\zeta} \sin \beta) \phi] \{\Phi_c''\} \{\Phi_c''\}^T + \\
& [-\frac{1}{2} \bar{EA}\eta_a w_{,x} + (\cos^2 \beta) (\bar{S}'_x)] \{\Phi_c''\} \{\Phi_c'\}^T - \\
& (\sin^2 \beta) (\bar{S}'_x) \{\Phi_c'\} \{\Phi_c''\}^T) dx
\end{aligned}$$

$$[K_{13}^{NL}] = \int_0^{l_e} [(\bar{M}'_y) \cos \beta - (\bar{M}'_z) \sin \beta] \{\Phi_c''\} \{\Phi_q\}^T dx$$

$$\begin{aligned}
[K_{21}^{NL}] = & \int_0^{l_e} ([\bar{EAB}_2 \cos \beta (v_{,x} \sin \beta - w_{,x} \cos \beta) - \\
& (\bar{EI}_{\eta\eta} \cos \beta + \bar{EI}_{\zeta\eta} \sin \beta) \phi] \{\Phi_c''\} \{\Phi_c''\}^T - \\
& [\frac{1}{2} \bar{EA}\zeta_a v_{,x} + (\sin^2 \beta) (\bar{S}'_x)] \{\Phi_c''\} \{\Phi_c'\}^T + \\
& (\cos^2 \beta) (\bar{S}'_x) \{\Phi_c'\} \{\Phi_c''\}^T) dx
\end{aligned}$$

$$\begin{aligned}
[K_{22}^{NL}] = & \int_0^l ((\bar{V}_x) \{\Phi_c'\} \{\Phi_c'\}^T + [\overline{EAB}_2 \sin \beta (v_{,x} \sin \beta - w_{,x} \cos \beta) + \\
& (\overline{EI}_{\eta\zeta} \cos \beta + \overline{EI}_{\zeta\zeta} \sin \beta) \phi] \{\Phi_c''\} \{\Phi_c''\}^T + \\
& [-\frac{1}{2} \overline{EA}\zeta_a w_{,x} + (\sin \beta \cos \beta) (\bar{S}'_x)] \{\Phi_c''\} \{\Phi_c'\}^T + \\
& (\sin \beta \cos \beta) (\bar{S}'_x) \{\Phi_c'\} \{\Phi_c''\}^T) dx
\end{aligned}$$

$$[K_{23}^{NL}] = \int_0^l [(\bar{M}'_y) \sin \beta + (\bar{M}'_z) \cos \beta] \{\Phi_c''\} \{\Phi_q\}^T dx$$

$$\begin{aligned}
[K_{31}^{NL}] = & \int_0^l [(\bar{M}'_y) \cos \beta - (\bar{M}'_z) \sin \beta] \{\Phi_q\} \{\Phi_c''\}^T + \\
& [(GJ)(\cos \beta)(-v_{,x} \sin \beta + w_{,x} \cos \beta) + \overline{EAB}_2 \phi] \\
& \{\Phi_q'\} \{\Phi_c''\}^T + (\frac{1}{2} EAB_0 v_{,x}) \{\Phi_q'\} \{\Phi_c'\}^T) dx
\end{aligned}$$

$$\begin{aligned}
[K_{32}^{NL}] = & \int_0^l [(\bar{M}'_y) \sin \beta + (\bar{M}'_z) \cos \beta] \{\Phi_q\} \{\Phi_c''\}^T + \\
& [(GJ)(\sin \beta)(-v_{,x} \sin \beta + w_{,x} \cos \beta) - \overline{EAB}_1 \phi] \\
& \{\Phi_q'\} \{\Phi_c''\}^T + (\frac{1}{2} EAB_0 w_{,x}) \{\Phi_q'\} \{\Phi_c'\}^T) dx
\end{aligned}$$

$$[K_{33}^{NL}] = \int_0^l [\frac{1}{2} EAB_4 \phi_{,x} + (\bar{T}_x)] \{\Phi_q'\} \{\Phi_q'\}^T dx$$

$$\begin{aligned}
[K_{41}^{NL}] = & \int_0^l [(EAB_0)(\cos \beta)(-v_{,x} \sin \beta + w_{,x} \cos \beta) + \overline{EA}\zeta_a \phi] \\
& \{\Phi_q'\} \{\Phi_c''\}^T + (\frac{1}{2} EA v_{,x}) \{\Phi_q'\} \{\Phi_c'\}^T) dx
\end{aligned}$$

$$[K_{42}^{NL}] = \int_0^l ((EAB_0)(\sin \beta)(-v_{,x} \sin \beta + w_{,x} \cos \beta) - \overline{EA\eta_a}\phi) \{\Phi_q'\}\{\Phi_c''\}^T + (\frac{1}{2}EAw_{,x}) \{\Phi_q'\}\{\Phi_c'\}^T dx$$

$$[K_{43}^{NL}] = \int_0^l (\frac{1}{2}EAC_0\phi_{,x}) \{\Phi_q'\}\{\Phi_q'\}^T dx$$

$$[K_{51}^{NL}] = \int_0^l ((\frac{1}{2}EAD_0v_{,x}) \{\Phi_q'\}\{\Phi_c'\}^T + (\overline{EAD_2}\phi) \{\Phi_q'\}\{\Phi_c''\}^T + [\frac{1}{2}(EAD_0' + EAB_5)v_{,x}] \{\Phi_q'\}\{\Phi_c'\}^T + [(EAB_{14})(\cos \beta)(-v_{,x} \sin \beta + w_{,x} \cos \beta) + (\overline{EAD_2}' + \overline{EAB_7})\phi] \{\Phi_q'\}\{\Phi_c''\}^T) dx$$

$$[K_{52}^{NL}] = \int_0^l ((\frac{1}{2}EAD_0w_{,x}) \{\Phi_q'\}\{\Phi_c'\}^T - (\overline{EAD_1}\phi) \{\Phi_q'\}\{\Phi_c''\}^T + [\frac{1}{2}(EAD_0' + EAB_5)w_{,x}] \{\Phi_q'\}\{\Phi_c'\}^T + [(EAB_{14})(\sin \beta)(-v_{,x} \sin \beta + w_{,x} \cos \beta) - (\overline{EAD_1}' + \overline{EAB_6})\phi] \{\Phi_q'\}\{\Phi_c''\}^T) dx$$

$$[K_{53}^{NL}] = \int_0^l ((\frac{1}{2}EAD_4\phi_{,x}) \{\Phi_q'\}\{\Phi_q'\}^T + [\frac{1}{2}(EAD_4' + EAB_9)\phi_{,x}] \{\Phi_q'\}\{\Phi_q'\}^T) dx$$

$$\begin{aligned}
[K_{61}^{NL}] &= \int_0^{l_e} \left( [(EAB_{12})(\cos \beta)(-v_{,x} \sin \beta + w_{,x} \cos \beta) + \right. \\
&\quad \left. \overline{G_\eta A \zeta_b \phi}] \{\Phi_q\} \{\Phi_c''\}^T + \left(\frac{1}{2}EA\eta_a v_{,x}\right) \{\Phi_q'\} \{\Phi_c'\}^T + \right. \\
&\quad \left. \left[\frac{1}{2}(G_\eta A + \tau_0 EA \zeta_a) v_{,x}\right] \{\Phi_q\} \{\Phi_c'\}^T \right) dx
\end{aligned}$$

$$\begin{aligned}
[K_{62}^{NL}] &= \int_0^{l_e} \left( [(EAB_{12})(\sin \beta)(-v_{,x} \sin \beta + w_{,x} \cos \beta) - \right. \\
&\quad \left. \overline{G_\eta A \eta_b \phi}] \{\Phi_q\} \{\Phi_c''\}^T + \left(\frac{1}{2}EA\eta_a w_{,x}\right) \{\Phi_q'\} \{\Phi_c'\}^T + \right. \\
&\quad \left. \left[\frac{1}{2}(G_\eta A + \tau_0 EA \zeta_a) w_{,x}\right] \{\Phi_q\} \{\Phi_c'\}^T \right) dx
\end{aligned}$$

$$[K_{63}^{NL}] = \int_0^{l_e} \left(\frac{1}{2}G_\eta J \phi_{,x}\right) \{\Phi_q\} \{\Phi_q'\}^T dx$$

$$\begin{aligned}
[K_{71}^{NL}] &= \int_0^{l_e} \left( [(EAB_{10})(\cos \beta)(-v_{,x} \sin \beta + w_{,x} \cos \beta) + \right. \\
&\quad \left. \overline{G_\zeta A \zeta_c \phi}] \{\Phi_q\} \{\Phi_c''\}^T + \left(\frac{1}{2}EA\zeta_a v_{,x}\right) \{\Phi_q'\} \{\Phi_c'\}^T + \right. \\
&\quad \left. \left[\frac{1}{2}(G_\zeta A - \tau_0 EA \eta_a) v_{,x}\right] \{\Phi_q\} \{\Phi_c'\}^T \right) dx
\end{aligned}$$

$$\begin{aligned}
[K_{72}^{NL}] &= \int_0^{l_e} \left( [(EAB_{10})(\sin \beta)(-v_{,x} \sin \beta + w_{,x} \cos \beta) - \right. \\
&\quad \left. \overline{G_\zeta A \eta_c \phi}] \{\Phi_q\} \{\Phi_c''\}^T + \left(\frac{1}{2}EA\zeta_a w_{,x}\right) \{\Phi_q'\} \{\Phi_c'\}^T + \right. \\
&\quad \left. \left[\frac{1}{2}(G_\zeta A - \tau_0 EA \eta_a) w_{,x}\right] \{\Phi_q\} \{\Phi_c'\}^T \right) dx
\end{aligned}$$

$$[K_{73}^{NL}] = \int_0^{l_e} \left(\frac{1}{2}G_\zeta J \phi_{,x}\right) \{\Phi_q\} \{\Phi_q'\}^T dx$$

All the other sub-matrices in  $[K^{NL}]$  are equal to zero.

## B.2 FINITE ELEMENT MATRICES ASSOCIATED WITH THE KINETIC ENERGY VARIATION

The finite element matrices which are associated with the kinetic energy variation include the mass matrix,  $[M]$ , the Coriolis damping matrix,  $[M^C]$ , the centrifugal stiffening matrix,  $[K^{CF}]$ , and the centrifugal force vector,  $\{F^{CF}\}$ . In order to express these finite element matrices in terms of their sub-matrices, the following constants are defined:

$$\overline{m\eta_m} = m\eta_m \cos \beta - m\zeta_m \sin \beta$$

$$\overline{m\zeta_m} = m\eta_m \sin \beta + m\zeta_m \cos \beta$$

$$\overline{Im_{\eta\zeta}} = Im_{\eta\zeta} \cos \beta - Im_{\eta\eta} \sin \beta$$

$$\overline{Im_{\eta\eta}} = Im_{\eta\zeta} \sin \beta + Im_{\eta\eta} \cos \beta$$

$$\overline{Im_{\zeta\zeta}} = Im_{\zeta\zeta} \cos \beta - Im_{\eta\zeta} \sin \beta$$

$$\overline{Im_{\zeta\eta}} = Im_{\zeta\zeta} \sin \beta + Im_{\eta\zeta} \cos \beta$$

$$\overline{mD_1} = mD_1 \cos \beta - mD_2 \sin \beta$$

$$\overline{mD_2} = mD_1 \sin \beta + mD_2 \cos \beta$$

$$\overline{h\Omega_x} = (\Omega_y^2 + \Omega_z^2)h_x - (\Omega_x\Omega_y - \dot{\Omega}_z)h_y - (\Omega_x\Omega_z + \dot{\Omega}_y)h_z - \Omega_y V_{bz} + \Omega_z V_{by} - \dot{V}_{bx}$$

$$\overline{h\Omega_y} = (\Omega_x^2 + \Omega_z^2)h_y - (\Omega_x\Omega_y + \dot{\Omega}_z)h_x - (\Omega_y\Omega_z - \dot{\Omega}_x)h_z - \Omega_z V_{bx} + \Omega_x V_{bz} - \dot{V}_{by}$$

$$\overline{h\Omega_z} = (\Omega_x^2 + \Omega_y^2)h_z - (\Omega_x\Omega_z - \dot{\Omega}_y)h_x - (\Omega_y\Omega_z + \dot{\Omega}_x)h_y - \Omega_x V_{by} + \Omega_y V_{bx} - \dot{V}_{bz}$$

The mass matrix, [M], is defined by the following non-zero sub-matrices:

$$[M_{11}] = \int_0^{l_e} m \{\Phi_c\} \{\Phi_c\}^T dx$$

$$[M_{13}] = \int_0^{l_e} -\overline{m\zeta_m} \{\Phi_c\} \{\Phi_q\}^T dx$$

$$[M_{14}] = \int_0^{l_e} -\overline{m\eta_m} \{\Phi_c'\} \{\Phi_q\}^T dx$$

$$[M_{15}] = \int_0^{l_e} -\overline{mD_1} \{\Phi_c'\} \{\Phi_q\}^T dx$$

$$[M_{16}] = \int_0^{l_e} -\overline{m\zeta_\zeta} \{\Phi_c'\} \{\Phi_q\}^T dx$$

$$[M_{17}] = \int_0^{l_e} -\overline{m\eta_\zeta} \{\Phi_c'\} \{\Phi_q\}^T dx$$

$$[M_{22}] = \int_0^{l_e} m \{\Phi_c\} \{\Phi_c\}^T dx$$

$$[M_{23}] = \int_0^{l_e} \overline{m\eta_m} \{\Phi_c\} \{\Phi_q\}^T dx$$

$$[M_{24}] = \int_0^{l_e} -\overline{m\zeta_m} \{\Phi_c'\} \{\Phi_q\}^T dx$$

$$[M_{25}] = \int_0^{l_e} -\overline{mD_2} \{\Phi_c'\} \{\Phi_q\}^T dx$$

$$[M_{26}] = \int_0^{l_e} -\overline{Im}_{\zeta\eta} \{\Phi_c'\} \{\Phi_q\}^T dx$$

$$[M_{27}] = \int_0^{l_e} -\overline{Im}_{\eta\eta} \{\Phi_c'\} \{\Phi_q\}^T dx$$

$$[M_{31}] = [M_{13}]^T$$

$$[M_{32}] = [M_{23}]^T$$

$$[M_{33}] = \int_0^{l_e} (Im_{\eta\eta} + Im_{\zeta\zeta}) \{\Phi_q\} \{\Phi_q\}^T dx$$

$$[M_{41}] = [M_{14}]^T$$

$$[M_{42}] = [M_{24}]^T$$

$$[M_{44}] = \int_0^{l_e} m \{\Phi_q\} \{\Phi_q\}^T dx$$

$$[M_{45}] = \int_0^{l_e} mD_0 \{\Phi_q\} \{\Phi_q\}^T dx$$

$$[M_{46}] = \int_0^{l_e} m\eta_m \{\Phi_q\} \{\Phi_q\}^T dx$$

$$[M_{47}] = \int_0^{l_e} m\zeta_m \{\Phi_q\} \{\Phi_q\}^T dx$$

$$[M_{51}] = [M_{15}]^T$$

$$[M_{52}] = [M_{25}]^T$$

$$[M_{54}] = [M_{45}]^T$$

$$[M_{55}] = \int_0^{l_e} mD_3 \{\Phi_q\} \{\Phi_q\}^T dx$$

$$[M_{56}] = \int_0^{l_e} mD_1 \{\Phi_q\} \{\Phi_q\}^T dx$$

$$[M_{57}] = \int_0^{l_e} mD_2 \{\Phi_q\} \{\Phi_q\}^T dx$$

$$[M_{61}] = [M_{16}]^T$$

$$[M_{62}] = [M_{26}]^T$$

$$[M_{64}] = [M_{46}]^T$$

$$[M_{65}] = [M_{56}]^T$$

$$[M_{66}] = \int_0^{l_e} Im_{\zeta\zeta} \{\Phi_q\} \{\Phi_q\}^T dx$$

$$[M_{67}] = \int_0^{l_e} Im_{\eta\zeta} \{\Phi_q\} \{\Phi_q\}^T dx$$

$$[M_{71}] = [M_{17}]^T$$

$$[M_{72}] = [M_{27}]^T$$

$$[M_{74}] = [M_{47}]^T$$

$$[M_{75}] = [M_{57}]^T$$

$$[M_{76}] = [M_{67}]^T$$

$$[M_{77}] = \int_0^{l_e} I m_{\eta\eta} \{\Phi_q\} \{\Phi_q\}^T dx$$

All the other sub-matrices in  $[M]$  are equal to zero.

The Coriolis damping matrix,  $[M^C]$ , is defined by the following non-zero sub-matrices:

$$[M_{11}^C] = \int_0^{l_e} 2\Omega_z \overline{m\eta_m} (\{\Phi_c'\} \{\Phi_c\}^T - \{\Phi_c\} \{\Phi_c'\}^T) dx$$

$$[M_{12}^C] = \int_0^{l_e} -2(\Omega_x m \{\Phi_c\} \{\Phi_c\}^T + \Omega_y \overline{m\eta_m} \{\Phi_c'\} \{\Phi_c\}^T + \Omega_z \overline{m\zeta_m} \{\Phi_c\} \{\Phi_c'\}^T) dx$$

$$[M_{13}^C] = \int_0^{l_e} -2\Omega_x \overline{m\eta_m} \{\Phi_c\} \{\Phi_q\}^T dx$$

$$[M_{14}^C] = \int_0^{l_e} 2\Omega_z m \{\Phi_c\} \{\Phi_q\}^T dx$$

$$[M_{15}^C] = \int_0^{l_e} 2\Omega_z m D_0 \{\Phi_c\} \{\Phi_q\}^T dx$$

$$[M_{16}^C] = \int_0^{l_e} 2\Omega_z m \eta_m \{\Phi_c\} \{\Phi_q\}^T dx$$

$$[M_{17}^C] = \int_0^{l_e} 2\Omega_z m \zeta_m \{\Phi_c\} \{\Phi_q\}^T dx$$

$$[M_{21}^C] = -[M_{12}^C]^T$$

$$[M_{22}^C] = \int_0^{l_e} -2\Omega_y \overline{m\zeta_m} (\{\Phi_c'\}\{\Phi_c\}^T - \{\Phi_c\}\{\Phi_c'\}^T) dx$$

$$[M_{23}^C] = \int_0^{l_e} -2\Omega_x \overline{m\zeta_m} \{\Phi_c\}\{\Phi_q\}^T dx$$

$$[M_{24}^C] = \int_0^{l_e} -2\Omega_y m \{\Phi_c\}\{\Phi_q\}^T dx$$

$$[M_{25}^C] = \int_0^{l_e} -2\Omega_y m D_0 \{\Phi_c\}\{\Phi_q\}^T dx$$

$$[M_{26}^C] = \int_0^{l_e} -2\Omega_y m \eta_m \{\Phi_c\}\{\Phi_q\}^T dx$$

$$[M_{27}^C] = \int_0^{l_e} -2\Omega_y m \zeta_m \{\Phi_c\}\{\Phi_q\}^T dx$$

$$[M_{31}^C] = -[M_{13}^C]^T$$

$$[M_{32}^C] = -[M_{23}^C]^T$$

$$[M_{34}^C] = \int_0^{l_e} -2(\Omega_y \overline{m\eta_m} + \Omega_z \overline{m\zeta_m}) \{\Phi_q\}\{\Phi_q\}^T dx$$

$$[M_{35}^C] = \int_0^{l_e} -2(\Omega_y \overline{mD_1} + \Omega_z \overline{mD_2}) \{\Phi_q\}\{\Phi_q\}^T dx$$

$$[M_{36}^C] = \int_0^{l_e} -2(\Omega_y \overline{m\zeta_\zeta} + \Omega_z \overline{m\zeta_\eta}) \{\Phi_q\}\{\Phi_q\}^T dx$$

$$[M_{37}^C] = \int_0^{l_e} -2(\Omega_y \overline{m}_{\eta\zeta} + \Omega_z \overline{m}_{\eta\eta}) \{\Phi_q\} \{\Phi_q\}^T dx$$

$$[M_{41}^C] = -[M_{14}^C]^T$$

$$[M_{42}^C] = -[M_{24}^C]^T$$

$$[M_{43}^C] = -[M_{34}^C]^T$$

$$[M_{51}^C] = -[M_{15}^C]^T$$

$$[M_{52}^C] = -[M_{25}^C]^T$$

$$[M_{53}^C] = -[M_{35}^C]^T$$

$$[M_{61}^C] = -[M_{16}^C]^T$$

$$[M_{62}^C] = -[M_{26}^C]^T$$

$$[M_{63}^C] = -[M_{36}^C]^T$$

$$[M_{71}^C] = -[M_{17}^C]^T$$

$$[M_{72}^C] = -[M_{27}^C]^T$$

$$[M_{73}^C] = -[M_{37}^C]^T$$

All the other sub-matrices in  $[M^C]$  are equal to zero.

The centrifugal stiffening matrix,  $[K^{CF}]$ , is defined by the following sub-matrices:

$$[K_{11}^{CF}] = \int_0^l [ -(\Omega_x^2 + \Omega_z^2) m \{\Phi_c\} \{\Phi_c\}^T - (\Omega_x \Omega_y + \dot{\Omega}_z) \overline{m\eta_m} \{\Phi_c\} \{\Phi_c'\}^T - (\Omega_x \Omega_y - \dot{\Omega}_z) \overline{m\eta_m} \{\Phi_c'\} \{\Phi_c\}^T ] dx$$

$$[K_{12}^{CF}] = \int_0^l \langle (\Omega_y \Omega_z - \dot{\Omega}_x) m \{\Phi_c\} \{\Phi_c\}^T - (\Omega_x \Omega_z + \dot{\Omega}_y) \overline{m\eta_m} \{\Phi_c'\} \{\Phi_c\}^T - (\Omega_x \Omega_y + \dot{\Omega}_z) \overline{m\zeta_m} \{\Phi_c\} \{\Phi_c'\}^T + [h\overline{\Omega_y} - (\Omega_x \Omega_y + \dot{\Omega}_z) x] m\zeta_m \cos^3 \beta \{\Phi_c'\} \{\Phi_c'\}^T \rangle dx$$

$$[K_{13}^{CF}] = \int_0^l \langle [(\Omega_y \Omega_z - \dot{\Omega}_x) \overline{m\eta_m} + (\Omega_x^2 + \Omega_z^2) \overline{m\zeta_m}] \{\Phi_c\} \{\Phi_q\}^T - [h\overline{\Omega_x} + (\Omega_y^2 + \Omega_z^2) x] \overline{m\zeta_m} \{\Phi_c'\} \{\Phi_q\}^T \rangle dx$$

$$[K_{14}^{CF}] = \int_0^l [(\Omega_x \Omega_y + \dot{\Omega}_z) m \{\Phi_c\} \{\Phi_q\}^T + (\Omega_y^2 + \Omega_z^2) \overline{m\eta_m} \{\Phi_c'\} \{\Phi_q\}^T] dx$$

$$[K_{15}^{CF}] = \int_0^l [(\Omega_x \Omega_y + \dot{\Omega}_z) m D_0 \{\Phi_c\} \{\Phi_q\}^T + (\Omega_y^2 + \Omega_z^2) \overline{m D_1} \{\Phi_c'\} \{\Phi_q\}^T] dx$$

$$[K_{16}^{CF}] = \int_0^l [(\Omega_x \Omega_y + \dot{\Omega}_z) m \eta_m \{\Phi_c\} \{\Phi_q\}^T + (\Omega_y^2 + \Omega_z^2) \overline{m\eta_{\zeta\zeta}} \{\Phi_c'\} \{\Phi_q\}^T] dx$$

$$[K_{17}^{CF}] = \int_0^l [(\Omega_x \Omega_y + \dot{\Omega}_z) m \zeta_m \{\Phi_c\} \{\Phi_q\}^T + (\Omega_y^2 + \Omega_z^2) \overline{m\eta_{\zeta}} \{\Phi_c'\} \{\Phi_q\}^T] dx$$

$$[K_{21}^{CF}] = \int_0^l \langle (\Omega_y \Omega_z + \dot{\Omega}_x) m \{\Phi_c\} \{\Phi_c\}^T - (\Omega_x \Omega_z - \dot{\Omega}_y) \overline{m\eta_m} \{\Phi_c\} \{\Phi_c'\}^T - (\Omega_x \Omega_y - \dot{\Omega}_z) \overline{m\zeta_m} \{\Phi_c'\} \{\Phi_c\}^T + [h\overline{\Omega_y} - (\Omega_x \Omega_y + \dot{\Omega}_z) x] m\zeta_m \cos^3 \beta \{\Phi_c'\} \{\Phi_c'\}^T \rangle dx$$

$$[K_{22}^{CF}] = \int_0^{l_e} [ - (\Omega_x^2 + \Omega_y^2) m \{ \Phi_c \} \{ \Phi_c \}^T - (\Omega_x \Omega_z - \dot{\Omega}_y) \overline{m \zeta_m} \{ \Phi_c \} \{ \Phi_c' \}^T - (\Omega_x \Omega_z + \dot{\Omega}_y) \overline{m \zeta_m} \{ \Phi_c' \} \{ \Phi_c \}^T ] dx$$

$$[K_{23}^{CF}] = \int_0^{l_e} \langle - [(\Omega_y \Omega_z + \dot{\Omega}_x) \overline{m \zeta_m} + (\Omega_x^2 + \Omega_y^2) \overline{m \eta_m}] \{ \Phi_c \} \{ \Phi_q \}^T + [\overline{h \Omega_x} + (\Omega_y^2 + \Omega_z^2) x] \overline{m \eta_m} \{ \Phi_c' \} \{ \Phi_q \}^T \rangle dx$$

$$[K_{24}^{CF}] = \int_0^{l_e} [(\Omega_x \Omega_z - \dot{\Omega}_y) m \{ \Phi_c \} \{ \Phi_q \}^T + (\Omega_y^2 + \Omega_z^2) \overline{m \zeta_m} \{ \Phi_c' \} \{ \Phi_q \}^T] dx$$

$$[K_{25}^{CF}] = \int_0^{l_e} [(\Omega_x \Omega_z - \dot{\Omega}_y) m D_0 \{ \Phi_c \} \{ \Phi_q \}^T + (\Omega_y^2 + \Omega_z^2) \overline{m D_2} \{ \Phi_c' \} \{ \Phi_q \}^T] dx$$

$$[K_{26}^{CF}] = \int_0^{l_e} [(\Omega_x \Omega_z - \dot{\Omega}_y) m \eta_m \{ \Phi_c \} \{ \Phi_q \}^T + (\Omega_y^2 + \Omega_z^2) \overline{m \zeta_\eta} \{ \Phi_c' \} \{ \Phi_q \}^T] dx$$

$$[K_{27}^{CF}] = \int_0^{l_e} [(\Omega_x \Omega_z - \dot{\Omega}_y) m \zeta_m \{ \Phi_c \} \{ \Phi_q \}^T + (\Omega_y^2 + \Omega_z^2) \overline{m \eta_\eta} \{ \Phi_c' \} \{ \Phi_q \}^T] dx$$

$$[K_{31}^{CF}] = \int_0^{l_e} \langle [(\Omega_y \Omega_z + \dot{\Omega}_x) \overline{m \eta_m} + (\Omega_x^2 + \Omega_z^2) \overline{m \zeta_m}] \{ \Phi_q \} \{ \Phi_c \}^T - [\overline{h \Omega_x} + (\Omega_y^2 + \Omega_z^2) x] \overline{m \zeta_m} \{ \Phi_q \} \{ \Phi_c' \}^T \rangle dx$$

$$[K_{32}^{CF}] = \int_0^{l_e} \langle - [(\Omega_y \Omega_z - \dot{\Omega}_x) \overline{m \zeta_m} + (\Omega_x^2 + \Omega_y^2) \overline{m \eta_m}] \{ \Phi_q \} \{ \Phi_c \}^T + [\overline{h \Omega_x} + (\Omega_y^2 + \Omega_z^2) x] \overline{m \eta_m} \{ \Phi_q \} \{ \Phi_c' \}^T \rangle dx$$

$$[K_{33}^{CF}] = \int_0^{l_e} \{(\Omega_z^2 - \Omega_y^2) [(Im_{\zeta\zeta} - Im_{\eta\eta})(\cos^2\beta - \sin^2\beta) - 4Im_{\eta\zeta} \sin\beta \cos\beta] \\ - 4\Omega_y\Omega_z [(Im_{\zeta\zeta} - Im_{\eta\eta}) \sin\beta \cos\beta + Im_{\eta\zeta}(\cos^2\beta - \sin^2\beta)]\} \\ \{\Phi_q\}\{\Phi_q\}^T dx$$

$$[K_{34}^{CF}] = \int_0^{l_e} [(\Omega_x\Omega_z - \dot{\Omega}_y) \overline{m\eta_m} - (\Omega_x\Omega_y + \dot{\Omega}_z) \overline{m\zeta_m}] \{\Phi_q\}\{\Phi_q\}^T dx$$

$$[K_{35}^{CF}] = \int_0^{l_e} [(\Omega_x\Omega_z - \dot{\Omega}_y) \overline{mD_1} - (\Omega_x\Omega_y + \dot{\Omega}_z) \overline{mD_2}] \{\Phi_q\}\{\Phi_q\}^T dx$$

$$[K_{36}^{CF}] = \int_0^{l_e} [(\Omega_x\Omega_z - \dot{\Omega}_y) \overline{m\zeta_\zeta} - (\Omega_x\Omega_y + \dot{\Omega}_z) \overline{m\zeta_\eta}] \{\Phi_q\}\{\Phi_q\}^T dx$$

$$[K_{37}^{CF}] = \int_0^{l_e} [(\Omega_x\Omega_z - \dot{\Omega}_y) \overline{m\eta_\zeta} - (\Omega_x\Omega_y + \dot{\Omega}_z) \overline{m\eta_\eta}] \{\Phi_q\}\{\Phi_q\}^T dx$$

$$[K_{41}^{CF}] = \int_0^{l_e} [(\Omega_x\Omega_y - \dot{\Omega}_z) m \{\Phi_q\}\{\Phi_c\}^T + (\Omega_y^2 + \Omega_z^2) \overline{m\eta_m} \{\Phi_q\}\{\Phi_c'\}^T] dx$$

$$[K_{42}^{CF}] = \int_0^{l_e} [(\Omega_x\Omega_z + \dot{\Omega}_y) m \{\Phi_q\}\{\Phi_c\}^T + (\Omega_y^2 + \Omega_z^2) \overline{m\zeta_m} \{\Phi_q\}\{\Phi_c'\}^T] dx$$

$$[K_{43}^{CF}] = \int_0^{l_e} [(\Omega_x\Omega_z + \dot{\Omega}_y) \overline{m\eta_m} - (\Omega_x\Omega_y - \dot{\Omega}_z) \overline{m\zeta_m}] \{\Phi_q\}\{\Phi_q\}^T dx$$

$$[K_{44}^{CF}] = \int_0^{l_e} -(\Omega_y^2 + \Omega_z^2) m \{\Phi_q\}\{\Phi_q\}^T dx$$

$$[K_{45}^{CF}] = \int_0^{l_e} -(\Omega_y^2 + \Omega_z^2) mD_0 \{\Phi_q\}\{\Phi_q\}^T dx$$

$$[K_{46}^{CF}] = \int_0^{l_e} -(\Omega_y^2 + \Omega_z^2) m \eta_m \{\Phi_q\} \{\Phi_q\}^T dx$$

$$[K_{47}^{CF}] = \int_0^{l_e} -(\Omega_y^2 + \Omega_z^2) m \zeta_m \{\Phi_q\} \{\Phi_q\}^T dx$$

$$[K_{51}^{CF}] = \int_0^{l_e} [(\Omega_x \Omega_y - \dot{\Omega}_z) m D_0 \{\Phi_q\} \{\Phi_c\}^T + (\Omega_y^2 + \Omega_z^2) \overline{m D_1} \{\Phi_q\} \{\Phi_c'\}^T] dx$$

$$[K_{52}^{CF}] = \int_0^{l_e} [(\Omega_x \Omega_z + \dot{\Omega}_y) m D_0 \{\Phi_q\} \{\Phi_c\}^T + (\Omega_y^2 + \Omega_z^2) \overline{m D_2} \{\Phi_q\} \{\Phi_c'\}^T] dx$$

$$[K_{53}^{CF}] = \int_0^{l_e} [(\Omega_x \Omega_z + \dot{\Omega}_y) \overline{m D_1} - (\Omega_x \Omega_y - \dot{\Omega}_z) \overline{m D_2}] \{\Phi_q\} \{\Phi_q\}^T dx$$

$$[K_{54}^{CF}] = [K_{45}^{CF}]^T$$

$$[K_{55}^{CF}] = \int_0^{l_e} -(\Omega_y^2 + \Omega_z^2) m D_3 \{\Phi_q\} \{\Phi_q\}^T dx$$

$$[K_{56}^{CF}] = \int_0^{l_e} -(\Omega_y^2 + \Omega_z^2) m D_1 \{\Phi_q\} \{\Phi_q\}^T dx$$

$$[K_{57}^{CF}] = \int_0^{l_e} -(\Omega_y^2 + \Omega_z^2) m D_2 \{\Phi_q\} \{\Phi_q\}^T dx$$

$$[K_{61}^{CF}] = \int_0^{l_e} [(\Omega_x \Omega_y - \dot{\Omega}_z) m \eta_m \{\Phi_q\} \{\Phi_c\}^T + (\Omega_y^2 + \Omega_z^2) \overline{m \zeta_\zeta} \{\Phi_q\} \{\Phi_c'\}^T] dx$$

$$[K_{62}^{CF}] = \int_0^{l_e} [(\Omega_x \Omega_z + \dot{\Omega}_y) m \eta_m \{\Phi_q\} \{\Phi_c\}^T + (\Omega_y^2 + \Omega_z^2) \overline{m \zeta_\eta} \{\Phi_q\} \{\Phi_c'\}^T] dx$$

$$[K_{63}^{CF}] = \int_0^{l_e} [(\Omega_x \Omega_z + \dot{\Omega}_y) \overline{Im}_{\zeta\zeta} - (\Omega_x \Omega_y - \dot{\Omega}_z) \overline{Im}_{\zeta\eta}] \{\Phi_q\} \{\Phi_q\}^T dx$$

$$[K_{64}^{CF}] = [K_{46}^{CF}]^T$$

$$[K_{65}^{CF}] = [K_{56}^{CF}]^T$$

$$[K_{66}^{CF}] = \int_0^{l_e} -(\Omega_y^2 + \Omega_z^2) Im_{\zeta\zeta} \{\Phi_q\} \{\Phi_q\}^T dx$$

$$[K_{67}^{CF}] = \int_0^{l_e} -(\Omega_y^2 + \Omega_z^2) Im_{\eta\zeta} \{\Phi_q\} \{\Phi_q\}^T dx$$

$$[K_{71}^{CF}] = \int_0^{l_e} [(\Omega_x \Omega_y - \dot{\Omega}_z) m_{\zeta m} \{\Phi_q\} \{\Phi_c\}^T + (\Omega_y^2 + \Omega_z^2) \overline{Im}_{\eta\zeta} \{\Phi_q\} \{\Phi_c'\}^T] dx$$

$$[K_{72}^{CF}] = \int_0^{l_e} [(\Omega_x \Omega_z + \dot{\Omega}_y) m_{\zeta m} \{\Phi_q\} \{\Phi_c\}^T + (\Omega_y^2 + \Omega_z^2) \overline{Im}_{\eta\eta} \{\Phi_q\} \{\Phi_c'\}^T] dx$$

$$[K_{73}^{CF}] = \int_0^{l_e} [(\Omega_x \Omega_z + \dot{\Omega}_y) \overline{Im}_{\eta\zeta} - (\Omega_x \Omega_y - \dot{\Omega}_z) \overline{Im}_{\eta\eta}] \{\Phi_q\} \{\Phi_q\}^T dx$$

$$[K_{74}^{CF}] = [K_{47}^{CF}]^T$$

$$[K_{75}^{CF}] = [K_{57}^{CF}]^T$$

$$[K_{76}^{CF}] = [K_{67}^{CF}]^T$$

$$[K_{77}^{CF}] = \int_0^{l_e} -(\Omega_y^2 + \Omega_z^2) Im_{\eta\eta} \{\Phi_q\} \{\Phi_q\}^T dx$$

The centrifugal force vector,  $\{F^{CF}\}$ , is defined by the following sub-vectors:

$$\begin{aligned}
\{F_1^{CF}\} = & \int_0^l \langle \{ - [\overline{h\Omega_y} - (\Omega_x\Omega_y + \dot{\Omega}_z)x] m - (\Omega_x^2 + \Omega_z^2) \overline{m\eta_m} + \\
& (\Omega_y\Omega_z - \dot{\Omega}_x) \overline{m\zeta_m} \} \{\Phi_c\} + \{ [\overline{h\Omega_x} + (\Omega_y^2 + \Omega_z^2)x] \overline{m\eta_m} - \\
& (\Omega_x\Omega_y - \dot{\Omega}_z) (\text{Im}_{\zeta\zeta} \cos^2\beta + \text{Im}_{\eta\eta} \sin^2\beta - 2\text{Im}_{\eta\zeta} \sin\beta \cos\beta) - \\
& (\Omega_x\Omega_z + \dot{\Omega}_y) [(\text{Im}_{\zeta\zeta} - \text{Im}_{\eta\eta}) \sin\beta \cos\beta + \text{Im}_{\eta\zeta} (\cos^2\beta - \sin^2\beta)] \} \\
& \{\Phi_c'\} \rangle dx
\end{aligned}$$

$$\begin{aligned}
\{F_2^{CF}\} = & \int_0^l \langle \{ - [\overline{h\Omega_z} - (\Omega_x\Omega_z - \dot{\Omega}_y)x] m - (\Omega_x^2 + \Omega_y^2) \overline{m\zeta_m} + \\
& (\Omega_y\Omega_z + \dot{\Omega}_x) \overline{m\eta_m} \} \{\Phi_c\} + \{ [\overline{h\Omega_x} + (\Omega_y^2 + \Omega_z^2)x] \overline{m\zeta_m} - \\
& (\Omega_x\Omega_y - \dot{\Omega}_z) [(\text{Im}_{\zeta\zeta} - \text{Im}_{\eta\eta}) \sin\beta \cos\beta + \text{Im}_{\eta\zeta} (\cos^2\beta - \sin^2\beta)] - \\
& (\Omega_x\Omega_z + \dot{\Omega}_y) (\text{Im}_{\eta\eta} \cos^2\beta + \text{Im}_{\zeta\zeta} \sin^2\beta + 2\text{Im}_{\eta\zeta} \sin\beta \cos\beta) \} \\
& \{\Phi_c'\} \rangle dx
\end{aligned}$$

$$\begin{aligned}
\{F_3^{CF}\} = & \int_0^l \{ - [\overline{h\Omega_z} - (\Omega_x\Omega_z - \dot{\Omega}_y)x] \overline{m\eta_m} + [\overline{h\Omega_y} - (\Omega_x\Omega_y + \dot{\Omega}_z)x] \overline{m\zeta_m} + \\
& (\text{Im}_{\eta\eta} + \text{Im}_{\zeta\zeta}) \dot{\Omega}_x - \\
& (\Omega_y^2 - \Omega_z^2) [(\text{Im}_{\zeta\zeta} - \text{Im}_{\eta\eta}) \sin\beta \cos\beta + \text{Im}_{\eta\zeta} (\cos^2\beta - \sin^2\beta)] + \\
& \Omega_y\Omega_z [(\text{Im}_{\zeta\zeta} - \text{Im}_{\eta\eta}) (\cos^2\beta - \sin^2\beta) - 4\text{Im}_{\eta\zeta} \sin\beta \cos\beta] \} \{\Phi_q\} dx
\end{aligned}$$

$$\begin{aligned}
\{F_4^{CF}\} = & \int_0^l \{ - [\overline{h\Omega_x} + (\Omega_y^2 + \Omega_z^2)x] m + (\Omega_x\Omega_y - \dot{\Omega}_z) \overline{m\eta_m} + \\
& (\Omega_x\Omega_z + \dot{\Omega}_y) \overline{m\zeta_m} \} \{\Phi_q\} dx
\end{aligned}$$

$$\{F_5^{CF}\} = \int_0^{l_e} \{ - [\overline{h\Omega_x} + (\Omega_y^2 + \Omega_z^2)x] mD_0 + (\Omega_x\Omega_y - \dot{\Omega}_z) \overline{mD_1} + (\Omega_x\Omega_z + \dot{\Omega}_y) \overline{mD_2} \} \{\Phi_q\} dx$$

$$\{F_6^{CF}\} = \int_0^{l_e} \{ - [\overline{h\Omega_x} + (\Omega_y^2 + \Omega_z^2)x] m\eta_m + (\Omega_x\Omega_y - \dot{\Omega}_z) \overline{m\zeta\zeta} + (\Omega_x\Omega_z + \dot{\Omega}_y) \overline{m\zeta\eta} \} \{\Phi_q\} dx$$

$$\{F_7^{CF}\} = \int_0^{l_e} \{ - [\overline{h\Omega_x} + (\Omega_y^2 + \Omega_z^2)x] m\zeta_m + (\Omega_x\Omega_y - \dot{\Omega}_z) \overline{m\eta\zeta} + (\Omega_x\Omega_z + \dot{\Omega}_y) \overline{m\eta\eta} \} \{\Phi_q\} dx$$

### B.3 FINITE ELEMENT MATRICES ASSOCIATED WITH THE VIRTUAL WORK OF THE EXTERNAL LOADS

The finite element matrices which are associated with the virtual work of the external loads include the applied moment stiffening matrix,  $[K^I]$ , and the applied force vector,  $\{F^I\}$ .

The applied moment stiffening matrix,  $[K^I]$ , has the following non-zero sub-matrices:

$$[K_{12}^I] = \int_0^{l_e} q_x \{\Phi_c'\} \{\Phi_c'\}^T dx$$

$$[K_{21}^I] = \int_0^{l_e} -q_x \{\Phi_c'\} \{\Phi_c'\}^T dx$$

$$[K_{31}^I] = \int_0^{l_e} -q_y \{\Phi_q\} \{\Phi_c'\}^T dx$$

$$[K_{32}^I] = \int_0^{l_e} -q_z \{\Phi_q\} \{\Phi_c'\}^T dx$$

$$[K_{41}^I] = \int_0^{l_e} q_z \{\Phi_q'\} \{\Phi_c'\}^T dx$$

$$[K_{42}^I] = \int_0^{l_c} -q_y \{\Phi_q'\} \{\Phi_c'\}^T dx$$

All the other sub-matrices in  $[K^I]$  are equal to zero.

The non-zero sub-vectors associated with the applied force vector,  $\{F^I\}$ , are:

$$\{F_1^I\} = \int_0^{l_e} (-p_y \{\Phi_c\} - q_z \{\Phi_c'\}) dx$$

$$\{F_2^I\} = \int_0^{l_e} (-p_z \{\Phi_c\} + q_y \{\Phi_c'\}) dx$$

$$\{F_3^I\} = \int_0^{l_e} -q_x \{\Phi_q\} dx$$

$$\{F_4^I\} = \int_0^{l_e} -p_x \{\Phi_q\} dx$$

All the other sub-vectors in  $\{F^I\}$  are equal to zero.

## Appendix C

### LOCAL-TO-GLOBAL TRANSFORMATION MATRICES

#### C.1 TRANSFORMATION FOR ROTATIONAL DEGREES OF FREEDOM

Assume that each transformation matrix is written in the form

$$[T] = \begin{bmatrix} T_{11} & T_{12} & T_{13} \\ T_{21} & T_{22} & T_{23} \\ T_{31} & T_{32} & T_{33} \end{bmatrix}$$

The nonzero elements of the matrix  $[T^K]$  are:

$$T_{11}^K = \cos \Lambda_s \sin \Lambda_a w_{,x}^G - \sin \Lambda_s \sin^2 \Lambda_a v_{,x}^G$$

$$T_{21}^K = \cos \Lambda_s \sin^2 \Lambda_a v_{,x}^G$$

$$T_{22}^K = -\sin \Lambda_s \sin \Lambda_a \phi^G$$

$$T_{31}^K = \sin^2 \Lambda_s \cos \Lambda_a w_{,x}^G$$

$$T_{33}^K = \cos \Lambda_s \sin \Lambda_a (\sin \Lambda_s \cos \Lambda_a \phi^G - \cos \Lambda_s w_{,x}^G)$$

The nonzero elements of the matrix  $[T^C]$  are:

$$T_{11}^C = \cos \Lambda_s \sin \Lambda_a w_{,x}^G - \sin \Lambda_s \sin^2 \Lambda_a v_{,x}^G$$

$$T_{12}^C = -\cos \Lambda_s \sin \Lambda_a \phi^G$$

$$T_{13}^C = -\sin \Lambda_s \sin^2 \Lambda_a \dot{\phi}^G$$

$$T_{21}^C = \cos \Lambda_s \sin^2 \Lambda_a \dot{v}_{,x}^G + \sin \Lambda_s \sin \Lambda_a \dot{w}_{,x}^G$$

$$T_{22}^C = -\sin \Lambda_s \sin \Lambda_a \dot{\phi}^G$$

$$T_{23}^C = \cos \Lambda_s \sin^2 \Lambda_a \dot{\phi}^G$$

$$T_{31}^C = \sin^2 \Lambda_s \cos \Lambda_a \dot{w}_{,x}^G + \cos \Lambda_s \sin \Lambda_s \cos \Lambda_a \sin \Lambda_a \dot{v}_{,x}^G$$

$$T_{32}^C = -\sin^2 \Lambda_s \cos \Lambda_a \dot{\phi}^G + \cos^2 \Lambda_s \sin \Lambda_a \dot{v}_{,x}^G$$

$$T_{33}^C = \cos \Lambda_s \sin \Lambda_a (\sin \Lambda_s \cos \Lambda_a \dot{\phi}^G - \cos \Lambda_s \dot{w}_{,x}^G)$$

The nonzero elements of the matrix  $[T^M]$  are:

$$T_{11}^M = \cos \Lambda_s \sin \Lambda_a \dot{w}_{,x}^G - \sin \Lambda_s \sin^2 \Lambda_a \dot{v}_{,x}^G$$

$$T_{12}^M = -\cos \Lambda_s \sin \Lambda_a \dot{\phi}^G$$

$$T_{13}^M = -\sin \Lambda_s \sin^2 \Lambda_a \dot{\phi}^G$$

$$T_{21}^M = \cos \Lambda_s \sin^2 \Lambda_a \dot{v}_{,x}^G + \sin \Lambda_s \sin \Lambda_a \dot{w}_{,x}^G$$

$$T_{22}^M = -\sin \Lambda_s \sin \Lambda_a \dot{\phi}^G$$

$$T_{23}^M = \cos \Lambda_s \sin^2 \Lambda_a \dot{\phi}^G$$

$$T_{31}^M = \sin^2 \Lambda_s \cos \Lambda_a \dot{w}_{,x}^G + \cos \Lambda_s \sin \Lambda_s \cos \Lambda_a \sin \Lambda_a \dot{v}_{,x}^G$$

$$T_{32}^M = -\sin^2 \Lambda_s \cos \Lambda_a \dot{\phi}^G + \cos^2 \Lambda_s \sin \Lambda_a \dot{v}_{,x}^G$$

$$T_{33}^M = \cos \Lambda_s \sin \Lambda_a (\sin \Lambda_s \cos \Lambda_a \dot{\phi}^G - \cos \Lambda_s \dot{w}_{,x}^G)$$

## C.2 TRANSFORMATION FOR THE VECTOR OF NODAL DEGREES OF FREEDOM

The transformation for the vector of nodal degrees of freedom are 23 by 23 matrices where a typical element at the  $i$ -th row and  $j$ -th column of a transformation matrix  $[\Lambda]$  is denoted by  $\Lambda(i, j)$ .

The nonzero elements of the linear transformation matrix  $[\Lambda^L]$  are:

$$\Lambda^L(1, 1) = \cos \Lambda_s$$

$$\Lambda^L(1, 5) = \sin \Lambda_s \sin \Lambda_a$$

$$\Lambda^L(1, 12) = \sin \Lambda_s \cos \Lambda_a$$

$$\Lambda^L(2, 2) = \cos \Lambda_a$$

$$\Lambda^L(2, 9) = -\sin \Lambda_a$$

$$\Lambda^L(3, 3) = \cos \Lambda_s$$

$$\Lambda^L(3, 7) = \sin \Lambda_s \sin \Lambda_a$$

$$\Lambda^L(3, 14) = \sin \Lambda_s \cos \Lambda_a$$

$$\Lambda^L(4, 4) = \cos \Lambda_a$$

$$\Lambda^L(4, 11) = -\sin \Lambda_a$$

$$\Lambda^L(5, 5) = \cos \Lambda_a$$

$$\Lambda^L(5, 12) = -\sin \Lambda_a$$

$$\Lambda^L(6, 2) = -\sin \Lambda_s \sin \Lambda_a$$

$$\Lambda^L(6, 6) = \cos \Lambda_s$$

$$\Lambda^L(6, 9) = -\sin \Lambda_s \cos \Lambda_a$$

$$\Lambda^L(7, 7) = \cos \Lambda_a$$

$$\Lambda^L(7, 14) = -\sin \Lambda_a$$

$$\Lambda^L(8, 4) = -\sin \Lambda_s \sin \Lambda_a$$

$$\Lambda^L(8, 11) = -\sin \Lambda_s \cos \Lambda_a$$

$$\Lambda^L(9, 2) = \cos \Lambda_s \sin \Lambda_a$$

$$\Lambda^L(9, 6) = \sin \Lambda_s$$

$$\Lambda^L(9, 9) = \cos \Lambda_s \cos \Lambda_a$$

$$\Lambda^L(10, 2) = \frac{1}{2} \cos \Lambda_s \sin \Lambda_a$$

$$\Lambda^L(10, 4) = \frac{1}{2} \cos \Lambda_s \sin \Lambda_a$$

$$\Lambda^L(10, 6) = \frac{1}{2} \sin \Lambda_s$$

$$\Lambda^L(10, 8) = \frac{1}{2} \sin \Lambda_s$$

$$\Lambda^L(10, 10) = \cos \Lambda_s \cos \Lambda_a$$

$$\Lambda^L(11, 4) = \cos \Lambda_s \sin \Lambda_a$$

$$\Lambda^L(11, 8) = \sin \Lambda_s$$

$$\Lambda^L(11, 11) = \cos \Lambda_s \cos \Lambda_a$$

$$\Lambda^L(12, 1) = -\sin \Lambda_s$$

$$\Lambda^L(12, 5) = \cos \Lambda_s \sin \Lambda_a$$

$$\Lambda^L(12, 12) = \cos \Lambda_s \cos \Lambda_a$$

$$\Lambda^L(13, 1) = -\frac{1}{2} \sin \Lambda_s$$

$$\Lambda^L(13, 3) = -\frac{1}{2} \sin \Lambda_s$$

$$\Lambda^L(13, 5) = \frac{1}{2} \cos \Lambda_s \sin \Lambda_a$$

$$\Lambda^L(13, 7) = \frac{1}{2} \cos \Lambda_s \sin \Lambda_a$$

$$\Lambda^L(13, 13) = \cos \Lambda_s \cos \Lambda_a$$

$$\Lambda^L(14, 3) = -\sin \Lambda_s$$

$$\Lambda^L(14, 7) = \cos \Lambda_s \sin \Lambda_a$$

$$\Lambda^L(14, 14) = \cos \Lambda_s \cos \Lambda_a$$

$$\Lambda^L(15, 15) = \cos \Lambda_s \cos \Lambda_a$$

$$\Lambda^L(16, 16) = \cos \Lambda_s \cos \Lambda_a$$

$$\Lambda^L(17, 17) = \cos \Lambda_s \cos \Lambda_a$$

$$\Lambda^L(18, 18) = \cos \Lambda_a$$

$$\Lambda^L(19, 19) = \cos \Lambda_a$$

$$\Lambda^L(20, 20) = \cos \Lambda_a$$

$$\Lambda^L(21, 18) = -\sin \Lambda_s \sin \Lambda_a$$

$$\Lambda^L(21, 21) = \cos \Lambda_s$$

$$\Lambda^L(22, 19) = -\sin \Lambda_s \sin \Lambda_a$$

$$\Lambda^L(22, 22) = \cos \Lambda_s$$

$$\Lambda^L(23, 20) = -\sin \Lambda_s \sin \Lambda_a$$

$$\Lambda^L(23, 23) = \cos \Lambda_s$$

The nonzero elements of the nonlinear transformation matrix  $[\Lambda^K]$  are:

$$\Lambda^K(2, 2) = \cos \Lambda_s \sin \Lambda_s \cos \Lambda_a \sin \Lambda_a \phi^J - \cos^2 \Lambda_s \sin \Lambda_a w_{,x}^J$$

$$\Lambda^K(2, 9) = \sin^2 \Lambda_s \cos \Lambda_a w_{,x}^J$$

$$\Lambda^K(6, 6) = -\sin \Lambda_s \sin \Lambda_a \phi^J$$

$$\Lambda^K(6, 9) = -\cos \Lambda_s \sin^2 \Lambda_a v_{,x}^J$$

$$\Lambda^K(9, 9) = \cos \Lambda_s \sin \Lambda_a w_{,x}^J - \sin \Lambda_s \sin^2 \Lambda_a v_{,x}^J$$

The nonzero elements of the nonlinear transformation matrix  $[\Lambda^C]$  are:

$$\Lambda^C(2, 2) = \cos \Lambda_s \sin \Lambda_s \cos \Lambda_a \sin \Lambda_a \phi^J - \cos^2 \Lambda_s \sin \Lambda_a w_{,x}^J$$

$$\Lambda^C(2, 6) = \sin^2 \Lambda_s \cos \Lambda_a \phi^J - \cos^2 \Lambda_s \sin \Lambda_a v_{,x}^J$$

$$\Lambda^C(2, 9) = \sin^2 \Lambda_s \cos \Lambda_a w_{,x}^J + \cos \Lambda_s \sin \Lambda_s \cos \Lambda_a \sin \Lambda_a v_{,x}^J$$

$$\Lambda^C(6, 2) = -\cos \Lambda_s \sin^2 \Lambda_a \phi^J$$

$$\Lambda^C(6, 6) = -\sin \Lambda_s \sin \Lambda_a \phi^J$$

$$\Lambda^C(6, 9) = -\cos \Lambda_s \sin^2 \Lambda_a v_{,x}^J - \sin \Lambda_s \sin \Lambda_a w_{,x}^J$$

$$\Lambda^C(9, 2) = -\sin \Lambda_s \sin^2 \Lambda_a \phi^J$$

$$\Lambda^C(9, 6) = \cos \Lambda_s \sin \Lambda_a \phi^J$$

$$\Lambda^C(9, 9) = \cos \Lambda_s \sin \Lambda_a w_{,x}^J - \sin \Lambda_s \sin^2 \Lambda_a v_{,x}^J$$

The nonzero elements of the nonlinear transformation matrix  $[\Lambda^M]$  are:

$$\Lambda^M(2, 2) = \cos \Lambda_s \sin \Lambda_s \cos \Lambda_a \sin \Lambda_a \dot{\phi}^J - \cos^2 \Lambda_s \sin \Lambda_a \dot{w}_{,x}^J$$

$$\Lambda^M(2, 6) = \sin^2 \Lambda_s \cos \Lambda_a \dot{\phi}^J - \cos^2 \Lambda_s \sin \Lambda_a \dot{v}_{,x}^J$$

$$\Lambda^M(2, 9) = \sin^2 \Lambda_s \cos \Lambda_a \dot{w}_{,x}^J + \cos \Lambda_s \sin \Lambda_s \cos \Lambda_a \sin \Lambda_a \dot{v}_{,x}^J$$

$$\Lambda^M(6, 2) = -\cos \Lambda_s \sin^2 \Lambda_a \dot{\phi}^J$$

$$\Lambda^M(6, 6) = -\sin \Lambda_s \sin \Lambda_a \dot{\phi}^J$$

$$\Lambda^M(6, 9) = -\cos \Lambda_s \sin^2 \Lambda_a \dot{v}_{,x}^J - \sin \Lambda_s \sin \Lambda_a \dot{w}_{,x}^J$$

$$\Lambda^M(9, 2) = -\sin \Lambda_s \sin^2 \Lambda_a \dot{\phi}^J$$

$$\Lambda^M(9, 6) = \cos \Lambda_s \sin \Lambda_a \dot{\phi}^J$$

$$\Lambda^M(9, 9) = \cos \Lambda_s \sin \Lambda_a \dot{w}_{,x}^J - \sin \Lambda_s \sin^2 \Lambda_a \dot{v}_{,x}^J$$

The superscript J in the expressions given above denotes the nodal value at the junction of the straight portion and the swept tip.



REPORT DOCUMENTATION PAGE			Form Approved OMB No. 0704-0188	
Public reporting burden for this collection of information is estimated to average 1 hour per response, including the time for reviewing instructions, searching existing data sources, gathering and maintaining the data needed, and completing and reviewing the collection of information. Send comments regarding this burden estimate or any other aspect of this collection of information, including suggestions for reducing this burden, to Washington Headquarters Services, Directorate for Information Operations and Reports, 1215 Jefferson Davis Highway, Suite 1204, Arlington, VA 22202-4302, and to the Office of Management and Budget, Paperwork Reduction Project (0704-0188), Washington, DC 20503.				
1. AGENCY USE ONLY (Leave blank)	2. REPORT DATE May 1995	3. REPORT TYPE AND DATES COVERED Contractor Report		
4. TITLE AND SUBTITLE Aeroelasticity and Structural Optimization of Composite Helicopter Rotor Blades with Swept Tips			5. FUNDING NUMBERS G NAG1-833 WU 505-63-36-06	
6. AUTHOR(S) K. A. Yuan and P. P. Friedmann				
7. PERFORMING ORGANIZATION NAME(S) AND ADDRESS(ES) University of California Mechanical, Aerospace and Nuclear Engineering Department Los Angeles, CA 90024			8. PERFORMING ORGANIZATION REPORT NUMBER	
9. SPONSORING / MONITORING AGENCY NAME(S) AND ADDRESS(ES) National Aeronautics and Space Administration Langley Research Center Hampton, Virginia 23681-0001			10. SPONSORING / MONITORING AGENCY REPORT NUMBER NASA CR-4665	
11. SUPPLEMENTARY NOTES Langley Technical Monitor: Howard M. Adelman				
12a. DISTRIBUTION / AVAILABILITY STATEMENT Unclassified - Unlimited Subject Category 05  Availability: NASA CASI, (301) 621-0390			12b. DISTRIBUTION CODE	
13. ABSTRACT (Maximum 200 words) <p>This report describes the development of an aeroelastic analysis capability for composite helicopter rotor blades with straight and swept tips, and its application to the simulation of helicopter vibration reduction through structural optimization. A new aeroelastic model is developed in this study which is suitable for composite rotor blades with swept tips in hover and in forward flight. The hingeless blade is modeled by beam type finite elements. A single finite element is used to model the swept tip. Arbitrary cross-sectional shape, generally anisotropic material behavior, transverse shears and out-of-plane warping are included in the blade model. The nonlinear equations of motion, derived using Hamilton's principle, are based on a moderate deflection theory. Composite blade cross-sectional properties are calculated by a separate linear, two-dimensional cross section analysis. The aerodynamic loads are obtained from quasi-steady, incompressible aerodynamics, based on an implicit formulation. The trim and steady state blade aeroelastic response are solved in a fully coupled manner. In forward flight, where the blade equations of motion are periodic, the coupled trim-aeroelastic response solution is obtained from the harmonic balance method. Subsequently, the periodic system is linearized about the steady state response, and its stability is determined from Floquet theory.</p>				
14. SUBJECT TERMS Rotor Blades, Optimization, Aeroelasticity, Composite Structures			15. NUMBER OF PAGES 432	
			16. PRICE CODE A19	
17. SECURITY CLASSIFICATION OF REPORT Unclassified	18. SECURITY CLASSIFICATION OF THIS PAGE Unclassified	19. SECURITY CLASSIFICATION OF ABSTRACT	20. LIMITATION OF ABSTRACT	





National Aeronautics and  
Space Administration  
Langley Research Center  
Mail Code 180  
Hampton, VA 23681-0001

Official Business  
Penalty for Private Use, \$300

**BULK RATE**  
**POSTAGE & FEES PAID**  
NASA  
Permit No. G-27